U.S. Department
of Transportation

**Federal Railroad
Administration**

**Office of Research,
Development and Technology
Washington, DC 20590**

Side Impact Test and Analyses of a Legacy DOT-113 Tank Car

DOT/FRA/ORD-21/28

Final Report | September 2021

REPORT DOCUMENTATION PAGE	*Form Approved* *OMB No. 0704-0188*

1. REPORT DATE *(DD-MM-YYYY*	**2. REPORT TYPE** Technical Report	**3. DATES COVERED** *(From - To)* November 2019

4. TITLE AND SUBTITLE Side Impact Test and Analyses of a Legacy DOT 113 Tank Car	**5a. CONTRACT NUMBER** DTFR53-11-D-00008
	5b. GRANT NUMBER
	5c. PROGRAM ELEMENT NUMBER
6. AUTHOR(S) Shawn Trevithick*0000-0001-6155-5526 Michael Carolan**0000-0002-8758-5739 Shaun Eshraghi**0000-0002-8152-0838 Nicholas Wilson*0000-0003-1140-7108	**5d. PROJECT NUMBER**
	5e. TASK NUMBER TO 0008
	5f. WORK UNIT NUMBER
7. PERFORMING ORGANIZATION NAME(S) AND ADDRESS(ES) *Transportation Technology Center, Inc. 55500 DOT Road, Pueblo, CO 81001-0130 **Volpe National Transportation Systems Center 55 Broadway, Cambridge, MA 02142	**8. PERFORMING ORGANIZATION REPORT NUMBER**
9. SPONSORING/MONITORING AGENCY NAME(S) AND ADDRESS(ES) U.S. Department of Transportation Federal Railroad Administration Office of Railroad Policy and Development Office of Research, Development, and Technology Washington, DC 20590	**10. SPONSOR/MONITOR'S ACRONYM(S)**
	11. SPONSOR/MONITOR'S REPORT NUMBER(S) DOT/FRA/ORD-21/28

12. DISTRIBUTION/AVAILABILITY STATEMENT
This document is available to the public through the FRA website.

13. SUPPLEMENTARY NOTES
COR: Francisco González, III

14. ABSTRACT

On November 19, 2019, the Federal Railroad Administration (FRA) contracted Transportation Technology Center, Inc. (TTCI) to conduct a side impact test of the DOT-113C120W (DOT-113) cryogenic tank car to evaluate the performance of the tank car and to provide data for the verification and refinement of a computational model. The tank car was filled to approximately 82.4 percent of its volume with water. It was then sealed and pressurized to approximately 50 pound-force per square inch (psig). Pre-test modeling had estimated a puncture range of between 16 and 18 mph. Based on these results, the target test speed was 16.5 mph ±0.5 mph. The tank car was impacted by a 296,975-pound ram car traveling at 16.7 mph. A 12-inch by 12-inch ram head fitted to the ram car impacted the tank shell. The impact resulted in the puncture of both the outer and inner shells of the tank car. The residual kinetic energy after puncture drove the ram far enough into the tank car that it lodged in the tank car, indicating that 16.7 mph exceeded the speed necessary to just result in the puncture of both tanks. Pre-test finite element (FE) modeling was used to estimate the overall response of the tank to the impact, including the force-displacement response. The post-test model was updated to include the actual material behavior. Volpe National Transportation Systems Center (Volpe) made several adjustments to the post-test models to investigate the effects of material failure models for the inner tank, strain-rate sensitivity of the inner tank's material, and the influence of the perlite insulation between the inner and outer tanks.

15. SUBJECT TERMS
Impact test, DOT-113 tank car, tank car performance, transportation safety, cryogenic liquids, finite element analysis, FEA

16. SECURITY CLASSIFICATION OF:			**17. LIMITATION OF ABSTRACT**	**18. NUMBER OF PAGES**	**19a. NAME OF RESPONSIBLE PERSON**
a. REPORT	**b. ABSTRACT**	**c. THIS PAGE**		276	Francisco González, III
Unclassified	Unclassified	Unclassified			**19b. TELEPHONE NUMBER** *(Include area code)* (202) 689-4316

Standard Form 298 (Rev. 8/98)
Prescribed by ANSI Std. Z39.18

METRIC/ENGLISH CONVERSION FACTORS

ENGLISH TO METRIC

LENGTH (APPROXIMATE)

1 inch (in) = 2.5 centimeters (cm)
1 foot (ft) = 30 centimeters (cm)
1 yard (yd) = 0.9 meter (m)
1 mile (mi) = 1.6 kilometers (km)

AREA (APPROXIMATE)

1 square inch (sq in, in^2) = 6.5 square centimeters (cm^2)
1 square foot (sq ft, ft^2) = 0.09 square meter (m^2)
1 square yard (sq yd, yd^2) = 0.8 square meter (m^2)
1 square mile (sq mi, mi^2) = 2.6 square kilometers (km^2)
1 acre = 0.4 hectare (he) = 4,000 square meters (m^2)

MASS - WEIGHT (APPROXIMATE)

1 ounce (oz) = 28 grams (gm)
1 pound (lb) = 0.45 kilogram (kg)
1 short ton = 2,000 pounds (lb) = 0.9 tonne (t)

VOLUME (APPROXIMATE)

1 teaspoon (tsp) = 5 milliliters (ml)
1 tablespoon (tbsp) = 15 milliliters (ml)
1 fluid ounce (fl oz) = 30 milliliters (ml)
1 cup (c) = 0.24 liter (l)
1 pint (pt) = 0.47 liter (l)
1 quart (qt) = 0.96 liter (l)
1 gallon (gal) = 3.8 liters (l)
1 cubic foot (cu ft, ft^3) = 0.03 cubic meter (m^3)
1 cubic yard (cu yd, yd^3) = 0.76 cubic meter (m^3)

TEMPERATURE (EXACT)

[(x-32)(5/9)] °F = y °C

METRIC TO ENGLISH

LENGTH (APPROXIMATE)

1 millimeter (mm) = 0.04 inch (in)
1 centimeter (cm) = 0.4 inch (in)
1 meter (m) = 3.3 feet (ft)
1 meter (m) = 1.1 yards (yd)
1 kilometer (km) = 0.6 mile (mi)

AREA (APPROXIMATE)

1 square centimeter (cm^2) = 0.16 square inch (sq in, in^2)
1 square meter (m^2) = 1.2 square yards (sq yd, yd^2)
1 square kilometer (km^2) = 0.4 square mile (sq mi, mi^2)
10,000 square meters (m^2) = 1 hectare (ha) = 2.5 acres

MASS - WEIGHT (APPROXIMATE)

1 gram (gm) = 0.036 ounce (oz)
1 kilogram (kg) = 2.2 pounds (lb)
1 tonne (t) = 1,000 kilograms (kg)
= 1.1 short tons

VOLUME (APPROXIMATE)

1 milliliter (ml) = 0.03 fluid ounce (fl oz)
1 liter (l) = 2.1 pints (pt)
1 liter (l) = 1.06 quarts (qt)
1 liter (l) = 0.26 gallon (gal)
1 cubic meter (m^3) = 36 cubic feet (cu ft, ft^3)
1 cubic meter (m^3) = 1.3 cubic yards (cu yd, yd^3)

TEMPERATURE (EXACT)

[(9/5) y + 32] °C = x °F

QUICK INCH - CENTIMETER LENGTH CONVERSION

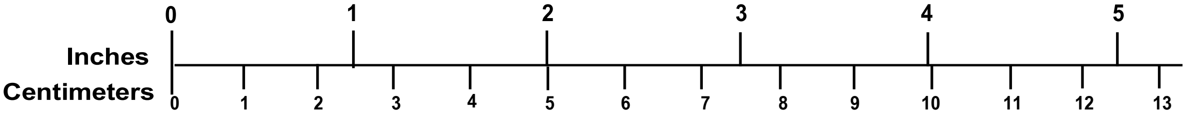

QUICK FAHRENHEIT - CELSIUS TEMPERATURE CONVERSIO

°F	-40°	-22°	-4°	14°	32°	50°	68°	86°	104°	122°	140°	158°	176°	194°	212°
°C	-40°	-30°	-20°	-10°	0°	10°	20°	30°	40°	50°	60°	70°	80°	90°	100°

For more exact and or other conversion factors, see NIST Miscellaneous Publication 286, Units of Weights and Measures. Price $2.50 SD Catalog No. C13 10286

Updated 6/17/98

Acknowledgements

The authors of this report gratefully acknowledge the cooperation and assistance of Scott Nason of Chart Industries and Ken Dorsey of the Association of American Railroads Tank Car Committee in obtaining engineering drawings and design information for the DOT-113 tank car used in this test.

The authors of this report gratefully acknowledge the technical assistance of the Volpe National Transportation Systems Center's Senior Engineer Benjamin Perlman. Additionally, input from Francisco González, III of the Federal Railroad Administration's (FRA) Office of Research, Development and Technology were valuable in developing this testing program. The authors also gratefully acknowledge technical discussions and assistance in developing the testing plan from Mark Maday from FRA's Office of Railroad Safety, and Leonard Majors and Alex Cheng with Pipeline and Hazardous Materials Safety Administration's Office of Engineering. The authors also gratefully acknowledge technical discussions and calculations of outage volume and pressure provided by Dr. Phani Raj with FRA's Office of Railroad Safety.

Contents

Figures

Tables

Executive Summary

The tests and analyses described in this report support the overall objective of the Federal Railroad Administration's (FRA) research program to improve transportation safety for tank cars. This report documents the combined efforts of Transportation Technology Center, Inc. (TTCI) and the Volpe National Transportation Systems Center (Volpe) to test and analyze the side impact puncture performance of a DOT-113C120W (DOT-113) tank car. On November 19, 2019, TTCI conducted the side impact test of the DOT-113 cryogenic tank car to evaluate the performance of the tank car and to provide data for the verification and refinement of a computational model. All test requirements were met. Volpe performed both pre-test and post-test analyses of the impact response to evaluate, validate, and improve the puncture modeling capabilities.

The tank car was filled to approximately 82.4 percent of its volume with water. It was then sealed and pressurized to approximately 50 psig. Pre-test modeling had estimated a puncture range of between 16 and 18 mph. Based on these results, the target test speed was 16.5 mph ±0.5 mph. The tank car was impacted by a 296,975-pound ram car traveling at 16.7 mph. A 12-inch by 12-inch ram head fitted to the ram car impacted the tank shell. The impact resulted in the puncture of both the outer and inner shells of the tank car. The residual kinetic energy after puncture drove the ram far enough into the tank car that it became lodged in the tank car, indicating that 16.7 mph exceeded the speed necessary to just result in the puncture of both tanks. Pre-test finite element (FE) modeling was used to estimate the overall response of the tank to the impact, including the force-displacement response.

Pre-test material behavior for the A516 carbon steel outer shell and the T304 stainless steel inner shell of the car was estimated based on publicly available data. After the test, material coupons were cut from the outer and inner shells of the tank car and subjected to tensile testing. The outer tank's material was tested at room temperature, and the inner tank's material was tested both at room temperature and at a range of cryogenic temperatures. The post-test model was updated to include the actual material behavior. Volpe made several adjustments to the post-test models to investigate the effects of material failure models for the inner tank, strain-rate sensitivity of the inner tank's material, and the influence of the perlite insulation between the inner and outer tanks.

1. Introduction

This report documents the analyses and test results for a side impact test performed on a specification DOT-113C120W (DOT-113) tank car. A DOT-113 is a specially designed tank car intended to transport cryogenic liquid commodities. Previously tested tank cars in the Federal Railroad Administration's (FRA) side impact testing program have featured either an exterior jacket that was thinner than the commodity tank or have been unjacketed. The DOT-113 tank car used in this test had an outer tank made of 7/16-inch carbon steel and an inner tank made of 1/4-inch stainless steel. This report documents the impact test and describes the FE model development and pre-test estimates. This report also includes comparisons of the test measurements and outputs from the analyses. Additionally, the report describes subsequent post-test analyses performed to address the variations between the pre-test analyses and actual test conditions.

1.1 Background

In the past decade, significant research has been conducted to analyze and improve the impact behavior and puncture resistance of railroad tank cars. Ultimately, the results of this research will be used by Federal regulatory agencies (i.e., FRA and the Pipeline and Hazardous Materials Safety Administration [PHMSA] in the United States) to establish performance-based testing requirements and to develop methods to evaluate the crashworthiness and structural integrity of different tank car designs when subjected to a standardized shell impact scenario. A performance-based requirement for tank car head impact protection has already been defined within the current regulations [1], and an optional performance-based requirement for tank car shell impact resistance is applicable to DOT-117P tank cars [2].

FRA has a continuing research program to provide the technical basis for rulemaking on enhanced and alternative performance standards for tank cars and review of new and innovative designs that are developed by the industry and other countries. In support of this ongoing research program, full-scale tests are necessary to provide the technical information to validate modeling efforts and to inform regulatory activities. These tests evaluate the crashworthiness of tank cars used in the transportation of hazardous materials, including designs that comply with current regulations as well as innovative new designs that have improved puncture resistance.

At the time that this test was being planned, the Hazardous Materials Regulations (HMR) permitted the transportation of several cryogenic liquids via DOT-113 tank cars, including argon and ethylene. Refrigerated liquid methane—more commonly referred to as liquefied natural gas (LNG)—was not authorized for transportation via DOT-113 tank car. However, there has been considerable interest in transporting this commodity via DOT-113 tank cars. Because the existing fleet of DOT-113 tank cars is small compared to the overall tank car fleet and limited accident data exists regarding the performance of these cars in derailments or collisions, a series of full-scale shell impact tests was planned to provide technical information on the puncture resistance of the DOT-113 tank car.

A DOT-113 tank car is a specialized tank car that is designed to transport cryogenic liquids. A cryogenic liquid is "a refrigerated liquefied gas having a boiling point colder than -90 °C

(-130 °F) at 101.3 kPa (14.7 psia) absolute."[1] The DOT-113 tank cars are "tank-within-a-tank" cars, where the inner tank is in contact with the cryogenic material and resists the pressure exerted by the lading, and an outer tank surrounds the inner tank and insulating materials and carries the in-train forces. The tank car used in this test was constructed to DOT-113C120W specification as defined in Title 49 Code of Federal Regulations (CFR) Part 179 Subpart F.[2] Table 1 shows a description of the alphanumeric code making up the DOT-113C120W specification.

Table 1. Description of Specification

Code	Description
DOT	Car built to meet a U.S. Department of Transportation specification
113	Specification 113
C	Inner tank design service temperature of -260 °F
120	Inner tank test pressure of 120 psig
W	Welded tank

All DOT-113 tank cars must include several design features that are not found on non-pressure (e.g., DOT-117) or pressure (e.g., DOT-105) tank cars because of the particular properties of cryogenic materials. The inner tank of a DOT-113 tank car will be exposed to cryogenic temperatures, and therefore, must be constructed of either ASTM A240 Type 304 (T304) or Type 304L stainless steel [3]. Those particular grades of steel maintain desirable properties at cryogenic temperatures. The specification requires that the inner tank for the tank car be a minimum of 3/16 inch thick.

Since the inner tank and lading must be kept at cryogenic temperatures during transit, the inner tank must be surrounded by highly effective insulation. This insulation may take the form of expanded perlite (i.e., a granular, lightweight, natural mineral) or multiple layers of "super" insulating materials (e.g., multi-layer insulation [MLI]). Additionally, a vacuum is typically used in conjunction with either perlite or MLI to further reduce heat transfer into the inner tank. The specification defines the maximum rate of heat transfer that is permissible through the insulation system.

The inner tank and insulation must be surrounded by an external tank to contain the insulation, maintain the vacuum, and carry the in-train forces. The specification requires that the outer tank be made of a carbon steel or stainless steel that is approved for use in tank car construction and be a minimum of 7/16 inch thick.

---

[1] 49 CFR § 173.115(g)

[2] 49 CFR § 179.302 Subpart F–Specification for Cryogenic Liquid Tank Car Tanks and Seamless Steel Tanks (Classes DOT-113 and 107A)

1.2 Objectives

The objective of this test was to quantify the deformation mode, impact load-time history, and puncture resistance of a tank car in a side impact. Moreover, the impact conditions were developed so that the side impact test was: 1) safe, 2) repeatable, and 3) analyzable. The test conditions were chosen to be representative of planned service conditions, subject to the limitation that LNG was not permitted to be carried via DOT-113 tank cars at the time the test conditions were developed. This test was intended to subject an existing, "legacy" tank car meeting specification DOT-113 to an impact of sufficient energy to puncture both the inner and outer tanks.

The objective of the pre- and post-test analyses was to provide estimates of the tank car impact response both for the pre-test planning and for the validation of tank car impact and puncture modeling capabilities.

This impact test was the first in a planned series of impacts to DOT-113 tank cars and tank car surrogates.[3] Each test in this series is planned to increase in both complexity and realism over the previous test in an incremental approach to representing planned service conditions. The objective of this test series is to examine the potential improvement in shell puncture resistance for a DOT-113 tank car with an outer shell made of 9/16-inch TC128-B carbon steel compared to a baseline DOT-113 with an outer shell constructed from 7/16-inch A516-70 carbon steel under LNG service conditions.

1.3 Overall Approach

Prior to this test, FRA conducted similar shell impact tests on DOT-105, DOT-111, DOT-112, and DOT-117 tank cars. These previous tests were all accompanied by companion finite element analysis (FEA). These previous tests covered a wide range of tank car designs (e.g., capacities, shell diameters, shell thicknesses, vintages, manufacturers, outage levels, outage pressures, etc.) While some of the previously tested tank cars were designed to transport liquids under elevated pressure (i.e., DOT-105 and DOT-112), each of these tank cars featured a shell made of carbon steel as the tanks were designed to transport commodities that were liquid at ambient temperature. Some of the previously tested tank cars featured both a commodity tank and an outer jacket, however, the outer jacket is typically 1/8-inch thick and, as such, had a limited contribution to the puncture resistance of a shell impact.

The goal of the testing and modeling program is to understand how a particular tank car performs under a standardized impact scenario that is representative of typical service conditions. For a DOT-113 tank car, typical service conditions mean 1) the presence of a cryogenic commodity within the inner tank and 2) the inner tank must be made of stainless steel to ensure compatibility with the in-service temperatures. These two conditions are a significant departure from the test conditions of the previously tested tank cars as well as from the FE modeling techniques that were demonstrated to be suitable for modeling the previous tests.

---

[3] A "surrogate" DOT-113 refers to a purpose-built test article including the features of a DOT-113 tank car necessary for a puncture test (e.g., materials of construction, shell thicknesses, shell diameters, etc.) but excluding various tank car components, such as safety appliances, couplers, brake rigging, and other features that would not influence the shell puncture performance of the tank car.

Thus, the experience gained in previous tests and modeling could be used as a starting point for the DOT-113 modeling and testing plan. However, it was expected that the DOT-113 impact test described in this report would only be a first test, as there would be significant information to be gained following this test. This first test would resemble the previous tests in several ways, including the use of water as the lading within the tank. The overall approach to understanding the behaviors of a DOT-113 tank car under impact conditions and the potential for improved performance through design changes would use both full-scale and laboratory testing with companion FE modeling of increasing complexity to ultimately represent a DOT-113 tank car under LNG service conditions subjected to a shell impact that punctures both inner and outer tanks. This approach would see future tests and corresponding analyses examine the influence of different materials/thicknesses used for the tank shell, examine the effect(s) of modeling both the lading and the inner tank steel using properties at cryogenic conditions, and ultimately modeling a DOT-113 tank car under "representative" conditions expected for LNG service.

The consideration of puncture of one or both tanks further complicates designs such as that of the DOT 113. The desired outcome of the impact test described in this report was puncture of both the inner and outer tanks, as that situation would lead to loss of the commodity in a real-world impact. One way to maximize the value of the test data would be to run a test in which the impactor is brought to a complete stop at the instant the second tank punctures. Such a test would be an experimental demonstration of the threshold puncture speed, as all the ram car's initial kinetic energy has been transferred into the tank car at the same instant that the tank car reaches the limit of its capacity. An incrementally slower test would have been a non-puncture test, and an incrementally faster test would have exceeded the capacity of the tank car to resist puncturing.

Neither a test that causes catastrophic damage to the tank car structure nor a test that scarcely creates a dent would be an effective tool for evaluating the puncture resistance of the car. The highly nonlinear force response of an impacted tank car makes extrapolation or interpolation of test results problematic when attempting to calculate the threshold speed between puncture and non-puncture in the event of an excessive-speed impact. The uncertainty of an interpolation or extrapolation increases when the test speed is either significantly higher or significantly lower than the threshold speed. A test that punctures both tanks but does not leave the impactor with an excessive amount of residual kinetic energy can be used to verify that a model captures both the overall response of the tank car and the suitability of the puncture modeling techniques defined for the materials of the car. However, achieving this outcome can be challenging.

Figure 1 and Figure 2 show the typical FE modeling and testing approach used for these tests. Volpe National Transportation Systems Center (Volpe), TTCI, and FRA collaborated before each test to determine the target test speed based on the model estimates, the desired outcome of the test, and such factors as ambient conditions (e.g., wind speed influencing actual impact speed) at the time of the test. After the test, the material coupon test data from both the inner and outer shells of the car, the measured internal pressure, and the measured test speed are used to update the pre-test model to reflect the actual test conditions. The post-test model results and the test measurements are then compared to one another.

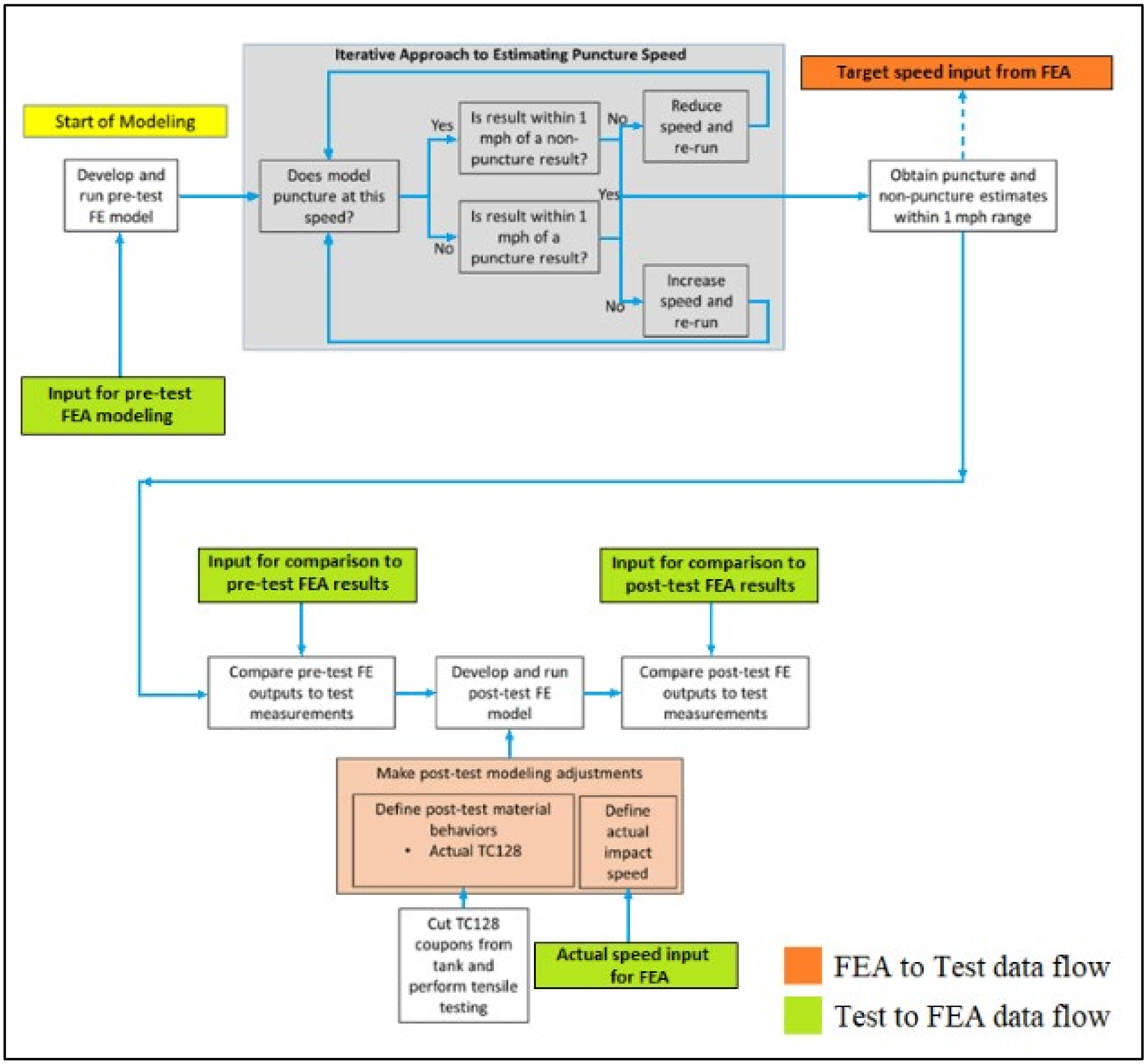

Figure 1. Flowchart Showing Typical FEA Modeling Approach

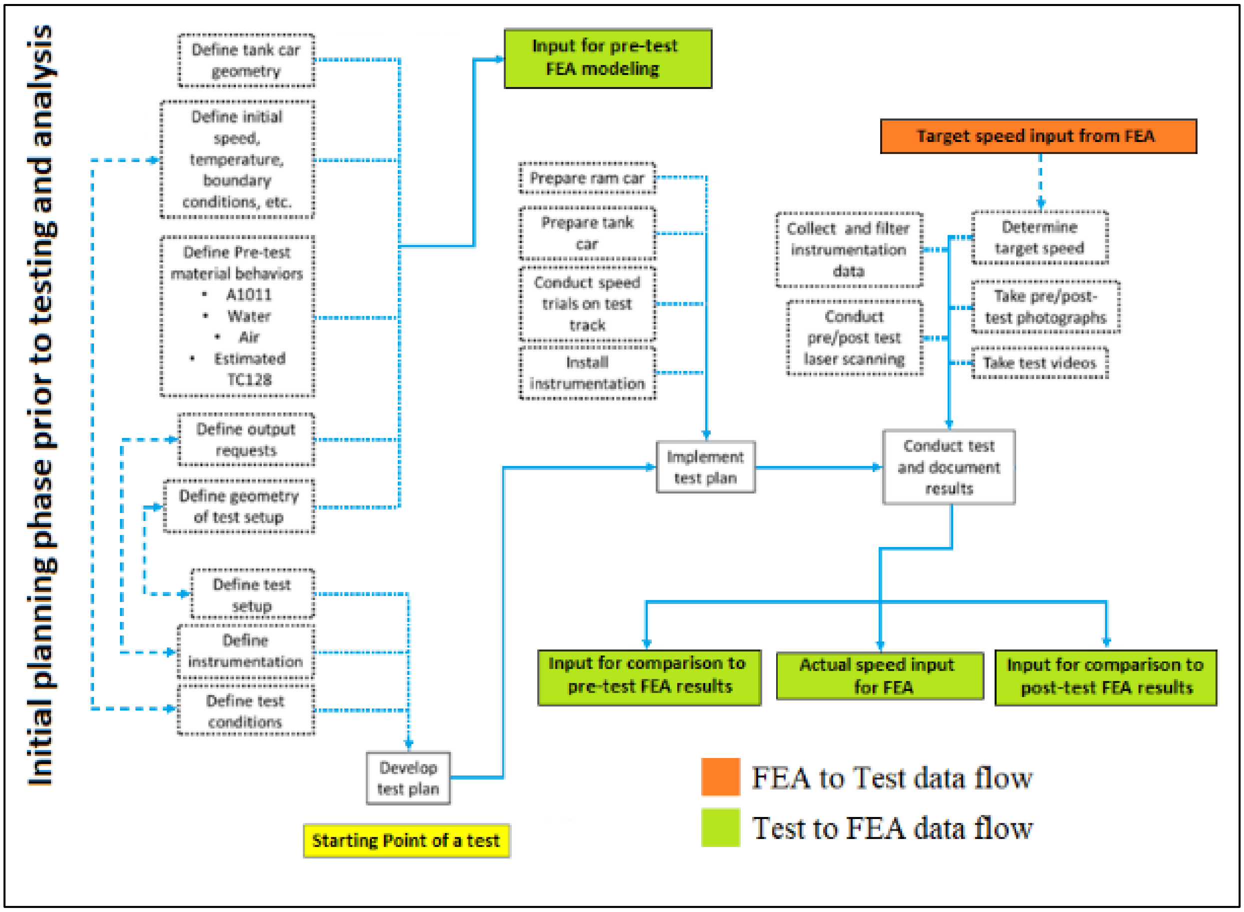

Figure 2. Flowchart Showing Typical Testing Approach

1.4 Scope

This report documents the analyses and test results for a side impact test performed on a legacy DOT-113 tank car. The report presents the test results, discusses the execution of the test, summarizes the overall results of the test, and includes the discussion of the post-test modeling adjustments. Finally, a comparison between the test measurements and the model results are presented.

The report includes an introduction to cryogenic tank car design requirements applicable to specification DOT-113 tank cars, summarizing the unique features of these tank cars compared to pressure and non-pressure tank cars carrying ambient temperature ladings. It includes a discussion of developing and executing the FE models used in this program, aspects of which include modeling the tank car steels, modeling the water within the tank, and modeling the gas phase outage within the tank.

This report does not include any results from further analyses using the DOT-113 tank car model, such as impact conditions outside the conditions of the test. While this report refers to previously performed shell impact tests on tank cars of different specifications [4] [5] [6] [7] [8], the scope of this report does not include a comparison of results from those different tests. Research into the puncture resistance of DOT-113 tank cars is ongoing and further testing and simulations of the puncture responses of DOT-113 tank cars under varied impact conditions (e.g., varied outage levels, impact speeds, and tank thicknesses, cryogenic lading conditions, etc.) are planned for this testing and analysis program and will be documented in future reports.

1.5 Organization of the Report

Section 1 introduces the research conducted and describes the organization of the report.

Section 2 describes the tank car undergoing testing and analysis, as well as the shell impact test setup.

Section 3 describes the instrumentation used during the test and its placement and includes a discussion of the cameras used to capture the impact event.

Section 4 presents the results of the test. These results include a description of the actual conditions of the impact, a description of the test itself, and a summary of the measured test data.

Section 5 describes the development of the FE models used in this program. This section describes the geometry used in the model, the different material models developed, and the modeling techniques used in the pre- and post-test models.

Section 6 details test measurements alongside the corresponding estimates from the pre-test FE models.

Section 7 presents test measurements alongside the corresponding estimates from the post-test FE models.

Section 8 details the post-test FE modeling with additional behaviors.

Section 9 includes a summary of the report and concluding remarks.

Appendix A describes the positions of the cameras and targets used in the test.

Appendix B contains the full set of test data as well as the material data measured during the tensile coupon tests for the steels making up the tank car's inner and outer shells and a micrographic analysis of selected samples taken from the impact zone.

Appendix C contains a full set of comparisons between the test measurements and the FE estimates. This appendix contains comparisons for pre-test models using different material behaviors and for the post-test model using the actual steel behaviors.

Appendix D describes the geometry and the mesh on each part used in the FE models.

Appendix E contains a description of the modeling techniques that were used in both the pre- and post-test FE models.

Appendix F contains a description of how each material behavior was developed in the FE models.

Appendix G contains the calculations used to determine the outage pressure and volume targeted for this test.

2. Test Conditions

FRA performed the side impact test on November 19, 2019, at the Transportation Technology Center (TTC) in Pueblo, CO, by sending a ram car into the side of a DOT-113. This section describes the tank car that was used in this test and the overall test setup used in the shell impact testing program.

2.1 Description of DOT-113 Tank Car Used in Test

The DOT-113 tank car used in this test was constructed in 1976 and originally intended for use in liquefied ethylene service. The inner tank was made of American Society for Testing and Materials (ASTM) A240 T304 [3] stainless steel having a minimum thickness of 1/4 inch on its shell and 3/8 inch for the heads. The outer tank was made of ASTM A516-70 [9] carbon steel having a minimum thickness of 7/16 inch on the shell, and 1/2 inch on the heads. The inner tank had a nominal capacity of 32,900 gallons of water.[4] The two tanks were separated by a 6-inch gap. This gap was filled with evacuated perlite and held under a vacuum. Additionally, this gap contained piping and structural members. The tank car had an overall length over strikers of approximately 76 feet. The car was equipped with a pressure relief valve (PRV) having a start-to-discharge pressure (STDP) of 75 psig. The PRV, as well as other loading and unloading valves, were contained in two cabinets at the two ends of the car, inboard of each bolster. Figure 3 shows the DOT-113 tank car used in this test.

Figure 3. DOT-113 Tank Car Used in Test

2.2 Test Setup

The test was performed by sending a ram car into the side of the tank car which was mounted on skids and backed by a rigid impact barrier as shown in Figure 4.

---

[4] Due to thermal contraction, the inner tank would have a lower capacity of cryogenic material based on the temperature of that material.

Figure 4. Target Tank Car Mounted on Support Skids

2.2.1 Test Arrangement

Due to its length, the DOT-113 tank car had to be offset by approximately 11 feet toward the west, resulting in an off-center impact. A centered impact would have resulted in the DOT-113 tank car fouling a right-of-way (ROW) adjacent to the impact wall and would have resulted in striking the car at a location with internal structure between the two tanks. The 11-foot offset ensured that the adjacent ROW was clear and that the point of impact included only the two tanks and perlite. Figure 5 shows an overhead view of the test setup with annotations indicating the A-end and the B-end of the tank car, as well as the east and west sides of the test site. Note that earthen berms were constructed prior to the test to channel the water away from the tank car in the event of a puncture. Additionally, a containment pond (not visible in the picture) was dug to catch the run-off from a puncture. The purpose of this catchment system was to evaluate ways of controlling and containing a liquid nitrogen spill during future impact testing.

Figure 5. Overhead View of Test Setup Extracted from Drone Video

Figure 6(a) shows one of the skids that the tank car was placed on oriented parallel to the track with one end near the impact barrier. Four sections of I-beams were welded to the tank car and skids for the attachment, as Figure 6(b) shows. The tank car with the attached skids was placed on 1-inch steel plates. These steel plates were placed on plywood sheets to raise the car above the concrete slab in which the rails are embedded at the impact wall. This test configuration was designed to minimize the tank car rollback and allow the tank car on the skids to slide on the steel plates during impact.

(a) Support Skids

(b) Welded I-beam Connection

Figure 6. Tank Support Skid System

The indenter was positioned to align as closely as possible with the mid height of the target tank car. The ram car was a modified flat car with an 8-foot ram installed on the leading end. This ram car was used in previous tank car tests and has a shortened tank attached to the ram end.

Figure 7 shows the ram car. For this test, a 12-inch by 12-inch indenter with 1-inch radii on the edges and corners was used. The same indenter was used in the impact test of a DOT-111 tank car [10], a DOT-112 tank car [11], a DOT-117 tank car [12], a DOT-105 tank car [13], and a second DOT-111 tank car meeting voluntary industry standard CPC-1232 [14]. This large indenter was expected to result in a considerable amount of fluid motion (i.e., "sloshing") during the test, requiring careful modeling of the lading to be able to capture this motion.

Figure 7. Ram Car and Head (Photo from Previous Test)

Figure 8 shows the 12-inch by 12-inch indenter attached to the ram car, and Figure 9 shows the ram car aligned with the tank car. The ram car was weighed before the test to confirm the actual weight. The measured weight was 296,975 pounds.

Figure 8. Ram Arm with 12-inch by 12-inch Indenter (Photo from Previous Test)

Figure 9. Ram Arm with 12-inch by 12-inch Indenter Aligned with Impact Zone on the Tank Car (Frame Extracted from High-Speed Video)

Due to the large offset in the tank car's position on the impact wall, one of the reinforcement rings would interfere with the typical interaction between the tank car and the impact wall. Because the reinforcement ring was on the outside of the outer tank, the initial point of contact between the DOT-113 tank car and the rigid wall during impact would be this reinforcement ring. Therefore, the decision was made to add sections of 4-inch thick plate steel to the wall to allow the entire outer tank to be initially in contact with the rigid wall, typical of the setup used in the previous tests. Five-foot wide sections of plate were mounted to the existing plate across the width of the wall with a 1-foot gap between the plates at one end to accommodate the structural ring. Figure 10 shows the layout of this plate on the wall.

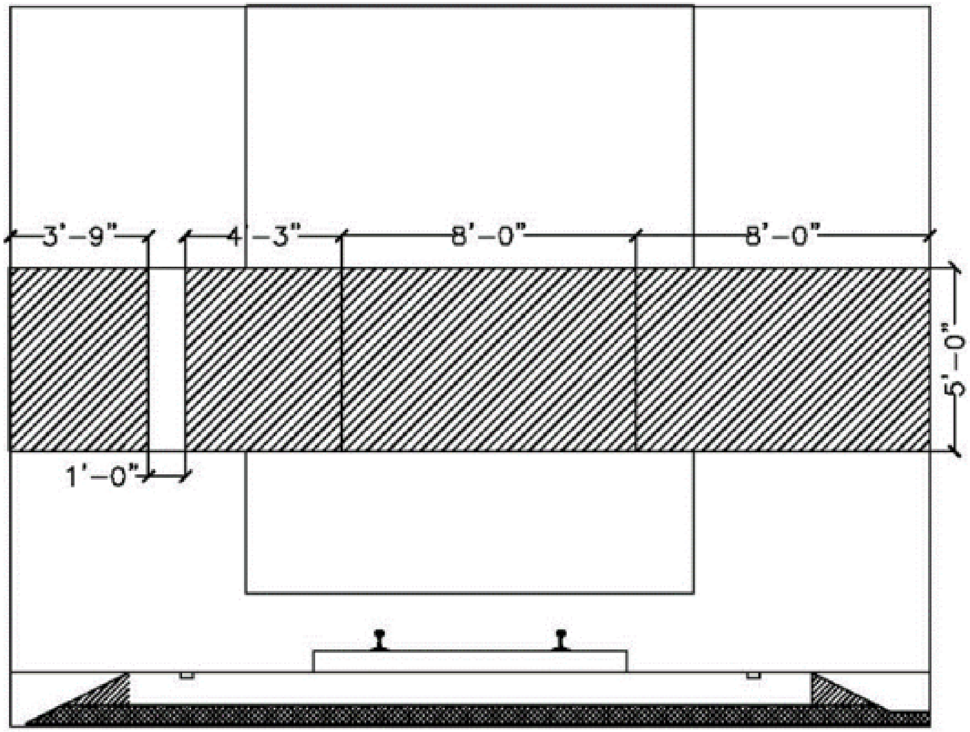

Figure 10. Offset Plate Layout

2.2.2 Lading and Outage Conditions

Three lading conditions needed to be defined prior to the test. First, the lading to be used in the car had to be selected. Second, the volume of the lading (thus, the volume of vapor space or "outage") to be placed in the car had to be chosen. Third, the desired pressure for the outage had to be chosen. This section discusses each of these three aspects and the values targeted for the test.

Careful consideration for the safety, environmental, logistical, and technical ramifications were given to the lading that was be used in the tank car during this test. As this was the first impact test using a DOT-113 tank car performed to-date, water was chosen over a cryogenic liquid to reduce the number of unknowns for this test. As previously described in Section 2.1, a DOT-113 tank car contains several unique design features that were not present, and therefore, not examined in the pressure and non-pressure tank cars that FRA previously tested. Using a cryogenic liquid in the tank car while testing would have presented a more realistic test condition, but using water would permit this test to examine the unique structural features of the DOT-113 (e.g., tank-within-a-tank design, puncture of both carbon and stainless steels in a single impact, etc.) under better-controlled conditions.

It must be noted that while the use of water as lading simplified the test setup in several ways, compared to using a cryogenic liquid, it also introduced several additional challenges into the test implementation process. For instance, water has a weight density of approximately 8.3 pounds per gallon [1,000 kg/m^3] at room temperature [15]. Liquid ethylene, the commodity this particular DOT-113 tank car was designed to transport, has a weight density of approximately 4.7 pounds per gallon at saturation conditions of 1 atmosphere pressure and -155.4 °F (568 kg/m^3

at 1 atmosphere pressure and 169.3 K) [16]. Therefore, if the tank car were filled to the same level with water as it would have been filled with liquid ethylene, the inner tank would be carrying a load that weighed approximately 1.8 times what the tank was initially designed to carry.[5] In turn, this extra load would result in higher stresses in the inner tank, the inner tank's attachments to the outer tank, and the outer tank at the start of the test.

Using water at ambient temperature also has a potential effect on the material behavior of the inner tank. The DOT-113 tank car used in this test was authorized to be loaded at or above -260 °F (i.e., the design service temperature, per 49 CFR § 179.401-1). While the outer tank of a properly functioning DOT-113 tank car should not reach this temperature, the inner tank will be at the same temperature as the lading. The mechanical properties of the stainless steel, namely the strength and ductility, would be expected to differ when the tank is at ambient temperature versus cryogenic temperature. As a means of addressing this difference, post-test material coupons were excised from the inner tank and subjected to tensile testing at temperatures of -320, -260, -100, and 71 °F. Section 4.5 discusses these material test results.

Post-test modeling is planned to investigate the effects of the temperature of the lading, the density of the lading, and the mechanical properties of the inner tank steel at cryogenic temperatures. As this modeling will not have been completed at the time of this report's writing, the results will not be discussed in this report.

The second aspect of the lading and outage conditions to be determined prior to the test was the filling level for the tank car. For cryogenic materials authorized to be transported by DOT-113 tank cars, 49 CFR § 173.319(d)(2) contains a table of maximum permitted filling densities[6] for different commodities, initial pressures, specification tank cars, and STDP for the tank car's PRV. During the planning of this test, the table at § 173.319(d)(2) did not list the filling density for LNG shipments in DOT 113C tank cars. Because the tank was going to be filled with water during the test, a target filling density had to be chosen based on the in-service condition expected to be encountered for a particular commodity.

At the time of this test, LNG could only be transported via DOT-113 tank car under a Special Permit. At the time of planning this test, PHMSA published a Notice of Proposed Rulemaking (NPRM) in the *Federal Register*[7] that proposed allowing the transportation of LNG by DOT-113C120W tank cars. This NPRM included a proposed updated version of the table contained in 49 CFR § 173.319(d)(2) that sets out the filling conditions. Test conditions were based on the proposed conditions in the NPRM at the time the test was planned. Subsequent to the November 2019 test, the final rule[8] was promulgated on July 24, 2020. The final rule specified slightly

---

[5] While not authorized for transportation in DOT-113 tank cars except under Special Permit at the time of the test, liquid methane (LNG) has a weight density of approximately 3.5 pounds/gallon at 1 atmosphere (see Methane - Density and Specific Weight). Thus, the inner tank of a DOT-113 car loaded with water to the same level as a DOT-113 loaded with LNG would be carrying approximately 2.3 times the weight of lading.

[6] 49 CFR § 173.319(d)(1) states: For the purposes of this section, "filling density" is defined as the percent ratio of the weight of lading in the tank to the weight of water that the tank will hold at the design service temperature.

7 Pipeline and Hazardous Materials Safety Administration, "Hazardous Materials: Liquefied Natural Gas by Rail," Federal Register/Vol 84, No. 206/October 24, 2019.

8 Pipeline and Hazardous Materials Safety Administration, "Hazardous Material: Liquefied Natural Gas by Rail," Federal Register/Vol 85, No. 143/July 24, 2020.

different filling density conditions than those proposed in the NPRM. Table 2 includes the two sets of conditions.

Table 2. Summary of Conditions from NPRM and Final Rule for LNG

Property	**NPRM**	**Final Rule**
Tank car specification	113C120W	113C120W9
Maximum STDP of the PRV	75 psig	75 psig
Maximum pressure when offered for transportation	15 psig	15 psig
Design service temperature	-260 °F	-260 °F
Maximum permitted filling density (percent by weight) Methane	32.5%	37.3%

A detailed description of the calculations and logic employed to define the lading conditions for the test can be found in Appendix G. The filling density is defined as the weight ratio of the cryogenic commodity at its design temperature loading conditions to water at atmospheric pressure and 60 °F. Due to the substitution of water for the commodity the tank car was designed to carry, the test team needed to determine an appropriate volume of water (and thus, outage volume) and outage pressure to simulate service conditions. Since water and liquid methane have different densities, the DOT-113 used in this test could be filled with water to either have a volume of liquid matching service conditions or a mass of liquid matching service conditions.

If the tank car was filled with a mass of water equal to the mass of LNG that DOT-113 could carry, the tank would have only been filled to 32.5 percent of its volume with water. While the mass of water in the tank would be equal to the mass of LNG permitted by the NPRM, the height of the water in the tank would be low due to the much lower volume of water compared to the volume of LNG having the same weight. Previous FRA-sponsored testing and analyses have shown that the height of the outage can have a significant effect on the structural response and puncture behavior of an impacted tank car under the standardized test conditions [10]. Thus, the filling level was chosen to match the approximate filling volume of LNG with an equivalent volume of water. As discussed previously in this section, that volume of water would result in a water-filled car that is considerably heavier than an LNG-filled car.

The density of the LNG also needed to be known to calculate the volume of the tank car that would be filled with LNG having a filling density of 32.5 percent. The density of LNG varies with the pressure at which the LNG is stored. Two bounding conditions were identified from conditions given in the NPRM. At one limit, just prior to the activation of the PRV, the tank would have a 75 psig pressure and a 15 percent outage volume. This represents the highest pressure expected in normal service and the smallest outage volume. At the other limit, a 15 psig loading pressure and a filling density (by weight) of 32.5 percent would result in a 21 percent outage by volume at the time of filling. This represents the lowest pressure expected to be encountered in normal service and the largest outage volume.

Because typical loading conditions, transit times, and heating rates are unknown due to a lack of service history for LNG transported via DOT-113 tank cars, the test outage pressure was chosen to represent a mid-range value. A 45 psig outage was chosen to represent a tank car that may be in transit but has not been in transit for so long that its PRV is imminently going to vent.

Assuming a 32.5 percent filling density and a filling pressure of 15 psig, by the time the internal pressure reached 45 psig, the outage volume would be reduced to 17.6 percent. Appendix G contains the calculations for the relationship between outage volume and outage pressure. Table 3 summarizes the target lading and outage conditions chosen for the test.

Table 3. Summary of Target Lading and Outage Conditions for Test

Loading Parameter	Target Value for Test
Commodity in Tank	Water
Outage Volume	17.6%
Outage Pressure	45 psig

3. Test Instrumentation

Data were collected during the test from instrumentation on board the ram car, instrumentation on board the DOT-113 tank car, high-speed video cameras, conventional-speed video cameras, and two cameras mounted to drones hovering over the test site. This section describes the instrumentation used and its placement.

3.1 Overview

The test configuration and instrumentation were consistent with the specifications of the test implementation plan [17]. Table 4 lists all the instrumentation types used for this test. Additional descriptions of the various types of instrumentation are provided in the following subsections.

Table 4. Instrumentation Summary

Type of Instrumentation	Channel Count
Accelerometers	11
Speed sensors	2
Pressure transducers	8
String potentiometers	4
Laser displacement transducers	15
Total data channels	40
Digital video	10 cameras (including 4 high speed cameras)

3.2 Ram Car Accelerometers and Speed Sensors

The local acceleration coordinate systems were defined relative to the ram car. Positive X, Y, and Z directions are forward, left, and up relative to the lead end of the ram. Three triaxial accelerometers were mounted on the longitudinal centerline of the ram car, one at the front, one at the rear, and one near the center of the car. One uniaxial accelerometer was mounted on the left side of the car and one on the right side of the car to supplement recording of longitudinal acceleration. Figure 11 illustrates the positions of these accelerometers, and Table 5 summarizes the ram car accelerometer types and positions.

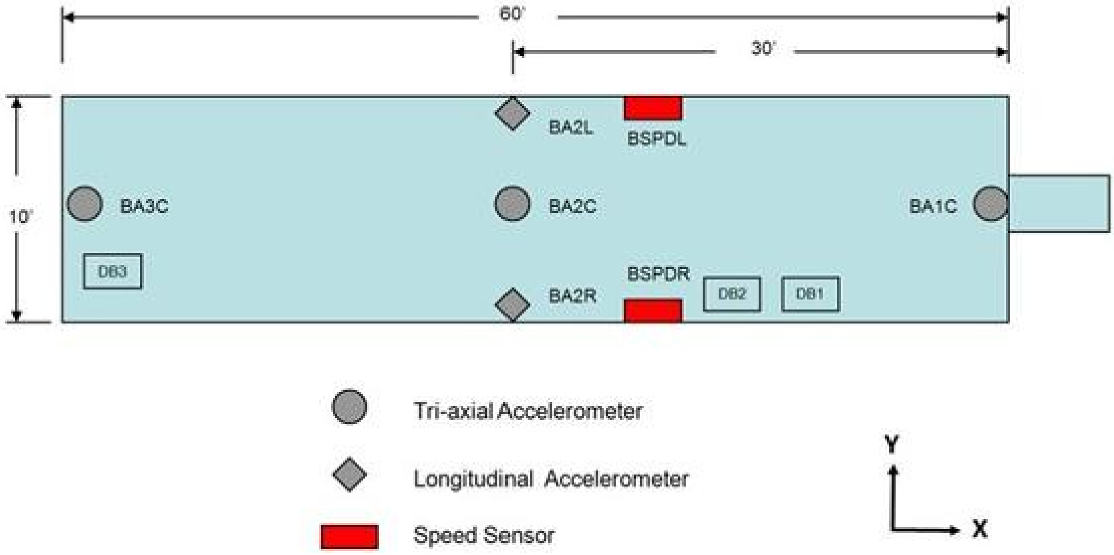

Figure 11. Ram Car Instrumentation

Table 5. Ram Car Accelerometers

Channel Name	Sensor Description	Range
BA1CX	Leading End, Centerline, X Accel	200 g
BA1CY	Leading End, Centerline, Y Accel	100 g
BA1CZ	Leading End, Centerline, Z Accel	200 g
BA2LX	Middle, Left Side, X Accel	100 g
BA2CX	Middle, Centerline, X Accel	50 g
BA2CY	Middle, Centerline, Y Accel	50 g
BA2CZ	Middle, Centerline, Z Accel	50 g
BA2RX	Middle, Right Side, X Accel	100 g
BA3CX	Trailing End, Centerline, X Accel	200 g
BA3CY	Trailing End, Centerline, Y Accel	100 g
BA3CZ	Trailing End, Centerline, Z Accel	200 g

Speed sensors were mounted on both sides of the ram car to provide accurate measurements of the car's velocity within 20 inches of the impact point. The speed sensors were reflector-based light sensors, which use reflectors on the ground separated by a known distance in conjunction with light sensors mounted on the car. These sensors were triggered as the car passed over the reflectors. The last reflector was positioned to align with the sensor when the ram head was within a few inches of the impact point. The time interval between passing the reflectors was recorded, and the speed was calculated from distance and time. A handheld radar gun was also used to take supplemental speed measurements.

3.3 Tank Car String Potentiometers and Pressure Transducers

The local displacement coordinate systems (except for the tank heads) were defined relative to the tank car. Positive X, Y, and Z directions are forward, right (away from the wall), and up relative to the A-end of the tank car. Tank head displacements were positive toward the impact wall.

Four string potentiometers were used to measure the tank motions. One string potentiometer was attached to each of the tank skids and one to the center of the tank heads at both ends of the car. Fixed anchor positions were established so that these measurements were limited to the longitudinal motions of the tank heads and skids. Table 6 lists all string potentiometers attached to the tank car. Figure 12 and Figure 13 show their placement.

Table 6. Tank Car String Potentiometers

Area	Location	Axis	Channel name	Range (in.)
Tank Head	A-end	Y	TDBend	50
Tank Head	B-end	Y	TDAend	50
Skid	A-end	Y	TDBskid	50
Skid	B-end	Y	TDAskid	50

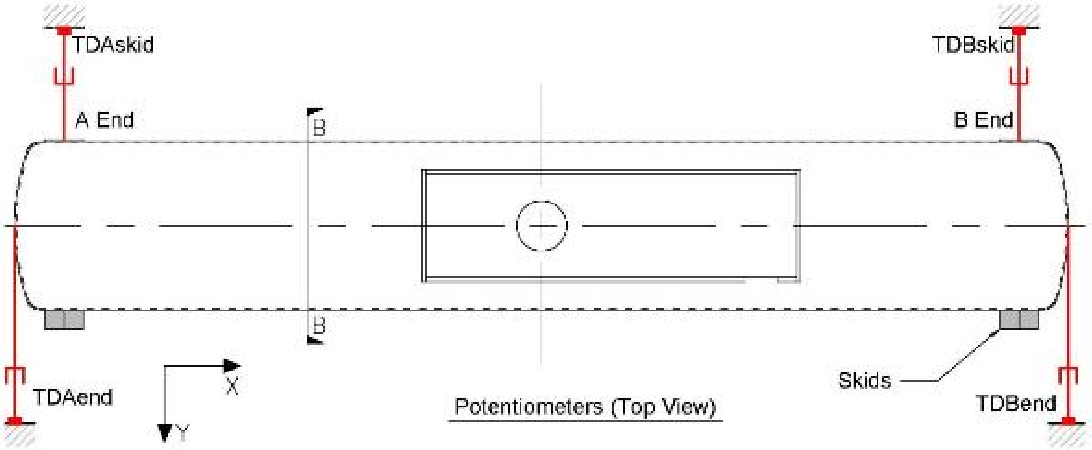

Figure 12. Tank Car String Potentiometers (top)

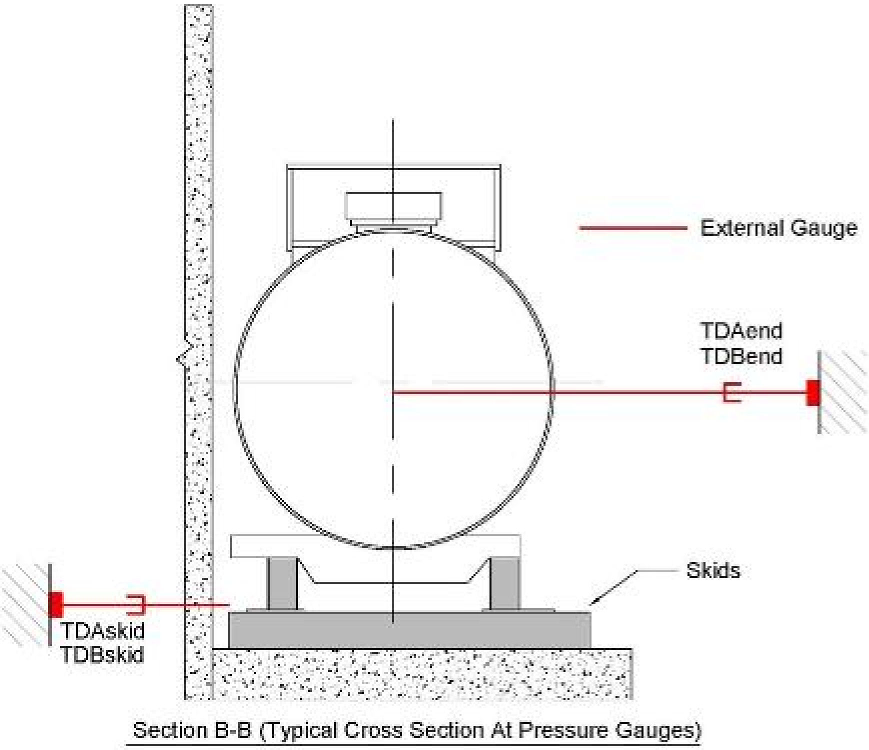

Figure 13. Tank Car String Potentiometers (end)

An array of seven pressure transducers was set up within the tank to record the pressure in the lading and the outage. They were mounted on the top, sides, and bottom of the inner tank near the manway. Table 7 provides a list of all pressure transducers used for the tank car. Figure 14 and Figure 15 show their placement.

Table 7. Tank Car Pressure Transducers

Location	Channel Name	Sensor Description	Range psi
B Top	TPB000	Top Pressure Toward B-End (Outage)	300
A Top	TPA000	Top Pressure Toward A-End (Outage)	300
C Top	TPC000	Center Top Pressure (Outage)	300
C Back wall	TPC090	Center Back Wall Pressure	300
C Floor	TPC180	Center Floor Pressure	300
C Front wall	TPC270	Center Front Wall Pressure	300
Manhole Lid	TPMH	Outage Pressure in the Manway	500
PR Valve	TPRV	Pressure Downstream from Relief Valve	500

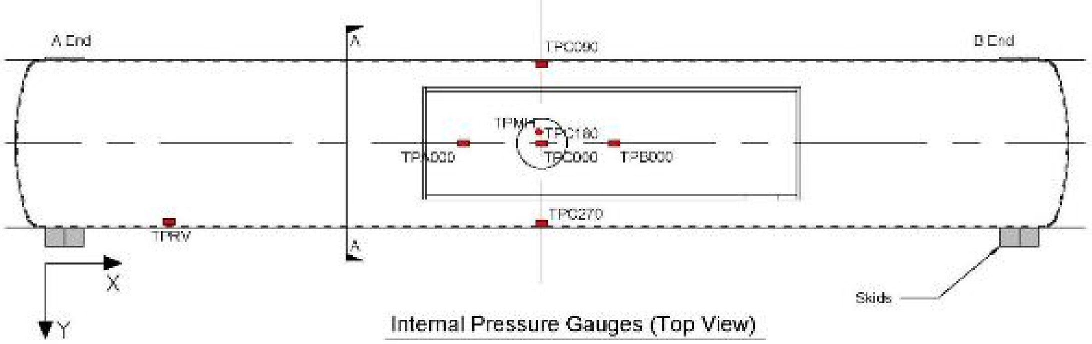

Figure 14. Tank Car Pressure Transducers (top)

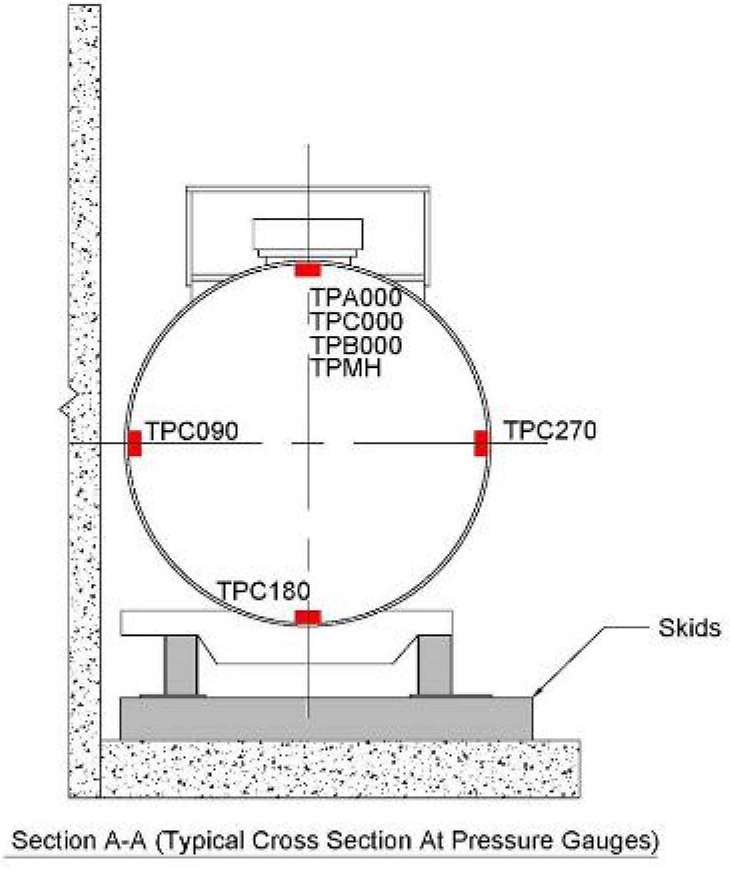

Figure 15. Tank Car Pressure Transducers (end)

3.4 Laser Displacement Transducers

In previous tests, string potentiometers were used to record the crush response and maximum deformation of the tank car during impact. However, due to limited access to the inside of the tank car, the decision was made to substitute a series of lasers mounted to the face of the ram car and in recesses cut into the offset plate mounted to the crash wall to record the tank car response. That data was used to calculate the deformation of the tank car at positions that were 24 and 48 inches on either side of the center of impact. The overall positional reference for these calculations was provided by a laser mounted at the top of the ram car and aimed at the crash wall which recorded the distance between the ram car and the crash wall. Table 8 provides a list of the laser displacement transducers used during the test. Figure 16 shows the position of the lasers mounted to the ram car. Figure 17 shows the lasers mounted to the crash wall and Figure 18 shows the relative positions of those lasers.

Table 8. Laser Displacement Transducers

Location	Channel Name	Sensor Description	Range (mm)
Ram Car	BD1Y	Displacement EAST	50–12,000
Ram Car	BD2Y	Displacement 2nd from EAST	50–12,000
Ram Car	BD3Y	Displacement 3rd from EAST Aimed at Crash Wall Above Tank Car	50–12,000
Ram Car	BD4Y	Displacement 4th from EAST	50–12,000
Ram Car	BD5Y	Displacement 5th from EAST	50–12,000
Crash Wall	TD1YS	Displacement Short Range EAST	35–110
Crash Wall	TD1YL	Displacement Long Range EAST	100–1,000
Crash Wall	TD2YS	Displacement Short Range 2nd from EAST	35–110
Crash Wall	TD2YL	Displacement Long Range 2nd from EAST	100–1,000
Crash Wall	TD3YS	Displacement Short Range 3rd from EAST	35–110
Crash Wall	TD3YL	Displacement Long Range 3rd from EAST	100–1,000
Crash Wall	TD4YS	Displacement Short Range 4th from EAST	35–110
Crash Wall	TD4YL	Displacement Long Range 4th from EAST	100–1,000
Crash Wall	TD5YS	Displacement Short Range 5th from EAST	35–110
Crash Wall	TD5YL	Displacement Long Range 5th from EAST	100–1,000

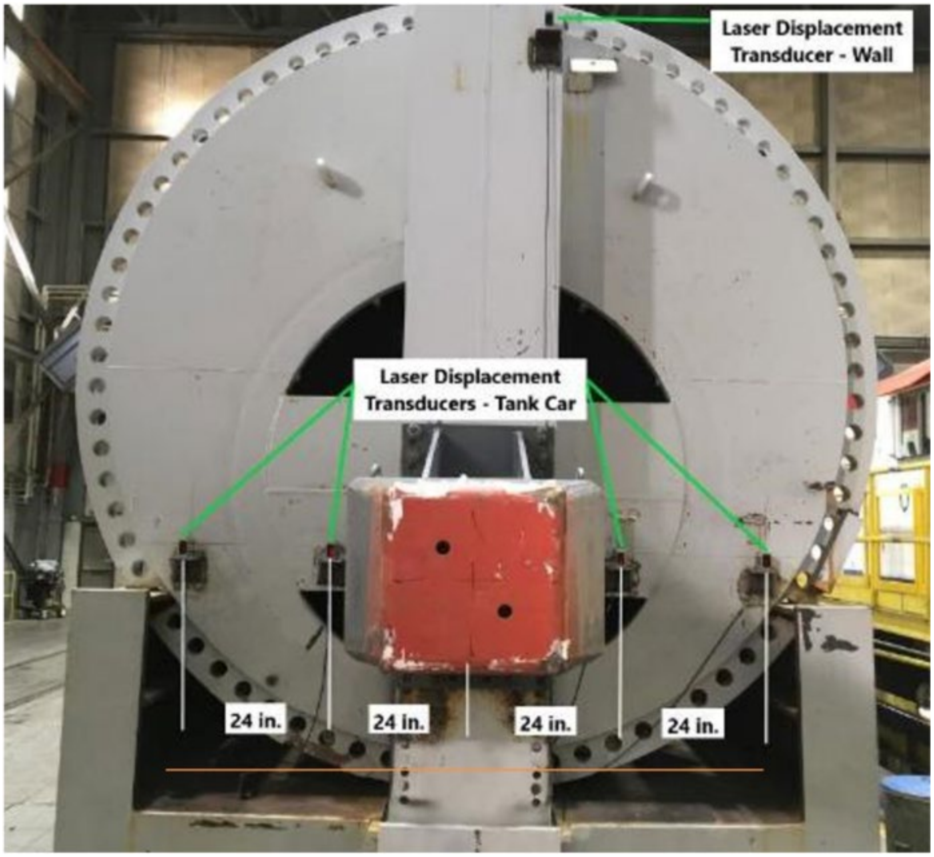

Figure 16. Laser Displacement Transducers on Ram Car

Figure 17. Laser Displacement Transducers on Crash Wall

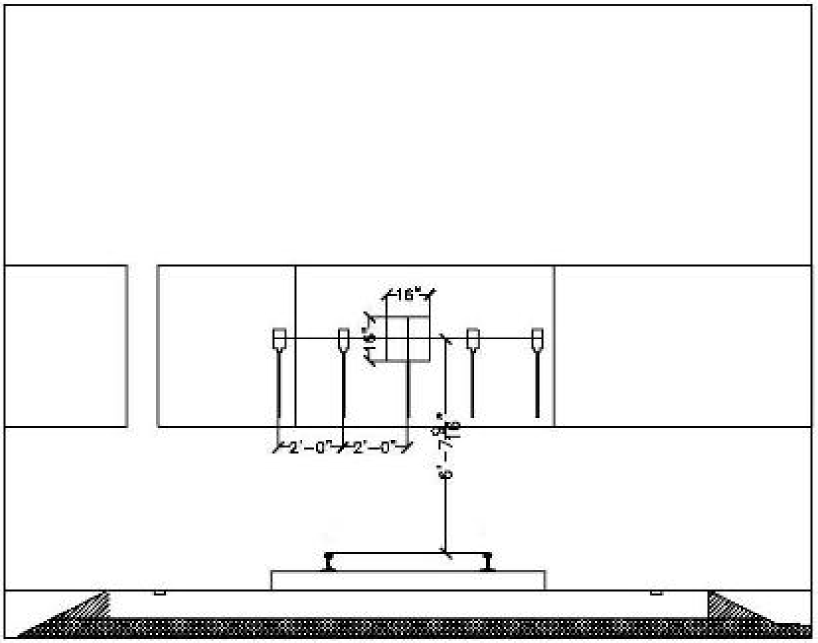

Figure 18. Relative Positions of Crash Wall Laser Transducers

3.5 Real Time and High-Speed Photography

Four high-speed and six real-time, high-definition video cameras were used to document the impact event. All high-speed cameras used were crashworthy and rated for peak accelerations of 100 g. The ram car and the impact barrier were painted with flat light gray. The tip of the indenter was painted red. High contrast targets were applied to the ram car and the indenter. Appendix A contains a schematic of the locations of the cameras and positions of the targets.

3.6 Data Acquisition

A set of eight-channel battery-powered onboard data acquisition systems was used to record the data from the instrumentation mounted on the ram car. These systems provided excitation to the instrumentation, analog anti-aliasing filtering of the signals, analog-to-digital conversion, and recording of each data stream. A similar set of ground-based data acquisition systems was used to record data from the pressure transducers and string potentiometers on the tank car.

The data acquisition systems were GMH Engineering Data BRICK Model III units. Data acquisition complied with the appropriate sections of SAE J211 [18]. Data from each channel was anti-alias filtered at 1,735 Hz, then sampled and recorded at 12,800 Hz. Data recorded on the data bricks were synchronized to time zero at initial impact. The time reference came from the closure of the tape switches on the front of the test vehicle. Each data brick was ruggedized for shock loading up to at least 100 g. Onboard battery power was supplied by GMH Engineering 1.7 Amp-hour 14.4 Volt NiCad Packs. Tape Switches, Inc., model 1201-131-A tape switches provided event initial contact.

Software in the data bricks was used to determine zero levels and calibration factors rather than relying on set gains and expecting no zero drift. The data bricks were set to record 1 second of data before initial impact and 4 seconds of data after initial impact.

4. Results

This section describes the actual conditions of the test, some of which varied from the target conditions summarized in Section 2. The section also presents the photographs of the test results and a discussion of the damage to the tank car, as well as graphs of test data. Researchers presented the results of pre- and post-test laser scans of the inner and outer tank, and used the test data and test videos to provide a reconstruction of the sequence of events that occurred during the test.

4.1 Test Conditions

As described in Sections 2.1 and 2.2, this test was a side impact on a specification DOT-113C120W tank car, performed on November 19, 2019. The test involved a 16.7-mph side impact from a structurally rigid 296,975-pound ram car with a 12-inch by 12-inch impactor head into the side of the tank car. The tank car was backed by a rigid impact barrier and filled to approximately 82.4 percent of its capacity with water to simulate the commodity lading volume of a DOT-113 tank car in LNG service based on the conditions in the proposed regulation. The inner tank was sealed and pressurized to 50 psig. At the time of the test, the ambient conditions included a wind speed of 2 mph out of the north-northeast and an air temperature of 66 °F.

4.2 Details of Test

Based on the estimated material properties for both the inner and outer tank steels, pre-test simulations estimated a puncture speed range of 16 to 18 mph. The target speed for the test was 16.5 mph, ±0.5 mph, near the low end of this speed range. Regardless of whether the tanks punctured or remained intact, one objective in choosing this target test speed was ensuring the actual impact speed was close to the threshold puncture/non-puncture speed. Section 6 contains a discussion of the pre-test simulations used to help select the target test speed. The actual calculated impact speed from the speed sensors was 16.7 mph.

The indenter punctured the outer tank under a corner on the left-hand side of the indenter. The initial puncture created a tear in the outer tank that spread circumferentially as the impactor continued to travel forward. The inner tank was punctured after the outer tank. The ram car continued to move forward following impact and came to rest embedded within the tanks. The continued forward travel of the impactor following the puncture of the inner tank created additional tearing and damage to both tanks until the ram finally came to a stop. Figure 19 shows the post-test positions of the DOT-113 and the ram car.

Figure 19. Post-Test Positions of DOT-113 and Ram Car

Figure 20 shows the post-test position of the tank car relative to the supporting wall as well as the damage to the back side of the tank car. Because of the length of the tank car and the 11-foot impact point offset, the west end of the tank car saw significantly less longitudinal motion than the east end, resulting in the west skid acting like a pivot point.

Figure 20. Post-Test Position of Tank Car (Wall Side)

Figure 21 contains side-by-side photographs taken prior to the ram's removal from the DOT-113. The left-side photograph was taken from inside the tank from the east side of the test setup. This photograph shows the tear to the inner tank through which the torn outer tank is also visible. The right-hand side of this image shows the outside of the DOT-113 viewed from the east side, prior to the ram's removal.

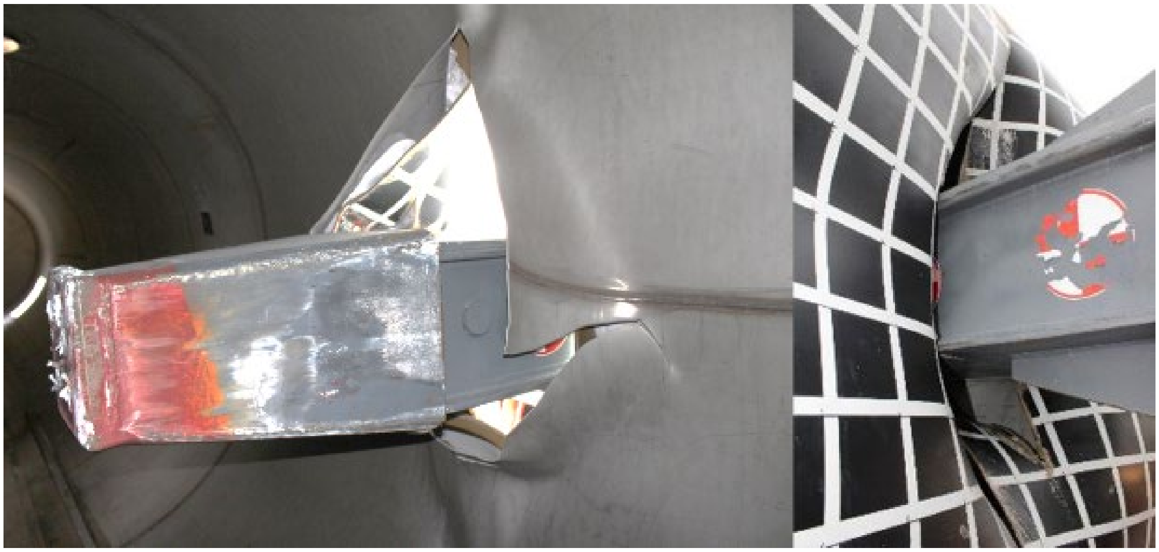

Figure 21. Interior (left) and Exterior (right) Views of Tank Damages from East Side (Prior to Impactor Removal)

Figure 22 includes the same interior view of the punctured tank shown in the previous image with the addition of an inset. This inset image features a zoomed-in view of the tears to both the inner and outer tanks. The outer tank's surface shows red paint transferred from the tip of the impactor. Based upon the position of the impactor relative to the tear, this location was determined to have originally aligned with the left (east) upper corner of the impactor prior to puncture. Note the pronounced bend in the outer tank that is adjacent to the limit of the red paint transfer. To the left of the torn outer tank, a similar sharp radius is seen in the inner tank's material, slightly lower in the photograph than the corner of the outer tank. This sharp radius in the inner tank is believed to have been caused by the inner tank wrapping itself around the impactor, which was in contact with the outer tank. Based on their final positions as shown in this Figure 22, the two bends have experienced some displacement relative to one another during either the impact or post-impact when each tank recovered its elastic energy.

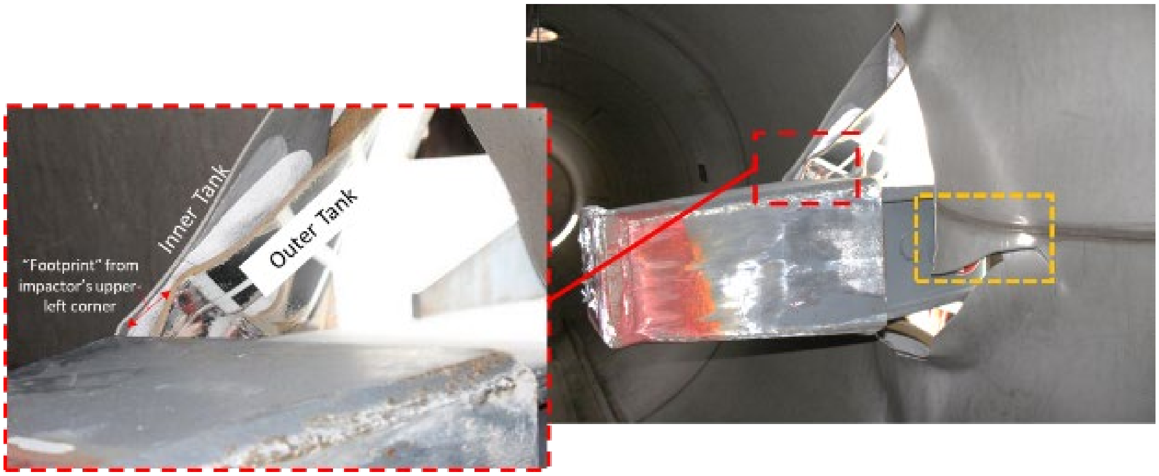

Figure 22. Interior View of Tank from East Side with Inset Showing Contact Area Between Inner and Outer Tank (Prior to Impactor Removal)

Figure 23 includes the same interior view of the punctured tank shown in Figure 21 with the addition of a different inset that highlights the area of torn tank on the left (east) side of the impactor. The inner tank of the DOT-113 featured a longitudinal weld at the approximate same height as the impactor. The inset image shows that the circumferential tear crosses the longitudinal weld without changing direction. Below the longitudinal weld, there is a tear extending upward and parallel to the longitudinal weld in the base metal of the inner tank. While the inner tank tore in the vicinity of this longitudinal weld, there is no evidence that the weld itself contributed to the puncture's initiation or to the propagation of the tear.

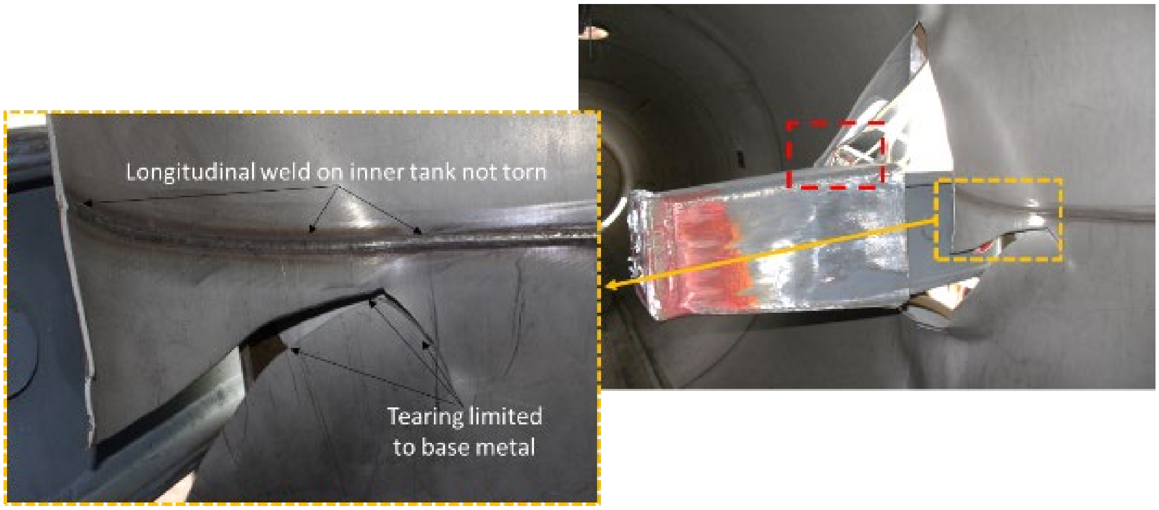

Figure 23. Interior View of Tank from East Side with Inset Showing Longitudinal Weld on Inner Tank (Prior to Impactor Removal)

Figure 24 contains side-by-side photographs taken prior to the ram's removal from the DOT-113. The left-side photograph was taken from outside the tank from the west side of the test setup. The right-hand side of this image shows the inside of the DOT-113 viewed from the west side, prior to the ram's removal. The right-hand image demonstrates that the inner tank tore on the left (east) side and formed a hinge on its right (west) side as the impactor pushed further into the tank. This view shows that the inner tank's tear extended across the longitudinal weld seam but does not appear to be influenced by the presence of an inner tank weld in the impact zone.

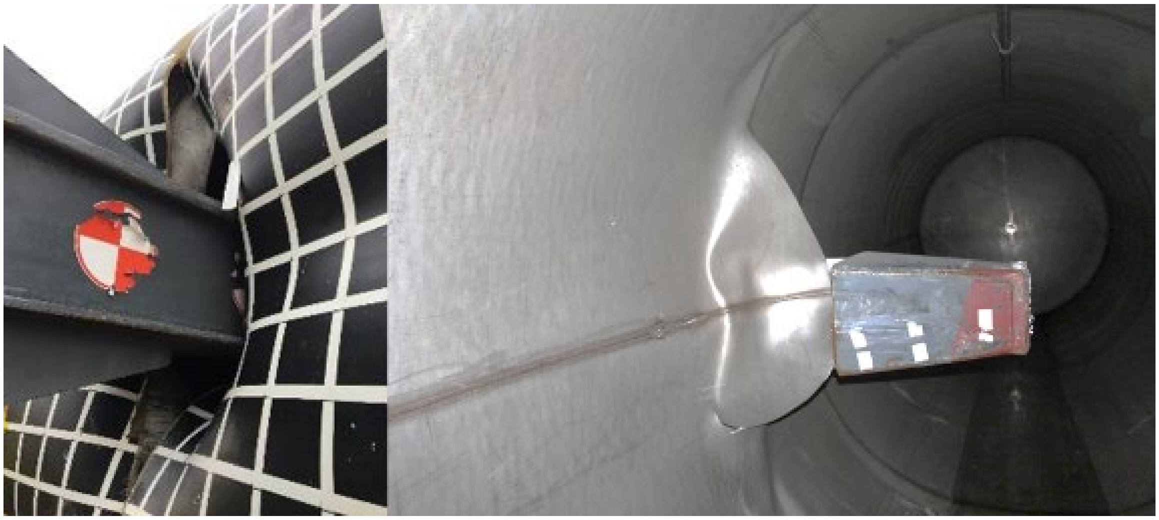

Figure 24. Exterior (left) and Interior (right) Views of Tank Damages from West Side (Prior to Impactor Removal)

Figure 25 shows two side-by-side photographs. The left-side photograph shows an interior view of the puncture zone above the impactor, and the right-side photograph shows an exterior view of the puncture zone above the impactor. The upper limit of the inner tank's tear is denoted on both images using an arrow. From the right-side photograph, it can be observed that the vertical extent of the outer tank's tear continued above the extent of the inner tank's tear.

Figure 25. Interior (left) and Exterior (right) Views of Punctured Tanks Above Impactor (Prior to Impactor Removal)

Figure 26 shows two side-by-side photographs. The left-side photograph shows an interior view of the puncture zone below the impactor, and the right-side photograph shows an exterior view of the puncture zone below the impactor. Common points on the torn outer tank are denoted on both images using arrows. From the right-side photograph, it can be observed that the downward vertical extent of the outer tank's tear continued below the extent of the inner tank's tear.

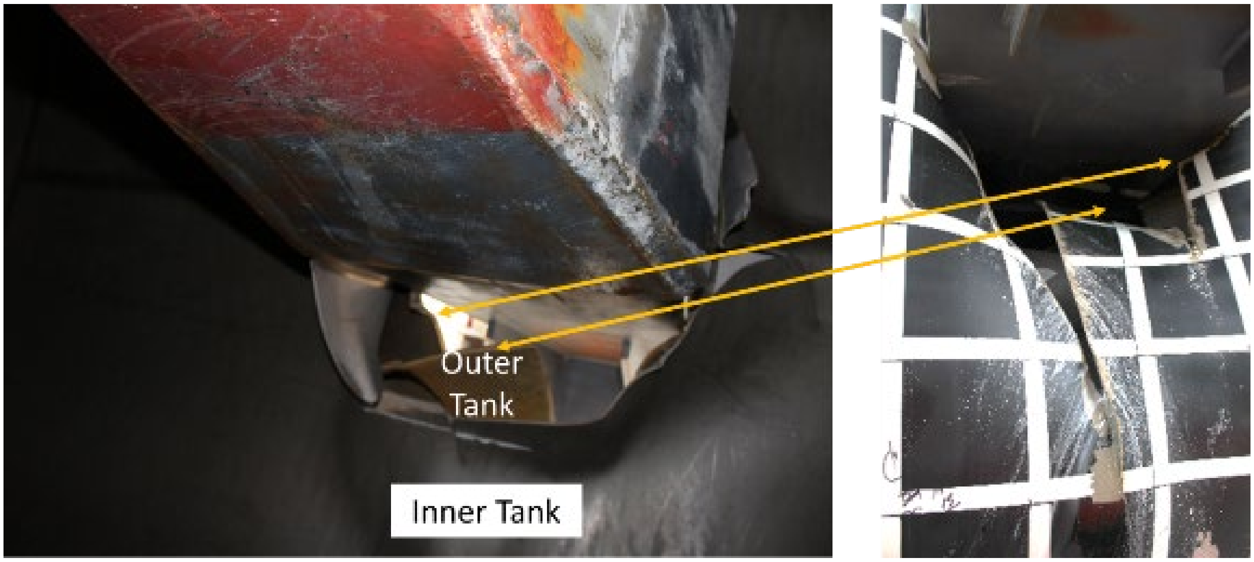

Figure 26. Interior (left) and Exterior (right) Views of Punctured Tanks Below Impactor (Prior to Impactor Removal)

Figure 27 shows the impact area on the outside of the tank car after the test. This photograph was taken after the ram car had been removed from the DOT-113. From this point forward, the impact zone will include tank damage that occurred both during the impact and during the process of extracting the ram from the DOT-113. Deformation outside of the black and white checkered area, which was a result of a secondary impact—occurring after puncture of the inner tank—from the side-frames of the ram car, is also visible on the outer tank. This type of impact is not typical in the side impact test program and was a result of a large residual ram car speed (7.9 mph) at the time of puncture of the inner tank.

Figure 27. Tank Car After Impact (Impact Side, After Impactor Removal)

Figure 28 shows two side-by-side photographs taken after the impactor's removal from the DOT-113. The left-side photograph shows an exterior view of the puncture zone taken from the east side of the impact site, and the right-side photograph shows an exterior view of the puncture zone taken from the west side of the impact site. In both photographs, the outer tank and inner tank are visible and have been denoted with callouts.

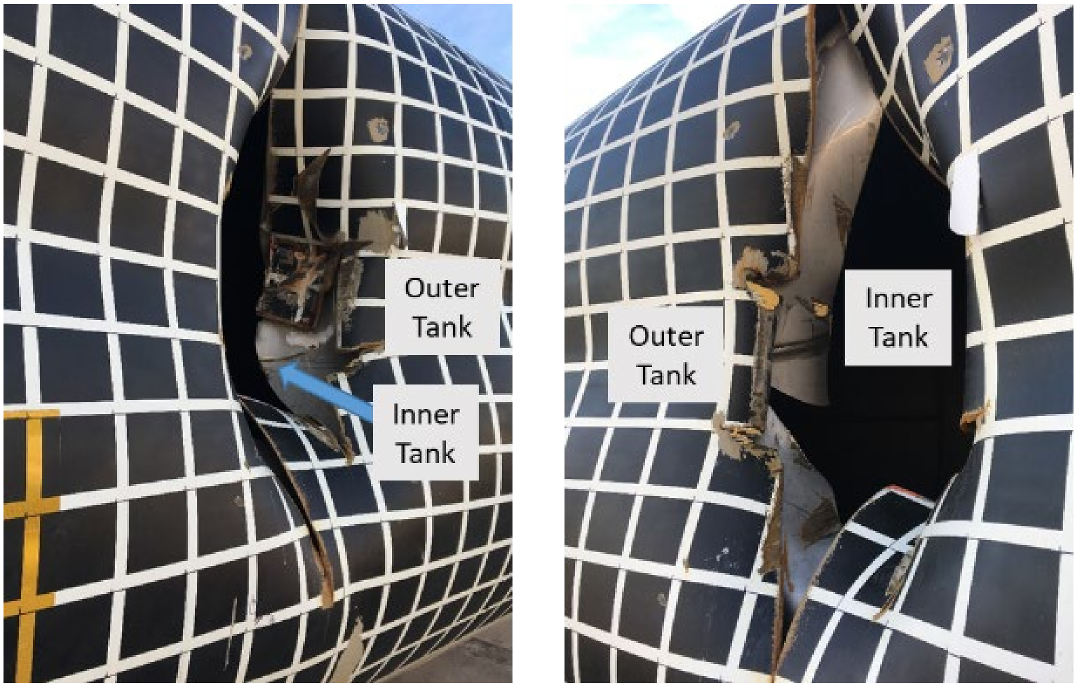

Figure 28. Post-Test Views of Impact Zone Taken from East (left) and West (right) (After Impactor Removal)

Figure 29 is an annotated cross section photograph taken through the outer tank, annular space, and inner tank. This photograph was taken at the end of the car where plates were removed from both the outer and inner tanks for material characterization. The test team chose to cut material samples from this area of the DOT-113 because it was remote from the impact zone, therefore the materials were expected to be representative of the pre-test condition of the car. This view illustrates the condition of the perlite in an area remote from the impact. While the plates have been removed from the tank, the perlite remained in the annular space unless "dug out," while a loose, granular material, the perlite had enough adhesion between particles to remain in the annular space even when unconstrained by the tanks.

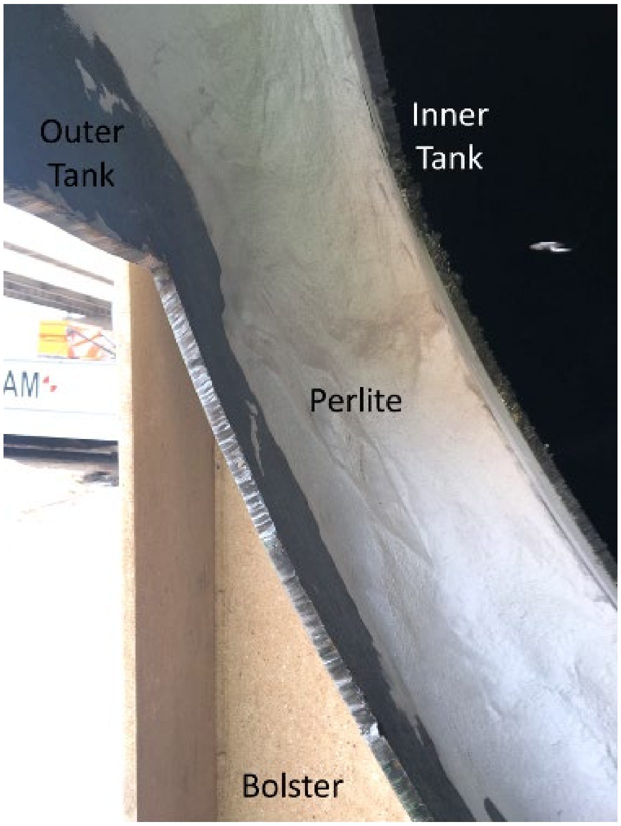

Figure 29. Cross Section Through Front of DOT-113 at Location of Removed Shell Plates

4.3 Laser Scanning

Prior to the test, a light detection and ranging (LIDAR) scan was performed on the interior of the test car and a companion DOT-113 tank car. The output of this scan is a full-scale, three-dimensional geometry file that can be compared with the geometry in the FE models. The pre-test geometry of the inner tank is shown in Figure 30. The individual views of the car shown in Figure 30 are (from top to bottom) top, front, and isometric. The same arrangement is also used in Figure 31 and Figure 32.

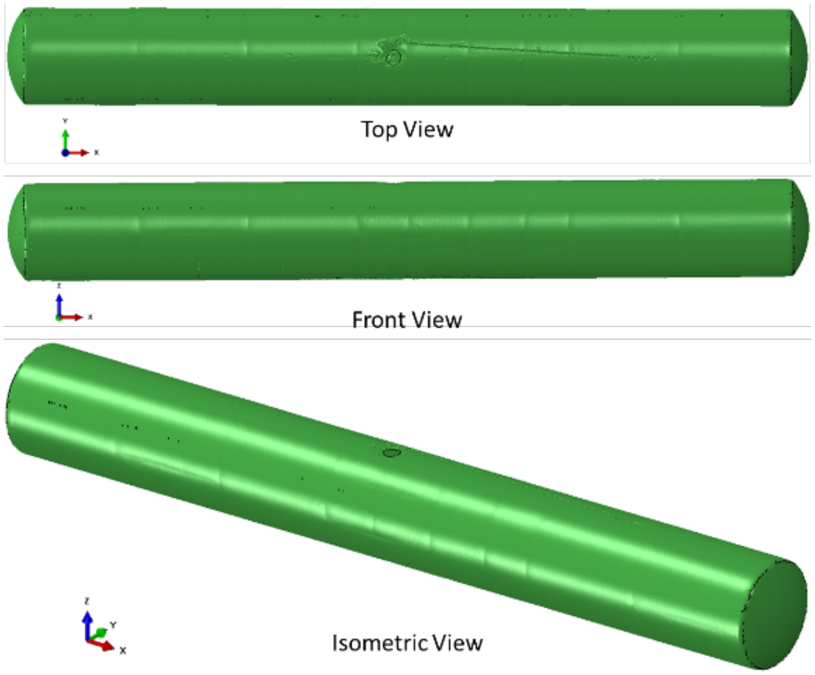

Figure 30. Pre-Test Geometry from Scan of Inner Tank

Following the test, complete scans of the inside and outside of the tested tank car were performed to document the deformation that occurred during the test. The post-test scan of the inner tank is shown in Figure 31. The area of impact is shown as the area of missing material on the left side of the tank, and the area that was cut away for material characterization (see Section 4.5) is shown at the right end of the tank. The post-test scan of the outer tank is shown in Figure 32.

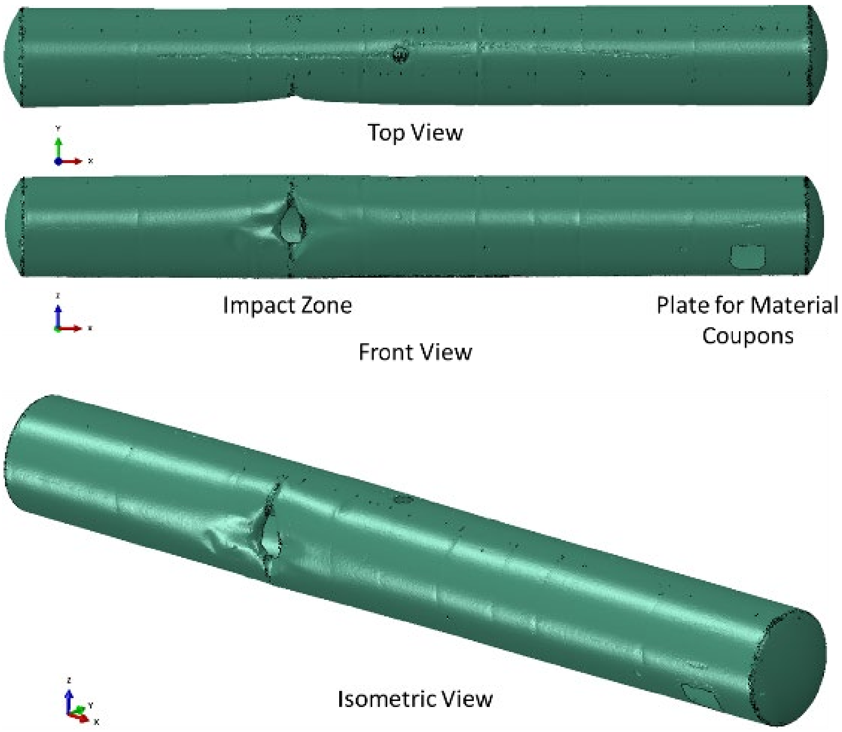

Figure 31. Post-Test Geometry from Scan of Inner Tank

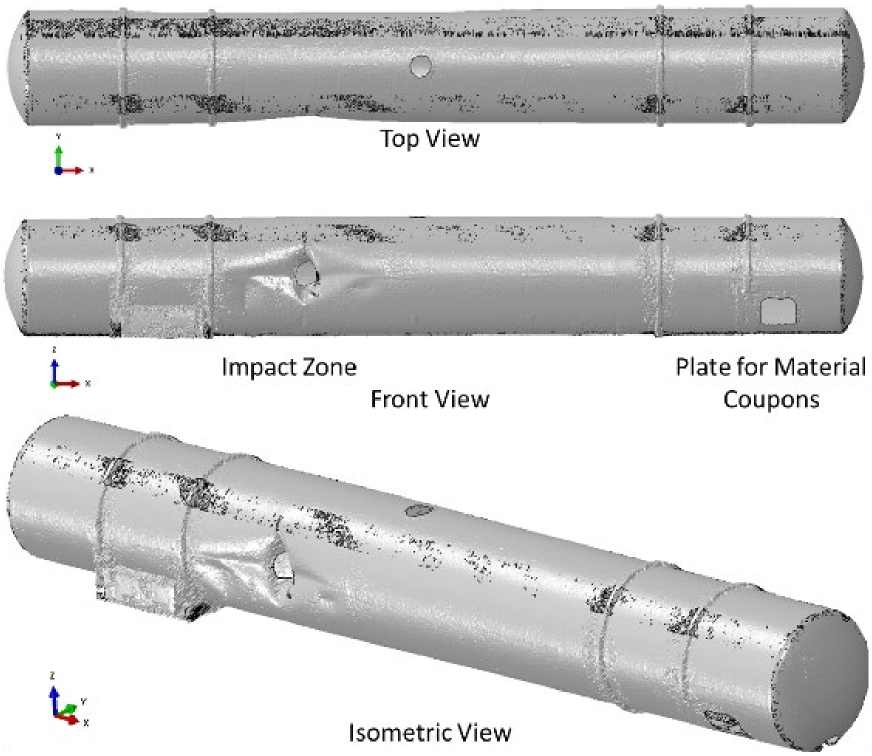

Figure 32. Post-Test Geometry from Scan of Outer Tank

Because the individual points of measurement in the pre- and post-test scans were not the same, obtaining an estimate of the relative indentation at different locations throughout the car posed a challenge. As an approximation, the post-test scan data was compared to the theoretical positions of a perfectly cylindrical tank having the same inner and outer diameter as the tested DOT-113 tank. One result of interest is the depth of the dent in the outer tank, and the extent to which the dent has spread along the length of the tank car. The post-test scan geometry of the dent zone in the outer tank is shown in Figure 33. In this figure, the vertical dashed line indicates a cross section through the punctured area that will be examined further.

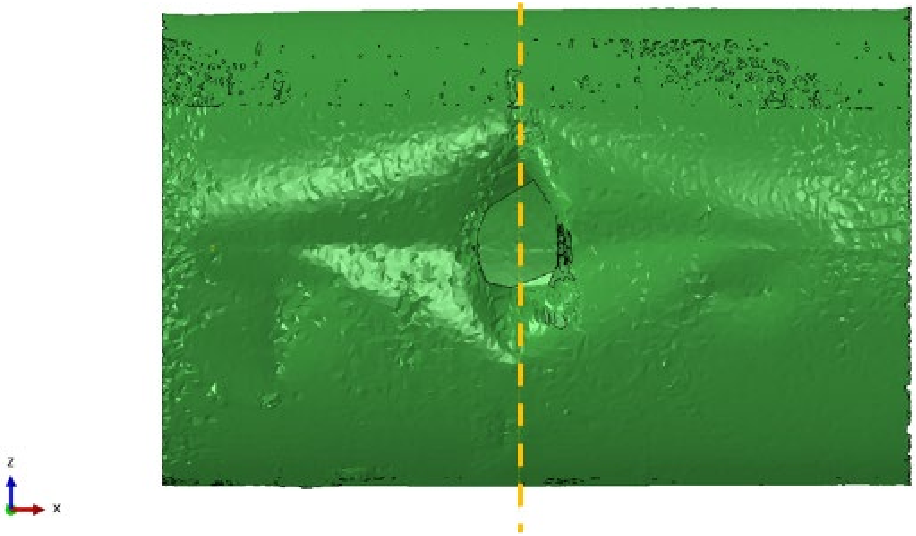

Figure 33. Dent Zone in Outer Tank

To determine the relative indentation of each point in the scanned point cloud, it was first necessary to calculate the original coordinates of each point on the undeformed tank surface using the coordinate system shown in Figure 34. Since the tank was originally a cylinder of known radius, the Z (vertical) and X (axial) coordinates of each point in the deformed point cloud could be used to calculate the Y (horizontal) coordinate of the corresponding point on the outer surface of the cylinder. This theoretical circle was then aligned with the approximate centerline of the deformed tank scan. Figure 34 shows a plot of a slice through the deformed tank car (individual points) at the center of the puncture alongside a circle having the same diameter as the pre-test outer tank. Note that because the scan points are not a perfect grid, the data points shown in Figure 34 include all points having an X coordinate within ± 1 inch of the dashed line in Figure 33. In Figure 34, the dented area is shown on the left side. Because the material tore, there is no single value that equals the maximum depth of the residual indentation. At both the top and bottom of the tank, the deformed shape is outside of the original circle. This indicates that some of the vertical "ovalization" that occurred during the test remained post puncture. At the right side of the figure, the diameter of the tank has been reduced and flattened, likely due to the permanent deformation of the outer tank resulting from the collision with the rigid impact wall.

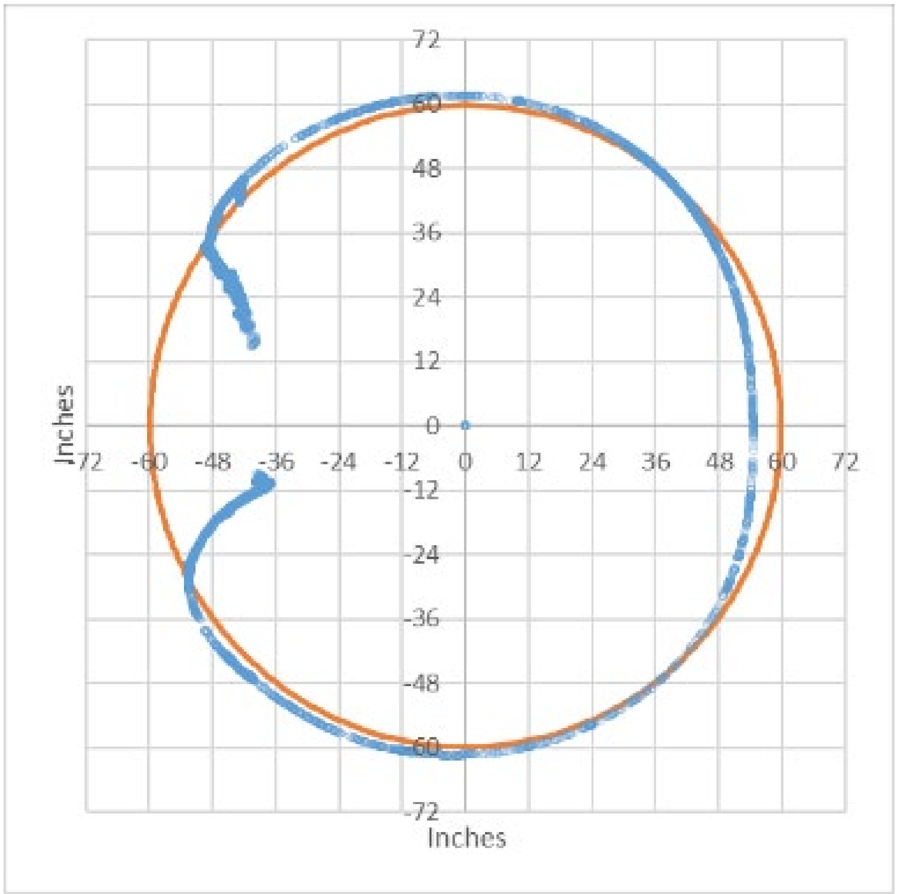

Figure 34. Cross Section of Deformed Outer Tank from Post-Test Scan and Undeformed Circle

4.4 Measured Data – Impact Test

TTCI initially processed the data collected in the test (e.g., offset corrections, filtering, etc.) and provided to Volpe for comparison to the analyses. The offset adjustment procedure ensured that the data that was plotted and analyzed contained only impact-related accelerations and strains and excluded electronic offsets or steady biases in the data. To determine the necessary offset, the data collected before impact was averaged. This offset was then subtracted from the entire data set for each channel. This post-test offset adjustment was made independent of and in addition to the pre-test offset adjustment made by the data acquisition system.

The post-test data filtering was accomplished with a phaseless four-pole digital filter algorithm consistent with the requirements of SAE J211 [18]. A 60 Hz channel frequency class (CFC) filter was applied to the filtered acceleration data shown in this report. A brief summary of the measured data is also provided in this section. Appendix B contains the plots of filtered data from all transducers.

The longitudinal acceleration of the ram car was one of the primary measurements taken during the test. Multiple accelerometers were installed on the ram car to capture this data. The data were used to derive the impact energy, the deceleration of the ram car, and the contact forces between the ram and target tank car. Figure 35 shows the average longitudinal acceleration history from all the accelerometers on the ram car.

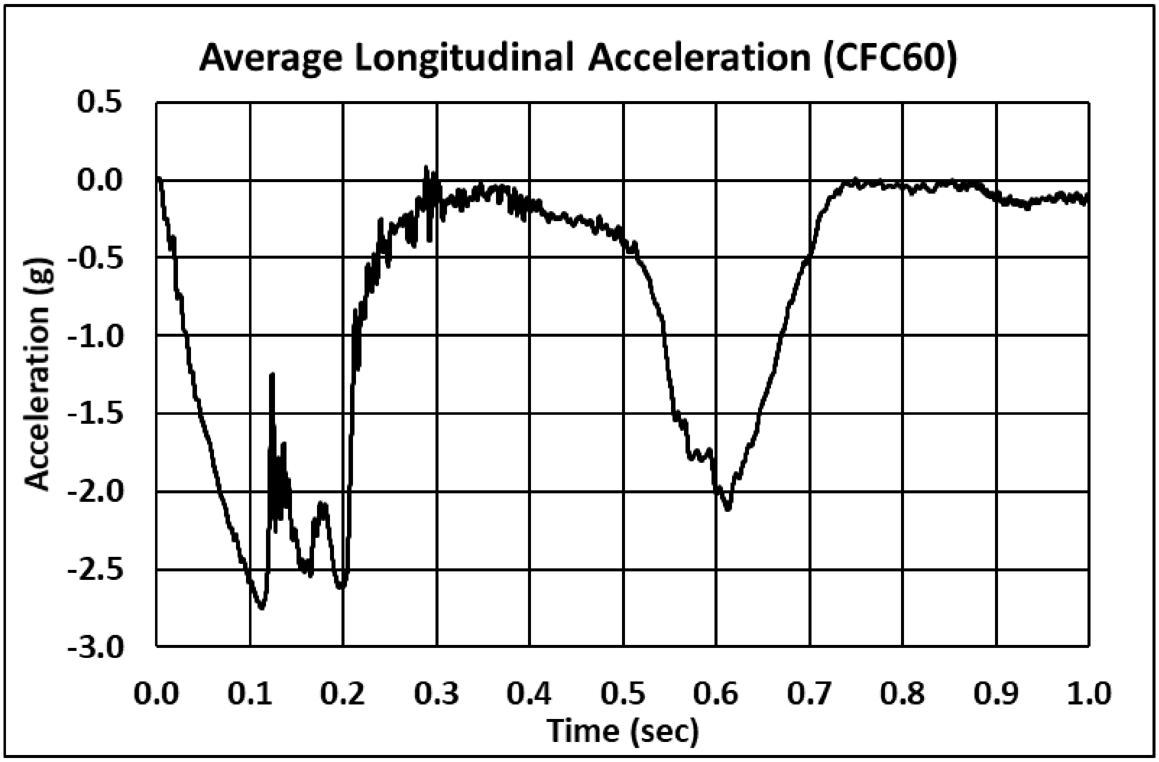

Figure 35. Longitudinal Acceleration Data (Averaged)

The ram car velocity history in the test was calculated by integrating the average longitudinal acceleration of the ram car and using the impact speed measurement as an initial condition. Contact forces between the ram and target tank car were calculated as the product of the average acceleration and the mass of the ram car. Figure 36 shows both the force-time and velocity-time histories. The longitudinal acceleration trace of Figure 35 and the impact force trace of Figure 36 show two distinct periods of heavy deceleration/impact forces. The first period corresponds to the initial impact with the tank car and subsequent puncture of both the outer and the inner tanks (i.e., approximately the first 250 milliseconds [ms]). The second period corresponds to the second collision between the front of the ram car and the rebounding east end of the tank car. Between the two is a period of reduced deceleration and force as the only significant interaction between the two vehicles is the frictional force between the ram "arm" and the wall of the tank car. This is also the reason for the "stepped" appearance of the speed trace of Figure 36.

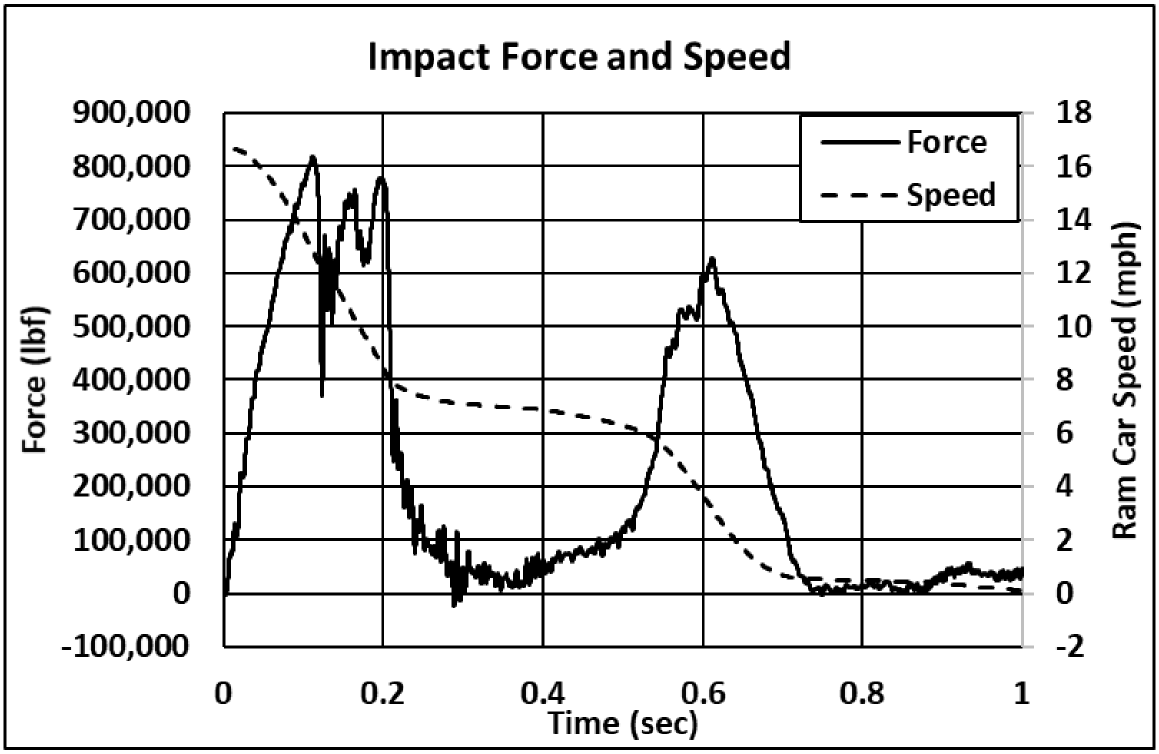

Figure 36. Impact Force and Ram Car Speed (Averaged)

Similarly, the kinetic energy was calculated for the ram car from the speed-time history and weight. Figure 37 shows the kinetic energy-time history of the ram car and the energy absorbed by the tank car. The kinetic energy of the ram car is calculated directly from the ram car's mass and speed-time history. The energy absorbed by the tank car is calculated as the difference between the ram car's current kinetic energy and its kinetic energy at the time of impact. This plot also has a "stepped" appearance with the energy absorbed by the tank car reaching its maximum shortly after the collision between the front of the ram car and the rebounding tank car.

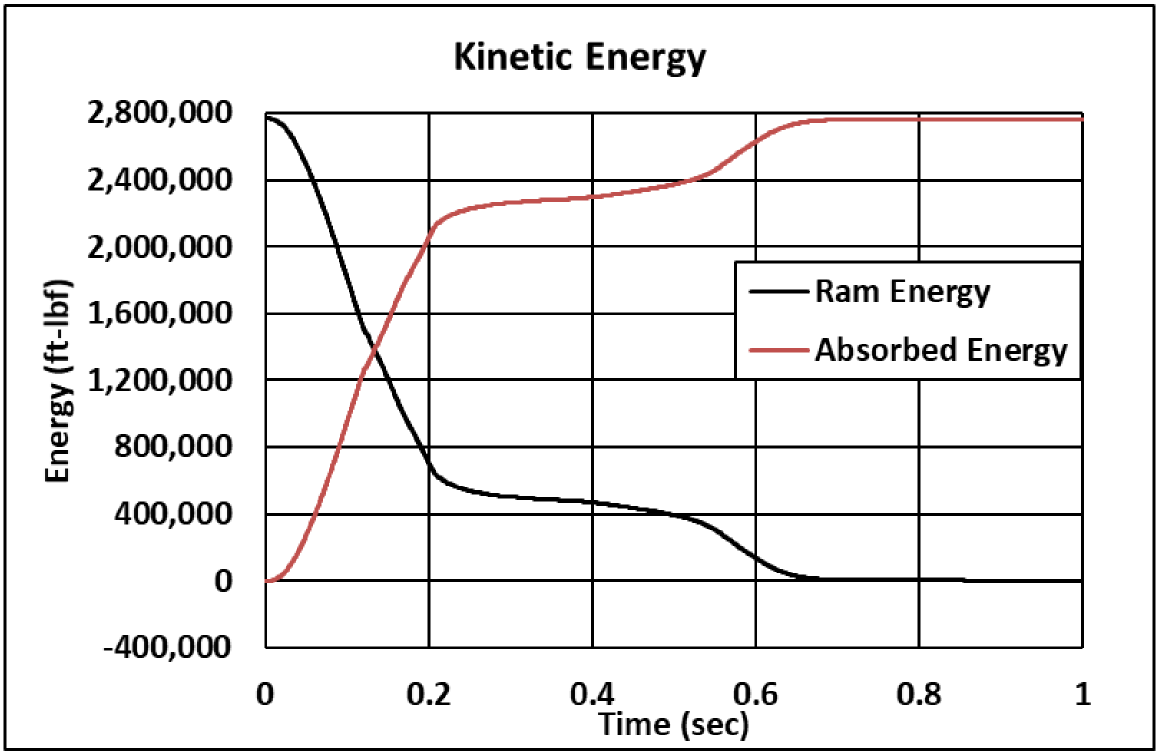

Figure 37. Kinetic Energy Time-History of Ram Car

The total kinetic energy of the ram car was approximately 2.77 million ft-lbf, and the energy absorbed by the tank car before puncture was approximately 2.14 million ft-lbf. The difference between the initial kinetic energy and the energy absorbed by the tank car before puncture was approximately 630,000 ft-lbf of excessive energy or about 22.5 percent of the initial kinetic energy.

Another significant impact response measured in the test was the effect of the internal pressure as the tank indentation formed and reduced the volume of the tank. The tank was filled to approximately a 17.6 percent outage volume with water, and the tank was pressurized to about 50 psig. Water can be approximated as incompressible for the impact behavior. As a result, the air volume in the outage, initially at 1 atmosphere of pressure, was compressed as the dent formation reduced the tank volume. This caused the internal pressure to rapidly increase. As described in Section 3.3, pressure transducers were mounted at several locations inside the tank car, both within the water/lading and at the pressure release valve and manhole within the air/outage.

Figure 38 shows pressure data from within the lading near the center of the tank car (i.e., transducers TPC090 on the back wall, TPC180 at the bottom, and TPC270 on the front wall).

Prior to puncture, the overall pressure in both the lading and the outage rose to about 60 psig. The sloshing of the water in the tank created local pressure variations of up to 25 psig (i.e., pressure transducer TPC090) within the lading while the pressure readings in the outage were significantly more stable. Note that the spikes seen in TPB000 in Figure 39 are not believed to be representative of any actual physical phenomena and are considered to be noise in the signal. Also, the separation of TPA000 (also in Figure 39) from the other signals is believed to be a result of a “zero offset” of that channel.

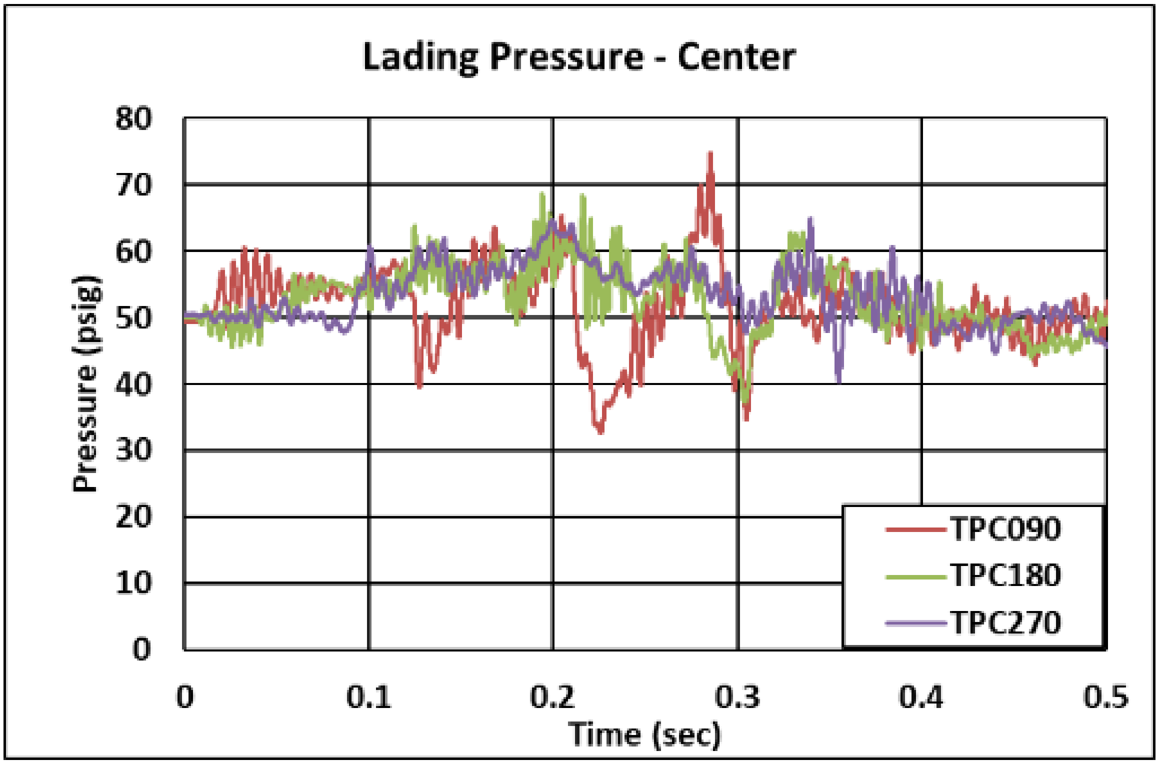

Figure 38. Lading Pressure Measured at the Center of the Tank Car

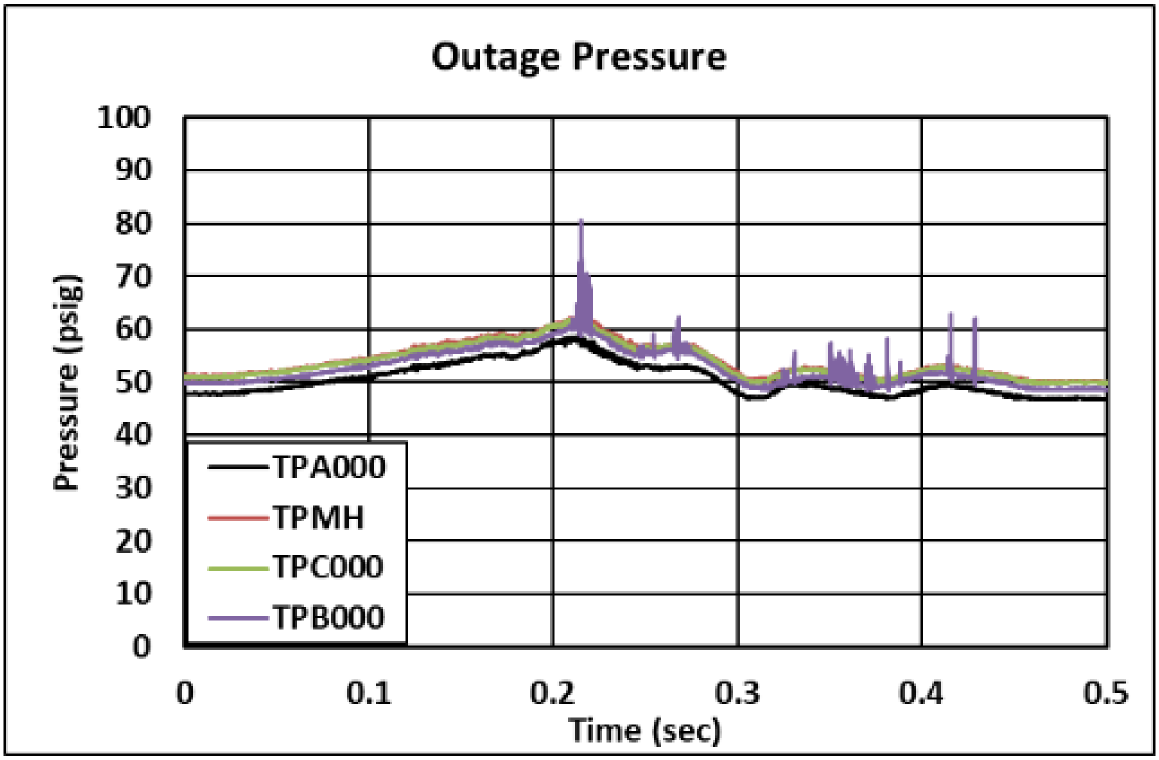

Figure 39. Pressure Measured in the Manway and the Outage

The remaining quantitative measurements taken from the tank impact behavior were displacement histories recorded with string potentiometers and laser displacement transducers. These measurements included external tank deformations (measured with lasers) and external tank movements at both ends of the tank (measured with string potentiometers). The layout of the string potentiometers was described in Section 3.3. The layout of the lasers was described in Section 3.4.

As discussed in Section 3.4, limited access to the interior of the tank car led the test team to use lasers to measure the deformation of the tank car. The most useful data for calculating the deformation of the outer tank in the area of the impact are the measurements from the lasers on the front of the ram car, which are presented in Figure 40. The data series BD1Y and BD5Y show the distance between the tank car and the front of the ram car 48 inches to the left and the right of the center of impact respectively, over time, from the ram car frame of reference. BD2Y and BD4Y show the distance between the tank car and the front of the ram car 24 inches to the left and the right of the center of impact respectively, over time. BD3Y shows the distance between the front of the ram car and the wall over time. By measuring the distance of the front of the ram car from the crash wall and the front of the ram car from the front of the tank car, the distance between the front of the tank and crash wall (and correspondingly the longitudinal deformation of the tank car) is easily calculated. The maximum longitudinal deformation is expected to correspond to the time at which puncture occurs (i.e., about 0.21 seconds after impact, see Section 4.6). After the ram breaches the wall of the tank car, the front of the ram car can move closer to the front of the tank car without any further longitudinal deformation of the tank car occurring. At the time of puncture, the calculated distances between the front of the tank car and the offset plate on the crash wall were 94.3 inches at BD1Y, 86.5 inches at BD2Y, 84.9 inches at BD4Y, and 93.4 inches at BD5Y. The nominal outside diameter of the tank car was 119.625 inches.

In previous tank car tests, in addition to measuring the longitudinal deformation of the tank car, the vertical deformation of the car was also measured using a string potentiometer. However, for this test, as with the longitudinal internal string potentiometers, limited access made it impossible to install a vertical string potentiometer, and, as no suitable external alternative was found, vertical deformation data were not captured for this test.

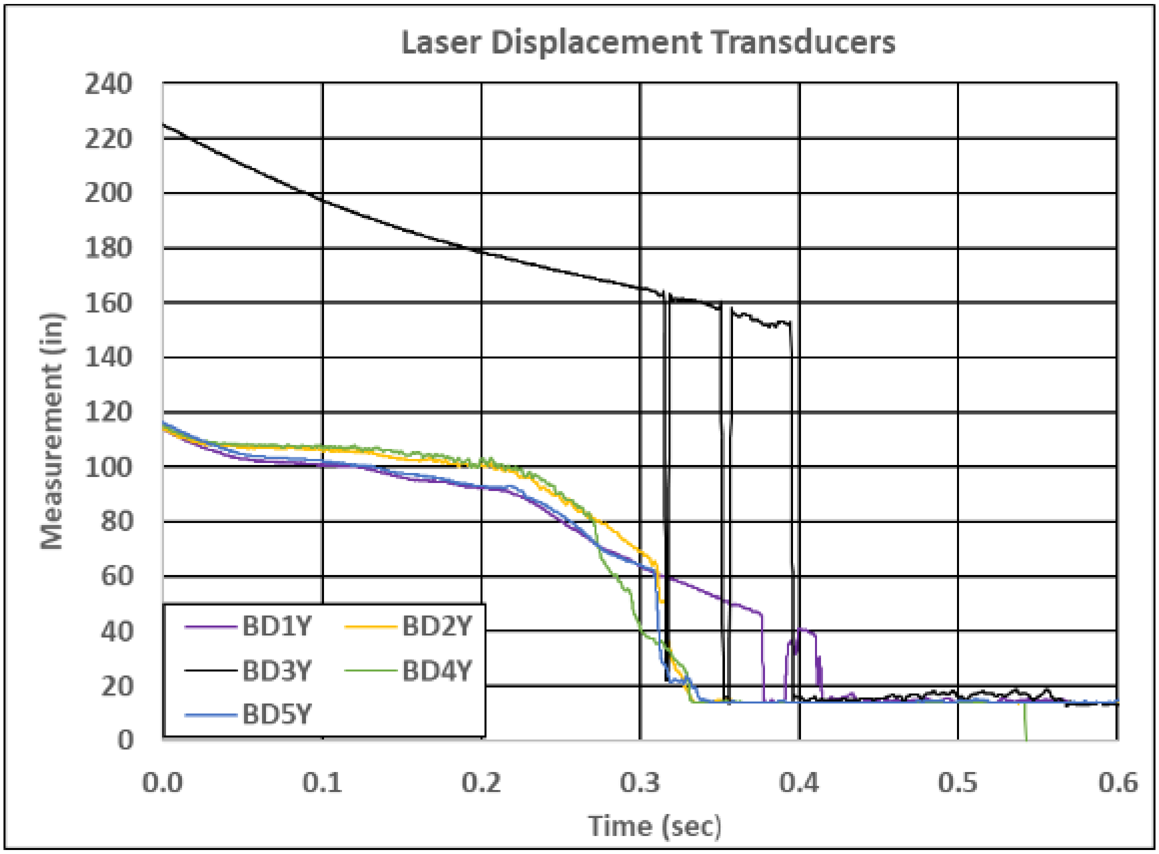

Figure 40. Tank Car Deformation Measured with Laser Displacement Transducers

Figure 41 and Figure 42 shows the measured displacements for the tank car's external string potentiometers. The car-end displacements were significantly delayed from the motions in the impact zone and little displacement is seen for the first 0.1 second of the response. The measurements of the car head displacements and the skid displacements were nearly identical at each end. However, the individual sets of responses were very different between the A-end and B-end of the tank. Due to the overall length of the car and the 11-foot offset of the point of impact, the A-end of the car saw more movement than the B-end, and the movements were much larger in magnitude.

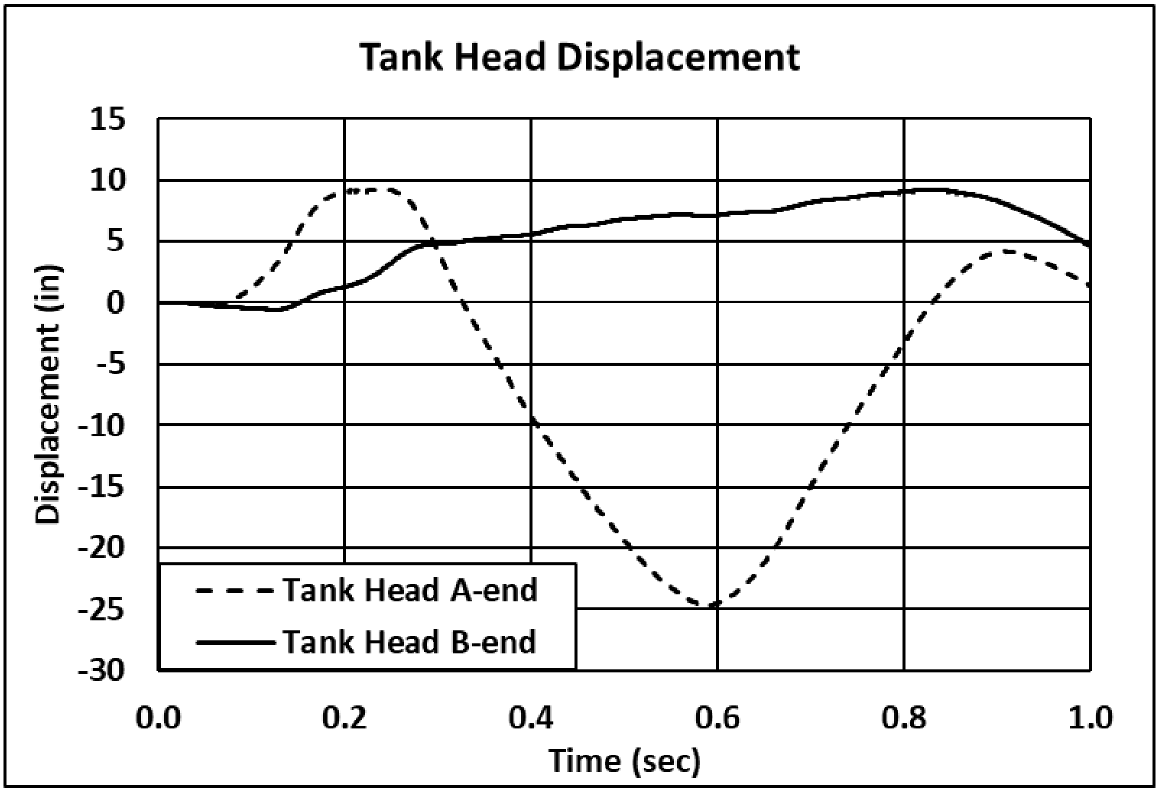

Figure 41. External Displacements–Tank Car Heads

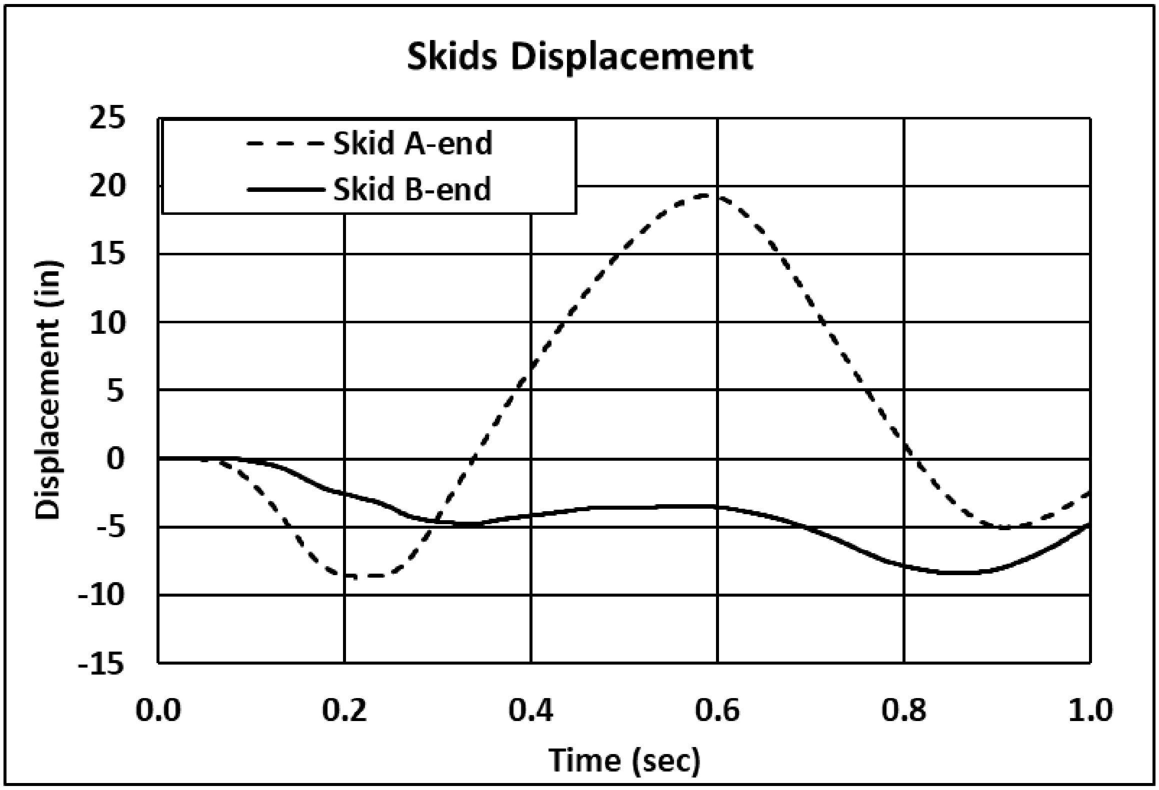

Figure 42. External Displacements - Skids

4.5 Measured Data – Material Testing

Following the test, a square panel measuring approximately 36 inches on a side was cut out of both the inner tank and the outer tank. Each panel was cut out of its respective tank from a shell ring outboard of the west-end bolster on the front (impact side) of the tank car. This region was selected as it was remote from the impact zone, and thus the material was expected to better represent the pre-test properties. Figure 43 shows the post-test tank car with the removed plates of material.

Figure 43. Photograph of DOT-113 with Area of Material Samples Removed Post-Test

Figure 44 shows the plates removed from the two tanks. The stainless-steel inner tank plate is shown on top of the carbon-steel inner tank plate.

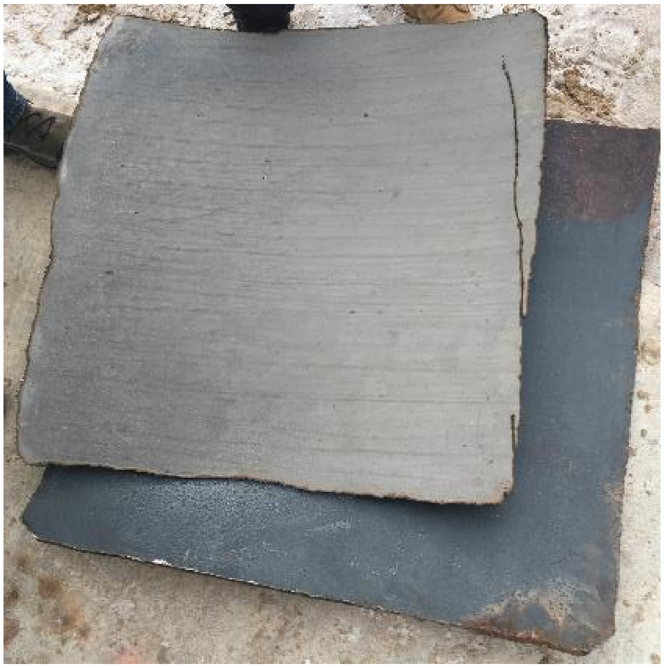

Figure 44. Stainless (top) and Carbon (bottom) Steel Panels Removed from Inner and Outer Tanks, Respectively

Tensile test specimens were machined from each panel according to the requirements of ASTM E-8 for a flat rectangular coupon having a 2-inch gage length [19]. Two rounds of tensile testing were planned for each material. An initial set of three specimens of each material were tested immediately after the test, at room temperature. This first round was intended to provide a quick answer to the question of how the material properties compared to the estimated values used in the pre-test modeling.

A second round of tensile testing was later conducted for the stainless steel at a range of cryogenic temperatures: -320 °F, -260 °F, -100 °F, and at room temperature. The mechanical properties of the stainless steel at cryogenic temperatures were required for future use in post-test modeling that will examine the puncture performance of the DOT-113 tank car under conditions more representative of service conditions. These four temperatures were chosen to provide a range of material performance data over the temperatures expected to be relevant to this testing program. A temperature of -260 °F corresponds to the boiling temperature of LNG at 1 atmosphere of pressure. At 1 atmosphere, liquid nitrogen (LN2) boils at -320 °F. This is an important data point, as future tests of DOT-113 tank cars are expected to be performed using LN2 as the commodity in the tank. A temperature of -100 °F was chosen as an intermediate point between LNG's boiling point and room temperature. Understanding the differences between stainless steel properties at room temperature, LN2's boiling point, and LNG's boiling point will be critical for future modeling and testing to define the expected level of performance of the DOT-113 under service conditions.

The carbon steel was also subjected to a second set of tensile tests at room temperature by the laboratory performing the cryogenic testing. This was done to ensure the consistency of the results from the two labs. Three carbon steel and three stainless steel specimens were tested at room temperature at each lab.

The results of the first round of testing revealed that the stainless steel had a yield strength (YS), ultimate tensile strength (UTS), and elongation at break (EB) as expected. However, the carbon steel had a YS and a UTS below the minimum values for ASTM A516-70 steel.

The results of the second round of testing were consistent with the results of the first round for both the carbon and stainless steels at room temperatures. Additionally, the cryogenic temperature tests performed on the stainless steel showed that as the temperature decreased, the YS and UTS increased while the EB decreased. The shape of the stainless-steel stress-strain curve also changed as the temperature decreased. Appendix B, Section 4 provides the complete set of material test results.

4.5.1 Stainless Steel (Inner Tank)

Table 9 summarizes the mechanical properties of the stainless-steel samples. The specification reference values shown in this table are from the 2019 edition of ASTM A240 [3]. It should be noted that ASTM A240 does not contain any minimum strength or ductility requirements for tests performed at cryogenic temperatures.

Table 9. Summary of YS, UTS, and EB from Tensile Tests of Stainless Steel

		Lab 1	**Lab 2**	**Lab 2**	**Lab 2**	**Lab 2**
	Kelvin:	**295**	**295**	**200**	**111**	**77**
	Fahrenheit:	**71**	**71**	**-100**	**-260**	**-321**
YS (thousand psi)	Coupon A	37	35.9	41.3	40.3	44.9
	Coupon B	43.1	37.4	40.8	41.7	44.1
	Coupon C	39.4	38.7	39.9	44.2	43.8
	Average	*39.8*	*37.3*	*40.7*	*42.1*	*44.3*
	Specification Requirement	***30***	***30***	***N/A***	***N/A***	***N/A***
UTS (thousand psi)	Coupon A	85.7	86	144	178.7	198
	Coupon B	87.3	87.4	140.4	186.7	207.5
	Coupon C	83.5	90.6	144.8	180.1	208.5
	Average	*85.5*	*88*	*143.1*	*181.8*	*208*
	Specification Requirement	***75***	***75***	***N/A***	***N/A***	***N/A***
EB (2-inch gage) (%)	Coupon A	70.1	73.5	38.8	41.3	42.9
	Coupon B	78.2	76.9	39.1	33	36.3
	Coupon C	65.4	77.5	51	36.2	53.2
	Average	*71.2*	*76*	*43*	*36.8*	*44.1*
	Specification Requirement	***40***	***40***	***N/A***	***N/A***	***N/A***

Figure 45 presents the YS data from Table 9 as a graph of YS versus temperature. The YS from each individual coupon is plotted as a solid circle, and the average YS from a given lab and a given temperature is plotted as an “X.” In general, the data show a modest increase in YS as the temperature decreases further below room temperature. At the extreme, the largest average value of YS at 77 K is approximately 18.8 percent higher than the smallest average value of YS at 295 K.

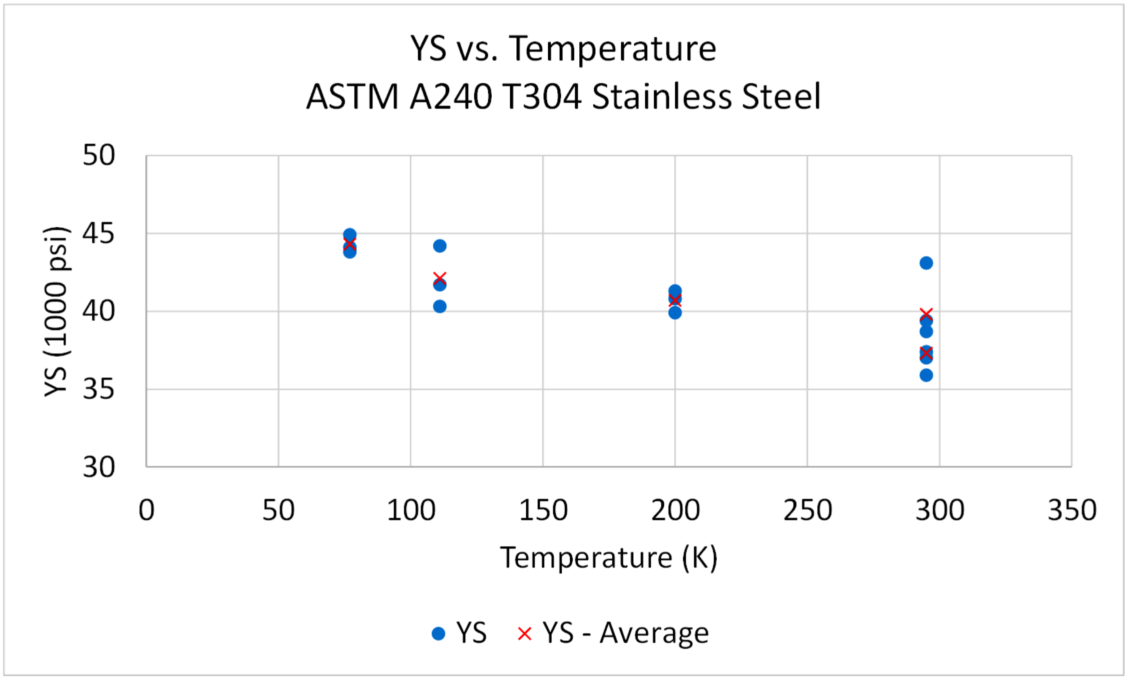

Figure 45. Graph of YS Versus Temperature for T304 Stainless Steel

Figure 46 presents the UTS data from Table 9 as a graph of UTS versus temperature. The UTS from each individual coupon is plotted as a solid circle, and the average UTS from a given lab and a given temperature is plotted as an "X." Overall, the data show a large increase in UTS as the temperature decreases further below room temperature. At the extreme, the largest average value of UTS occurring at 77 K is approximately 143 percent higher than the smallest average value of UTS occurring at 295 K.

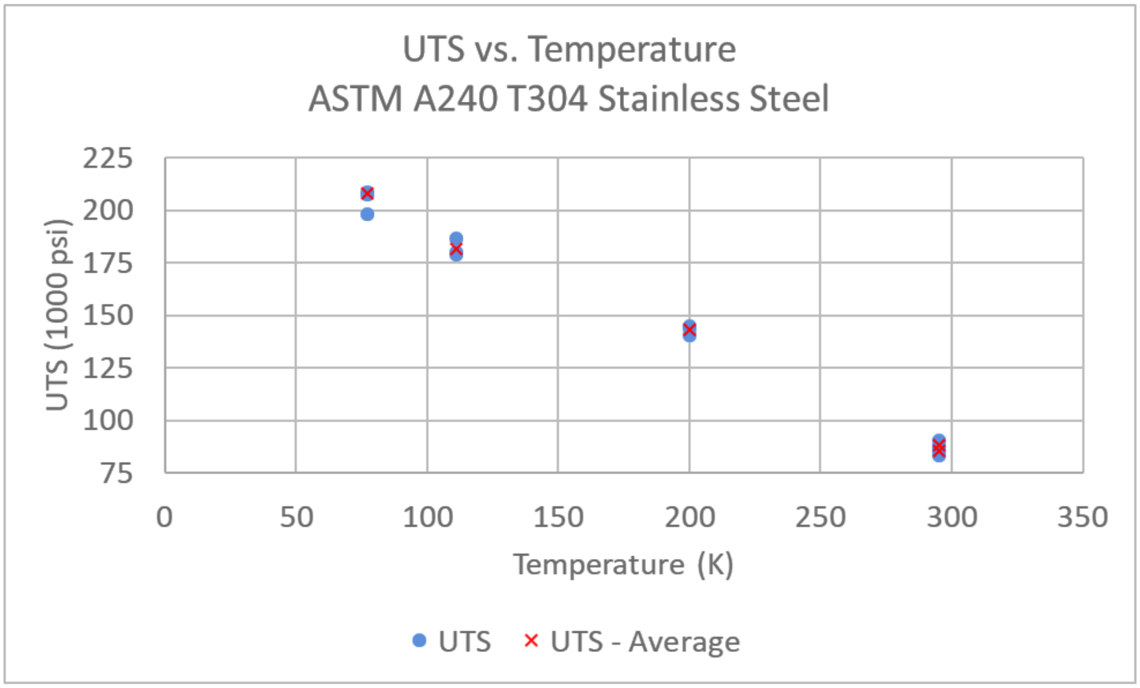

Figure 46. Graph of UTS Versus Temperature for T304 Stainless Steel

Figure 47 presents the EB data from Table 9 as a graph of EB versus temperature. The EB from each individual coupon is plotted as a solid circle and the average EB from a given lab and a given temperature is plotted as an "X." In general, the data show a decrease in EB as the temperature decreases further below room temperature.

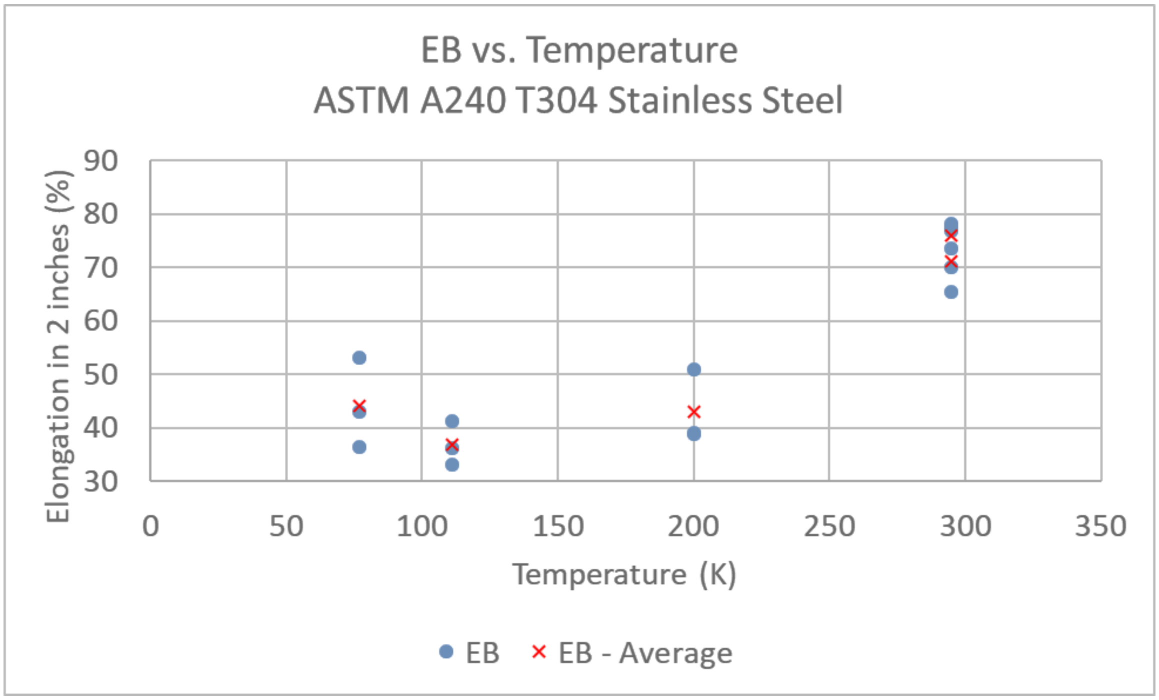

Figure 47. Graph of EB Versus Temperature for T304 Stainless Steel

It should be noted that at the lowest temperature of 77 K both the average EB and the EB of two individual coupons are higher than the EB at the next-lowest temperature of 110 K. Additionally, it should be pointed out that at all temperatures, the EB measurements exhibited considerable spread. While it is generally apparent that the EB at cryogenic temperatures is less than the EB at room temperature, further testing may be appropriate to better characterize whether the EB continues to decrease with further decreasing temperature. Additional testing may be able to better quantify the EB at each temperature.

The tensile testing demonstrated that the stainless steel in the inner tank exceeded the minimum values of YS, UTS, and EB required of ASTM A240 T304 stainless steel at room temperature.

4.5.2 Carbon Steel (Outer Tank)

Table 10 summarizes the mechanical properties of the carbon steel samples. The specification reference values in this table are taken from the 1969 edition of ASTM A516 [20], as the DOT-113 tank car used in this test was constructed in 1976.

Table 10. Summary of YS, UTS, and EB from Tensile Tests of Carbon Steel

	Sample	Lab 1	Lab 2
YS (thousand psi)	Coupon	33.8	33.3
	Coupon	37.1	33.9
	Coupon	34.9	34.3
	Average	*35.3*	*33.8*
	Specification Requirement	***38***	***38***
UTS (thousand psi)	Coupon	54.1	55.1
	Coupon	54.1	54.2
	Coupon	53.8	54.6
	Average	*54.0*	*54.6*
	Specification Requirement[9]	***70–85***	***70–85***
EB (2-inch gage) (%)	Coupon	44.4	42.0
	Coupon	41.5	63.0
	Coupon	42.6	43.9
	Average	*42.8*	*49.6*
	Specification Requirement	***21***	***21***

In addition to preparing the tensile specimens for mechanical testing, TTCI's laboratory performed a chemical analysis to determine whether the composition of the steel met the requirements of ASTM A516-70 [9] [20] steel. Table 11 presents the results of that analysis. This analysis revealed that the carbon steel plate in the tested DOT-113 tank car had levels of manganese and silicon that did not meet the minimum level required by the A516-70 specification. Reference values for the elements in A516-70 steel are shown from both the 2006 edition [9] of this specification and the 1969 edition [20] of the specification, as the DOT-113 tank car used in this test was built in 1976. While the allowable levels of certain elements changed between 1969 and 2006, the manganese and silicon levels in the DOT-113 carbon steel plate were below the minima specified in both editions.

---

[9] In the 2006 edition of ASTM A516-70, the UTS range is 70–90 ksi.

Table 11. Chemical Composition Analysis Results

Element	ASTM A516-70 (2006) Product Composition (%)	ASTM A516-70 (1969) Product Composition (%)	TTCI Product Analysis (%)	Note
Carbon (max.)	0.27	0.27	0.1356	Meets specification
Manganese	0.79–1.30	0.8–1.25	0.4824	Below specification minimum
Phosphorus (max.)	0.035	0.035	0.0059	Meets specification
Sulfur (max.)	0.035	0.04	0.0084	Meets specification
Silicon	0.13–0.45	0.13–0.33	0.0813	Below specification minimum

The tensile testing demonstrated that the outer tank exceeded the minimum value for EB but did not meet the minimum values for YS or UTS, required of ASTM A516-70 steel. The chemistry analysis demonstrated that the outer tank did not meet the minimum content requirements for silicon or for manganese as specified by ASTM A516-70.

Following the test, TTCI's material laboratory also performed microstructural analysis on three samples taken from the puncture zone of the inner stainless-steel tank. The areas of characterization are shown in Figure 48. Appendix B, Section 5 provides the results.

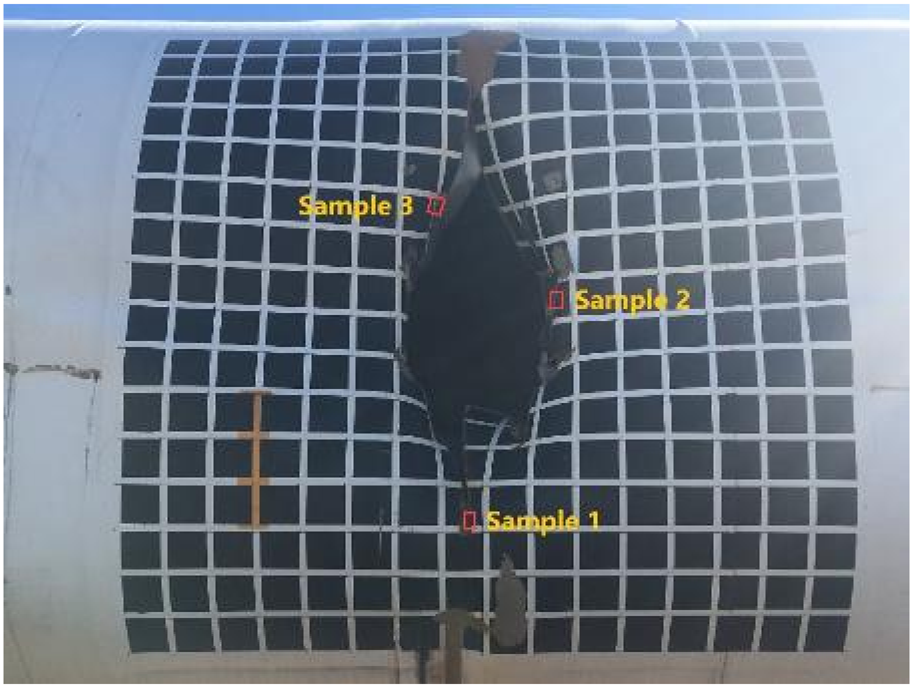

Figure 48. Areas of Puncture Selected for Post-Test Microstructural Analysis

4.6 Observations from Test Videos

After the test, the test videos were examined alongside the other data measured during the test. An analysis of the videos yielded several insights into behaviors measured during the impact test. Table 12 summarizes the key events observed during the impact test. In this section, the test data and corresponding still frames from test videos are discussed to better understand the sequence of events that occurred during this test. Based on the test video and test data correlation described in this section, the outer tank was confirmed to have torn first and the inner tank to have torn subsequently. This discussion is focused on the first 250 ms of the impact event, as that is the period of time during which the two tanks punctured.

Table 12. Summary of Key Events Observed in Test Data and Test Videos

Event	Source of Event Time	Time (ms)	Impactor Travel (in.)	Impact Force (kips)	Absorbed Energy (million ft. lbf.)	Air Pressure (psig)
Global peak force	Test data	113	30.4	817.1	1.14	54.2
Visible tear in outer tank	Onboard camera	125	33.1	488.5	1.29	55.1
Second peak force	Test data	195	46.0	770.8	2.00	58.3
First frame with visible water leakage	Onboard camera	209	48.1	487.7	2.12	59.9
Global peak pressure	Test data	211	48.4	328.4	2.14	59.9
First frame with visible water leakage	High-speed isometric camera	213	48.7	244.8	2.14	59.9

4.6.1 Time of Impact

For the high-speed isometric camera, the time of impact is known with a high degree of confidence. This high-speed camera captured 500 frames per second and featured a timestamp on each frame that was synchronized to a trigger in the impact zone. Additionally, a flashbulb was placed on the ram car within this camera's view. This flashbulb was also triggered at the moment of impact. Figure 49 (left) shows a still frame 0.002 second prior to impact from the isometric high-speed camera and Figure 49 (right) shows a still frame from the same camera at 0.0 second.

Note that in the frame at 0.0 second, the flashbulb is illuminated, indicating that the trigger has been activated.

Figure 49. Two Frames from Isometric High-Speed Video Showing t=-2 ms (left) and t=0.0 ms (right)

The camera on board the ram car was a ruggedized camera collecting video at approximately 240 frames per second. This camera was not tied into the triggering system. Thus, the frame corresponding to time of impact was estimated by examining this video frame-by-frame to find the first frame with visible deformation of the outer tank. The time of impact can only be known to occur between the prior frame and the first frame showing damage. At a framerate of approximately 240 frames per second, 4 ms elapses between consecutive frames. Thus, any frames extracted from the onboard video camera have a ± 0.004 second uncertainty associated with comparing the frame time with either the test data or corresponding frames from the isometric video. Figure 50 (left) shows the last frame without obvious deformation to the outer tank from the onboard video, and Figure 50 (right) shows the second frame with deformation to the outer tank (8.0 ms). The frame without deformation is used to establish a time of 0.0 seconds for all subsequent discussion of the onboard video.

Figure 50. Two Frames from Onboard Video Showing t=0.0 ms seconds (left) and t=8.0 ms (right)

4.6.2 Global Peak Force

The averaged force-time history data from four of the five onboard accelerometers was filtered with a CFC60 filter. Figure 51 shows the force-time history measured during the test, with a callout indicating the time and amplitude of the peak force. This global peak force occurred at a time of approximately 113 ms. This peak force occurred just prior to a drop in force of approximately 400 kips.

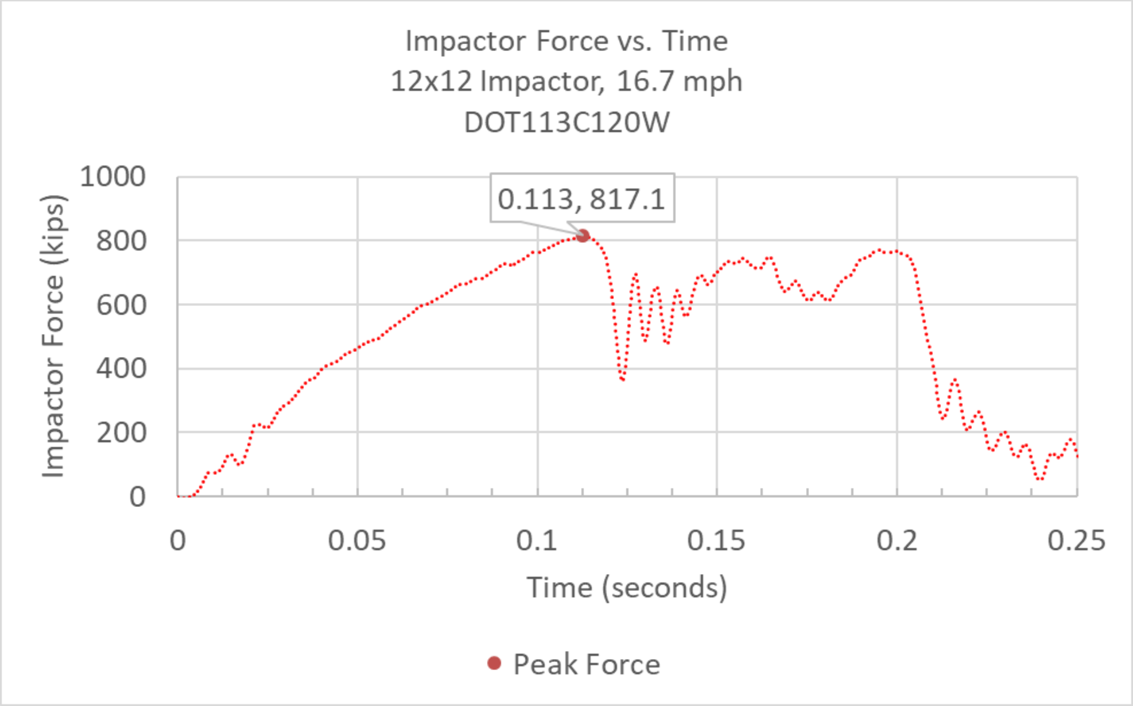

Figure 51. Impactor Force Versus Time with Peak Force Annotated

Figure 52 is a frame extracted from the high-speed isometric camera at a time of 113 ms. At this time, the indentation in the tank was apparent but there was no evidence of tank tearing based on what can be seen in the video frame.

Figure 52. Frame from High-Speed Isometric Video at 113 ms

4.6.3 Visible Tear in Outer Tank

Figure 53 contains a plot of impactor force versus time with an annotation for the time at which a visible tear was first observed in a frame from the onboard video. The error bars around this data point indicate ± 4 ms due to uncertainty around the exact time. From this figure, it is apparent that the time at which a tear was first visible in the outer tank occurred just after the 400 kip drop in force that followed the global peak force. Following this drop in force, the impact force partially recovered as the DOT-113's load-carrying capacity was not completely lost.

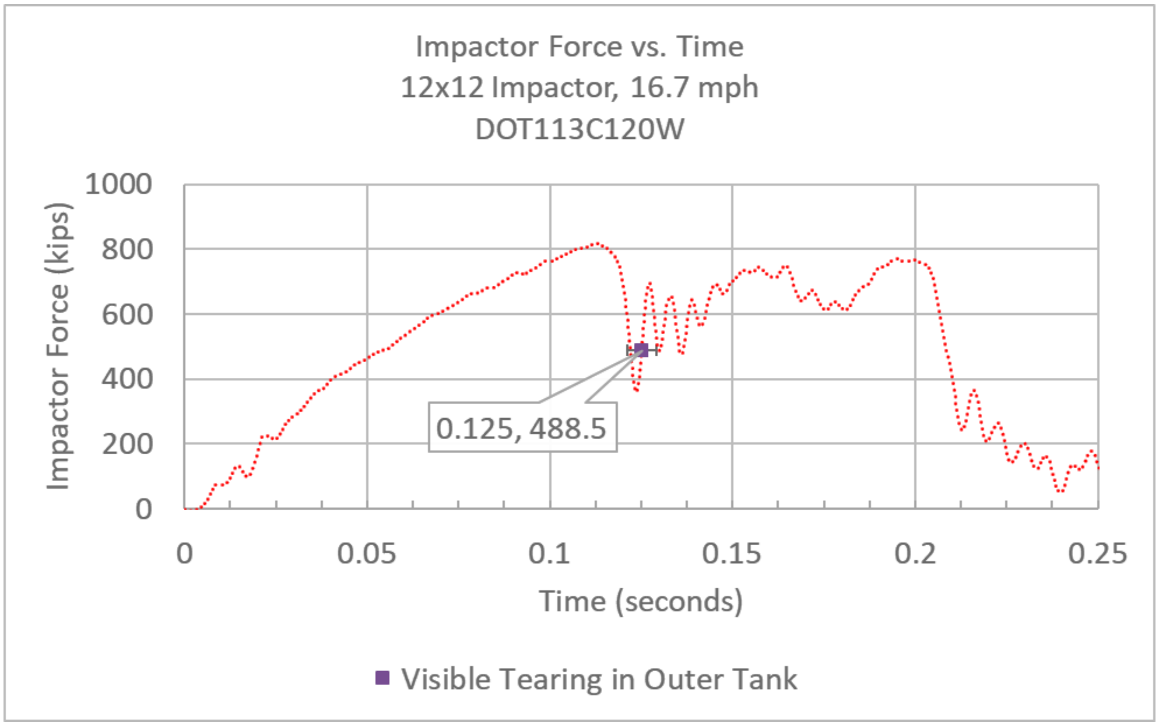

Figure 53. Impactor Force Versus Time with Time of Visible Tear Annotated

Figure 54 shows a frame extracted from the onboard video at approximately 125 ms. The inset image shows a focused view of the impact zone, with the region of the tear at the upper-left hand corner of the impactor indicated with the dashed box. Note that because the onboard video camera was mounted above the impactor, any tearing of the outer tank that occurred below the impactor was not captured by this camera. The frame indicates that tearing of the outer tank was first observable in the tank plate beneath the upper-left hand corner of the impactor in an area that was remote from any weld seams.

Figure 54. Frame from Onboard Video at 125 ms

Figure 55 shows a frame extracted from the high-speed isometric video at 125 ms. The indentation in the outer tank has extended outside of the painted grid by this point. By 125 ms, the impactor had traveled approximately 33.1 inches since it made first contact with the outer tank.

Figure 55. Frame from High Speed Isometric Video at 125 ms

4.6.4 *Second Peak Force*

Figure 56 contains a plot of impactor force versus time with an annotation for the time at which the second-highest peak force was measured during the test. The second peak force occurred at approximately 195 ms. This time is approximately 6 ms prior to a substantial drop in force. Following this second drop in force, the impact force does not recover.

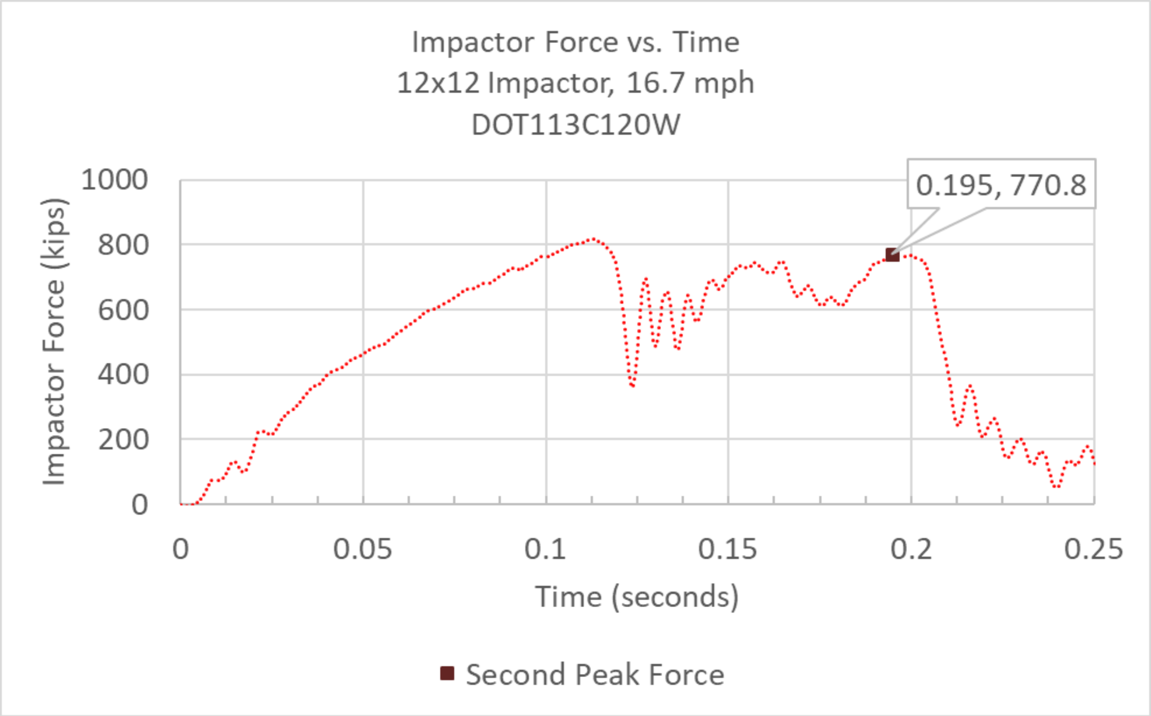

Figure 56. Impactor Force Versus Time with Time of Second Peak Force Annotated

Figure 57 shows a frame extracted from the high-speed isometric video at 195 ms, the time of the second peak force. The scope of the dent in the outer tank continued to extend and to sharpen since the frame shown at 125 ms (Figure 53). At 195 ms, the impactor had traveled approximately 46 inches since first making contact with the outer tank.

Figure 57. Frame from High-Speed Isometric Video at 195 ms

4.6.5 First Frame with Visible Water Escaping

Figure 58 contains a plot of impactor force versus time with annotations for the times at which water escaping the torn outer tank was first observed in a frame from the onboard video and from the high-speed isometric video. The error bars around the onboard data point indicate ± 4 ms due to uncertainty around the exact time. Taking the uncertainty of the onboard video timing into account, water leakage was observed in both videos at essentially the same time. This provides a good indication that the estimated time from the onboard video is reasonably close to the time triggered in the high speed isometric video.

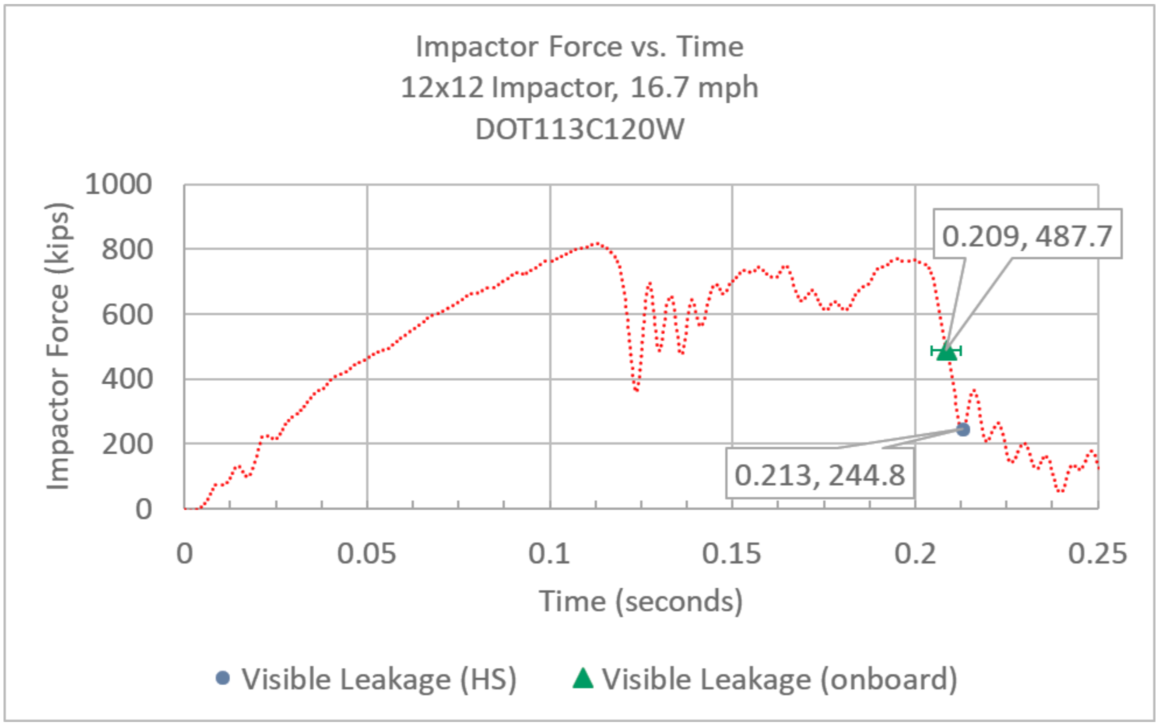

Figure 58. Impactor Force Versus Time with Visible Leakage

Figure 59 also demonstrates that the first observed water leakage through the torn outer tank occurred during the significant drop in impact force following the second peak force.

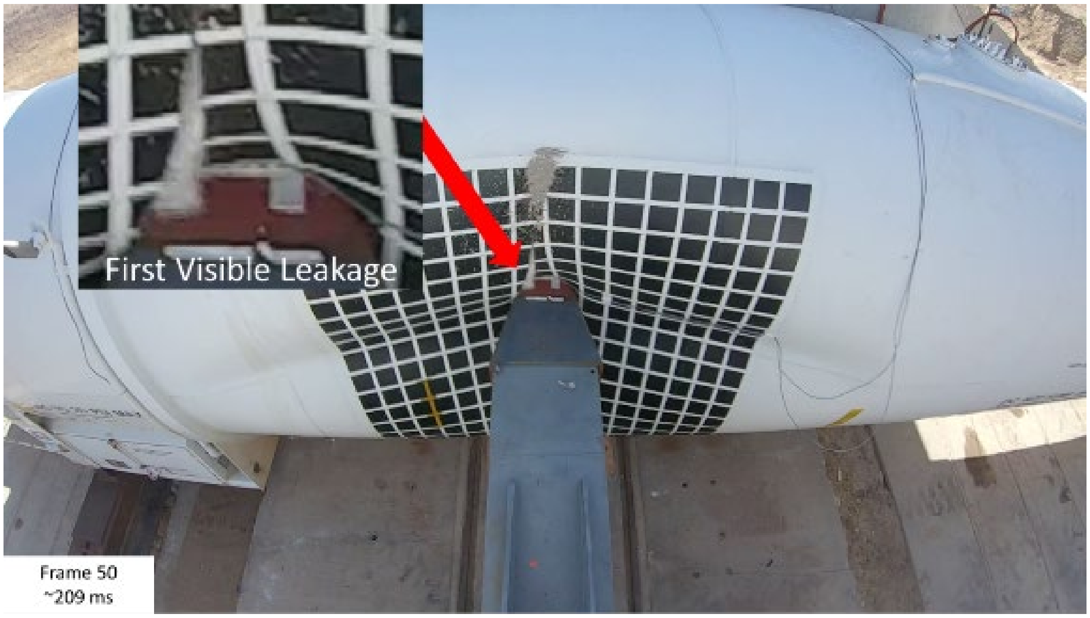

Figure 59. Frame from Onboard Video at 209 ms

Figure 60 shows a frame extracted from the high-speed isometric video at 213 ms. This is when water first visibly leaked from the tear in the outer tank under the upper-left corner of the impactor. This figure contains an inset image highlighting the visible water leakage. By 213 ms, the impactor had traveled approximately 48.7 inches since making first contact with the outer tank.

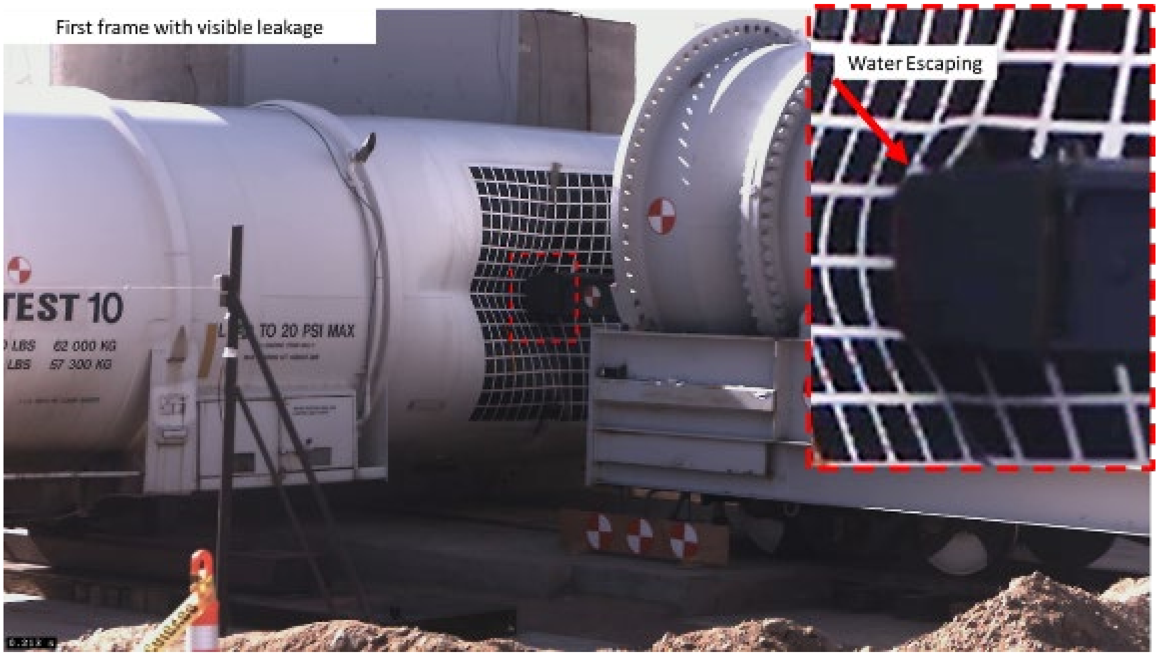

Figure 60. Frame from HS Isometric Video at 213 ms

4.6.6 Global Peak Internal Pressure

Figure 61 contains a plot of impactor force versus time with an annotation for the time at which the peak value of average outage pressure occurred during the test. The peak value of air pressure occurred at 211 ms which is between the time when water was first observed leaking from the outer tank as seen on the onboard video (209 ms) and on the high speed isometric video (213 ms). The peak average air pressure occurred toward the end of the sudden drop in force following the second peak force (195 ms).

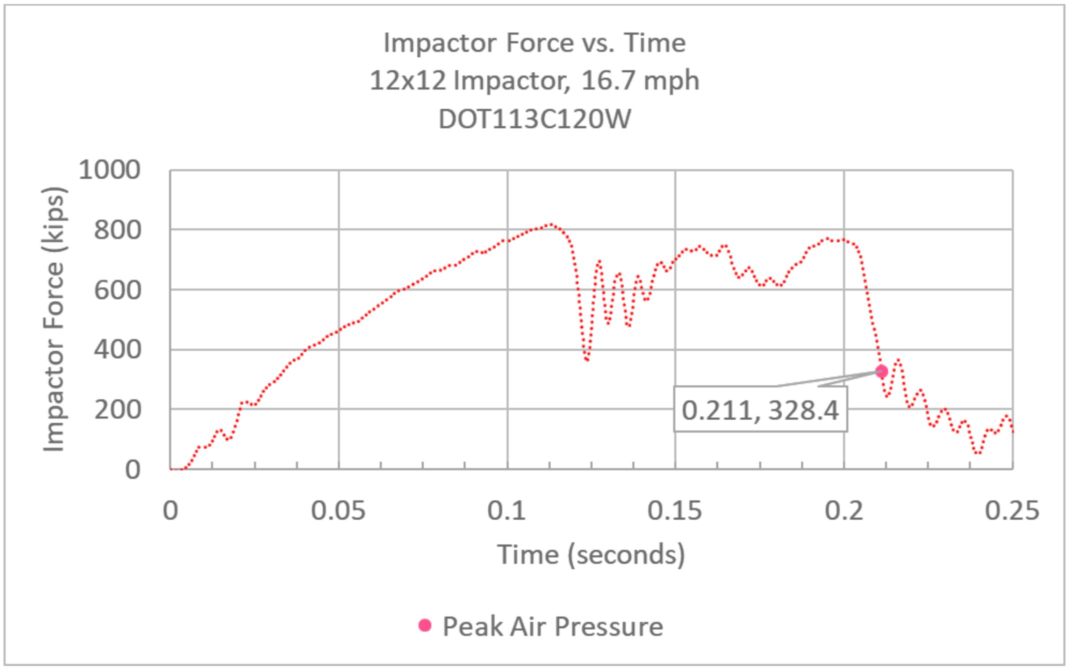

Figure 61. Impactor Force Versus Time with Time of Peak Average Air Pressure Annotated

Figure 62 contains a plot of the average outage pressure versus time, with the peak outage pressure (59.9 psig) annotated. As the DOT-113 tank car was initially pressurized to approximately 50 psig during the test, the pressure rise was approximately 10 psig, or 20 percent.

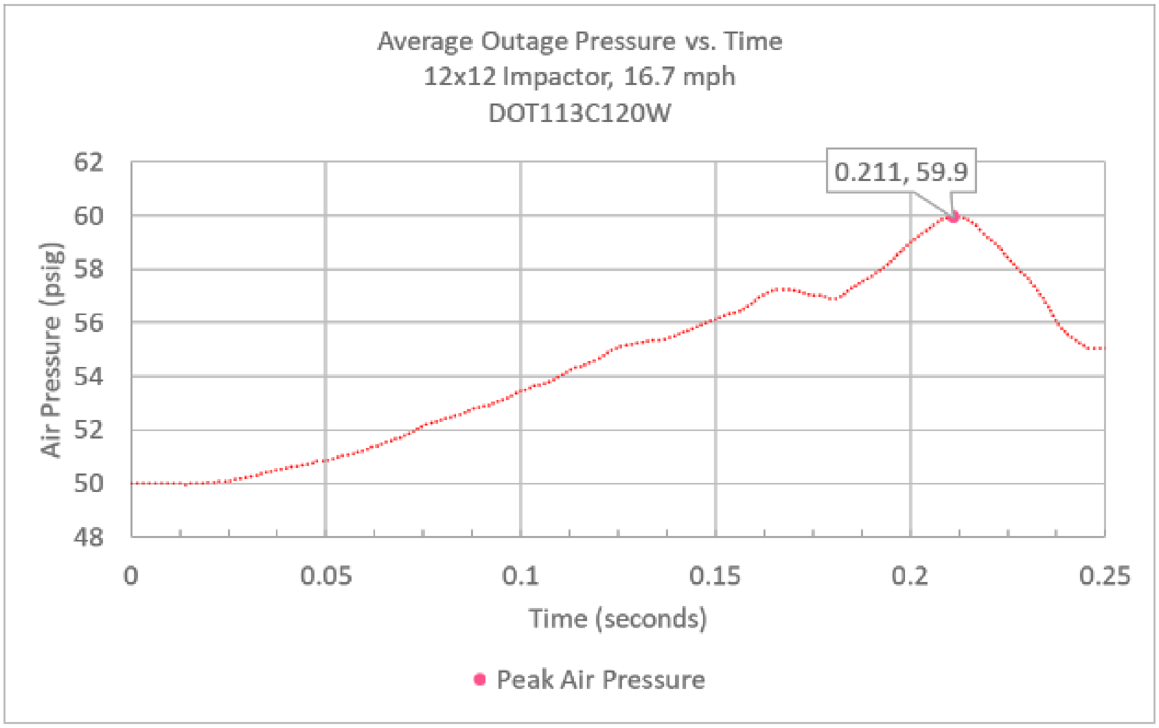

Figure 62. Average Air Pressure versus Time with Time of Peak Average Air Pressure Annotated

Because the inner tank reached its peak pressure at approximately the same time as when water was observed leaking out of the tear in the outer tank, there is evidence that the inner tank did not tear until approximately 210 ms.

4.6.7 Summary of Impact Sequence

Figure 63 shows the impactor force-time response. This figure includes annotations for all the events described in the previous sections. Based upon the correlation of test data and test videos, the test team concluded that the global peak force was limited by the tearing of the outer tank. The outer tank was visibly tearing just after measuring the peak force. The force continued to rise after this time until the second peak force was reached. This second peak force occurred just prior to when water was visibly leaking through the tear in the outer tank. The air pressure reached its maximum at a time nearly coincident with the observation of leakage through the outer tank. Thus, the test team concluded that failure of the inner tank corresponded to a time around when the second peak force was measured. The internal air pressure began to drop as the inner tank tore, allowing pressurized water to escape through the already-torn outer tank.

Figure 63. Annotated Plot of Impactor Force Versus Time

Figure 64 contains a plot of the impactor force versus impactor travel with the same annotations as the previous figure. Plotting force versus displacement rather than force versus time demonstrates that the impactor travelled a significant distance between the first and second peak forces.

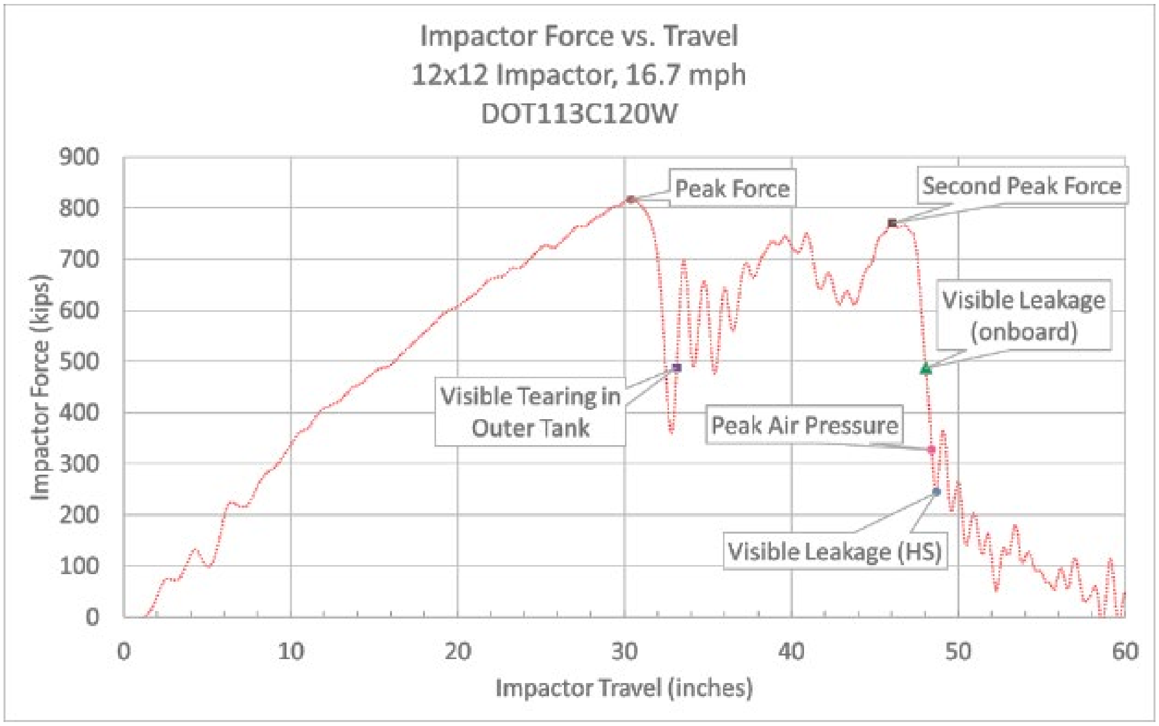

Figure 64. Annotated Plot of Impactor Force Versus Impactor Travel

Figure 65 contains a plot of the average outage pressure versus time with annotations for the key impact events. This figure demonstrates that the global peak force does not correspond to any significant response or change in behavior in the outage. Once a visible tear was observable in the outer tank, the outage pressure appeared to experience a change in slope but continued to increase its pressure. This reduction in slope may be attributed to the loss of annular space vacuum that occurred as the outer tank shell tore or to a redistribution of forces through the inner and outer tanks as the outer tank lost its load-carrying capacity due to the tear. This figure shows that a delay exists between the second peak force and the peak pressure, while the peak pressure and the observation of water spraying from the outer tank are coincident. The apparent lag between peak force and peak pressure may have been caused by a fluid inertia, where the moving fluids (air and water) took some time to "push back" against the now-compromised inner tank after being pushed away from the point of impact for the duration of the impact up to this point. The lag may also have been caused by the time necessary to propagate the tear in the inner tank to a size large enough to allow a significant volume of water to escape and thus reduce the pressure measured in the outage.

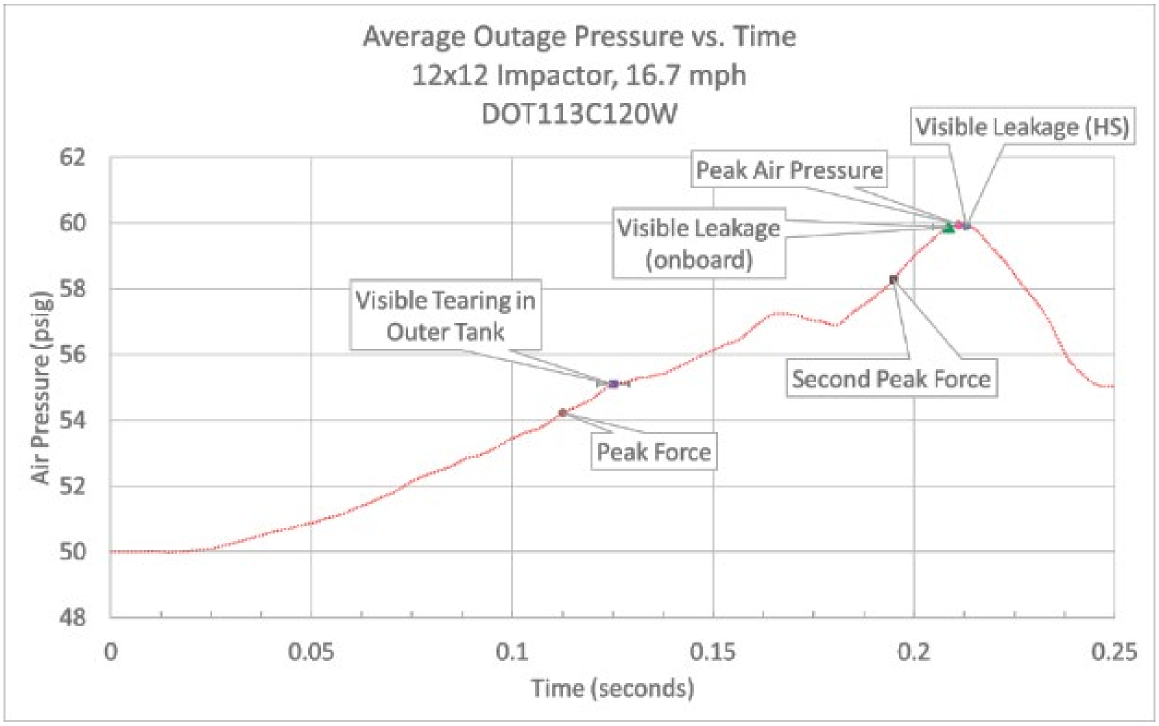

Figure 65. Annotated Plot of Average Outage Pressure versus Time

Figure 66 contains a plot of the absorbed energy versus time with annotations of key events. The absorbed energy was calculated by integrating the force-displacement response of the ram car. This plot shows that the slope of the energy-time response changed at approximately the same time that the visible tearing of the outer tank occurred. While the DOT-113 continued to absorb the impactor's energy, it did so at a slower rate once the outer tank tore and the force of resistance to the impactor motion dropped. This figure also visually illustrates the amount of energy absorbed by the DOT-113 prior to the outer tank tearing as well as the energy absorbed between the outer tank tearing and the inner tank tearing, as previously summarized in Table 12.

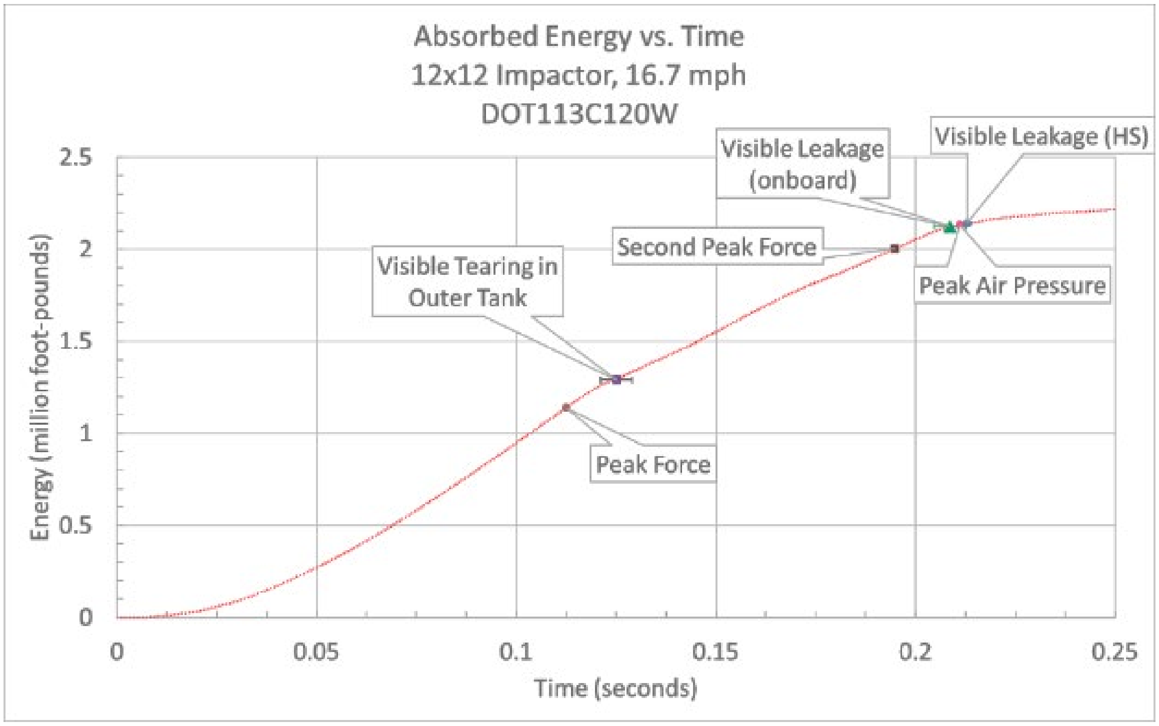

Figure 66**. Annotated Plot of Absorbed Energy Versus Time**

5. FE Model Development

Volpe developed FE models of the DOT-113 tank car prior to the test to estimate the desired impact speed while considering unknown parameters such as the exact material behaviors in the inner and outer tanks. The FE models incorporated and expanded upon several modeling techniques that had been used during simulations of previous tank car impact tests [10] [11] [12] [13] [14] [21]. The DOT-113 models required definition of the tank car geometry, geometry of the impact setup (e.g., impact wall, impactor, etc.), definition of boundary conditions, constraints, initial conditions, and development of several material models. Additionally, researchers selected modeling features such as element types, mesh sizes, and fluid/structure interactions . Three different sets of FE models are described in this report. Prior to the test, all FE models used estimated steel material behaviors for the inner and outer tanks. These models are referred to as pre-test models. Following the test, several updates were made to the material properties and other input conditions to better match the test conditions. These post-test models were updated in two stages and are described separately.

The models were assembled using the Abaqus/CAE preprocessor and executed in Abaqus/Explicit [22]. Abaqus/Explicit is a commercially available, general purpose nonlinear FE solver capable of simulating dynamic impacts involving complex material behaviors such as plasticity and puncture. The Abaqus software also includes several modeling techniques to represent the water and air phases of the lading, permitting these two parts to be modeled explicitly. The solid mechanics simulation features used in the DOT-113 models included modeling an elastic-plastic material response for the tank and jacket, ductile failure implementation of the Bao-Wierzbicki (B-W) [23] triaxiality-based damage initiation model, and ductile failure implementation of the Modified Mohr-Coulomb (MMC) [24] damage initiation model. Following the test, the model underwent several adjustments to better represent the actual test conditions.

After the test, these pre-test models were updated in two stages. Immediately after the test, several details of the test were apparent and could be implemented in the models right away. These models continued to use estimated pre-test material behaviors for the inner and outer tank steels and are referred to as post-test models using pre-test material behaviors. Finally, after the results of the material characterization tests were received, the post-test models were updated to reflect the actual test conditions, including the thicknesses and material behaviors of the actual tanks. These models are referred to as post-test models using post-test actual material behaviors.

5.1 Overview of Models

The pre-test and post-test FE models are made up of geometry representing the different components in the test setup, material parameters describing the behaviors of the materials making up the car and its lading, and numerous constraints, boundary conditions, and loads describing the conditions of the test. The DOT-113 tank car presented several unique FE modeling challenges compared to previously tested tank cars. The DOT-113 tank car featured an external tank and an internal tank. The desired test outcome was the puncture of both tanks. This required both tanks to be modeled with techniques that would simulate puncture. The outer tank was made of a carbon steel (A516-70) that had not been encountered in previous tank car tests, requiring the modelers to estimate the pre-test material behaviors. The inner tank was made of stainless steel that had not been encountered in previous tank car tests and required the modelers to estimate additional pre-test material models.

In an ideal pre-test model, the actual YS, UTS, EB, and the shape of the engineering stress-strain response would be known and used as inputs to the model. Prior to this test, the DOT-113's material properties could not be known without excising coupons from each tank. For the pre-test models, lower- and upper-bound estimates based on the ductility of each material were made based on published data from various sources found in Appendix F. The development of the pre-test upper- and lower-bound estimates of the A516-70 outer tank material responses is described in detail in Appendix F, Section 3.1. The development of the pre-test upper- and lower-bound estimates of the T304 inner tank material responses is described in detail in Appendix F, Section 4.1.

Puncture-capable FE models feature more complex material definitions and meshes than non-puncture models. These models include refined meshes on the inner and outer tanks in the areas of contact with the impactor and material modeling behaviors to simulate element degradation and removal. For the DOT-113, the refined area was meshed using solid elements on both the inner and outer tanks. Because the desired outcome of the DOT-113 test was puncture of both tanks, the solid patch of elements on the outer tank needed to be large enough to not only capture the initial tearing of the tank, which typically occurs beneath a corner of the impactor, but also to allow the tear to propagate until such a time as the inner tank punctured. This required a much larger solid patch of elements on the outer tank than had been used in previous tank car FE models. It was important to include a sufficiently large patch of solid elements in the outer tank to allow the tear to propagate fully without being artificially arrested by reaching the limits of the solid patch as that could result in the modeled DOT-113 placing less demand on the inner tank than would be experienced during an impact test. Outside of the impact zones, both the inner and outer tanks were meshed using shell elements.

The annular space featured both perlite and a vacuum, neither of which had been encountered in a previously tested tank car. The mechanical properties of perlite were not known prior to the test, and it was not well understood what role, if any, the perlite would play in the structural response of the tank car under the test's impact condition. Prior to the test, the condition of the perlite in the tested car was unknown. Because perlite is a granular material, it was possible that years of service in a railroad environment had led to the perlite settling. It was also not known whether repeated cycles of thermal expansion and contraction of the inner tank had led to redistribution of the perlite. As a simplification, the pre-test FE models did not include the perlite.

The vacuum in the annular space was modeled by using external pressure on the outside of the outer tank and defining the pressure within the inner tank to account for both the gage pressure and the atmospheric pressure. This simplification is only accurate up to the point when the outer tank experiences a through-tear which would allow atmospheric air to enter the tank during the test. The external pressure and gravity were simultaneously applied to the model over the course of a "settling" step prior to the impactor making contact with the tank. The pre-test FE models did not account for the loss of vacuum in the annular space. Several post-test FE models used a prescribed pressure-time history to simulate loss of vacuum following the tearing of the outer tank.

As the point of impact on the tested DOT-113 tank car was planned to be offset from the centerline of the car, a symmetry boundary condition could not be used to simplify the geometry in the FE models. Thus, all the models discussed in this report are full-length models. To reduce the runtimes associated with using full-length models, the tanks' geometry had a reduced level of detail in the model than in the tested DOT-113, and structures expected to have an insignificant effect on the puncture speed (e.g., the stub sills) were omitted. These approximations have a relatively minor effect on the impact response of the tank under the test conditions. Figure 67 shows the pre-test model. The assembly of the pre-test model was similar to that of the post-test model.

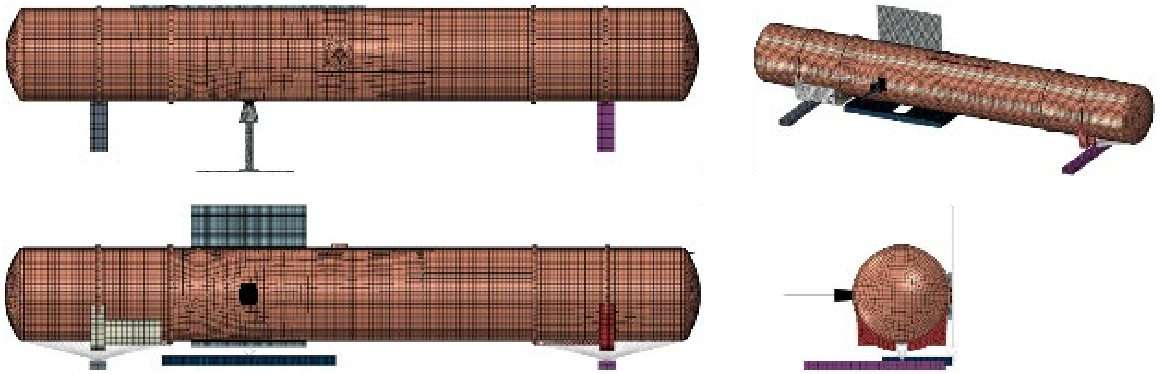

Figure 67. Four Views of Pre-Test FE Model

The combination of a large patch of solid elements in the outer tank, a second patch of solid elements in the inner tank, a need for a "settling" step for the initial pressures to equalize, and a lack of symmetry in the model led to the DOT-113 FE models having a significant runtime of multiple days on a dedicated simulation server. This long runtime limited the number of pre-test simulations that could be conducted. The need to include these features also led to certain other simplifications to the geometry and fluid representations of the tank car to prevent the runtime from growing even longer.

The lading in the DOT-113 FE model was represented using a hydraulic cavity for the water phase and a pneumatic cavity for the pressurized air phase. This approach is the same as was used for the pre- and post-test models of two previous tests of DOT-105 tank cars in the FRA testing program [13] [25]. The cavity approach is a simplified modeling technique that represents the fluid species, either gas or liquid, using an average pressure over the entire volume of that species. As the volume enclosing the pneumatic cavity is reduced through tank deformation, this average pressure will change over the course of the impact simulation. This dual-cavity approach to fluid modeling gave satisfactory representation of the fluid response seen in this test with a pressurized DOT-113 tank car, while offering considerable computational efficiency over an explicit representation of the liquid phase geometry and hydrodynamic behaviors (e.g., Lagrangian, Eulerian, or smoothed particle hydrodynamics [SPH] representations).

The parts included in the model can generally be divided into three categories: rigid bodies, deformable bodies made of steel, and deformable bodies made of other materials. A section view, with the cutting plane passing through the center of the impactor, is shown in Figure 68. This image includes annotations denoting the various parts making up the assembly of the DOT-113 tank car FE model.

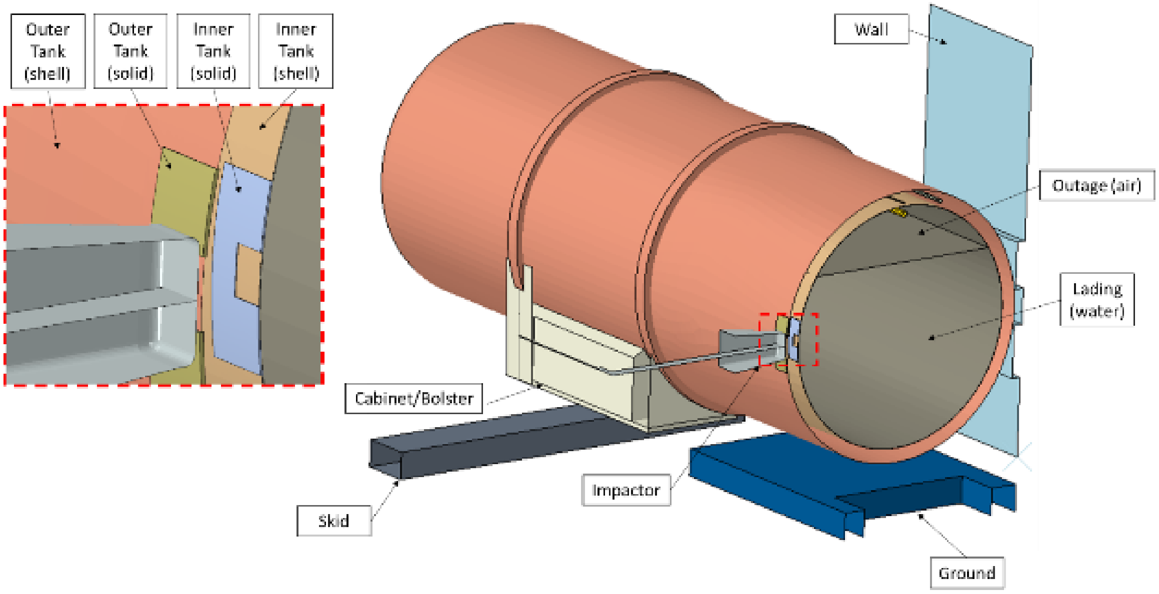

Figure 68. Section View Through Impact Plane with Annotated Parts

Table 13 contains a summary of the parts making up the FE model used in the pre-test puncture simulations including the weight of the part in the model and the number of elements in that part's mesh. Due to the adjustments made between the pre- and post-test models, the meshes and part weights were slightly different in the post-test models. Appendix D provides a full description of each part in both the pre-test and post-test models.

Table 13. Summary of Parts in Pre-Test FE Models

Type of body	Part name	Number of elements	Part weight (lbf)
Rigid	Impactor	5,782	297,126
Rigid	Rigid wall	9,658	N/A
Rigid	Skid	371	9,600
Rigid	Ground	11,973	N/A
Deformable, steel	Outer tank (shell elements)	23,803	45,850
Deformable, steel	Outer tank (solid elements)	927,392	43
Deformable, steel	Inner tank (shell elements)	23,382	25,100
Deformable, steel	Inner tank (solid elements)	435,400	16
Deformable, steel	Piping	32,400	620
Deformable, steel	Bolster and cabinet	1,482	1,600
Deformable, non-steel	Internal membrane	23,866	232,950

From Table 13, the total weight of the parts in the pre-test FE model corresponding to the entire DOT-113 (e.g., inner and outer tanks, bolsters, cabinets, piping, and water) would be approximately 327,000 lbf. This weight exceeds the 263,000-pound weight limit to which the DOT-113 was originally designed. The single heaviest part in both the FE model and the test setup was the water within the tank car. As previously discussed in Section 2.2.2, water was used in the test to account for both the mass and the dynamic effects of a fluid-filled tank car. As this tank car was designed to carry cryogenic materials having a lower density than that of water, the tank car was intentionally overloaded (by weight) for the test to maintain a filling volume that was similar to what would be expected in cryogenic service. Thus, the model was loaded with water having a mass that matched the test condition.

5.2 Material Behaviors in FE Models

Several material definitions were used in both the pre and post-test FE models: ASTM A240 T304 stainless steel, ASTM A516-70 carbon steel, a membrane material, air, and water. An additional material, perlite, was only used in the post-test models. This section summarizes the material properties input to the FE models. Appendix F gives complete descriptions of the development of the stainless steel, carbon steel, and perlite material models.

5.2.1 ASTM A240 T304 Stainless Steel

One purpose of this test was to subject the tank car to a moderately high-speed impact that was sufficient to puncture both the inner and outer tanks, without leaving the ram car with excess of kinetic energy at the time of puncture. While it was known from the certificate of construction and other tank car documentation that the inner tank's shell had a nominal thickness of 0.25 inch and was made of ASTM A240 T304 stainless steel, the actual plastic stress-strain response and EB would not be known until coupons could be excised from the tank car's inner shell and subjected to tensile testing. Pre-test material properties were estimated from published sources of mechanical test results on similar stainless steels to T304. Post-test material properties were calibrated based on post-test tensile testing of the actual material making up the inner tank of the tested DOT-113.

Pre-Test

Publicly available mechanical test data from two alloys of stainless steel similar to the T304 used in the DOT-113's inner tank, T304L [26] and T316L [27], were compiled and analyzed as a means of developing upper- and lower-bound estimates for pre-test material models.

The published curves for a series of mechanical tests using different coupon geometries were used to develop the true stress-strain behaviors of the upper- and lower- ductility estimates of the T304 steel. Tensile coupon tests were simulated, and the simulation outputs were compared to the behaviors reported in these sources. The minimum and maximum engineering properties obtained from the outputs of the FE models of tensile tests of stainless coupons are summarized in Table 14. It should be noted that both the lower- and upper-ductility T304 material models exhibited YS, UTS, and EB in 2 inches that exceeded the minimum requirements of the specification [3]. Additional details on the development of the pre-test material behaviors for T304 can be found in Appendix F, Section 4.1.

Table 14. Summary of Mechanical Properties of T304 from Pre-Test Estimates

Name	YS (ksi)	UTS (ksi)	EB in 2 inches (%)
Pre-test upper ductility	46	90	79
Pre-test lower ductility	46	90	67

The material properties for the pre-test T304 materials are summarized in Table 15.

Table 15. Summary of Material Properties for Pre-Test T304

Parameter	Value
Mass density	7.35×10^{-4} lbf-s^2/in^4
Modulus of elasticity	3×10^7 psi
Poisson's ratio	0.25
Plasticity	Piecewise Nonlinear (see Appendix F, Section 4.1)
Damage initiation	MMC Surface (see Appendix F, Section 4.1)
Damage progression	Displacement = 0.03 in/in^2, exponent = -2 (upper ductility) Displacement = 0.0015 in/in^2, exponent = -2 (lower ductility)
Mesh implementation	0.05-inch reduced integration brick (C3D8R) elements

In addition to requiring a plastic stress-strain response, the pre-test FE models required that damage initiation and damage progression behaviors be defined for the upper- and lower-ductility estimates. As described in Appendix F, Section 2.3, a MMC damage initiation surface was calibrated based on a series of FE simulations of mechanical tests on a variety of coupon geometries. Figure 69 shows the nominal stress-strain response obtained from the tensile coupon simulation for the pre-test T304.

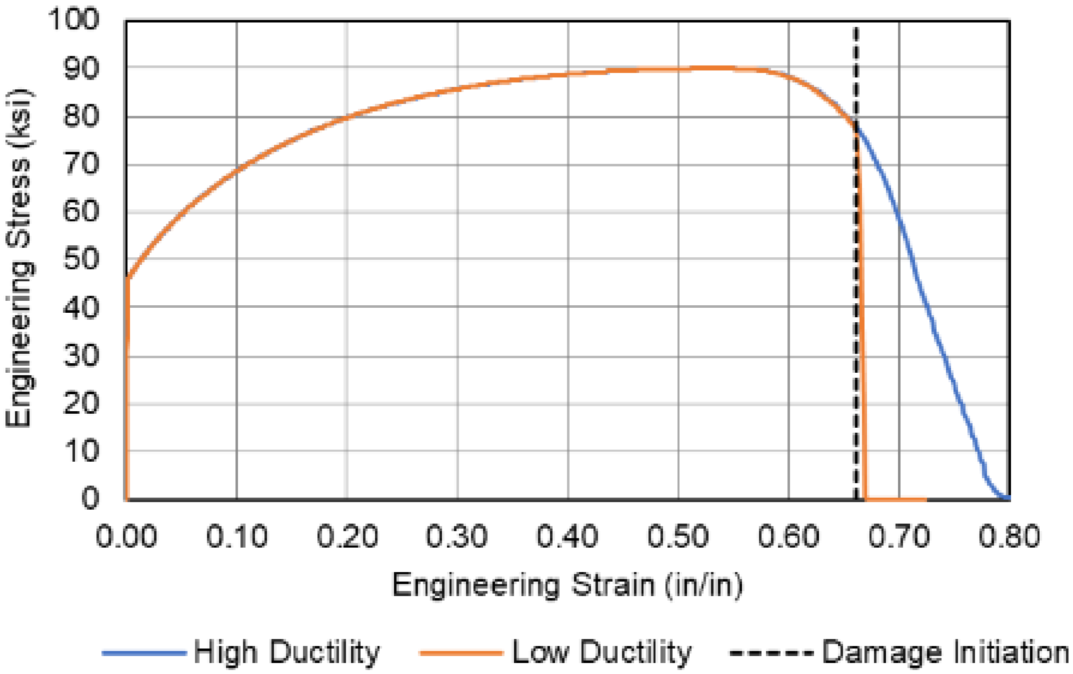

Figure 69. Pre-Test Engineering Stress-Strain Tensile Coupon FE Results for T304 Steel with High and Low Estimates of Ductility

Post-Test

After the impact test, material coupons were cut from an undamaged area of the tested DOT-113 tank car and subjected to tensile testing at room temperature at two different labs and at a variety of cryogenic temperatures by one of the labs. Rectangular dogbone (DB) coupons with a 2-inch gage length were cut from the plate removed from the inner tank's shell. The typical dimensions of the rectangular coupons were 2-inch gage length, 0.5-inch gage width, and 0.281-inch thickness. Note that the inner tank had a nominal thickness of 0.25 inch reported in its documentation, but all tensile coupons were reported to have a thickness in excess of the nominal thickness.

Post-test material testing of T304 stainless steel was performed at a range of cryogenic temperatures: -321 °F (77 K), -260 °F (111 K), -100 °F (200 K), and at room temperature (71 °F, or 295 K). The mechanical properties of the stainless steel at cryogenic temperatures were measured in anticipation of future modeling examining the puncture performance of the DOT-113 tank car under conditions more representative of service conditions. Post-test material model development for actual T304 was only performed for the room temperature properties, as the post-test DOT-113 model must first have been validated through successful simulation of the conditions of the test. Additional material model development for T304 at cryogenic temperatures is anticipated in support of future modeling and will be documented in a future technical report.

Three post-test material behaviors were calibrated for the T304 stainless steel in the inner tank in an attempt to estimate limit cases for the puncture response observed during the test. The first post-test material behavior used the MMC damage initiation envelope from the pre-test model, which happened to be in good agreement with the actual tensile properties of the inner tank.

However, the pre-test MMC damage initiation envelope resulted in an overestimation of the puncture resistance of the inner tank. The second post-test material behavior used a B-W damage initiation envelope and was closer to the actual puncture response observed in the test but still overestimated the puncture resistance.

While the first two material models were calibrated based on quasi-static (QS) tensile test data, research from Paik [28] and Kirkpatrick [26] showed that the mechanical properties of stainless steel are sensitive to rate effects. The third post-test material behavior used a B-W damage initiation envelope calibrated based on the tensile properties reported by Kirkpatrick [26] for T304L stainless steel tested at a rate of 0.1 in/in/s. This rate was chosen because it resulted in the lowest properties for UTS and EB out of the rates that were tested in the referenced report. This third post-test material behavior estimated a lower puncture resistance in the inner tank response, so the material calibration was stopped at this point.

Additional material calibration procedures could have been performed in an effort to achieve a response that matched what observed in the test. Such procedures, however, would have been focused on model calibration (tuning) instead of model validation. The lessons learned from this test on the damage initiation models and strain rate sensitivity of stainless steel will be applied in future tests with stainless steel tanks to validate the FE model.

The details of each post-test material calibration are provided in Appendix F, Section 4. Figure 70 shows the engineering stress-strain response from a model of the rectangular DB coupon cut from the inner tank using each of the three post-test material calibrations. This figure also includes the average QS UTS and EB from the tensile tests for comparison.

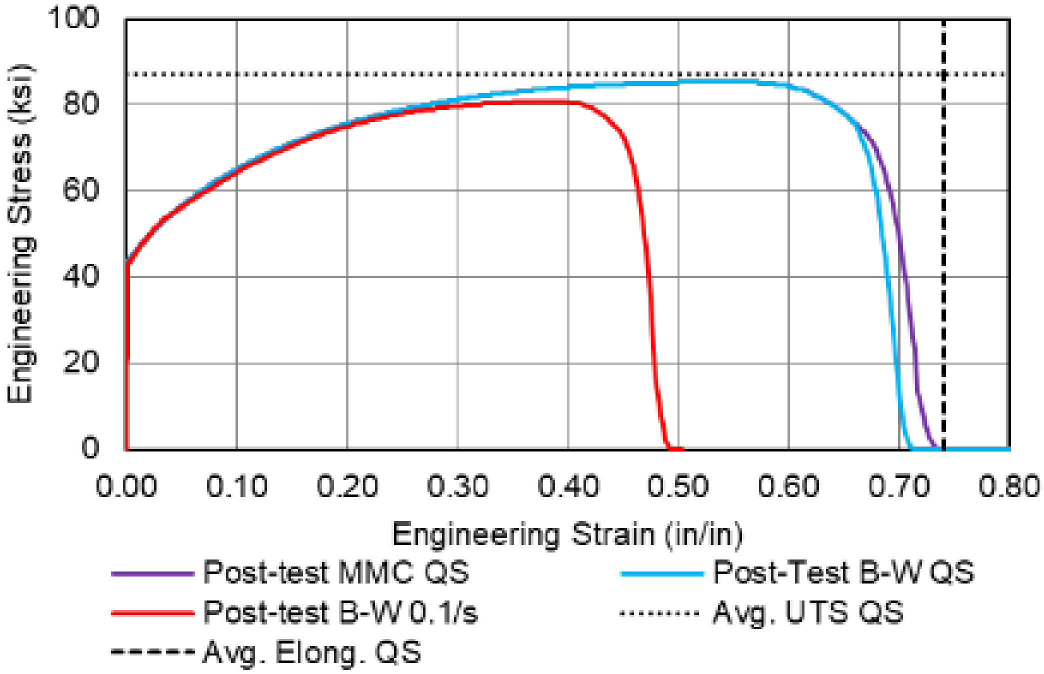

Figure 70. Engineering Stress-Strain Response from the Three T304 Post-Test Material Calibrations Applied to a Flat Tensile FE Model with Average Qs Tensile Properties (Dashed) For Comparison

From Figure 70, it is apparent that the QS MMC and B-W post-test material calibrations resulted in similar uniaxial tensile responses; however, a difference in puncture resistance was observed (refer to Section 7.2) when each material was applied to the full-scale tank car model. A significant reduction in EB was observed in the third post-test calibration based on 0.1 in/in/s tensile test data. This less ductile response also resulted in a significant reduction in puncture resistance in the inner tank (refer to Section 7.2).

5.2.2 ASTM A516-70 Carbon Steel

One goal of this test was to subject the tank car to a moderately high-speed impact that was sufficient to puncture both the inner and outer tanks without leaving the ram car with an excess of kinetic energy at the time of puncture. The certificate of construction and other tank car documentation showed that the outer tank's shell had a nominal thickness of 7/16 (0.4375) inch and was made of ASTM A516-70 carbon steel. However, the actual plastic stress-strain response and EB of this steel would not be known until coupons could be excised from the tank car's outer shell and subjected to tensile testing. Pre-test material properties were estimated from published sources of tensile test results on A516-70. Post-test material properties were based on post-test tensile testing of the actual material making up the outer tank of the tested DOT-113.

Pre-Test

The modeling team compiled and analyzed publicly available tensile test data from A516-70 steel as a means of developing upper- and lower-bound estimates for pre-test material models. The minimum, maximum, and average properties obtained from the compiled A516-70 data are summarized in Table 16. Additional detail on the development of the pre-test material behaviors for A516-70 can be found in Appendix F, Section 3.1.

Table 16. Material Properties from Published Sources for A516-70

Property	Min (including specification)	Min (excluding specification)	Average	Max
YS (*ksi*)	38	39.9	51.7	75.8
UTS (*ksi*)	70	70.9	77.2	86.4
EB in 2 inches (%)	21	28	34.1	40
EB in 8 inches (%)	17	17	23.9	30

Two published sources [26] [29] included engineering stress-strain curves over the full range of EBs measured during tensile tests. These stress-strain curves were used to develop the true stress-strain behaviors of the upper- and lower- ductility estimates of the A516-70 steel. The modeling team simulated tensile coupon tests and compared the simulation outputs against the engineering stress-strain behaviors reported in these sources. Table 17 summarizes the engineering properties of the two pre-test A516-70 materials.

Table 17. Summary of Engineering Properties for Pre-Test A516-70

Material Name	YS (ksi)	UTS (ksi)	EB in 2 inches(%)
Pre-test upper ductility	50	72	37
Pre-test lower ductility	54	73	29

Table 18 summarizes the material properties for the pre-test A516-70 materials.

Table 18. Summary of Material Properties for Pre-Test A516-70

Parameter	Value
Mass density	7.35×10^{-4} lbf-s^2/in^4
Modulus of elasticity	3×10^7 psi
Poisson's ratio	0.3
Plasticity	Piecewise nonlinear (see Appendix F, Section 3.1)
Damage initiation	(B-W) (see Appendix F, Section 3.1)
Damage progression	Displacement = 0.03 in/in^2, exponent = -8 (upper ductility) Displacement = 0.02 in/in^2, exponent = -2 (lower ductility)
Mesh implementation	0.05-inch reduced integration brick (C3D8R) elements

In addition to requiring a plastic stress-strain response, the pre-test FE models required that damage initiation envelopes and damage progression behaviors be defined for the upper- and lower-ductility estimates. As described in Appendix F, Section 3.1, the B-W damage initiation envelopes were iteratively calibrated to result in the desired EB for a 2-inch gage tensile coupon FE model based on the published stress-strain responses. The nominal stress-strain responses obtained from the tensile coupon simulations for the pre-test A516-70 materials are shown in Figure 71.

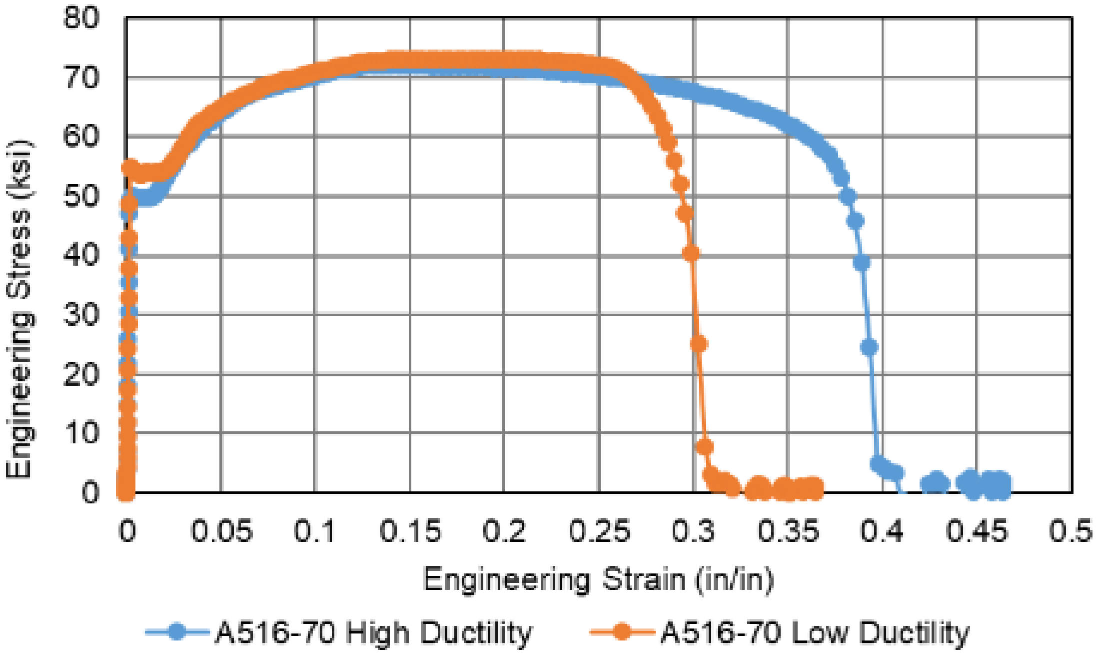

Figure 71. Pre-Test Engineering Stress-Strain Coupon Simulation Results for A516-70 Material Models

Post-Test

After the impact test, material coupons were cut from an undamaged area of the tested DOT-113 tank car and subjected to tensile testing by two different labs. Rectangular DB coupons with a 2-inch gage length was cut from the plate removed from the outer tank's shell. The typical dimensions of the rectangular coupons were 2-inch gage length, 0.5-inch gage width, and 0.463-inch thickness. Note that the outer tank had a nominal thickness of 7/16 inch (0.4375) reported in its documentation, but all tensile coupons were reported to have a thickness exceeding the nominal thickness.

Points were manually specified in the Lüder's (slip) band region of the true stress-true plastic equivalent (PEEQ) strain curve up to a PEEQ strain of 0.04 in/in. A curve fit based on the Swift-Voce Hardening Law relationship was applied for PEEQ strains from 0.045 in/in up to 2.0 in/in at an increment of 0.005 in/in.

The Lee-Wierzbicki "quick calibration" procedure [30] [31] was used to create a B-W damage initiation envelope using the results of the post-test A516-70 coupon testing. The damage progression was empirically defined as displacement based with exponential softening, and the targeted displacement was set to 0.022 in/in^2 with an exponent of -5. Figure 72 shows the engineering stress-strain results from the tensile simulations of the pre- and post-test A516-70 material models. The actual A516-70 material exhibited a lower YS and UTS than either pre-test estimate but a larger EB than either pre-test estimate. The measured YS and UTS were below the minimum levels required by the material specification, and the EB exceeded the minimum required by the material specification.

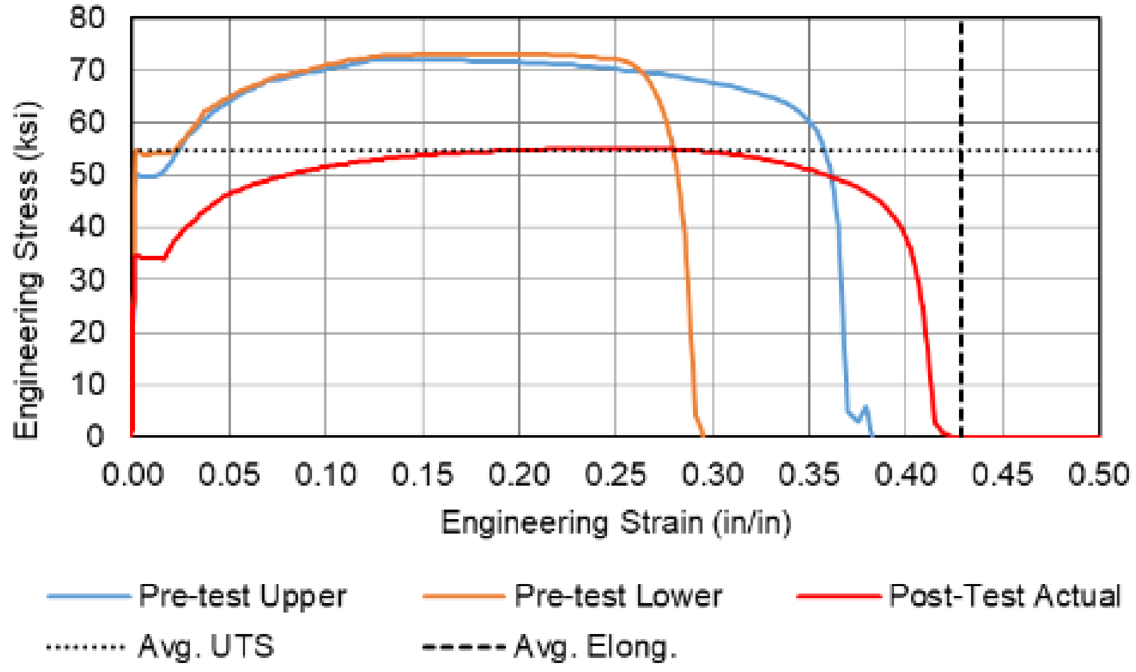

Figure 72. Post-Test Engineering Stress-Strain Coupon Simulation Results for A516-70 Material Models

5.2.3 Membrane

As described in Appendix D, Section 9, an artificial surface was modeled within the tank to define the limits of the hydraulic and pneumatic cavities. Because this surface did not correspond to any physical structure within the tank, modeling techniques were chosen to minimize the increase in either mass or stiffness introduced into the model by the membrane. The membrane material was modeled as having the mass density of steel to avoid the minimum time increment becoming dominated by the artificial material in the membrane. Table 19 summarizes the material properties of the membrane.

Table 19. Material Properties Defined for Membrane Material

Parameter	Value
Density	7.35×10^{-4} lbf·s^2/in^4
Modulus of Elasticity	3×10^4 psi

Additionally, a nonstructural mass was added to the membrane around the hydraulic cavity to account for the mass of the water within the tank. This nonstructural mass is described further in Appendix D, Section 9.

5.2.4 Air

The gas phase of the lading was modeled as air at a gauge pressure of 45 psi, as this was the desired internal pressure for the tank car at the beginning of the test within Abaqus, the air within the outage was modeled as an ideal gas, using a pneumatic cavity modeling technique. This modeling technique requires a surface that enclosed the cavity to be defined with a specific reference point within that cavity that was assigned an initial temperature and pressure. The initial pressure and temperature are discussed further in Appendix E, Section 9.

The pneumatic cavity approach models the entire cavity with a single average pressure and average temperature value, each of which can vary with time. The use of this technique allowed for a change in air pressure within the model as the volume of the tank changed due to the impact. The modeling inputs defined for the air phase of the model are summarized in Table 20 using the unit system used in the FE models.

Table 20. Properties for Air Used in FE Models

Property	**Value in Pre-Test Models**	**Value in Post-Test Models**	**Reference**
Universal Gas Constant (R): *in-lbf/(mol·K)*	73.583	73.583	[32]
Molecular Weight (MW): $(lbf{\cdot}s^2/in)/mol$	1.654×10^{-4}	1.654×10^{-4}	[33]
Constant Temperature: *K*	277	283	
Initial Pressure: *psig*	50	50	

The molar specific heat capacity for air was calculated according to Equation 1.

$$c_{P.m} = c_P \cdot MW$$

Equation 1. Calculation of Molar Specific Heat

Values for the specific heat capacity of air (c_p) were obtained from published values [34]. Table 21 shows the values calculated for molar specific heat at different temperatures using Equation 1. These values were defined in the FE model's unit system.

Table 21. Molar Specific Heat for Air

Temperature *K*	$c_{p,m}$ *in-lbf/(mol·K)*
250	257.2
300	257.7
350	258.5
400	259.7

5.2.5 Water

The initial conditions targeted for the side impact test of the DOT-113 tank car were set to an outage volume of 17.6 percent and internal pressure of 45 psig. The liquid phase of the lading was modeled as water at approximately 39 °F (277 K) in the pre-test models and approximately 50 °F (283 K) in the post-test models with corresponding property values within Abaqus, a hydraulic cavity model was used to describe the behavior of the liquid water. The key properties that must be input to this material model are the material's density and its bulk modulus. Values for density and speed of sound were obtained by interpolating published tabular values to the anticipated test temperature of 39 °F. Initial conditions are discussed further in Appendix E, Section 9.

The speed of sound (c) in a fluid can be determined from the fluid's bulk modulus (K) and density (ρ) according to the Newton-Laplace equation given in Equation 2 [35].

$$K = c^2\rho$$

Equation 2. Calculation of Bulk Modulus

The properties used in the DOT-113 tank car model are shown in Table 22. This table includes the specific units used in the unit system of the FE model.

Table 22. Properties of Water Used in FE Models

Property	Value in Pre-Test Models	Value in Post-Test Models	Reference
Mass Density (ρ): $lbf{\cdot}s^2/in^4$	9.42×10^{-5}	9.41×10^{-5}	[15]
Speed of Sound (c): in/s	55,930	56,990	[36]
Bulk Modulus (K): lbf/in^2	294,695	305,626	Equation 2

While density is among the parameters defined for the water in the hydraulic cavity, this value of density is only used by the solver to calculate the bulk modulus of the liquid in the hydraulic cavity. The mass of the water in the tank was represented as a distributed, nonstructural mass assigned to the membrane surrounding the hydraulic cavity. This nonstructural mass is described further in Appendix D, Section 9.

5.2.6 Perlite

The tested DOT-113 had approximately 6 inches of annular space between the inner and outer tanks. This space was filled with granular perlite and was under vacuum during the test, typical of service conditions. Pre-test modeling included the vacuum but did not include any representation of the perlite. The results from previously performed FRA-sponsored tank car impact tests showed that insulation materials had varying levels of influence on the test measurements. Consequently, the insulation materials could be omitted from some previous FE models without influencing the level of agreement but needed to be included in other models to attain a better level of agreement between the test and FE model results. For example, the 2017 test of a DOT-117 tank car featured 0.5-inch fiberglass insulation between the jacket and tank. This insulation was omitted from FE models without an appreciable effect on the ability of the model to agree with the test measurements [12]. On the other hand, during two tests of DOT-105 tank cars that used 4 inches of urethane foam insulation, the FE models needed some representation of this foam material to better match the structural response behaviors measured during the test [13].

Prior to the test of the DOT-113 tank car, several references were reviewed to attempt to estimate the role, if any, perlite would have in the structural response of the tank car. If perlite were expected to enhance the puncture resistance of the tank car, then omitting the perlite from the FE models would lead to a conservative model. In this context, a conservative model is a model that predicts puncture at a lower energy than would have occurred in the test. If perlite were expected to have no effect on the puncture resistance of the tank car, then omitting the perlite from the FE model would be expected to have no effect on the level of agreement between the model and the test. If the perlite were expected to have a detrimental effect on the puncture resistance of the tank car, then omitting the perlite would lead to a non-conservative model, i.e., a model that predicted a non-puncture outcome under test conditions that would in fact lead to puncture of the tanks.

One report examined prior to the DOT-113 test contained an economic analysis of the benefits of using perlite versus multi-layer insulation on a large, stationary cryogenic vessel planned for construction. While not an engineering analysis, this report contained the statement:

> *[multi-layer insulation] offers no resistance to deformation of the outer shell with respect to the inner shell; therefore, it is not effective as a protective media. However, perlite completely fills the annular space between inner and outer shell with a resilient 5-ft. layer of low-density material which will absorb the shock loads impinging upon the outer shell, thereby helping to prevent damaging distortions of the dual shell structure* [37].

This report further states:

> *[b]ased upon qualitative analysis, perlite appears to be superior to [multi-layer insulation] from the aspect of resistance to damage to the inner vessel from shock or shrapnel. A quantitative analysis to determine the extent of this superiority would require design information concerning the vessel support structure and a testing program to determine the actual effectiveness of perlite as a shock absorber* [37].

An additional report examined prior to the test attempted to estimate the energy losses of a bullet traveling through perlite as a means of assessing the ability of perlite to offer some impact protection to a stationary cryogenic storage vessel. In this report, the energy-absorbing effects of perlite are estimated using relationships for dry and wet sand. This report also investigated the effectiveness of perlite at resisting impacts from larger objects, such as debris thrown during a tornado. This report includes the statement that "[s]ufficient information was not available to calculate the reduction in velocity due to perlite insulation and whether existence of this material would prevent perforation of the inner tank" [38].

Another report examined prior to the test documented various strategies for mitigating the effects of blast loading pipelines. One technology examined used 3-inch diameter compartments filled with perlite and wrapped around the pipeline to be protected. This report documented efforts at FE modeling of perlite, where the perlite was treated as a sandy soil material. However, this report concluded that the effectiveness of the blast mitigation offered by a 3-inch layer of perlite was essentially equivalent to the blast mitigation offered by a 3-inch air gap around the pipeline. Thus, the perlite "adds minimal structural resistance" for the blast loading examined [39].

Based on the limited data available prior to the test, it appeared that perlite would be expected to have either no effect or a positive effect on the puncture resistance of the DOT-113. Thus, by omitting the perlite from the pre-test FE models, the models were expected to be conservative.

Examination of the tank car after the test revealed that the perlite in the annular space was packed in fairly tightly, rather than the loose fill that was expected to be found. Additionally, a review of the test data and pre- and post-test models without perlite indicated discrepancies in the global force-time and force-displacement histories that were not corrected by including the actual material properties of the inner and outer tank car steels, the actual test pressure and temperature in the lading or the actual impact speed. The test outcome demonstrated that omitting the perlite from the pre-test FE models was, in fact, non-conservative.

Perlite Material Model 1: "Sandy Soil"

As a means of investigating whether the perlite was a likely source of discrepancy, a simplified approach to modeling this material was implemented in the post-test FE models. Because modern DOT-113 cars more typically use MLI in the annular space rather than perlite, a significant research effort at characterizing the mechanical properties of perlite for use in crashworthiness analyses would be of limited value. In lieu of a significant effort that would only be of limited value, a simplified FE representation of perlite was developed using data available in the literature.

One approach described in the literature was to treat perlite as a sandy soil, using an existing FE material model for the sandy soil and adjusting the properties of the sandy soil to better match perlite [39]. An existing model of sandy soil, developed for use in Abaqus/Explicit, was found in the literature [40] and adapted as described in Appendix F, Section 5. The properties of simplified perlite used in the post-test FE models are summarized in Table 23.

Table 23. Summary of Material Properties for "Sandy Soil" Perlite

Parameter	Value
Mass Density	9 x 10^{-6} lbf-s^2/in^4
Modulus of Elasticity	67.5 psi
Poisson's Ratio	0
Plasticity	Cap plasticity with cap hardening (see Appendix F, Section 5)
Mesh Implementation	3-inch reduced integration brick (C3D8R) elements

Perlite Material Model 2: "Crushable Foam"

After implementing the perlite-as-sandy-soil material model in the post-test FE models, the discrepancies between the test measurements and corresponding FE outputs were reduced but still remained significant. Further literature review was conducted to identify better material properties specifically for perlite, and a second material model for perlite was developed. This second perlite material model was implemented in the post-test FE models that used the actual steel properties from the tested tanks. This second perlite material model did not reuse any of the "sandy soil" material properties, but rather developed a new material model using the "crushable foam" elasticity definition within Abaqus. The development of the crushable foam material model for perlite is described more fully in Appendix F, Section 5.2. The material properties input to the FE model for the "crushable foam" are shown in Table 24.

Table 24. Summary of Material Properties for "Crushable Foam" Perlite

Parameter	Value
Mass Density	9 x 10^{-6} lbf-s^2/in^4
Modulus of Elasticity	Tabular, see Appendix F, Section 5.2

Parameter	Value
Poisson's Ratio	0.3
Tensile Cutoff Stress	40 psi

5.3 Modeling Techniques Adjusted between Pre-Test and Post-Test Models

Several modeling techniques were adjusted between the pre- and post-test models. The adjustments were made based on the actual test conditions and observations from the test outcomes and measurements. These modeling techniques and their adjustments are summarized in Table 25.

Table 25. Summary of Adjustments Made Between Pre- and Post-Test Models

Modeling feature	Condition in pre-test models	Condition in post-test models	Explanation
Impact speed	Varied	16.7 mph	Adjusted to match measured test speed
Outage pressure	45 psig	50 psig	Adjusted to match measured pressure at start of test
Lading temperature	39 °F	50 °F	Adjusted to match measured test-day temperature
Annular space pressure[10]	Vacuum	Prescribed pressure-time history	Adjusted to simulate loss of vacuum when outer tank tore
A516-70 carbon steel properties	Upper and lower estimates from literature	Calibrated material based on tensile test results	Adjusted based on post-impact measurements of steel properties
Outer tank shell thickness	0.4375 inch	0.463 inch	Adjusted to match actual thickness based on post-test measurements
Outer tank impact zone mesh	0.0546875 inch	0.058 inch	Mesh seed updated based on eight elements through updated thickness
Outer tank impact zone size	Approximately 25 inches by 16 inches	Approximately 27 inches by 18 inches	Solid patch of elements increased in size to keep tear from edge
A240 T304 stainless steel properties	Upper and lower estimates from literature	Calibrated material based on tensile test results	Adjusted based on post-impact measurements of steel properties
Inner tank shell thickness	0.25 inch	0.281 inch	Adjusted to match actual thickness based on post-test measurements
Inner tank impact zone mesh	0.05 inch	0.0562 inch	Mesh seed updated based on five elements through updated thickness

---

[10] Due to an input error discovered during preparations for a subsequent test, the annular space in all models had a pressure of 12.3 psia acting on the outer surface of the inner tank and a 0 psia pressure acting on the inner surface of the outer tank. This discrepancy is discussed further in Appendix E.

Modeling feature	Condition in pre-test models	Condition in post-test models	Explanation
Perlite	None	Simplified perlite based on sandy soil or crushable foam	Perlite included to better represent test conditions
Mass scaling	2 x 10^{-6} seconds	9 x 10^{-7} seconds	Reduced in post-test models to reduce artificial dynamic peak forces
Distortion control	None	Length ratio=0.1	Distortion control used in perlite
Initialization Step Duration	0.2 second	0.1 second	Reduced in post-test models to decrease runtime

5.3.1 Impact Speed

Pre-test FE models simulated impacts over a range of speeds from 16 to 18 mph. The purpose of the pre-test models was to aid in test planning by estimating the outcomes (e.g., impact forces, puncture of one or both tanks, etc.) over a range of speeds so that a target impact speed could be chosen. Post-test FE models were run using 16.7 mph, the measured impact speed from the test. The post-test models needed to be run at the same speed as the test to facilitate comparison of test and model results as part of a model validation program.

5.3.2 Outage Pressure

Pre-test models were run using an outage pressure of 45 psig. This value was chosen based on consideration of the pressure conditions proposed in PHMSA's NPRM at the time pre-test preparations were being made (see discussion in Section 2.2.2). Just prior to the test, the actual outage pressure was measured to be 50 psig. The post-test FE models were updated to use the actual test pressure of 50 psig.

5.3.3 Annular Space Pressure

All pre-test models and some post-test models were run without any attempt to simulate the loss of vacuum in the annular space that occurred after the outer tank began to tear. Post-test models that were run using "crushable foam" perlite insulation included a prescribed pressure-time history that caused the internal pressure in the annular space to increase to 1 atmosphere starting at the time the outer tank began to tear. This method required an iterative approach, as the time of the onset of tearing to the outer tank had to be known to define the pressure-time response.

Additionally, during preparations for a subsequent test of a DOT-113 surrogate using LN2 (see Section 9.2) the modeling team observed a discrepancy in the way annular space pressure was defined in all Test 10 models. This discrepancy resulted in a simulated vacuum acting on the inner surface of the outer tank, but a simulated 1 atmosphere pressure (12.3 psia) acting on the outer surface of the inner tank. The effects of this discrepancy were investigated for a limited number of post-test models.

5.3.4 Lading Temperature

The pre-test FE models used a lading temperature for the air and water cavities of 39 °F. This temperature was chosen based on the estimated historical temperatures for Pueblo during the planned test date. The post-test FE models used a lading temperature of 50°F based on the actual temperature at the time of the test.

5.3.5 A516-70 Carbon Steel Properties

All pre-test FE models used estimated mechanical properties for the A516-70 carbon steel making up the outer tank. After the test, coupons were extracted from the outer tank of the DOT-113 in an area remote from the impact zone and sent to two materials labs for tensile testing. The post-test FE models were updated to use A516-70 material properties based on the measured properties of the actual steel making up the outer tank of the tested DOT-113.

5.3.6 Outer Tank Shell Thickness

All pre-test models used the nominal thickness of the outer tank's shell, 7/16 inch (0.4375 inch). After the test, coupons were extracted from the outer tank of the DOT-113 in an area remote from the impact zone and sent to two materials labs for tensile testing. Each of those laboratories reported sample thicknesses in excess of 7/16 inch. The average thickness of the outer tank coupons was 0.463 inch, or 5.8 percent thicker than the nominal thickness. The post-test models were updated to use a thickness of 0.463 inch on the outer tank's shell.

5.3.7 Outer Tank Impact Zone Mesh

All the FE models (pre- and post-test) used eight elements through the thickness of the solid patch of the outer tank in the impact zone. The mesh size was updated between the pre- and post-test models based on the pre-test models using the nominal thickness of the outer tank's shell and the post-test models using the actual thickness of the outer tank's shell. The pre-test models used a mesh seed of approximately 0.055 inch while the post-test models used a mesh seed of 0.058 inch.

5.3.8 Outer Tank Impact Zone Size

The solid patch of elements in the puncture zone had to be large enough to allow the extent of material failure to be fully captured by puncture-capable elements. Particularly for the outer tank, the solid patch needed to be large enough for the impactor to both initiate and propagate a tear without reaching the edge of the solid patch to allow the inner tank to be loaded in a realistic way. If the tearing of the outer tank was inhibited by using a too-small span of elements in the solid patch, the outer tank could have carried more of the impact load in the model than would have been carried by the outer tank in the test. At the same time, the solid patch of elements was computationally expensive and needed to have its size limited to reduce the models' runtimes.

As different A516-70 material properties were used in the pre-test and post-test FE models, the size of the solid patch needed to be varied as the size of the tear varied with the material properties. The outer dimensions of the solid patch in the outer tank measured approximately 25 inches high by 16 inches wide in the pre-test models. The outer dimensions of the solid patch measured approximately 27 inches high by 15 inches wide in the post-test models run using the pre-test material behaviors. The outer dimensions of the solid patch measured approximately 27 inches by 18 inches wide in the post-test models run using the actual material behaviors.

5.3.9 A240 T304 Stainless Steel Properties

All pre-test FE models used estimated mechanical properties for the A240 T304 stainless steel making up the inner tank. After the test, coupons were extracted from the inner tank of the DOT-113 in an area remote from the impact zone and sent to two materials labs for tensile testing. The post-test FE models were updated to use A240 T304 material properties based on the measured properties of the actual steel making up the inner tank of the tested DOT-113.

5.3.10 Inner Tank Shell Thickness

All pre-test models used 0.25 inches, the nominal thickness of the inner tank's shell. After the test, coupons were extracted from the inner tank of the DOT-113 in an area remote from the impact zone and sent to two materials labs for tensile testing. Each of those laboratories reported sample thicknesses in excess of 0.25 inch. The average thickness of the inner tank coupons was 0.281 inch, or 12.4 percent thicker than the nominal thickness. The post-test models were updated to use a thickness of 0.281 inch on the inner tank's shell.

5.3.11 Inner Tank Impact Zone Mesh

All the FE models (pre- and post-test) used five elements through the thickness of the solid patch of the inner tank in the impact zone. The mesh size was updated between the pre- and post-test models based on the pre-test models using the nominal thickness of the inner tank's shell and the post-test models using the actual thickness of the inner tank's shell. The pre-test models used a mesh seed of 0.05 inch while the post-test models used a mesh seed of 0.056 inch.

5.3.12 Perlite

The pre-test FE models were run with a vacuum, but no perlite, in the annular space between the two tanks. Based on the level of disagreement observed between the force-time and force-displacement histories from the test and the pre-test models, perlite was included in the post-test models along with a vacuum. The post-test models were also run without perlite, as a means of demonstrating the influence of perlite on the global impact response of the DOT-113 model. Three different material models for perlite were developed, which are described in Appendix F, Section 5.

5.3.13 Mass Scaling

The pre-test models used a variable mass scaling technique to reduce simulation runtimes so that the pre-test modeling could be completed prior to the planned test date. Because of the need for a refined mesh of solid elements in the impact zone on both the inner and outer tanks, the puncture-capable models featured a large number of very small elements. Additionally, the models were full length, as the impact zone was off center for this test. These two factors combined to create models with significant runtimes, even when executed on multiple processor workstations. Variable mass scaling was employed in the FE models to decrease the runtime without decreasing either the span or the resolution of the refined meshes. Variable mass scaling is a technique in which the user sets a target-time increment for a set of elements within the model (i.e., up to and including all elements within the model), and the Abaqus solver increases the mass of each element to attempt to bring the minimum timestep up to the user-defined minimum. “Variable” refers to the software’s ability to increase the mass of each element by a different amount based on the material and geometry of each element. While mass scaling is an efficient way of reducing runtime without re-meshing a model, care must be exercised when using this technique with highly dynamic simulations. If overly aggressive mass scaling is applied, the amount of artificial mass added to the model in the refined mesh area can significantly affect both the overall dynamic response as well as the puncture behavior of the model.

The pre-test models used a target-time increment of 2 x 10^{-6} seconds. A review of the pre-test FE model results revealed a significant artificial peak corresponding to the impactor making contact first with the outer tank and subsequently when the outer tank made contact with the inner tank. This peak was attributed to the increase in mass of the refined meshes in the impact zones from the mass scaling. The post-test FE models used variable mass scaling with a target-time increment of 9 x 10^{-7} seconds. This reduction in target-time increment resulted in the post-test FE models requiring a longer runtime but reduced the artificial peaks caused by the mass scaling.

5.3.14 Distortion Control

The pre-test FE models did not use distortion control. The post-test FE models that included perlite used distortion control with a characteristic length of approximately 0.1. Distortion control was used to prevent the relatively soft perlite elements from becoming highly distorted and reducing the critical timestep or causing premature termination of the FE model through excessive distortion.

5.3.15 Initialization Step Duration

The pre-test models used a 0.2-second initialization step to apply the pressure inside the inner tank, the ambient pressure on the outer tank, and the effects of gravity. In the post-test models, this initialization step was shortened to 0.1 second, as the additional mesh refinements and reduced mass scaling factors applied to the post-test models resulted in an increase to the models’ runtimes. Reducing the initialization step partially offset the longer runtimes by reducing the total duration of time analyzed by the post-test models.

6. Comparison of Test Responses to Pre-Test Analyses

One of the intended uses of the pre-test models was to assist in test planning by estimating the range of impact speeds over which the puncture of both the inner and outer tanks would be likely to occur. The pre-test models were run using an iterative approach to attempt to determine a speed that would cause the puncture of both tanks without resulting in an excessive amount of residual energy in the impactor at the time of puncture. If the tank steels resembled the lower-ductility estimates, a 16-mph impact speed was estimated to cause puncture of only the outer tank while a speed of 18 mph was estimated to cause puncture of both the inner and outer tanks. If the tank steels were more similar to the upper-ductility estimates, an 18-mph impact would partially tear the outer tank but would not tear the inner tank. Thus, the range of speeds where puncture of both tanks could be expected began at 17.5 mph and extended to more than 18 mph, depending on the material behaviors in the tanks. Table 25 summarizes the pre-test FE models and their outcomes.

Table 25. Summary of Pre-Test FE Model Outcomes

Simulated impact speed (mph)	Tank steels	Outer tank state	Inner tank state	Reason for ending simulation
16	Lower ductility	Puncture	No elements lost	Impactor rebounding
17	Lower ductility	Puncture running to edge of solid patch	No elements lost	Impactor rebounding
17.5	Lower ductility	Puncture running to edge of solid patch	No elements lost	Impactor rebounding
18	Lower ductility	Puncture running to edge of solid patch	Puncture running to edge of solid patch	Puncture of both tanks
18	Upper ductility	Through tear under two corners	No elements lost	Impactor rebounding

The pre-test models were limited by the size of the solid patch of elements in the outer tank. For models run using the lower-ductility material at speeds greater than 16 mph, the tear in the outer tank extended to the limits of the solid patch of elements with failure properties defined. This behavior is undesirable, as the tear is forced to arrest in the model because of a modeling simplification, while in the actual DOT-113 the tear could continue to propagate. As a result of the tear being arrested in the model, the outer tank may be capable of carrying more of the impact load in the FE model than would be expected in an actual test as the tank became more compromised. Thus, the 17, 17.5, and 18 mph pre-test results using the lower-ductility material estimates needed to be interpreted cautiously as they could overpredict the contribution of the outer tank to the DOT-113's impact response.

On the basis of the pre-test modeling results, the target speed chosen for the test was 16.5 mph. This speed was expected to be conservative for a DOT-113 made out of material being similar to the upper-ductility pre-test estimates. However, if a higher test speed were specified and the DOT-113 was made from material similar to the lower-ductility pre-test estimate, the impact would have overwhelmed the tank car. This could have resulted in widespread damage to the tank car, the test fixtures, and the equipment. The range of expected test impact speeds was ± 0.5 mph around the 16.5 mph target speed, (i.e., 16 to 17 mph), a speed range where puncture of both tanks was possible but not certain. The actual test speed was 16.7 mph and resulted in puncture of both tanks, with the impactor continuing into the DOT-113 after the inner tank punctured.

Pre-test results using the lower ductility estimated steel behaviors were available at 16 and 17 mph. These results are compared to the test measurements in this section as the actual impact speed of 16.7 mph was between the speeds of these two pre-test FE models. Pre-test FE simulation results at all speeds and using both pre-test estimated material behaviors are contained within Appendix C, Section 1.

The impact force versus impactor travel is compared between the pre-test FE models using lower estimates of ductility for carbon and stainless steels and the test measurements in Figure 73. While the FE model used a rigid impactor with a single acceleration-time history, the ram car in the test featured five longitudinal accelerometers. The test force reported is calculated from the average of the five longitudinal accelerometer channels. Both the test and FE forces reported in this section were filtered using a CFC60 filter [18].

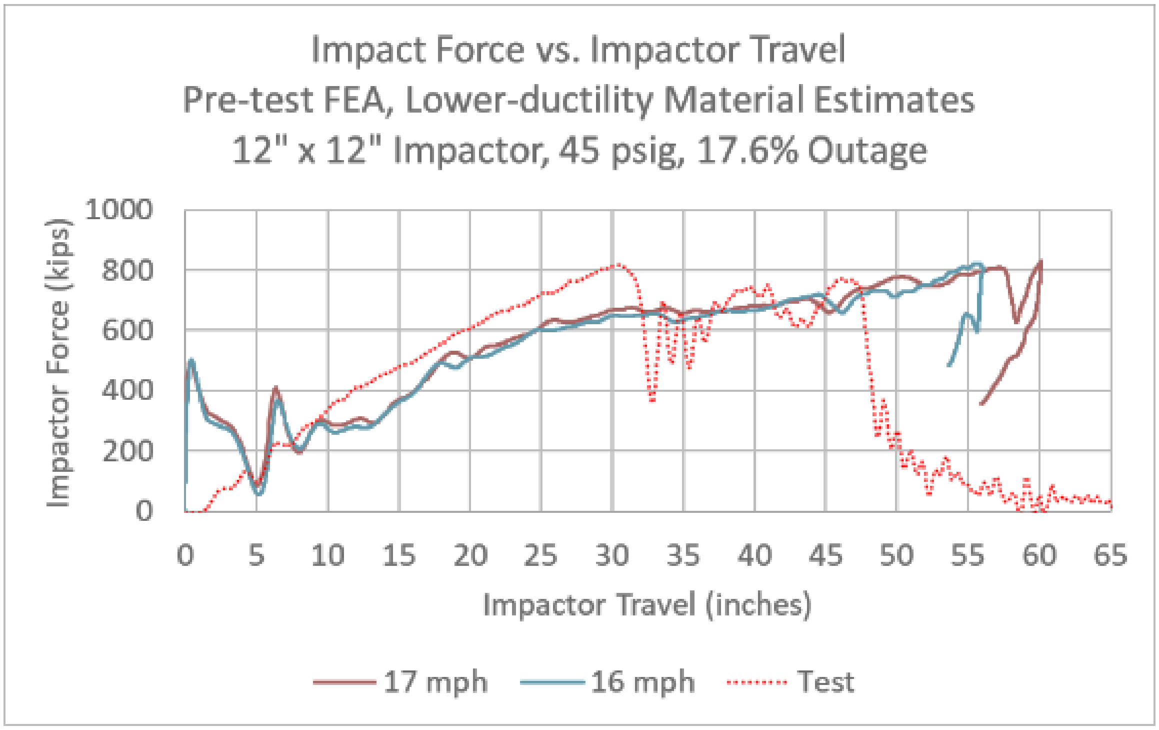

Figure 73. Force-Displacement Responses from Pre-Test FEA with Lower Estimates of Steels at 16 and 17 mph Compared to Test Results at 16.7 mph

The pre-test FEA using the lower-ductility materials did not exhibit a satisfactory level of agreement with the force versus impactor travel measurements from the test. The initial spikes exhibited by the FE models occurring within the first 7 inches of impactor travel are likely caused by the impactor first contacting the outer tank and then, after indenting the tank through the annular space, making contact with the inner tank. After these spikes, the FE models followed a lower slope than what was measured during the test. After approximately 30 inches of impactor travel, the FE models predicted a near-flat "plateau" response. This plateau continued until approximately 55 inches for the 16-mph impact and approximately 57 inches for the 17-mph impact, at which point the force dropped. After the force drop, the impactor travel began to decrease, indicating that the impactor had been brought to a stop and was beginning to rebound from the tank.

Figure 74 shows a side-by-side view of the solid patches on the outer (left) and inner (right) tanks at the end of the 16-mph simulation. This figure shows that the outer tank's tear did not extend to the limits of the solid patch of elements. Since there are additional puncture-capable elements in the path between the extent of the tear and the solid-shell transition, the tear has not been artificially arrested by the size of the solid patch in the model. Additionally, the model predicted tearing initiating on the left-hand side of the outer tank, which is consistent with the initial tear location observed from the video camera on board the ram car (see Section 4.6.3). It is also apparent that the inner tank has not yet begun to tear. However, as this pre-test model was run at 16 mph and the test occurred at 16.7 mph, a lack of puncture to the inner tank at a lower impact speed is not itself evidence of a discrepancy in the model.

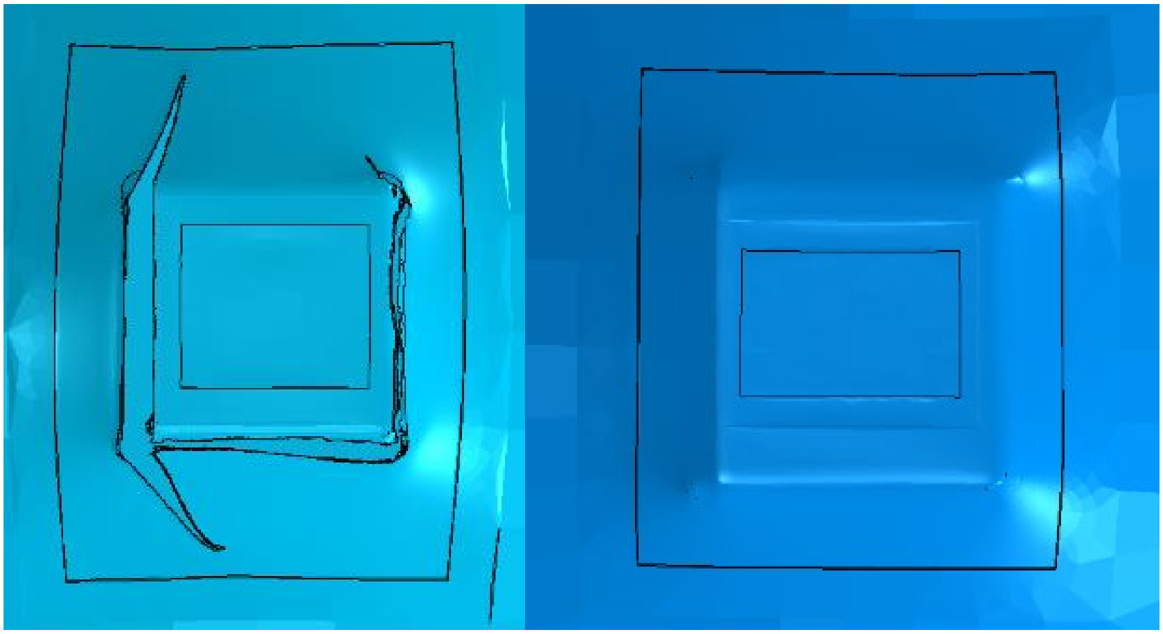

Figure 74. Exterior Views of Outer (left) and Inner (right) Tank Solid Patches from 16 mph Pre-Test FEA at 0.4 Seconds

Figure 75 shows a side-by-side view of the solid patches on the outer (left) and inner (right) tanks at the end of the 17-mph simulation. This figure shows that the outer tank's tear extended to the limits of the solid patch of elements. This is an undesirable result because the tear in the outer tank has been artificially arrested by a transition in the mesh to shell elements that do not have the ability to tear. It is apparent that by 0.4 seconds of simulated impact time the tear has reached the top of the solid patch. Thus, any model results beyond this time must be viewed with some skepticism, as the impact response may not be proceeding the same way that it would if the tear were allowed to continue propagating. However, it is apparent that the model predicted tearing initiating on the left-hand side of the outer tank, which is consistent with the initial tear location observed from the video camera onboard the ram car (see Section 4.6.3).

From this figure, it is apparent that the inner tank has not yet begun to tear. As this pre-test model was run at 17 mph and the test occurred at 16.7 mph, the lack of puncture of the inner tank at a higher impact speed was an indication that the pre-test model needed to be improved by, at a minimum, replacing the estimated pre-test steel properties with steel properties based on the actual material behaviors in the tested DOT-113 tank car.

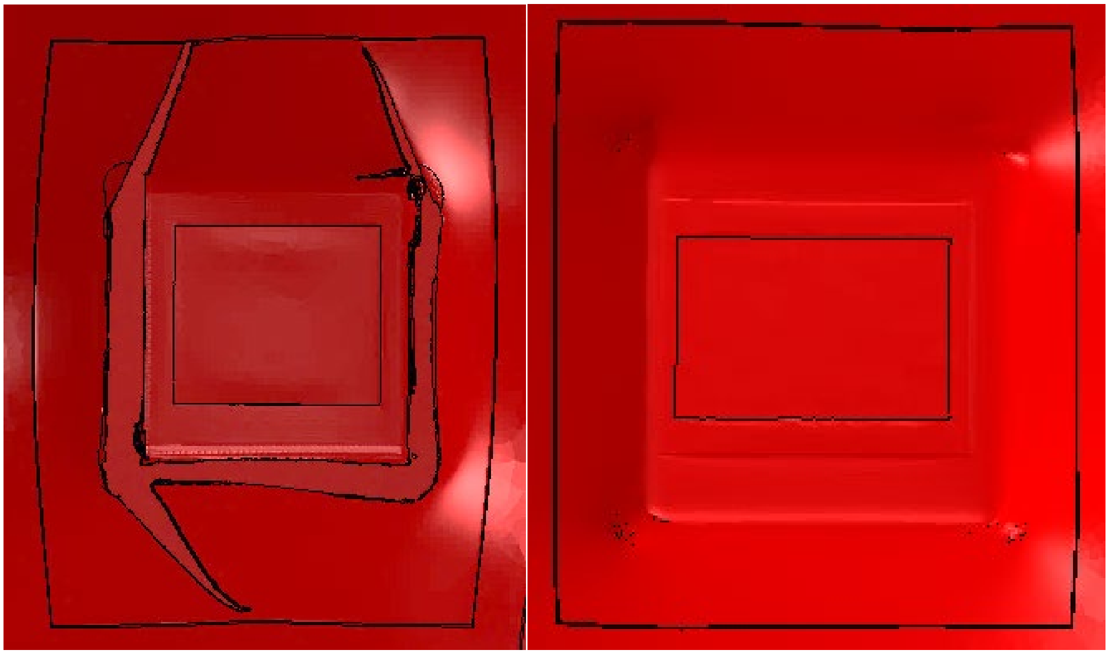

Figure 75. Exterior Views of Outer (left) and Inner (right) Tank Solid Patches from 17 mph Pre-Test FEA at 0.4 Seconds

7. Comparison of Test Responses to Post-Test Analyses

Post-test analyses were conducted in two stages. In the first stage, the pre-test FE model was updated to reflect the actual test speed, temperature, and initial outage pressure. These models were run immediately after the test was performed but prior to the material characterization tests being performed. The pre-test material properties for the inner and outer tanks were used in this first stage. The second stage of post-test analyses used the actual test speed, temperature, initial outage pressure, and material behaviors developed following the tensile tests of the actual stainless and carbon steels used in the tested tank car. This section contains results and a discussion of the post-test models made using pre-test and post-test steel properties using either no perlite or "sandy-soil" perlite properties as summarized in Table 26.

Table 26. Summary of Post-Test FE Model Outcomes, Models without Perlite or "Sandy Soil" Perlite

Simulated impact speed (mph)	Perlite	Tank steels	Outer tank state	Inner tank state	Reason for termination	Report section
16.7	None	Upper ductility	Small number of elements lost under impactor corner	No elements lost	Impactor rebounding	7.1.1
16.7	"Sandy Soil" Perlite	Upper ductility	Puncture	No elements lost	Impactor rebounding	7.1.1
16.7	None	Lower ductility	Puncture	No elements lost	Impactor rebounding	7.1.2
16.7	"Sandy Soil" Perlite	Lower ductility	Puncture running to edge of solid patch	Puncture	Puncture of both tanks	7.1.2
16.7	None	Actual	Puncture	No elements lost	Impactor rebounding	7.2.1
16.7	"Sandy Soil" Perlite	Actual	Puncture	No elements lost	Impactor rebounding	7.2.2

The levels of agreement between the test measurements and the model results presented in this section were lower than desired. Additional post-test models were run to examine the properties of perlite and stainless steel beyond those included in the post-test models discussed in this section. These additional post-test models are discussed in Section 8.

7.1 Post-Test Analyses using Pre-Test Steel Properties

Immediately after the test, the pre-test FE model was updated to reflect the measured impact speed, outage pressure, and temperature. While awaiting the results of material coupon tests from testing labs, the post-test models were first run using the estimated lower- and upper-ductility material models that had been used in the pre-test models. After observing the condition of the perlite in the annular space of the DOT-113 (Figure 29) and the level of discrepancies between the pre-test FEA and the test measurements (see Section 6), the post-test models were updated to include a simplified representation of the perlite between the tanks based on a "sandy soil" material model identified in literature (see Section 5.2.6). Post-test models were run both with and without perlite to assess its effects, as summarized in Table 27.

Table 27. Summary of Post-Test FE Model Outcomes, Models Using Pre-Test Steel Behaviors

Simulated impact speed (mph)	Perlite	Tank steels	Outer tank state	Inner tank state	Reason for termination	Report section
16.7	None	Upper ductility	Small number of elements lost under impactor corner	No elements lost	Impactor rebounding	7.1.1
16.7	"Sandy soil" Perlite	Upper ductility	Puncture	No elements lost	Impactor rebounding	7.1.1
16.7	None	Lower ductility	Puncture	No elements lost	Impactor rebounding	7.1.2
16.7	"Sandy soil" Perlite	Lower ductility	Puncture running to edge of solid patch	Puncture	Puncture of both tanks	7.1.2

Of the four cases described in Table 27, the only situation that resulted in the same puncture outcome as the test (i.e., puncture of both the inner and outer tanks) was the model using "sandy soil" perlite and the lower-ductility pre-test materials. This outcome supported the post-test hypothesis that the perlite in the annular space may have been responsible for the significant discrepancies between the models run without perlite and the test measurements. Additionally, this outcome suggested the possibility that the perlite effectively decreased the impact speed that would be necessary to puncture both tanks under the tested conditions. The results of each model summarized in Table 28 are described in the subsequent sections.

7.1.1 Post-Test Models with Pre-Test Upper-Ductility Steels

Figure 76 shows the force-displacement responses of two post-test FE models run at test conditions. One FE model excluded perlite, and the other included the "sandy soil" model of perlite. Both models used the pre-test upper ductility steel behaviors for both inner and outer tanks. While this figure demonstrates an increase in stiffness of the overall force-displacement response in the model that included perlite, neither model exhibited significantly improved agreement compared to the pre-test models. The impactor came to a stop and rebounded without puncturing the inner tank in both post-test models.

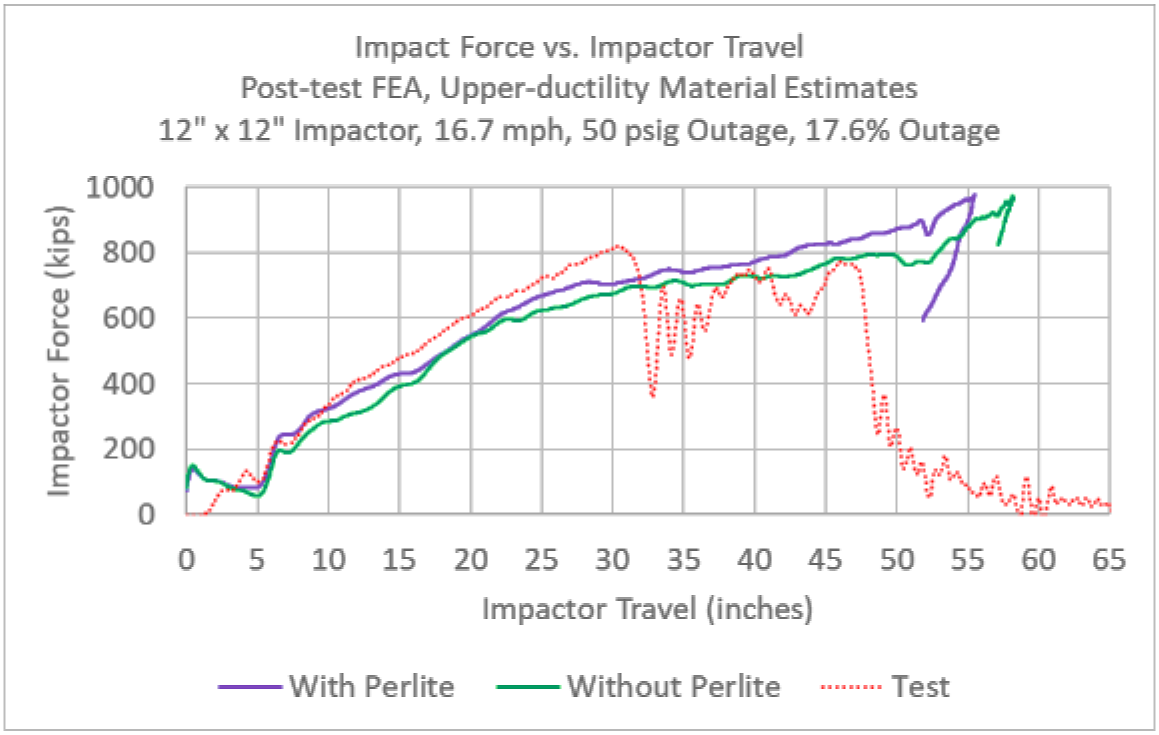

Figure 76. Force-Displacement Responses from Post-Test FEA with Upper Estimates of Steels with and without "Sandy Soil" Perlite Compared to Test Results

7.1.2 Post-Test Models with Pre-Test Lower-Ductility Steels

Figure 77 shows the force-displacement responses of two post-test FE models run at test conditions, both using the pre-test lower ductility steel behaviors for the inner and outer tanks. One FE model excluded perlite, and the other included the "sandy soil" model of perlite. Similar to the behavior observed in the models using the pre-test upper-ductility steels, the results from the models using the lower-ductility steels also indicates an increase in stiffness of the overall force-displacement response in the model that included perlite. However, neither model exhibited significantly improved agreement compared to the pre-test models. The impactor came to a stop and rebounded in both post-test models.

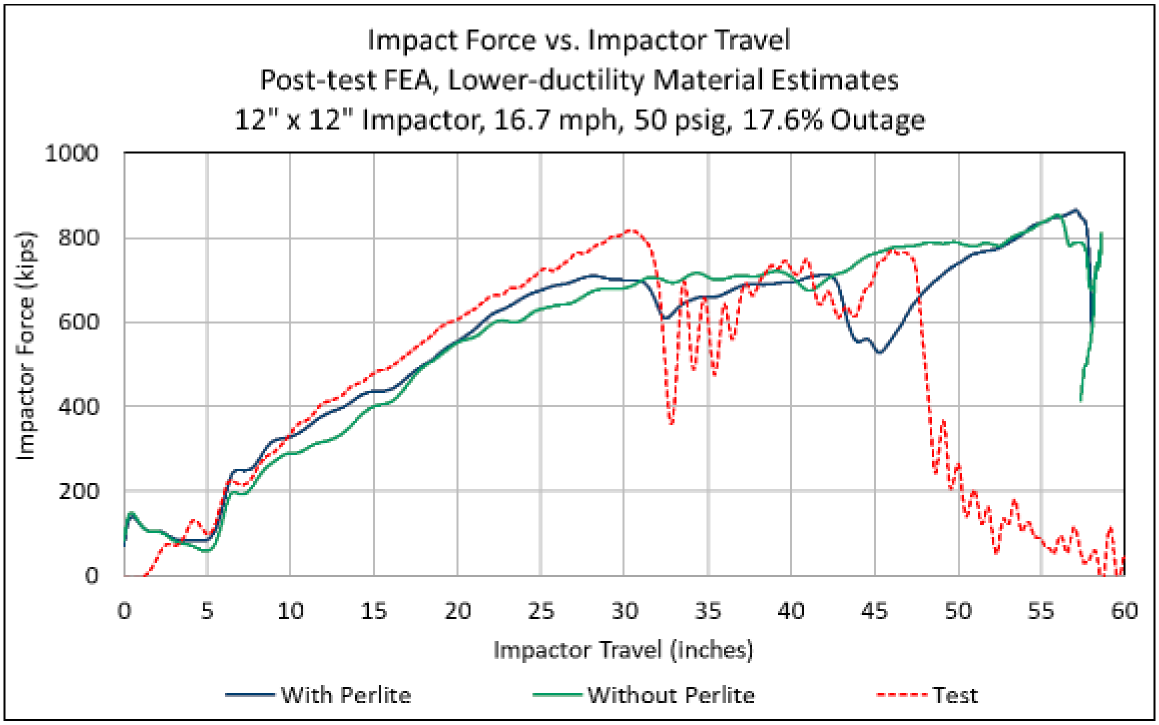

Figure 77. Force-Displacement Responses from Post-Test FEA with Lower Estimates of Steels with and without "Sandy Soil" Perlite Compared to Test Results

The level of agreement exhibited between the post-test model that included perlite and the test measurements was higher than the level of agreement exhibited between the post-test model without perlite and the test measurements. The post-test model with perlite demonstrated a series of drops in force, including a final drop in force associated with the puncture of the inner tank, exhibiting a response similar to the measurements of the test. The post-test model using the pre-test lower-ductility steels and perlite still overestimated both the impact force and impactor travel at puncture of the inner tank. However, based upon these results, the researchers agreed that perlite appeared to have played a significant role in the global impact response measured in this test. Thus, perlite was deemed important enough to continue to include in the post-test model as further post-test models were run. Subsequently, the mechanical properties of perlite and the material implementation within Abaqus would be re-examined (Section 8.1.1), as the initial stiffness of the post-test model using "sandy soil" perlite was still low compared to the test measurement.

7.2 Post-Test Analyses using Actual Steel Properties

Post-test analyses were conducted using the actual impact speed, temperature, and initial outage pressure, as well as the inner and outer tank steel properties based on the results of post-test tensile testing performed on coupons removed from the actual tested car. Post-test FE modeling activities also included the development of several material models for the perlite used in the annular space between the inner and outer tanks in the tested DOT-113.

A full description of the different perlite models can be found in Appendix F, Section 5. Comparisons between the test measurements and the DOT-113 FE models using different modeling approaches for perlite can be found in Appendix C, Section 3. Table 28 contains a summary of the outcomes of different FE post-test models that used two different approaches to represent the perlite.

Table 28. Summary of Post-Test FE Model Outcomes, Models Using Actual Steel Behaviors

Impact Speed (mph)	Perlite	Tank Steels	Inner Tank Damage Model	Outer Tank State	Inner Tank State	Reason for Termination	Report Section
16.7	None	Actual	MMC	Puncture	No elements lost	Impactor rebounding	7.2.1
16.7	“Sandy Soil” Perlite	Actual	MMC	Puncture	No elements lost	Impactor rebounding	7.2.2

The modeling approach that gave the best agreement between the test measurements and the simulation outputs used a crushable foam material model within Abaqus to represent the perlite. The process of developing this perlite material model is found in Appendix F, Section 5.2. The results of this FE model and its comparison to the test measurements are included in this section.

7.2.1 Post-Test Model with Actual Steel Behaviors, no Perlite

Incorporating the actual carbon and stainless steel material properties alone did not result in a significant improvement in model-test correlation. Figure 78 compares the force-displacement responses of the test with a post-test FE model that used the actual test conditions and actual material behaviors for both the inner and outer tank steels. This model did not include any representation of the perlite insulation to allow the effects of the steel behaviors to be assessed independently. Consistent with the previously described FE models that neglected perlite, this post-test model exhibited a force-displacement response that was softer than the response measured in the test. This post-test FE model also experienced a rebounding impactor without puncturing both tanks which was inconsistent with the outcome of the test. The full set of results from this model can be found in Appendix C, Section 3.1.

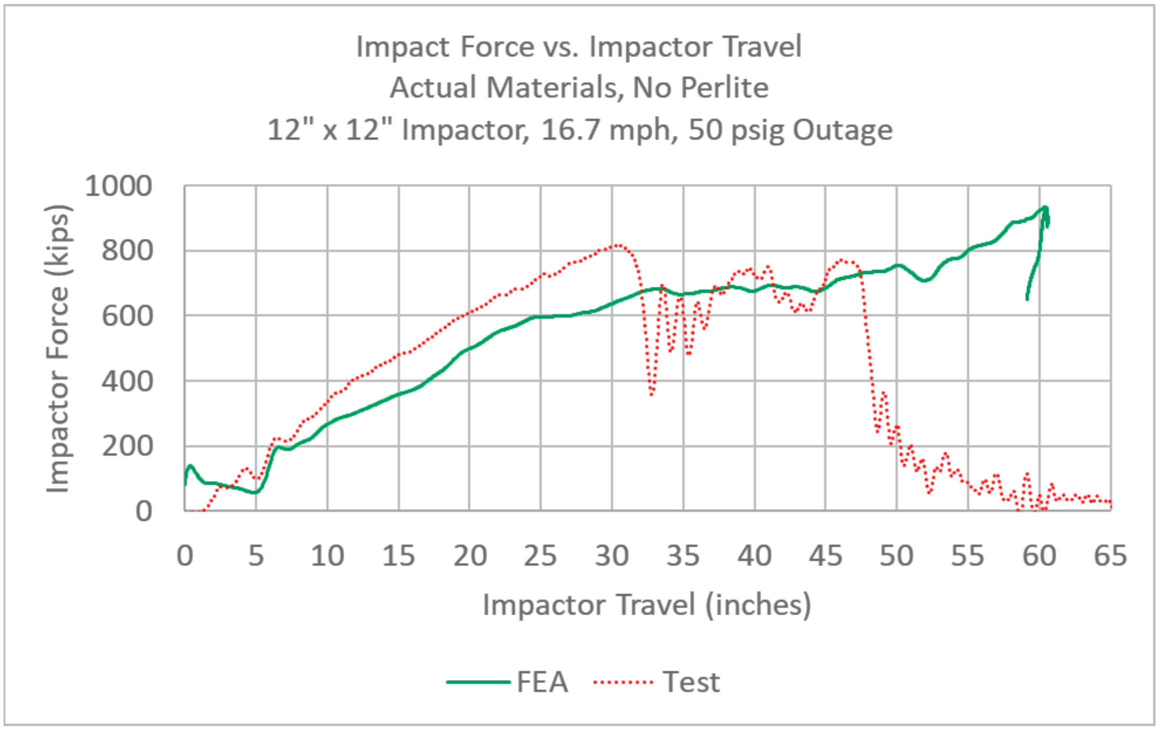

Figure 78. Impactor Force Versus Impactor Travel from Test and Post-Test FEA with No Perlite

7.2.2 Post-Test Model with Actual Steel Behaviors, "Sandy Soil" Perlite

Since including the actual material properties for the carbon and stainless steels in the DOT-113 did not attain a satisfactory level of test-model agreement, the next step was to incorporate perlite insulation into the post-test FE model. Figure 79 compares the force-displacement responses of the test with a post-test FE model that used the actual test conditions and actual material behaviors for both the inner and outer tank steels. The perlite insulation was modeled using the "sandy soil" material model described in Section 5.2.6. Compared to the post-test FE model using actual steel behaviors but neglecting perlite, this FE model demonstrated an increased stiffness in its force-displacement response. However, the force-displacement response of this model was still softer than the response measured in the test. This post-test FE model also experienced a rebounding impactor without puncturing both tanks, which was inconsistent with the outcome of the test. Thus, while modeling perlite using a material model based upon sandy soil improved the stiffness of the overall DOT-113 response, the resulting model still exhibited significant room for improvement in the model-test correlation. The full set of results from this model can be found in Appendix C, Section 3.2.

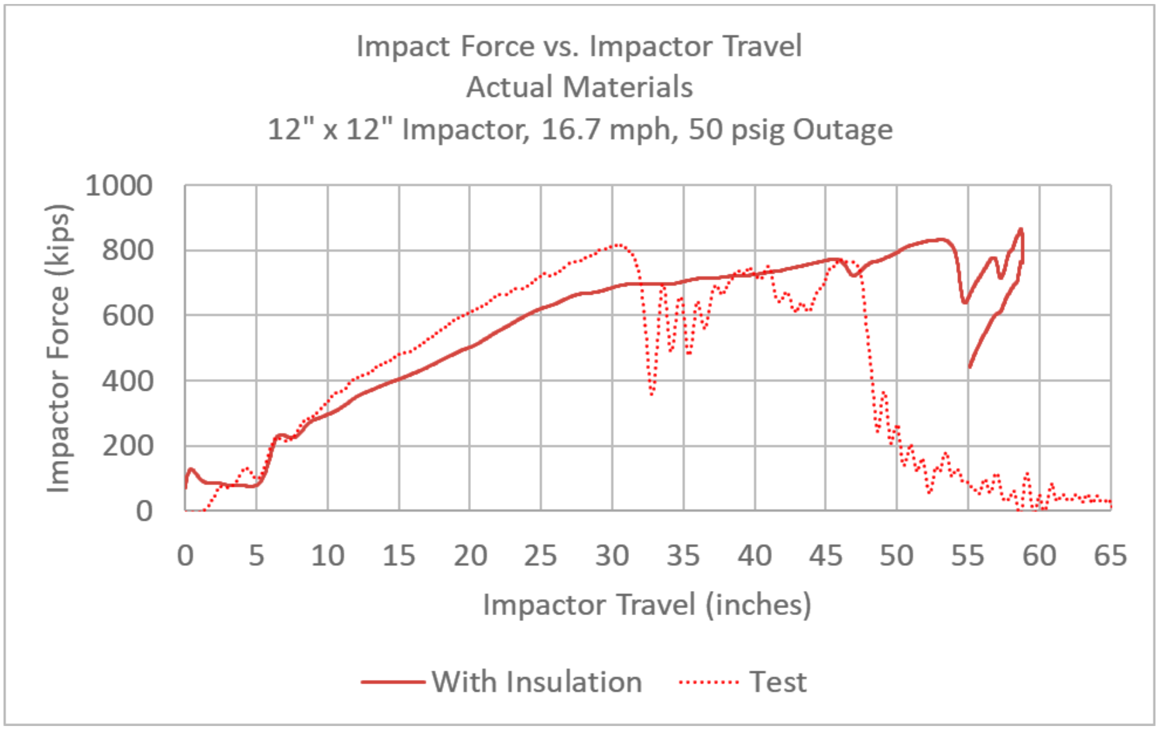

Figure 79. Impactor Force Versus Impactor Travel from Test and Post-Test FEA with "Sandy Soil" Perlite Material

8. Post-Test Modeling of Additional Behaviors

The agreement between the test measurements and the output from the post-test FE model using actual material properties and “sandy soil” perlite (see Section 7.2.2) was lower than expected. Additional post-test modeling was performed to investigate potential causes for the disagreement. This post-test examination focused on two notable areas of disagreement. First, the post-test FE models did not closely follow the same force-displacement response measured in the test, even prior to the puncture of the outer tank. This suggested that there was some disagreement, unrelated to the puncture behaviors defined in the FE model, between a global parameter in the FE model and the test condition. Second, the FE model experienced puncture of both tanks at different forces and displacements than those observed during the test. This suggested that additional review of the material definitions for the tank steels in the FE model was warranted.

Additional post-test modeling was first focused on understanding the discrepancy in the global force-displacement response, as that behavior should exhibit a high level of agreement with the test measurements up to the point of puncture regardless of the properties of the puncture material used. The mechanical properties of the perlite insulation were re-visited in this model. Ultimately, both the input properties and the approach to modeling the perlite insulation were changed in the post-test model compared to the previous “sandy soil” perlite material. Changing the perlite material model led to better agreement in the overall response in the post-test FE model and better agreement with the occurrence of puncture of the outer tank when compared to the test measurements. However, the FE model still overpredicted the force, displacement, and energy necessary to cause puncture of the inner tank.

Further investigation of the failure behavior defined for the inner tank was performed, using an FE model with the new “crushable foam” perlite material model. Both MMC and B-W damage initiation models were implemented for the stainless steel material. While the B-W envelope resulted in a smaller force and displacement at the inner tank failure than the MMC material model, the FE model still overestimated the energy needed to puncture the inner tank compared with the test data.

Finally, strain-rate effects for stainless steel were investigated for the inner tank in conjunction with the “crushable foam” perlite and the B-W damage initiation envelope. The post-test FE model incorporating a strain-rate effect underpredicted the energy to puncture the inner tank. Thus, neglecting strain-rate effects for stainless steel resulted in an overestimate of the energy required to puncture both tanks, and a simplified approximation of strain-rate effects for stainless steel resulted in an underestimate of energy. Further refinement of the strain-rate effect model for the inner tank was not undertaken as a part of this study but may be considered in conjunction with future DOT-113 testing.

Finally, a discrepancy was discovered in the way the Test 10 models accounted for atmospheric pressure and annular space vacuum outside of the hydraulic and pneumatic cavities representing water and air, respectively. The model that used the B-W envelope derived from quasi-static tensile test results for the stainless steel was re-run using an adjusted ambient pressure value in the cavity definitions.

The additional post-test FE models used to investigate the perlite and stainless-steel behaviors are summarized in Table 29.

Table 29. Summary of Post-Test FE Model Outcomes, Models Investigating Perlite and Stainless-Steel Properties

Impact Speed (mph)	Perlite	Tank Steels	Inner Tank Damage Model	Outer Tank State	Inner Tank State	Ambient Pressure (psi)	Report Section
16.7	"Crushable Foam" Perlite	Actual	MMC	Puncture	Puncture	12.3	8.1.1
16.7	"Crushable Foam" Perlite	Actual	B-W	Puncture	Puncture	12.3	8.1.2
16.7	"Crushable Foam" Perlite	Actual carbon steel, rate-dependent stainless steel	B-W	Puncture	Puncture	12.3	8.1.3
16.7	"Crushable Foam" Perlite	Actual	B-W	Puncture	Puncture	0	8.1.4

8.1 Post-Test Model with Actual Steel Behaviors, Crushable Foam Perlite, MMC Failure for Stainless Steel

While the "sandy soil" perlite showed promise, significant discrepancies remained between the post-test FEA and the corresponding test measurements. A second perlite material model was developed using material properties obtained from a thorough literature search and implemented in Abaqus using a crushable foam material model. The post-test FE model was run using this perlite implementation with the actual steel behaviors and the actual impact conditions. This second perlite material model was based on a crushable foam material and was primarily included in the post-test FE model to investigate whether different properties for perlite would lead to a higher level of agreement in this model than in the "sandy soil" perlite model Section 5.2.6 describes the development of this second perlite model. The inclusion of "sandy soil" perlite in previous models indicated that perlite could not be neglected; the development of a crushable foam perlite material was intended to attain better agreement with the test measurements. Further, this post-test FE model included a prescribed pressure-time history acting on the surfaces enclosing the annular space to represent the loss of vacuum associated with tearing of the outer tank.

Figure 80 contains a plot comparing the force-displacement responses of the test with a post-test FE model that used the actual test conditions and actual material behaviors for both the inner and outer tank steels. Overall, the force-displacement response from the post-test FE model using this second perlite model exhibited an improvement in both the qualitative and quantitative agreement with the test results. The overall stiffness of the force-displacement response agreed with the test measurements for approximately the first 25 inches of indentation. As the displacement increased beyond this point, the model began to soften, and the outer tank punctured. The outer tank in the test punctured with a smaller indentation than the outer tank in the FE model. Following the puncture of the outer tank, both the test and the FE model's stiffness rose as the load transferred to the inner tank. Both the FE model and the test resulted in the puncture of the inner tank. However, the FE model overestimated both the force and the amount of impactor travel at the inner tank's puncture.

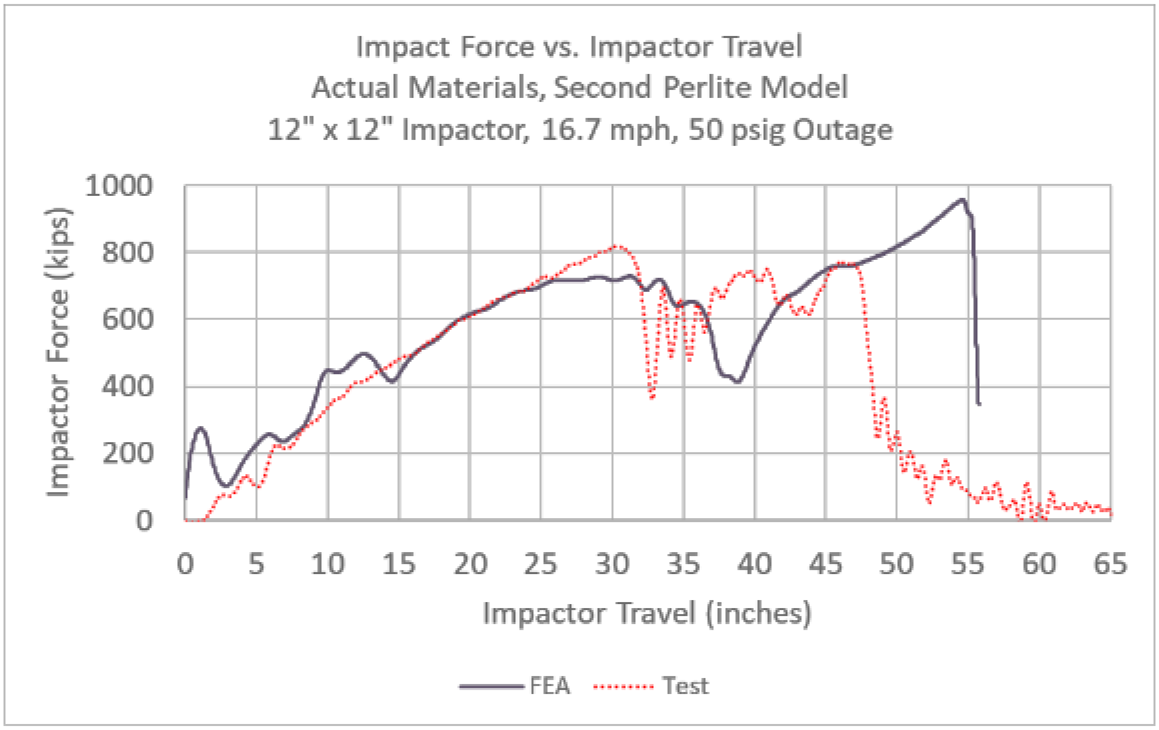

Figure 80. Impactor Force Versus Impactor Travel from Test and Post-Test FEA with Crushable Foam Perlite Material and MMC Damage Initiation

Figure 81 shows the impactor velocity versus impactor travel for both the test and the post-test FE model using the second perlite model and the actual steel properties for both tanks. This figure demonstrates that the FE model exhibited agreement with the test measurements over approximately the first 46 inches of impactor travel. Beyond this point, the FE model continued to slow down more rapidly than the test. This discrepancy can be attributed to the delayed inner tank puncture estimated by the model. When the outer tank punctured during the test, the tank car offered little resistance to the impactor's continued motion. Thus, the impactor in the test experienced a more gradual deceleration following the inner tank puncture. As the FE model estimated the inner tank would puncture after a larger deformation, the impactor in the FE model decelerated more rapidly until the inner tank punctured.

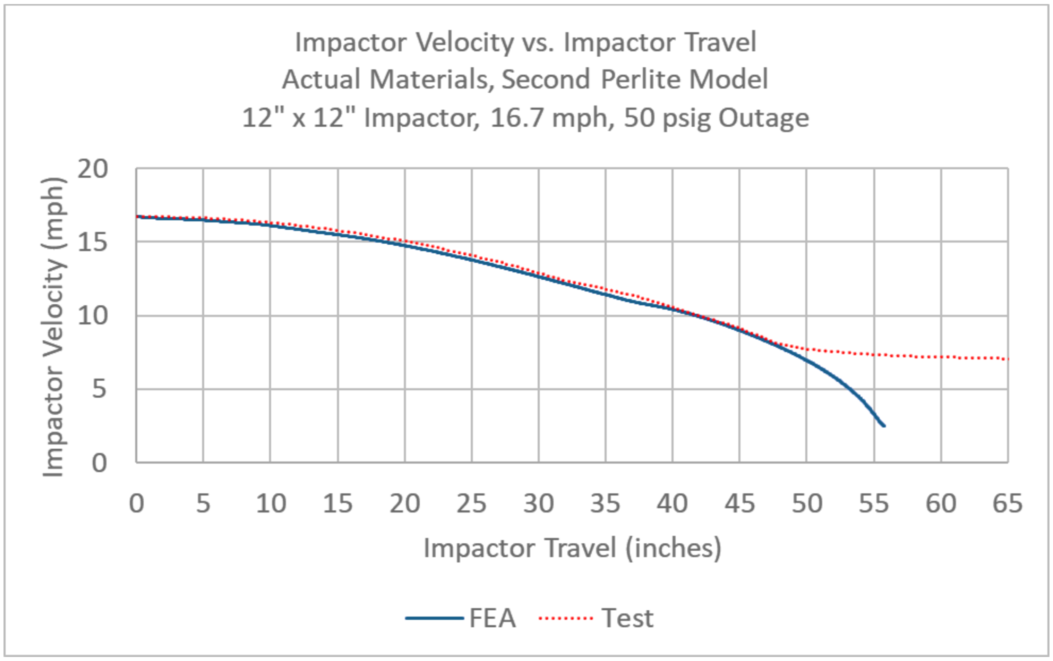

Figure 81. Impactor Velocity Versus Impactor Travel from Test and Post-Test FEA with Crushable Foam Perlite Material and MMC Damage Initiation

Figure 82 plots the energy absorbed by the DOT-113 versus the impactor travel. This energy was calculated by integrating the force-displacement response (Figure 80). This figure demonstrates that the FE model and the test were in agreement until the inner tank punctured in the test at approximately 46 inches of impactor travel. Because the inner tank in the FE model did not puncture at this displacement, the model continued to absorb energy beyond the point when puncture actually occurred during the test. The crushable foam perlite material model improved the agreement between the initial force-displacement response in the model and the test and improved the agreement for puncture energy of the outer tank. However, the model overestimated the puncture energy of the inner tank. This suggests that while the crushable foam perlite lead to a better overall level of agreement between the test and the FE model, discrepancies remained in the inner tank's material model.

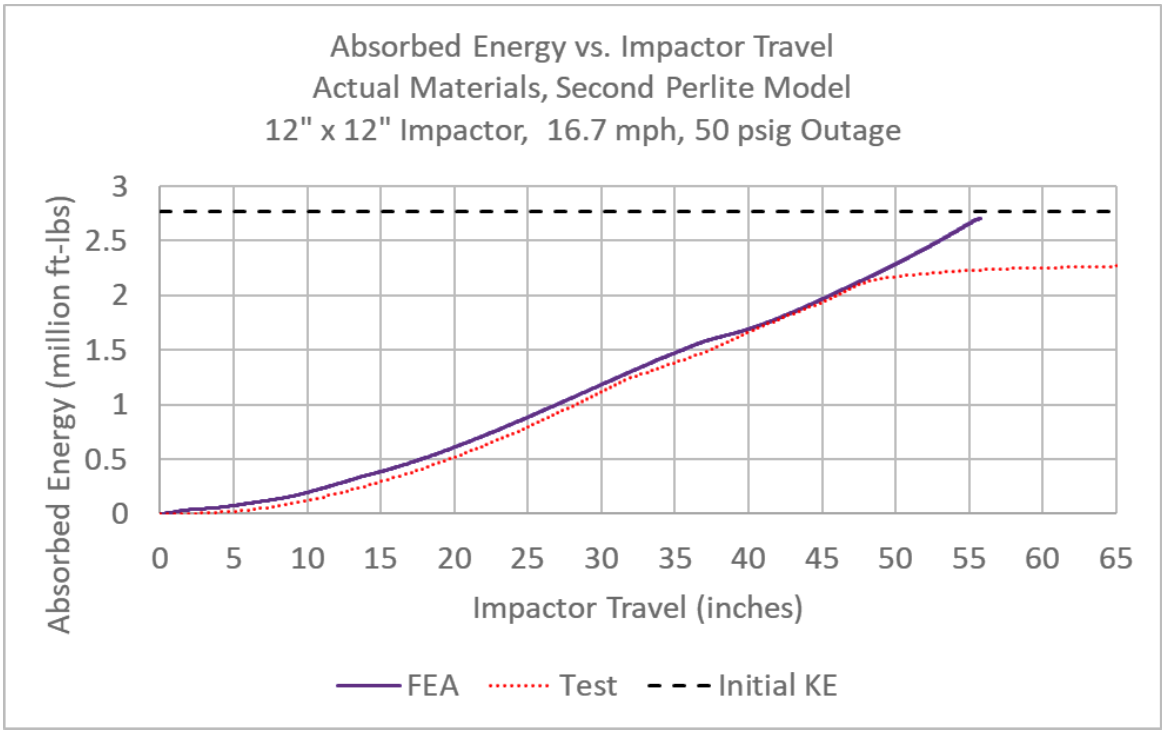

Figure 82. Impactor Velocity Versus Impactor Travel from Test and Post-Test FEA with Crushable Foam Perlite Material and MMC Damage Initiation

Table 30 presents a comparison of the peak values for numerous measurements from the test and the post-test FE model using the crushable foam perlite material model. The full set of FE results is found in Appendix C, Section 3.3.

Table 30. Comparison of Peak Results from Test and Post-Test FEA with Crushable Foam Perlite Material and MMC Damage Initiation

Peak Measurement	**Test *Value***	**FEA *Value***	**FEA *% Difference***
Force at Outer Tank Puncture (kips)	817.1	727.9	-10.9
Displacement at Outer Tank Puncture (inches)	30.4	31.3	3.1
Absorbed Energy at Outer Tank Puncture (million foot-pounds)	1.1	1.3	10.6
Force at Inner Tank Puncture (kips)	770.8	957.1	24.2
Displacement at Inner Tank Puncture (inches)	46.0	54.6	18.6
Absorbed Energy at Inner Tank Puncture (million foot-pounds)	2.0	2.6	31.1
East Skid String Potentiometer (inches)	-8.6	-7.7	-11.0
West Skid String Potentiometer (inches)	-4.7	-1.4	-71.5
East Head String Potentiometer (inches)	-9.3	-9.0	-3.0
West Head String Potentiometer (inches)	-6.8	-0.8	-88.0
Average Air Pressure (psi)	61.9	62.1	0.3

8.1.1 Post-Test Model with Actual Steel Behaviors, Crushable Foam Perlite, QS B-W Failure for Stainless Steel

The post-test model using the second perlite material model exhibited a higher level of agreement than the previously discussed material models. However, that model still overestimated the inner tank puncture energy by a significant amount. That FE model used a B-W failure envelope for the outer, carbon steel tank, and an MMC failure surface for the inner stainless steel tank. A second post-test model was executed using the crushable foam perlite and a B-W failure model for both the carbon and stainless steels. This post-test FE model also included a prescribed pressure-time history acting on the surfaces enclosing the annular space to represent the loss of vacuum associated with tearing of the outer tank. The techniques used to develop the B-W damage initiation envelope for the stainless-steel material are described in Appendix F, Section 4.2. Note that this B-W envelope was based on QS tensile test data.

The impact force versus impactor travel for this model is shown in Figure 83. This model exhibits both qualitative and quantitative agreement with the test measurements. The model experienced two distinct puncture events with the puncture of the outer tank occurring at both a similar force and displacement as seen in the test. The overall slopes of the force-displacement responses were also in agreement over much of the impact event. This model's response was similar to that seen in the post-test model using the MMC failure model for the stainless steel inner tank.

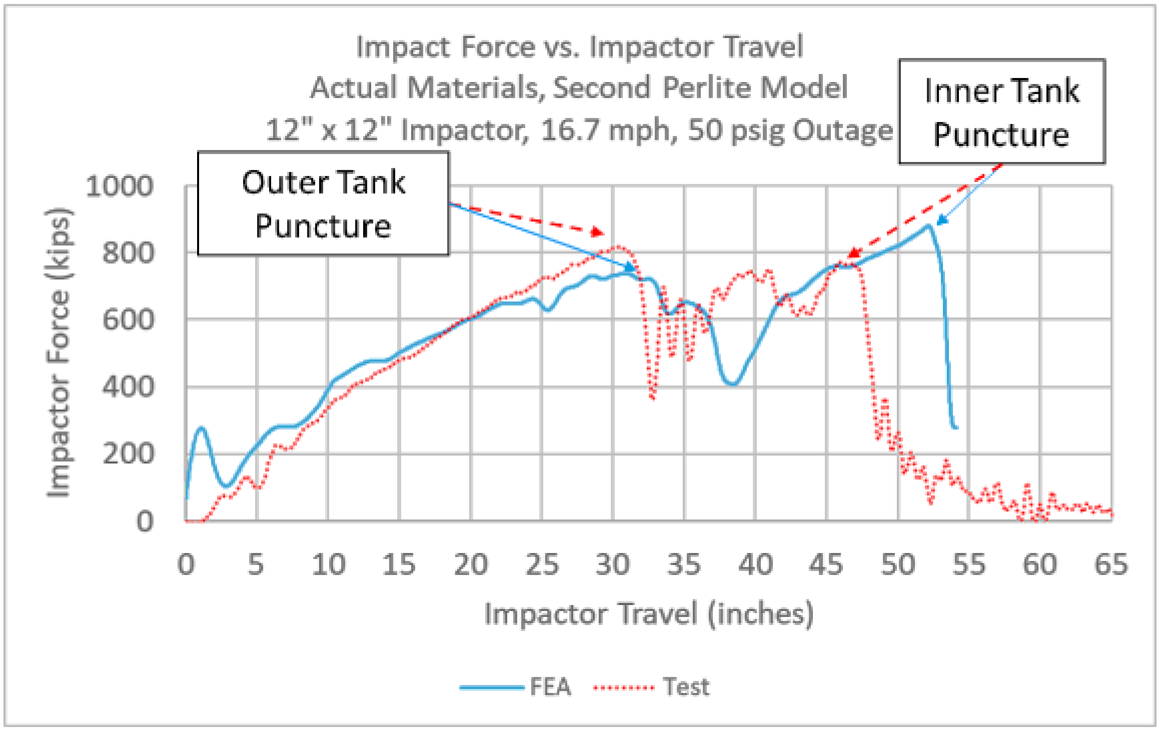

Figure 83. Impactor Force Versus Impactor Travel from Test and Post-Test FEA with Crushable Foam Perlite Material and B-W Damage Initiation

Figure 84 presents the impactor velocity versus impactor travel from the test and the post-test FEA using crushable foam perlite. The FE model matches the test velocity closely, up to approximately 47 inches of travel. This was approximately the displacement at which the inner tank punctured in the test. However, as seen in the force-displacement response (Figure 83), the

FE model did not experience puncture until approximately 53 inches of impactor travel. Since the impactor force continued to rise during this additional travel, the impactor's velocity was lower when the inner tank punctured in the FE model than in the test. Figure 84 shows that the impactor had a residual velocity of approximately 8 mph at the inner tank puncture during the test and approximately 5 mph at the inner tank puncture in the FE model.

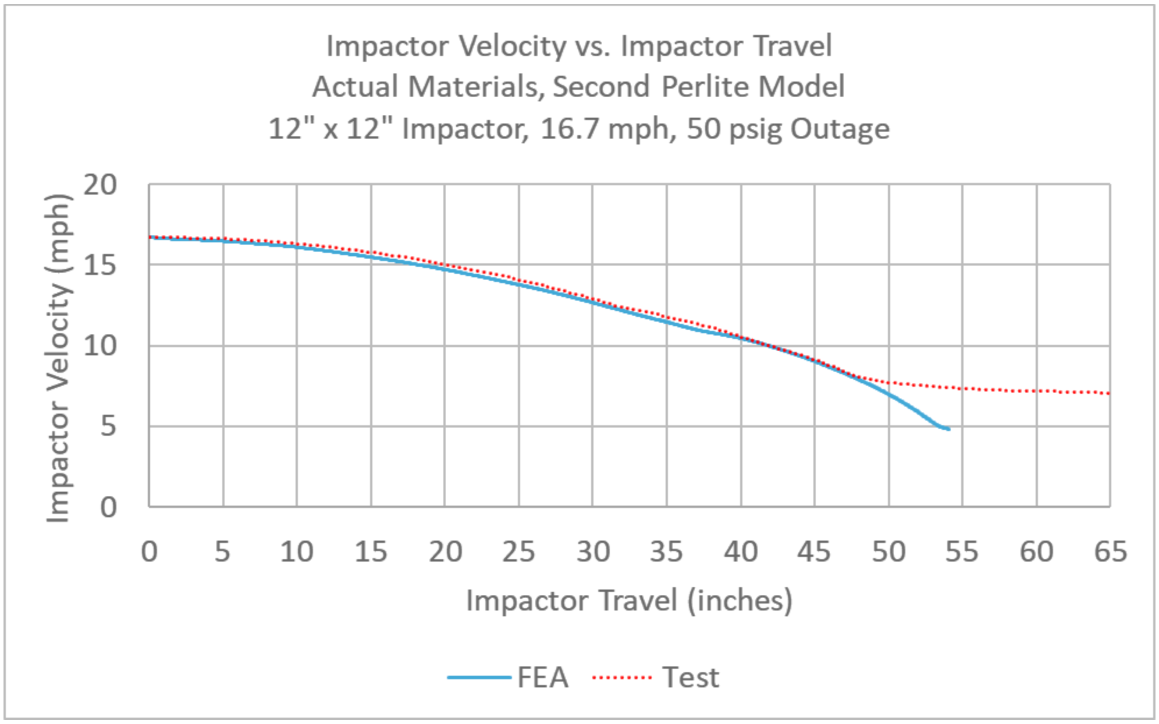

Figure 84. Impactor Velocity Versus Impactor Travel from Test and Post-Test FEA with Crushable Foam Perlite Material and B-W Damage Initiation

Figure 85 contains a plot of the energy absorbed by the DOT-113 versus the travel of the impactor. This energy was calculated by integrating the force-displacement response (Figure 83). This figure demonstrates that the FE model and the test were in agreement until approximately 48 inches of impactor travel. Beyond this distance, the FE model overpredicted the absorbed energy as the FE model's inner tank did not puncture until approximately 53 inches of impactor travel.

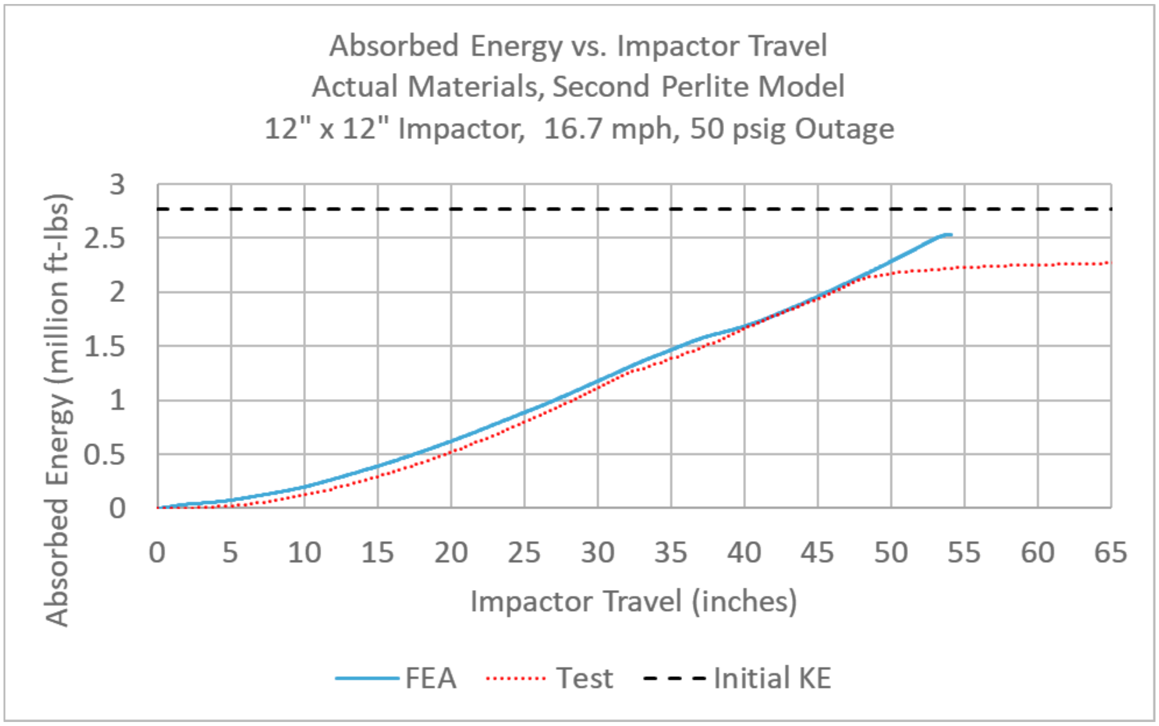

Figure 85. Absorbed Energy Versus Impactor Travel from Test and Post-Test FEA with Crushable Foam Perlite Material and B-W Damage Initiation

Table 31 presents a comparison of the peak values for numerous measurements from the test and the post-test FE model using the crushable foam perlite material model and the B-W damage initiation envelope for both steels. The full set of FE results is found in Appendix C, Section 3.4.

Table 31. Comparison of Peak Results from Test and Post-Test FEA with Crushable Foam Perlite Material and B-W Damage Initiation

Peak Measurement	**Test *Value***	**FEA *Value***	**FEA *% Difference***
Force at Outer Tank Puncture (kips)	817.1	737.4	-9.8
Displacement at Outer Tank Puncture (inches)	30.4	31.0	2.1
Absorbed Energy at Outer Tank Puncture (million foot-pounds)	1.1	1.2	8.5
Force at Inner Tank Puncture (kips)	770.8	878.5	14.0
Displacement at Inner Tank Puncture (inches)	46.0	52.2	13.3
Absorbed Energy at Inner Tank Puncture (million foot-pounds)	2.0	2.4	21.5
East Skid String Potentiometer (inches)	-8.6	-7.6	-12.3
West Skid String Potentiometer (inches)	-4.7	-1.3	-73.3
East Head String Potentiometer (inches)	-9.3	-8.9	-4.1
West Head String Potentiometer (inches)	-6.8	-0.8	-88.4
Average Air Pressure (psi)	61.9	61.0	-1.4

The results of the post-test FE model using the B-W failure model for the stainless-steel inner tank exhibited slightly better agreement than the results of the post-test FE model using the MMC failure model. However, both post-test models still overestimated the force, displacement, and energy at the puncture of the inner tank.

8.1.2 Post-Test Model with Actual Steel Behaviors, 0.1/s Stainless Steel Plasticity, Crushable Foam Perlite, B-W Failure for Stainless Steel

The post-test FE model to attain closest agreement with the force-displacement response measured during the test used the actual material properties of the steels, a crushable foam material model for perlite, simulated loss of vacuum, and the B-W failure initiation envelope for both the carbon steel outer tank and the stainless-steel inner tank. While this model captured the force, indentation, and energy absorbed at the time of the outer tank puncture reasonably well, the model overestimated the force, indentation, and amount of energy absorbed by the DOT-113 at the time of inner tank puncture.

One additional consideration that was examined using a post-test model was the potential for strain-rate effects to have an influence on the puncture response of the DOT-113 tank car. Typically, the tensile tests that are used to characterize the YS, UTS, EB, as well as the shape of the stress-strain response are conducted at a very low strain rate, referred to as a QS test. The tank car impact test is a dynamic test, and therefore, the impact zone is expected to experience strain rates that are higher than QS load rates. For some steel alloys, including tank car steels TC128-B and A516-70, this QS stress-strain response provides a reasonable description of the steel’s behavior when subjected to loading at a higher strain rate. However, for stainless steels, strain rate effects are thought to be more significant. These strain rate effects can affect the YS, UTS, EB, and therefore, the energy to fail the material sample [26].

A previous study of the strain rate effects of ASTM A240 T304L stainless steel (similar to the T304 used in the tested DOT-113) included engineering stress-strain curves demonstrating the effects of strain rate on the YS, UTS, and EB of T304L stainless steel [26]. This study tested A304L coupons in tension at rates of 0.01/s, 0.1/s, 1/s, and 10/s. In general, this study reported that UTS was lowest at an intermediate strain rate (0.1/s) and highest at 10/s. The lowest rate examined, 0.01/s, was reported to have a UTS that measured between intermediate strain rates and the highest strain rates. Additionally, the 0.01/s data reported the highest EB, while all other rates appeared to have about the same EB. Thus, as the 0.1/s data reported both a strength and a ductility that was lower than the QS data, the strain rate effects appeared to be a potential explanation for the DOT-113 post-test model estimating a higher energy to puncture than what was measured during the test. Therefore, when compared to a QS test rate for a stainless steel similar to the stainless steel found in the inner tank of the tested car, the material was expected to require less energy to break when loaded at an intermediate strain rate.

The Abaqus FE software allows strain rate effects to be incorporated into several different material behaviors. A strain rate dependent stress-strain response can be defined, as can a strain rate dependent damage initiation envelope (either B-W or MMC). Ideally, a series of tensile tests will be performed at different strain rates against which a family of stress-strain responses and damage initiation envelopes can be calibrated. The Abaqus FE software determines the strain rate at material integration points for which rate-dependent effects have been defined and then interpolates the material properties for each integration point among the defined stress-strain and damage initiation responses. During a dynamic impact, the strain rate in a given element may vary significantly, and the material behaviors must be updated at each timestep as the strain rate changes.

Because the QS material properties from the inner tank of the DOT-113 were found to be in reasonable agreement with the QS T304L results reported in [26], it was assumed that the stainless steel from the DOT-113 would exhibit similar trends at different rates. As a simple check on whether strain rate effects could be a factor in the apparent overestimation of inner tank puncture force, displacement, and energy, the most conservative rate-dependent response from [26] was employed in the post-test DOT-113 model using actual steel behaviors and crushable foam perlite. The researchers hypothesized that using the 0.1/s strain rate properties in the DOT-113 model would result in a decrease in the estimated energy needed to puncture the inner tank, compared with using the actual T304 stainless-steel properties measured at a QS rate. The properties of the 0.1/s stainless steel material behavior defined in this post-test model are described in Appendix F, Section 4.2.

Figure 86 shows the impactor force versus impactor travel for the test and for the post-test FE model that used 0.1/s material properties (e.g., stress-strain and B-W envelope) for the stainless-steel inner tank. This FE model had the same level of agreement as the previous two FE models up to the point of puncture of the outer tank. While the previous two models overpredicted the puncture force, displacement, and energy of the inner tank, the model using 0.1/s properties for stainless steel estimated a puncture at a lower force, energy, and displacement than measured during the test.

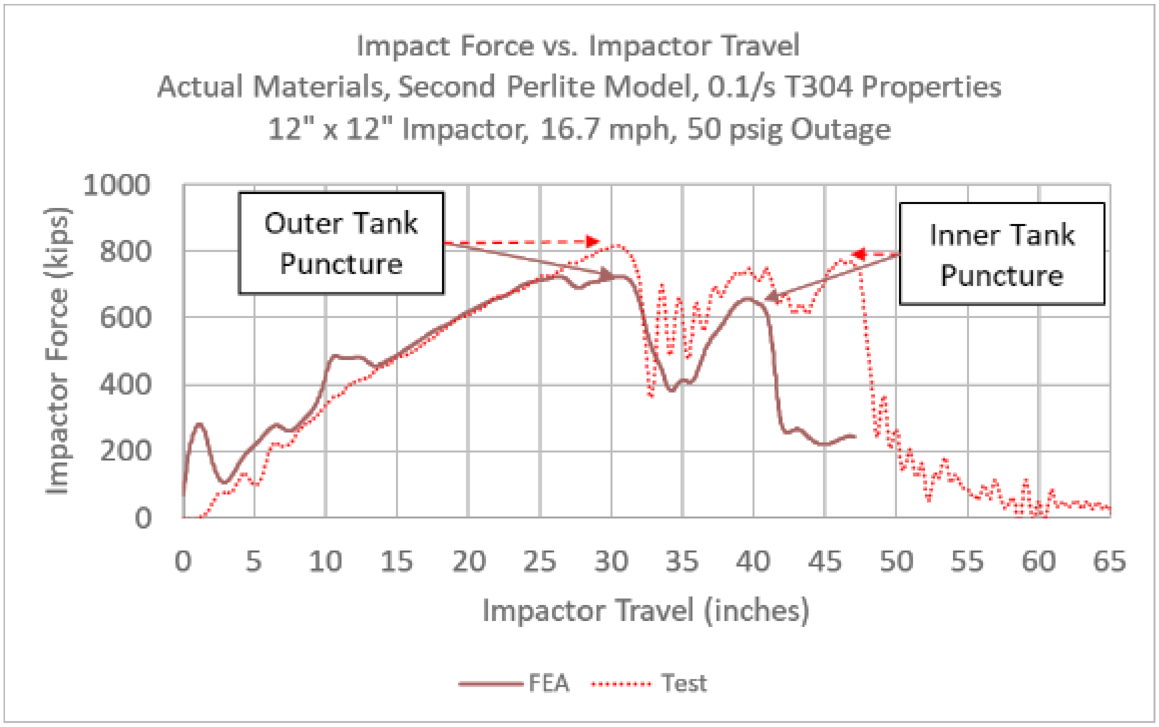

Figure 86. Impactor Force Versus Impactor Travel from Test and Post-Test FEA with Crushable Foam Perlite Material and 0.1/s T304 Properties

Figure 87 contains a plot of impactor velocity versus impactor travel for the FE model and the test measurements. Both results are in agreement until an impactor travel of approximately 40 inches. At that displacement, the FE model estimated puncture of the inner tank would occur while the test did not experience puncture until later. Thus, the FE model estimated a higher residual impactor velocity at puncture than was measured during the test.

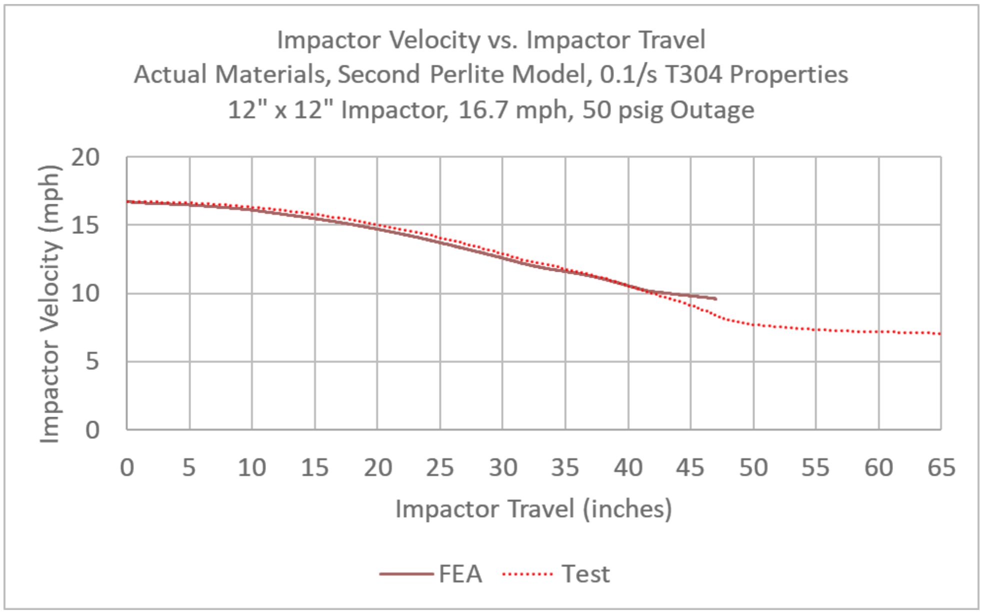

Figure 87. Impactor Velocity Versus Impactor Travel from Test and Post-Test FEA with Crushable Foam Perlite Material and 0.1/s T304 Properties

Figure 88 contains a plot of the energy absorbed by the DOT-113 versus the travel of the impactor. This energy was calculated by integrating the force-displacement response (Figure 86). This figure demonstrates that the FE model and the test were in agreement until approximately 40 inches of impactor travel. Beyond this distance, the FE model underpredicted the absorbed energy as the inner tank in the test did not puncture until approximately 46 inches of impactor travel.

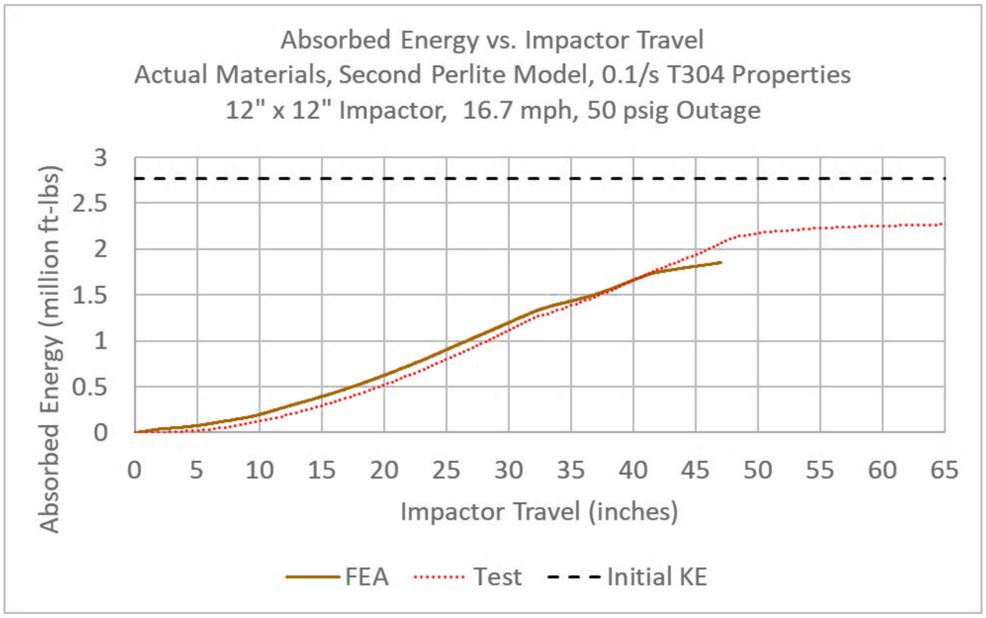

Figure 88. Absorbed Energy Versus Impactor Travel from Test and Post-Test FEA with Crushable Foam Perlite Material and 0.1/s T304 Properties

Table 32 presents a comparison of the peak values for numerous measurements from the test and the post-test FE model using 0.1/s data for the stainless steel. The full set of FE results is found in Appendix C, Section 3.5.

Table 32. Comparison of Peak Results from Post-Test FEA with Actual Steels Using 0.1/s Properties for T304 and Test Results

Peak Measurement	**Test *Value***	**FEA *Value***	**FEA *% Difference***
Force at Outer Tank Puncture (kips)	817.1	723.4	-11.5
Displacement at Outer Tank Puncture (inches)	30.4	26.4	-13.1
Absorbed Energy at Outer Tank Puncture (million foot-pounds)	1.1	1.0	-13.6
Force at Inner Tank Puncture (kips)	770.8	656.1	-14.9
Displacement at Inner Tank Puncture (inches)	46.0	39.6	-13.9
Absorbed Energy at Inner Tank Puncture (million foot-pounds)	2.0	1.6	-18.1
East Skid String Potentiometer (inches)	-8.6	-7.0	-19.1
West Skid String Potentiometer (inches)	-4.7	-1.4	-69.6
East Head String Potentiometer (inches)	-9.3	-8.7	-6.0
West Head String Potentiometer (inches)	-6.8	-1.3	-81.6
Average Air Pressure (psi)	61.9	56.1	-9.3

The post-test FE model using crushable foam perlite, B-W failure envelopes for both steels, and 0.1/s stress-strain and B-W properties for the inner tank was the first post-test FE model to underestimate the force, displacement, and energy necessary to puncture both tanks, compared to the test measurements. Further material modeling to develop a series of stress-strain responses and B-W envelopes at different strain rates could be undertaken to attempt to further improve the level of agreement between the test and the FE models. That work was not performed for this test but is expected to be included in future FE modeling in support of future DOT-113 impact tests. The results of this modeling study illustrated the potential for strain-rate effects on stainless steel to have a substantial influence on the puncture response of a stainless-steel tank, even at ambient temperature.

8.1.3 Post-Test Model with Actual Steel Behaviors, Crushable Foam Perlite, QS B-W Failure for Stainless Steel, 0 psi Ambient Pressure

During preparations for a subsequent test in this testing program, the modeling team discovered a discrepancy in the way in which the ambient pressure was applied to the air and water phases in all Test 10 FE models. As a result of this discrepancy, the inner tank in the FE models had a 12.3 psia ambient pressure applied to its outside surfaces, rather than a 0 psia pressure corresponding to the vacuum of the annular space. While this discrepancy was not expected to fundamentally alter the results of the FE models, its effects were still investigated. The post-test FE model described in Section 8.1.2, which used the QS B-W envelope for inner tank failure, was modified. The modification consisted of re-defining the ambient pressure outside of the hydraulic and pneumatic cavities to be 0 psia. Consequently, the initial gauge pressure defined in each cavity was increased to 62.3 psi from the previous 50 psi. This model continued the use of a prescribed pressure-time history to simulate loss of vacuum. Ambient pressure outside of the outer tank remained at 12.3 psi applied via a pressure load.

The impact force versus impactor travel for this model is shown in Figure 89. This model exhibits both qualitative and quantitative agreement with the test measurements. The model experienced two distinct puncture events, with the puncture of the outer tank occurring at both a similar force and displacement as seen in the test. The overall slopes of the force-displacement responses are also in agreement over much of the impact event. This model's response is generally similar to that from the model using a 12.3 psia ambient pressure for the cavities.

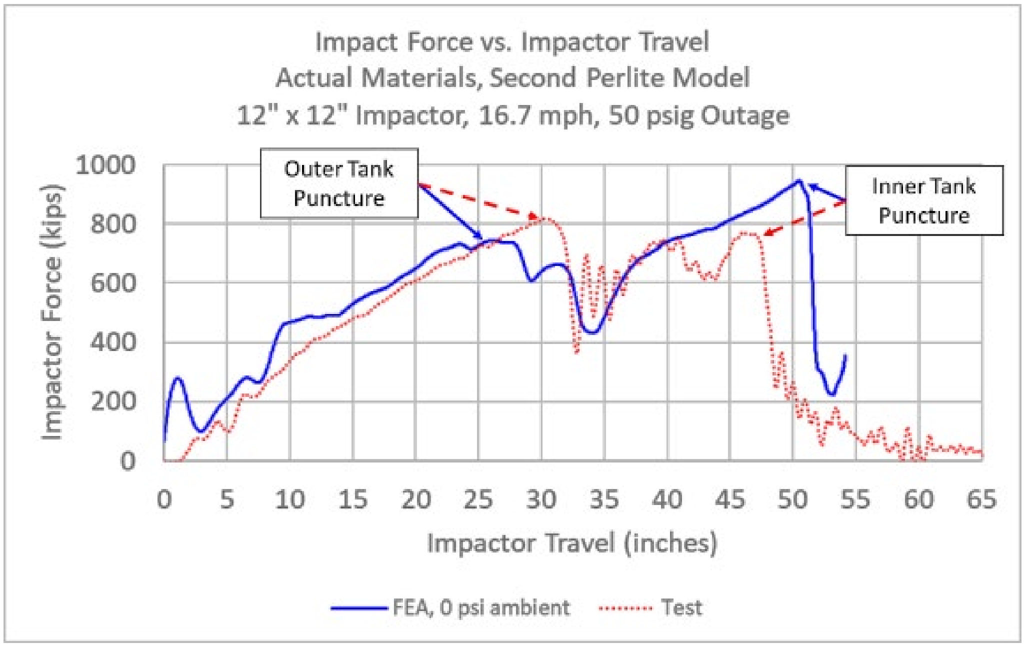

Figure 89. Impactor Force versus Impactor Travel from Test and Post-Test FEA with Crushable Foam Perlite Material, B-W Damage Initiation, and 0 psi Ambient Pressure

Figure 90 presents the impactor velocity versus impactor travel from the test and the post-test FEA using a 0-psi ambient pressure outside of the cavities. The FE model matches the test velocity closely, up to approximately 47 inches of travel. The level of agreement is similar to that see in the post-test FE model that used a 12.3 psia ambient pressure outside of the cavities (Figure 84).

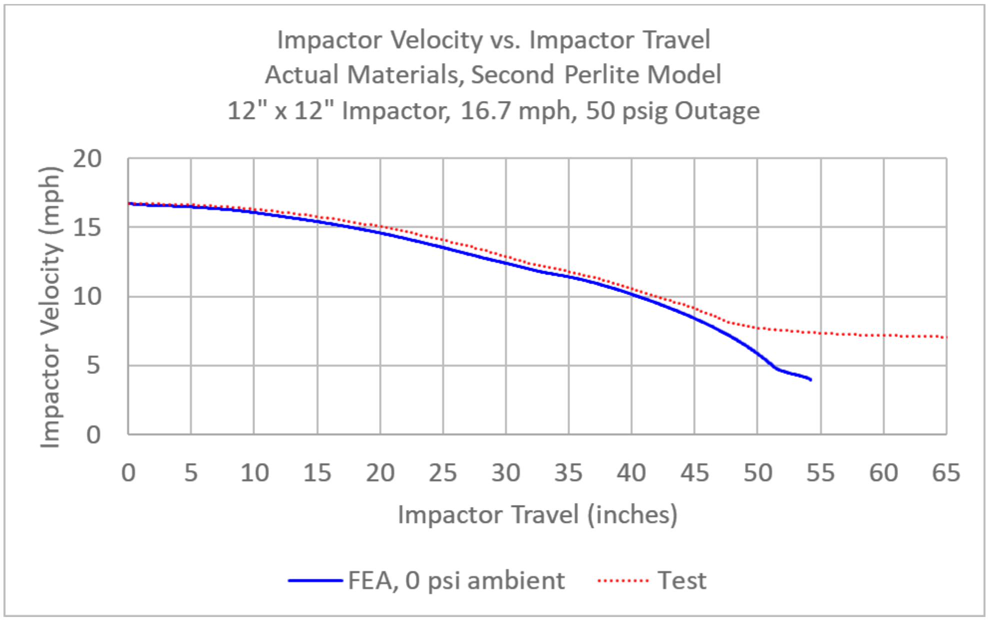

Figure 90. Impactor Velocity versus Impactor Travel from Test and Post-Test FEA with Crushable Foam Perlite Material, B-W Damage Initiation, and 0 psi Ambient Pressure

Figure 91 contains a plot of the energy absorbed by the DOT-113 versus the travel of the impactor. This energy was calculated by integrating the force-displacement response (Figure 89). This figure demonstrates that the FE model and the test were in agreement until approximately 48 inches of impactor travel. Beyond this distance, the FE model over-predicted the absorbed energy as the FE model's inner tank did not puncture until approximately 53 inches of impactor travel.

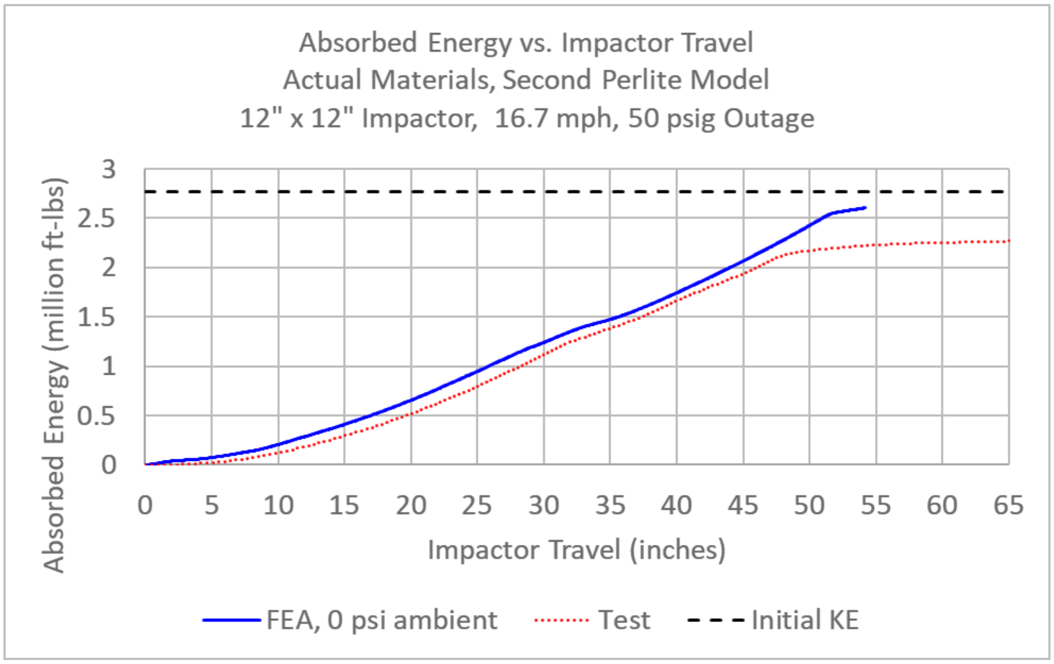

Figure 91. Absorbed Energy versus Impactor Travel from Test and Post-Test FEA with Crushable Foam Perlite Material, B-W Damage Initiation, and 0 psi Ambient Pressure

Table 33 presents a comparison of the peak values for numerous measurements from the test and the post-test FE model using the crushable foam perlite material model, the B-W damage initiation envelope for both steels, and an ambient pressure of 0 psi outside of both cavities. The full set of FE results is found in Appendix C, Section 3.6.

Table 33. Comparison of Peak Results from Test and Post-Test FEA with Crushable Foam Perlite Material and B-W Damage Initiation

Peak Measurement	**Test *Value***	**FEA *Value***	**FEA *% Difference***
Force at Outer Tank Puncture (kips)	817.1	743.9	-9.0
Displacement at Outer Tank Puncture (inches)	30.4	26.3	-13.6
Absorbed Energy at Outer Tank Puncture (million foot-pounds)	1.1	1.0	-10.1
Force at Inner Tank Puncture (kips)	770.8	944.4	22.5
Displacement at Inner Tank Puncture (inches)	46.0	50.5	9.7
Absorbed Energy at Inner Tank Puncture (million foot-pounds)	2.0	2.5	23.0
East Skid String Potentiometer (inches)	-8.6	-6.7	-22.0
West Skid String Potentiometer (inches)	-4.7	-1.4	-70.4
East Head String Potentiometer (inches)	-9.3	-7.7	-17.1
West Head String Potentiometer (inches)	-6.8	-1.2	-82.8
Average Air Pressure (psi)	61.9	59.3	-4.2

The results of the post-test FE model using an ambient pressure of 0 psi outside of the two cavities exhibited qualitatively similar results to the model run using an ambient pressure of 12.3 psi. The timing and amplitude of the force-time and force-displacement responses did change due to the removal of this extraneous atmospheric pressure on the outside of the inner tank. Both models still overestimated the energy required to cause puncture of both the inner and outer tanks.

9. Conclusion

This research supports FRA's tank car research program to provide the technical basis for rulemaking on enhanced and alternative performance standards for tank cars. This report documents the combined efforts of Volpe and TTCI to test and analyze the side impact performance of a specification DOT-113 tank car. The tank car was filled with water to approximately 82.4 percent of its volume. It was then sealed and pressurized to 50 psig. The test was intended to strike the tank car at a speed high enough to puncture both of the tank's shells. The tank car was impacted by a 297,126-pound ram car traveling at 16.7 mph. The impact deformed and tore both the outer and inner tanks, resulting in loss of lading. The post-test FE model and the test results were compared, with several discrepancies remaining even after making several adjustments to the post-test FE model.

9.1 Discussion

Video of the point of impact taken from onboard the ram car successfully captured the initiation of puncture and its propagation on the outer tank. Analysis of the test data and videos confirmed that the outer tank of the DOT-113 punctured first and its inner tank punctured subsequently. While the inner tank had a longitudinal weld in the vicinity of the puncture, neither the initiation nor the propagation of the puncture was influenced by this weld.

Material coupons were cut from the inner tank's stainless steel shell and subjected to tensile testing at both room temperature and cryogenic temperatures. The room temperature properties were within the expected range for the type of stainless steel used in the inner tank and were used to develop the post-test material model for the inner tank The cryogenic material properties were not used in the post-test modeling but are expected to be used to develop future material models. Future tests and models are planned to examine the performance of a DOT-113 tank car at cryogenic temperatures corresponding to both LN2 and LNG.

Material coupons were also cut from the outer tank's carbon steel shell and subjected to tensile testing at room temperature. The EB was found to exceed the minimum required by the material specification, but the YS and UTS were each found to be below the minimum levels required by the material specification. Additional chemical testing on this outer tank revealed that both the silicon and manganese content fell below the minimum required by the material specification. The post-test material model was developed based on the room temperature properties for the outer tank.

The overall response of the DOT-113 tank car was significantly influenced by the presence of perlite insulation in the annular space between the two tanks. The perlite influenced both the overall shape of the force-displacement response and the sequence of tank punctures in the post-test FE models. When perlite was omitted from the FE models, regardless of the steel properties modeled, an inner tank puncture did not occur under the impact conditions of the test. Various approaches to modeling perlite were attempted in the post-test modeling effort, using data from existing sources.

The perlite appeared to both stiffen the impact response and concentrate the load experienced by the inner tank. In models with the perlite omitted, the outer tank was free to move in response to the impactor as the annular space was simply a gap between the tanks. The outer tank could bend and deform as the impactor pushed through the annular space. The deformation of the outer tank affected the contact patch between the inner tank and the outer tank once the outer tank had deformed through the annular space.

When perlite was included in the model, the impactor needed to exert a larger force to indent the outer tank by a given distance, as the outer tank's motion was inhibited by the perlite within the annular space. Consequently, the outer tank reached a force level sufficient to initiate puncture at a lower displacement than if the annular space was empty. Further, because the perlite inhibited the outer tank from freely bending and flexing through the annular space, the inner tank "saw" a more localized contact from the impactor through the outer tank. Finally, because the DOT-113 was against a rigid wall in the test, the presence of perlite inhibited the outer tank from crushing on the side opposite the impactor. Inhibiting the outer tank from crushing on the wall side also served to increase the stiffness of the tank car in response to the impactor.

Based on the pre-test FE modeling, the tank car was expected to survive a 16.7 mph impact with the inner tank intact if the annular space was empty. Thus, the perlite appeared to decrease the puncture resistance of the DOT-113 in this particular test setup. It is important to note that the role of perlite may have been more significant due to the presence of the rigid backing wall as the tank car was limited in its ability to displace in response to the impact. Additionally, discussions with manufacturers of DOT-113 tank cars and others within the tank car industry indicated that perlite was largely discontinued in favor of MLI in the late 20th century. However, there is currently no prohibition on the use of perlite as an insulating material in cryogenic tank cars. If perlite will no longer be used on future cryogenic tank car designs, there is limited usefulness in further research characterizing its mechanical performance in impact events. However, if there is a renewed interest in the use of perlite as an insulating material in cryogenic tank cars in the future, it may be appropriate to perform additional studies on the mechanical behaviors of perlite to investigate any negative effects this type of insulation may have on the puncture resistance of perlite-equipped tank cars.

Even with inclusion of the perlite and inner and outer tank steel properties based on tensile tests of the actual materials of construction of the DOT-113's tanks, the post-test FE model overpredicts the force, displacement, and energy needed to puncture the inner tank. This non-conservative model differs from previous tank car FE models developed by Volpe, which, historically, have conservatively underpredicted the energy necessary to puncture the tank car. One behavior that has been identified as a potential source of this non-conservative outcome is the strain rate sensitivity of stainless steel. In previous FE models of carbon steel tank cars (i.e., TC128-B), strain rate effects have been negligible over the range of strain rates typically encountered during an impact test. However, stainless steel has a greater sensitivity to the rate at which it is loaded. As stainless steel's loading rate increases, its apparent strength increases but its ductility decreases. As both strength and ductility contribute to puncture resistance, QS loading rates (i.e., typical of rates used in tensile testing) are expected to have a higher apparent toughness (i.e., area beneath the stress-strain curve) than accelerated loading rates for stainless steel. Additional modeling work is planned to investigate the significance of strain rate effects on the specific stainless steels used in DOT-113 tank cars and to develop material models that incorporate these strain rate effects. Furthermore, additional future modeling and testing of stainless-steel materials is planned to investigate the simultaneous effects of accelerated strain rates and cryogenic temperatures. These combined effects would be encountered during a dynamic impact test or an in-service impact to a cryogenically loaded DOT-113 and must be well-understood.

9.2 Planned Future Work

This test was the first test in a planned series of four tests to be conducted on DOT-113 tank cars and tank car surrogates. The objective of this test series is to examine the potential improvement in shell puncture resistance for a DOT-113 tank car with an outer shell made of 9/16-inch thick TC128-B compared to a baseline DOT-113 using 7/16-inch thick A516-70 under LNG service conditions. Four tests are planned, with each test increasing in both complexity and realism compared to the previous test. Companion FE modeling is planned for each test, with the FE model expected to increase in complexity as results and observations from each test are studied and synthesized. Details of the planned testing sequence are summarized in Table 34.

Table 34. Summary of Planned DOT-113 Side Impact Test Conditions

	Test 10 (this report)	Test 11	Test 12	Test 13
Test Date	November 2019	June 2020	TBD 2021	TBD2021/2022
Test Article	DOT-113C120W	DOT-113 surrogate	DOT-113 surrogate	DOT-113C120W9
Thickness (Outer Tank)	7/16-inch (0.4375 inch)	9/16-inch (0.5625 inch)	~0.6-inch	9/16-inch (0.5625 inch)
Material (Outer Tank)	A516-70	TC128-B	TC128-B	TC128-B
Diameter (Outer Tank)	~119 inches	~120 inches	~120 inches	~120 inches
Length (Outer Tank)	~74 feet	~45 feet	TBD	TBD, typical of service
Thickness (Inner Tank)	1/4-inch (0.25 inch)	1/4-inch (0.25 inch)	1/4-inch (0.25 inch)	1/4-inch (0.25 inch)
Material (Inner Tank)	T304 stainless steel	T304 stainless steel	T304 stainless steel	T304 stainless steel
Diameter (Inner Tank)	~106 inches	~106 inches	~106 inches	~106 inches
Volume (Inner Tank)	32,900	19,300	TBD	TBD, Typical of service
Tank Lading	Water	Water	LN2	LN2
Outage	17.6%	17.6%	TBD, typical of service	TBD, typical of service
Pressure	50 psig	50 psig	TBD, typical of service	TBD, typical of service
Insulation	Perlite	MLI	MLI	MLI
Annular Pressure	Vacuum	Atmospheric	Vacuum	Vacuum
Impact Speed	16.7 mph	17.3 mph (actual)	TBD	TBD

The next test in this planned series (Test 11) will use a DOT-113 surrogate tank having a 9/16-inch outer tank made of TC128-B, where the Test 10 DOT-113C120W had a 7/16-inch outer tank made of A516-70 steel. Test 11 will also use water as the lading within the tank, with similar planned outage volume and outage pressure as the test described in this report. Beyond

Test 11, future tests are planned where the water within the tank is replaced by LN2, a cryogenic liquid. These future tests will more closely approximate the in-service conditions expected for a DOT-113 in LNG service by using a cryogenic liquid within the tank. It is anticipated that the material testing performed at various cryogenic temperatures after the November 2019 test will provide useful input data to guide future modeling of tank cars when the inner vessel is at cryogenic temperatures.

References

[1] Pipeline and Hazardous Materials Safety Administration, "Title 49 Code of Federal Regulations Section 179.16–Tank-head puncture-resistance systems," 2015.

[2] Pipeline and Hazardous Materials Safety Administration, "Title 49 Code of Federal Regulations Section 179.202-12–Performance standard requirements (DOT-117P)," U.S. Government Publishing Office, 2015.

[3] American Society for Testing and Materials, "ASTM A240/A240M: Standard Specification for Chromium and Chromium-Nickel Stainless Steel Plate, Sheet, and Strip for Pressure Vessels and for General Applications," ASTM International, Conshocken, PA, 2019.

[4] Kirkpatrick, S. W., Rakoczy, P., & MacNeill, R. A., "Side Impact Test and Analyses of a DOT-111 Tank Car," U.S. Department of Transportation, Federal Railroad Administration, Technical Report No. DOT/FRA/ORD/15-30, Washington DC, 2015.

[5] Rakoczy, P., & Carolan, M., "Side Impact Test and Analysis of a DOT-112 Tank Car," U.S. Department of Transportation, Federal Railroad Administration, Technical Report No. DOT/FRA/ORD-16/38, Washington, DC, 2016.

[6] Rakoczy, P., Carolan, M., Gorhum, T., & Eshraghi, S., "Side Impact Test and Analyses of a DOT-117 Tank Car," U.S. Department of Transportation, Federal Railroad Administration, Technical Report No. DOT/FRA/ORD-19/13, Washington, DC, 2019.

[7] Carolan, M., & Rakoczy, P., "Side Impact Test and Analyses of a DOT-105 Tank Car," U.S. Department of Transportation, Federal Railroad Administration, Technical Report No. DOT/FRA/ORD-19/12, Washington DC, 2019.

[8] Kirkpatrick, S. W., "Detailed Puncture Analyses of Various Tank Car Designs: FInal Report - Revision 1," January 2010.

[9] American Society for Testing and Materials, "ASTM A516/A516M: Standard Specification for Pressure Vessel Plates Carbon Steel for Moderate- and Lower-Temperature Service," ASTM International, Conshocken, PA, 2006.

[10] Kirkpatrick, S. W., Rakoczy, P., MacNeill, R. A., & Anderson, A., "Side Impact Test and Analyses of a DOT-111 Tank Car," U.S. Department of Transportation, Federal Railroad Administration, Technical Report No. DOT/FRA/ORD/15-30, Washington, DC, 2015.

[11] Rakoczy, P., & Carolan, M., "Side Impact Test and Analysis of a DOT-112 Tank Car," U.S. Department of Transportation, Federal Railroad Administration, Technical Report No. DOT/FRA/ORD-16-38, Washington, DC, 2016.

[12] Rakoczy, P., Carolan, M., Eshraghi, S., & Gorhum, T., "Side Impact Test and Analyses of a DOT-117 Tank Car," U.S. Department of Transportation, Federal Railroad Administration, Technical Report No. DOT/FRA/ORD-19/13, Washington, DC, 2019.

[13] Carolan, M., & Rakoczy, P., "Side Impact Test and Analyses of a DOT-105 Tank Car," U.S. Department of Transportation, Federal Railroad Administration, Technical Report No. DOT/FRA/ORD-19/12, Washington, DC, 2019.

[14] Eshraghi, S., Trevithick, S., Carolan, M., Rakoczy, P., Wilson, N., "Side Impact Test and Analyses of a DOT-111 (CPC-1232) Tank Car," U.S. Department of Transportation, Federal Railroad Administration, Technical Report No. DOT/FRA/ORD-20/43, Washington, DC, 2020.

[15] The Engineering Toolbox, "Water - Density, Specific Weight and Thermal Expansion Coefficient," 2003.

[16] Encyclopedia Air Liquide, "Ethylene - Gas Encyclopedia by Air Liquide," 2020.

[17] Transportation Technology Center, Inc., "Test Implementation Plan for FRA Tank Car Side Impact, Revision 2," Pueblo, CO, 2019.

[18] SAE International, *Instrumentation for Impact Test - Part 1: Electronic Instrumentation,* Warrendale, PA: SAE, 2007.

[19] American Society for Testing and Materials, *ASTM E8/E8M: Standard Test Methods for Tension Testing of Metallic Materials,* West Conshocken, PA, PA: ASTM International, 2013.

[20] American Society for Testing and Materials, *Standard Specification for Carbon Steel Plates for Pressure Vessels for Moderate and Lower Temperature Service,* Philadelphia, PA, 1969.

[21] Kirkpatrick, S. W., "Detailed Puncture Analyses of Various Tank Car Designs: Final Report - Revision 1," U.S. Departmen to Transportation, Federal Railroad Administration, Washington, DC, 2010.

[22] Dassault Systèmes Simulia Corp., *Abaqus 2017,* Providence, RI, 2017.

[23] Bao, Y., & Wierzbicki, T., "On fracture locus in the equivalent strain and stress triaxiality space," *International Journal of Mechanical Sciences, 46*(2004), p. 81–98, 2004.

[24] Bai, Y., & Wierzbicki, T., "A new model of metal plasticity and fracture with pressure and Lode dependence," *International Journal of Plasticity, 24*(6), p. 1071–1096, 2008.

[25] Wilson, N., Eshraghi, S., Trevithick, S., Carolan, M., & Rakoczy, P., "Side Impact Test and Analyses of a DOT-105 Tank Car – 6 X 6 Inch Indenter," U.S. Department of Transportation, Federal Railroad Administration, Technical Report No. DOT/FRA/ORD-20/38, Washington, DC, 2020.

[26] Kirkpatrick, S. W., & McKeighan, P. C., "Correlating Material Properties to Puncture Resistance to Enhance the Safety and Security of Tank Cars: Final Technical Report for Project TWP-10 - Revision 1," U.S. Department of Transportation, Federal Railroad Administration, Washington, DC, 2018.

[27] Paredes, M., Grolleau, V., & Wierzbicki, T., "On Ductile Fracture of 316L Stainless Steels at Room and Cryogenic Temperature Level: An Engineering Approach to Determine Material Parameters," *Maerialia,* vol. 100624, 2020.

[28] Paik, J. K., Kim, K. J., Lee, J. W., Jung, G. B., & Kim, S. J., "Test database of the mechanical properties of mild, high-tensile and stainless steel and aluminium alloy associated with cold temperatures and strain rates," *Ships and Offshore Structures, 12*(sup1), p. S230–S256, 2017.

[29] Cherry, J. L., "Analyses of Containment Structures with Corrosion Damage," in *1996 International Mechanical Engineering Congress and Exhibition*, SAND-96-0004c, CONF-961105-17, DE96014031, 97:007635, AC04-94AL85000 Atlanta, GA, 1996.

[30] Lee, Y. -W., & Wierzbicki, T., "Quick Fracture Calibration for Industrial Use," MIT Impact & Crashworthiness Laboratory, Cambridge, MA, 2004.

[31] Lee, Y. -W., "Fracture Prediction in Metal Sheets," Massachusetts Institute of Technology, Cambridge, MA, 2005.

[32] The Engineering ToolBox, "Universal and Individual Gas Constants," 2004.

[33] The Engineering ToolBox, "Air - Molecular Weight and Composition," 2004.

[34] Urieli, I., "Specific Heat Capacities of Air," Ohio University, 2008.

[35] Smits, A. J., A Physical Introduction to Fluid Mechanics, New York: John Wiley and Sons, 2000.

[36] The Engineering ToolBox, "Speed of Sound in Water," 2004.

[37] Rotter, L. L., "Economic Analysis of Perlite versus Super Insulation in Liquid Hydrogen Storage and Run Vessels for the M-1 Program," National Aeronautics and Space Administration (NASA), Covina, CA, 1965.

[38] Fecht, B. A., Gates, T. E., Nelson, K. O., & Marr, G. D., "Comparative Safety Analysis of LNG Storage Tanks," U.S. Department of Energy, United States, 1982.

[39] "Pipeline Blast Mitigation Technologies," United States. Combating Terrorism Technical Support Office. Technical Support Working Group, 2011.

[40] Chiroux, R. C., Foster Jr., W. A., Johnson, C. E., Shoop, S. A., & Raper, R. L., "Three-dimensional finite element analysis of soil interaction with a rigid wheel," *Applied Mathematics and Computation, 162*(2005), p. 707–722, 2005.

[41] The Engineering ToolBox, "Air - Altitude, Density and Specific Volume," 2003.

[42] Paredes, M., Sarzosa, D., Savioli, R., Wierzbicki, T., Jeong, D., & Tyrell, D., "Ductile Tearing Analysis of TC128 Tank Car Steel Under Mode I Loading Condition," *Theoretical and Applied Fracture Mechanics,* vol. 96, p. 658–675, 2018.

[43] Swift, H. W., "Plastic instability under plane stress," *Journal of the Mechanics and Physics of Solids, 1*(1), p. 1–18, 1952.

[44] Voce, E., "The relationship between stress and strain for homogeneous deformations," *Journal of the Institute of Metals,* vol. 74, p. 537–562, 1948.

[45] Eshraghi, S., & Carolan, M., "Quick Calibration of Fracture Behaviors in TC128 Steel for Finite Element Modeling," U.S. Department of Transportation, Federal Railroad Administration, Technical Report No. DOT/FRA/ORD-20/46, Washington, DC, 2020.

[46] Bai, Y., & Wierzbicki, T., "Application of extended Mohr-Coulomb criterion to ductile fracture," *International Journal of Fracture,* vol. 161, p. 1–20, 2010.

[47] Wierzbicki, T., & Xue, L., "On the effect of the third invariant of the stress deviator on ductile fracture," Massachusetts Institute of Technology Impact & Crashworthiness Laboratory, Cambridge, MA, 2005.

[48] Fasanella, E. L., Jackson, K. E., & Sotiris, K., "Soft Soil Impact Testing and Simulation of Aerospace Structures," in *10th International LS-DYNA User''s Conference*, Dearborn, MI, 2008.

[49] Wilson, H. S., "Lightweight Aggregates - Vermiculite, Perlite, Pumice - For Insulating Concretes," Canada Centre for Mineral and Energy Technology, Ottawa, Ontario, 1981.

[50] Mancuso, S., Mazzolai, B., Comparini, D., Popova, L., Azzarello, E., Masi, E., Bazihizina, N., Sinibaldi, E., & Pandolfi, C., "Subsurface investigation and interaction by self-burying bio-inspired probes: Self-burial strategy and performance in Erodium cicutarium - SeeDriller Final Report," No. 12-6401, European Space Agency, Advanced Concepts Team, 2014.

[51] Haery, H. A., "Elastic and Mechanical Properties of Expanded Perlite and Perlite/Epoxy Foams," University of Newcastle, Australia, Newcastle, Australia, 2017.

[52] American Society of Heating, Refrigerating and Air-Conditioning Engineers, ASHRAE Thermodynamic Properties of Refrigerants, New York: American Society of Heating, Refrigerating and Air-Conditioning Engineers, 1969.

[53] Duncan, A., Lam, P. -S., & Adams, T., "Tensile Testing of Carbon Steel in High Pressure Hydrogen," in *ASME 2007 Pressure Vessels and Piping Conference*, San Antonio, TX, 2007.

[54] Goel, G. S., "A Numerical Study of Tillage Tool Wear During Plowing of Sandy Soil," University of North Carolina at Charlotte, Charlotte, NC, 2013.

[55] Rodriguez, E. A., & Duffey, T. A., "Fracture-Safe and Fatigue Design Criteria for Detonation-Induced Pressure Loading in Containment Vessels," Welding Research Council Bulletin, 2004.

[56] Mehta, V., "Evaluation of the Fracture Parameters for SA-516 Grade 70 Material," *IOSR Journal of Mechanical and Civil Engineering, 13*(3), p. 38–45, 2016.

[57] Succop, L. N., Pense, A. W., & Stout, R. D., "The Effects of Warm Overstressing on Pressure Vessel Steel Properties," in *AWS 51st Annual Meeting*, Cleveland, OH, 1970.

[58] Brust, F. W., Yang, Y. P., & Scott, P. M., "Evaluation of Reactor Pressure Vessel (RPV) Nozzle to Hot-Leg Piping Bimetallic Weld Joint Integrity for the V.C. Summer Nuclear Power Plant," United States Nuclear Regulatory Commission, Washington, DC, 2002.

[59] Weber, R. A., "Weldability Characteristics of Construction Steels A36, A514, and A516," United States Army Corps of Engineers, Champaign, IL, 1981.

[60] Thomas, J. K., "Failure strain and mechanical property data for the Type IIIA waste tank liners," U.S. Department of Energy, Technical Report No. WSRC-RP-92-859, Washington, DC, 1992.

[61] McKinley, J., Xu, S., Gesing, M., & Williams, B., Strength, creep, and toughness of two tank car steels, TC128B and A516-70, CanmetMATERIALS, Ed., Ottawa, Canada: Transport Canada, 2019, p. 92.

Appendix A. Camera and Target Positions

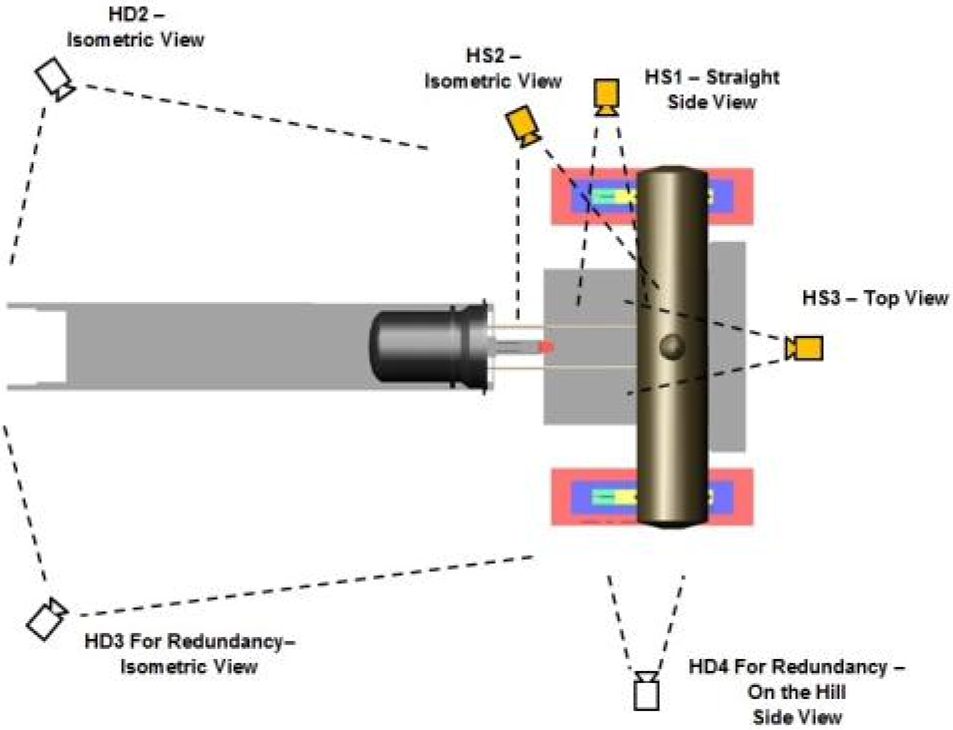

Figure A1. Camera Positions (Top) — High Speed, High Definition

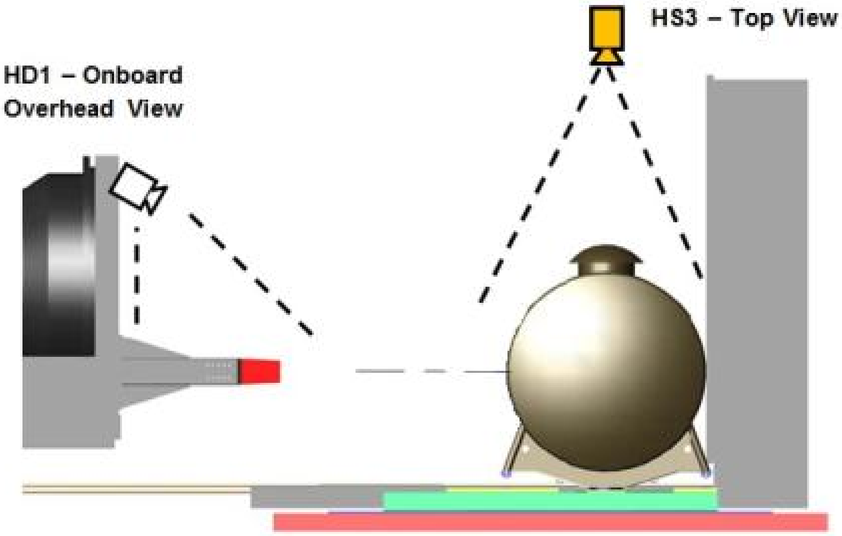

Figure A2. Camera Positions (side) — High Speed, High Definition

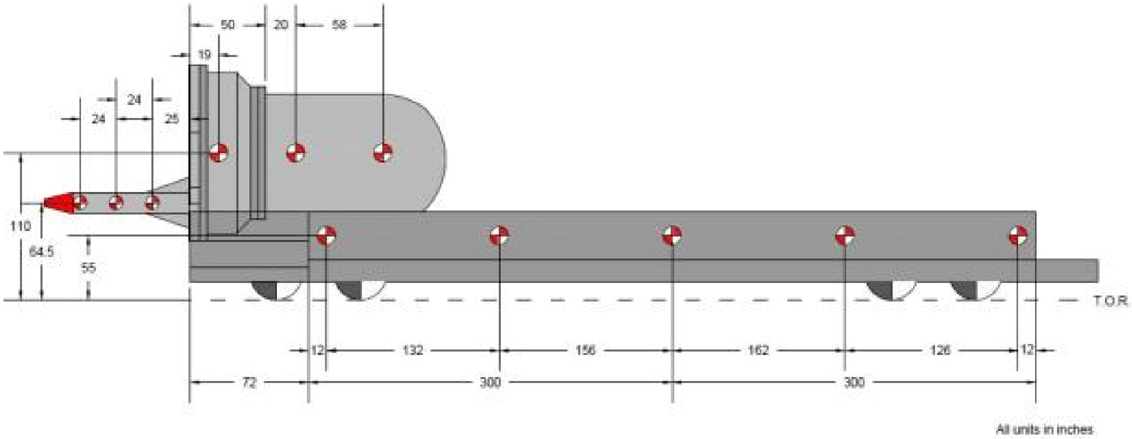

Figure A3. Ram Car Target Positions

Appendix B. Test Data

Section 1, Section 2, and Section 3 of this appendix contain raw and filtered test data. The raw accelerations and internal pressures measured on different locations on the ram car were processed as follows: the test data from -1 second to -0.1 second on each channel were averaged, and this value was subtracted from the test measurements in order to remove any initial offsets in the data. Each channel was then filtered to channel frequency class (CFC) 60 using the procedures given in SAE J211 [18]. Displacement data did not require any filtration.

Appendix B, Section 4 contains laboratory test results from material samples taken after the test of both the inner shell (T304 stainless steel) and outer shell (A-516 carbon steel) of the tank car.

Section 1 – Accelerations

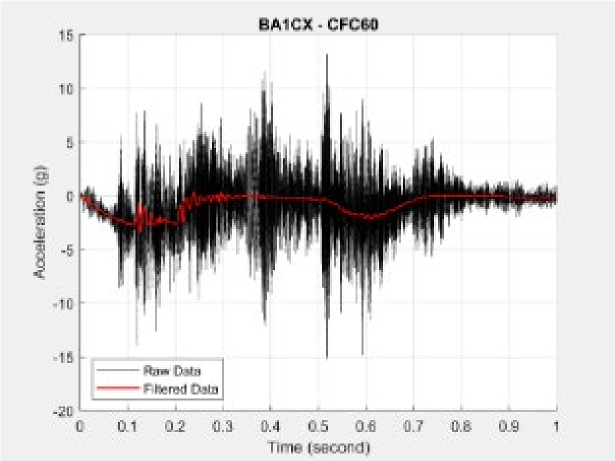

Figure B1. Raw and CFC60 Filtered Acceleration-Time Data from BA1CX

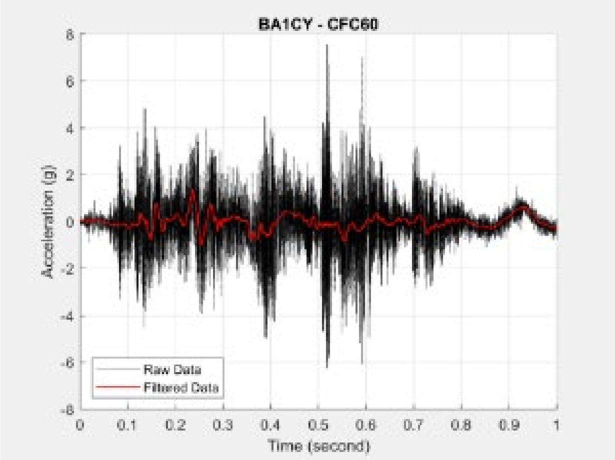

Figure B2. Raw and CFC60 Filtered Acceleration-Time Data from BA1CY

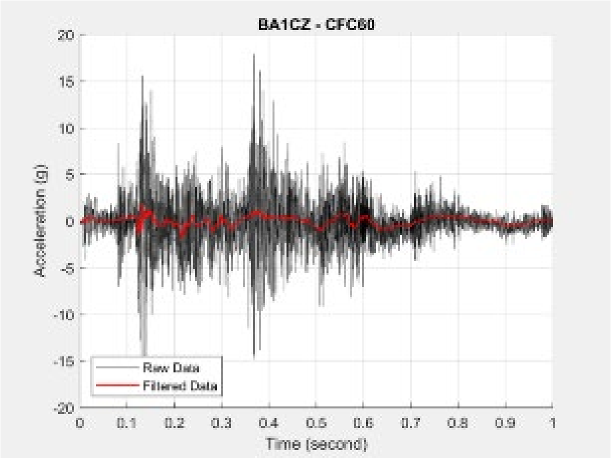

Figure B3. Raw and CFC60 Filtered Acceleration-Time Data from BA1CZ

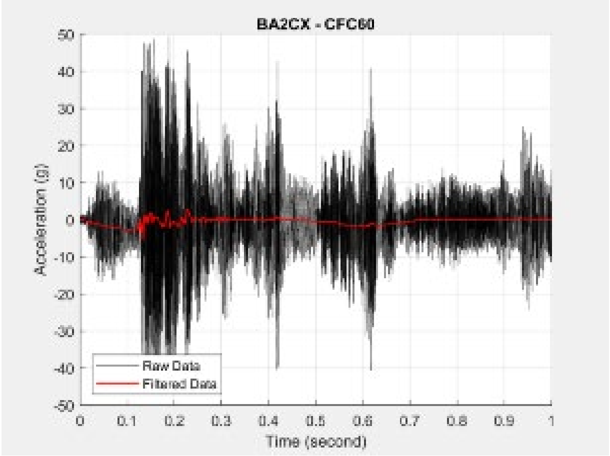

Figure B4. Raw and CFC60 Filtered Acceleration-Time Data from BA2CX

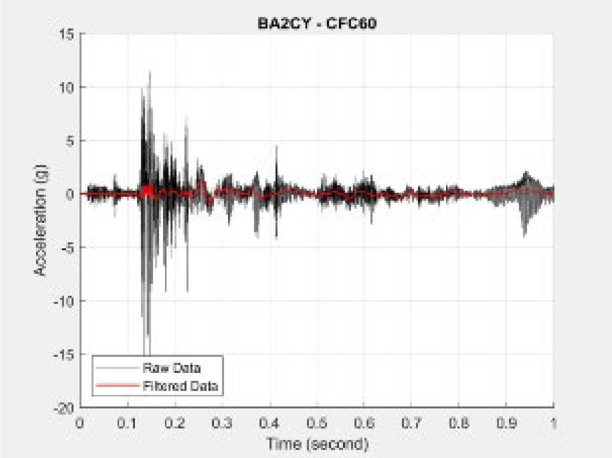

Figure B5. Raw and CFC60 Filtered Acceleration-Time Data from BA2CY

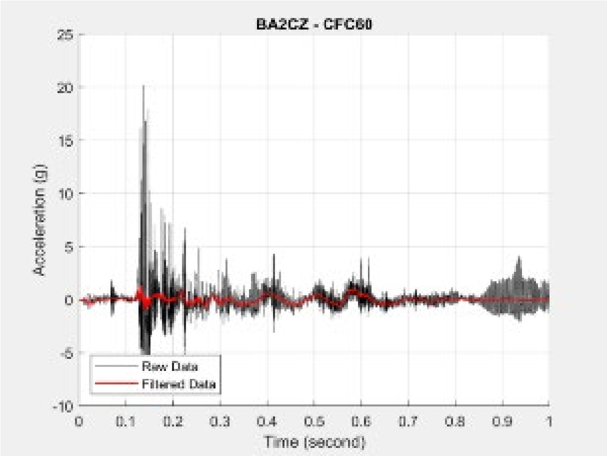

Figure B6. Raw and CFC60 Filtered Acceleration-Time Data from BA2CZ

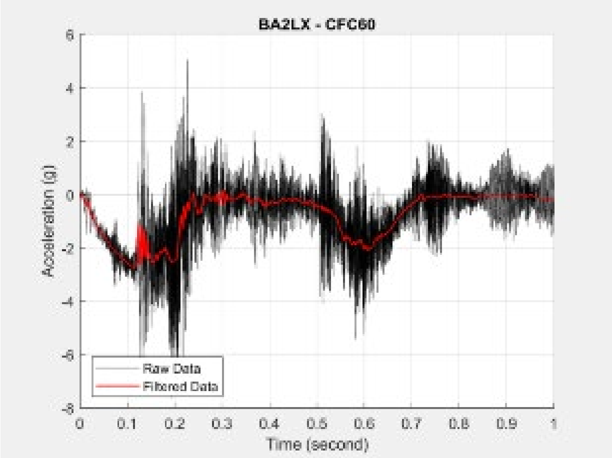

Figure B7. Raw and CFC60 Filtered Acceleration-Time Data from BA2LX

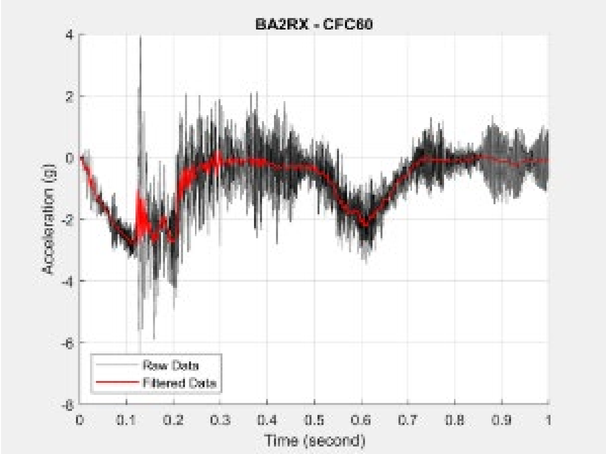

Figure B8. Raw and CFC60 Filtered Acceleration-Time Data from BA2RX

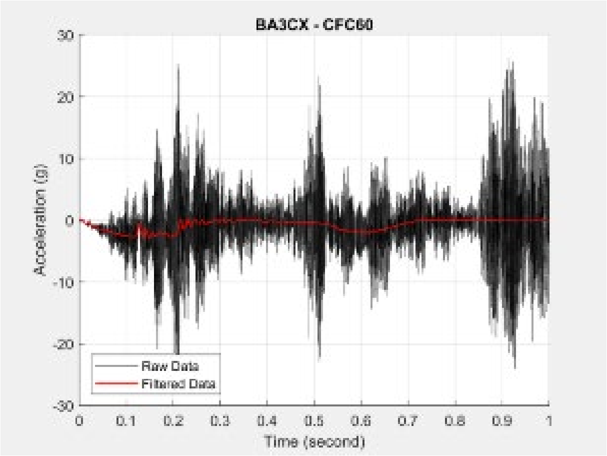

Figure B9. Raw and CFC60 Filtered Acceleration-Time Data from BA3CX

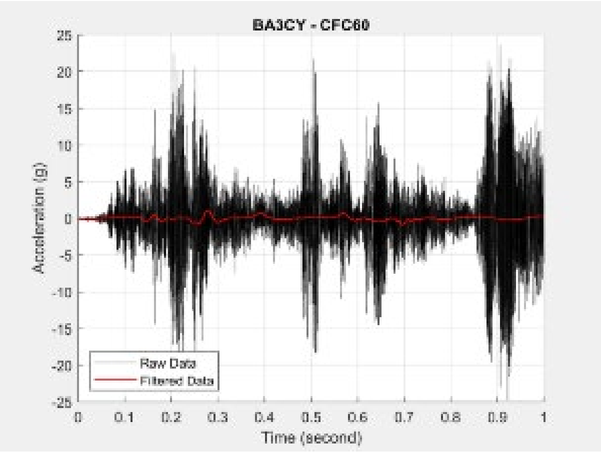

Figure B10. Raw and CFC60 Filtered Acceleration-Time Data from BA3CY

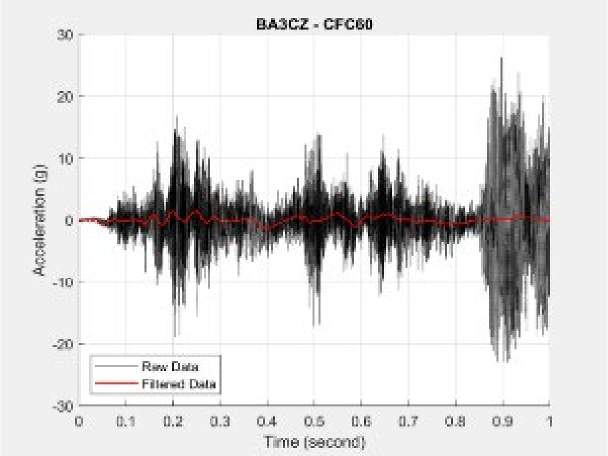

Figure B11. Raw and CFC60 Filtered Acceleration-Time Data from BA3CZ

Section 2 – Pressures

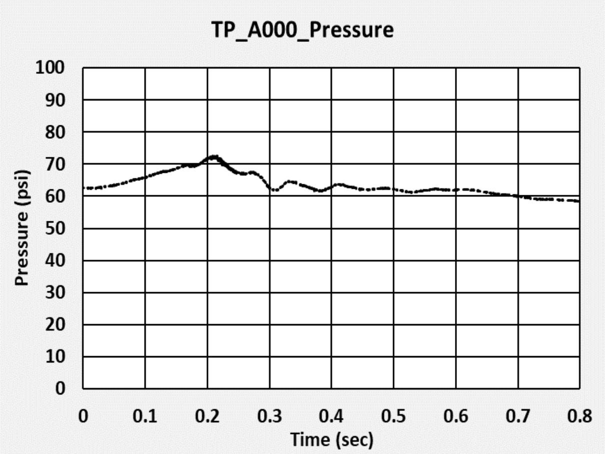

Figure B12. Raw Pressure-Time Data from TP_A000

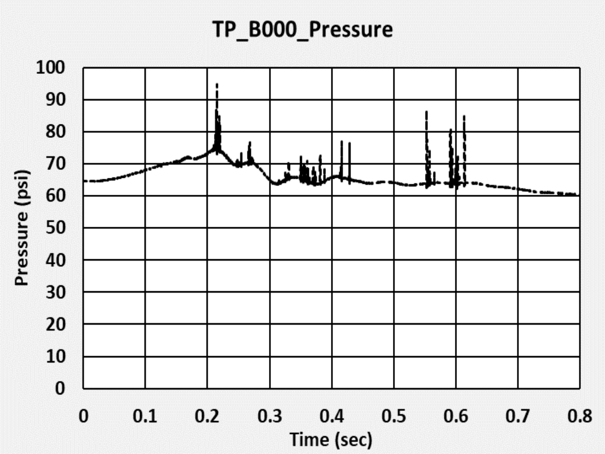

Figure B13. Raw Pressure-Time Data from TP_B000

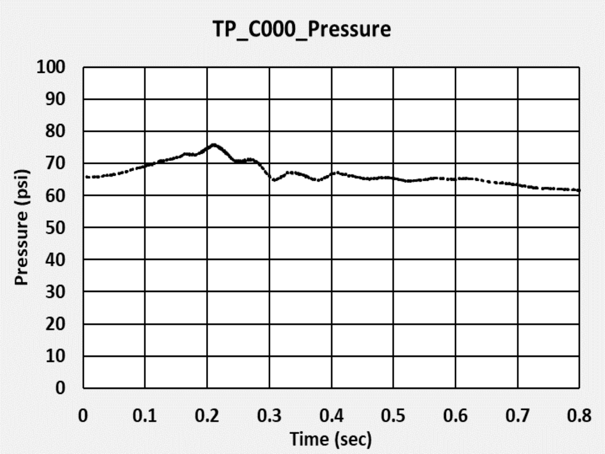

Figure B14. Raw Pressure-Time Data from TP_C000

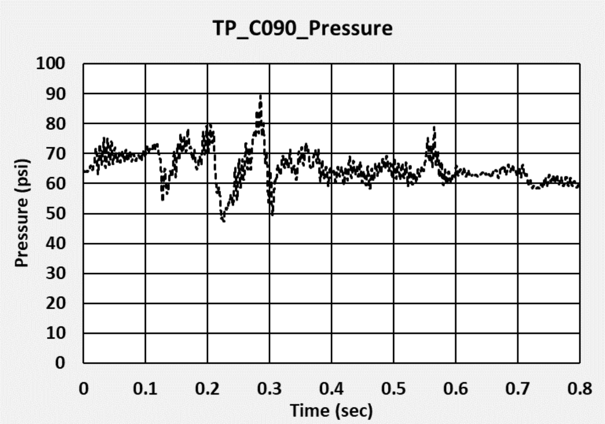

Figure B15. Raw Pressure-Time Data from TP_C090

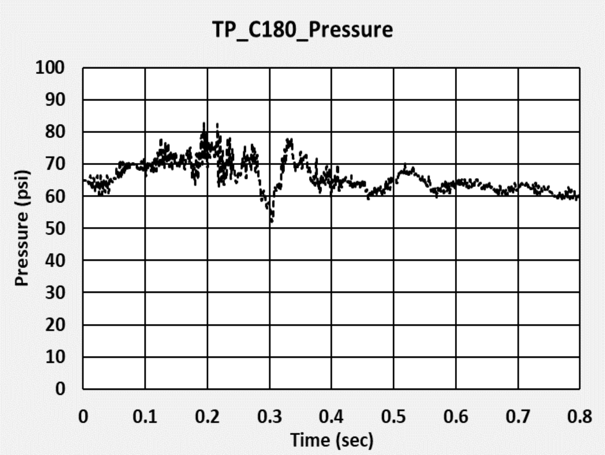

Figure B16. Raw Pressure-Time Data from TP_C180

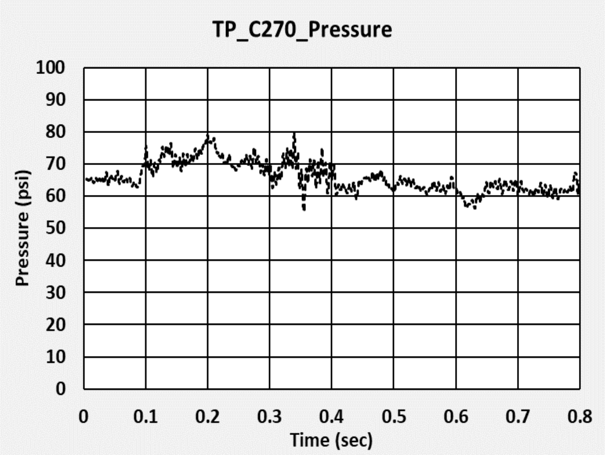

Figure B17. Raw Pressure-Time Data from TP_C270

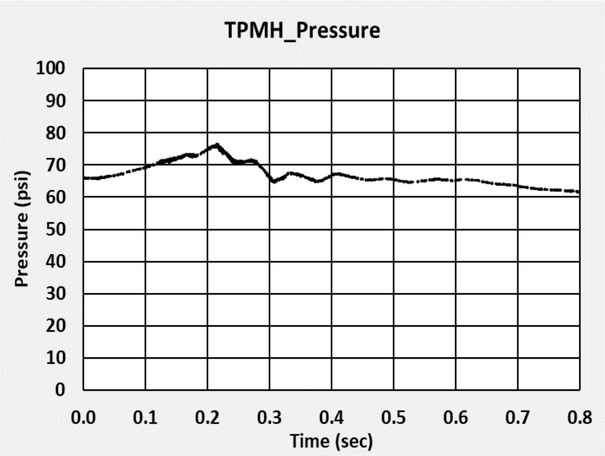

Figure B18. Raw Pressure-Time Data from TPMH

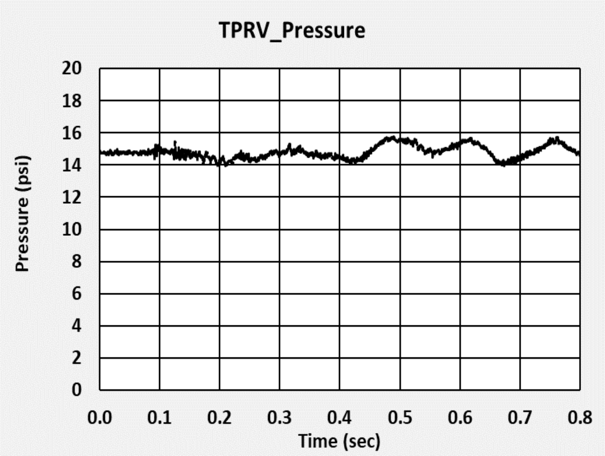

Figure B19. Raw Pressure-Time Data from TPRV

Section 3 – Displacements

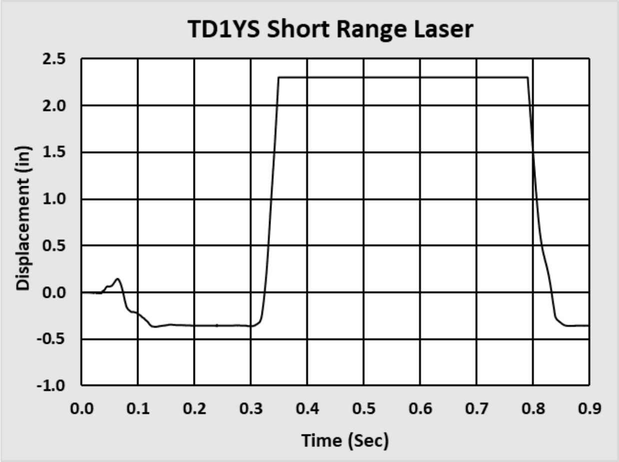

Figure B20. Raw Displacement-Time Data from Short Range Wall Mounted Laser Displacement Transducer (Range: 1.4 in to 4.3 in)

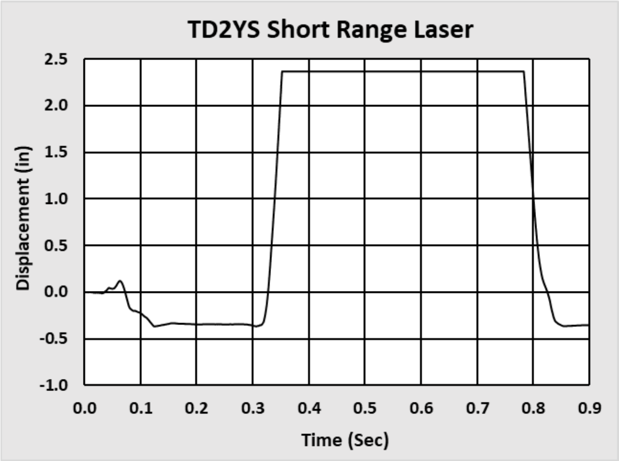

Figure B21. Raw Displacement-Time Data from Short Range Wall Mounted Laser Displacement Transducer (Range: 1.4 in to 4.3 in)

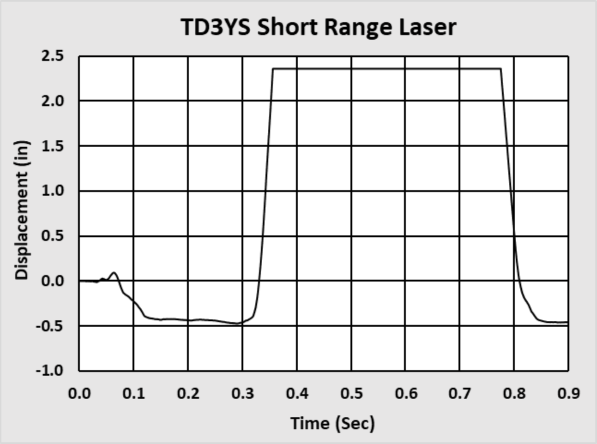

Figure B22. Raw Displacement-Time Data from Short Range Wall Mounted Laser Displacement Transducer (Range: 1.4 in to 4.3 in)

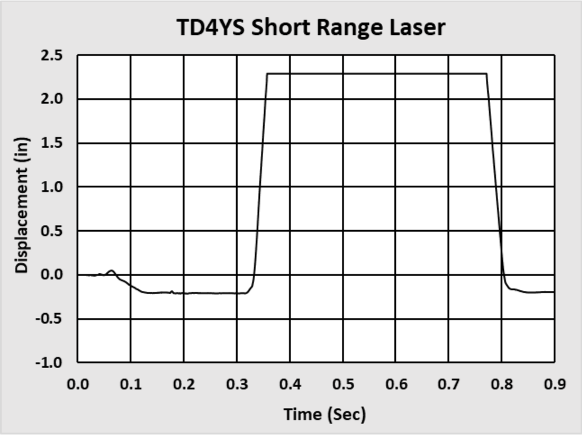

Figure B23. Raw Displacement-Time Data from Short Range Wall Mounted Laser Displacement Transducer (Range: 1.4 in to 4.3 in)

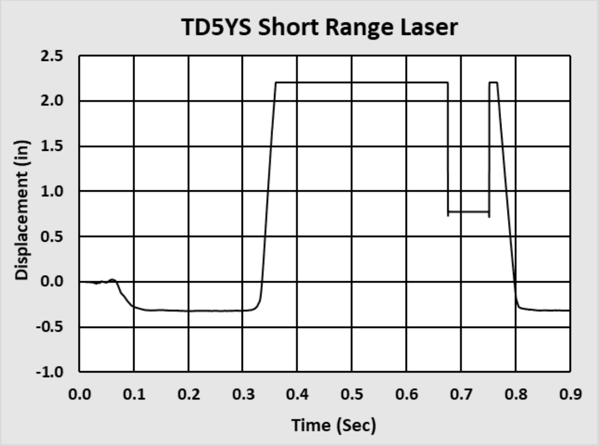

Figure B24. Raw Displacement-Time Data from Short Range Wall Mounted Laser Displacement Transducer (Range: 1.4 in to 4.3 in)

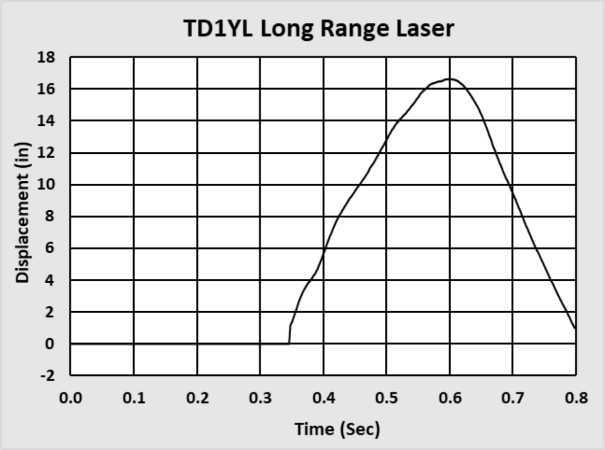

Figure B25. Raw Displacement-Time Data from Long Range Wall Mounted Laser Displacement Transducer (Range: 4 in to 39 in)

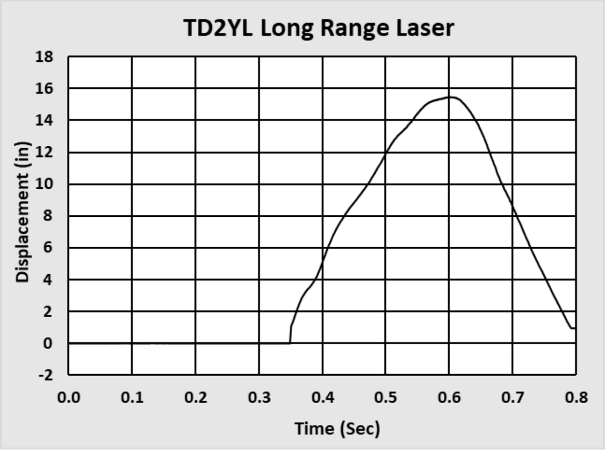

Figure B26. Raw Displacement-Time Data from Long Range Wall Mounted Laser Displacement Transducer (Range: 4 in to 39 in)

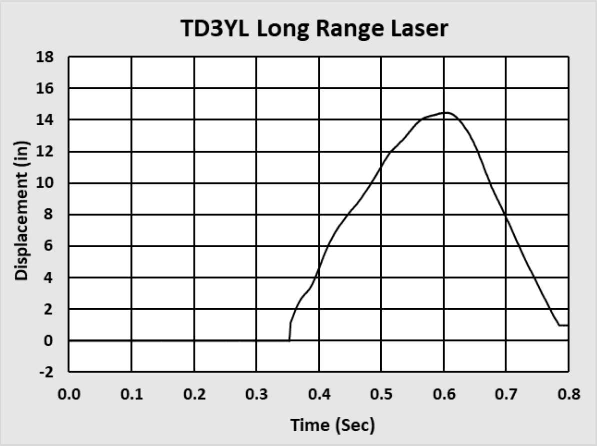

Figure B27. Raw Displacement-Time Data from Long Range Wall Mounted Laser Displacement Transducer (Range: 4 in to 39 in)

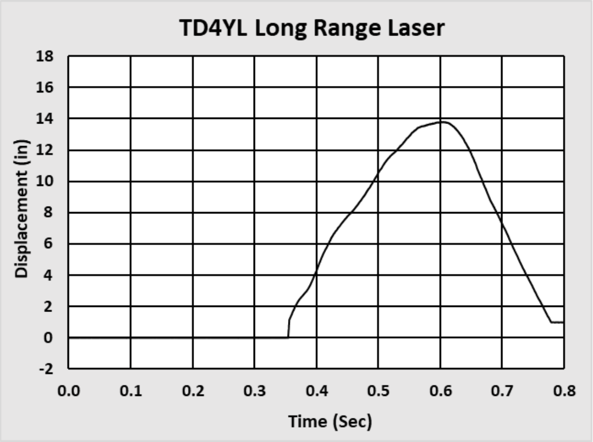

Figure B28. Raw Displacement-Time Data from Long Range Wall Mounted Laser Displacement Transducer (Range: 4 in to 39 in)

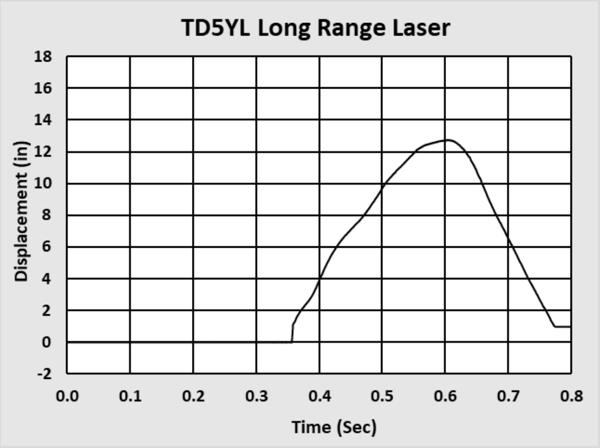

Figure B29. Raw Displacement-Time Data from Long Range Wall Mounted Laser Displacement Transducer (Range: 4 in to 39 in)

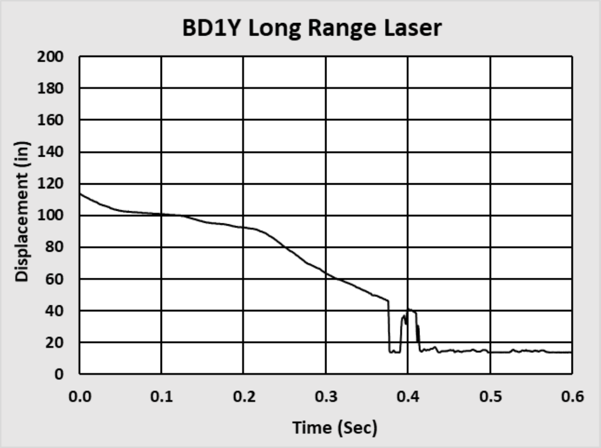

Figure B30. Raw Displacement-Time Data from Long Range Ram Car Mounted Laser Displacement Transducer (Range: 2 in to 39 ft)

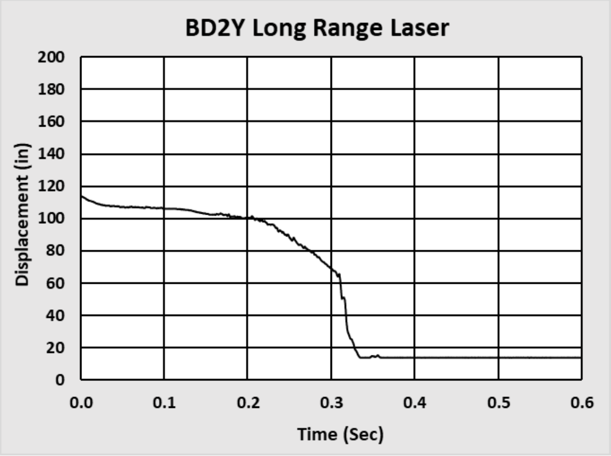

Figure B31. Raw Displacement-Time Data from Long Range Ram Car Mounted Laser Displacement Transducer (Range: 2 in to 39 ft)

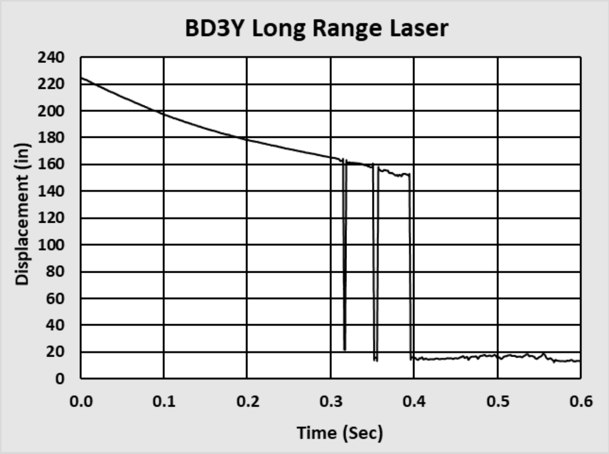

Figure B32. Raw Displacement-Time Data from Long Range Ram Car Mounted Laser Displacement Transducer (Range: 2 in to 39 ft)

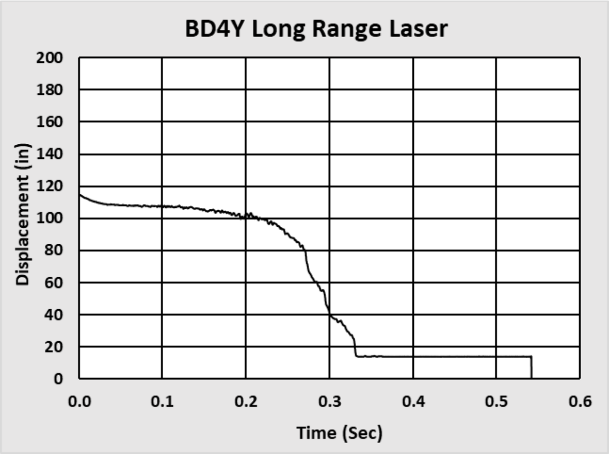

Figure B33. Raw Displacement-Time Data from Long Range Ram Car Mounted Laser Displacement Transducer (Range: 2 in to 39 ft)

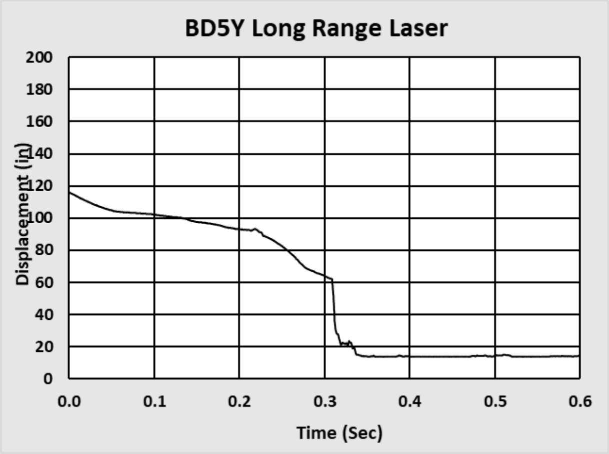

Figure B34. Raw Displacement-Time Data from Long Range Ram Car Mounted Laser Displacement Transducer (Range: 2 in to 39 ft)

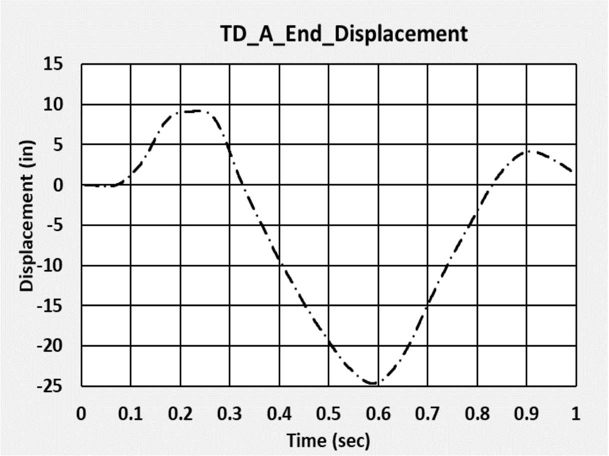

Figure B35. Raw Displacement-Time Data from Displacement Transducer on A-End Head

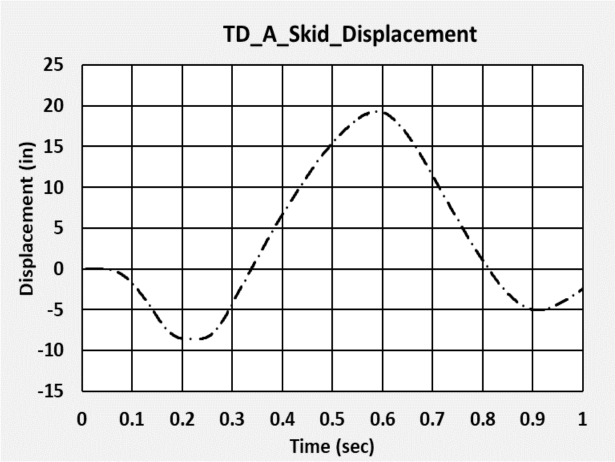

Figure B36. Raw Displacement-Time Data from Displacement Transducer on A-End Skid

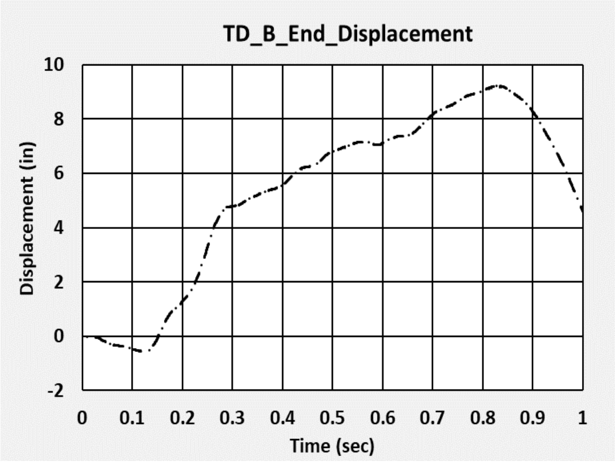

Figure B37. Raw Displacement-Time Data from Displacement Transducer on B-End Head

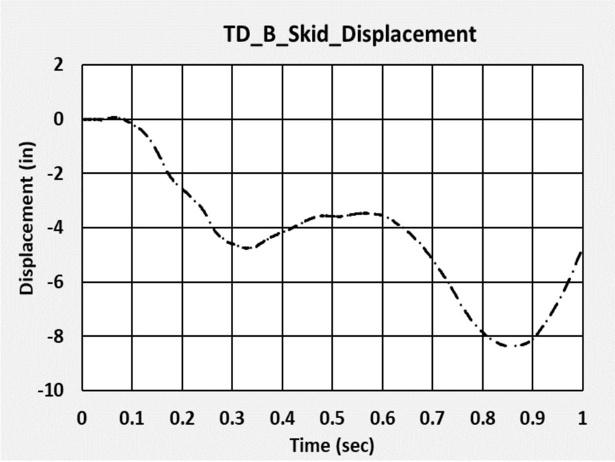

Figure B38. Raw Displacement-Time Data from Displacement Transducer on B-End Skid

Section 4. – Material Characterization Results

Table B1. Summary of Results from Room Temperature Tensile Tests of ASTM A240, T304 Stainless Steel

Lab	Coupon	Temp	YS	UTS	EB (2-inch)
#	-	*K*	*ksi*	*ksi*	*%*
1	A	295	37.0	85.7	70.1
1	B	295	43.1	87.3	78.2
1	C	295	39.4	83.5	65.4
2	A	295	35.9	86.0	73.5
2	B	295	37.4	87.4	76.9
2	C	295	38.7	90.6	77.5
Specification Requirements			>30	>75	>40

Table B2. Summary of Results from Cryogenic Temperature Tensile Tests of ASTM A240, T304 Stainless Steel

Lab	Coupon	Temp	YS	UTS	EB (2-inch)
#	-	*K*	*ksi*	*ksi*	*%*
2	A	200	41.3	144	38.8
2	B	200	40.8	140.4	39.1
2	C	200	39.9	144.8	51.0
2	A	111	40.3	178.7	41.3
2	B	111	41.7	186.7	33.0
2	C	111	44.2	180.1	36.2
2	A	77	44.9	198	42.9
2	B	77	44.1	207.5	36.3
2	C	77	43.8	208.5	53.2

Table B3. Summary of Results from Tensile Tests of ASTM A516, Grade 70 Carbon Steel

Lab	**Coupon**	**Temp**	**YS**	**UTS**	**EB (2-inch)**
#	*-*	*K*	*ksi*	*ksi*	*%*
1	A	295	33.8	54.1	44.4
1	B	295	37.1	54.1	41.5
1	C	295	34.9	53.8	42.6
2	A	295	33.3	55.1	42.0
2	B	295	33.9	54.2	63.0
2	C	295	34.3	54.6	43.9
Specification Requirement			>38*	70-85*	>21

*ASTM A516-70 tensile coupons did not meet specification requirements for YS or UTS

Section 5. – Micrographic Analysis of Material Samples from Puncture Zone

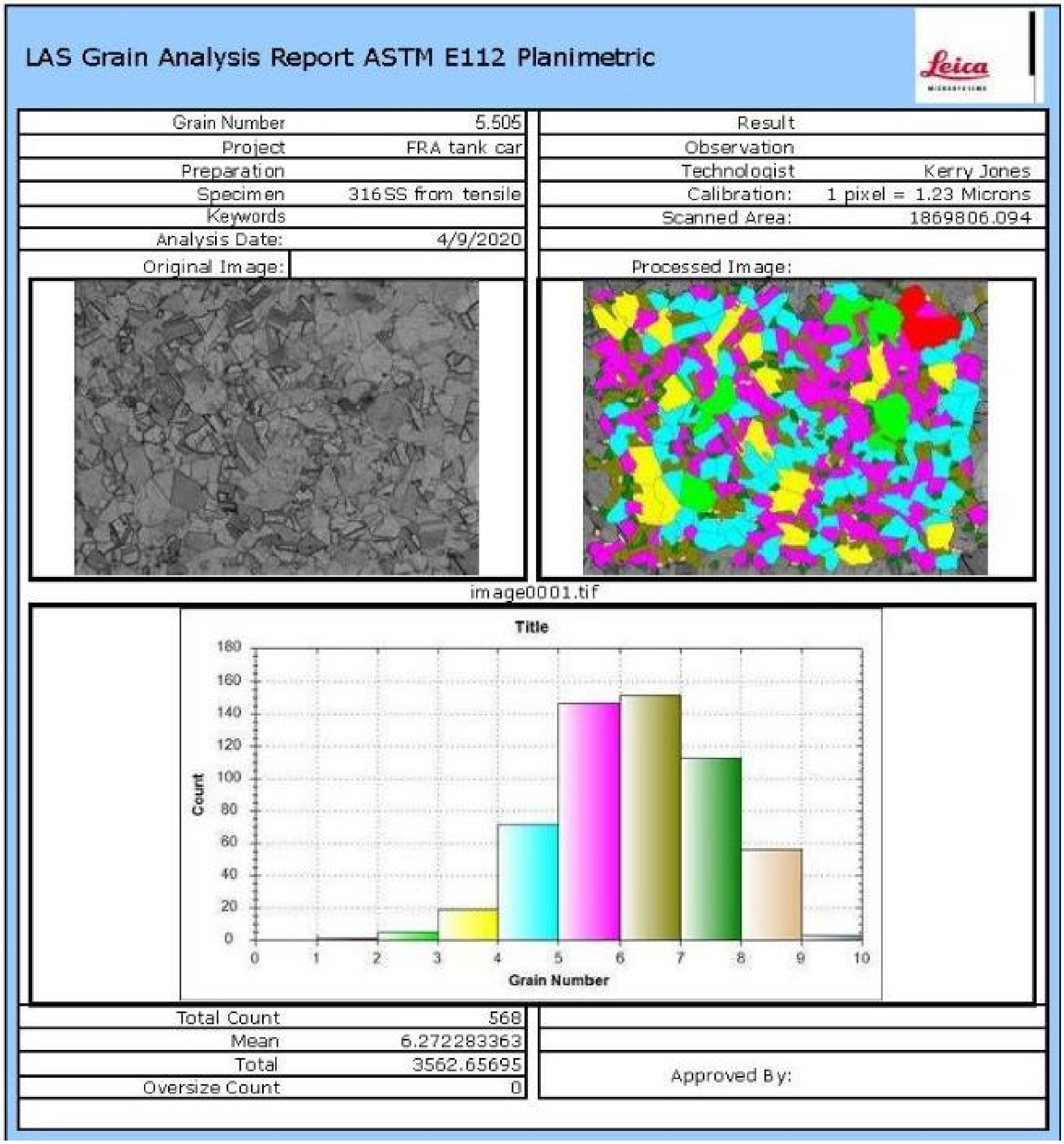

LAS Grain Analysis Report ASTM E112 Planimetric

Grain Number	5.505	Result	
Project	FRA tank car	Observation	
Preparation		Technologist	Kerry Jones
Specimen	316SS from tensile	Calibration:	1 pixel = 1.23 Microns
Keywords		Scanned Area:	1869806.094
Analysis Date:	4/9/2020		
Original Image:		Processed Image:	

image0001.tif

Total Count	568		
Mean	6.272283363		
Total	3562.65695	Approved By:	
Oversize Count	0		

Figure B39. Stainless Steel Grain Structure Analysis Sample 1

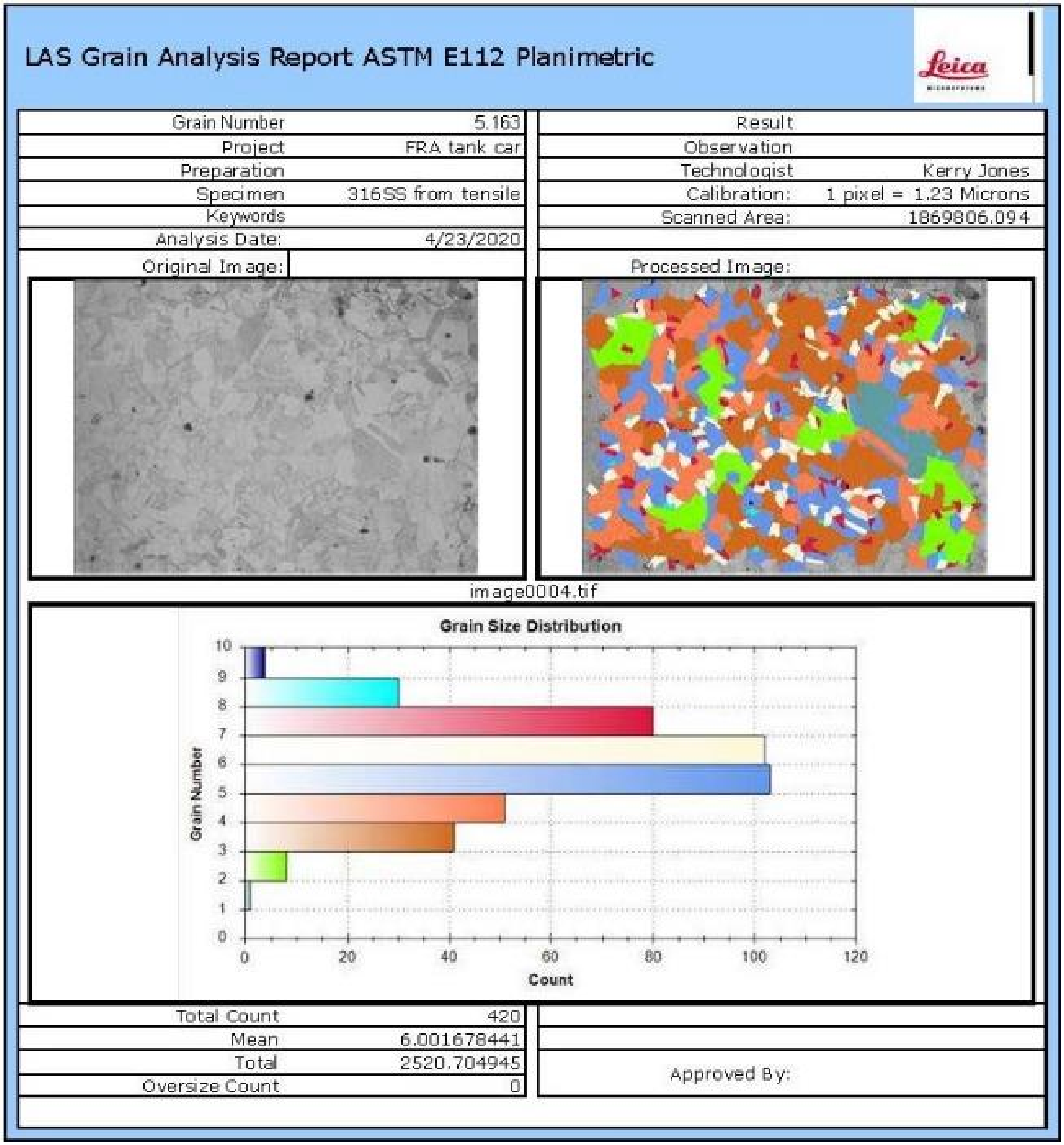

LAS Grain Analysis Report ASTM E112 Planimetric

Grain Number	5.163	Result	
Project	FRA tank car	Observation	
Preparation		Technologist	Kerry Jones
Specimen	316SS from tensile	Calibration:	1 pixel = 1.23 Microns
Keywords		Scanned Area:	1869806.094
Analysis Date:	4/23/2020		

Original Image:

Processed Image:

image0004.tif

Total Count	420		
Mean	6.001678441		
Total	2520.704945	Approved By:	
Oversize Count	0		

Figure B40. Stainless Steel Grain Structure Analysis Sample 2

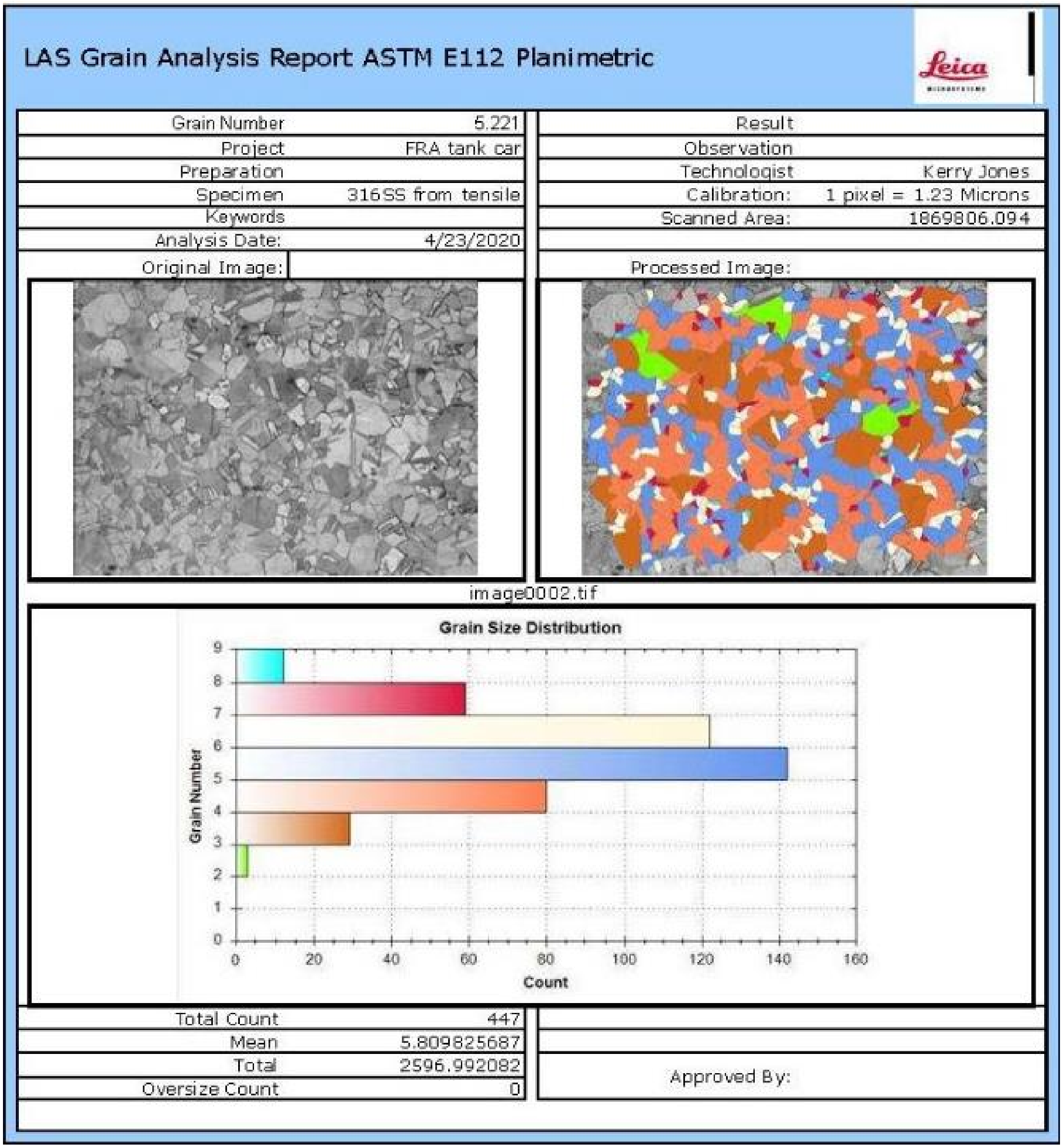

LAS Grain Analysis Report ASTM E112 Planimetric

Grain Number	5.221	Result	
Project	FRA tank car	Observation	
Preparation		Technologist	Kerry Jones
Specimen	316SS from tensile	Calibration:	1 pixel = 1.23 Microns
Keywords		Scanned Area:	1869806.094
Analysis Date:	4/23/2020		

Original Image:

Processed Image:

image0002.tif

Total Count	447		
Mean	5.809825687		
Total	2596.992082	Approved By:	
Oversize Count	0		

Figure B41. Stainless Steel Grain Structure Analysis Sample 3

Appendix C. FEA and Test Results

For all results presented in this appendix, the acceleration data from the test and output from the FE model have been filtered using a CFC60 filter. Three different sets of FE model results are presented in this appendix. Pre-test FEA was run at a variety of impact speeds using estimated lower- and upper-ductility steel behaviors for the inner and outer tanks. Following the test, post-test FEA was run at the impact conditions and using the pre-test lower- and upper-ductility material estimates. Finally, post-test FEA was run at the impact conditions and using steel properties and thicknesses as measured from the actual tanks in the tested DOT-113.

Section 1. Pre-Test Puncture FEA and Test Results

A pre-test puncture FEA was performed using estimated material properties for the inner and outer tanks. To minimize the total number of simulations needed to provide upper- and lower-bound estimates of puncture speed, models were only run using the upper- or lower-ductility estimates for both tanks. While it would be possible to have a DOT-113 with upper-ductility material in one tank and lower-ductility material in the other tank, this case was assumed to have a puncture speed bounded by the cases with both tanks having lower-ductility materials and both tanks having upper-ductility materials.

Table C1. Summary of Pre-Test FE Models

Simulated Impact Speed (mph)	Tank Steels	Outer Tank State	Inner Tank State	Reason for Ending Simulation
16	Lower-ductility	Puncture	No elements lost. Maximum DUCTCRT 0.83	Impactor rebounding
17	Lower-ductility	Puncture running to edge of solid patch	No elements lost. Maximum DUCTCRT 0.91	Impactor rebounding
17.5	Lower-ductility	Puncture running to edge of solid patch	No elements lost. Maximum DUCTCRT 0.93	Impactor rebounding
18	Lower-ductility	Puncture running to edge of solid patch	Puncture running to edge of solid patch	Puncture of both tanks
18	Upper-ductility	Through-tear under two corners	No elements lost. Maximum DUCTCRT 0.52.	Impactor rebounding

Section 1.1. 16 mph, Lower-Ductility Steels

The pre-test model using lower-ductility steels and a 16 mph impact speed punctured the outer tank but did not puncture the inner tank. The outer tank tear was contained entirely within the solid patch of elements with defined failure behaviors and did not reach any of the edges of the solid patch. The states of the solid patches of elements in the outer (left) and inner (right) tanks at a time of 420 ms are shown in Figure C1.

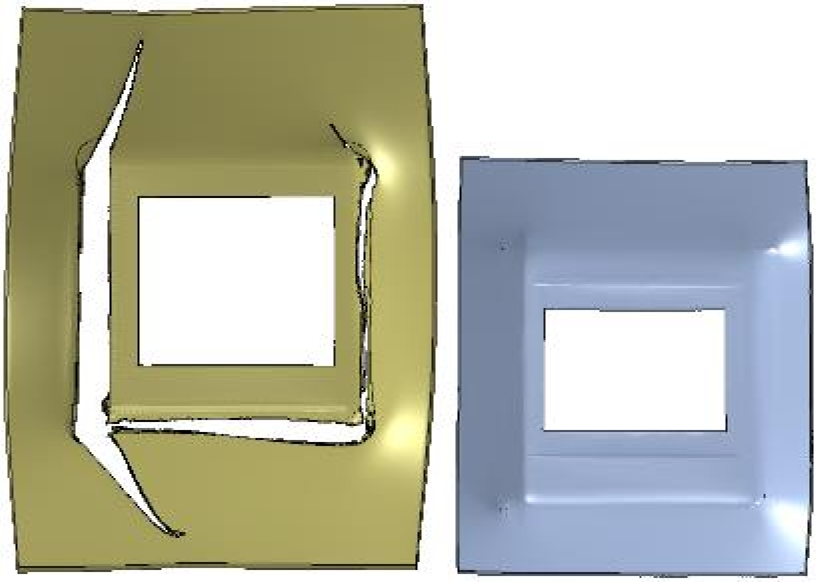

Figure C1. Solid Patch in Outer (left) and Inner (right) Tanks, 16 mph Pre-Test Model at 420 ms

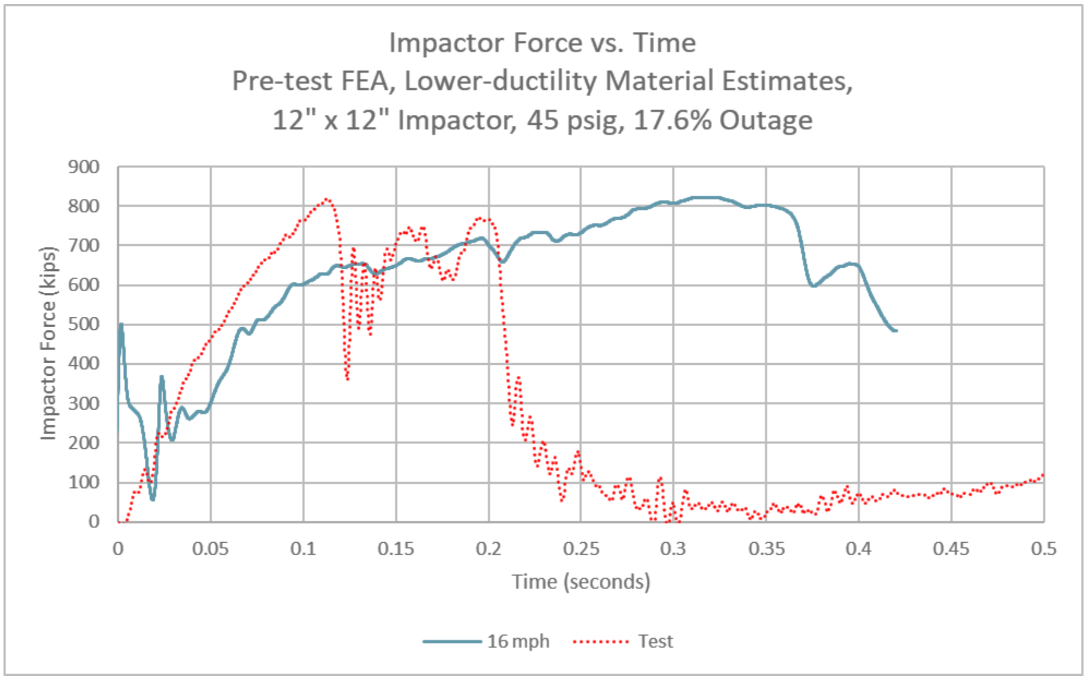

Figure C2. Impactor Force Versus Time for Pre-Test Model Using Lower-Ductility Material at 16 mph

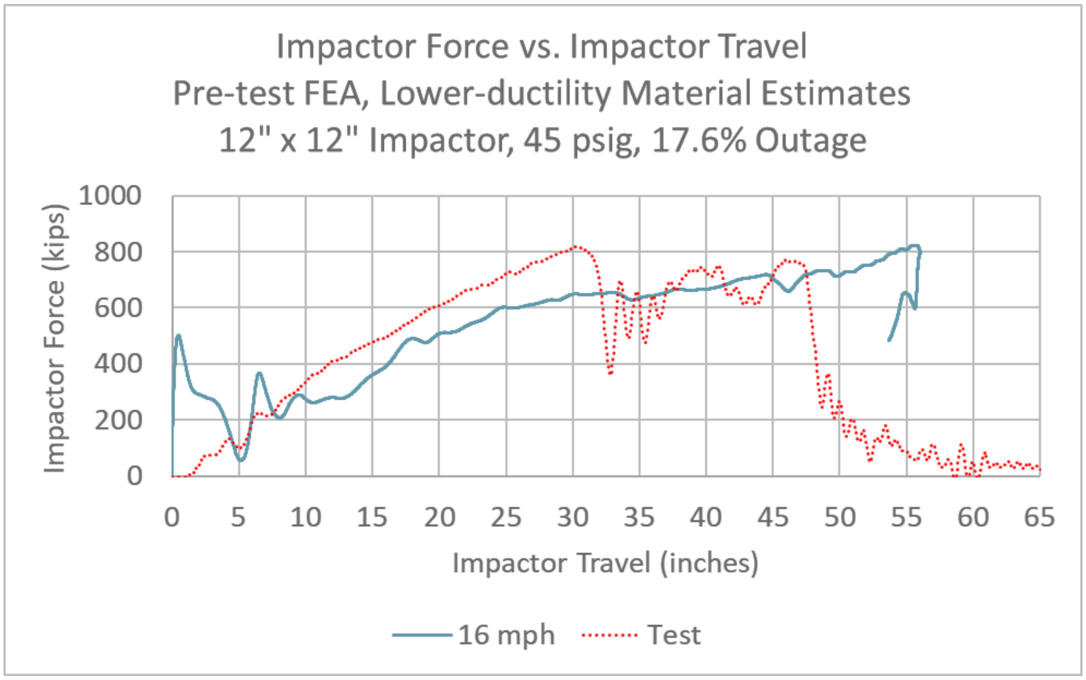

Figure C3. Impactor Force Versus Travel for Pre-Test Model Using Lower-Ductility Material at 16 mph

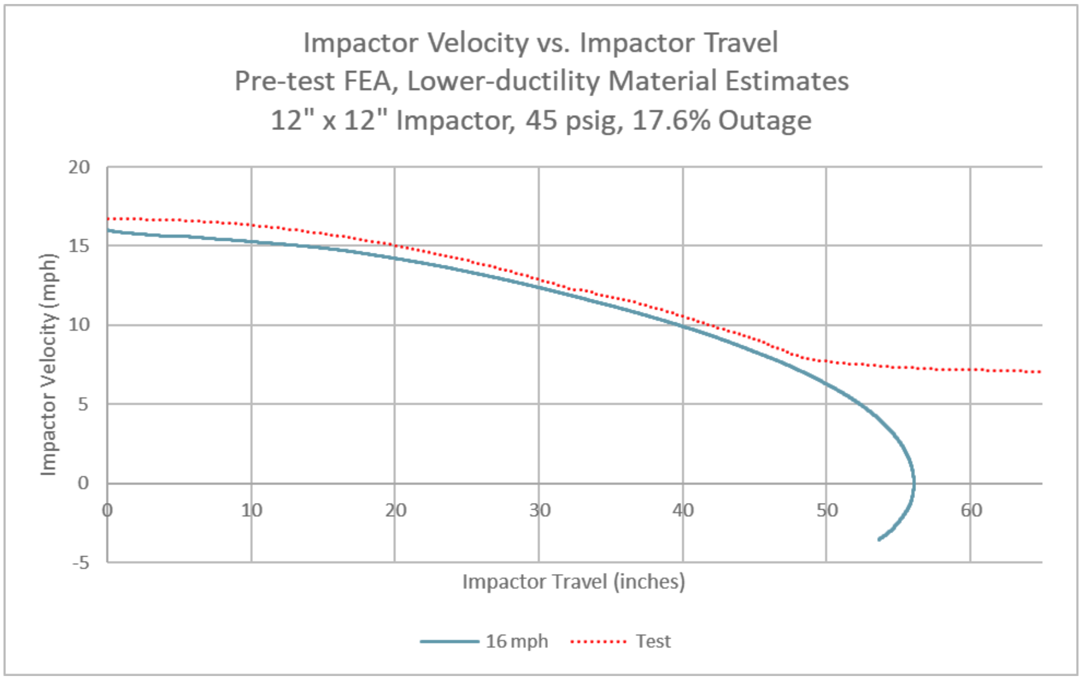

Figure C4. Impactor Velocity Versus Travel for Pre-Test Model Using Lower-Ductility Material at 16 mph

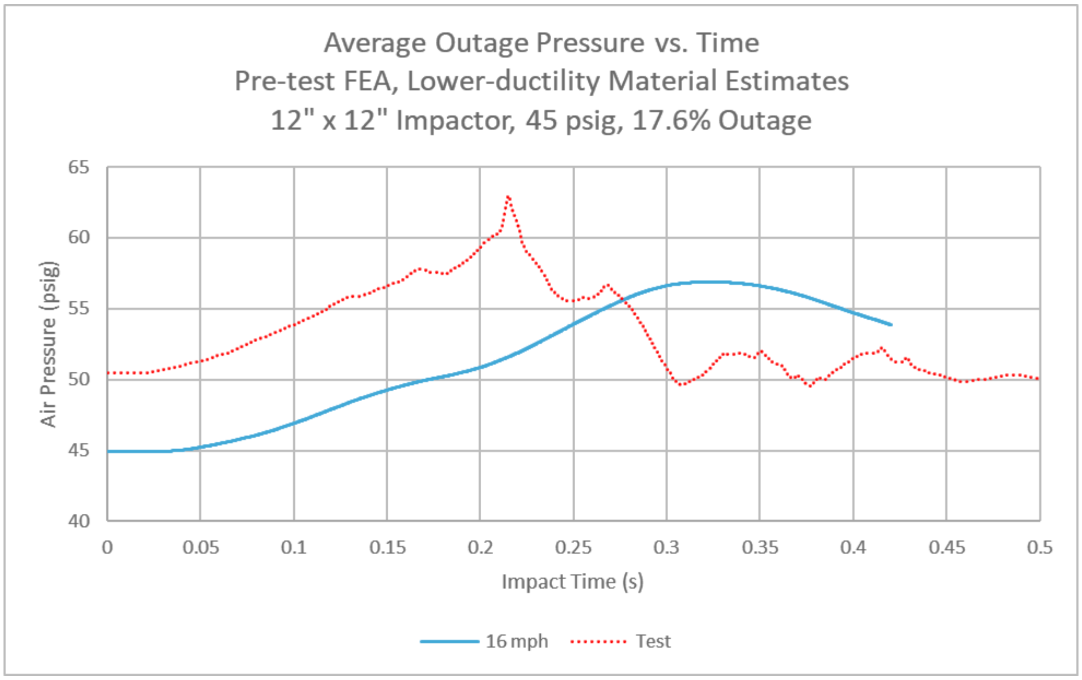

Figure C5. Average Outage Pressure Versus Time for Pre-Test Model Using Lower-Ductility Material at 16 mph

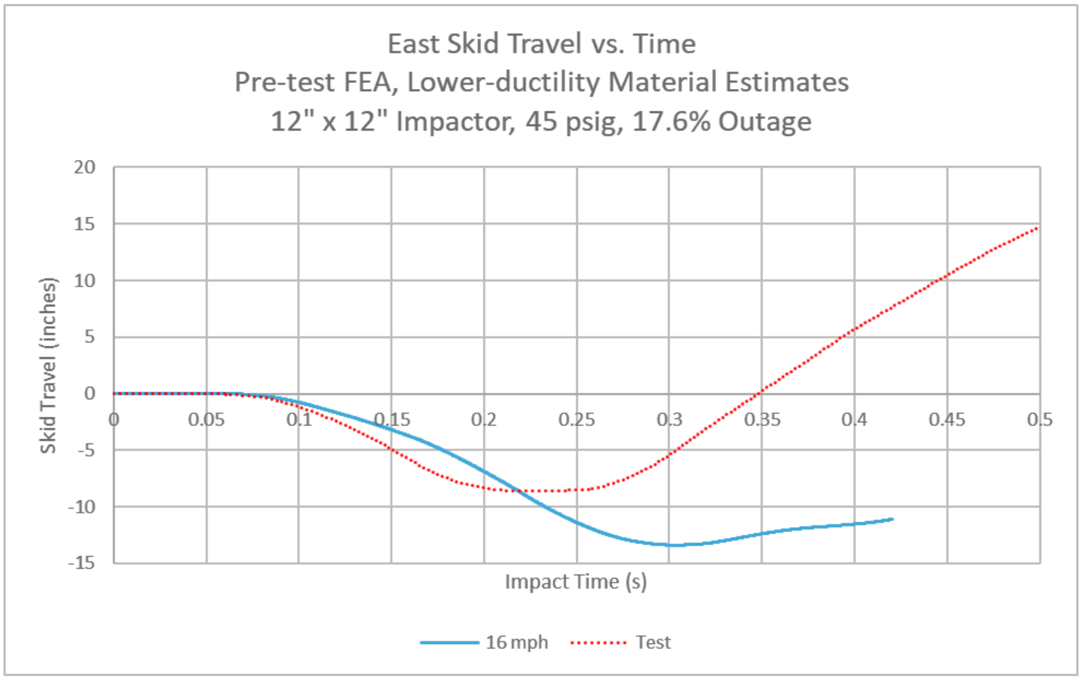

Figure C6. East Skid Travel Versus Time for Pre-Test Model Using Lower-Ductility Material at 16 mph

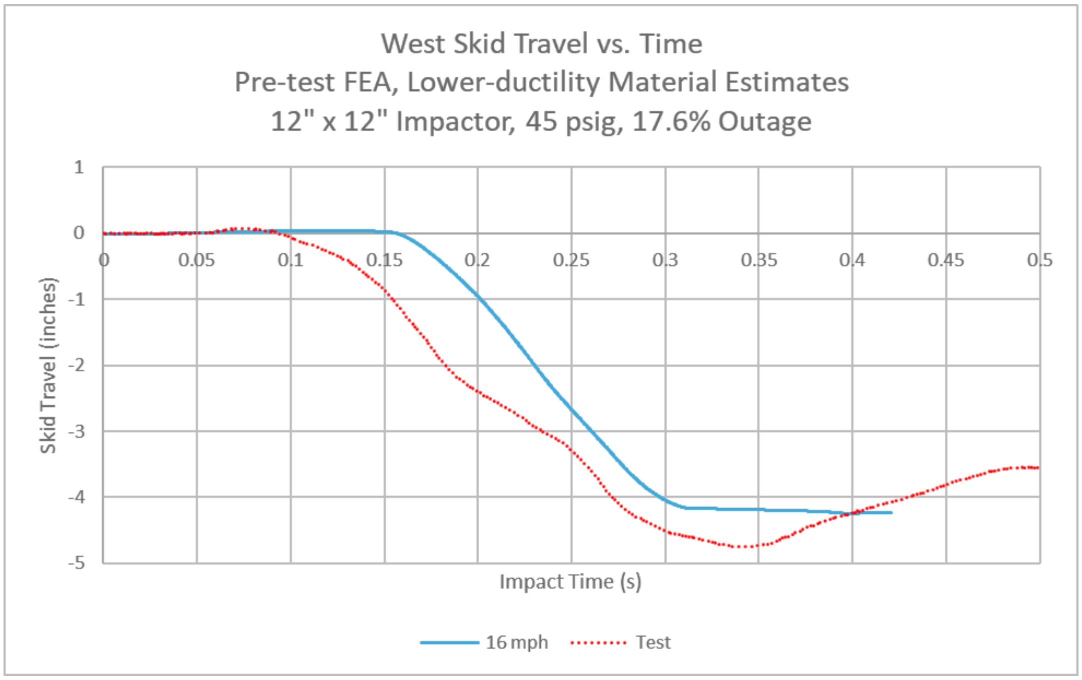

Figure C7. West Skid Travel Versus Time for Pre-Test Model Using Lower-Ductility Material at 16 mph

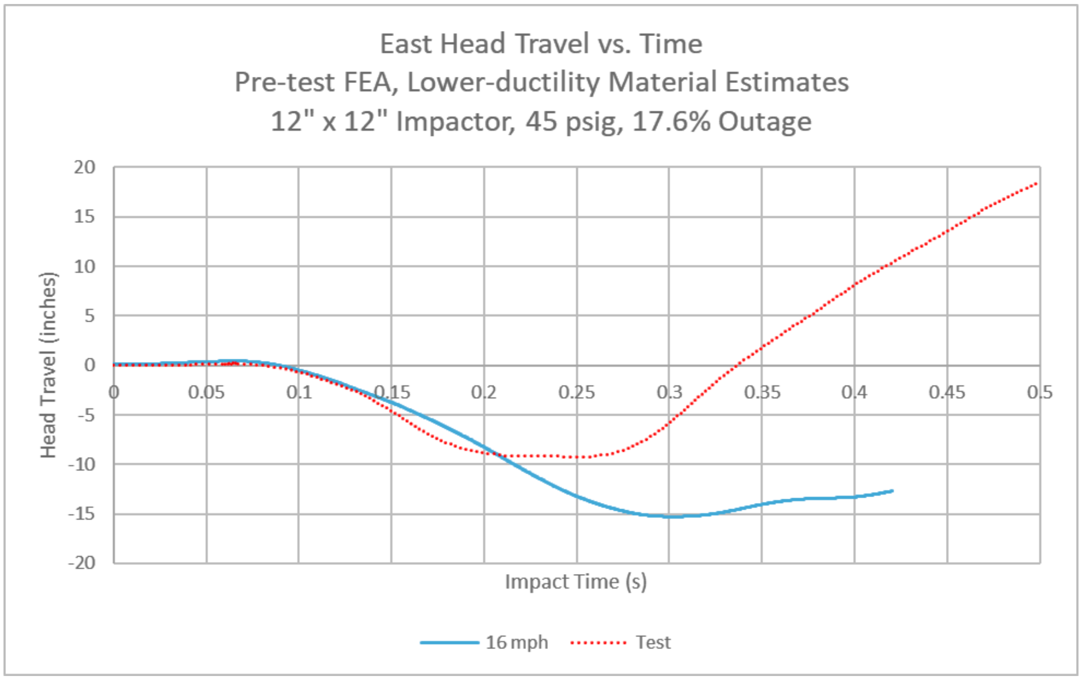

Figure C8. East Head Travel Versus Time for Pre-Test Model Using Lower-Ductility Material at 16 mph

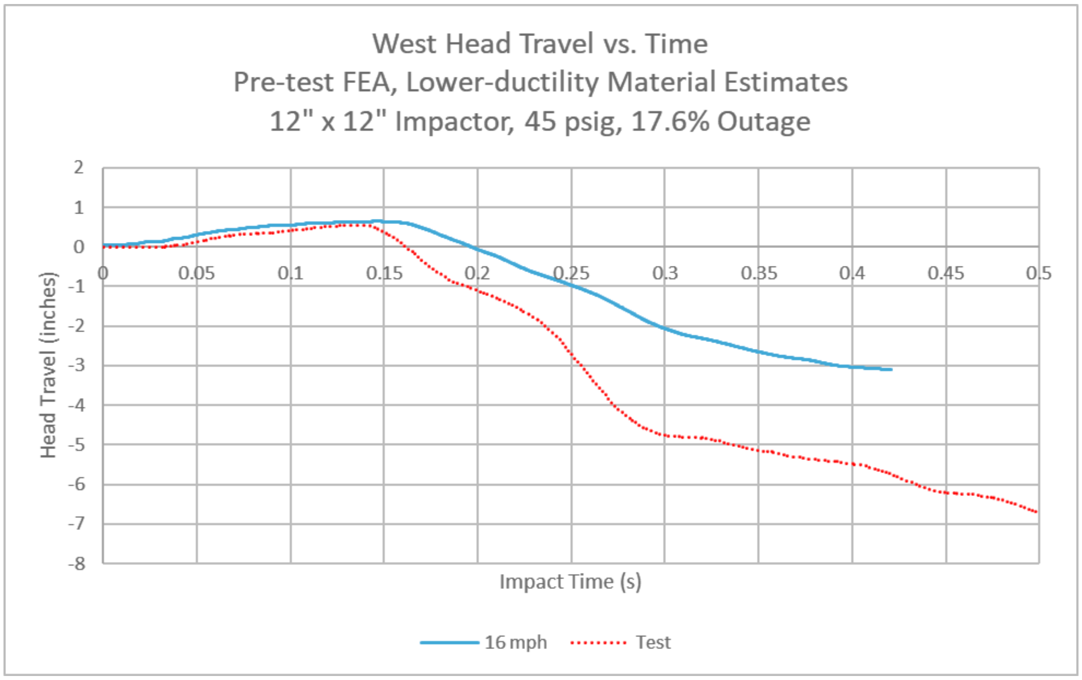

Figure C9. West Head Travel Versus Time for Pre-Test Model Using Lower-Ductility Material at 16 mph

Section 1.2. 17 mph, Lower-Ductility Steels

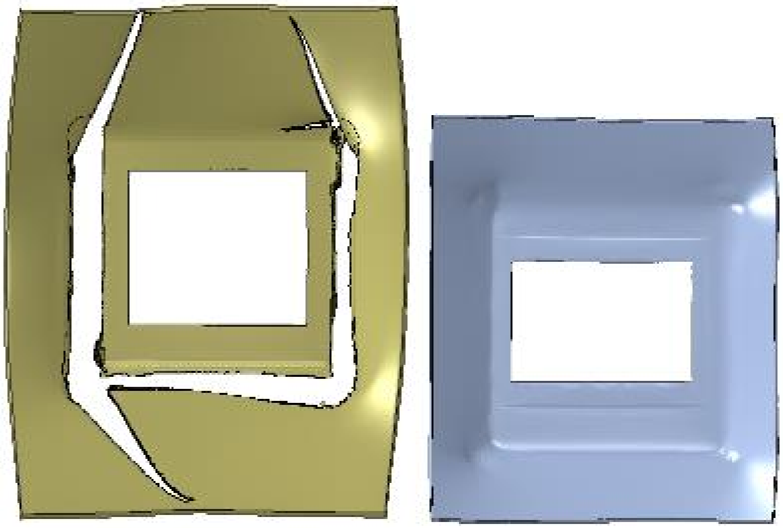

Figure C10. Solid Patch in Outer (left) and Inner (right) Tanks, 17 mph Pre-Test Model at 450 ms

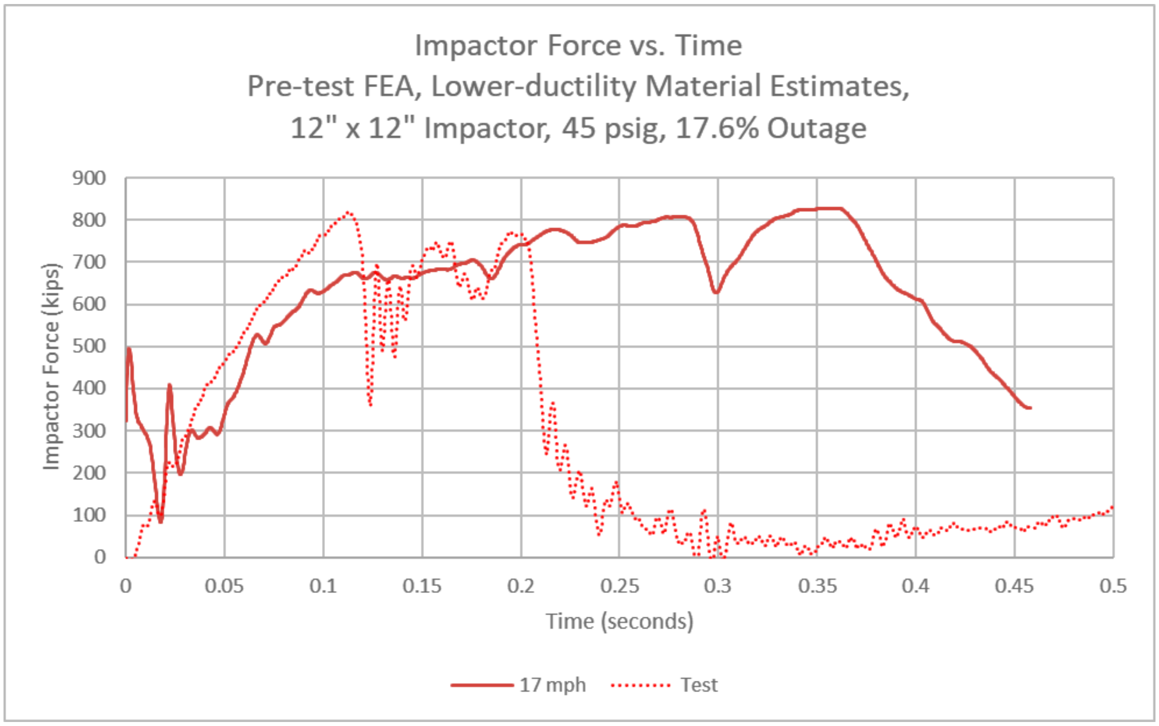

Figure C11. Impactor Force Versus Time for Pre-Test Model Using Lower-Ductility Material at 17 mph

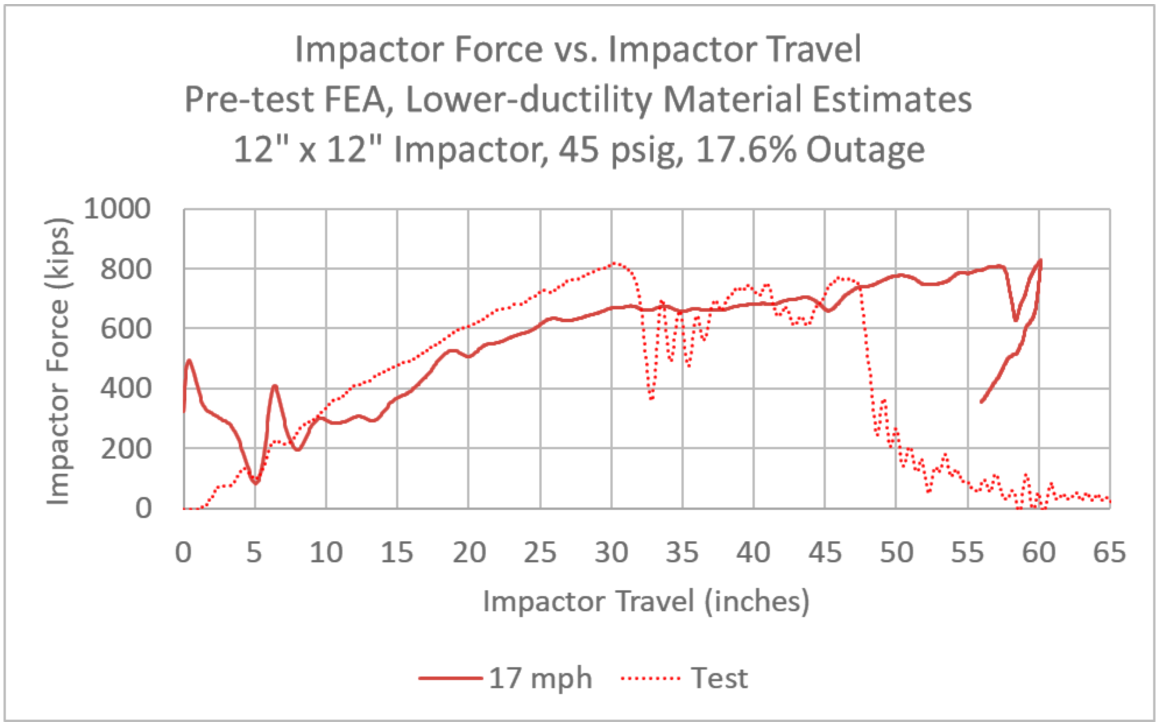

Figure C12. Impactor Force Versus Travel for Pre-Test Model Using Lower-Ductility Material at 17 mph

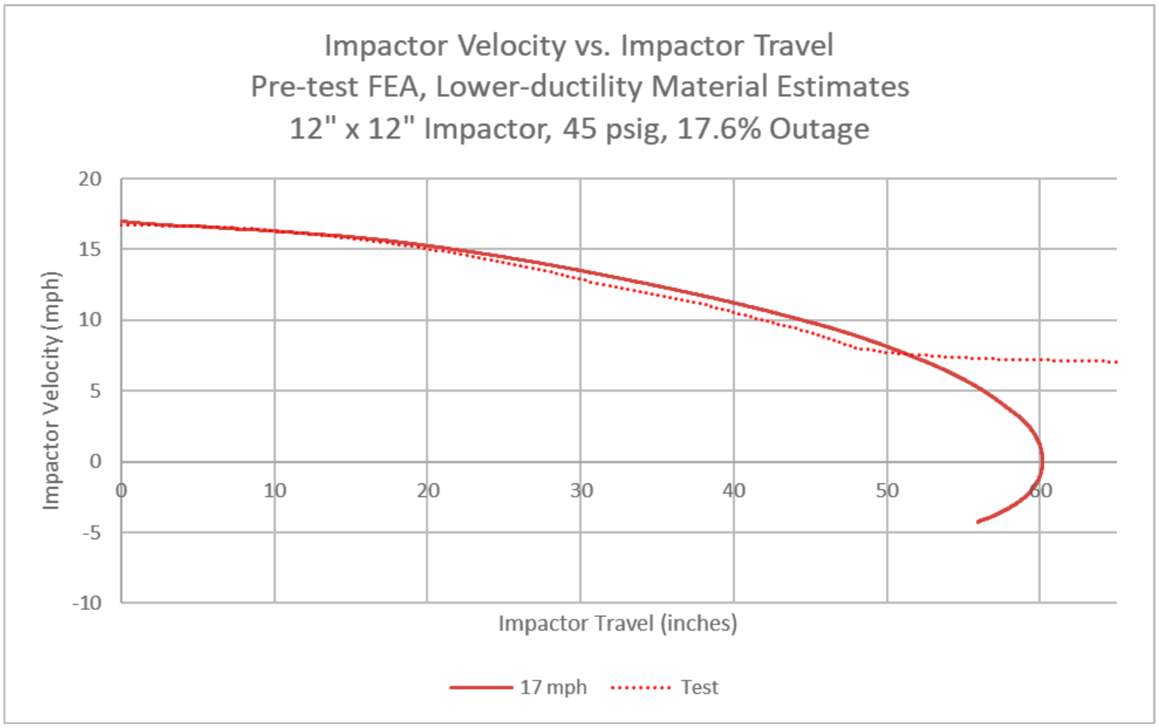

Figure C13. Impactor Velocity Versus Travel for Pre-Test Model Using Lower-Ductility Material at 17 mph

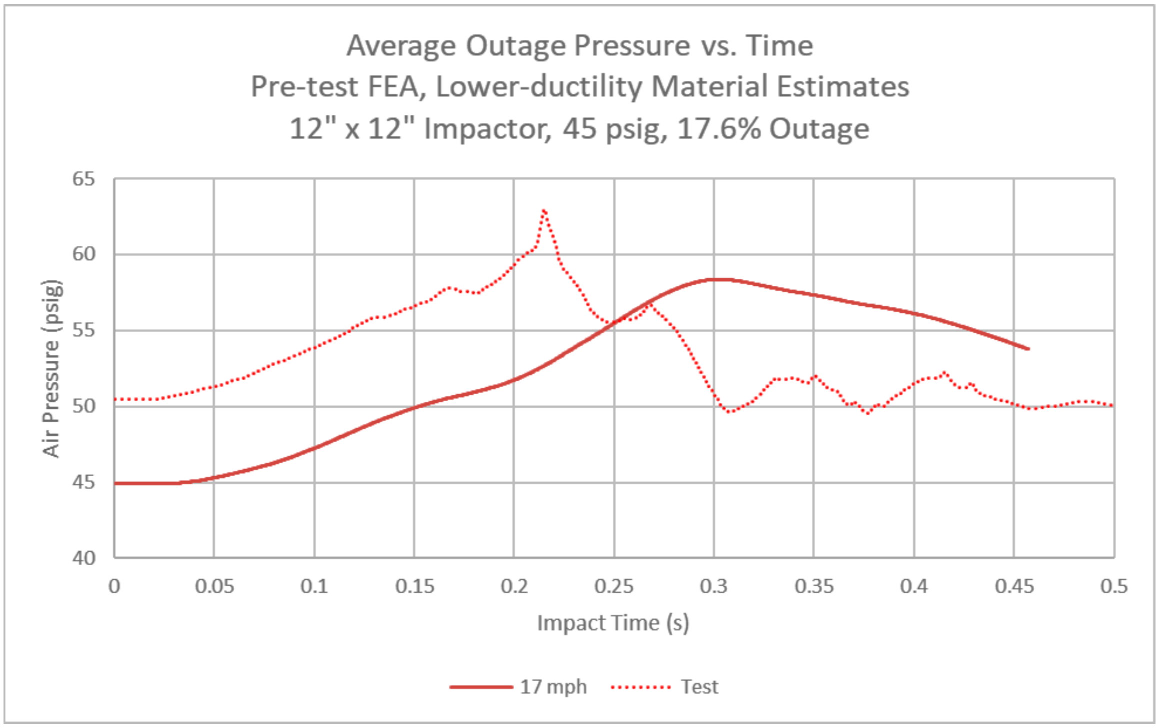

Figure C14. Outage Pressure Versus Time for Pre-Test Model Using Lower-Ductility Material at 17 mph

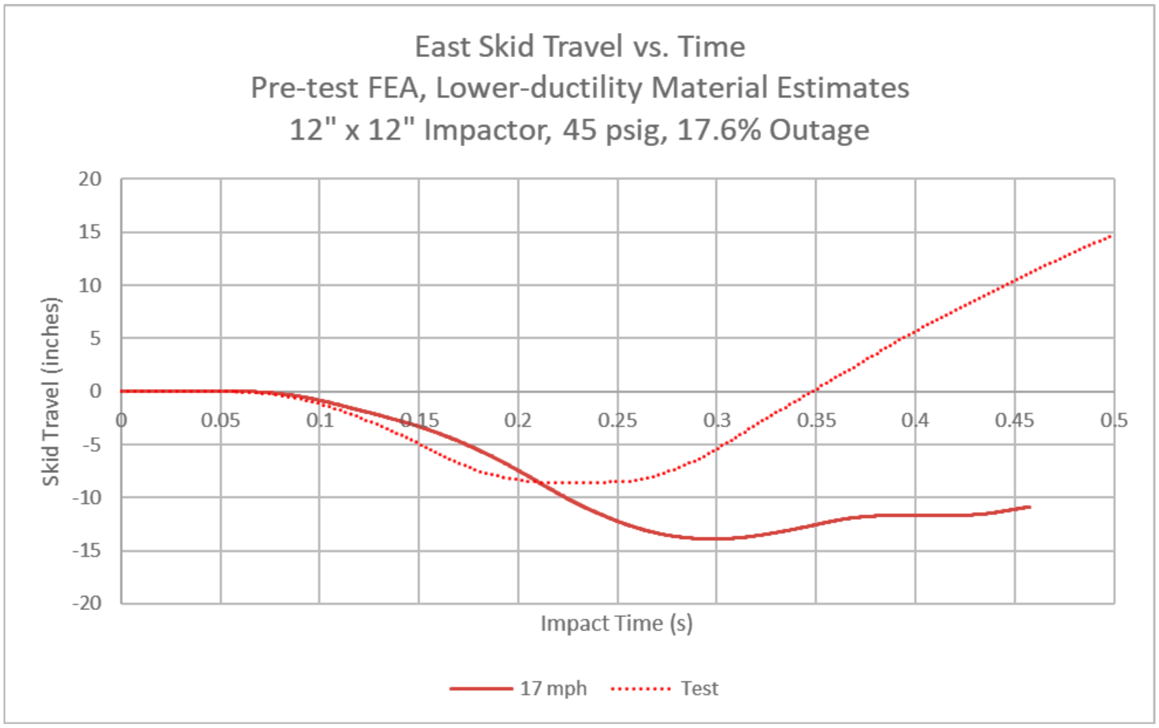

Figure C15. East Skid Travel Versus Time for Pre-Test Model Using Lower-Ductility Material at 17 mph

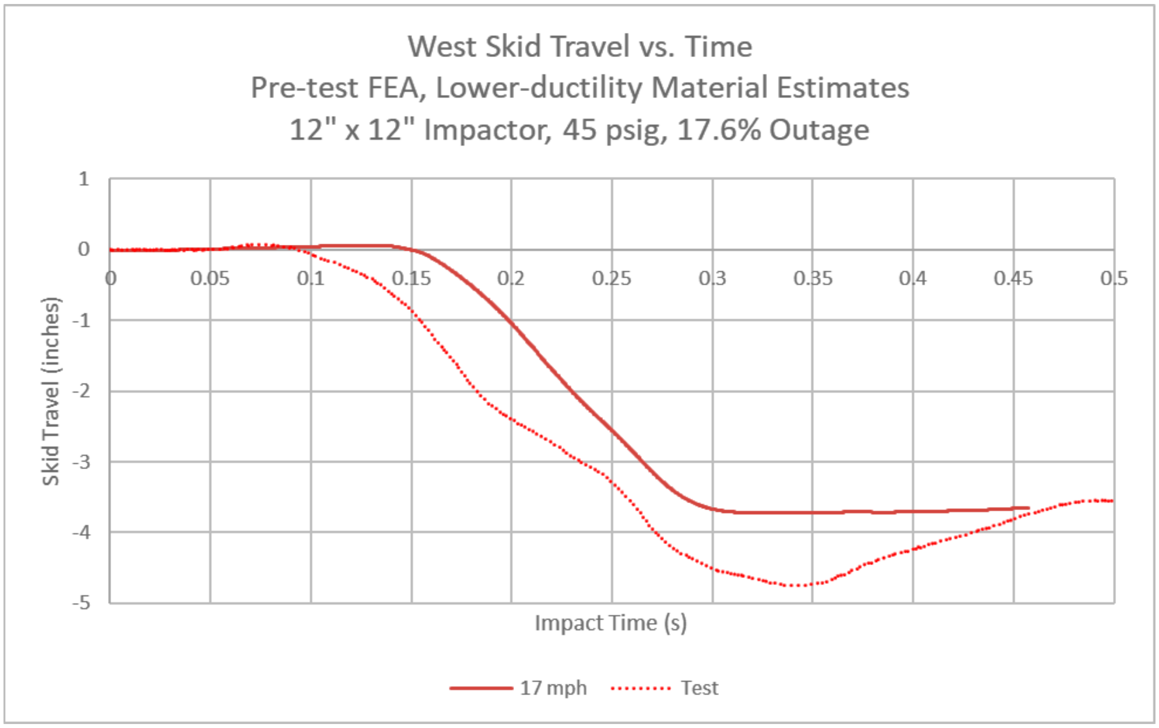

Figure C16. West Skid Travel Versus Time for Pre-Test Model Using Lower-Ductility Material at 17 mph

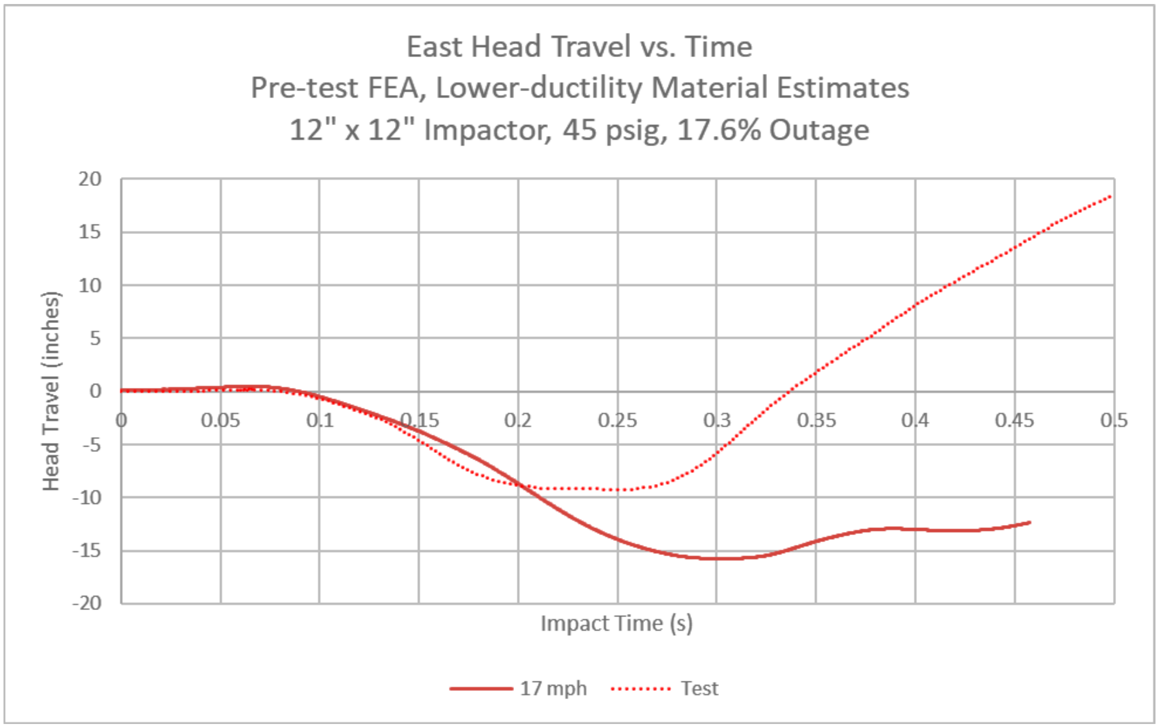

Figure C17. East Head Travel Versus Time for Pre-Test Model Using Lower-Ductility Material at 17 mph

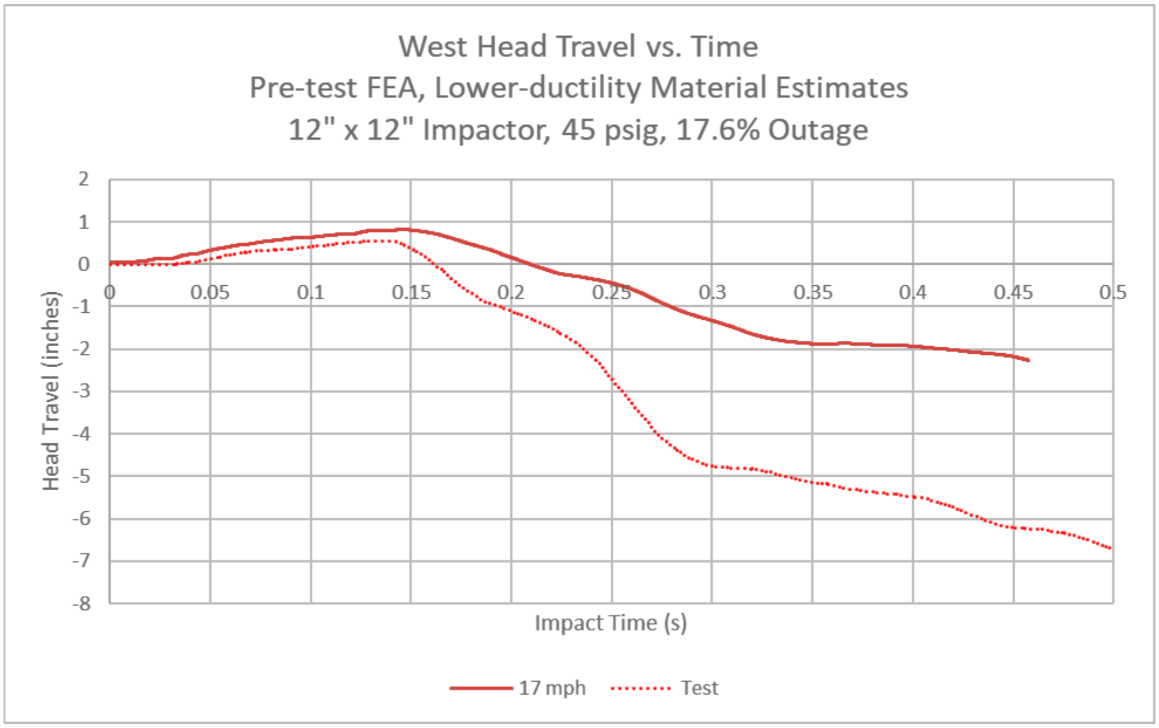

Figure C18. West Head Travel Versus Time for Pre-Test Model Using Lower-Ductility Material at 17 mph

Section 1.3. 17.5 mph, Lower-Ductility Steels

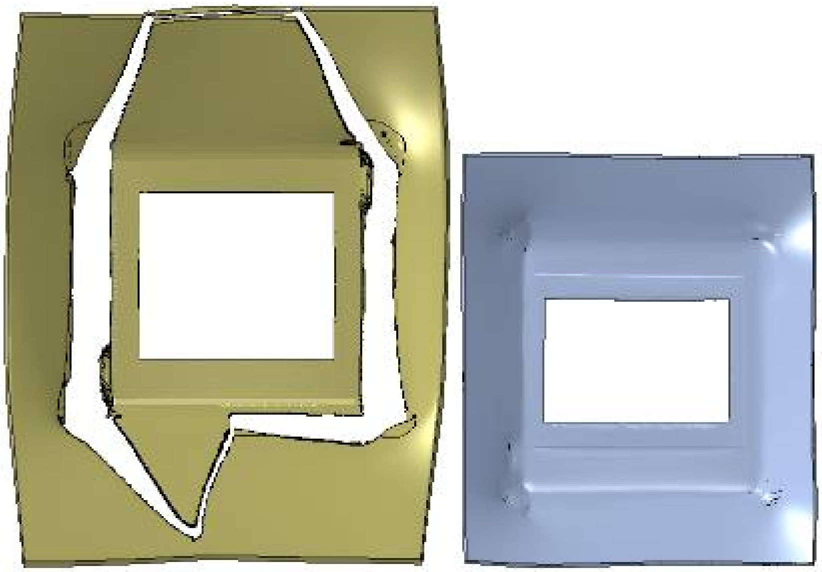

Figure C19. Solid Patch in Outer (left) and Inner (right) Tanks, 17.5 mph Pre-Test Model (Lower-Ductility Materials) at 500 ms

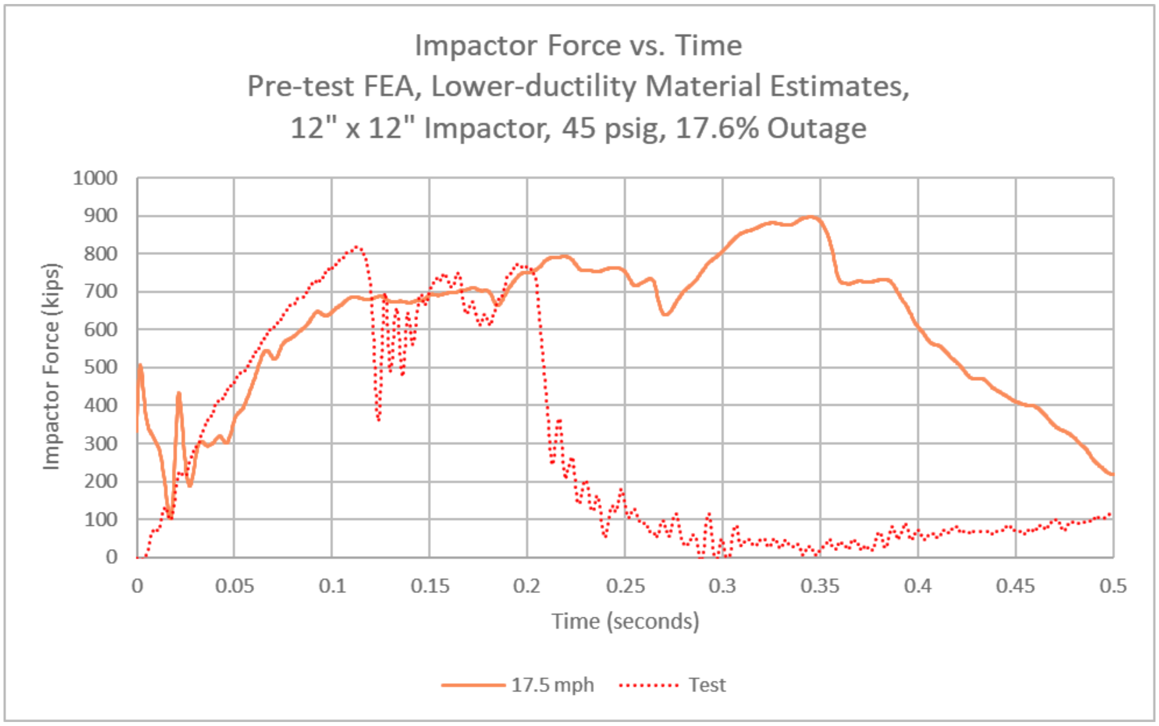

Figure C20. Impactor Force Versus Time for Pre-Test Model Using Lower-Ductility Material at 17.5 mph

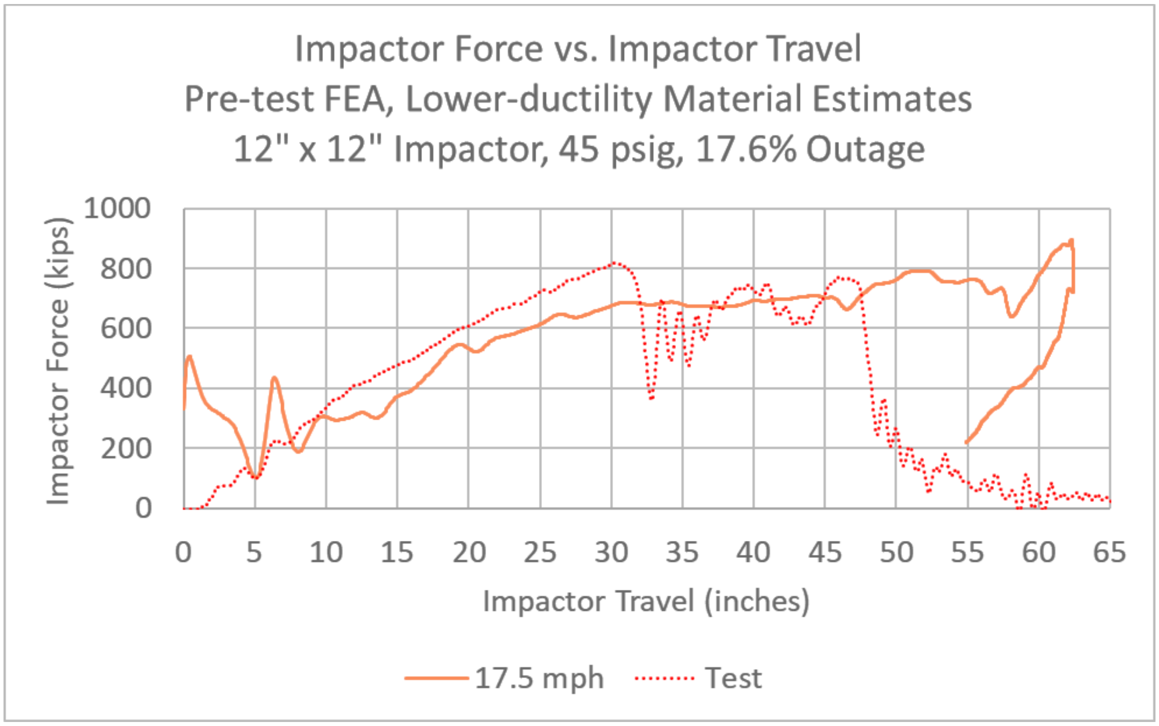

Figure C21. Impactor Force Versus Travel for Pre-Test Model Using Lower-Ductility Material at 17.5 mph

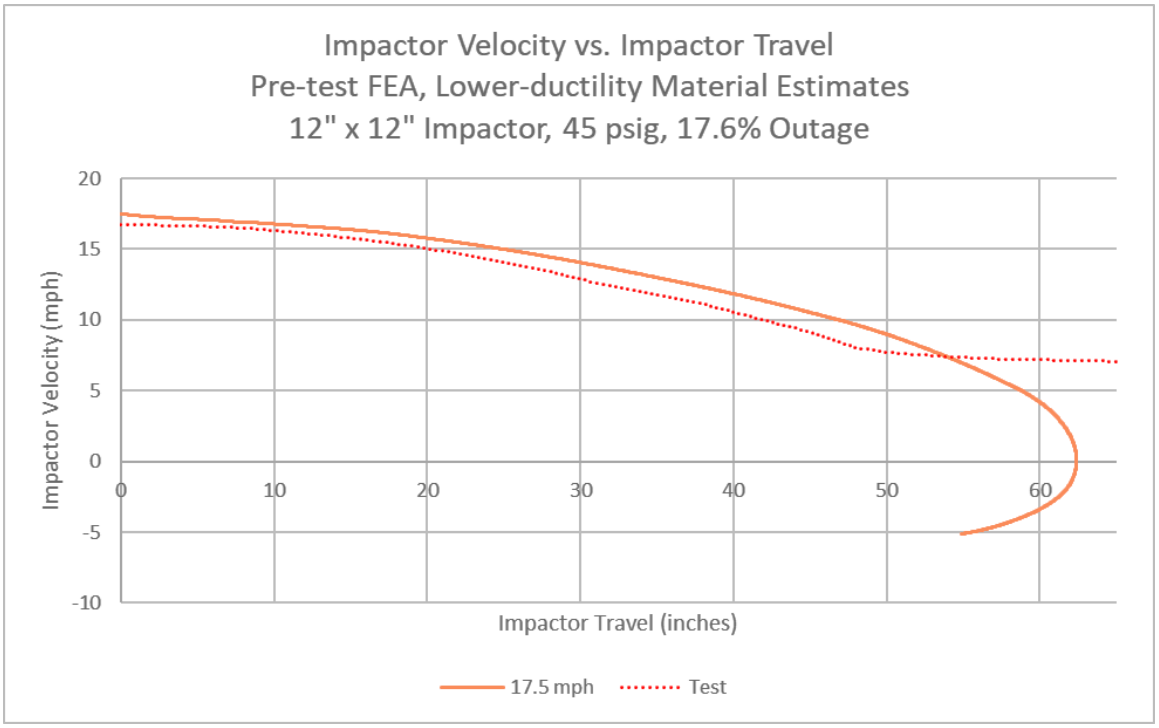

Figure C22. Impactor Velocity Versus Travel for Pre-Test Model Using Lower-Ductility Material at 17.5 mph

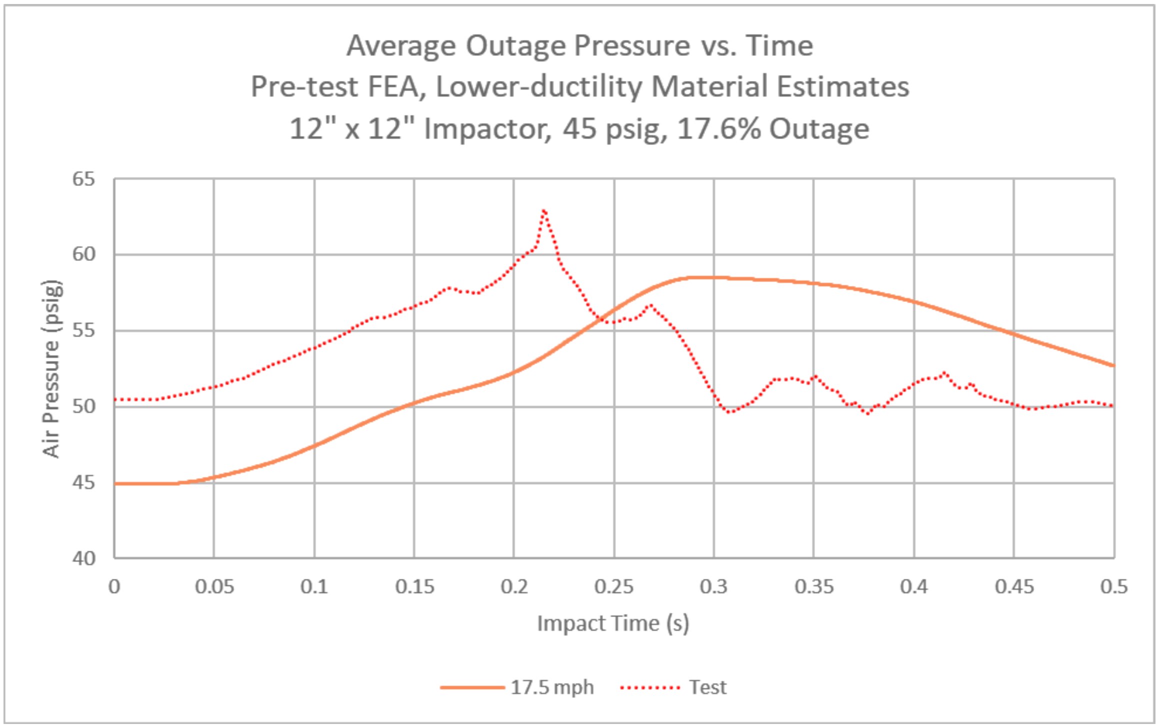

Figure C23. Average Outage Pressure Versus Time for Pre-Test Model Using Lower-Ductility Material at 17.5 mph

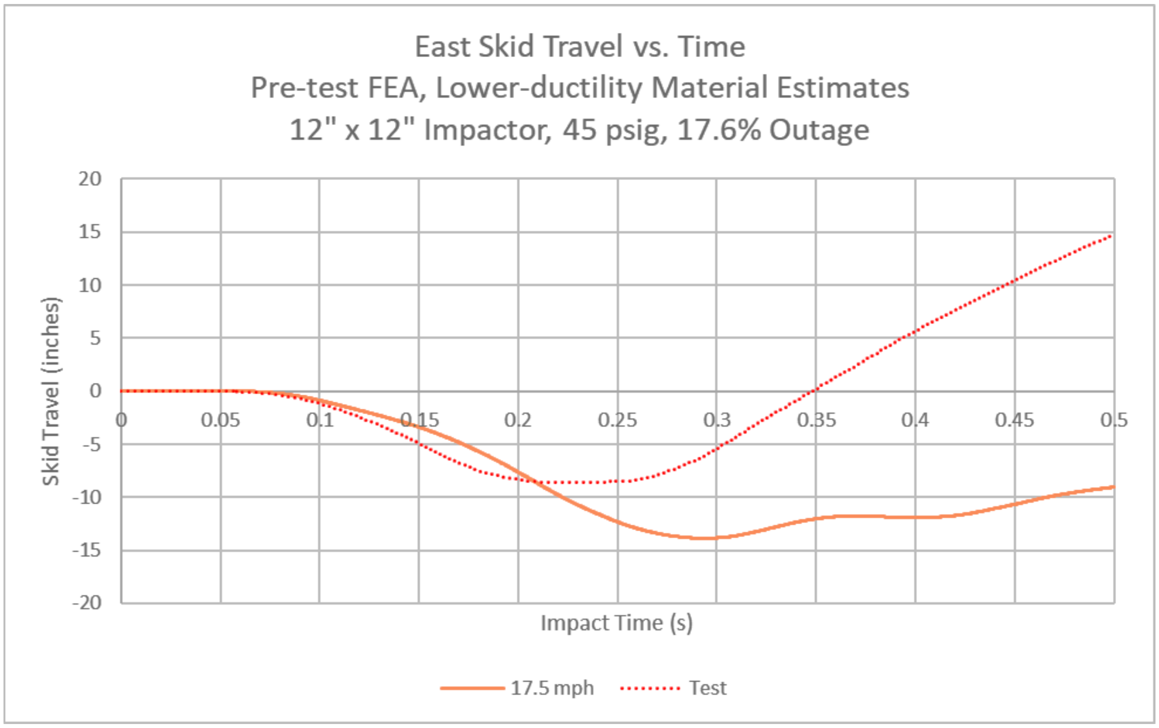

Figure C24. East Skid Travel Versus Time for Pre-Test Model Using Lower-Ductility Material at 17.5 mph

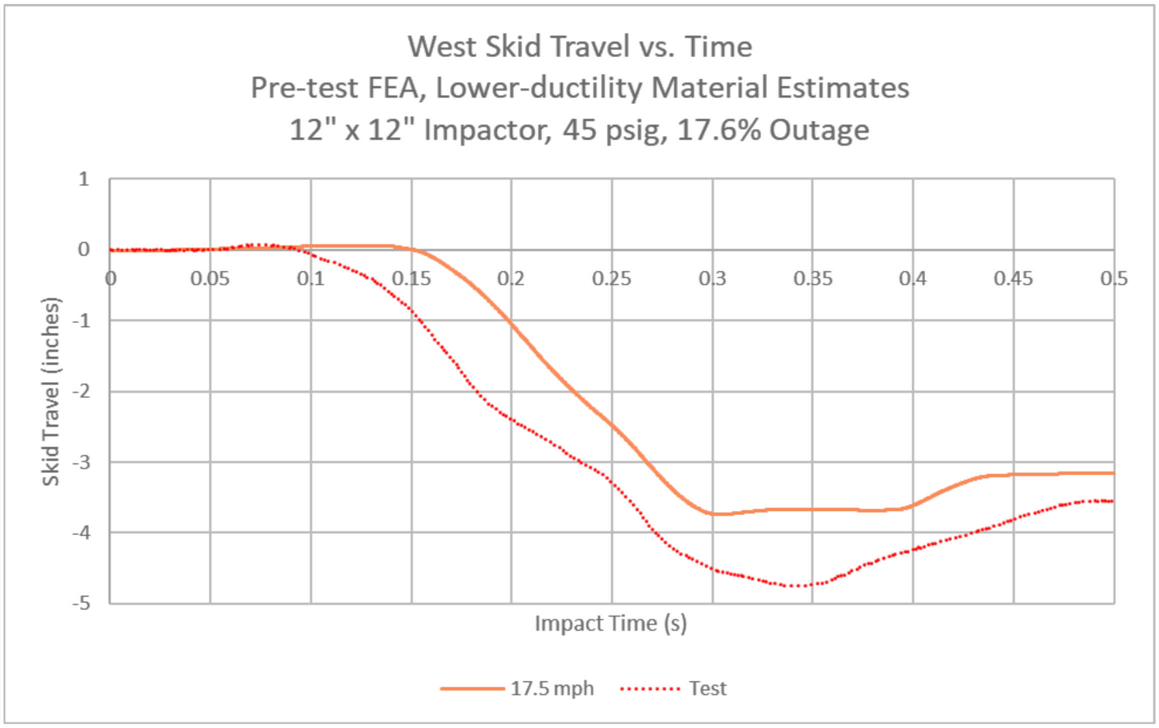

Figure C25. West Skid Travel Versus Time for Pre-Test Model Using Lower-Ductility Material at 17.5 mph

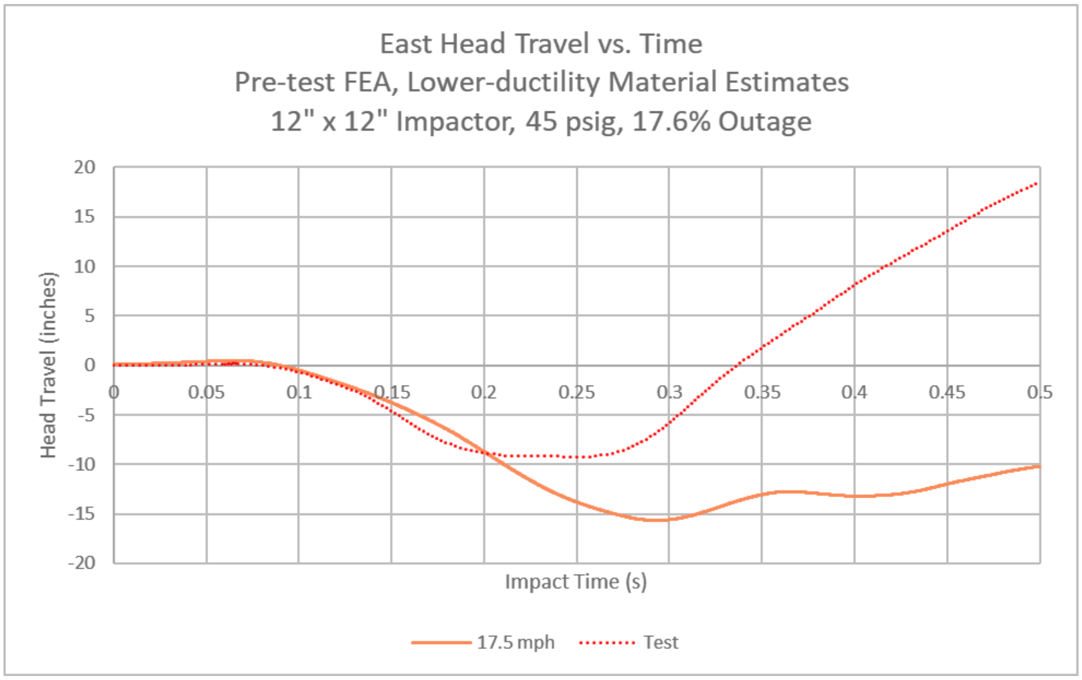

Figure C26. East Head Travel Versus Time for Pre-Test Model Using Lower-Ductility Material at 17.5 mph

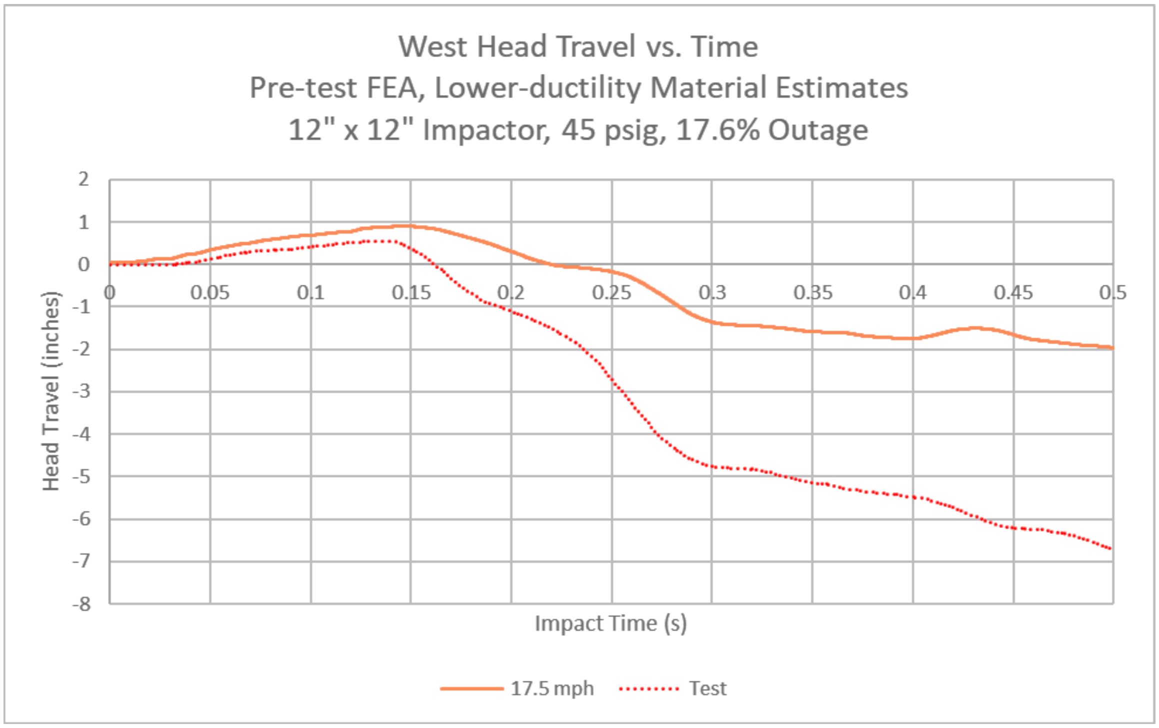

Figure C27. West Head Travel Versus Time for Pre-Test Model Using Lower-Ductility Material at 17.5 mph

Section 1.4. 18 mph, Lower-Ductility Steels

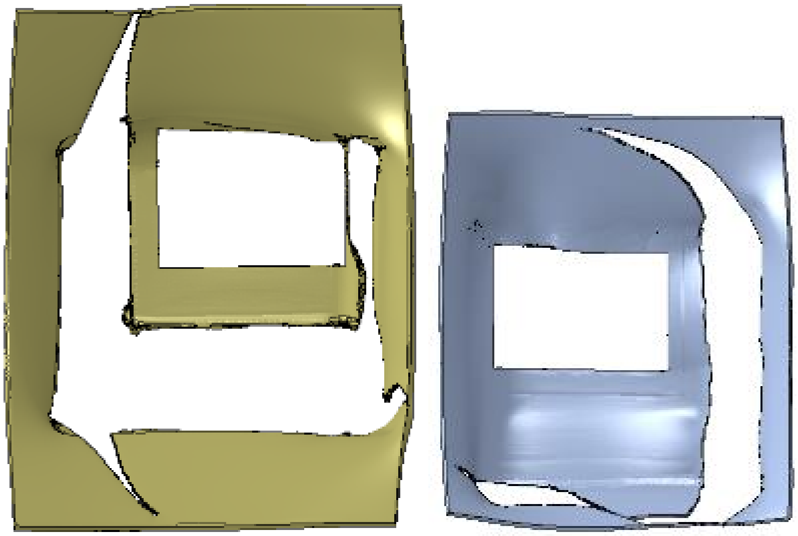

Figure C28. Solid Patch in Outer (left) and Inner (right) Tanks, 18 mph Pre-Test Model (Lower-Ductility Materials) at 230 ms

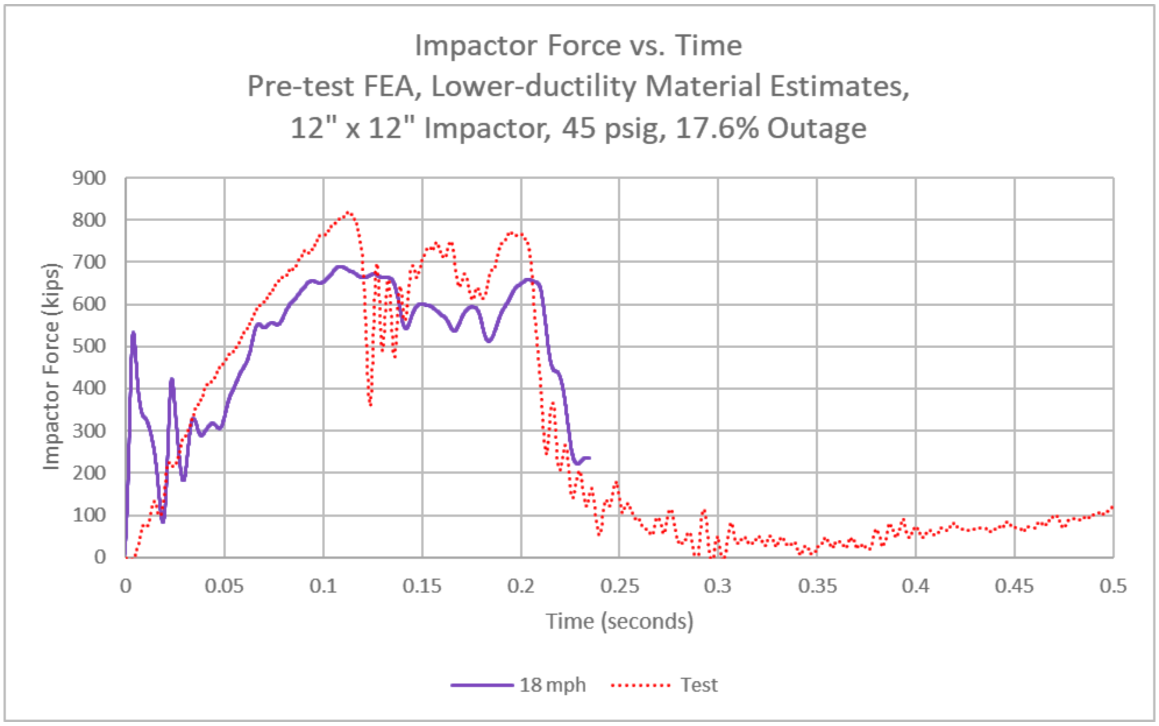

Figure C29. Impactor Force Versus Time for Pre-Test Model Using Lower-Ductility Material at 18 mph

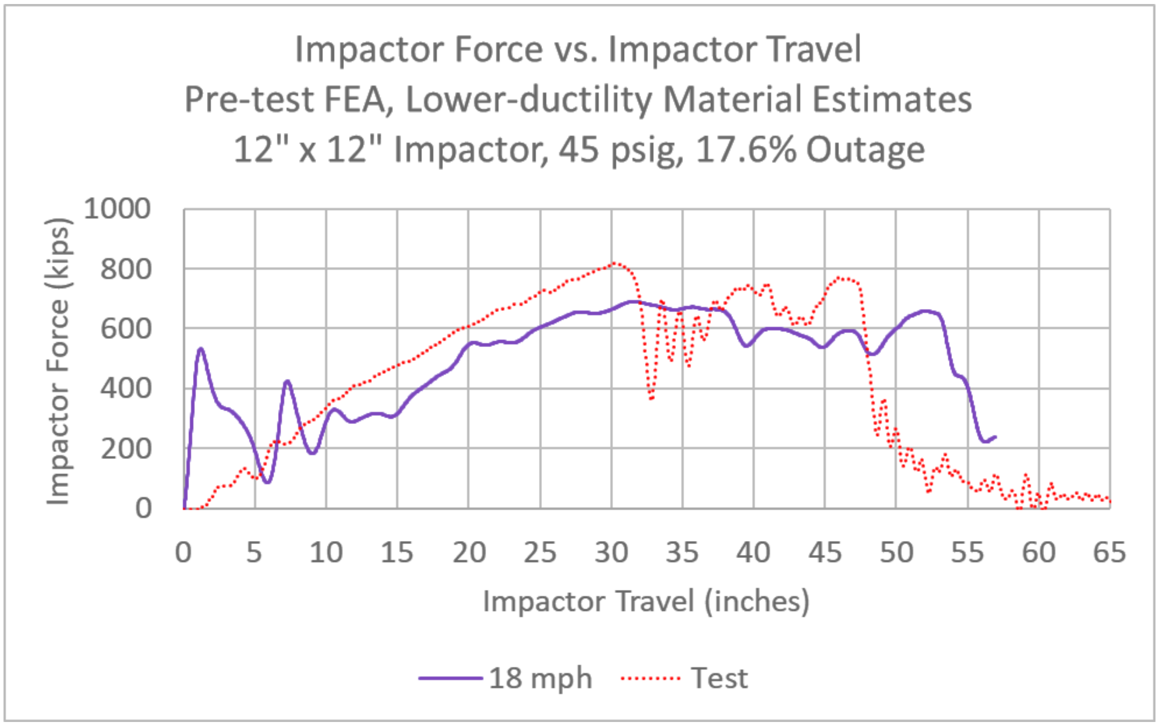

Figure C30. Impactor Force Versus Travel for Pre-Test Model Using Lower-Ductility Material at 18 mph

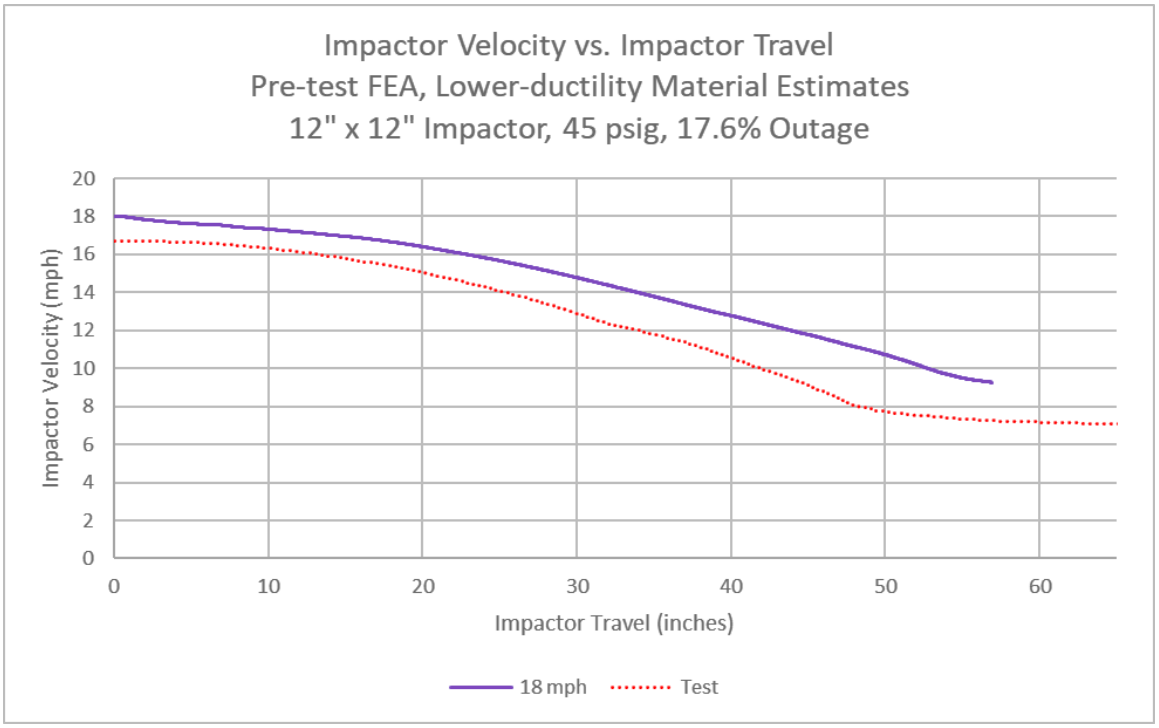

Figure C31. Impactor Velocity Versus Travel for Pre-Test Model Using Lower-Ductility Material at 18 mph

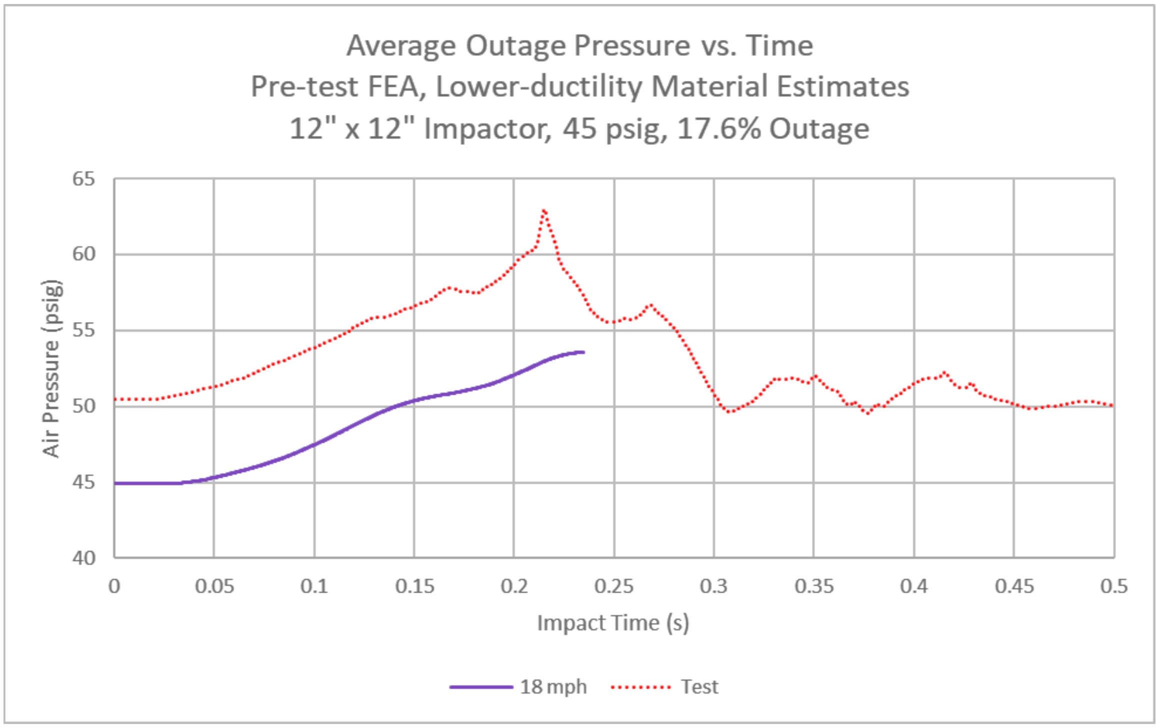

Figure C32. Average Outage Pressure Versus Time for Pre-Test Model Using Lower-Ductility Material at 18 mph

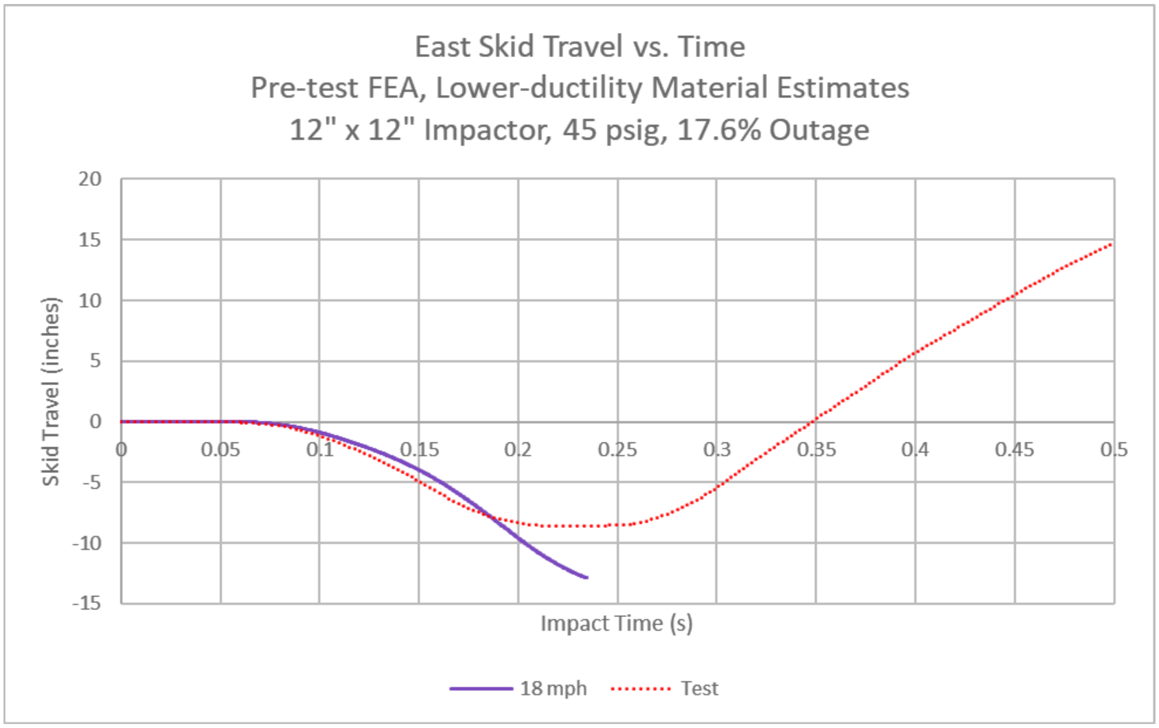

Figure C33. East Skid Travel Versus Time for Pre-Test Model Using Lower-Ductility Material at 18 mph

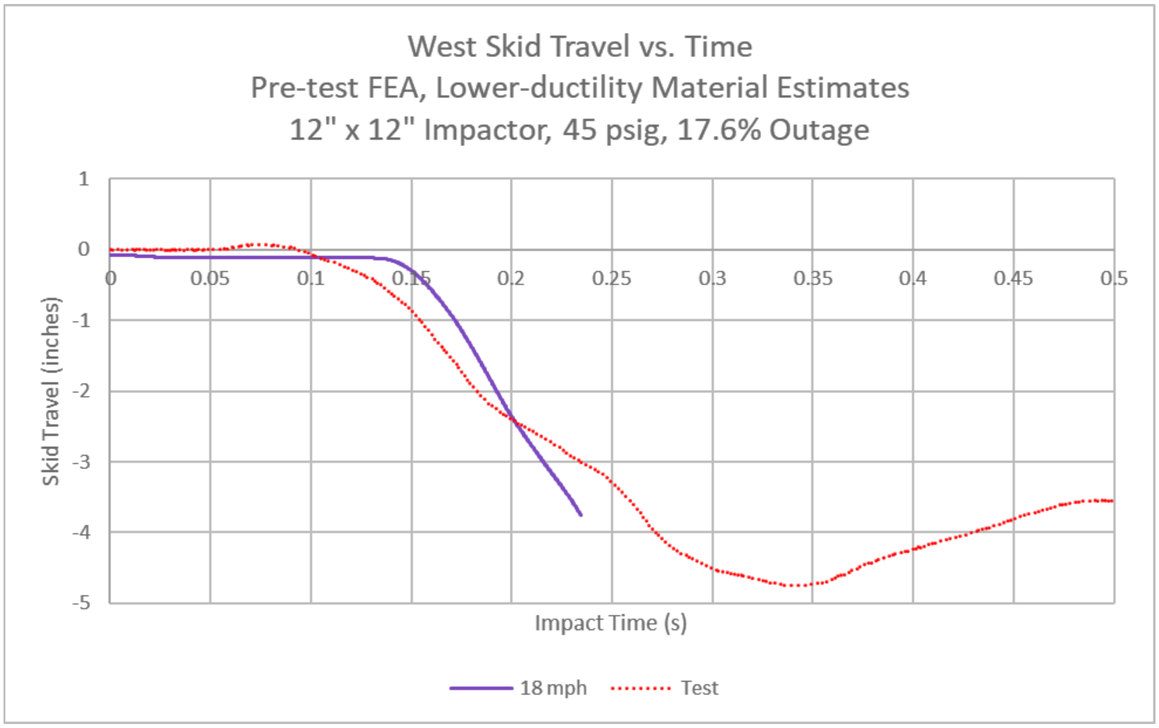

Figure C34. West Skid Travel Versus Time for Pre-Test Model Using Lower-Ductility Material at 18 mph

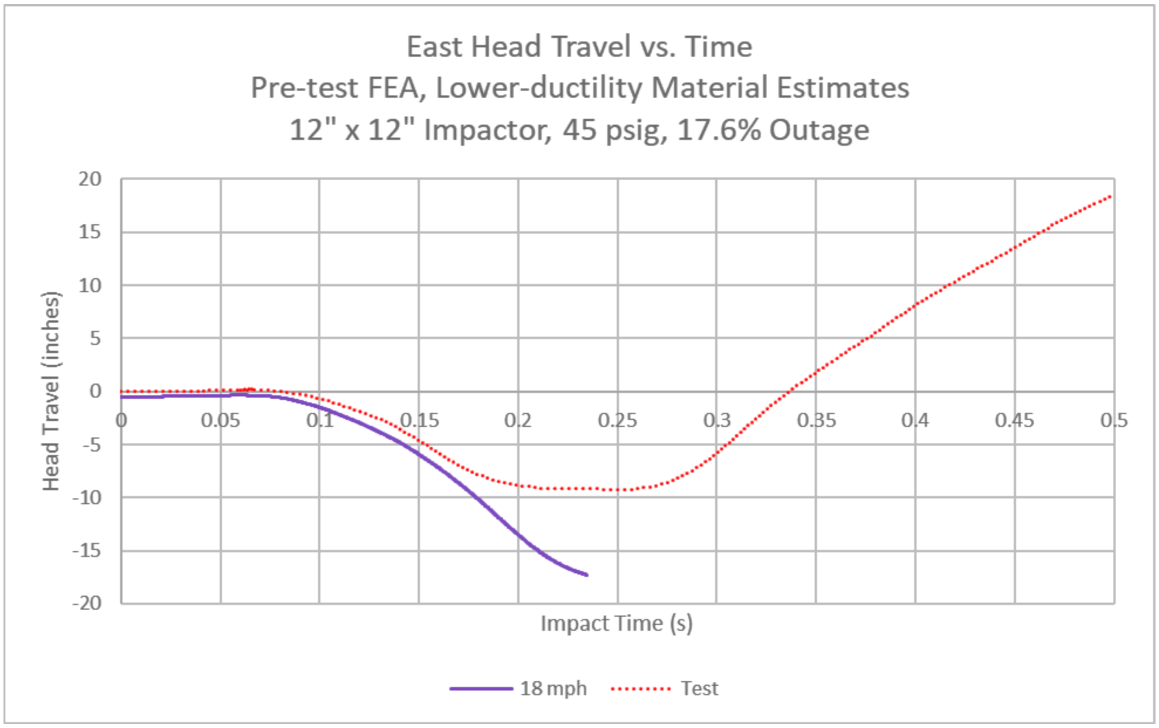

Figure C35. East Head Travel Versus Time for Pre-Test Model Using Lower-Ductility Material at 18 mph

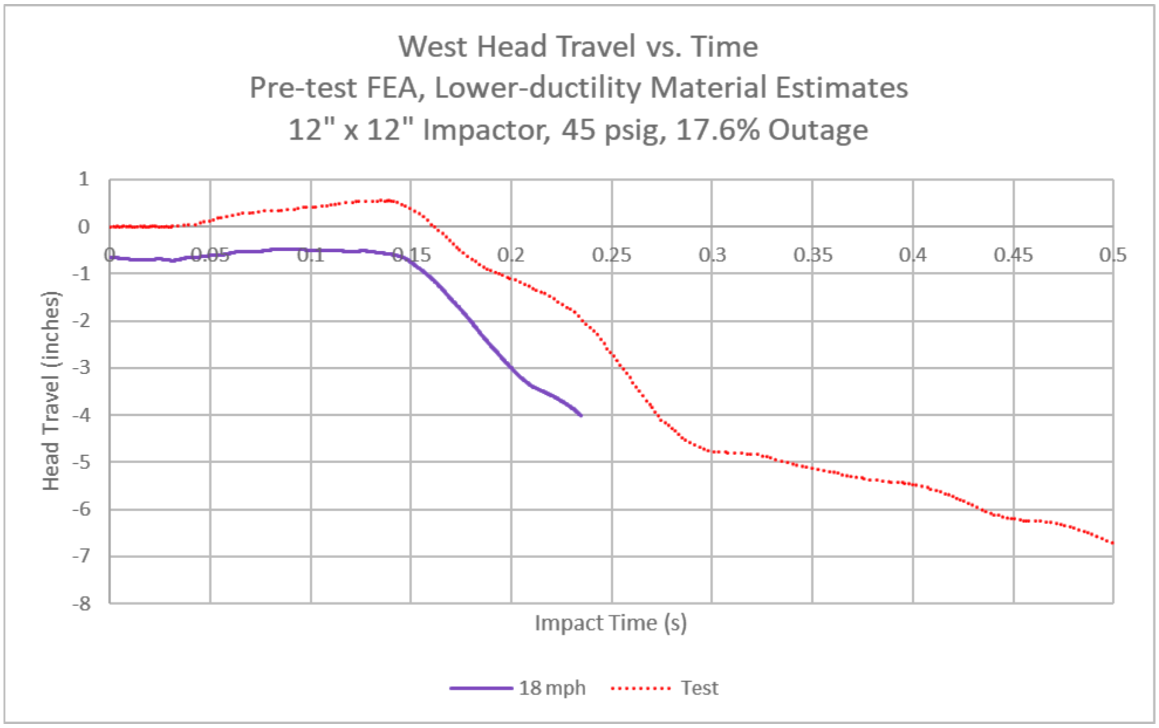

Figure C36. West Head Travel Versus Time for Pre-Test Model Using Lower-Ductility Material at 18 mph

Section 1.5. 18 mph, Upper-Ductility Steels

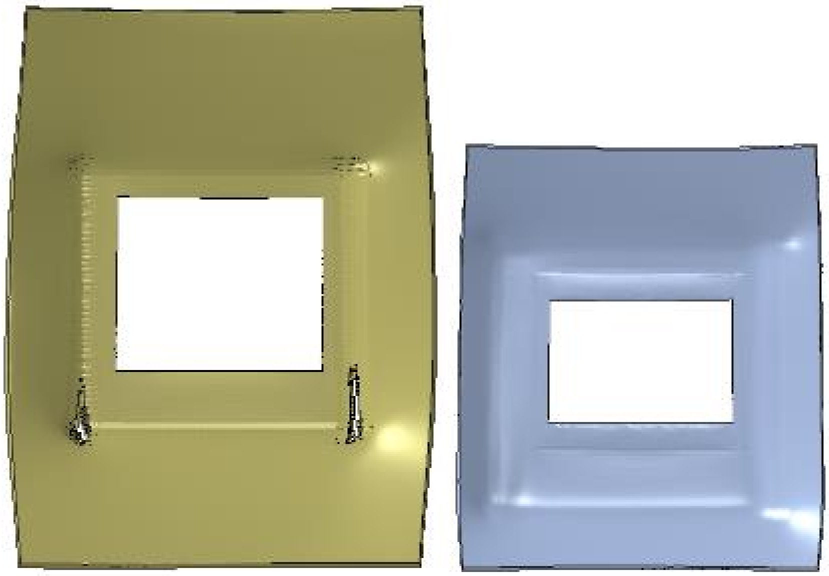

Figure C37. Solid Patch in Outer (left) and Inner (right) Tanks, 18 mph Pre-Test Model (Upper-Ductility Materials) at 500 ms

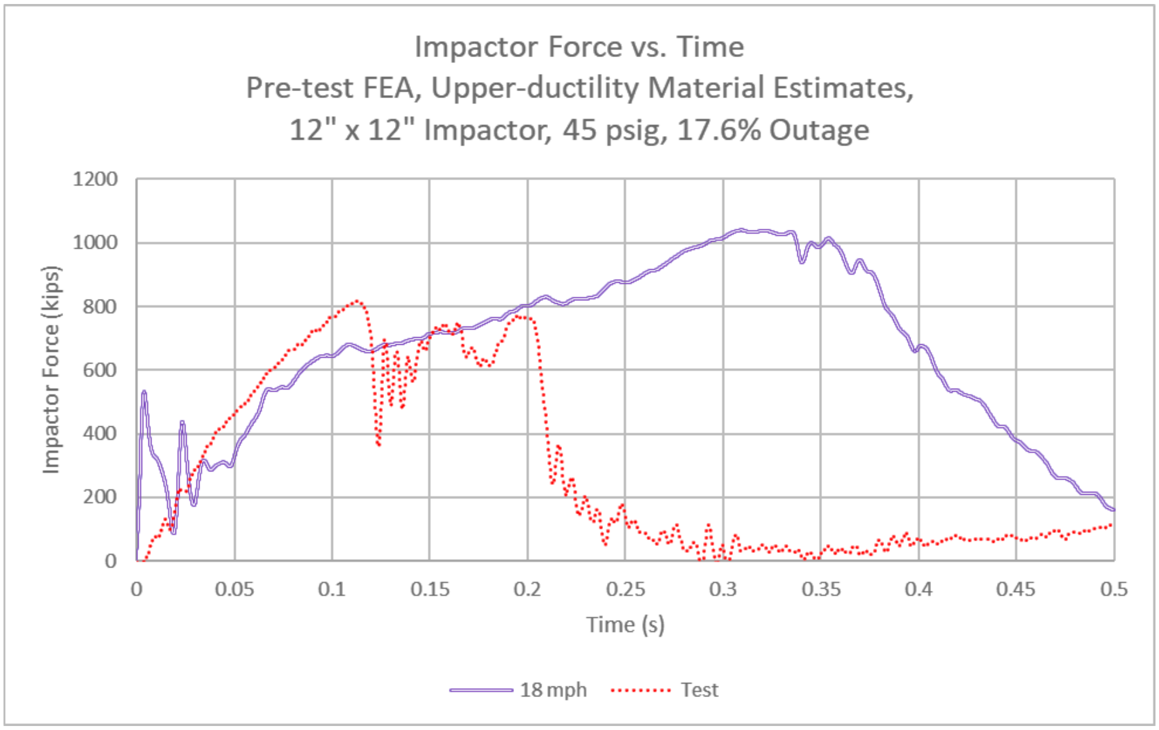

Figure C38. Impactor Force Versus Time for Pre-Test Model Using Upper-Ductility Material at 18 mph

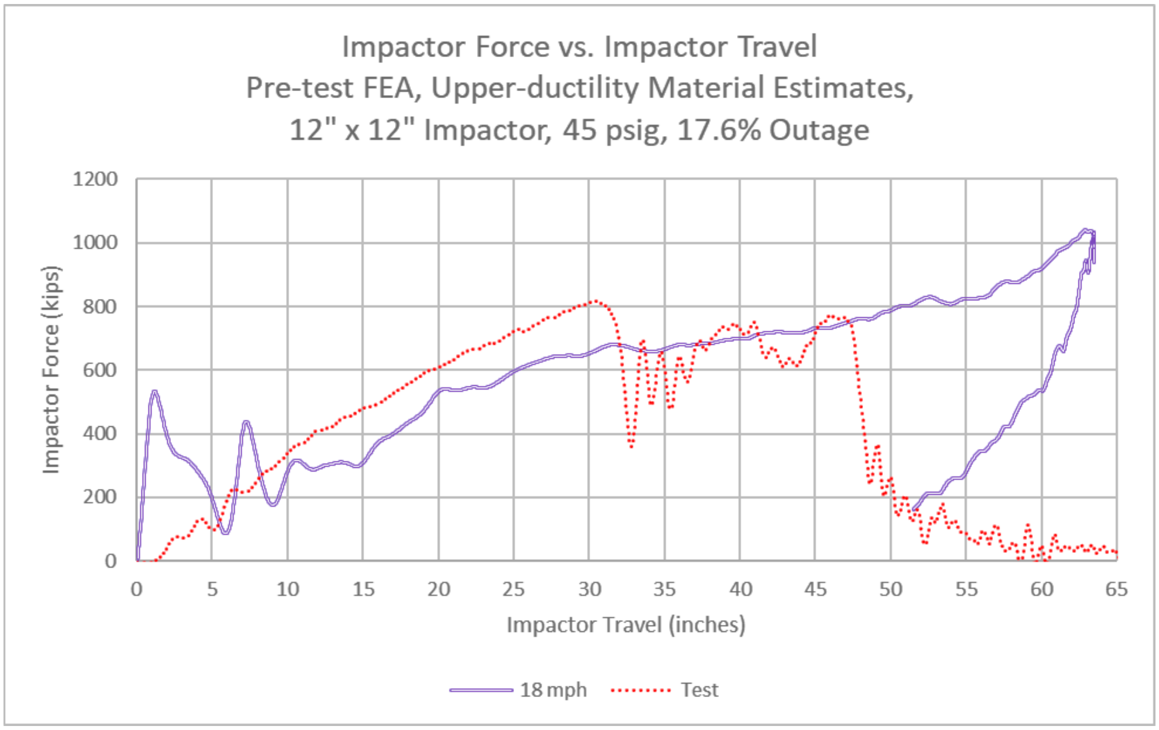

Figure C39. Impactor Force Versus Travel for Pre-Test Model Using Upper-Ductility Material at 18 mph

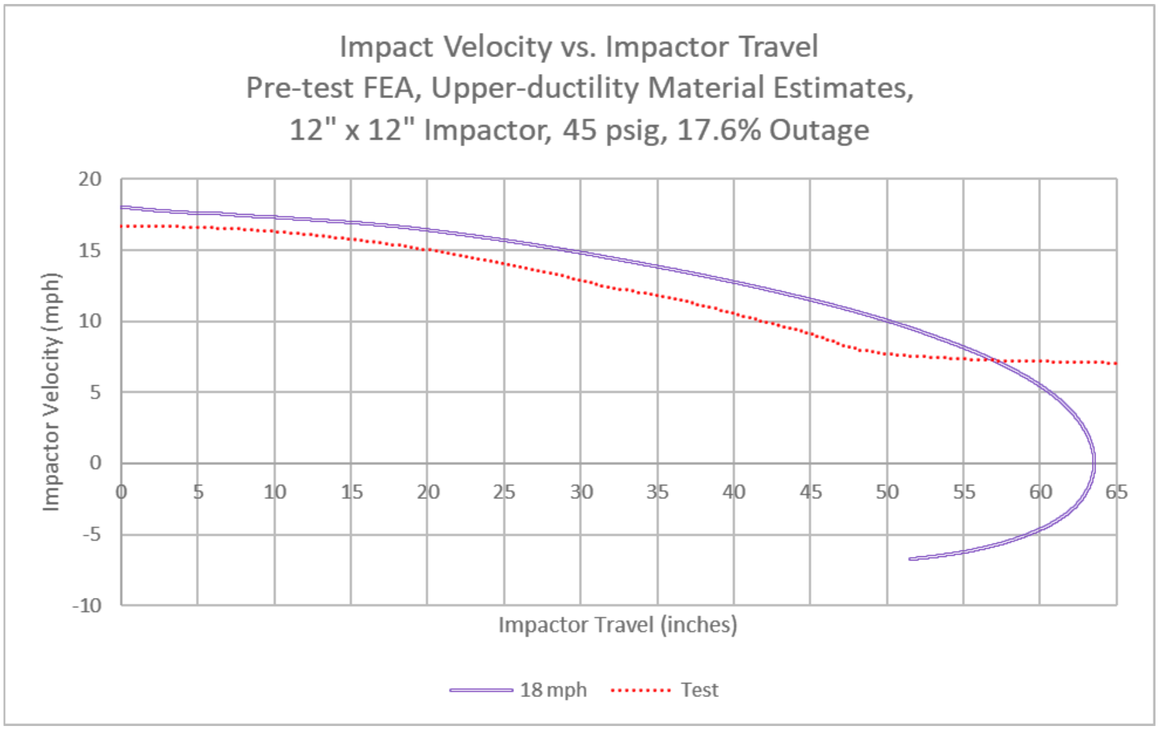

Figure C40. Impactor Velocity Versus Travel for Pre-Test Model Using Upper-Ductility Material at 18 mph

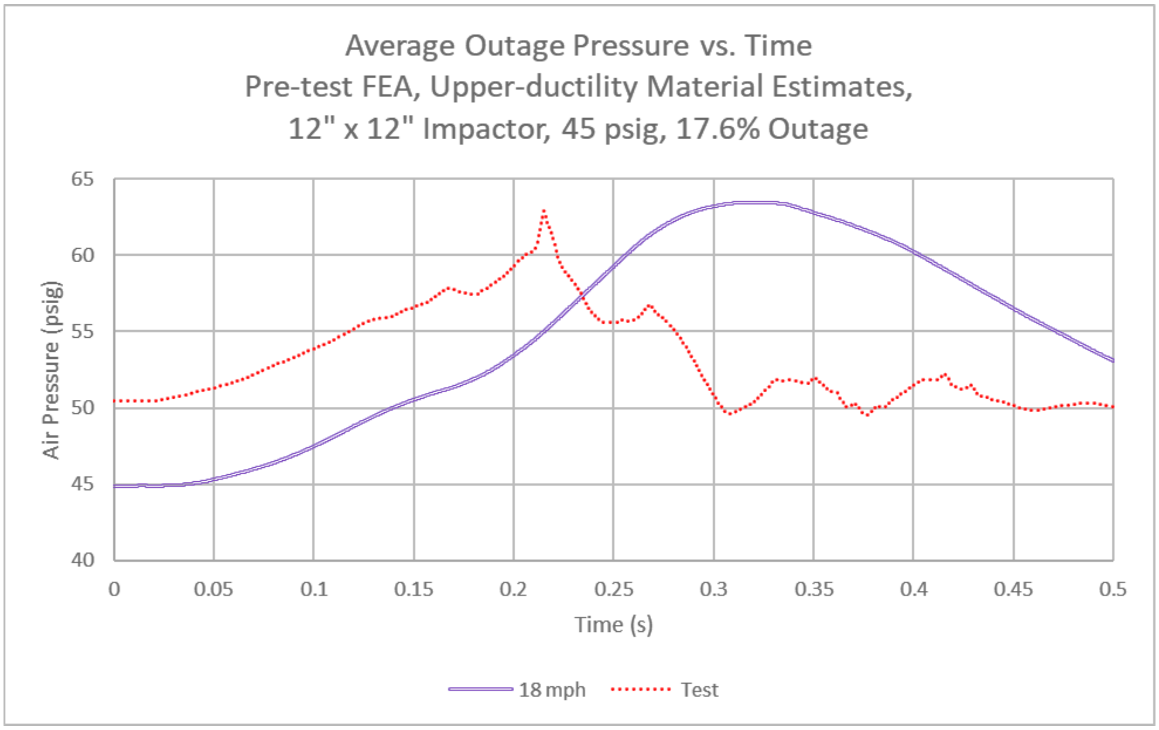

Figure C41. Average Outage Pressure Versus Time for Pre-Test Model Using Upper-Ductility Material at 18 mph

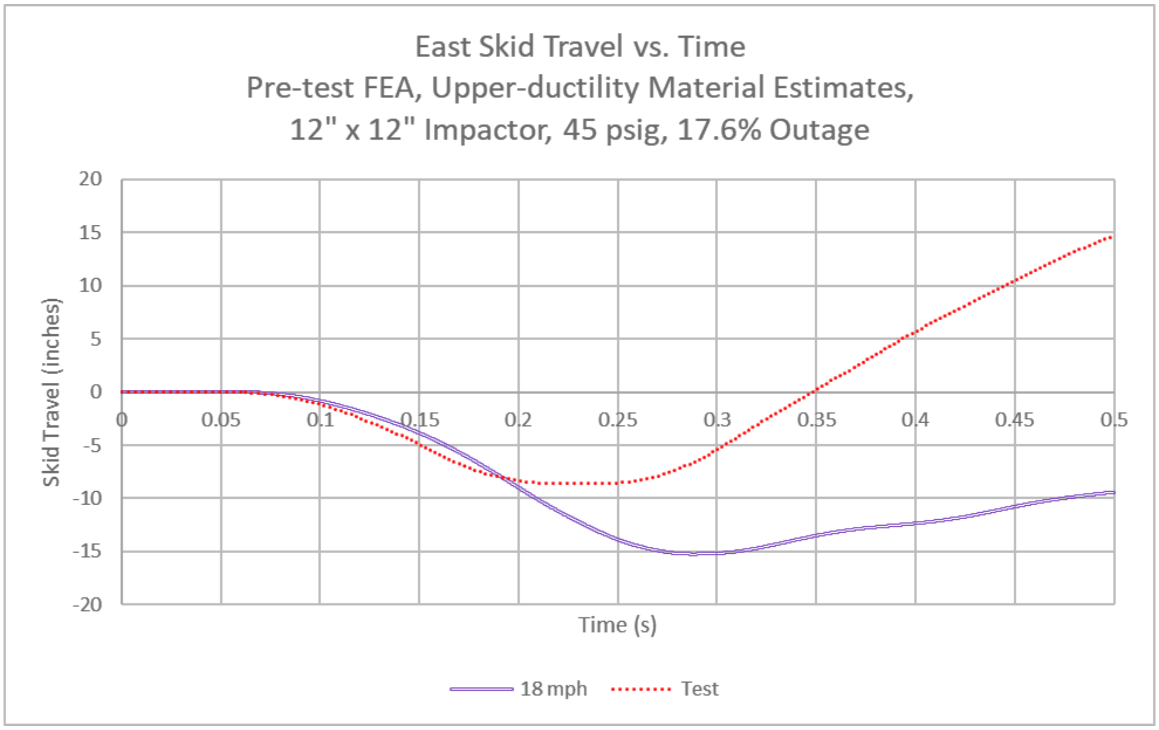

Figure C42. East Skid Travel Versus Time for Pre-Test Model Using Upper-Ductility Material at 18 mph

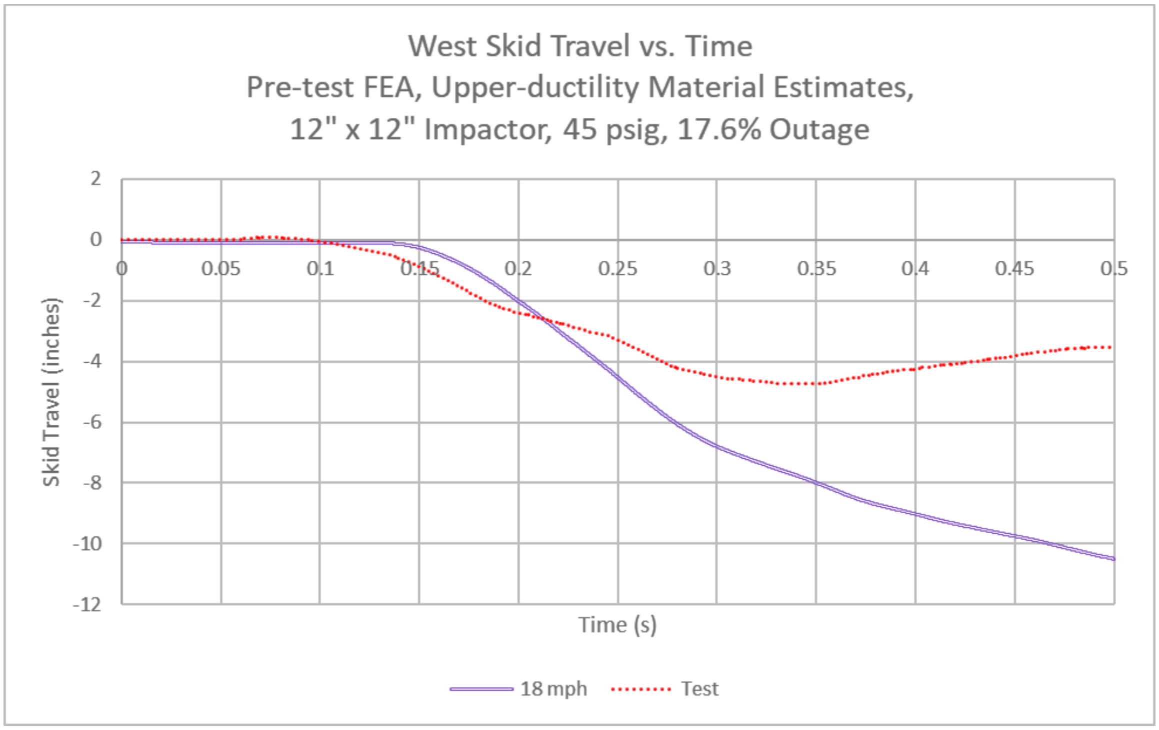

Figure C43. West Skid Travel Versus Time for Pre-Test Model Using Upper-Ductility Material at 18 mph

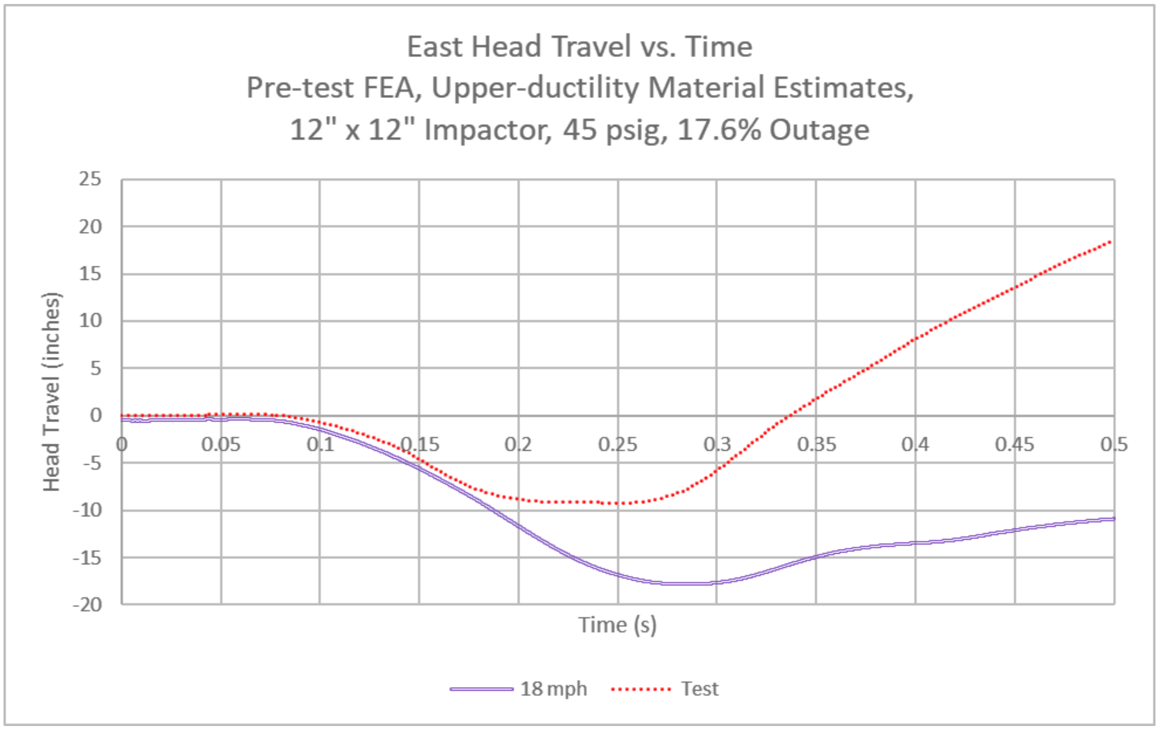

Figure C44. East Head Travel Versus Time for Pre-Test Model Using Upper-Ductility Material at 18 mph

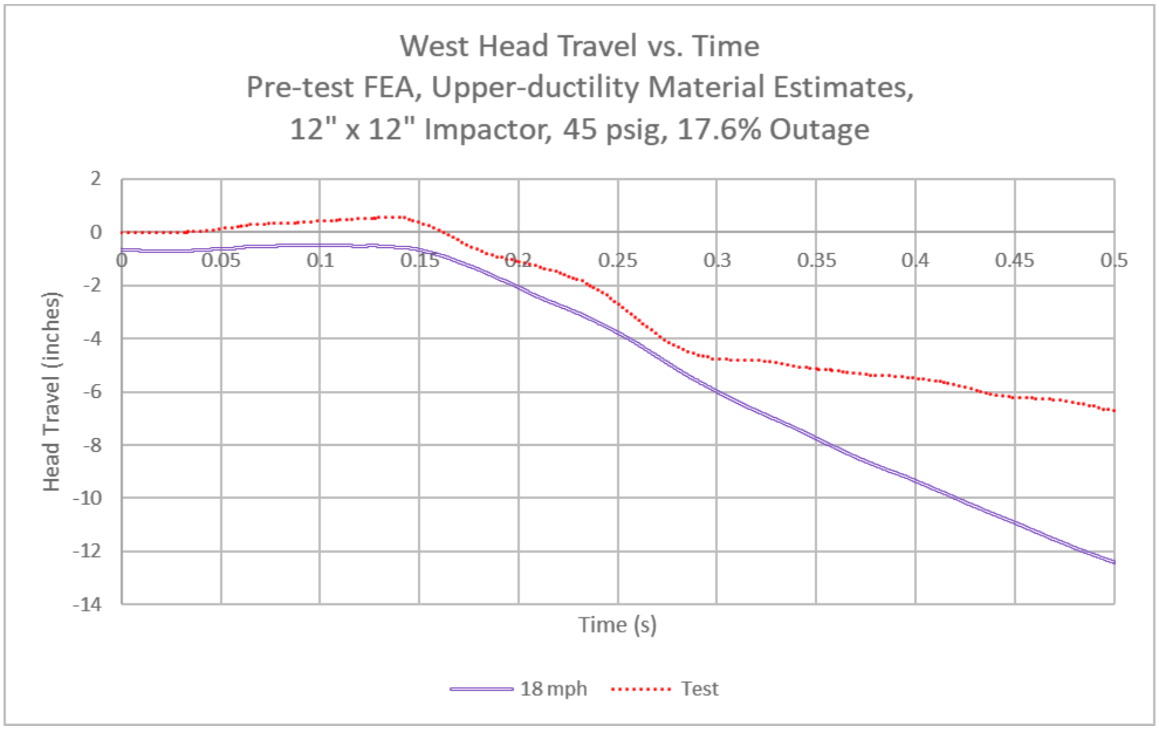

Figure C45. West Head Travel Versus Time for Pre-Test Model Using Upper-Ductility Material at 18 mph

Section 1.6. Summary of Pre-Test Puncture FEA and Test Results

The pre-test FEA estimated that a speed of 18 mph was needed to puncture both the inner and outer tanks if both tanks were made of steels having properties close to the lower-ductility estimates. At 18 mph, the outer tank would experience localized tearing, and the inner tank was not expected to tear if the steels had properties similar to the upper-ductility estimates.

One concern with targeting a speed of 18 mph or more was associated with the residual impactor speed. If both tanks were made of material equal to or better than the upper-bound estimate, a higher impact speed would increase the likelihood of puncturing both tanks. However, if the tanks were made of material having properties similar to (or worse than) the lower-ductility estimates, a higher impact speed would lead to an excess-energy impact, allowing the ram car to continue through the tank cars. This situation could potentially damage the test facilities, especially if the ram car were able to penetrate the tank to the point where the rigid impactor made contact with the rigid backing wall.

The pre-test FEA using the lower materials and an 18-mph impact speed estimated that the impactor would still be traveling at more than 9 mph when the inner tank punctured. Reducing the impact speed to 17.5 mph led to a pre-test estimate where the impactor was brought to a stop and rebounded from the tank without puncturing the inner tank. These two results underscored the challenges with modeling puncture using unknown materials and might indicate a particular sensitivity of tank-within-a tank designs to impact speeds. To minimize the potential for an over-speed impact, a target speed of 16.5 mph ± 0.5 mph was chosen for the test.

Section 2. Post-Test Puncture FEA and Test Results, Pre-Test Material Properties

After the test, the pre-test FE models were updated to better reflect the test conditions. Post-test modeling updates were made in two stages. Immediately following the test, the pre-test models were updated to reflect both the measured impact speed and initial pressure as well as the temperature of the fluids filling the tanks. Certain modeling changes, such as increasing the size of the solid mesh in the impact zone of the outer tank, were also undertaken based on the outcome of the pre-test model. Additionally, the post-test models were updated to include an approximation of the perlite in the annular space between the tanks. Once material coupon data were available from the testing labs, a second set of post-test FE models were run using the actual material properties and thicknesses as measured by the testing lab. This appendix describes the first set of post-test FE results. The second set of FE results are plotted alongside the test data in Appendix C, Section 3.

The first set of post-test simulations were run using the lower- and upper-ductility pre-test material models. To understand the effects of including the perlite, the post-test models were all run both with and without the perlite included using the "sandy soil" material simplification. Thus, the first set of post-test FE results include four different combinations of tank materials and perlite, as summarized in Table C2.

Table C2. Summary of Post-Test FE Models Using Pre-Test Material Properties

Simulated Impact Speed (mph)	Perlite	Tank Steels	Outer Tank State	Inner Tank State	Reason for Termination
16.7	No	Lower ductility	Puncture	No elements lost. Maximum DUCTCRT 0.97	Impactor rebounding
16.7	"Sandy Soil" Perlite	Lower ductility	Puncture running to edge of solid patch	Puncture	Puncture of both tanks
16.7	No	Upper ductility	Small number of elements lost under impactor corner	No elements lost. Maximum DUCTCRT 0.41	Impactor rebounding
16.7	"Sandy Soil" Perlite	Upper ductility	Puncture	No elements lost. Maximum DUCTCRT 0.50	Impactor rebounding

Section 2.1. 16.7 mph, Lower-Ductility Steels, No Perlite

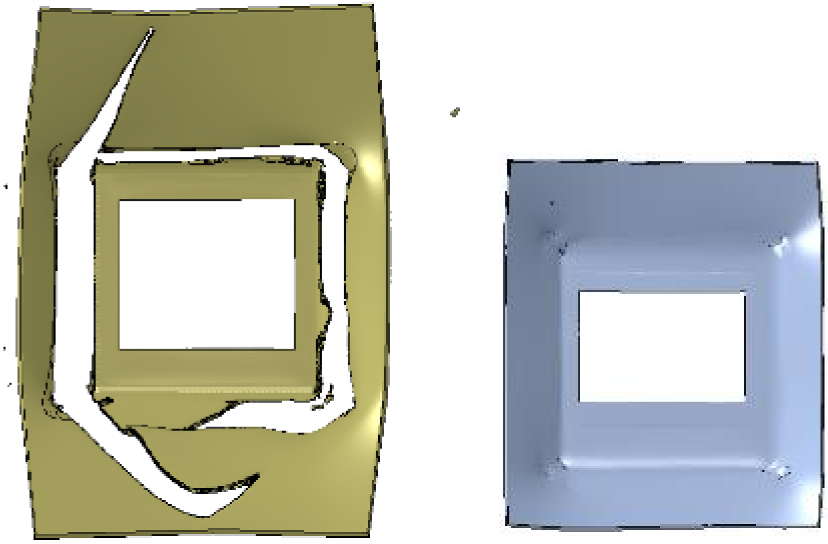

Figure C46. Solid Patch in Outer (left) and Inner (right) Tanks, 16.7 mph Post-Test Model (Lower-Ductility Materials) without Perlite at 400 ms

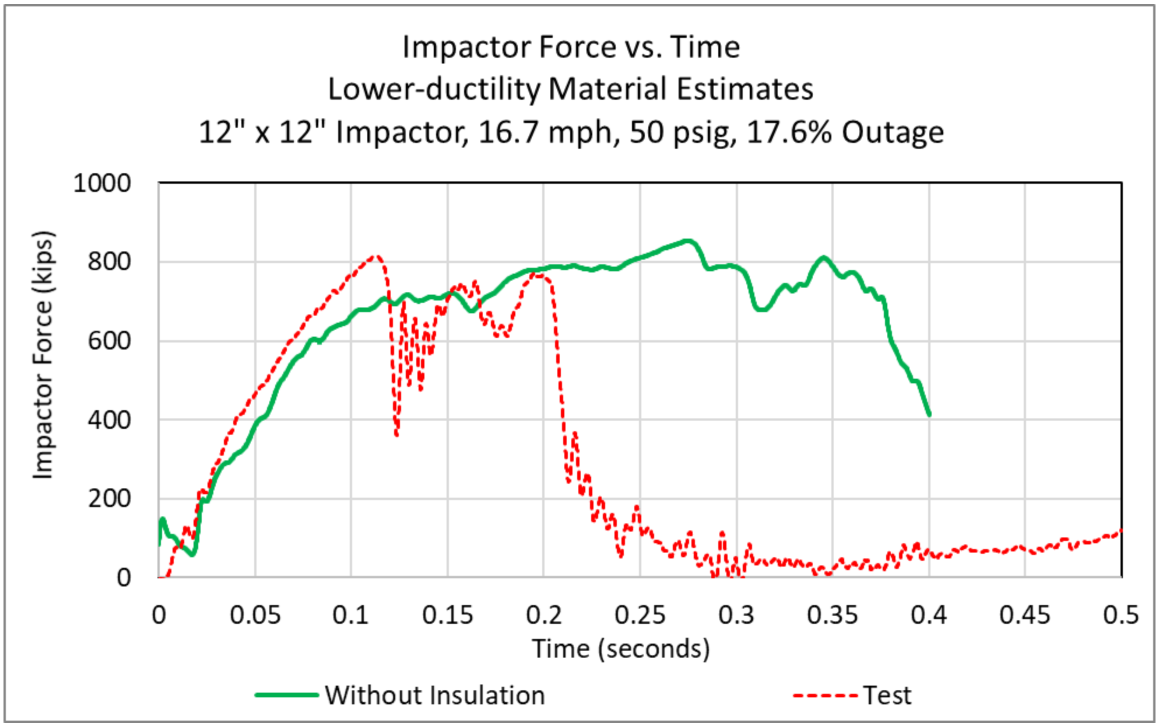

Figure C47. Impactor Force Versus Time, 16.7 mph Post-Test Model (Lower-Ductility Materials) Without Perlite

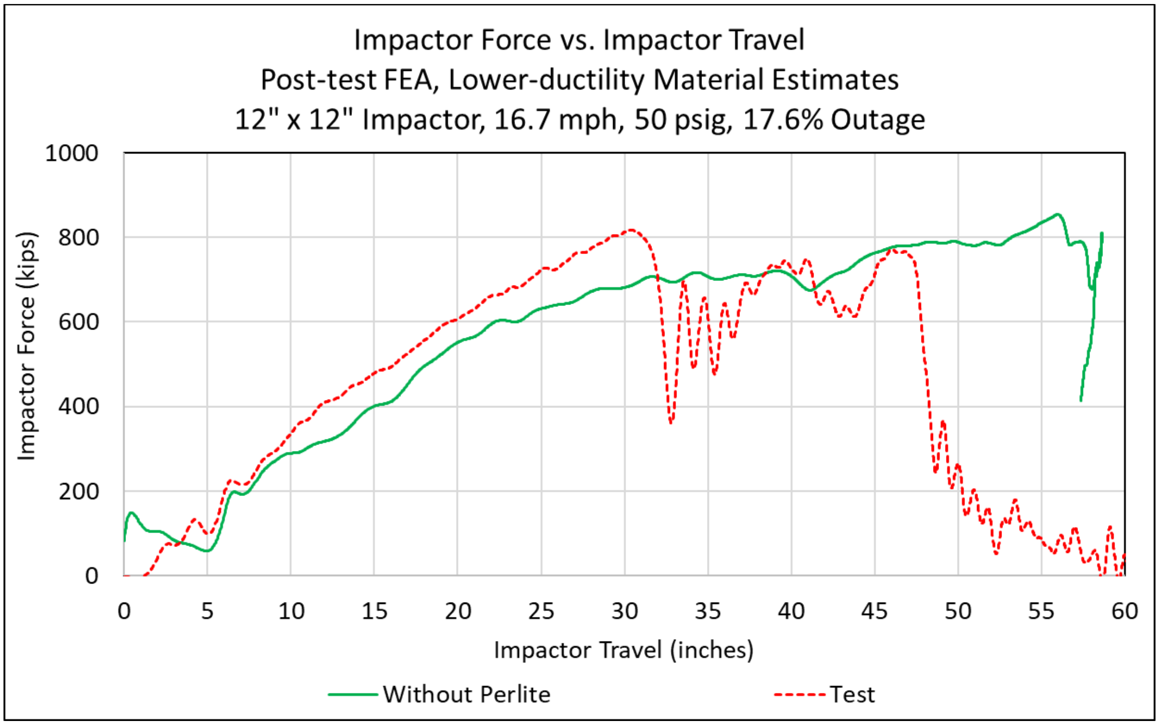

Figure C48. Impactor Force Versus Travel, 16.7 mph Post-Test Model (Lower-Ductility Materials) Without Perlite

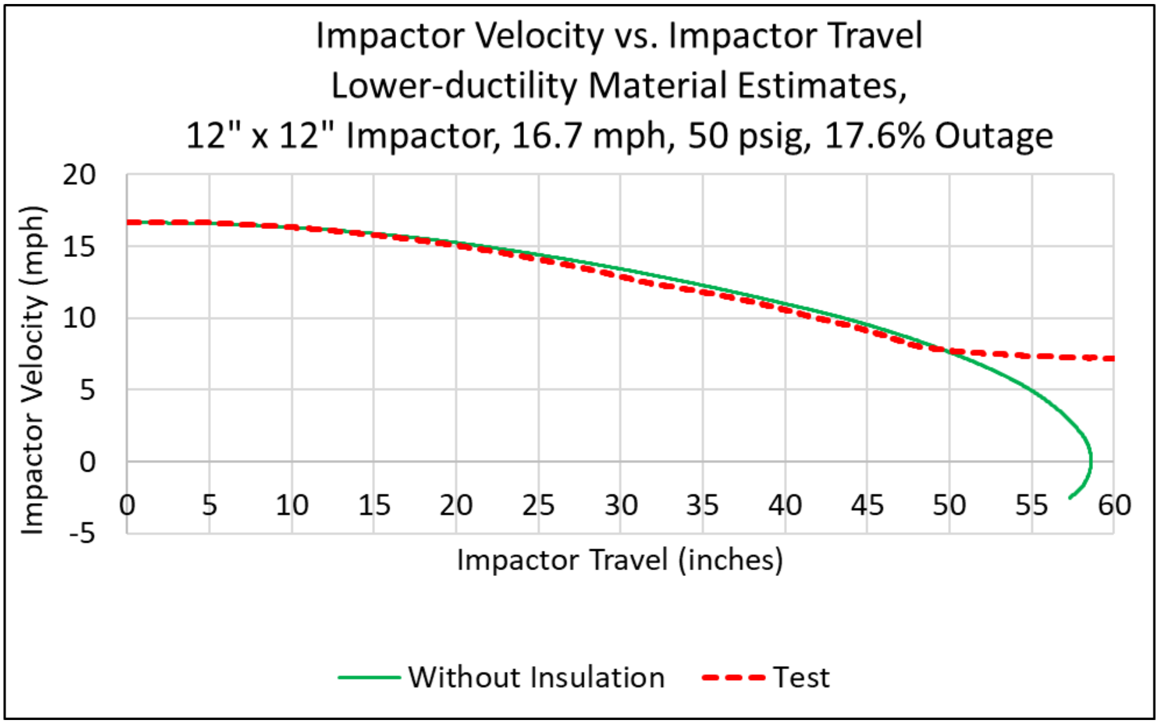

Figure C49. Impactor Velocity Versus Travel, 16.7 mph Post-Test Model (Lower-Ductility Materials) Without Perlite

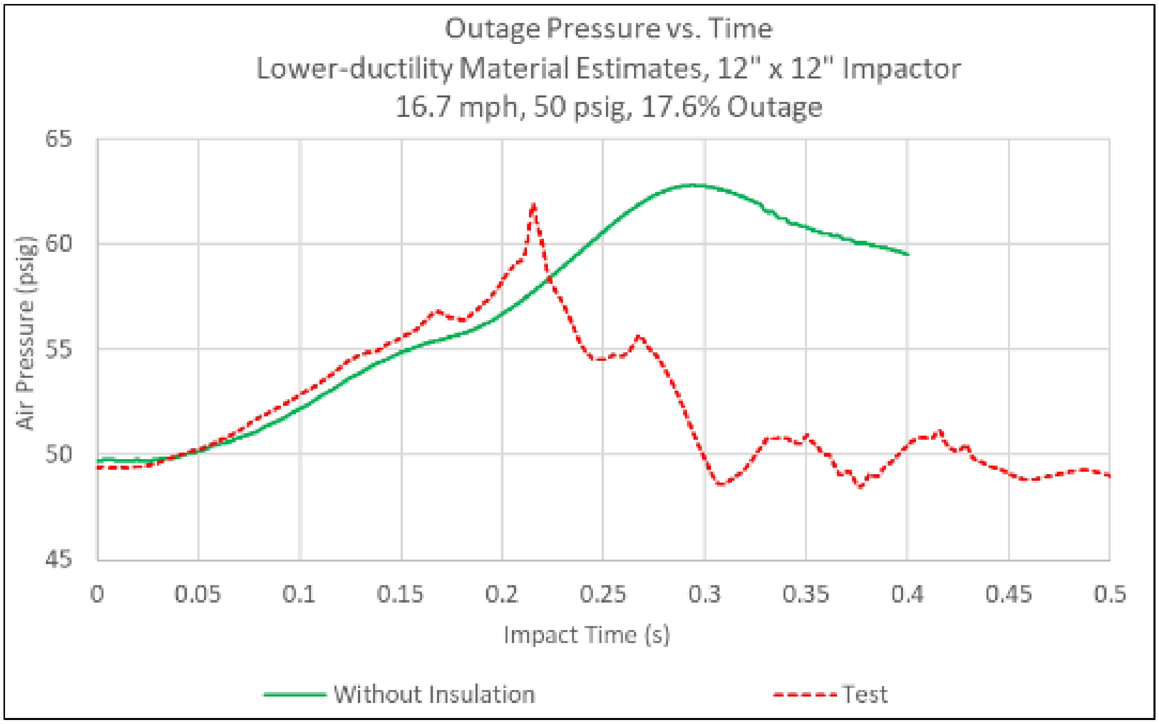

Figure C50. Average Outage Pressure Versus Time, 16.7 mph Post-Test Model (Lower-Ductility Materials) Without Perlite

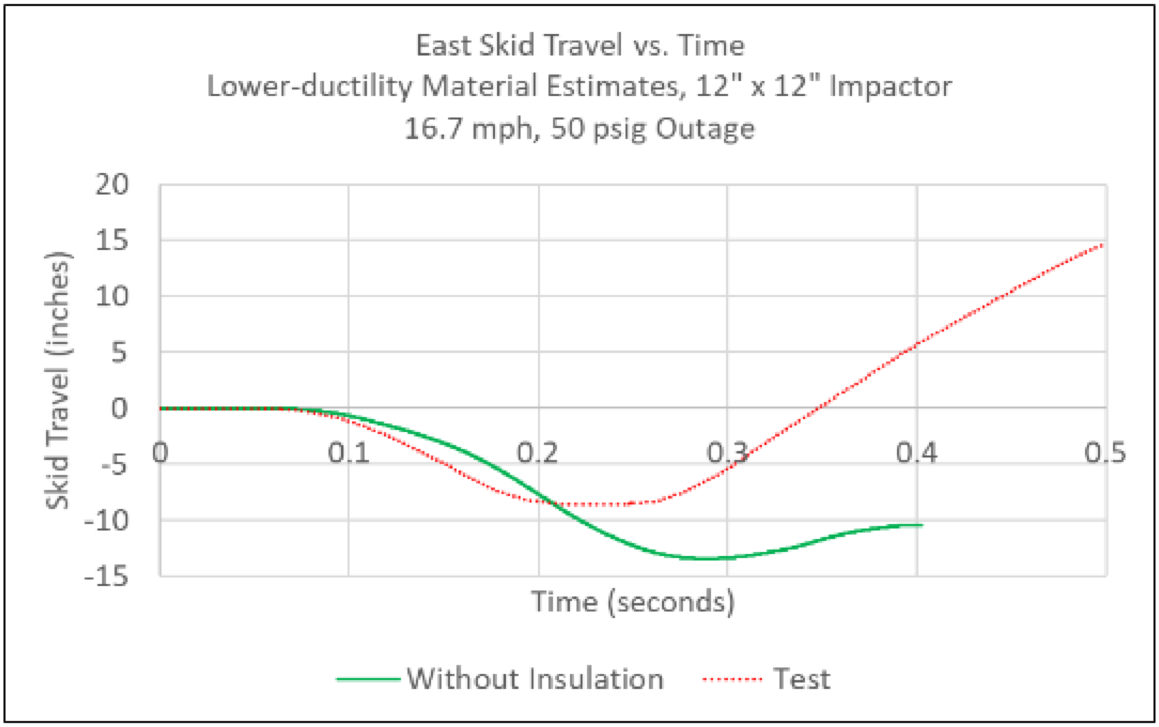

Figure C51. East Skid Travel Versus Time, 16.7 mph Post-Test Model (Lower-Ductility Materials) Without Perlite

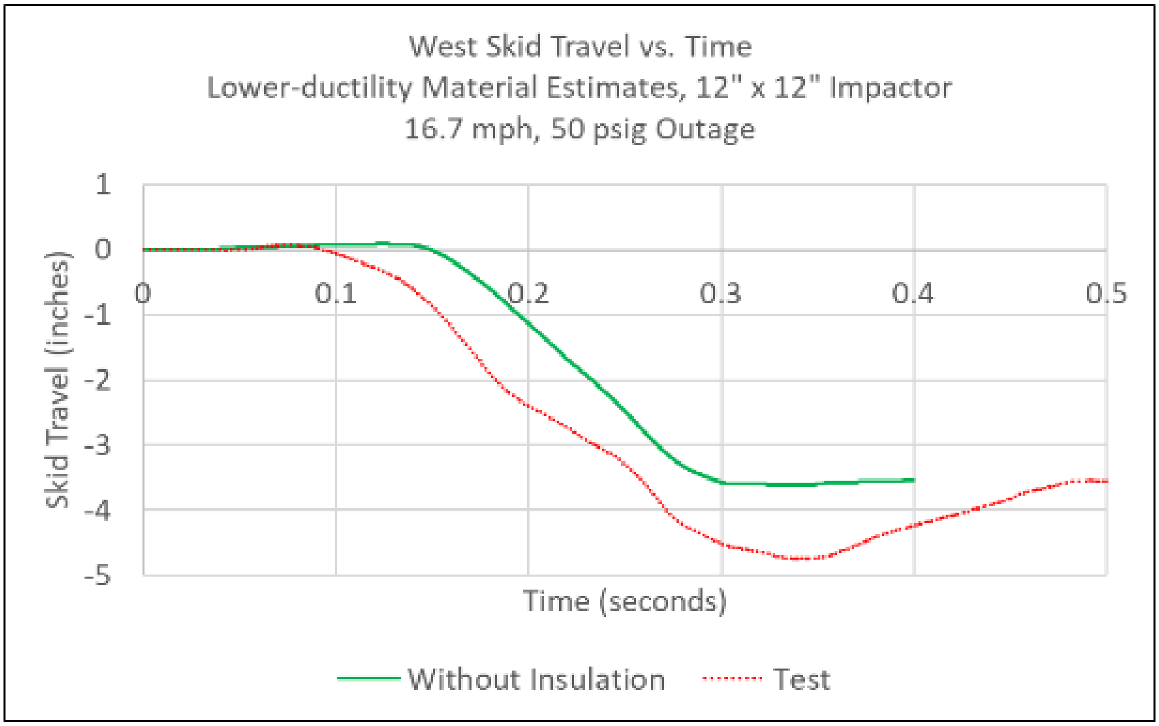

Figure C52. West Skid Travel Versus Time, 16.7 mph Post-Test Model (Lower-Ductility materials) without Perlite

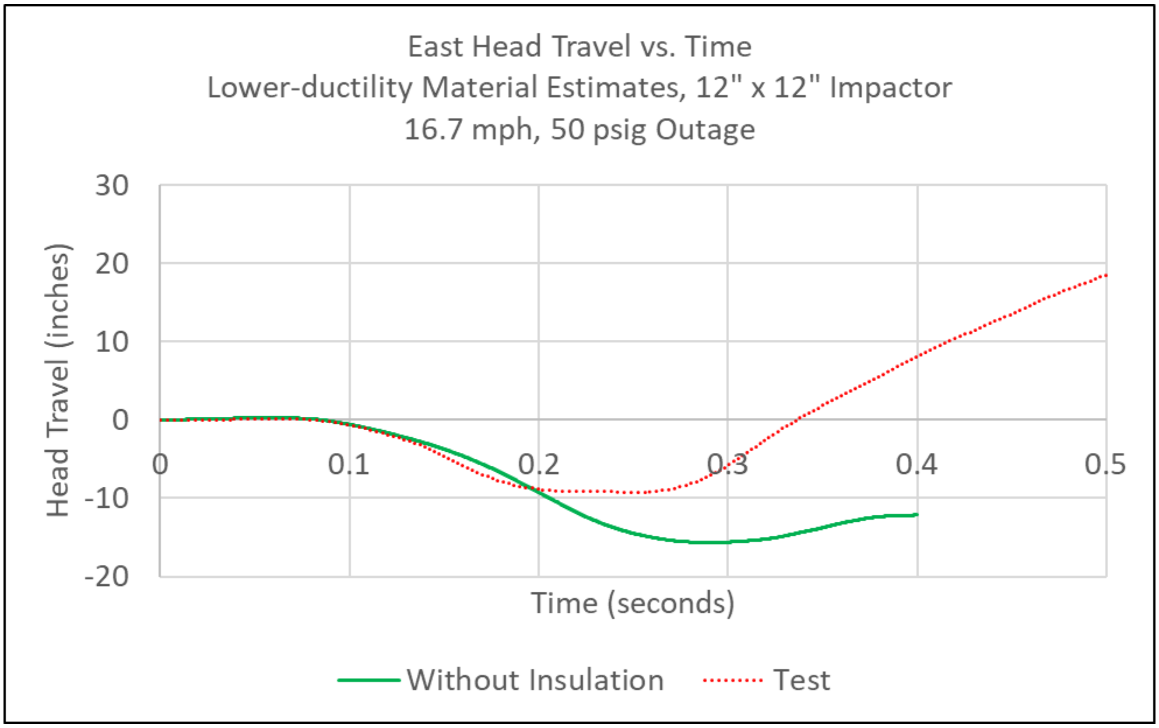

Figure C53. East Head Travel Versus Time, 16.7 mph Post-Test Model (Lower-Ductility Materials) Without Perlite

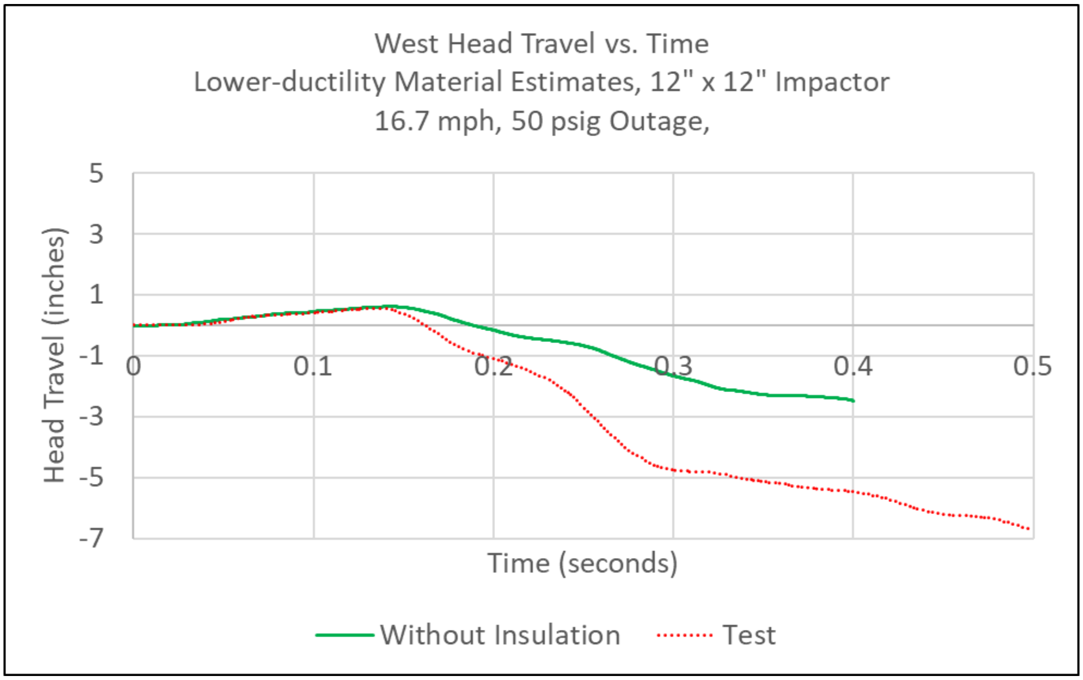

Figure C54. West Head Travel Versus Time, 16.7 mph Post-Test Model (Lower-Ductility Materials) Without Perlite

Section 2.2. 16.7 mph, Lower-Ductility Steels, "Sandy Soil" Perlite

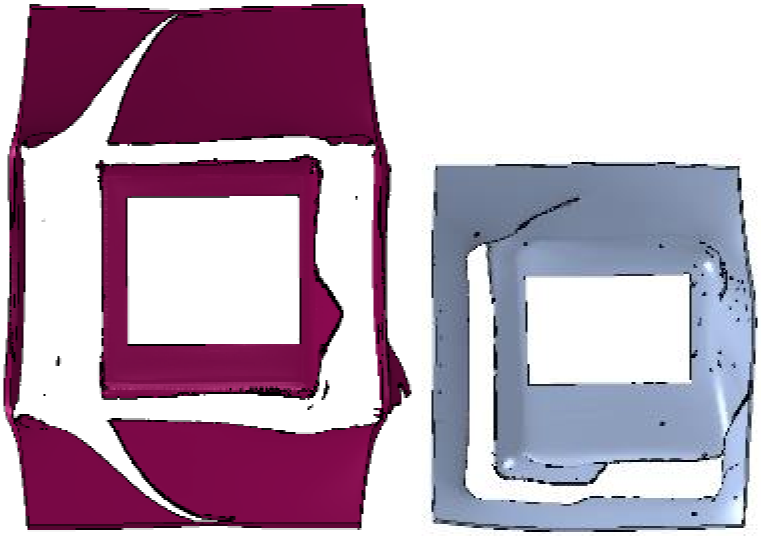

Figure C55. Solid Patch in Outer (left) and Inner (right) Tanks, 16.7 mph Post-Test Model (Lower-Ductility Materials) with "Sandy Soil" Perlite at 310 ms

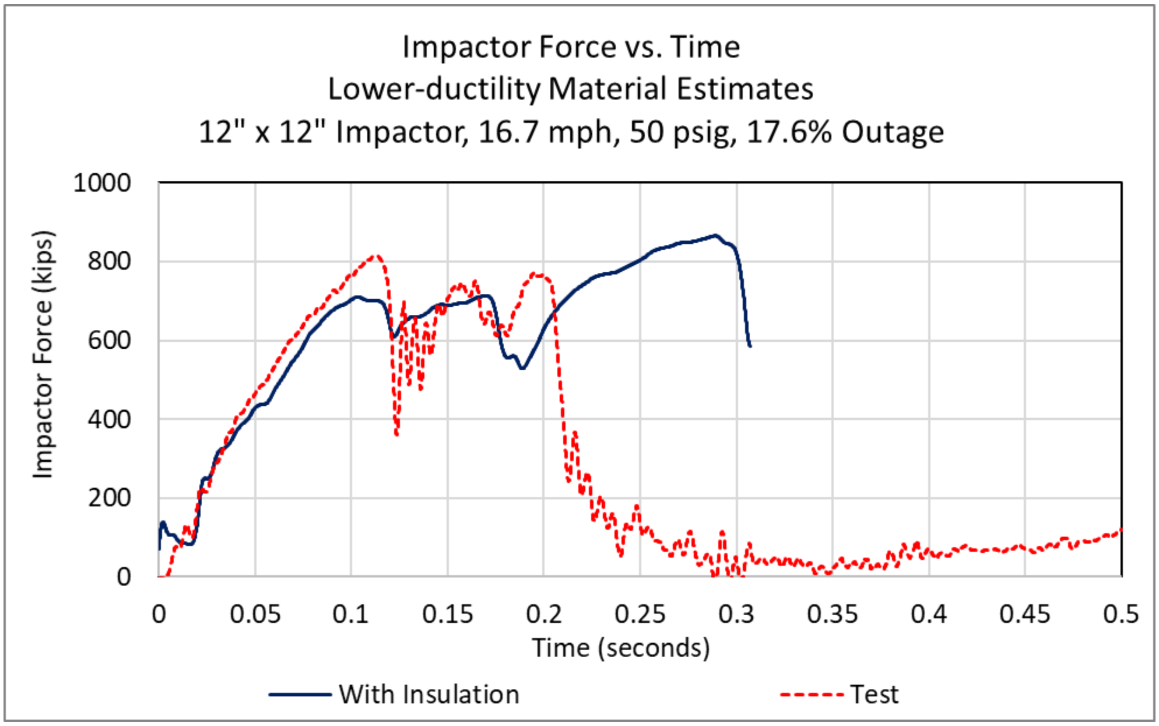

Figure C56. Impactor Force Versus Time, 16.7 mph Post-Test Model (Lower-Ductility Materials) with "Sandy Soil" Perlite

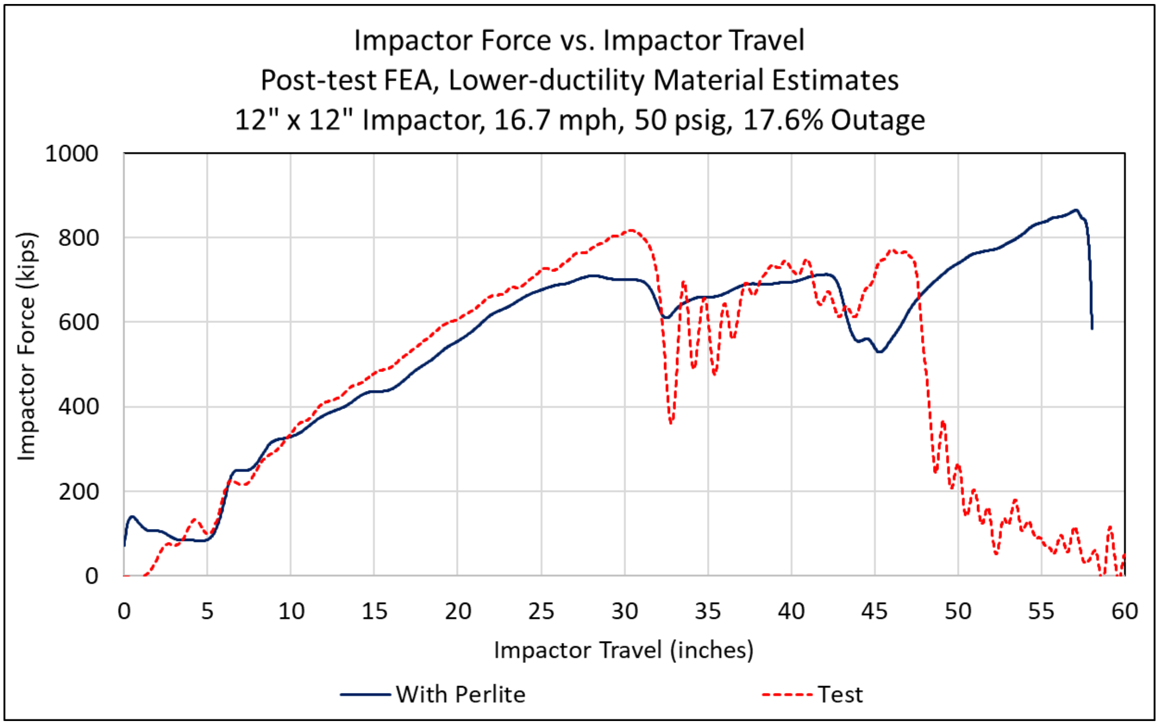

Figure C57. Impactor Force Versus Travel, 16.7 mph Post-Test Model (Lower-Ductility Materials) with "Sandy Soil" Perlite

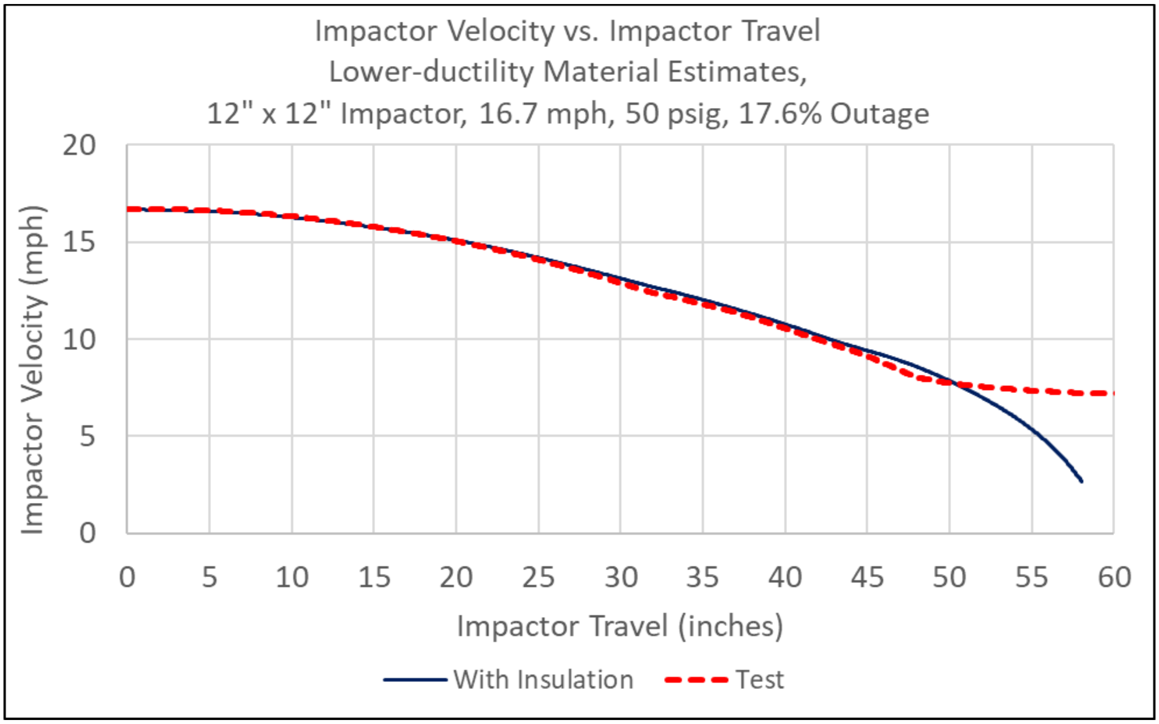

Figure C58. Impactor Velocity Versus Travel, 16.7 mph Post-Test Model (Lower-Ductility Materials) with "Sandy Soil" Perlite

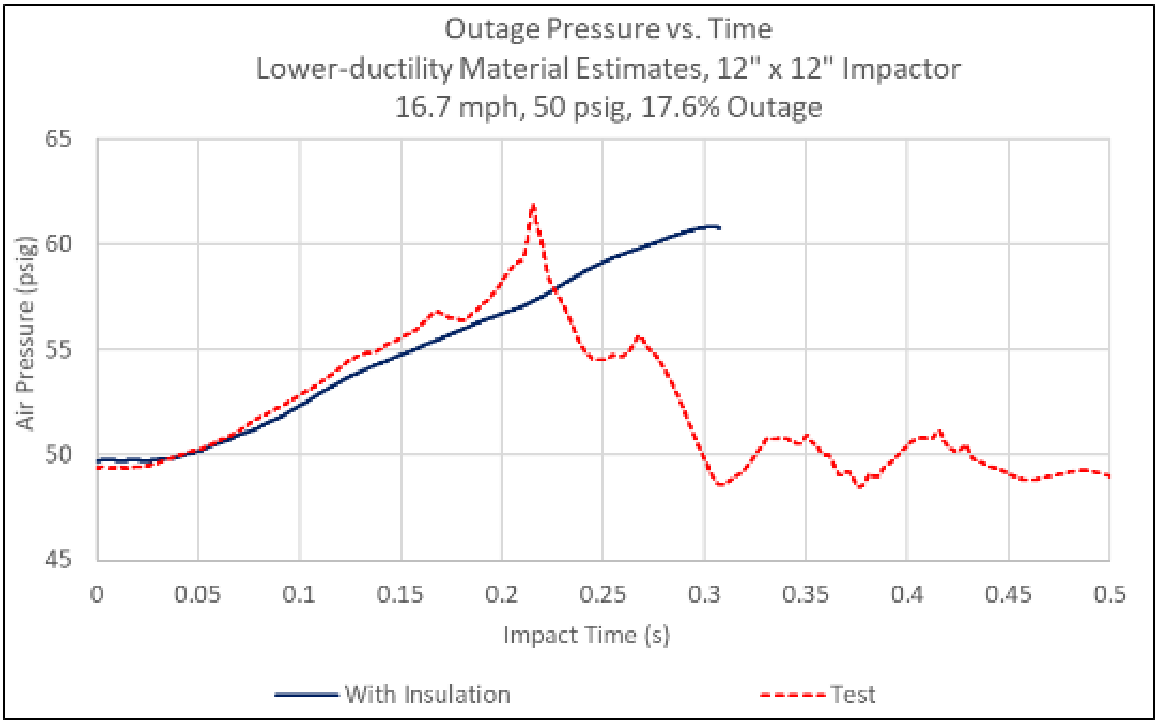

Figure C59. Outage Pressure Versus Time, 16.7 mph Post-Test Model (Lower-Ductility Materials) with "Sandy Soil" Perlite

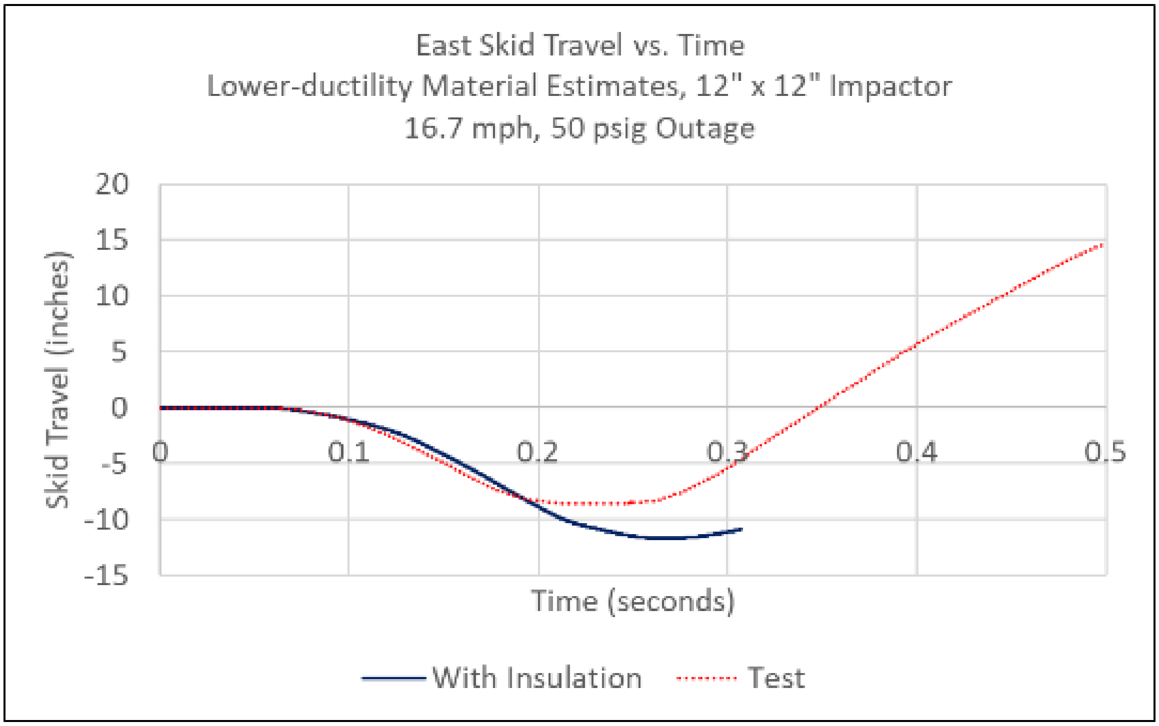

Figure C60. East Skid Travel Versus Time, 16.7 mph Post-Test Model (Lower-Ductility Materials) with "Sandy Soil" Perlite

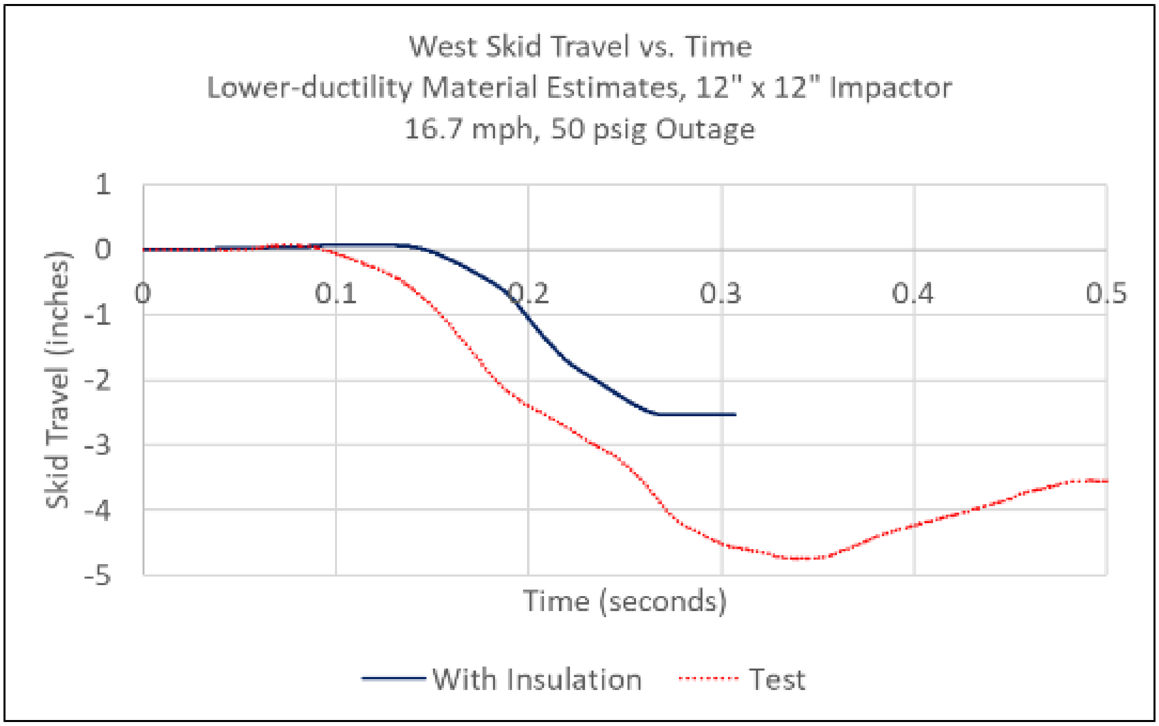

Figure C61. West Skid Travel Versus Time, 16.7 mph Post-Test Model (Lower-Ductility Materials) with "Sandy Soil" Perlite

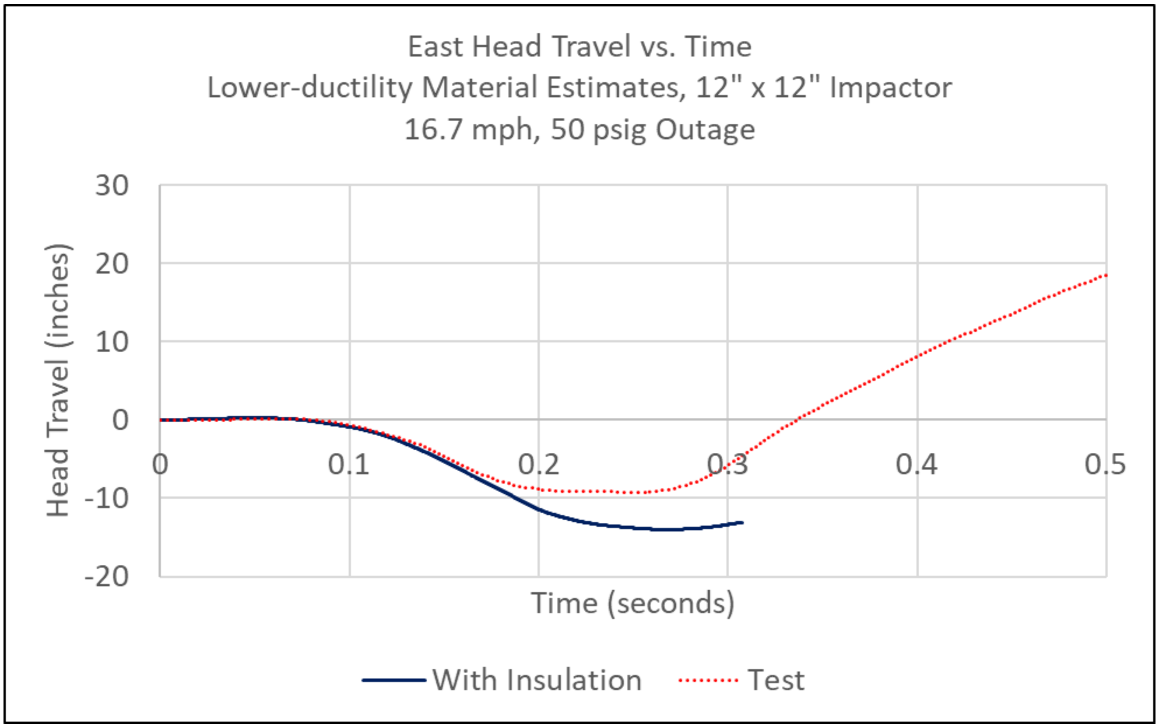

Figure C62. East Head Travel Versus Time, 16.7 mph Post-Test Model (Lower-Ductility Materials) with "Sandy Soil" Perlite

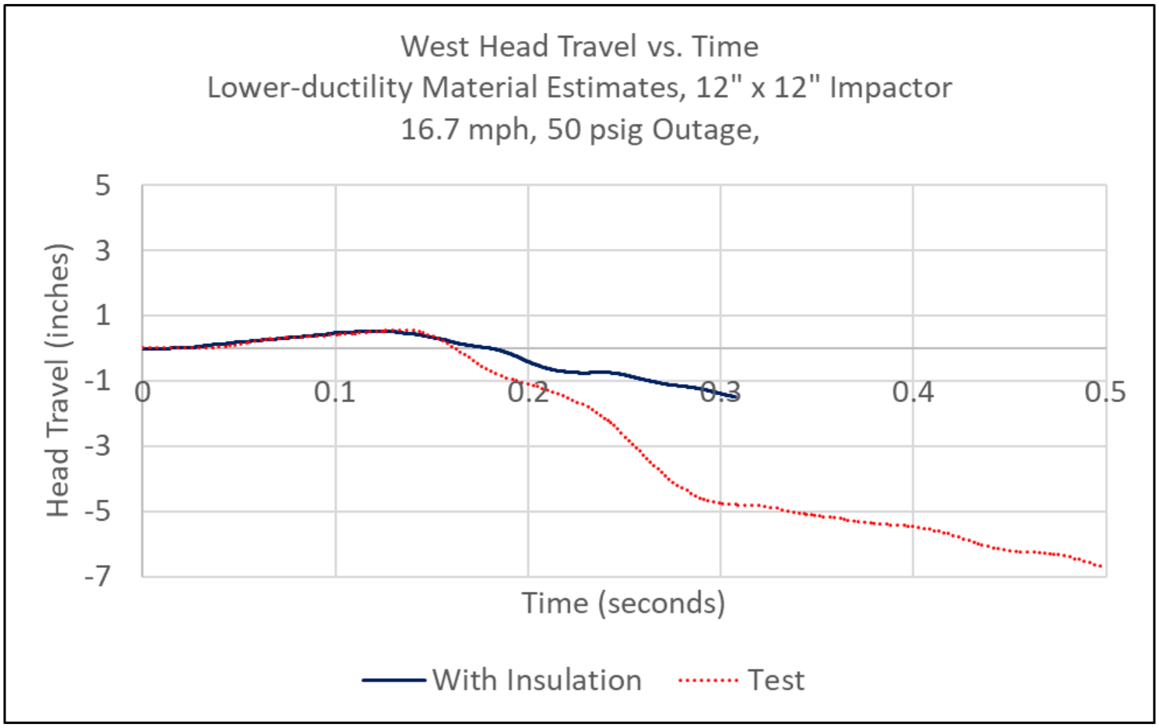

Figure C63. West Head Travel Versus Time, 16.7 mph Post-Test Model (Lower-Ductility Materials) with "Sandy Soil" Perlite

Section 2.3. 16.7 mph, Upper-Ductility Steels, No Perlite

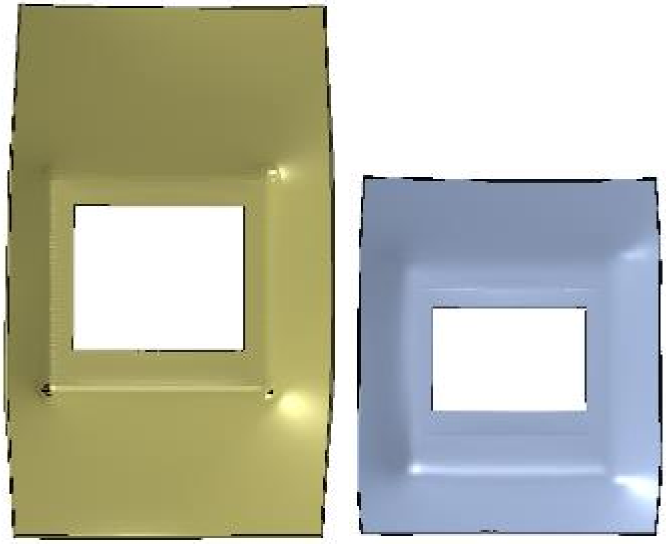

Figure C64. Solid Patch in Outer (left) and Inner (right) Tanks, 16.7 mph Post-Test Model (Upper-Ductility Materials) without Perlite at 400 ms

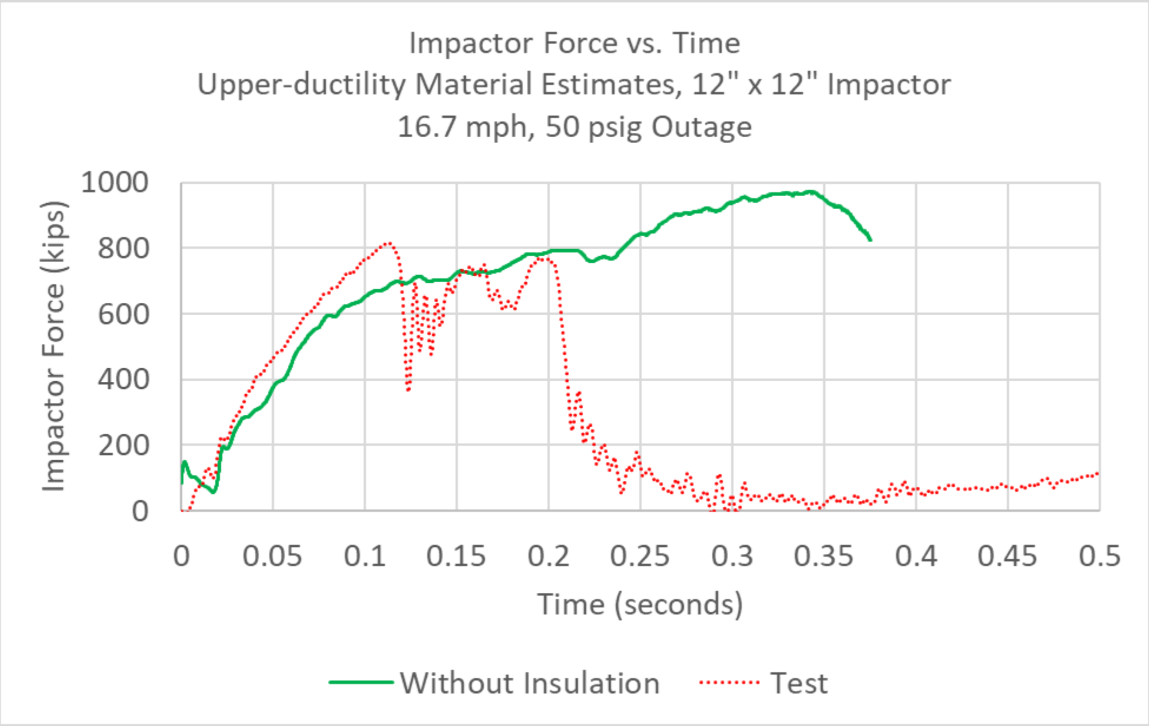

Figure C65. Impactor Force Versus Time, 16.7 mph Post-Test Model (Upper-Ductility Materials) without Perlite

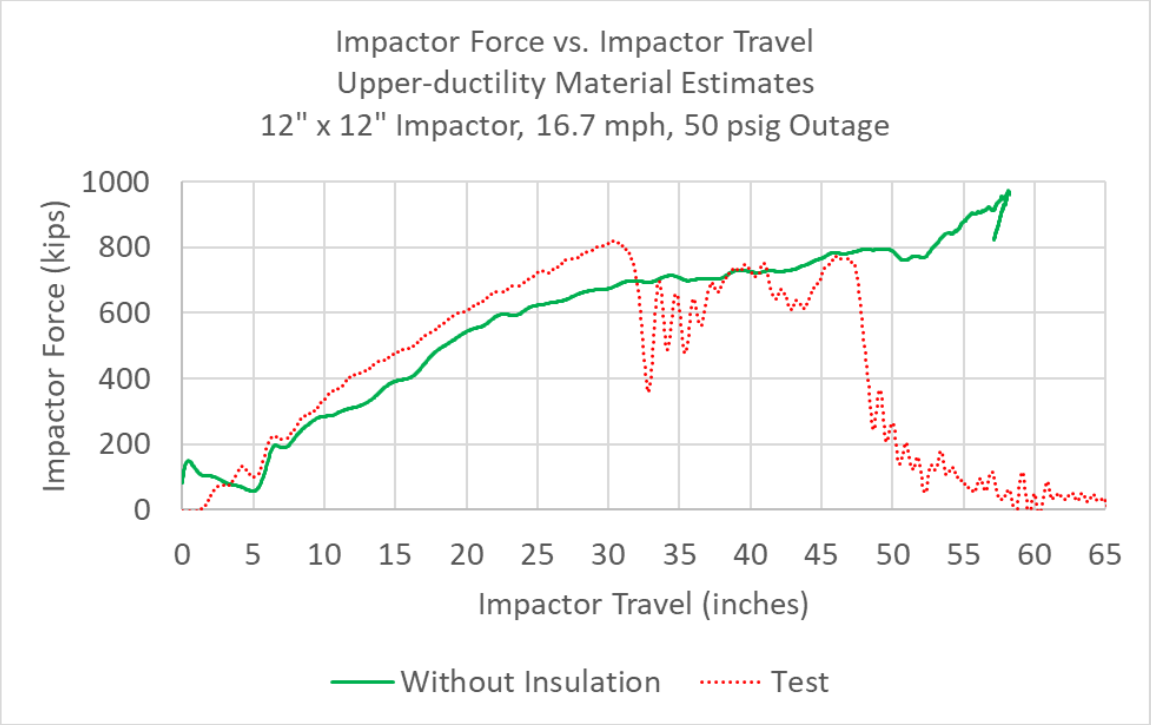

Figure C66. Impactor Force Versus Travel, 16.7 mph Post-Test Model (Upper-Ductility Materials) Without Perlite

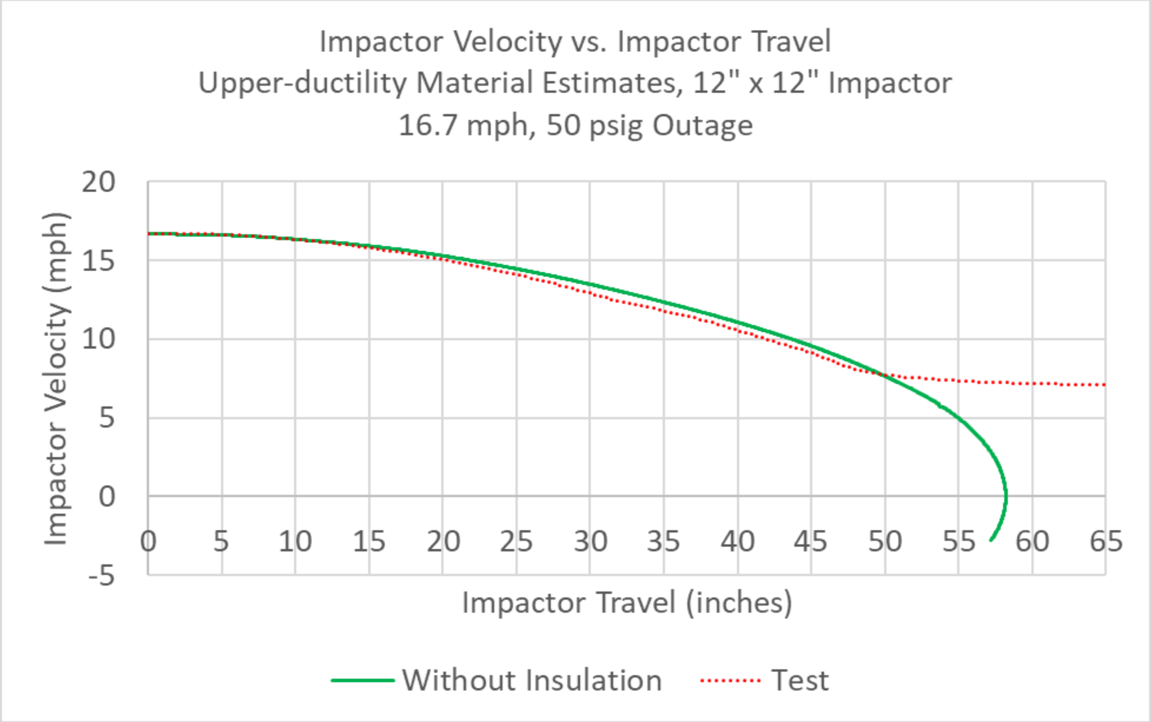

Figure C67. Impactor Velocity Versus Travel, 16.7 mph Post-Test Model (Upper-Ductility Materials) Without Perlite

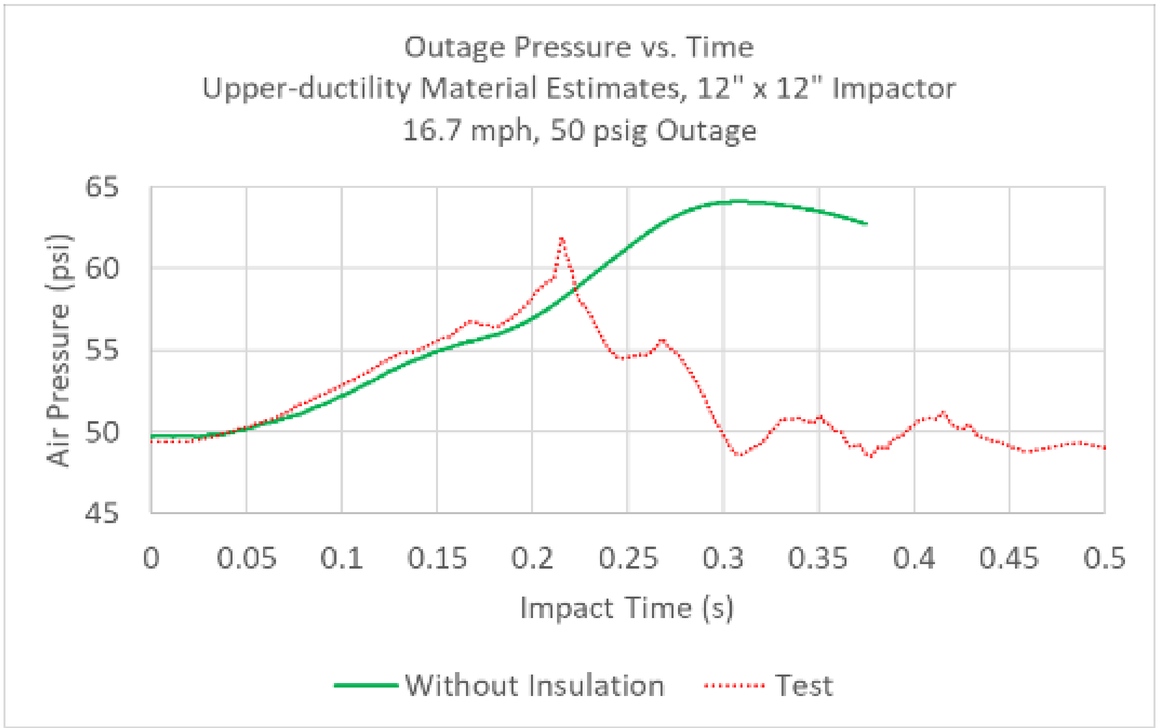

Figure C68. Outage Pressure Versus Time, 16.7 mph Post-Test Model (Upper-Ductility Materials) Without Perlite

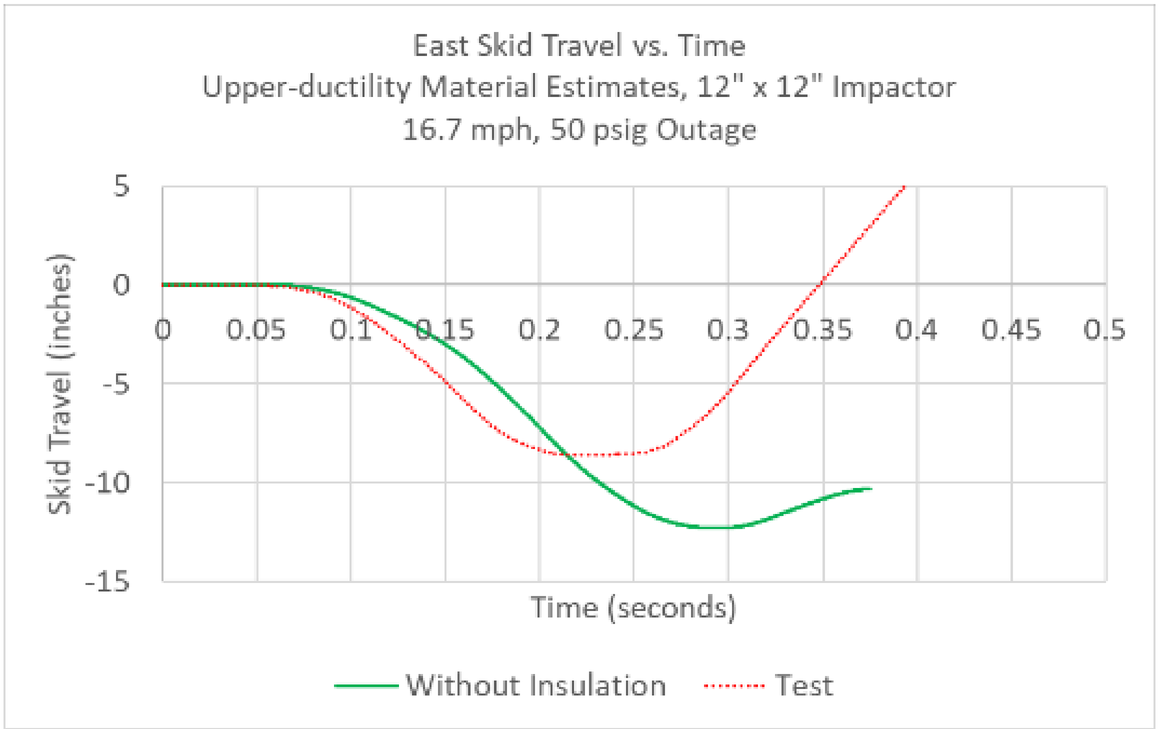

Figure C69. East Skid Travel Versus Time, 16.7 mph Post-Test Model (Upper-Ductility Materials) Without Perlite

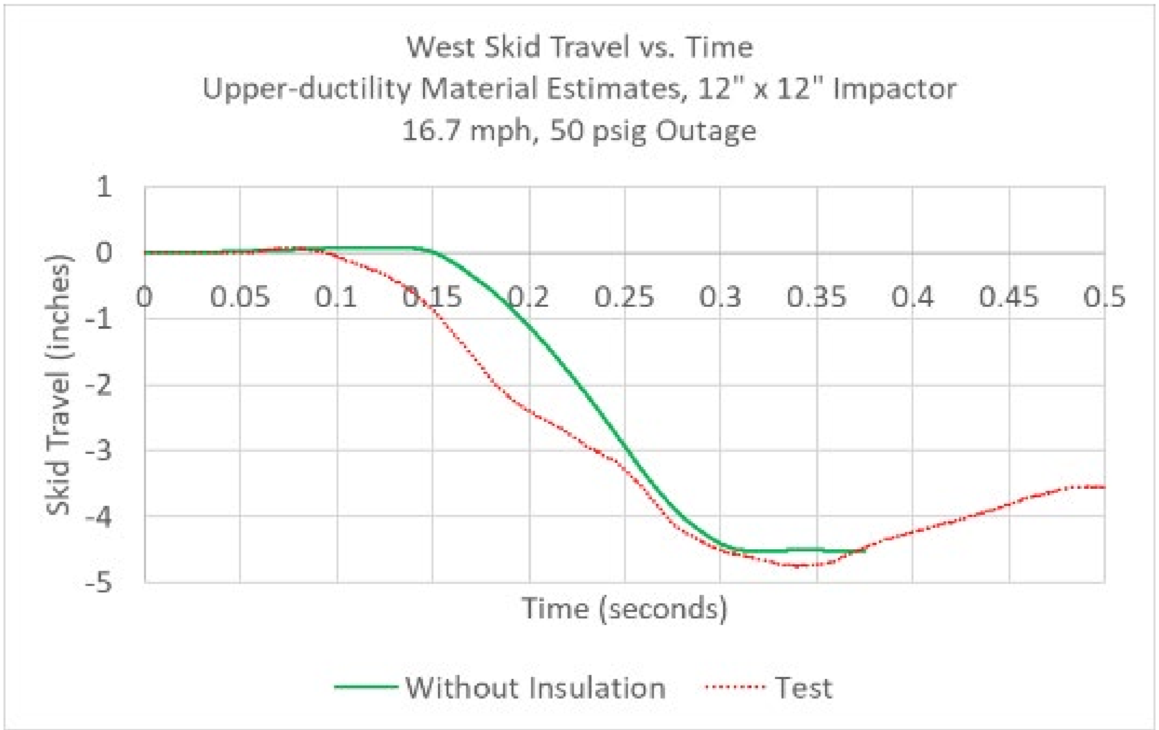

Figure C70. West Skid Travel Versus Time, 16.7 mph Post-Test Model (Upper-Ductility Materials) Without Perlite

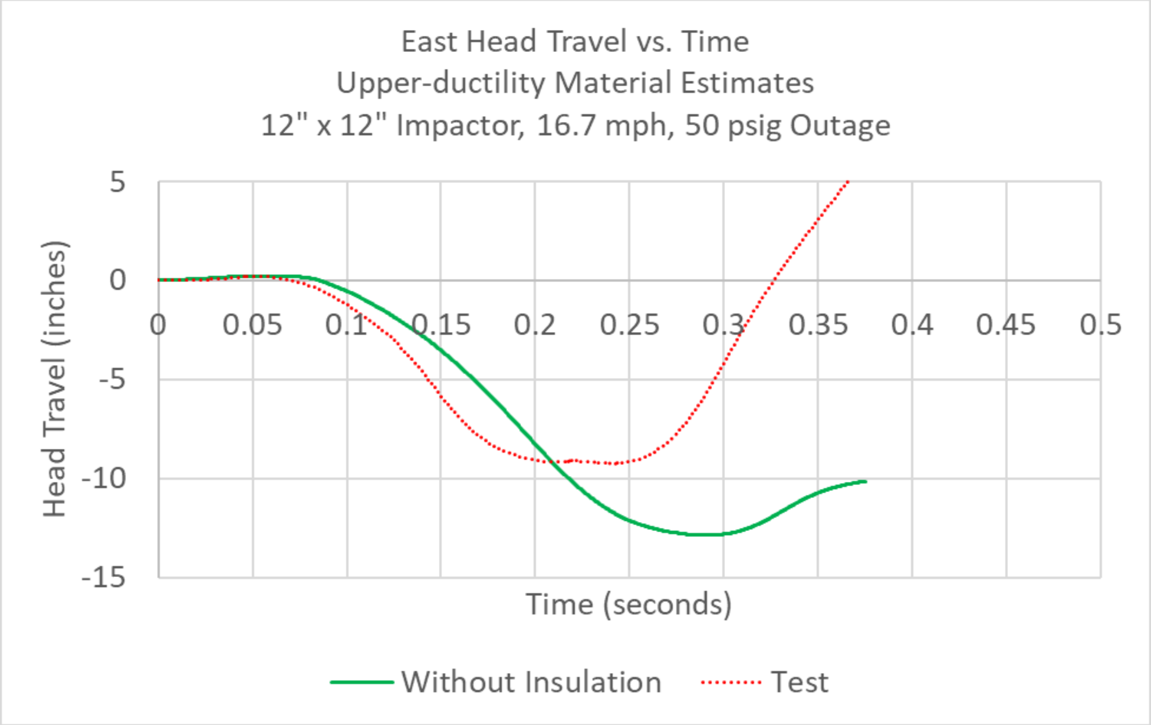

Figure C71. East Head Travel Versus Time, 16.7 mph Post-Test Model (Upper-Ductility Materials) Without Perlite

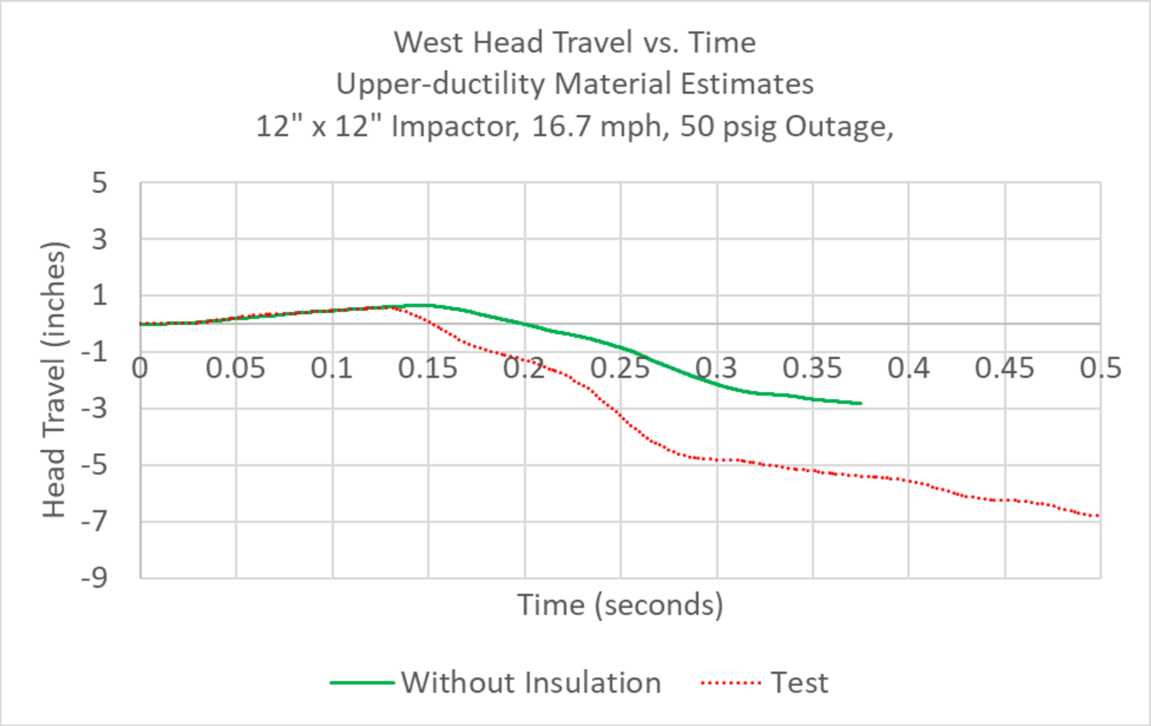

Figure C72. West Head Travel Versus Time, 16.7 mph Post-Test Model (Upper-Ductility Materials) without Perlite

Section 2.4. 16.7 mph, Upper-Ductility Steels, "Sandy Soil" Perlite

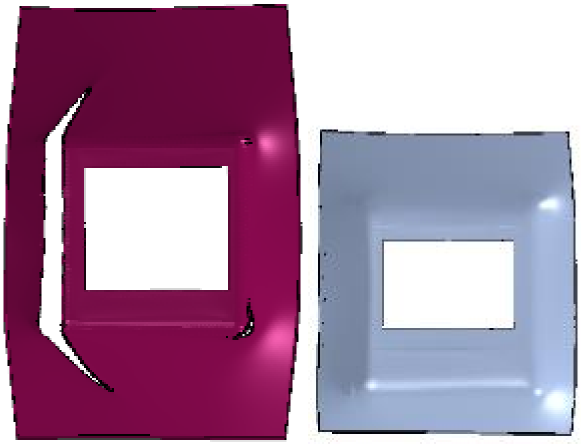

Figure C73. Solid Patch in Outer (left) and Inner (right) Tanks, 16.7 mph Post-Test Model (Upper-Ductility Materials) with Perlite at 400 ms

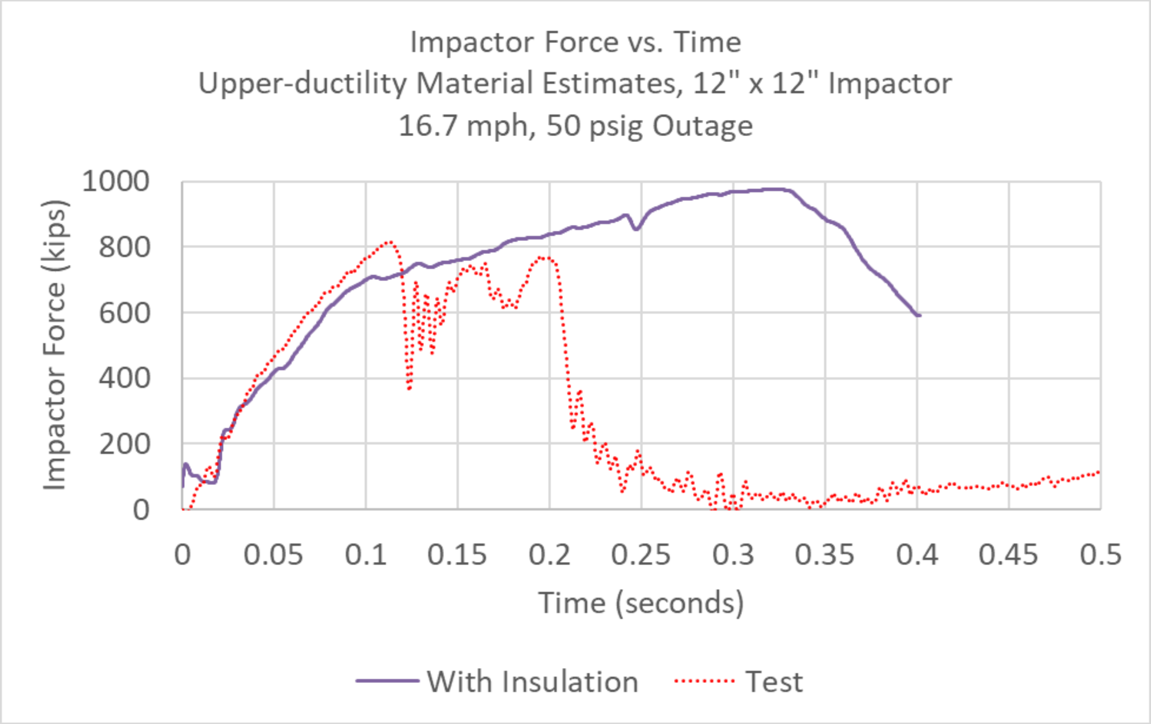

Figure C74. Impactor Force Versus Time, 16.7 mph Post-Test Model (Upper-Ductility Materials) with Perlite

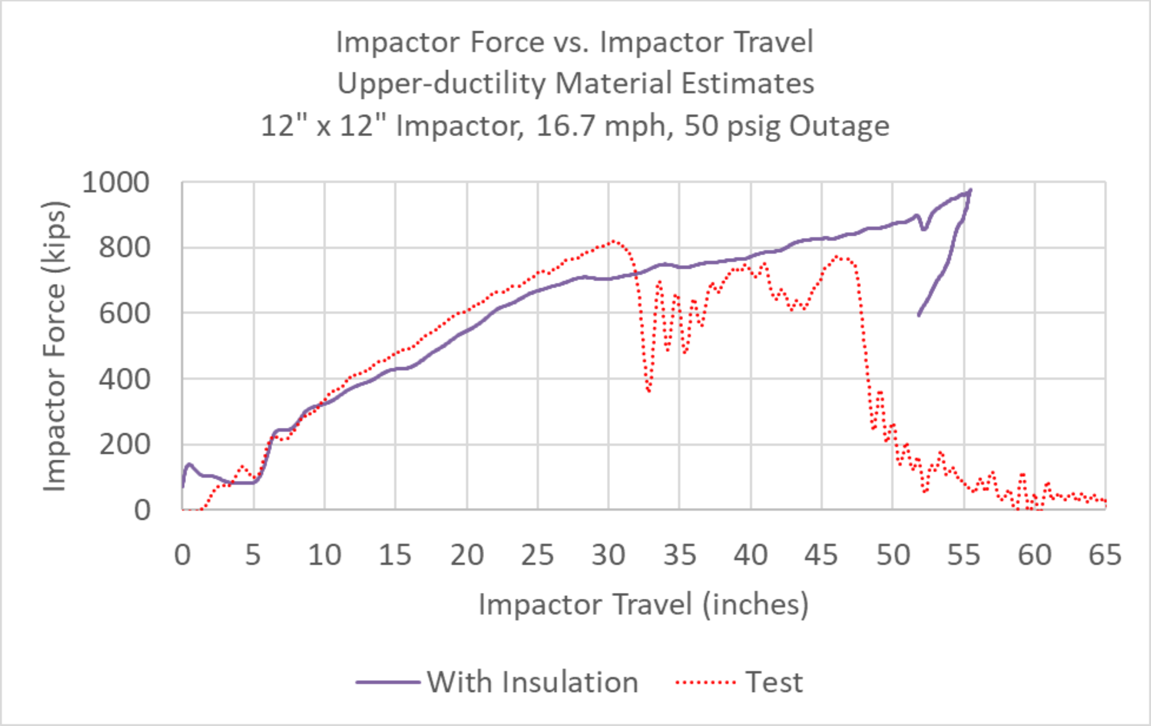

Figure C75. Impactor Force Versus Travel, 16.7 mph Post-Test Model (Upper-Ductility Materials) with Perlite

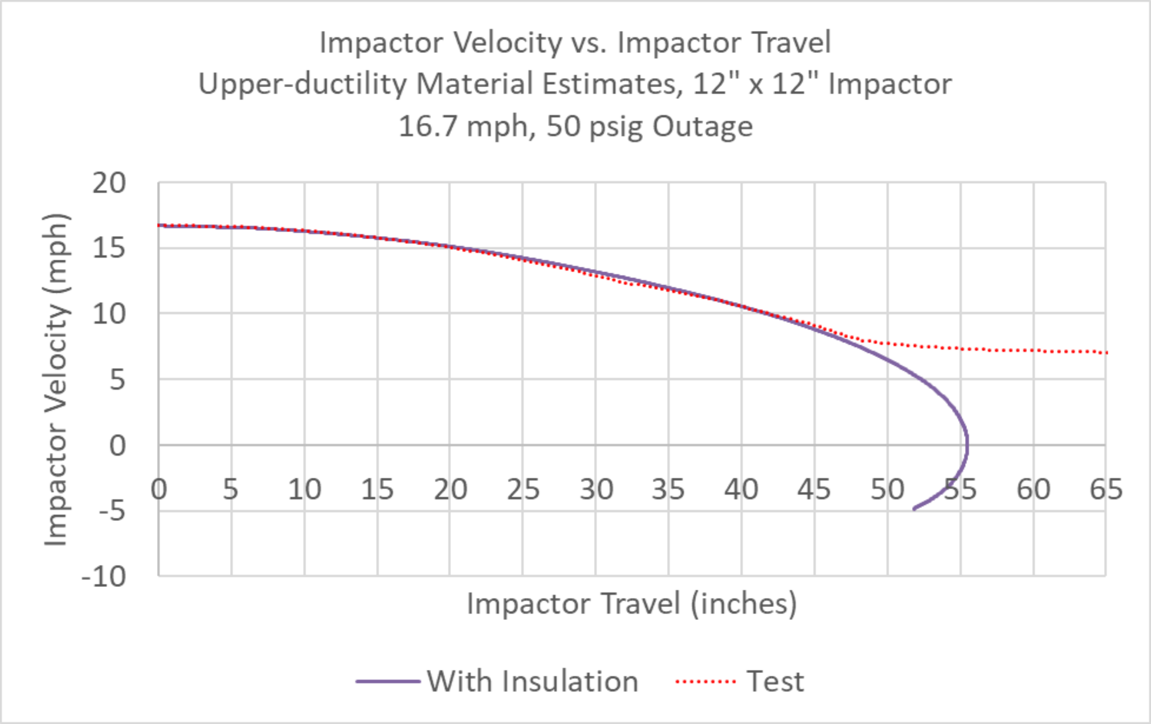

Figure C76. Impactor Velocity Versus Travel, 16.7 mph Post-Test Model (Upper-Ductility Materials) with Perlite

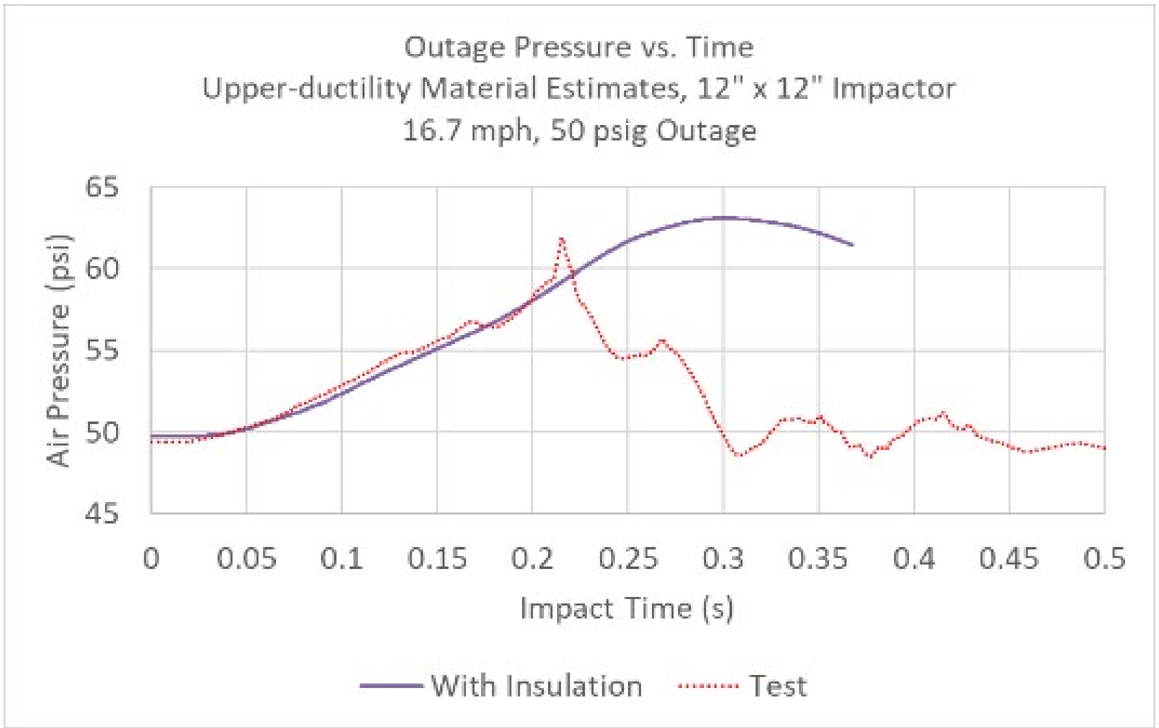

Figure C77. Outage Pressure Versus Time, 16.7 mph Post-Test Model (Upper-Ductility Materials) with Perlite

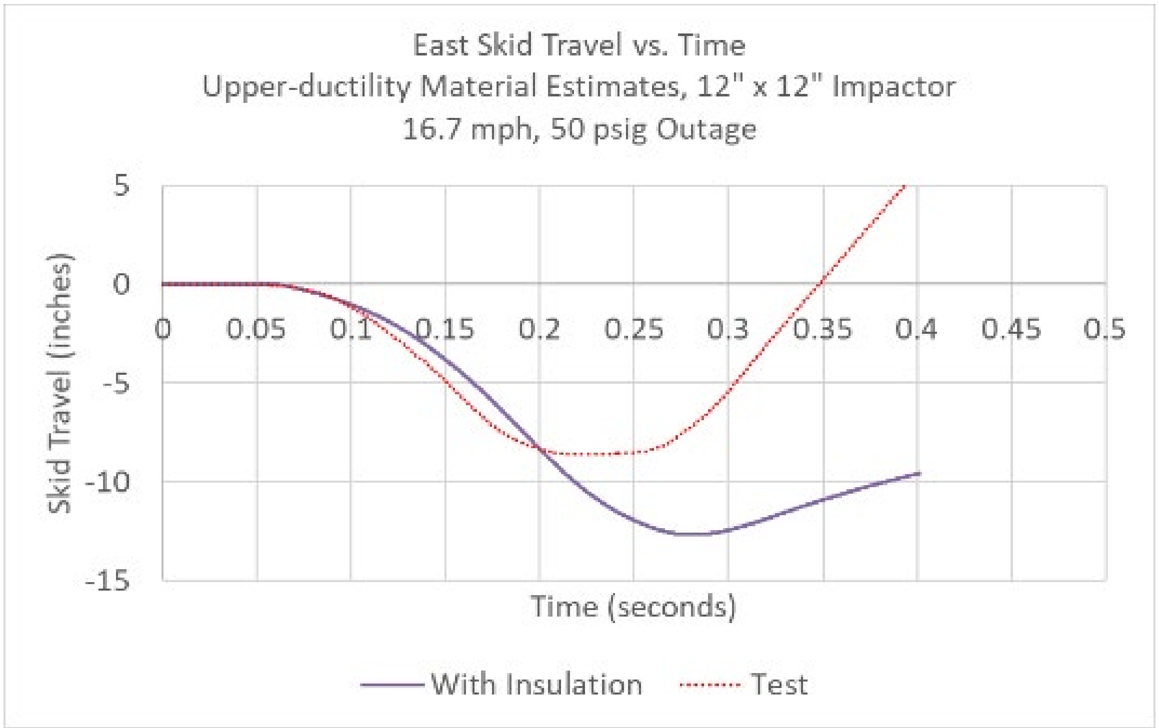

Figure C78. East Skid Travel Versus Time, 16.7 mph Post-Test Model (Upper-Ductility Materials) with Perlite

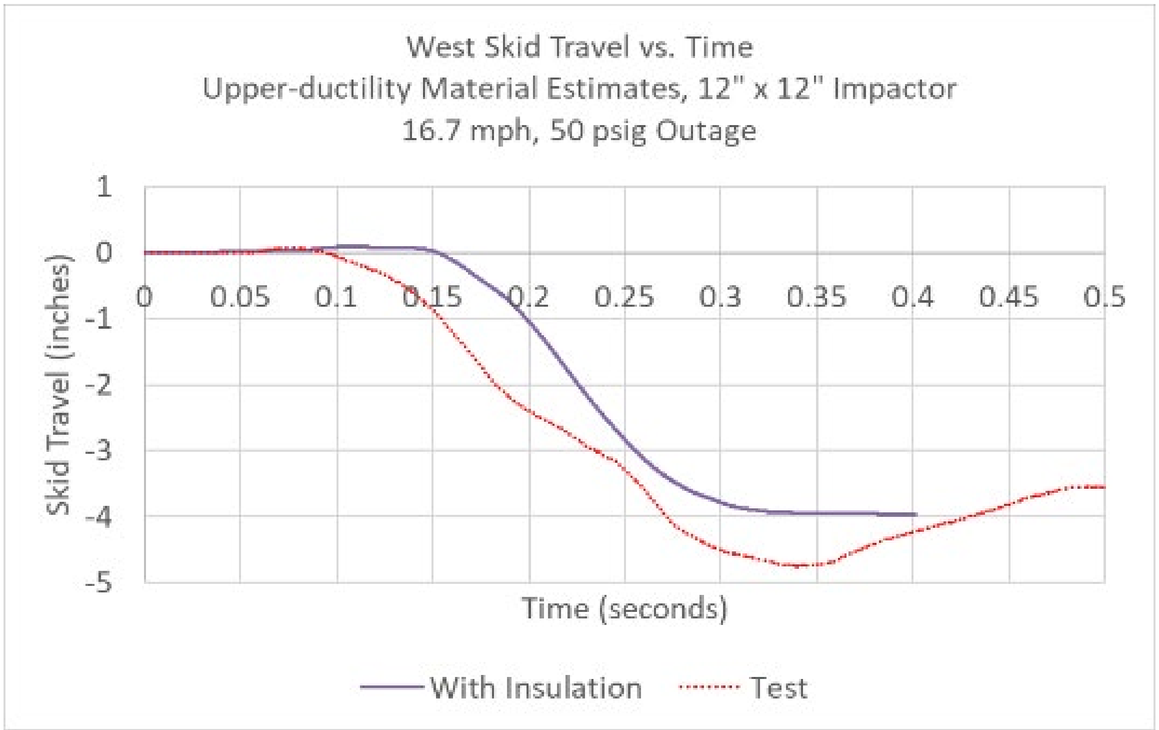

Figure C79. West Skid Travel Versus Time, 16.7 mph Post-Test Model (Upper-Ductility Materials) with Perlite

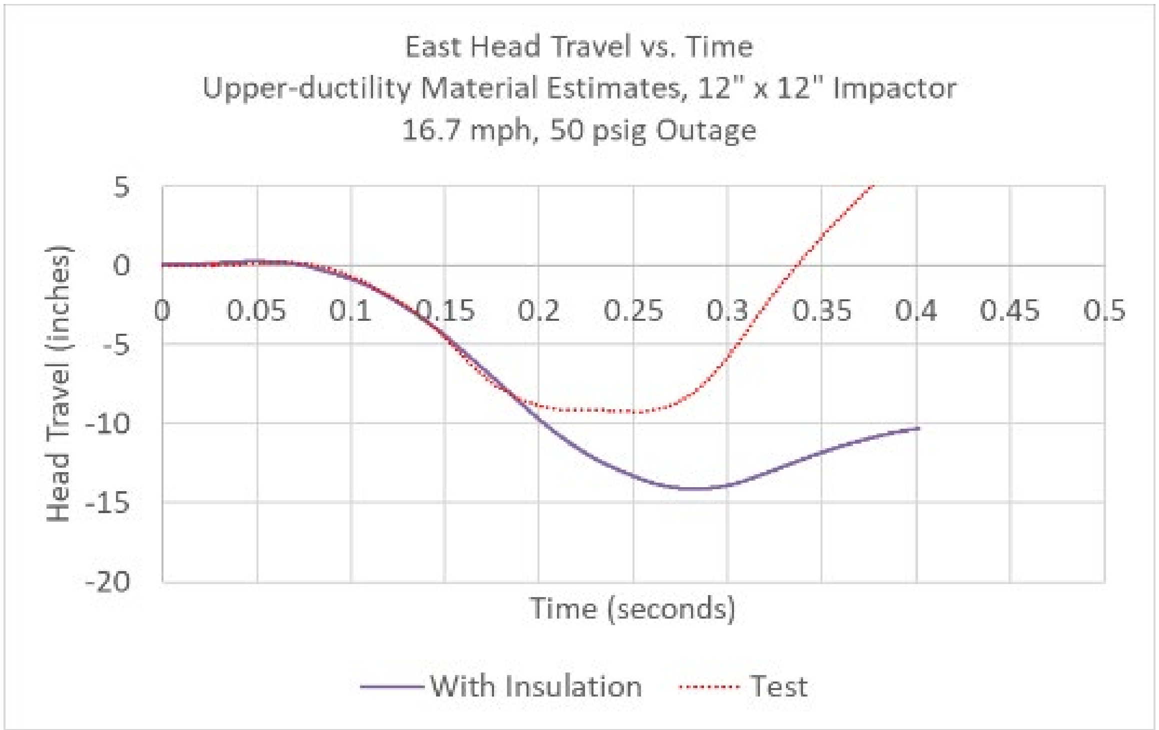

Figure C80. East Head Travel Versus Time, 16.7 mph Post-Test Model (Upper-Ductility Materials) with Perlite

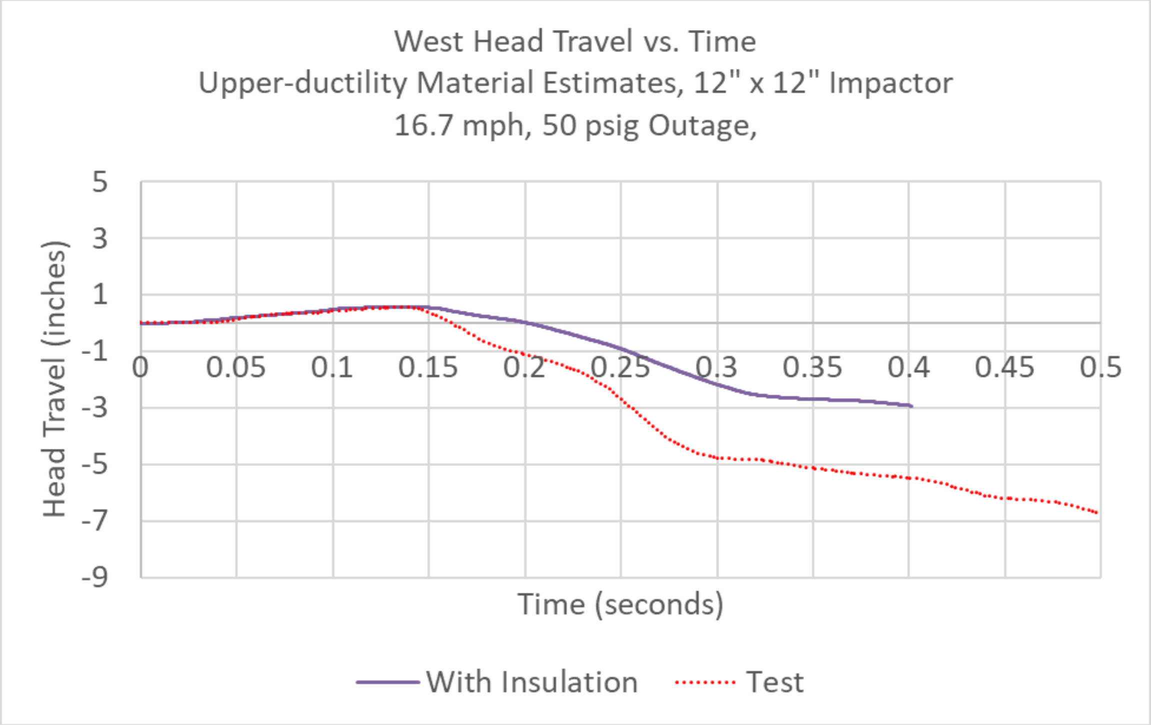

Figure C81. West Head Travel Versus Time, 16.7 mph Post-Test Model (Upper-Ductility Materials) with Perlite

Section 3. Post-Test Puncture FEA and Test Results, Post-Test Actual Material Properties

After the test, the pre-test FE models were updated to better reflect the test conditions. Post-test modeling updates were made in two stages. The first set of post-test model results are plotted alongside the test data in Section 2 of this appendix. Once material coupon data were available from the testing labs, a second set of post-test FE models were run using the actual material properties and thicknesses as measured by the testing lab. This appendix describes the second set of post-test FE results.

To understand the effects of including the perlite, all the post-test models were run with and without the perlite included, as summarized in Table C3. When the post-test model using actual steel properties and the "sandy soil" approach to modeling perlite continued to show discrepancies with the test measurements, a more in-depth material model was developed for perlite, using a crushable foam material modeling approach.

Table C3. Summary of Post-Test FE Models Using Actual Material Properties

Simulated Impact Speed (mph)	Perlite	Tank Steels	Outer Tank State	Inner Tank State	Reason for Termination
16.7	"Sandy Soil" Perlite	Actual	Puncture	No elements lost. Maximum DUCTCRT 0.99	Impactor rebounding
16.7	None	Actual	Puncture	No elements lost. Maximum DUCTCRT 0.70	Impactor rebounding
16.7	"Crushable Foam" Perlite	Actual	Puncture	Puncture	Inner tank punctured
16.7	"Crushable Foam" Perlite	Actual, 0.1/s T304 Properties	Puncture	Puncture	Inner tank punctured

Section 3.1. 16.7 mph, Actual Steels, No Perlite

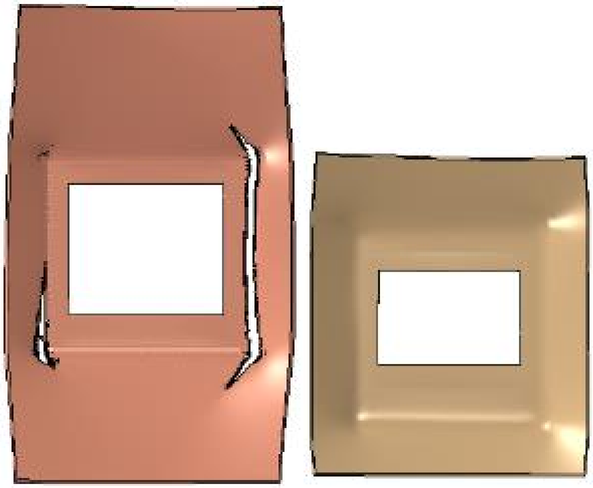

Figure C82. Solid Patch in Outer (left) and Inner (right) Tanks, 16.7 mph Post-Test Model (Actual Materials) without Perlite at 400 ms

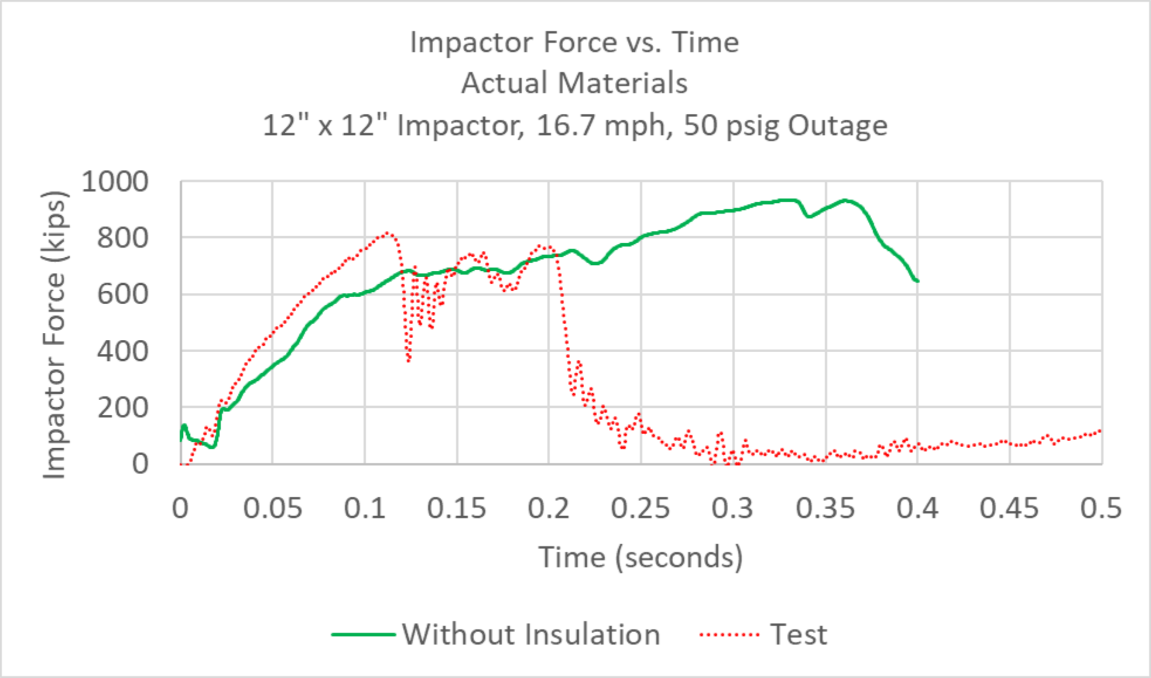

Figure C83. Impactor Force Versus Time, 16.7 mph Post-Test Model (Actual Materials) Without Perlite

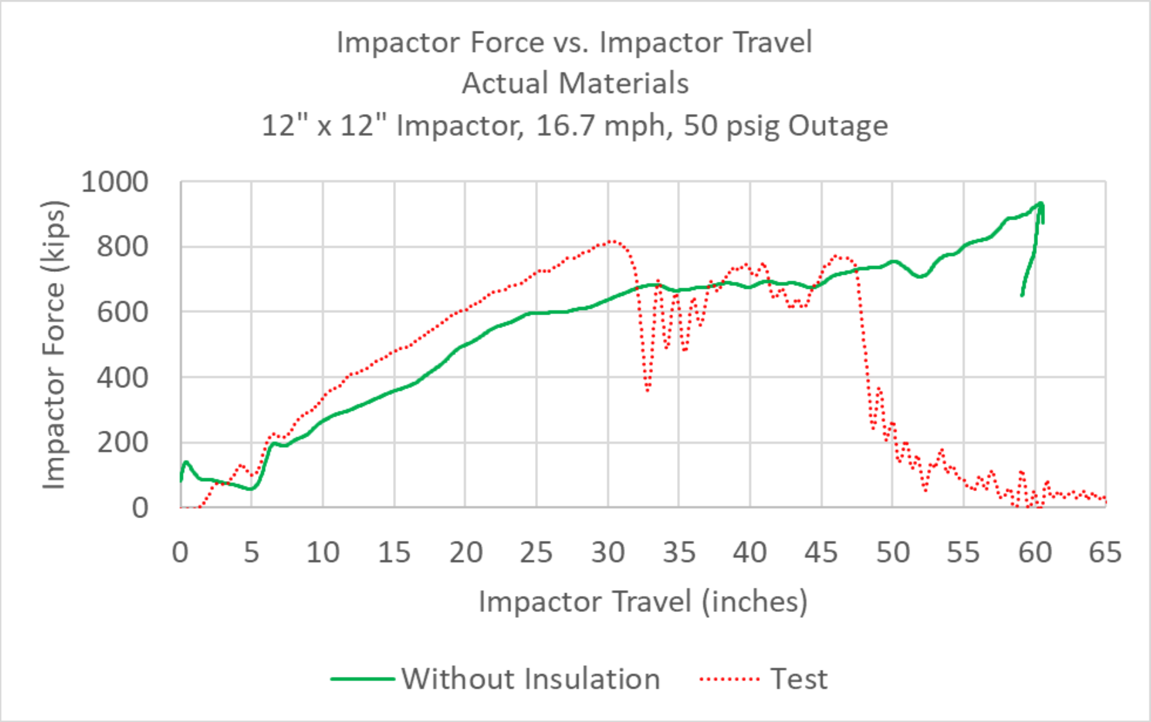

Figure C84. Impactor Force Versus Travel, 16.7 mph Post-Test Model (Actual Materials) Without Perlite

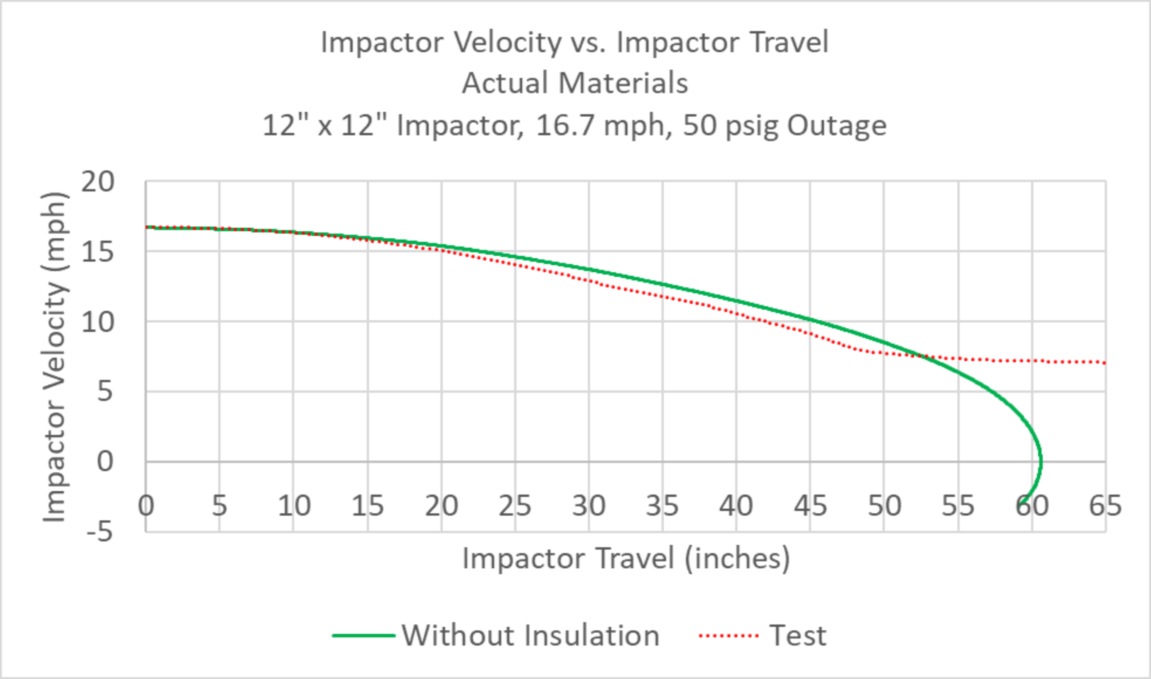

Figure C85. Impactor Velocity Versus Travel, 16.7 mph Post-Test Model (Actual Materials) Without Perlite

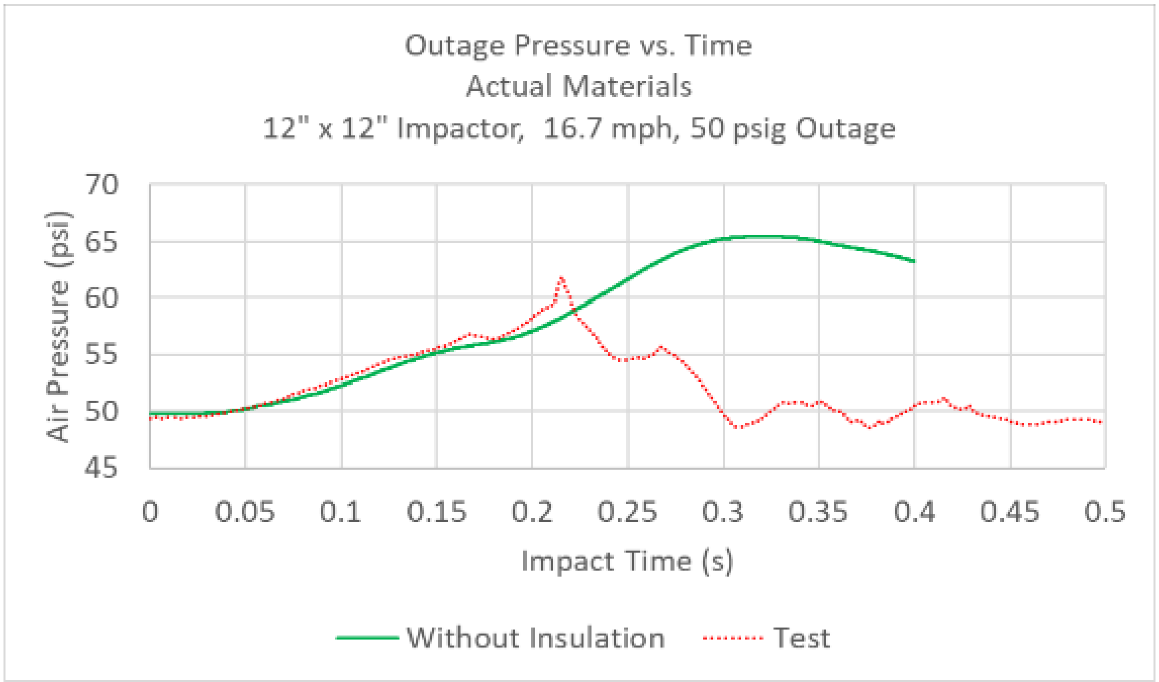

Figure C86. Outage Pressure Versus Time, 16.7 mph Post-Test Model (Actual Materials) Without Perlite

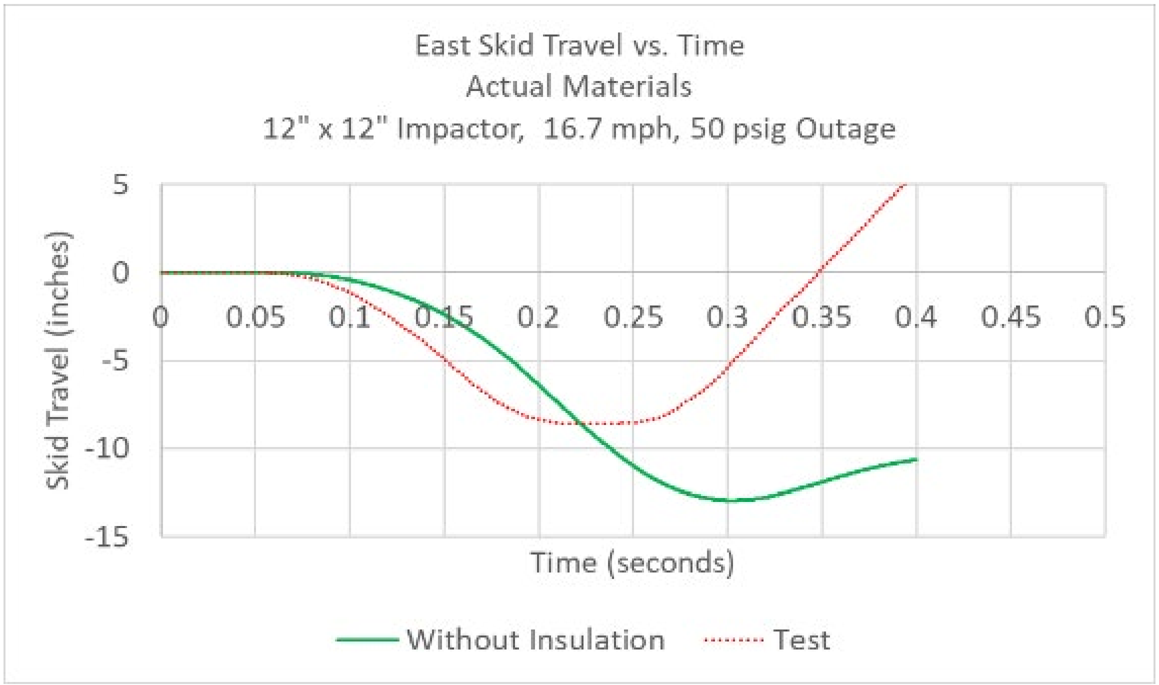

Figure C87. East Skid Travel Versus Time, 16.7 mph Post-Test Model (Actual Materials) Without Perlite

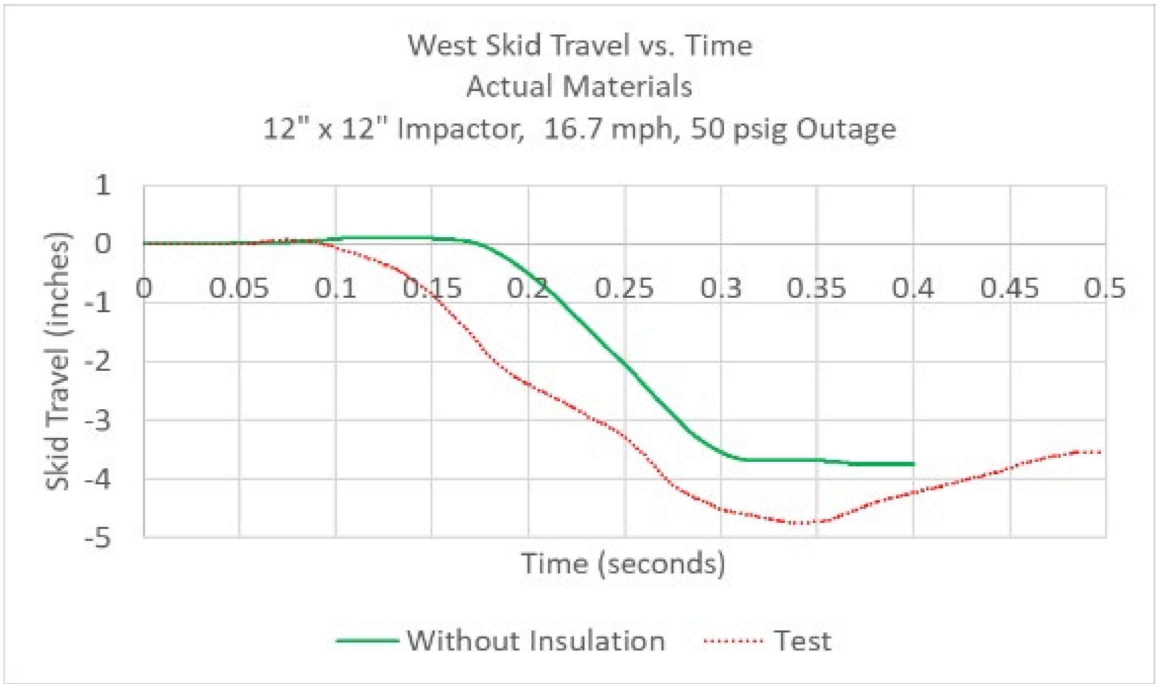

Figure C88. West Skid Travel Versus Time, 16.7 mph Post-Test Model (Actual Materials) Without Perlite

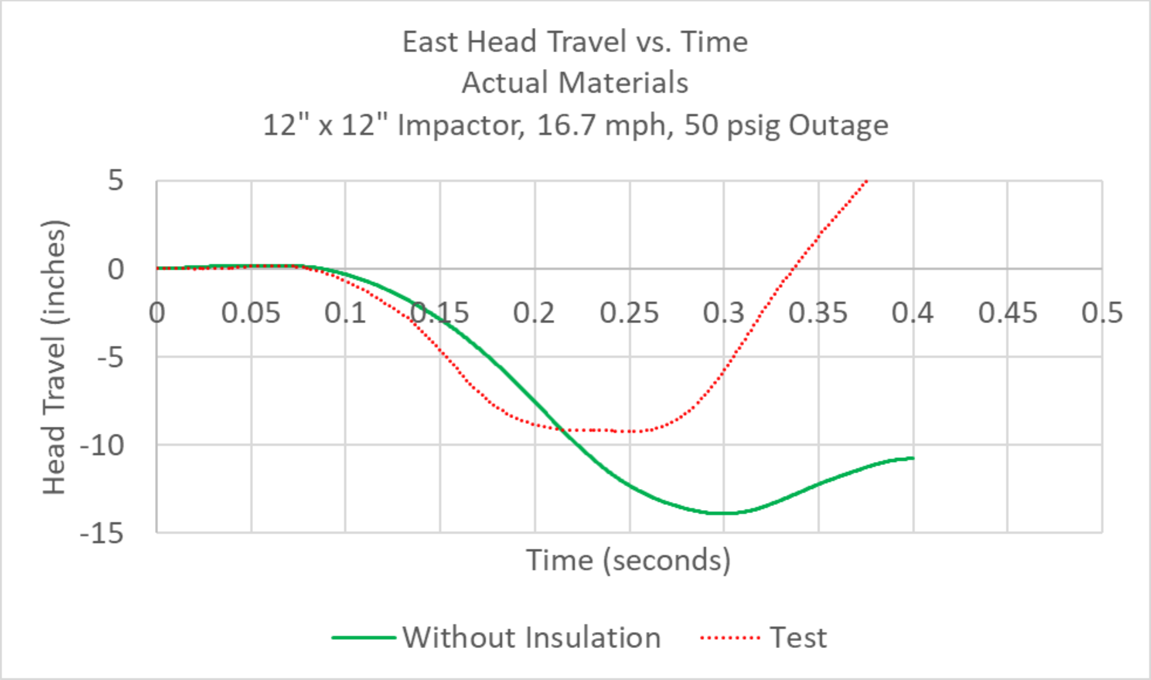

Figure C89. East Head Travel Versus Time, 16.7 mph Post-Test Model (Actual Materials) Without Perlite

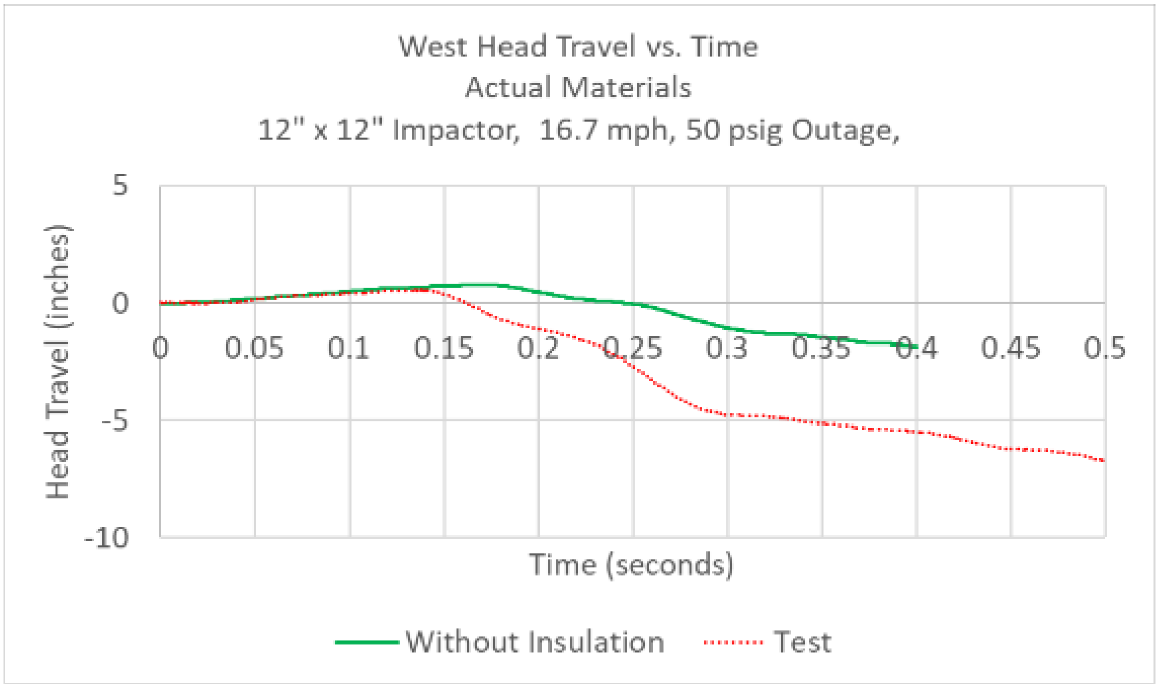

Figure C90. West Head Travel Versus Time, 16.7 mph Post-Test Model (Actual Materials) Without Perlite

Section 3.2. 16.7 mph, Actual Steels, "Sandy Soil" Perlite

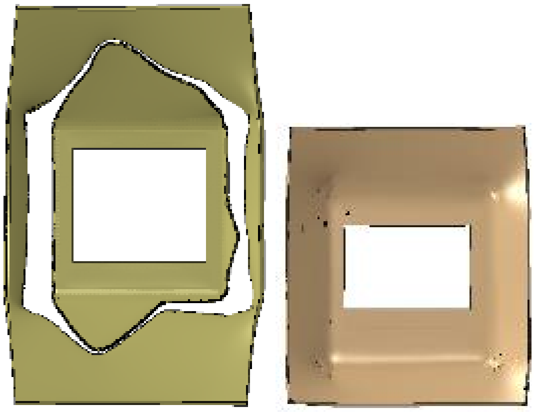

Figure C91. Solid Patch in Outer (left) and Inner (right) Tanks, 16.7 mph Post-Test Model (Actual Materials) with "Sandy Soil" Perlite at 450 ms

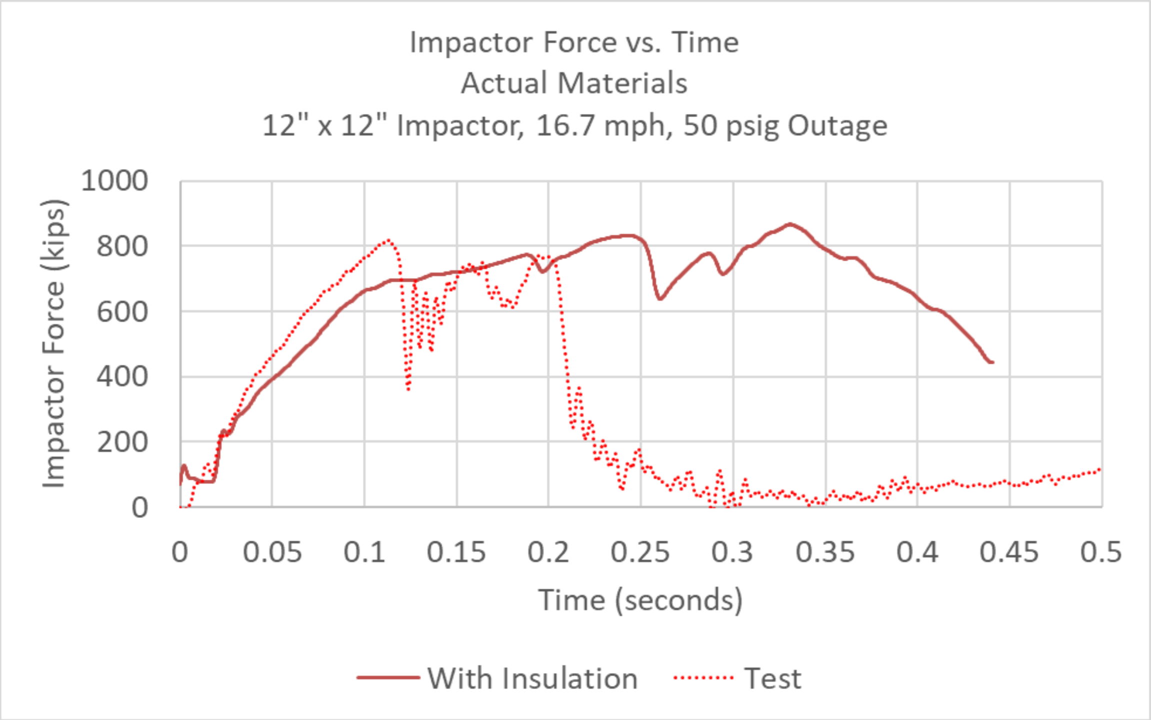

Figure C92. Impactor Force Versus Time, 16.7 mph Post-Test Model (Actual Materials) with "Sandy Soil" Perlite

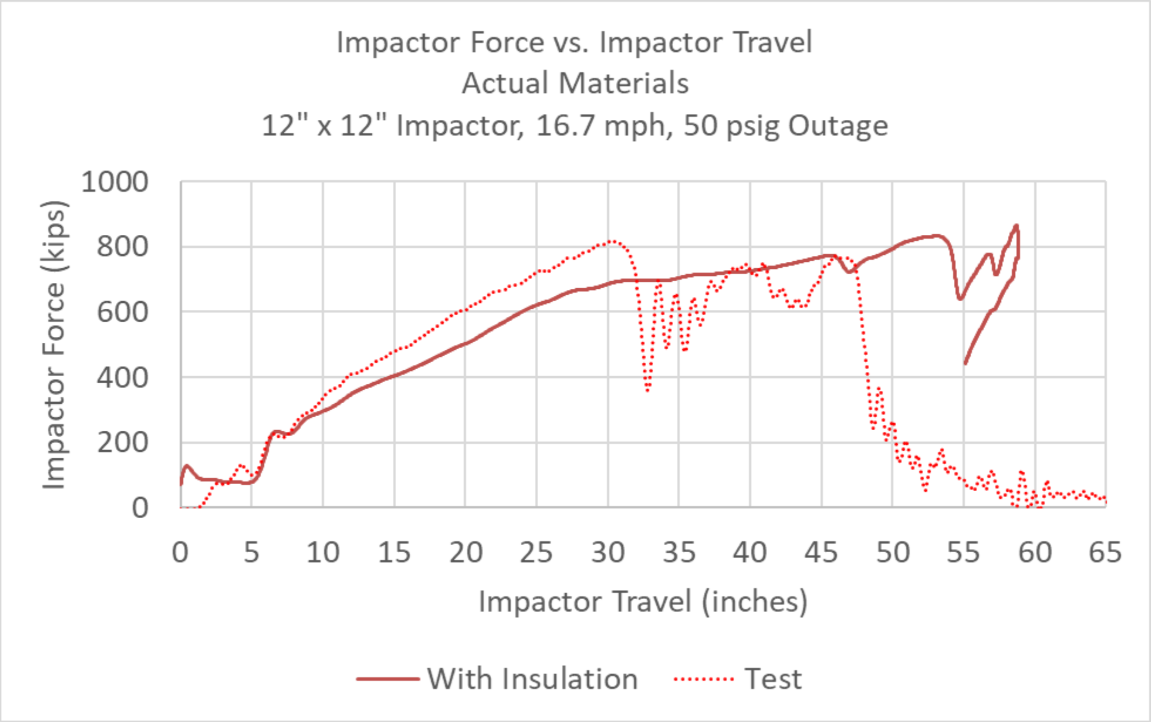

Figure C93. Impactor Force Versus Travel, 16.7 mph Post-Test Model (Actual Materials) with "Sandy Soil" Perlite

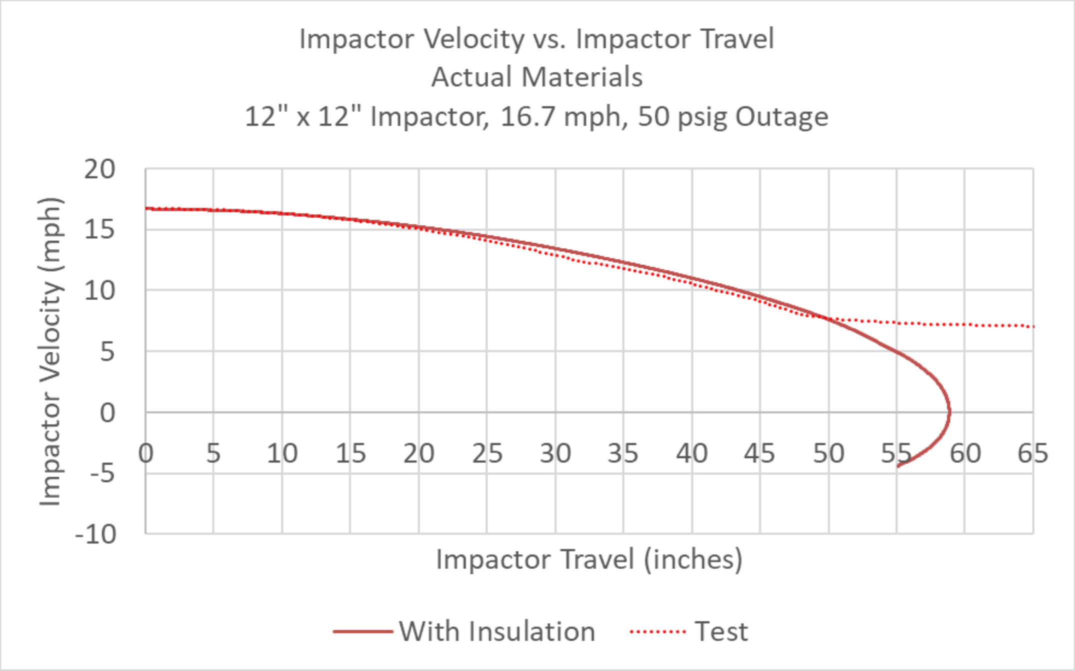

Figure C94. Impactor Velocity Versus Travel, 16.7 mph Post-Test Model (Actual Materials) with "Sandy Soil" Perlite

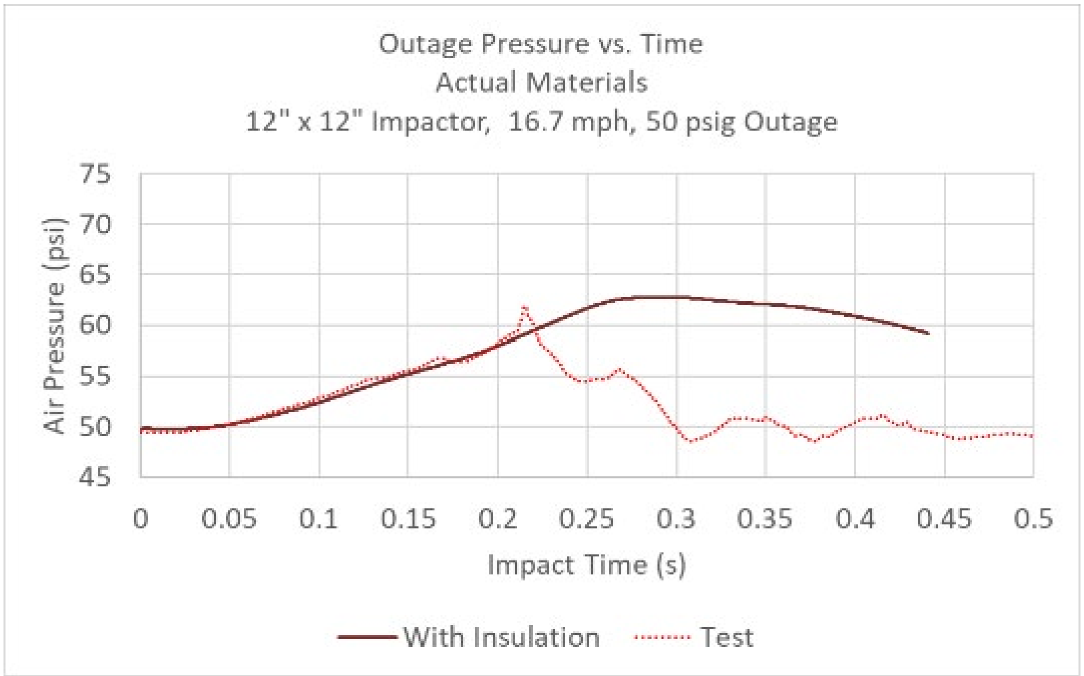

Figure C95. Outage Pressure Versus Time, 16.7 mph Post-Test Model (Actual Materials) with "Sandy Soil" Perlite

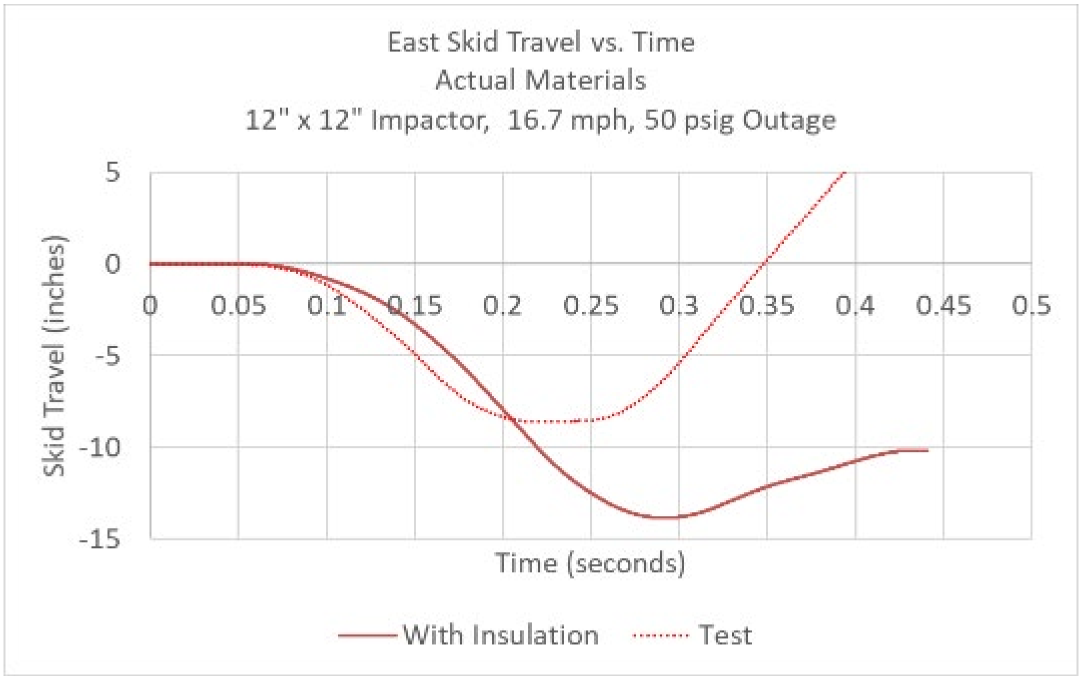

Figure C96. East Skid Travel Versus Time, 16.7 mph Post-Test Model (Actual Materials) with "Sandy Soil" Perlite

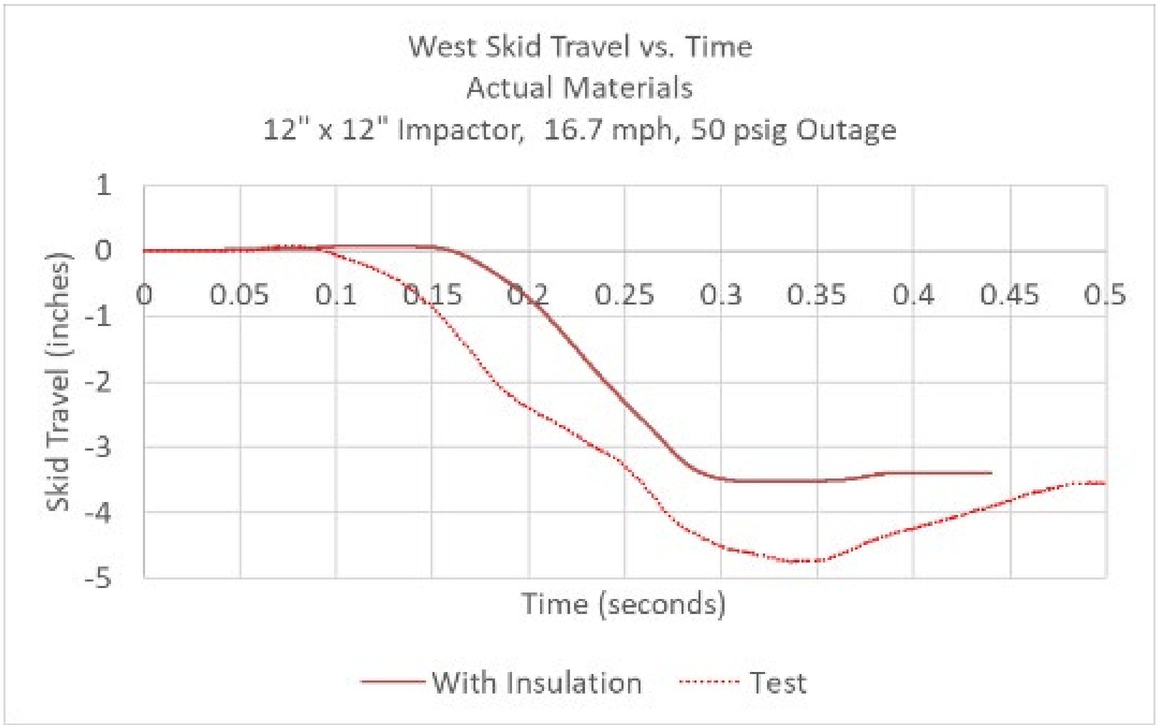

Figure C97. West Skid Travel Versus Time, 16.7 mph Post-Test Model (Actual Materials) with "Sandy Soil" Perlite

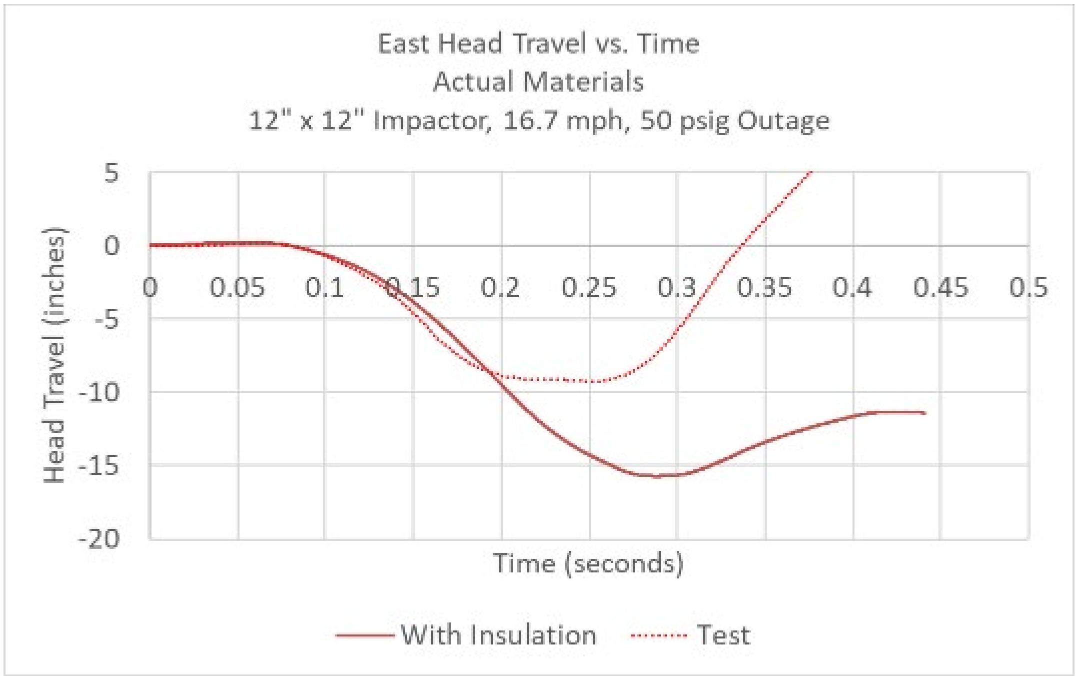

Figure C98. East Head Travel Versus Time, 16.7 mph Post-Test Model (Actual Materials) with "Sandy Soil" Perlite

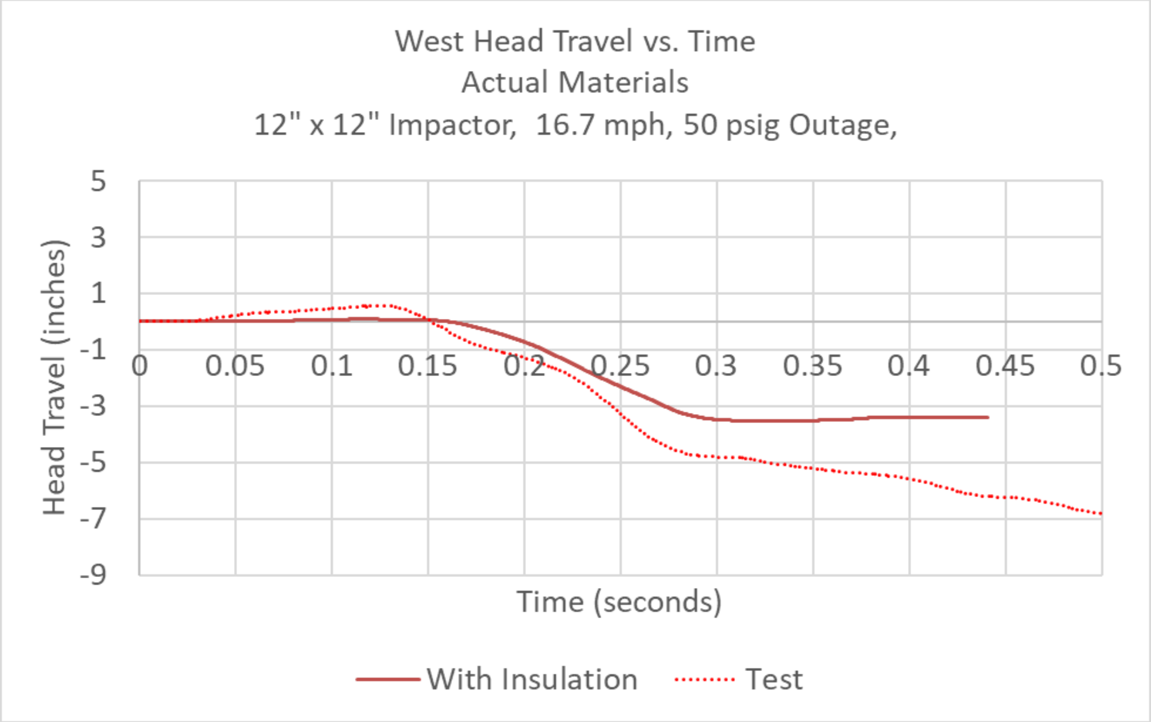

Figure C99. West Head Travel Versus Time, 16.7 mph Post-Test Model (Actual Materials) with "Sandy Soil" Perlite

Section 3.3. 16.7 mph, Actual Steels, “Crushable Foam” Perlite, MMC Damage Initiation for T304

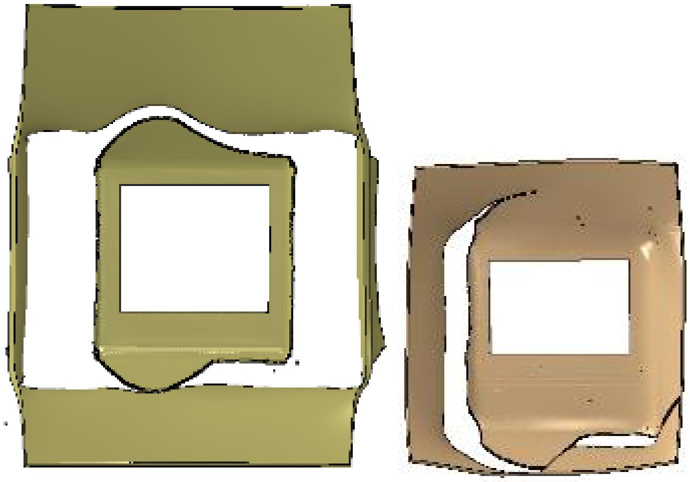

Figure C100. Solid Patch in Outer (left) and Inner (right) Tanks, 16.7 mph Post-Test Model (Actual Materials) with “Crushable Foam” Perlite and MMC Damage Initiation at 300 ms

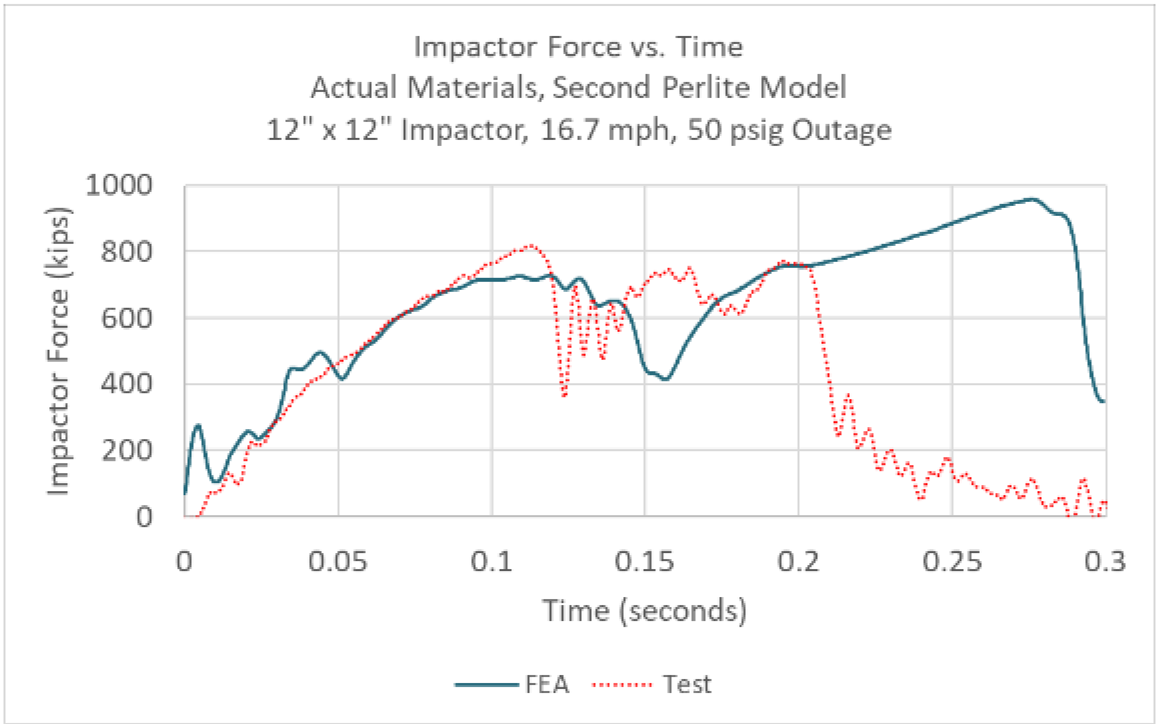

Figure C101. Impactor Force Versus Time, 16.7 mph Post-Test Model (Actual Materials) with “Crushable Foam” Perlite and MMC Damage Initiation

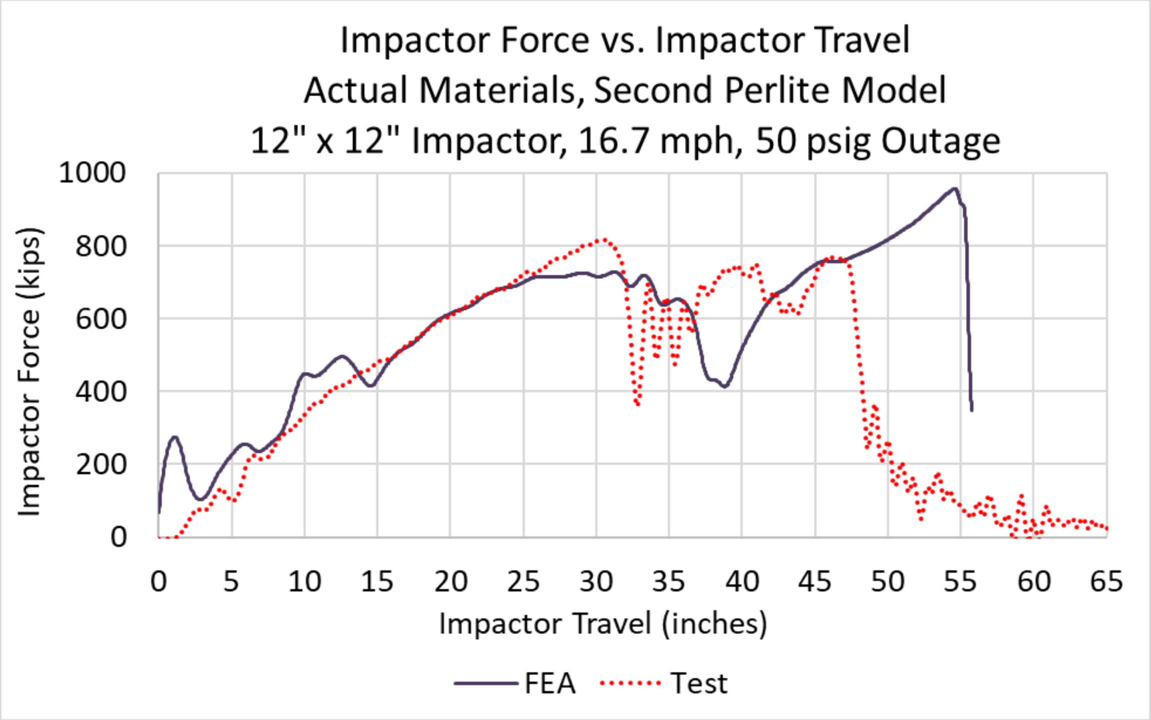

Figure C102. Impactor Force Versus Travel, 16.7 mph Post-Test Model (Actual Materials) with "Crushable Foam" Perlite and MMC Damage Initiation

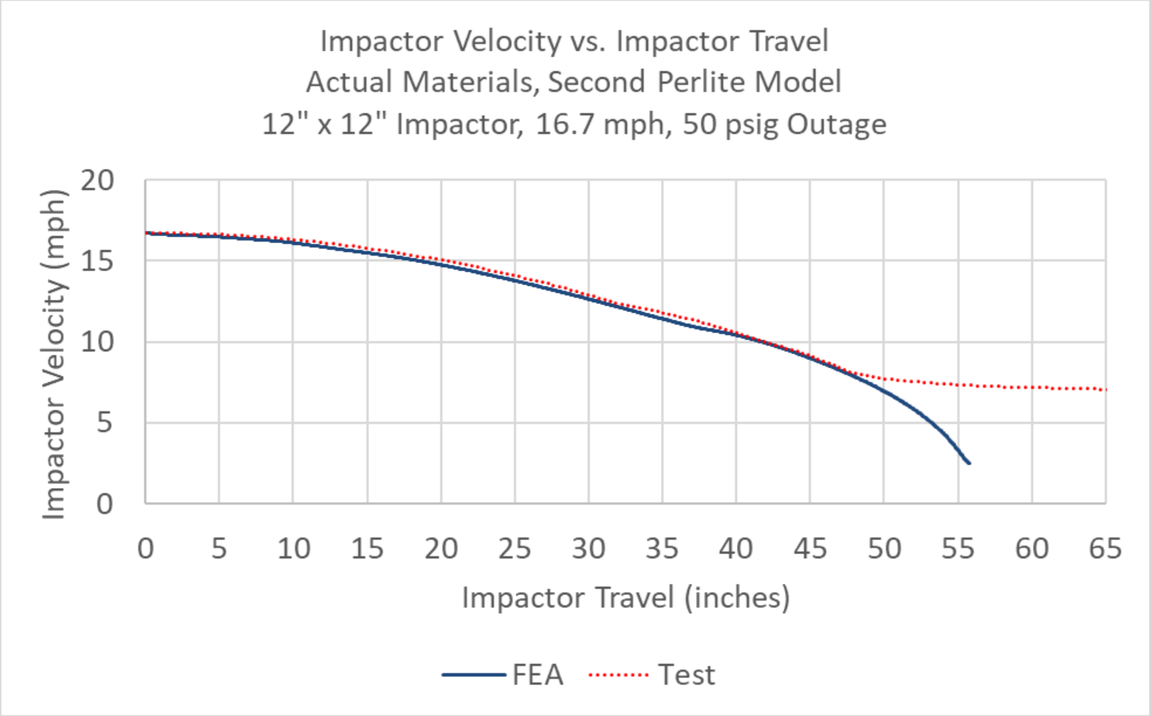

Figure C103. Impactor Velocity Versus Travel, 16.7 mph Post-Test Model (Actual Materials) with "Crushable Foam" Perlite and MMC Damage Initiation

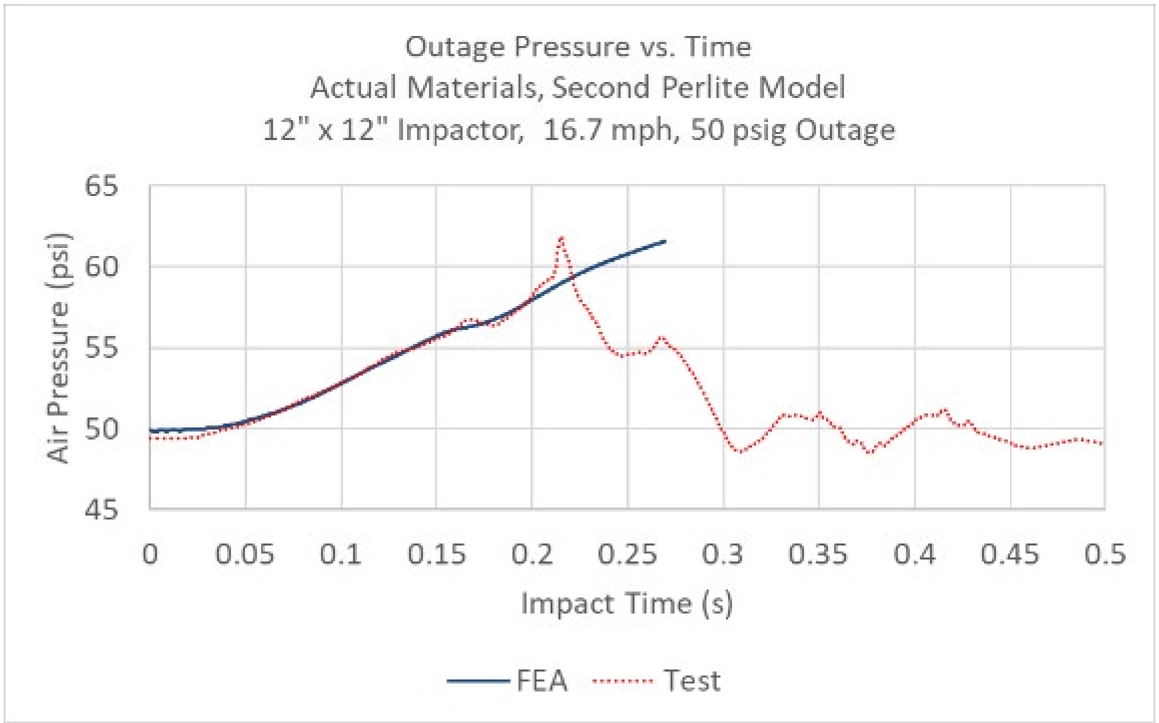

Figure C104. Outage Pressure Versus Time, 16.7 mph Post-Test Model (Actual Materials) with "Crushable Foam" Perlite and MMC Damage Initiation

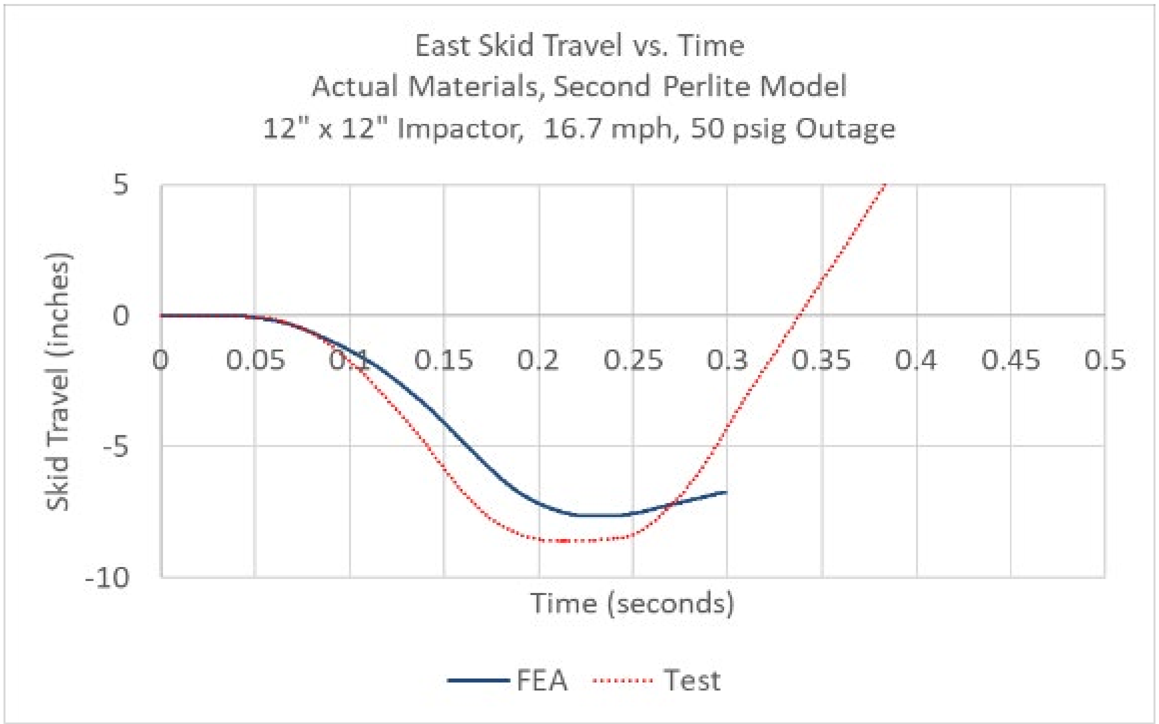

Figure C105. East Skid Travel Versus Time, 16.7 mph Post-Test Model (Actual Materials) with "Crushable Foam" Perlite and MMC Damage Initiation

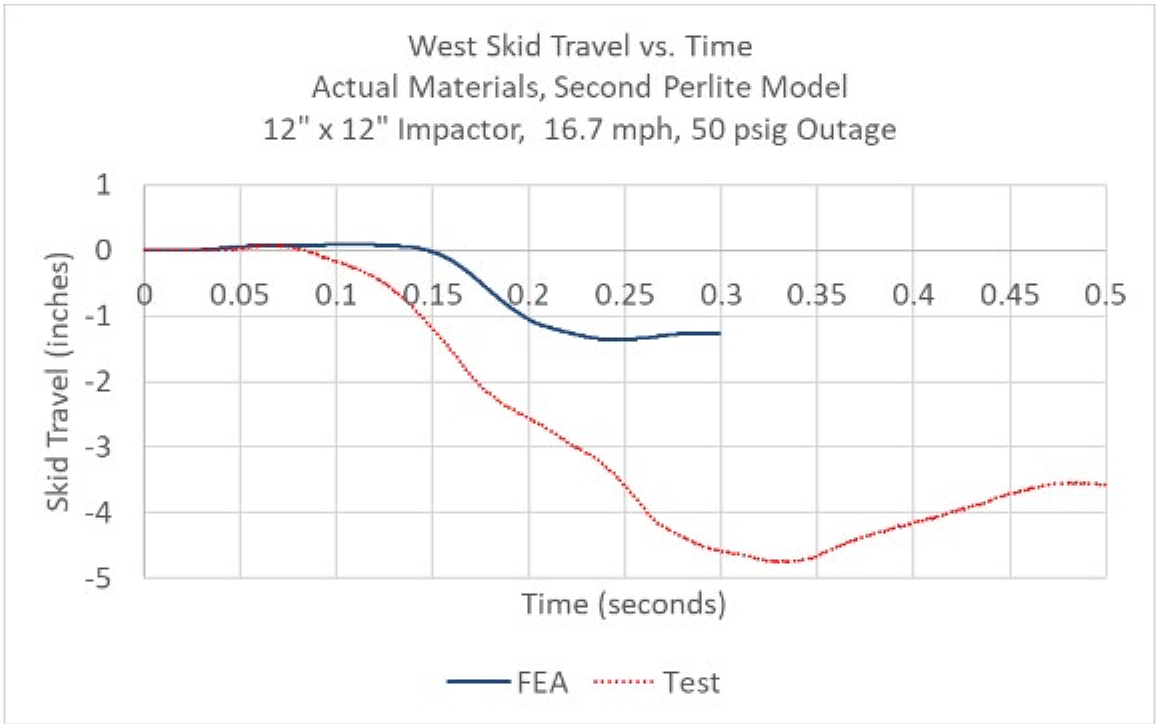

Figure C106. West Skid Travel Versus Time, 16.7 mph Post-Test Model (Actual Materials) with "Crushable Foam" Perlite and MMC Damage Initiation

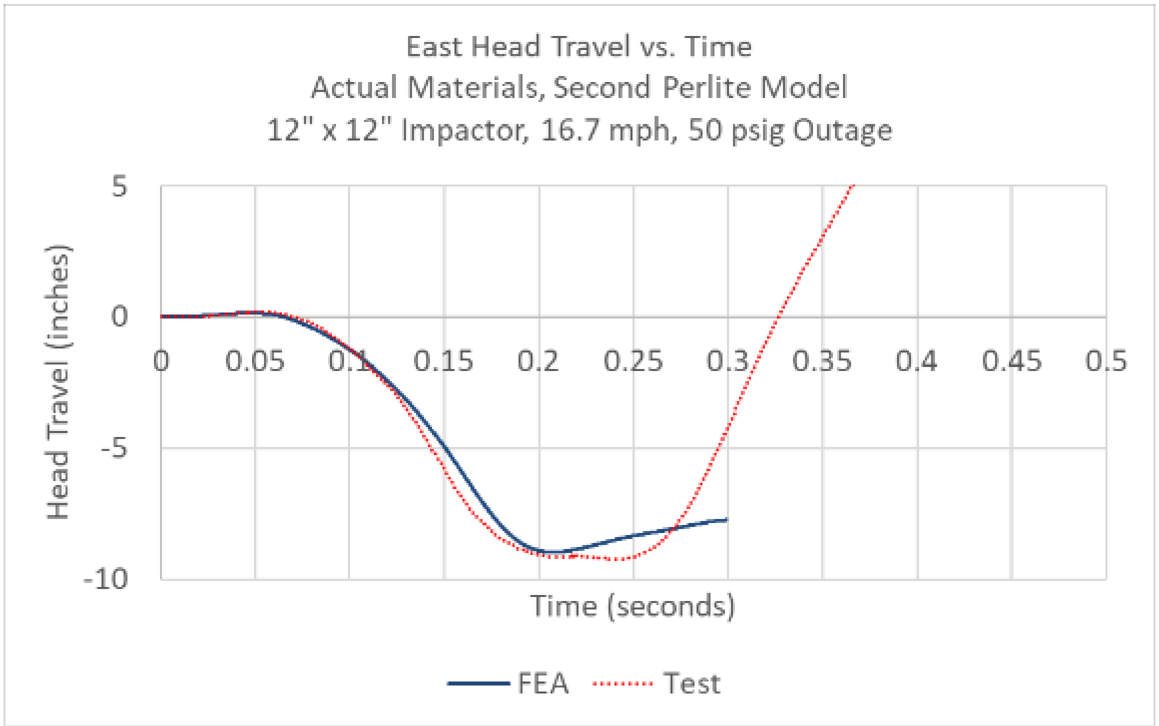

Figure C107. East Head Travel Versus Time, 16.7 mph Post-Test Model (Actual Materials) with "Crushable Foam" Perlite and MMC Damage Initiation

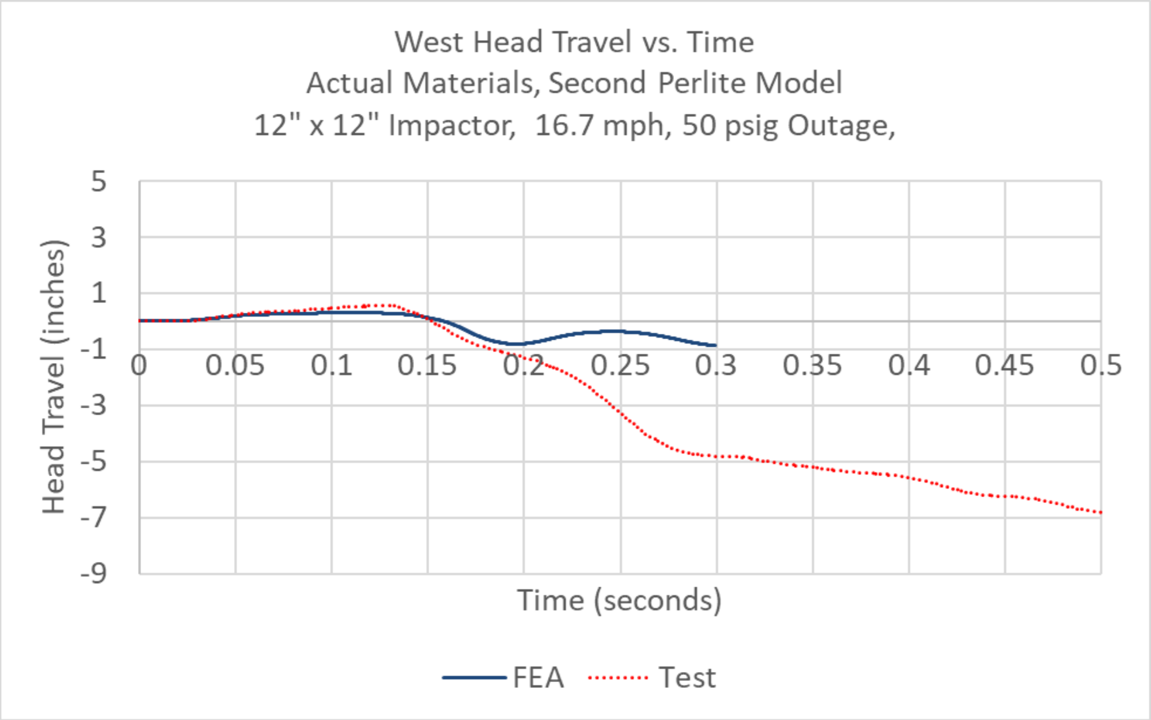

Figure C108. West Head Travel Versus Time, 16.7 mph Post-Test Model (Actual Materials) with "Crushable Foam" Perlite and MMC Damage Initiation

Section 3.4. 16.7 mph, Actual Steels, "Crushable Foam" Perlite, QS B-W Damage Initiation for T304

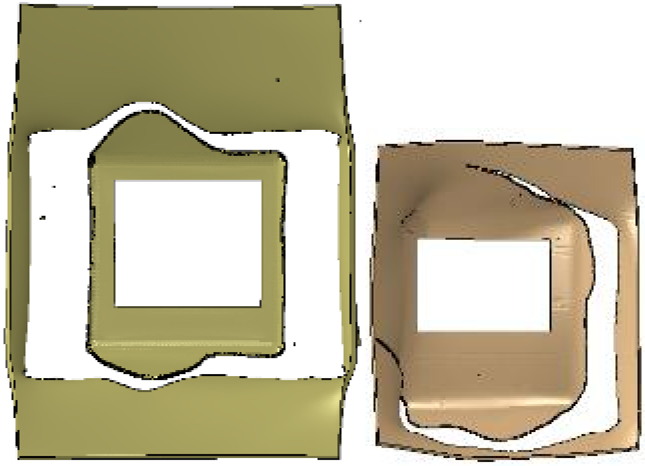

Figure C109. Solid Patch in Outer (left) and Inner (right) Tanks, 16.7 mph Post-Test Model (Actual Materials) with "Crushable Foam" Perlite and QS B-W Damage Initiation at 270 ms

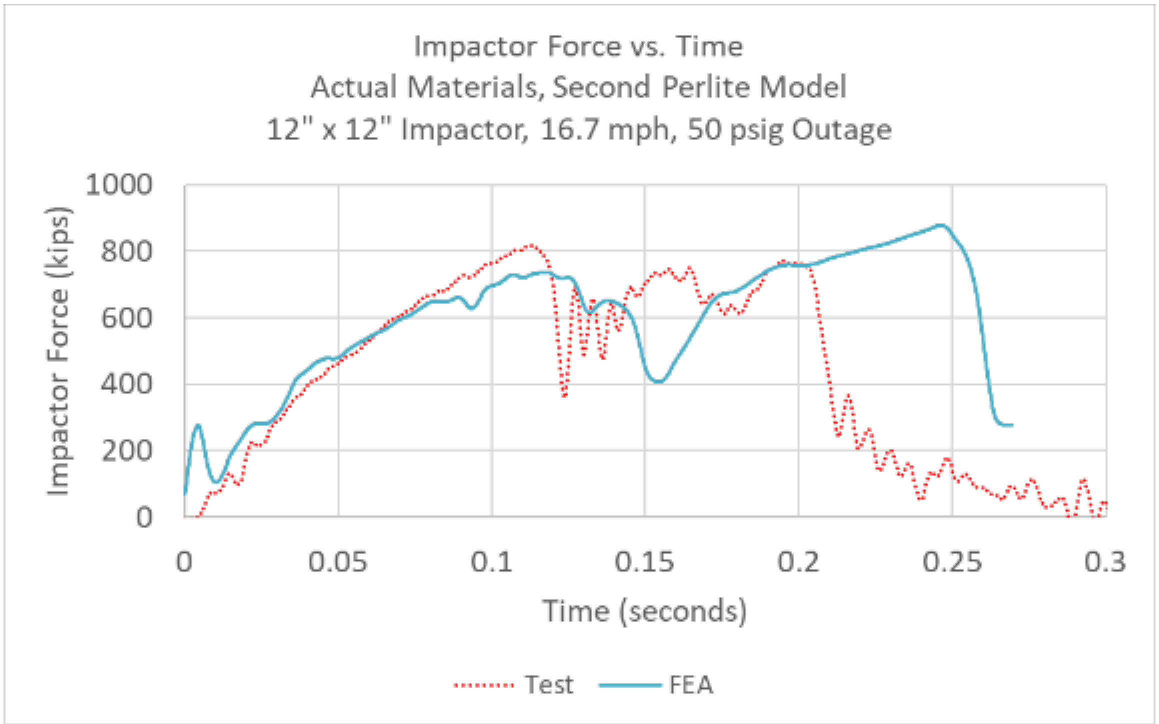

Figure C110. Impactor Force Versus Time, 16.7 mph Post-Test Model (Actual Materials) with "Crushable Foam" Perlite and QS B-W Damage Initiation

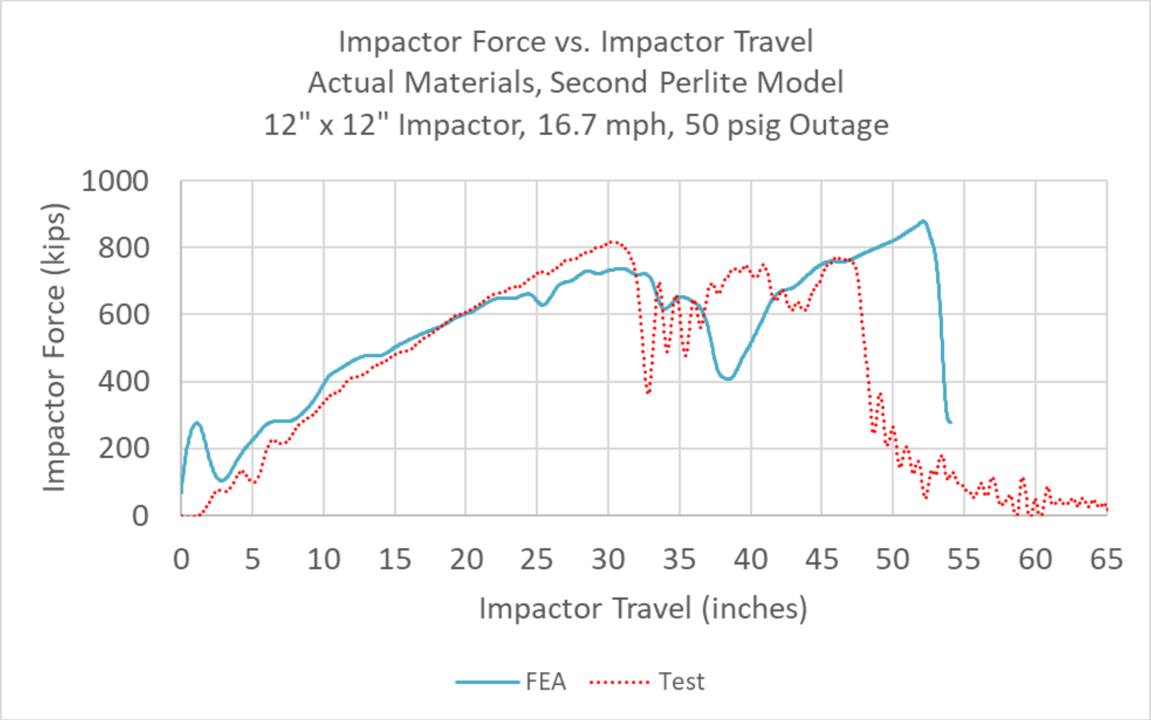

Figure C111. Impactor Force Versus Travel, 16.7 mph Post-Test Model (Actual Materials) with "Crushable Foam" Perlite and QS B-W Damage Initiation

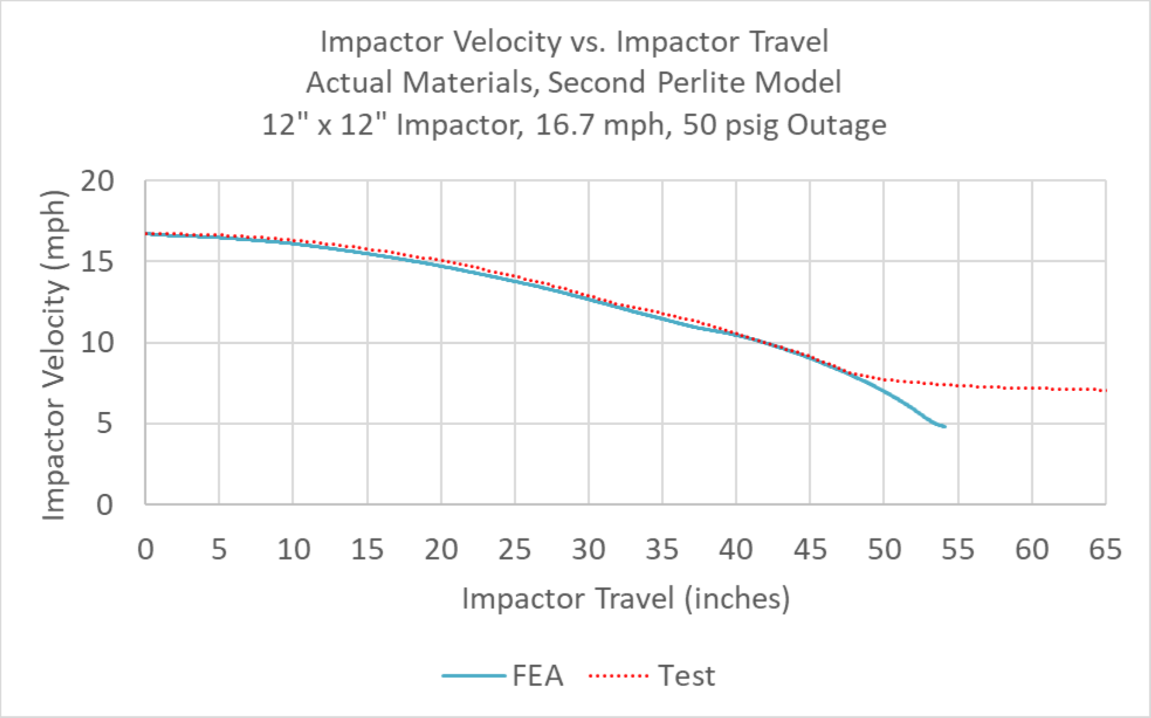

Figure C112. Impactor Velocity Versus Travel, 16.7 mph Post-Test Model (Actual Materials) with "Crushable Foam" Perlite and QS B-W Damage Initiation

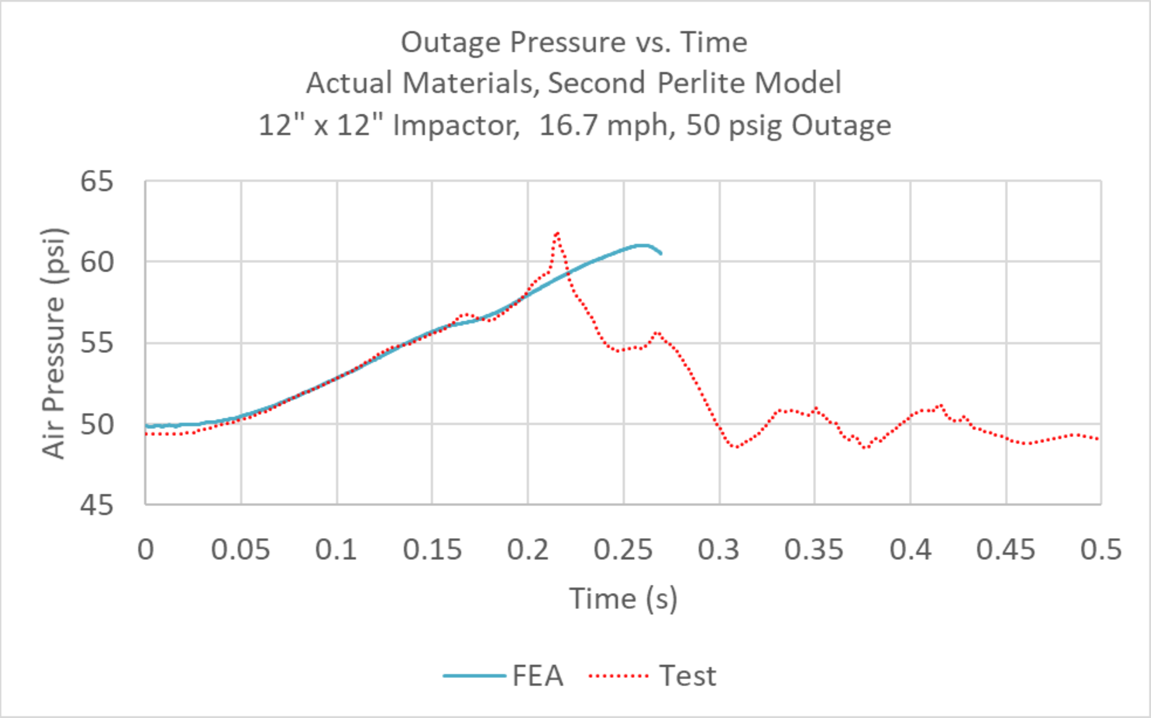

Figure C113. Outage Pressure Versus Time, 16.7 mph Post-Test Model (Actual Materials) with "Crushable Foam" Perlite and QS B-W Damage Initiation

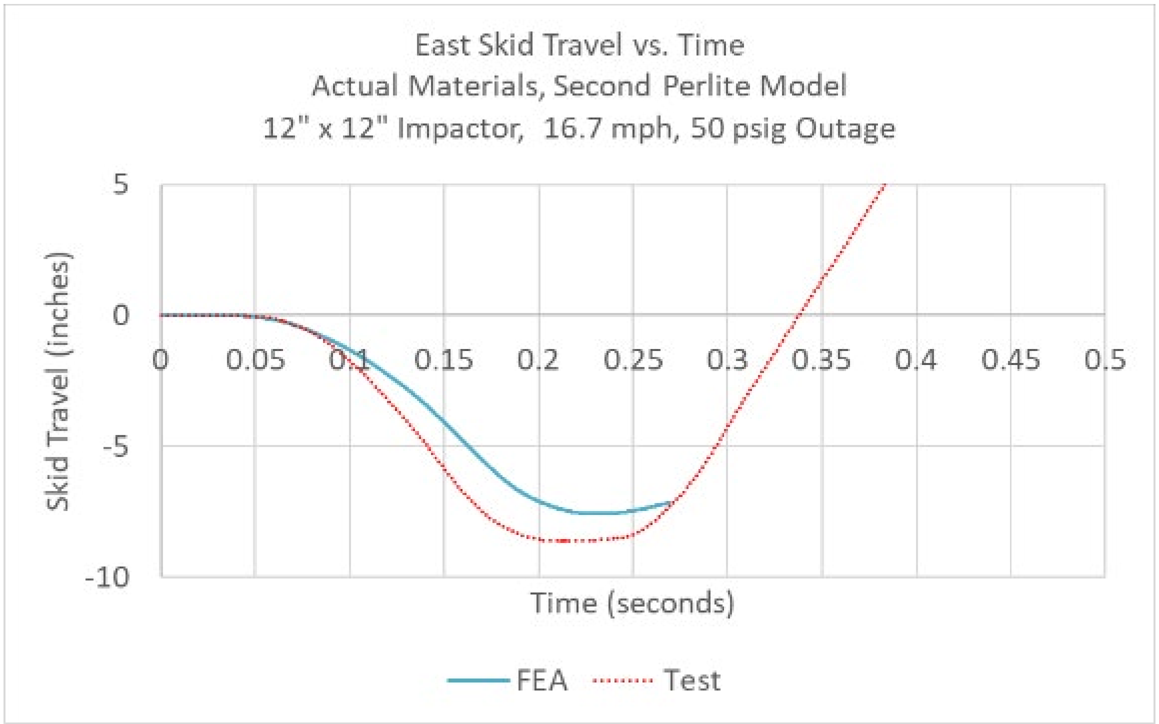

Figure C114. East Skid Travel Versus Time, 16.7 mph Post-Test Model (Actual Materials) with "Crushable Foam" Perlite and QS B-W Damage Initiation

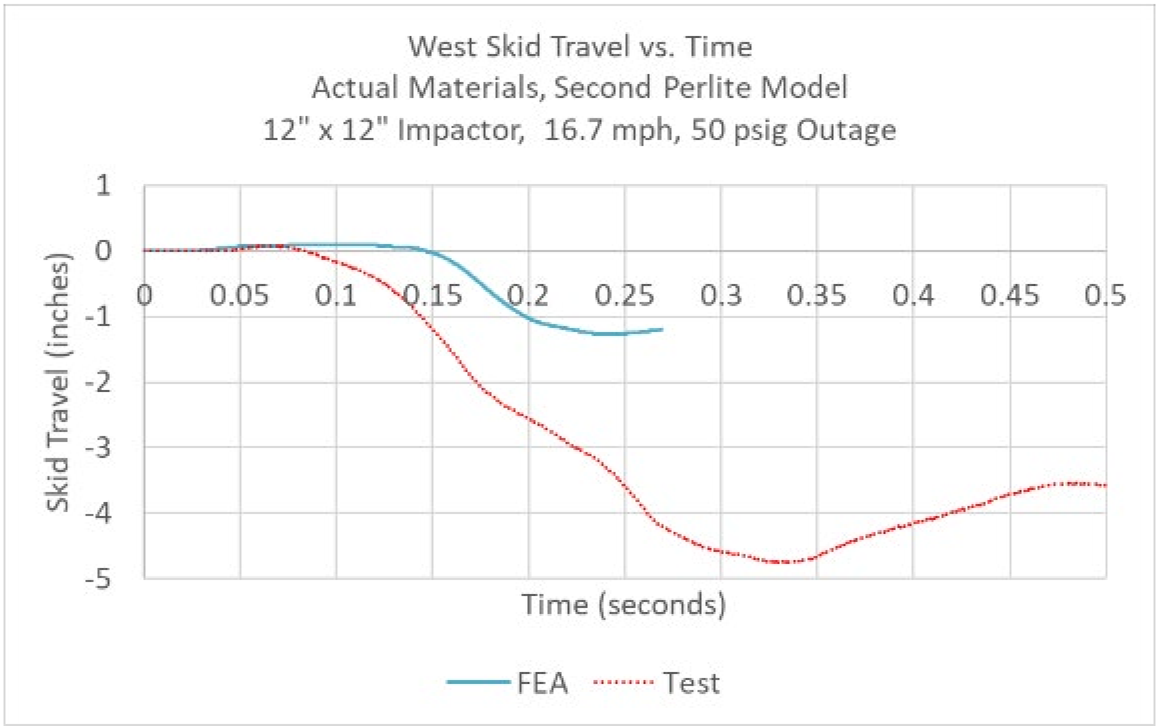

Figure C115. West Skid Travel Versus Time, 16.7 mph Post-Test Model (Actual Materials) with "Crushable Foam" Perlite and QS B-W Damage Initiation

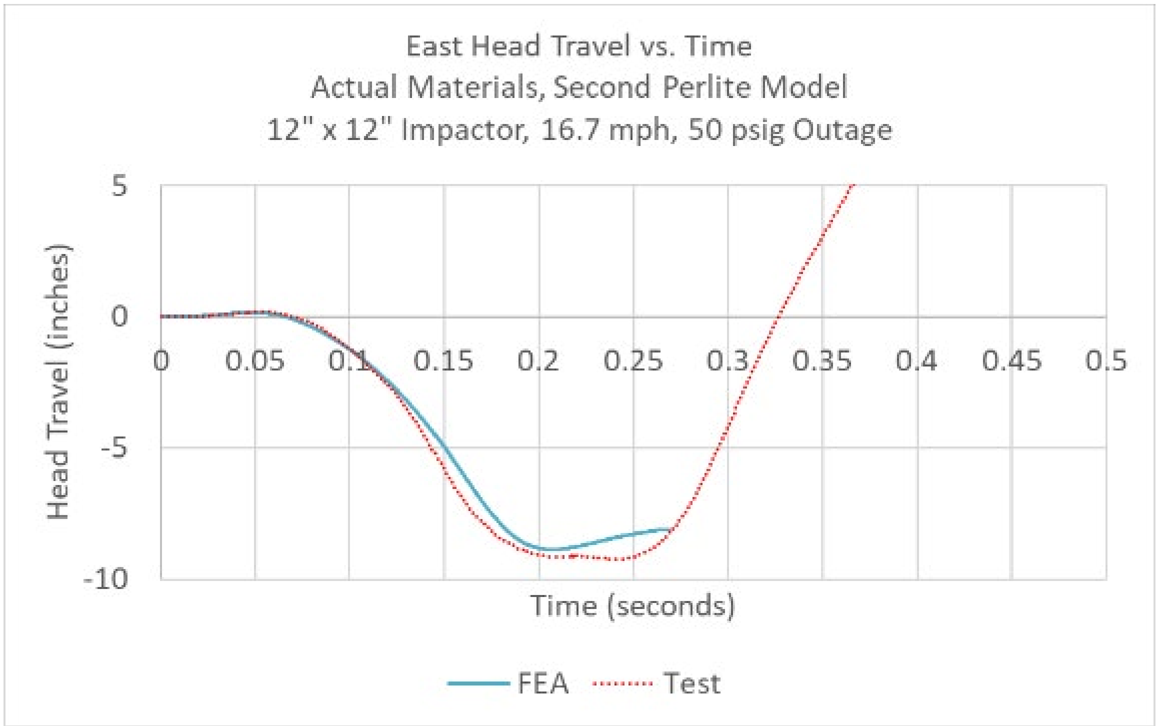

Figure C116. East Head Travel Versus Time, 16.7 mph Post-Test Model (Actual Materials) with “Crushable Foam” Perlite and QS B-W Damage Initiation

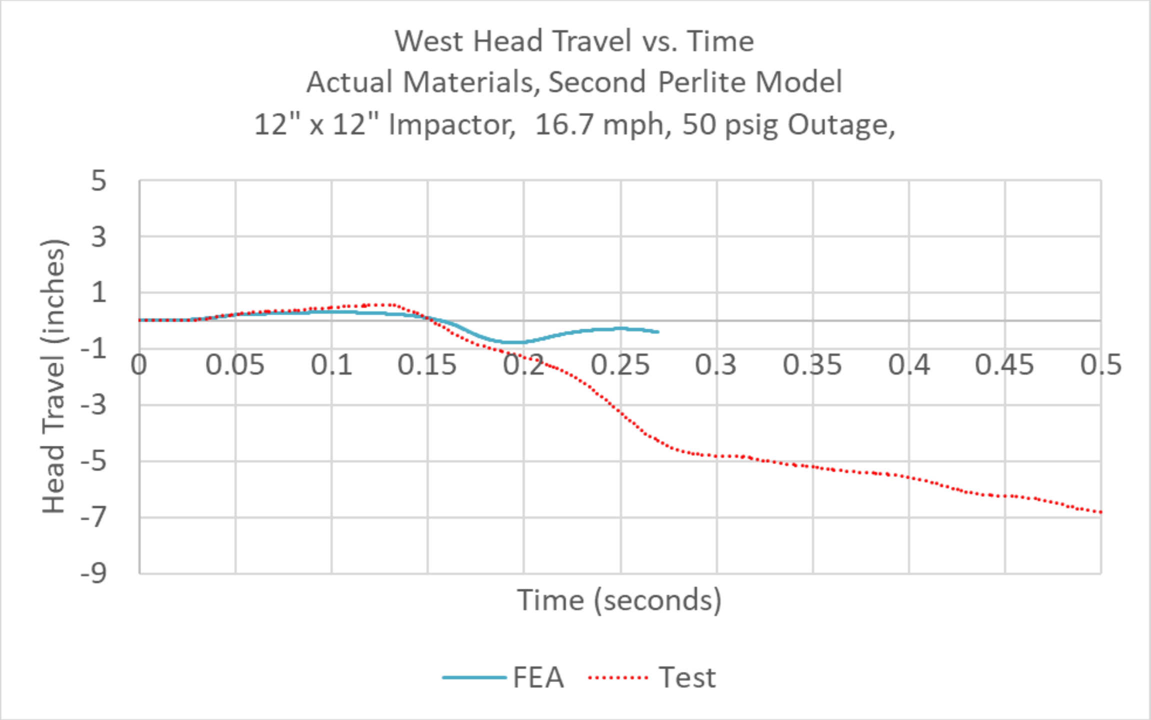

Figure C117. West Head Travel Versus Time, 16.7 mph Post-Test Model (Actual Materials) with “Crushable Foam” Perlite and QS B-W Damage Initiation

Section 3.5. 16.7 mph, Actual Steels, "Crushable Foam" Perlite, 0.1/s T304 Properties

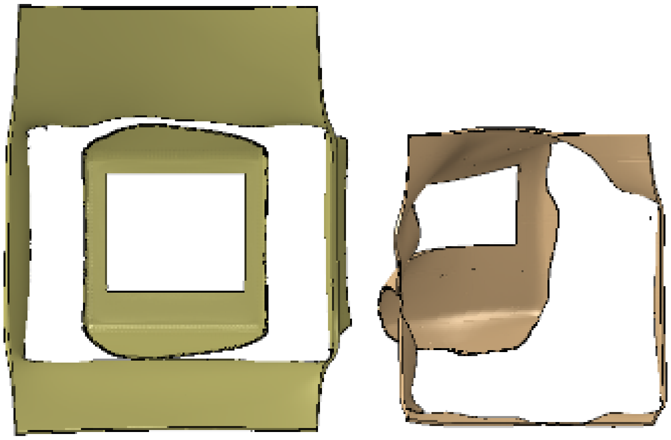

Figure C118. Solid Patch in Outer (left) and Inner (right) Tanks, 16.7 mph Post-Test Model (Actual Materials, 0.1/s T304 Properties) with "Crushable Foam" Perlite at 205 ms

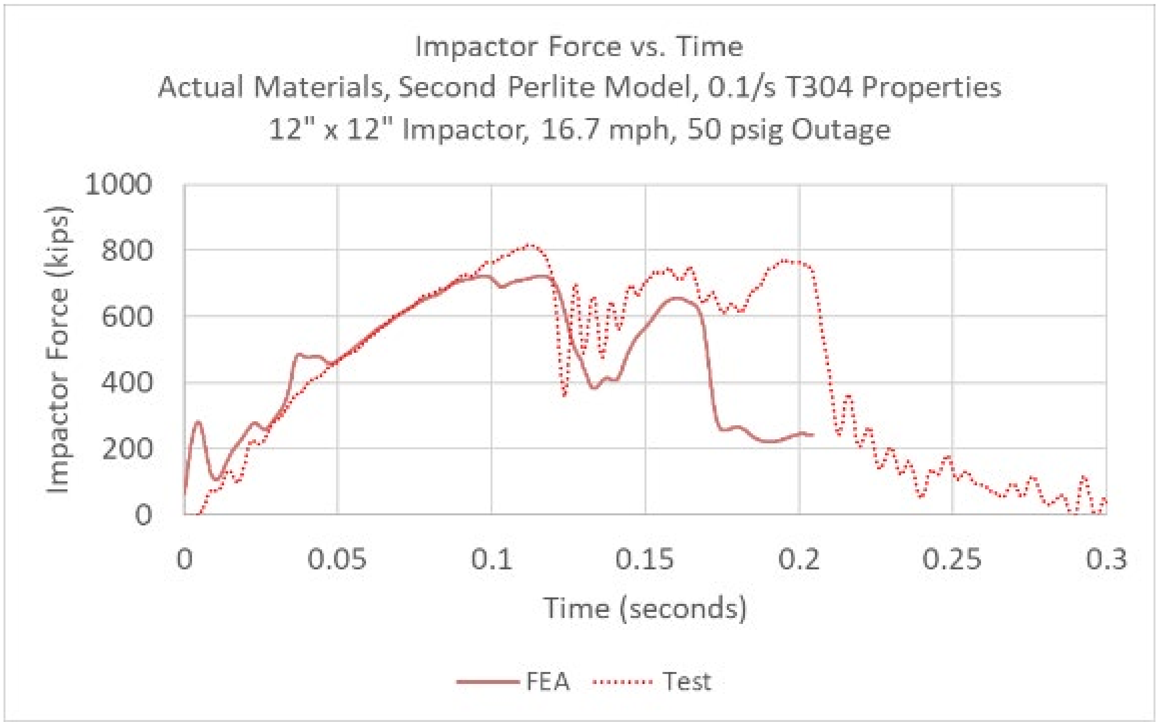

Figure C119. Impactor Force Versus Time, 16.7 mph Post-Test Model (Actual Materials, 0.1/s T304 Properties) with "Crushable Foam" Perlite

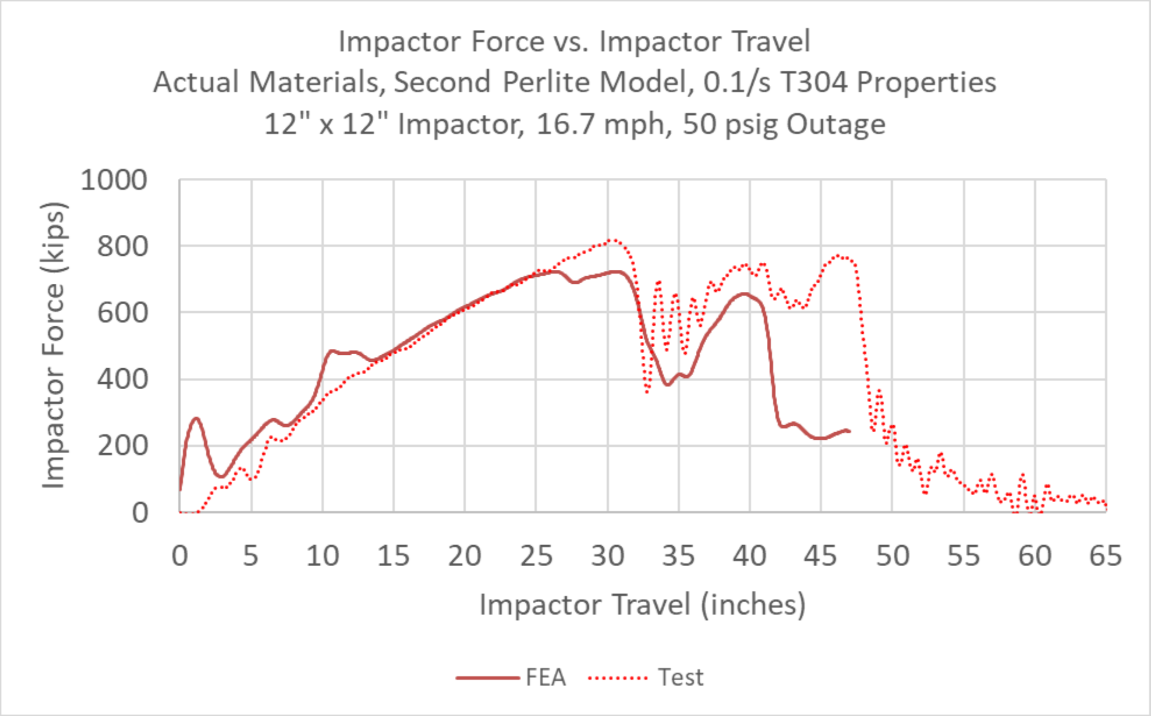

Figure C120. Impactor Force Versus Travel, 16.7 mph Post-Test Model (Actual Materials, 0.1/s T304 Properties) with "Crushable Foam" Perlite

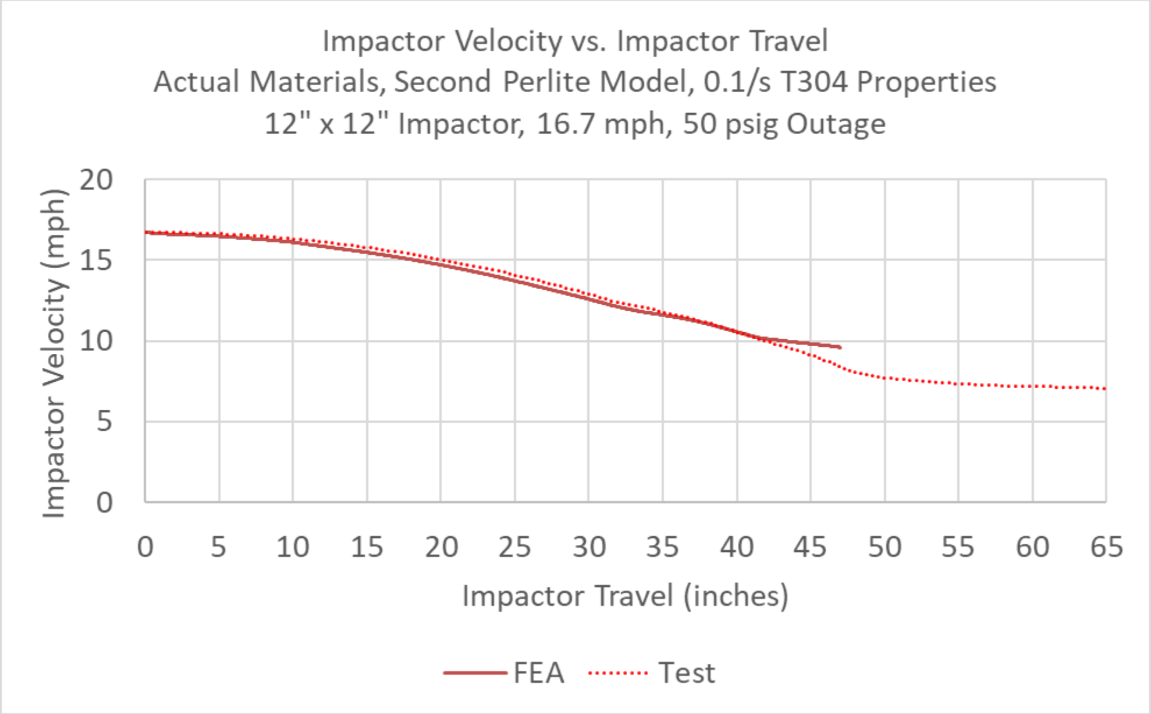

Figure C121. Impactor Velocity Versus Travel, 16.7 mph Post-Test Model (Actual Materials, 0.1/s T304 Properties) with "Crushable Foam" Perlite

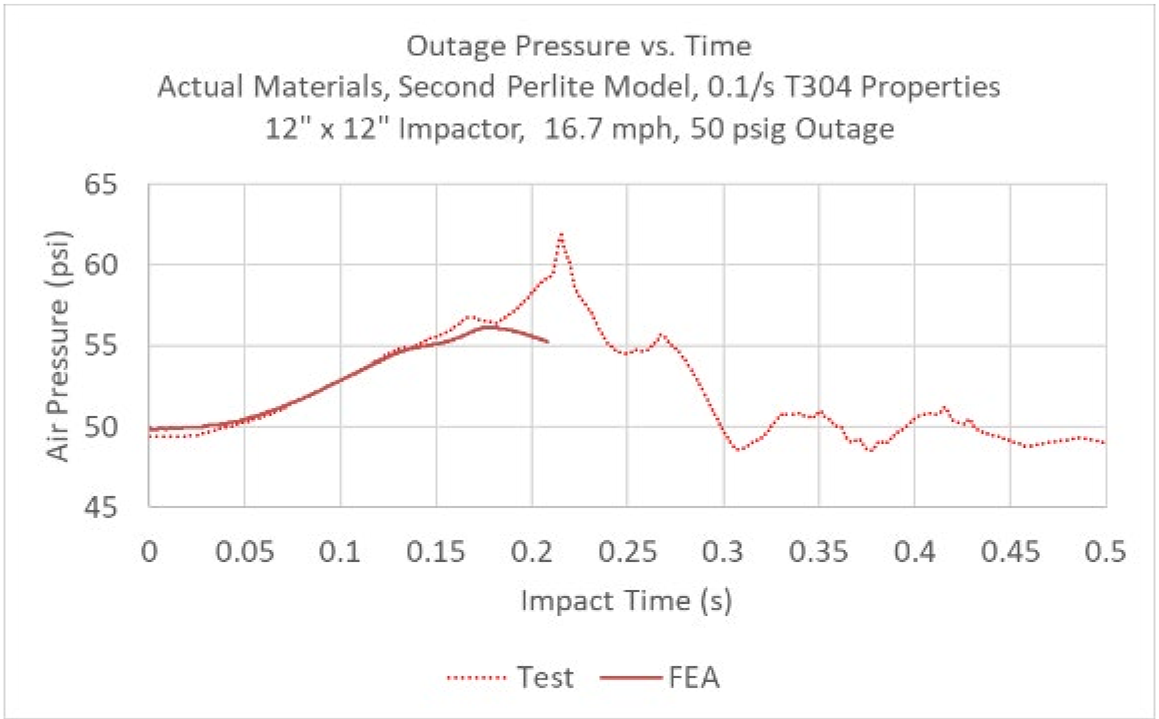

Figure C122. Outage Pressure Versus Time, 16.7 mph Post-Test Model (Actual Materials, 0.1/s T304 Properties) with "Crushable Foam" Perlite

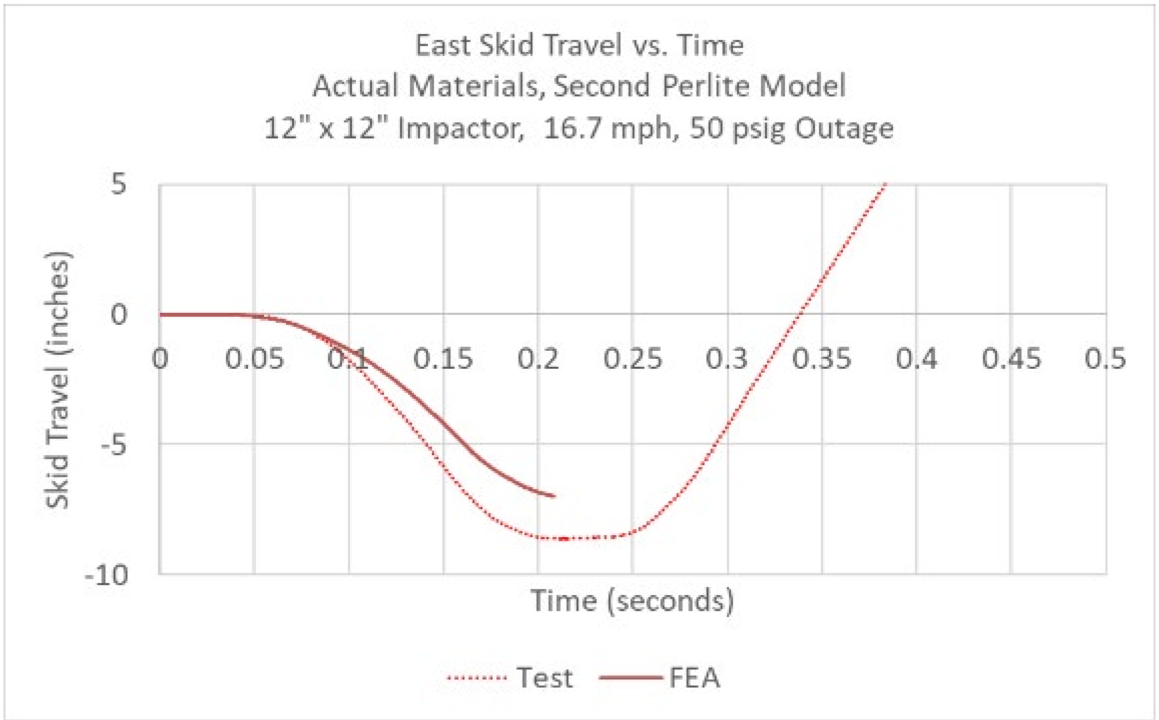

Figure C123. East Skid Travel Versus Time, 16.7 mph Post-Test Model (Actual Materials, 0.1/s T304 Properties) with "Crushable Foam" Perlite

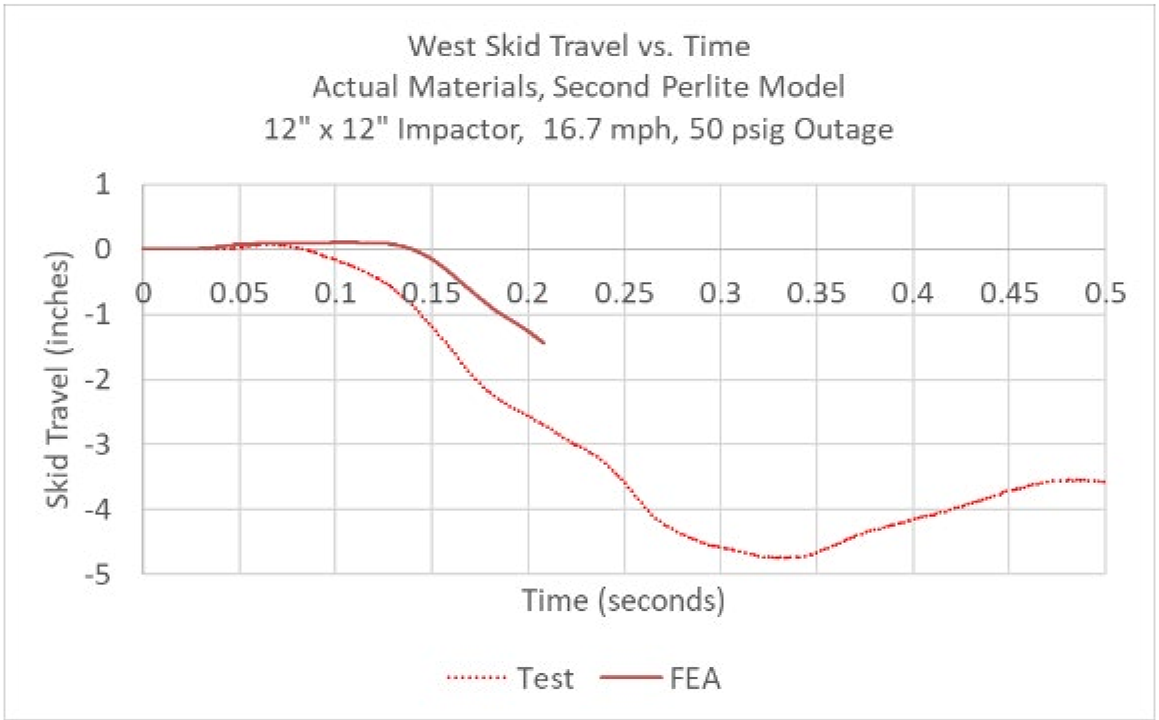

Figure C124. West Skid Travel Versus Time, 16.7 mph Post-Test Model (Actual Materials, 0.1/s T304 Properties) with "Crushable Foam" Perlite

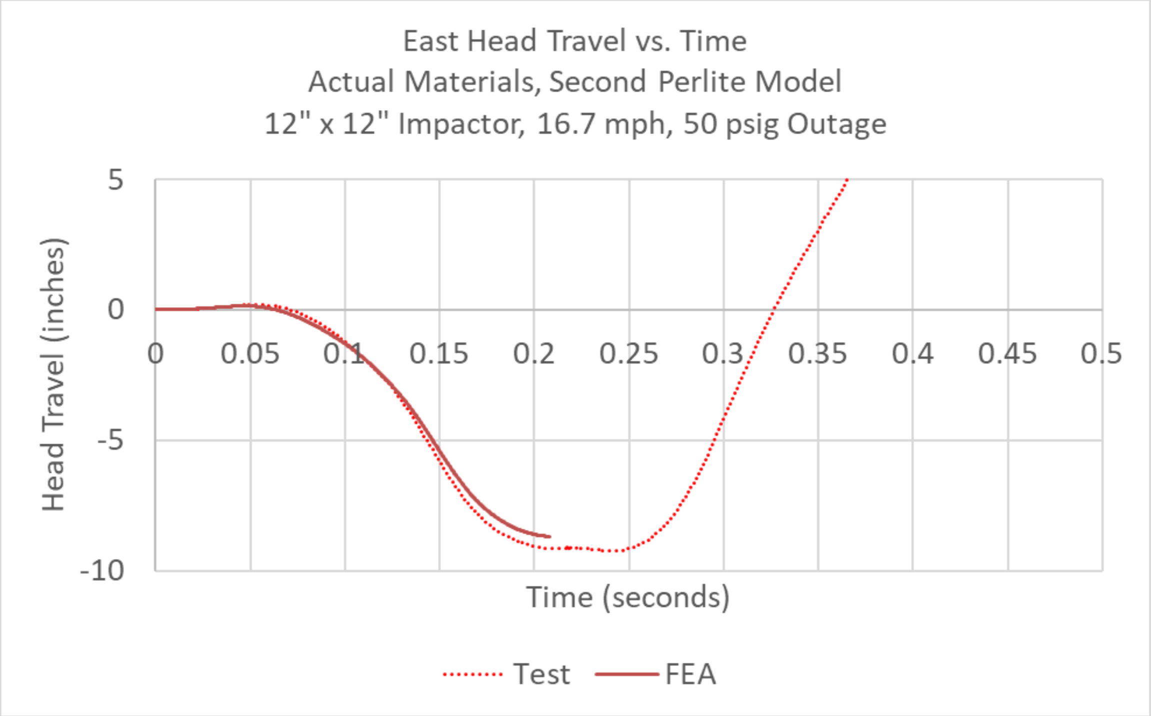

Figure C125. East Head Travel Versus Time, 16.7 mph Post-Test Model (Actual Materials, 0.1/s T304 Properties) with "Crushable Foam" Perlite

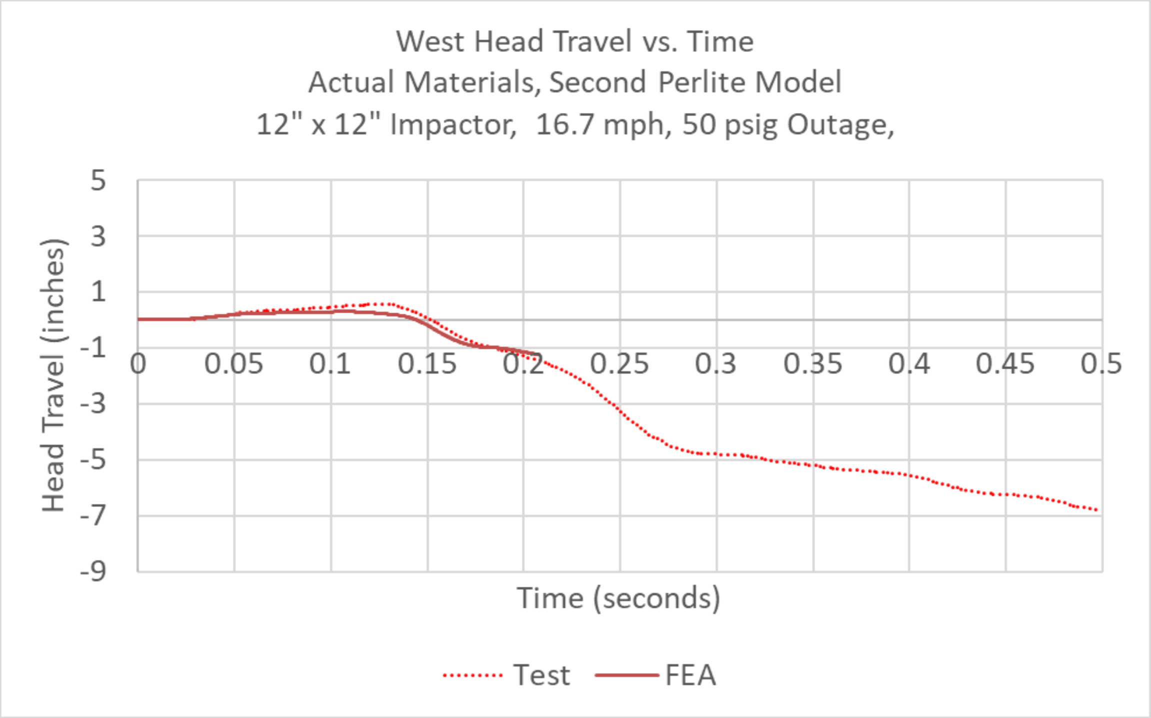

Figure C126. West Head Travel Versus Time, 16.7 mph Post-Test Model (Actual Materials, 0.1/s T304 Properties) with "Crushable Foam" Perlite

Section 3.6. 16.7 mph, Actual Steels, "Crushable Foam" Perlite, QS B-W Damage Initiation for T304, Zero Ambient Pressure

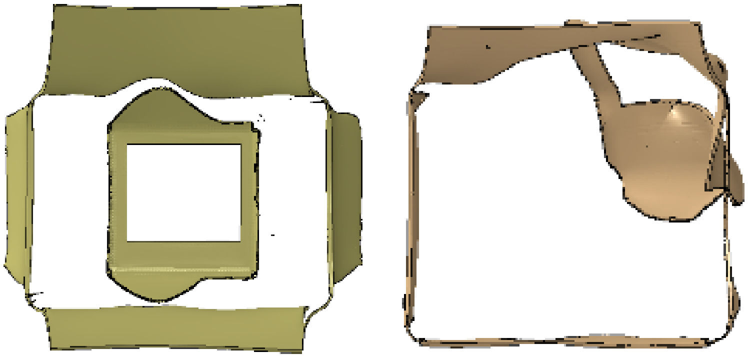

Figure C127. Solid Patch in Outer (left) and Inner (right) Tanks, 16.7 mph Post-Test Model (Actual Materials) with "Crushable Foam" Perlite, QS B-W Damage Initiation, and 0 psia Ambient Pressure at 287 ms

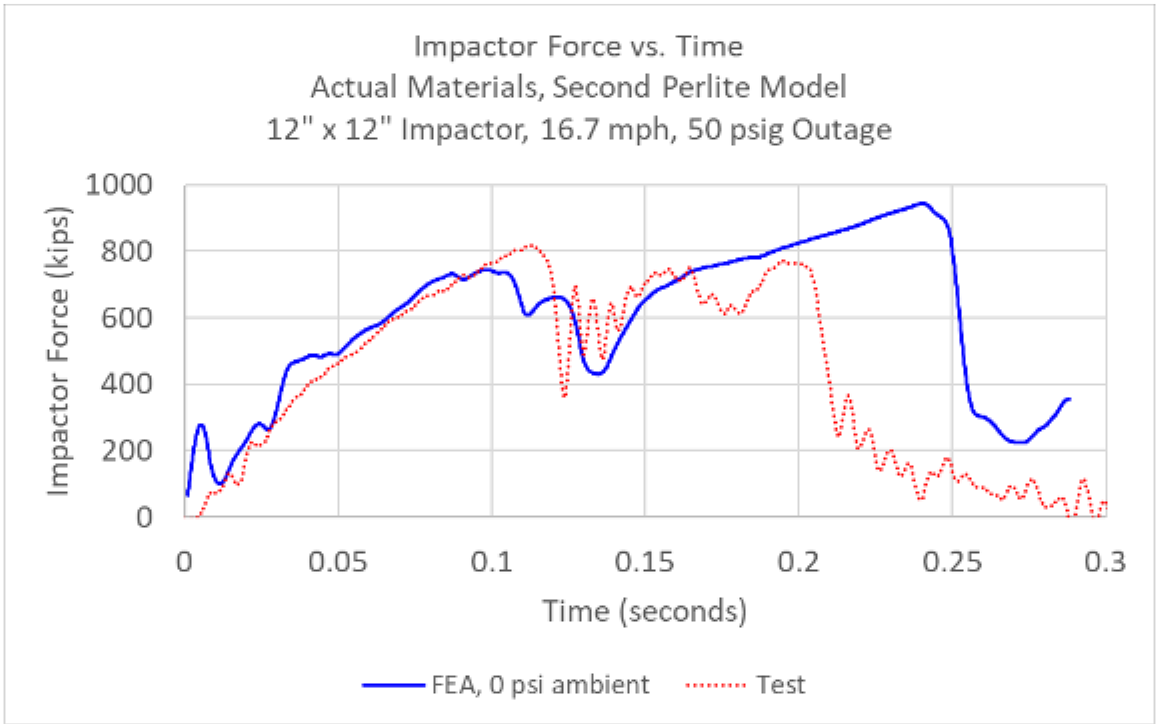

Figure C128. Impactor Force Versus Time, 16.7 mph Post-Test Model (Actual Materials) with "Crushable Foam" Perlite, QS B-W Damage Initiation, and 0 psia Ambient Pressure

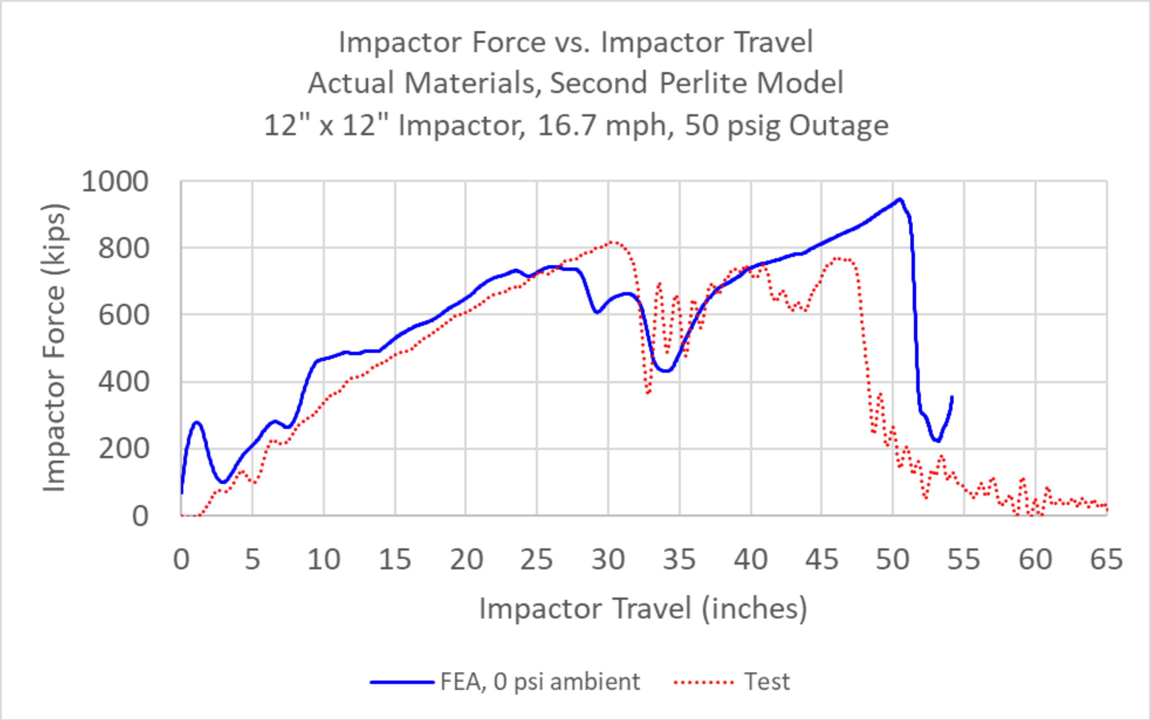

Figure C129. Impactor Force Versus Travel, 16.7 mph Post-Test Model (Actual Materials) with "Crushable Foam" Perlite, QS B-W Damage Initiation, and 0 psia Ambient Pressure

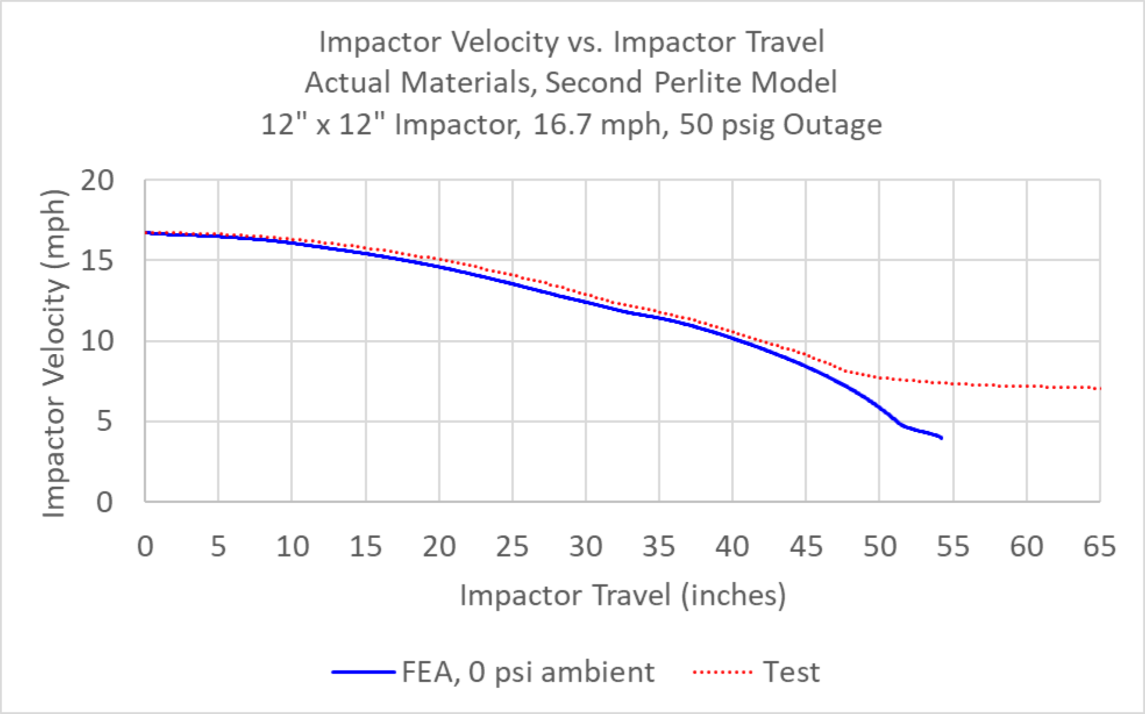

Figure C130. Impactor Velocity Versus Travel, 16.7 mph Post-Test Model (Actual Materials) with “Crushable Foam” Perlite, QS B-W Damage Initiation, and 0 psia Ambient Pressure

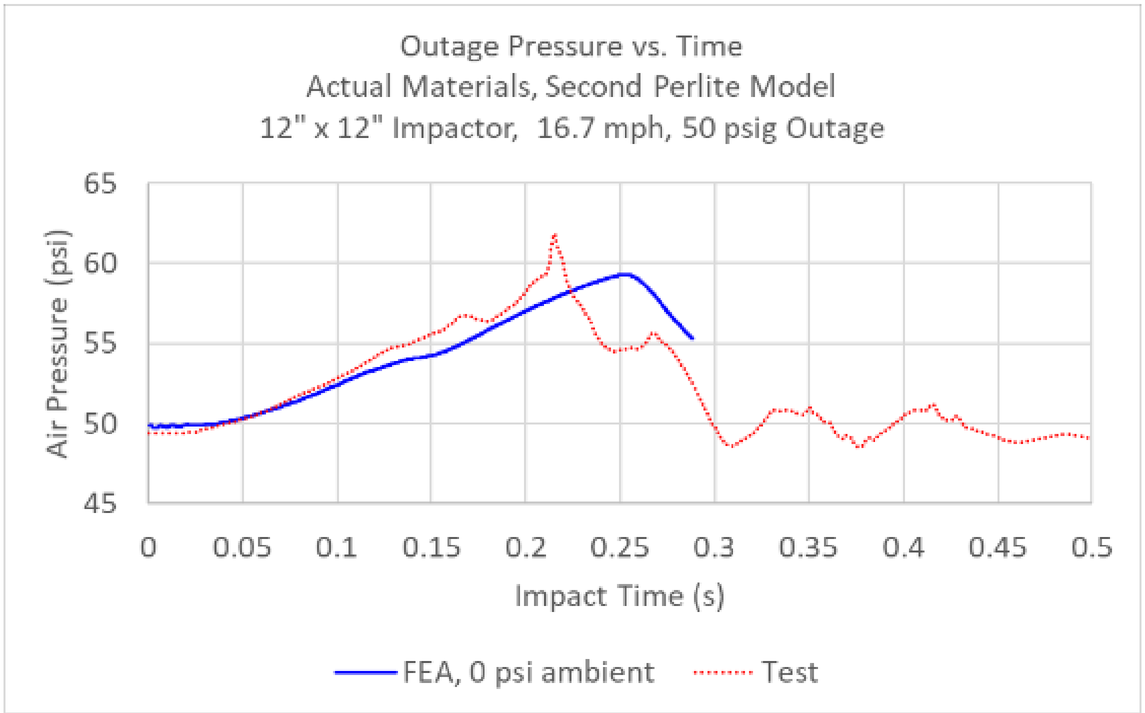

Figure C131. Outage Pressure Versus Time, 16.7 mph Post-Test Model Actual Materials (Actual Materials) with “Crushable Foam” Perlite, QS B-W Damage Initiation, and 0 psia Ambient Pressure

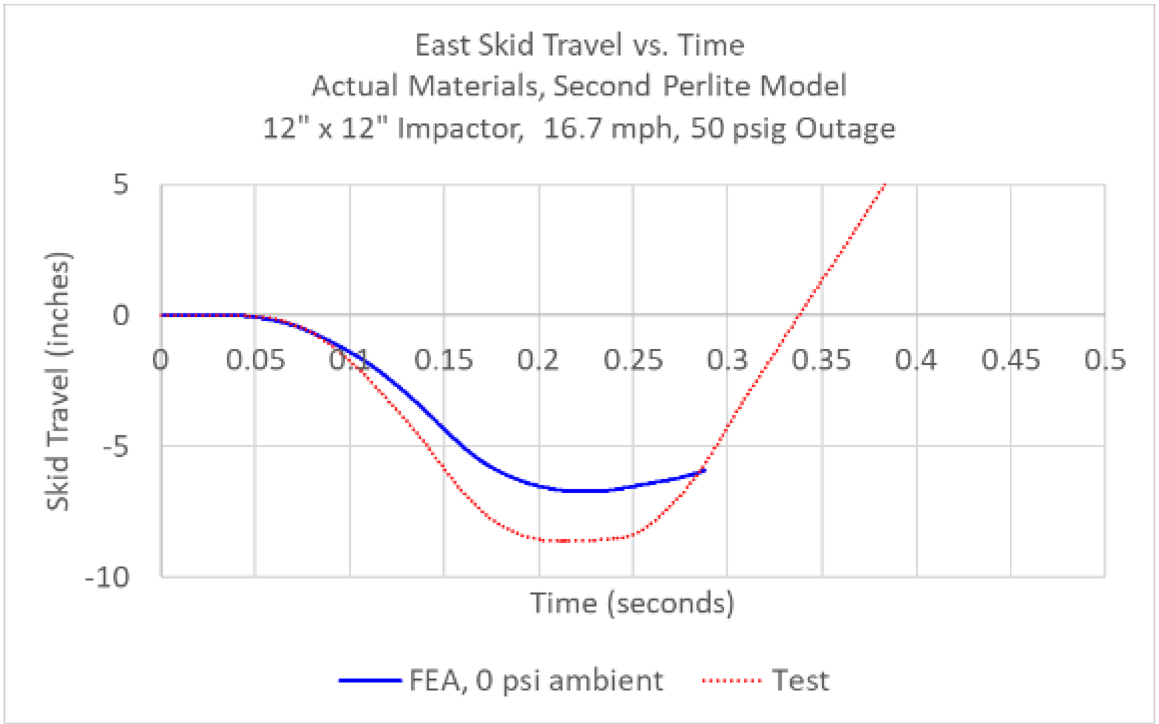

Figure C132. East Skid Travel Versus Time, 16.7 mph Post-Test Model (Actual Materials) with "Crushable Foam" Perlite, QS B-W Damage Initiation, and 0 psia Ambient Pressure

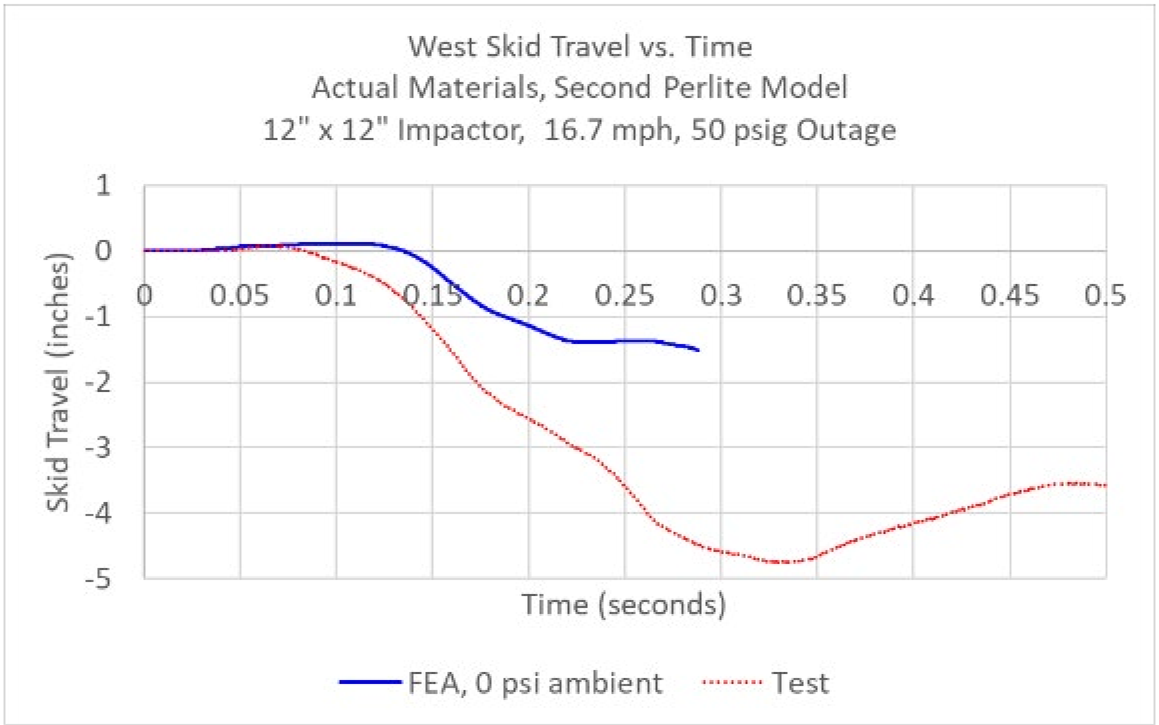

Figure C133. West Skid Travel Versus Time, 16.7 mph Post-Test Model (Actual Materials) with "Crushable Foam" Perlite, QS B-W Damage Initiation, and 0 psia Ambient Pressure

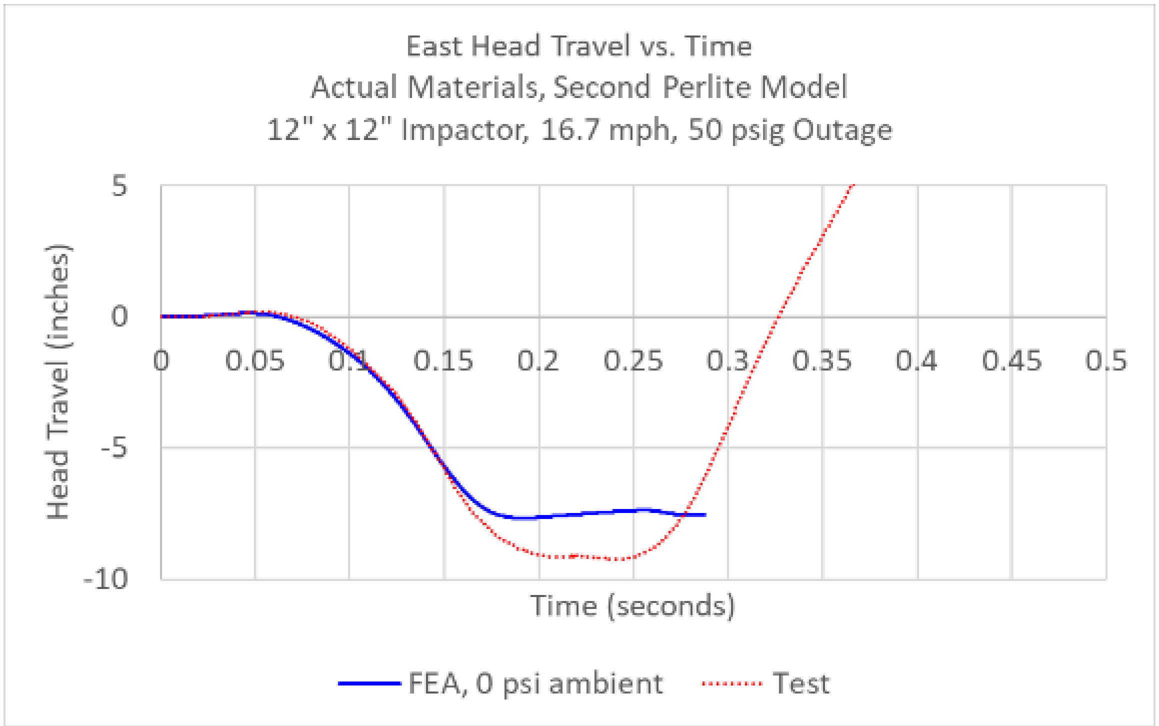

Figure C134. East Head Travel Versus Time, 16.7 mph Post-Test Model (Actual Materials) with "Crushable Foam" Perlite, QS B-W Damage Initiation, and 0 psia Ambient Pressure

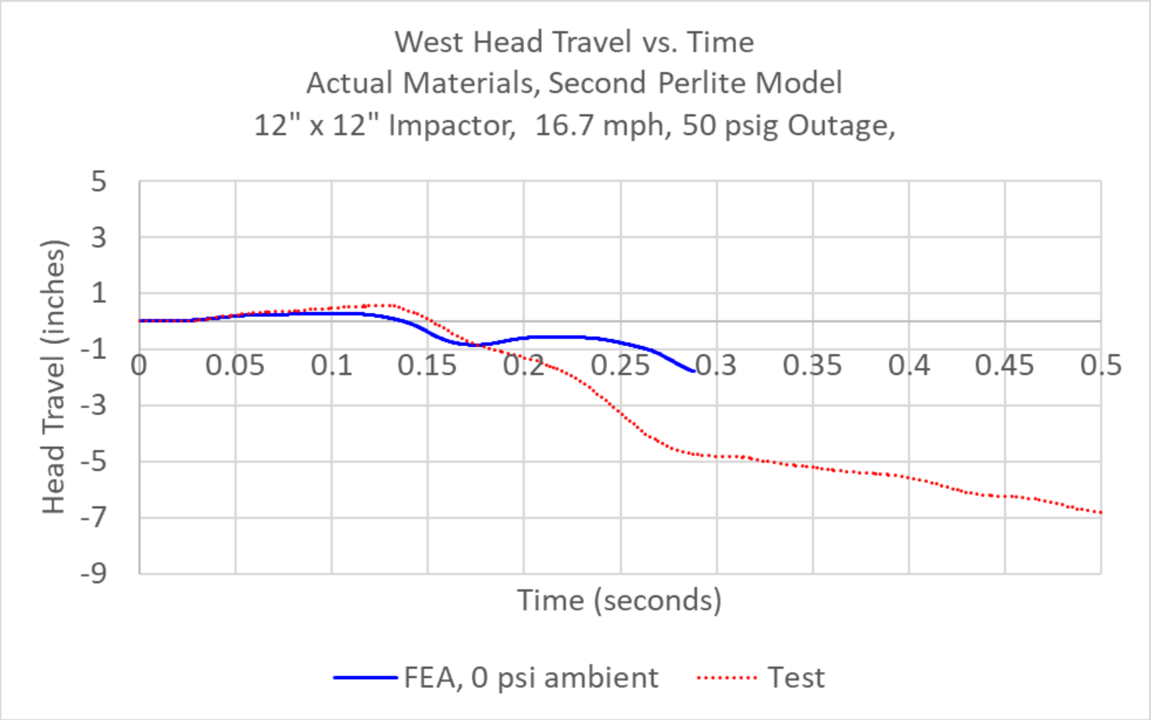

Figure C135. West Head Travel Versus Time, 16.7 mph Post-Test Model (Actual Materials) with "Crushable Foam" Perlite, QS B-W Damage Initiation, and 0 psia Ambient Pressure

Appendix D.
Geometry in Pre-Test and Post-Test FE Models

This appendix contains a discussion of each of the parts that made up the assemblies for the pre- and post-test FE models. Rigid parts were used when it was important to include a part for its inertia or its interaction through contact but where the deformation of the part could be neglected in the calculations. Four parts were modeled as rigid bodies. The remaining bodies were modeled as deformable bodies.

A summary of the element types used to mesh the model assembly is provided in Table D1.

Table D1. Summary of Element Types [22]

Element Designation	Description
C3D8	Eight-node linear brick element for stress and displacement modeling
C3D8R	Eight-node linear brick, reduced integration with hourglass control
CONN3D2	Connector element between two nodes or ground and a node
DCOUP3D	Three-dimensional distributing coupling element
M3D3	Three-node triangular membrane element
M3D4R	Four-node quadrilateral membrane element (reduced integration)
MASS	Point mass
R3D3	Three-dimensional, three-node triangular facet rigid element
R3D4	Three-dimensional, four-node bilinear quadrilateral rigid element
RNODE3D	Three-dimensional reference node
S3R	Three-node triangular general-purpose shell, finite membrane strains (identical to element S3)
S4R	Four-node general-purpose shell, reduced integration with hourglass control, finite membrane strains
SPRINGA	Axial spring between two nodes, whose line of action is the line joining the two nodes. This line of action may rotate in large-displacement analysis.

Section 1. Rigid Impactor

The impactor was modeled as a rigid body in the DOT-113 FE models. The simulations used a 12-inch by 12-inch square impactor with 1-inch radii edges around the impact face. The geometry included the impact face, the tapered cone back to the portion of the impactor where the impactor attached to the ram car, and a representation of the ram arm and the width of the ram car's body. The impactor, both with and without mesh, is shown in Figure D1.

Table D2. Properties of Impactor in Pre-Test and Post-Test FE Models

	Pre-Test Model	**Post-Test Model, Pre-Test Materials**	**Post-Test Model, Post-Test Materials**
Type of Part	Rigid	Rigid	Rigid
Number of Elements	R3D4: 5710 R3D3: 52 RNODE3D: 19 MASS: 1	R3D4: 5627 R3D3: 42 RNODE3D: 24 MASS: 1	R3D4: 5627 R3D3: 42 RNODE3D: 24 MASS: 1
Approximate Mesh Size (inches)	0.25–2	0.25–2	0.25–2
Approximate Part Weight (lbf)	297,126	297,126	297,126

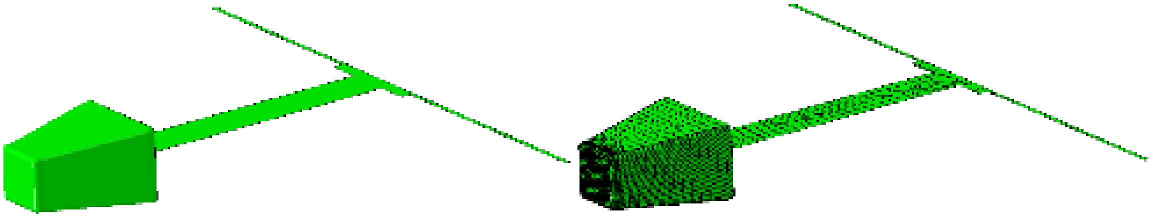

Figure D1. Impactor Geometry (left) and Mesh (right)

Section 2. Rigid Wall

The impact wall was modeled as a rigid body in the DOT-113 FE models. Because the wall was constrained against motion in any direction, no mass needed to be defined for this part. Figure D2 shows the wall's geometry and mesh. The wall's geometry and mesh were the same in all the pre- and post-test FE models.

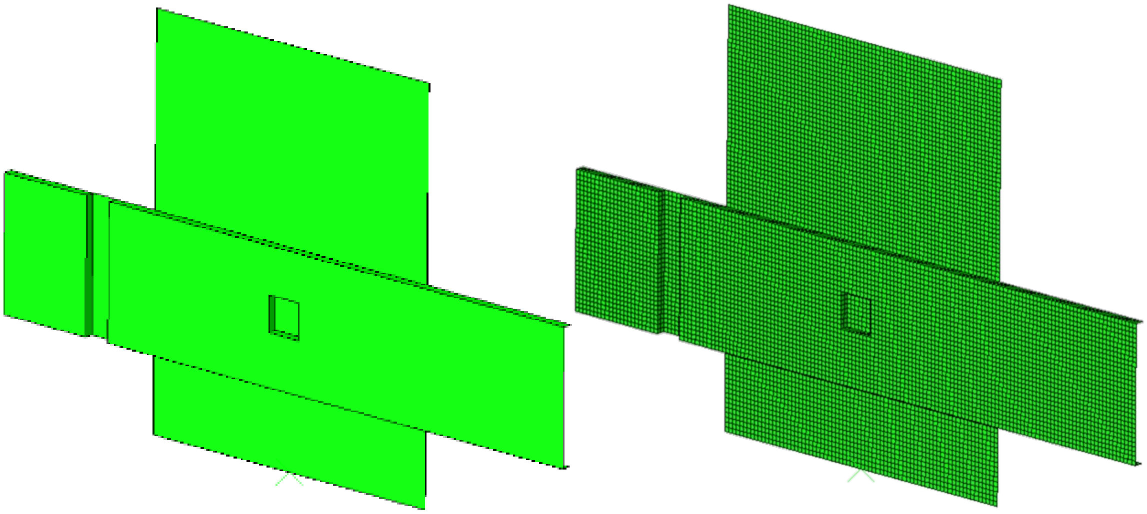

Figure D2. Rigid Wall Geometry (left) and Mesh (right)

Table D3. Properties of Rigid Wall in Pre-Test and Post-Test FE Models

Type of Part	Rigid
Number of Elements	R3D4: 9,640 RNODE3D: 18
Approximate Mesh Size (inches)	2

Section 3. Rigid Skid

The trucks of the tank car were removed prior to the test. The bolster of the car rested directly upon a set of skids, and the skids rested upon steel plates (see Figure 6). The skids were designed to inhibit the rigid body roll of the tank car following rebound from the rigid wall during a test. The skid geometry and mesh are shown in Figure D3. The skid's geometry and mesh were the same in all of the pre- and post-test FE models.

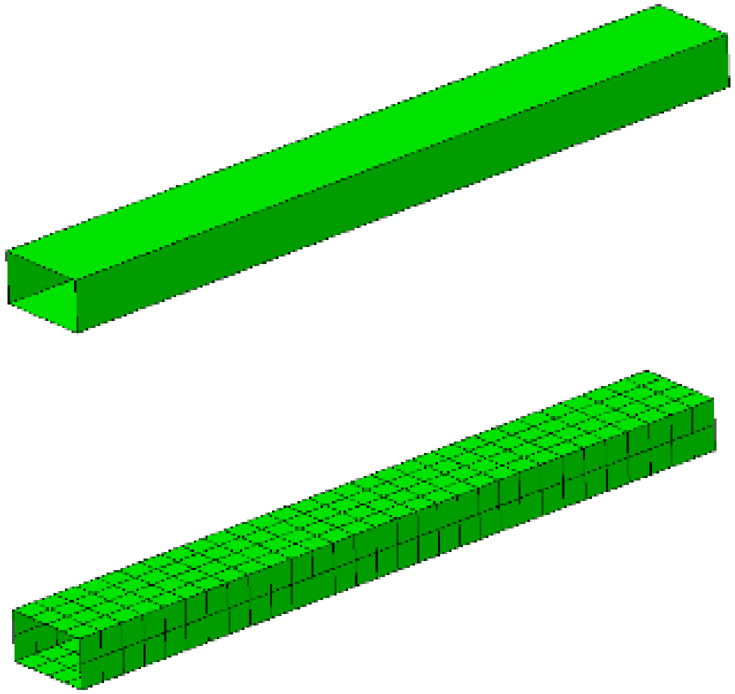

Figure D3. Skid Geometry (top) and Mesh (bottom)

Table D4. Properties of Skid in Pre-Test and Post-Test FE Models

Type of Part	Rigid
Number of Elements	R3D4: 368 MASS: 2 RNODE3D: 1
Approximate Mesh Size (inches)	1

The rigid skids used in the test weighed approximately 3,500 pounds each. This mass was included in the model through the use of a point mass at the rigid body reference node of each skid. As a simplified representation of the tank, the FE model does not include geometric details such as the draft sills, draft gear, or couplers, as these features were not expected to play a significant role in the puncture response for an impact away from the ends of the car. The masses of these components were included as a second point mass on the skid. For this car, the additional structure at each end of the car was assumed to have a weight of approximately 6,100 pounds. These additional point masses were added to both the pre- and post-test models without adjustment. Table D5 summarizes the masses on each skid.

Table D5. Point Masses Added to Skid Reference Point in Models

Component	**Approximate Weight** ***lbf***
Skid	3,500
Draft Sill, Draft Gear, Coupler, etc.	6,100

Section 4. Bolster and Cabinet

Each end of the DOT-113 tank car featured a structural bolster on the outer tank that served as the attachment point for the trucks. Each end of the car also featured a structural cabinet attached to the outer tank that served as a protective housing for the valves and piping that terminate outside of the tank. A simplified, shell element representation of both the bolster and cabinet was included on each end of the outer tank to ensure that any structural contribution of these additional features were captured by the models. Figure D4 shows the geometry of the bolster and cabinet part on the left, and the meshed bolster and cabinet part on the right.

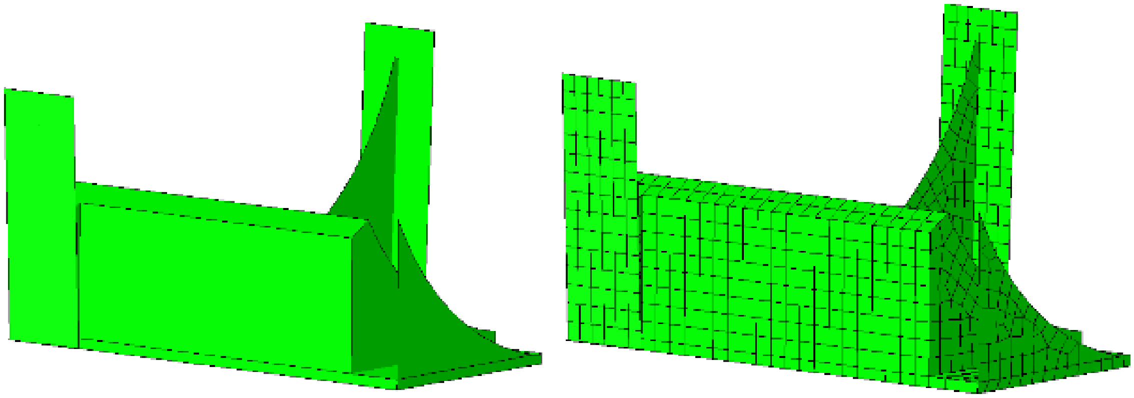

Figure D4. Bolster and Cabinet Geometry (left) and Mesh (right)

Table D6. Properties of Bolster and Cabinet in Pre-Test and Post-Test FE Models

Type of Part	**Deformable**
Number of Elements	S4R: 1,455 S3R: 27
Approximate Mesh Size (inches)	3.5
Material(s)	A516-70
Approximate Part Weight (lbf)	1,600

Section 5. Inner Tank – Shell Elements

The inner tank was modeled using two different techniques. The first technique, described in this section (see below), used shell elements to model the inner tank away from the impact zone. The second technique, described in Appendix D, Section 6, modeled the inner tank using solid "brick" elements in the impact zone. Figure D5 shows the shell portion of the inner tank. Note that in this figure certain structural details have been omitted from view. This part was globally meshed using quadrilateral reduced integration (S4R) elements. At the edges of the impact zone, the mesh was refined to provide a transition between the fine solid mesh of the impact zone and the coarse shell mesh of the distant tank. A technique referred to as shell-to-solid coupling was used to attach the solid patch to the edges of the shell mesh on the tank. The shell part of the tank represented the midplane surface of the tank. The shell part had a midplane diameter of 106.5 inches in the model. The models included a small number of triangular shell (S3R) elements.

The geometry of the inner tank was changed slightly from the pre-test model to the post-test model. In the pre-test model, and the post-test models run using the pre-test material properties, the nominal thickness of the inner tank shell was modeled. In the post-test model using the actual material behaviors of the tank car steels, the actual tank thickness was modeled.

The properties of the inner tank shell mesh in the pre-test and post-test FE models are summarized in Table D7.

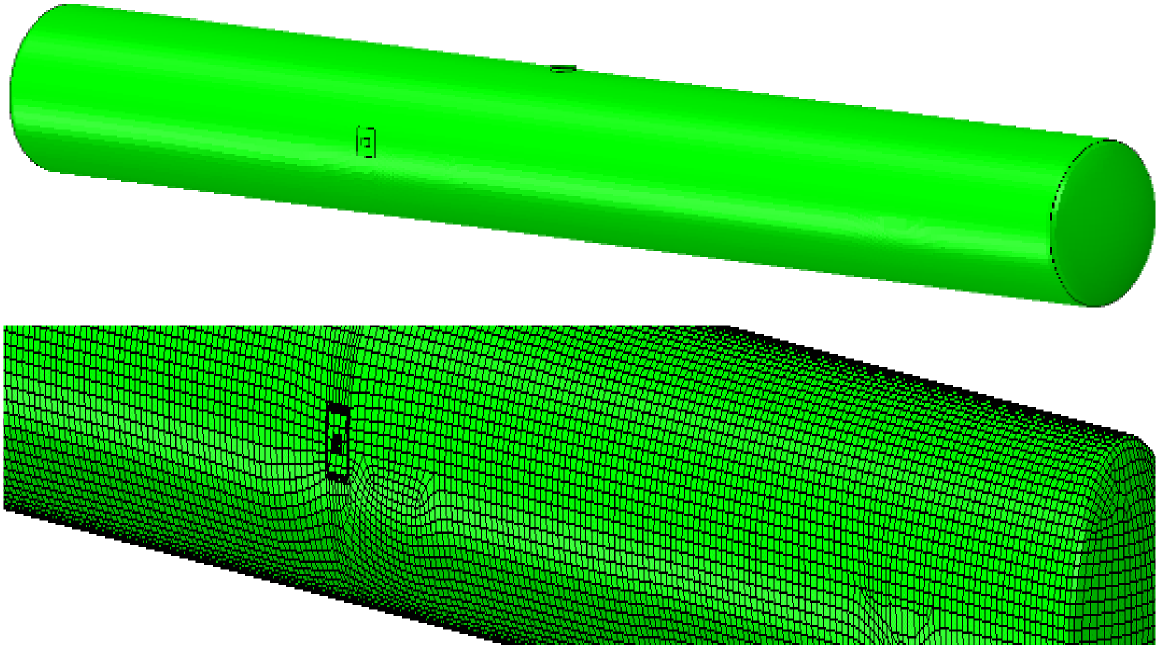

Figure D5. Inner Tank Shell Geometry (top) and Mesh (bottom)

Table D7. Properties of Inner Tank Shell Mesh in FE Models

	Pre-Test Model	Post-Test Model, Pre-Test Materials	Post-Test Model, Post-Test Materials
Type of Part	Deformable, Shell	Deformable, Shell	Deformable, Shell
Number of Elements	S4R: 23,238 S3R: 144	S4R: 23,238 S3R: 144	S4R: 23,238 S3R: 144
Approximate Mesh Size (inches)	4	4	4
Material(s)	ASTM T304 (upper) or ASTM T304 (lower)	ASTM T304 (upper) or ASTM T304 (lower)	ASTM T304 (actual)
Shell Thickness (inches)	0.25	0.25	0.28
Head Thickness (inches)	0.375	0.375	0.375
Approximate Part Weight (lbf)	25,100	25,100	27,550

Section 6. Inner Tank – Solid Elements

The second technique described below, modeled the inner tank using solid “brick” elements in the impact zone. Figure D6 shows the solid portion of the tank. Note that because of the fine mesh, the right-hand image appears to show the mesh as a solid-colored part. The outer dimensions of the part measured approximately 18 inches high by 14 inches wide in the pre- and post-test models. The inner cutout measured approximately 5 inches high by approximately 7 inches wide in the pre- and post-test models. The part was meshed using five elements through the thickness of the part. This through-thickness mesh density corresponded to a global mesh seed of 0.05 inch in the pre- and post-test models using the pre-test material behaviors, and a seed of 0.056 inch in the post-test model using the post-test material behaviors. The solid portion of the tank was meshed using 8-noded reduced integration hexahedral “brick” (C3D8R) elements. The solid tank mesh was attached to the shell tank mesh along the outer and inner edges using shell-to-solid coupling (SSC). The elements along the inner and outer edges of the solid tank that were involved in the shell-to-solid coupling were given the same elastic and plastic material responses as the rest of the solid patch but did not have failure behaviors defined. This was done to prevent elements involved in the SSC from being removed from the model, as that could cause the coupling itself to fail.

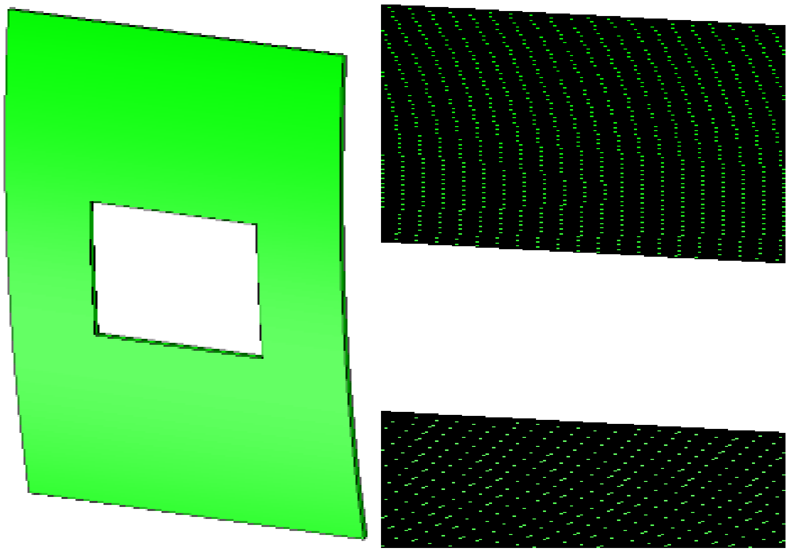

Figure D6. Inner Tank Solid Geometry (left) and Mesh (right)

Table D8. Properties of Inner Tank Solid Mesh in FE Models

	Pre-Test Model	Post-Test Model, Pre-Test Materials	Post-Test Model, Post-Test Materials
Type of Part	Deformable, Solid	Deformable, Solid	Deformable, Solid
Number of Elements	C3D8R: 435,400	C3D8R: 435,400	C3D8R: 345,340
Approximate Mesh Size (inches)	0.05	0.05	0.056
Material(s)	ASTM T304 (upper) or ASTM T304 (lower)	ASTM T304 (upper) or ASTM T304 (lower)	ASTM T304 (actual)
Thickness (inches)	0.25	0.25	0.28
Approximate Part Weight (lbf)	16	16	17

Section 7. Outer Tank – Shell Elements

The outer tank was modeled using two different techniques. The first technique shown below, used shell elements to model the inner tank away from the impact zone. The second technique, described in Appendix D, Section 8, modeled the inner tank using solid “brick” elements in the impact zone. Figure D7 shows the shell portion of the outer tank. This part was globally meshed using quadrilateral reduced integration (S4R) elements. At the edges of the impact zone, the mesh was refined to provide a transition between the fine solid mesh of the impact zone and the coarse shell mesh of the distant tank A technique referred to as SSC was used to attach the solid patch to the edges of the shell mesh on the tank. The shell part of the tank represented the midplane surface of the tank. The shell part in the model had a midplane diameter of approximately 119 inches. The models included a small number of triangular shell (S3R) elements.

The geometry of the outer tank was changed slightly from the pre-test model to the post-test model. In the pre-test models, and the post-test models run using the pre-test material properties, the nominal thickness of the outer tank shell was used. In the post-test models run using the actual material behaviors of the tank car steels, the actual tank thickness was used.

Additionally, in the post-test models, the size of the solid patch was expanded in an attempt to prevent the tear in the outer tank from reaching the edge of the solid patch of elements. The outer tank required a fairly large solid patch of elements, as the tear initiated in the outer tank well before the inner tank was on the verge of puncture. Thus, the tear in the outer tank needed to be able to propagate to ensure that the outer tank was not carrying more load in the model than it would have been able to carry in the test. The shell mesh of the outer tank was adjusted to ensure a compatible mesh with the solid part. The shell tank parts in the pre- and post-test models are summarized in Table D9.

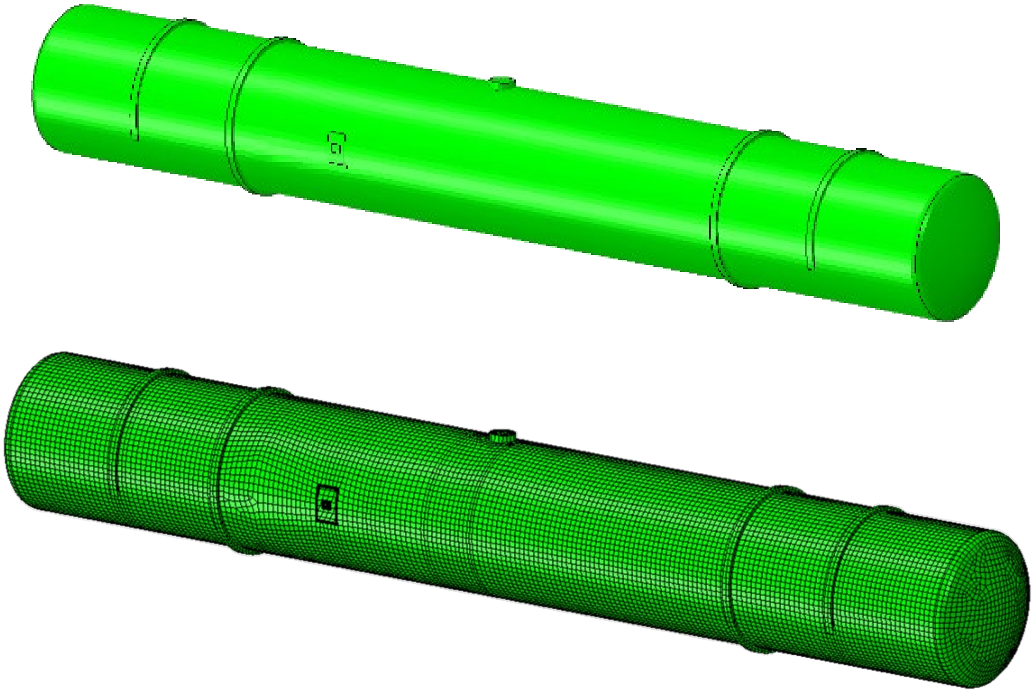

Figure D7. Outer Tank Shell Geometry (top) and Mesh (bottom)

Table D9. Properties of Outer Tank Shell Mesh in FE Models

	Pre-Test Model	Post-Test Model, Pre-Test Materials	Post-Test Model, Post-Test Materials
Type of Part	Deformable, Shell	Deformable, Shell	Deformable, Shell
Number of Elements	S4R: 23,523 S3R: 280	S4R: 23,450 S3R: 270	S4R: 23,535 S3R: 282
Approximate Mesh Size (inches)	4.25	4.25	4.25
Material(s)	A516-70 (lower) or A516-70 (upper)	A516-70 (lower) or A516-70 (upper)	A516-70 (actual)
Shell Thickness (inches)	0.4375	0.4375	0.463
Head Thickness (inches)	0.5	0.5	0.5
Approximate Part Weight (lbf)	45,850	45,850	48,100

Section 8. Outer Tank – Solid Elements

The second technique described see below, modeled the outer tank using solid "brick" elements in the impact zone. Figure D8 shows the solid portion of the outer tank. Note that because of the fine mesh, the right-hand image appears to show the mesh as a solid-colored part. The outer dimensions of the part measured approximately 25 inches high by 16 inches wide in the pre-test models. The outer dimensions of the part measured approximately 27 inches high by 15 inches wide in the post-test models run using the pre-test material behaviors. The outer dimensions of the part measured approximately 27 inches by 18 inches wide in the post-test models run using the actual material behaviors. The inner cutout measured approximately 7 inches high by approximately 8 inches wide in the pre-test models. The inner cutout measured approximately 7 inches high by approximately 8 inches wide in the post-test models run using the pre-test material behaviors. The inner cutout measured approximately 7 inches high by approximately 8 inches wide in the post-test models that used the actual material behaviors. The part was meshed using eight elements through the thickness of the part. This through-thickness mesh density corresponded to a global mesh seed of 0.055 inch in the pre-test models and the post-test models run using the pre-test material behaviors, and a seed of 0.058 inch in the post-test models using the post-test material behaviors. The solid portion of the tank was meshed using eight-noded reduced integration hexahedral "brick" (C3D8R) elements. The solid tank mesh was attached to the shell tank mesh along the outer and inner edges using SSC. The elements along the inner and outer edges of the solid tank that were involved in the SSC were given the same elastic and plastic material responses as the rest of the solid patch but did not have failure behaviors defined. Modeling the outer layers of elements with only elastic and plastic responses was done to prevent elements involved in the SSC from being removed from the model, as that could cause the coupling itself to fail.

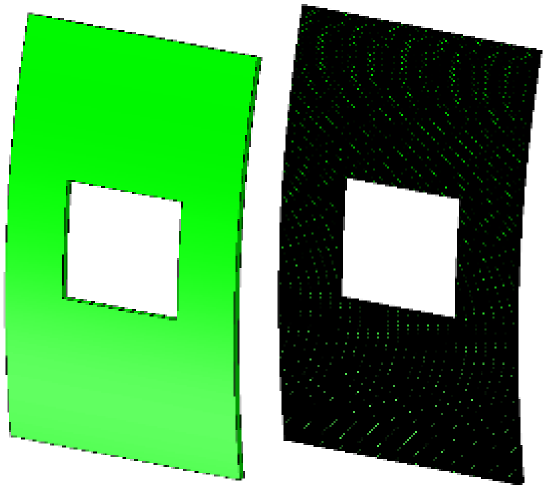

Figure D8. Outer Tank Solid Geometry (left) and Mesh (right)

Table D10. Properties of Outer Tank Solid Mesh in FE Models

	Pre-Test Model	Post-Test Model, Pre-Test Materials	Post-Test Model, Post-Test Materials
Type of Part	Deformable, Solid	Deformable, Solid	Deformable, Solid
Number of Elements	C3D8R: 927,392	C3D8R: 942,112	C3D8R:1,032,016
Approximate Mesh Size (inches)	0.055	0.055	0.058
Material(s)	A516-70 (lower) or A516-70 (upper)	A516-70 (lower) or A516-70 (upper)	A516-70 (actual)
Thickness (inches)	7/16	7/16	0.463
Approximate Part Weight (lbf)	43	44	57

Section 9. Membrane

The FE model of the DOT-113 tank car included a deformable membrane that represented the extent of the lading. The liquid and gas phases of the contents of the tank were modeled within the tank using a hydraulic and a pneumatic cavity, respectively. The material properties used to describe the behavior of the air are described in Section 5.2.4, and the material properties used to describe the water are described in Section 5.2.5. In the model, the outage volume was filled with air.

Hydraulic and pneumatic cavity modeling techniques are simplified approaches used to capture the inertial and pressure effects of the liquid lading and the pressure response of the air in the outage. The volume of the cavity is defined by the geometry within the model that encloses the limit of the fluid within each cavity. For the hydraulic cavity, the water in the tank was bounded by the shell of the tank itself and by the free surface of the membrane that represented the water-air interface. For the pneumatic cavity, the outage was bounded by the interior of the tank and free surface of the membrane that represented the water-air interface. Thus, the membrane's geometry represented the interior of the tank, using a horizontal plane to represent the boundary between the air and the water.

For each cavity defined within the membrane, the solver calculated the average pressure and temperature in each time increment during the impact. As the tank deformed from the impact, the hydraulic cavity changed shape. Because water is highly incompressible, the indentation of the tank reduced the volume of the air in the outage. The pneumatic cavity modeled the air as an ideal gas with user-defined initial pressure and temperature and a universal gas constant. Thus, as the volume of the tank was reduced, the volume of the pneumatic cavity decreased, and the pressure within the pneumatic cavity increased.

Because the pneumatic and hydraulic cavities only calculated the average pressures and temperatures within the cavity, and not the fluid pressure or temperature at discrete points throughout the volume of the lading, the cavity techniques reduced the simulation runtime compared to techniques that represented the fluid explicitly as a mesh or collection of particles. However, the average-behavior simplification may not be well suited to all conditions, such as an impact that features an extremely small outage, or a significant variation in pressure over the volume of either the air or liquid.

Both the hydraulic and pneumatic cavity models required a geometric surface to be defined within the model that defined the boundary of each cavity. Each cavity also required a reference point defined within the volume of the cavity. This reference point was used to define the interior of the cavity and was also the definition point for the initial temperatures and pressures for each cavity. As discussed in Appendix D, Section 5, the shell geometry of the tank represented the midplane geometry of the tank. If the midplane was used to define the outer surfaces of a cavity, the cavity volume would be larger than the actual tank being modeled, since the enclosed volume in the model would be based on the midplane surface and not on the inner surface of the tank. The part was defined to correspond to the inner surface of the tank's geometry.

The part was meshed using membrane elements for both the portion of the part that is in contact with the interior of the tank and the portion of the part that defined the interface between the water and the air within the tank. The membrane elements representing the inner surface of the tank were attached to the midplane surface of the inner tank using a tied constraint. Both the membrane mesh and the inner tank mesh were refined in the region of the impact zone. The geometry and mesh of the membrane are shown in Figure D9. Note that approximately half of the membrane has been removed from these views to allow for an interior view of the part. In the model, the membrane extended for the full length of the tank.

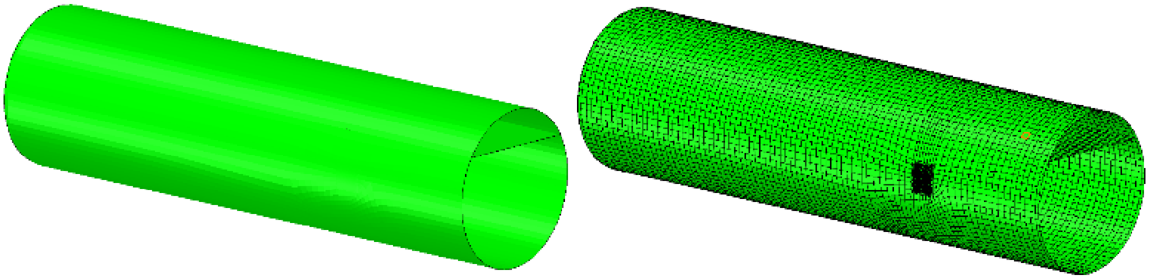

Figure D9. Membrane Geometry (left) and Mesh (right)

Because the portion of the membrane defined to divide the water and air boundary represents geometry that is not physically present within the tank, a membrane element representation was chosen to be as thin and flexible as practical within the model without causing the model to terminate due to excessively distorted membrane elements. with these constraints, a thickness of 0.05 inch was chosen for the membrane.

The height of the horizontal plane (measured from the bottom of the manway within the inner tank, as shown in Figure D10) was adjusted in a series of simulations to develop a relationship between outage height and outage volume for the inner tank. The relationship between outage height and outage volume for the DOT-113 models is shown in Figure D11. For the desired test outage of 17.6 percent, the model used an outage height of approximately 23.4 inches below the bottom of the manway inside the inner tank.

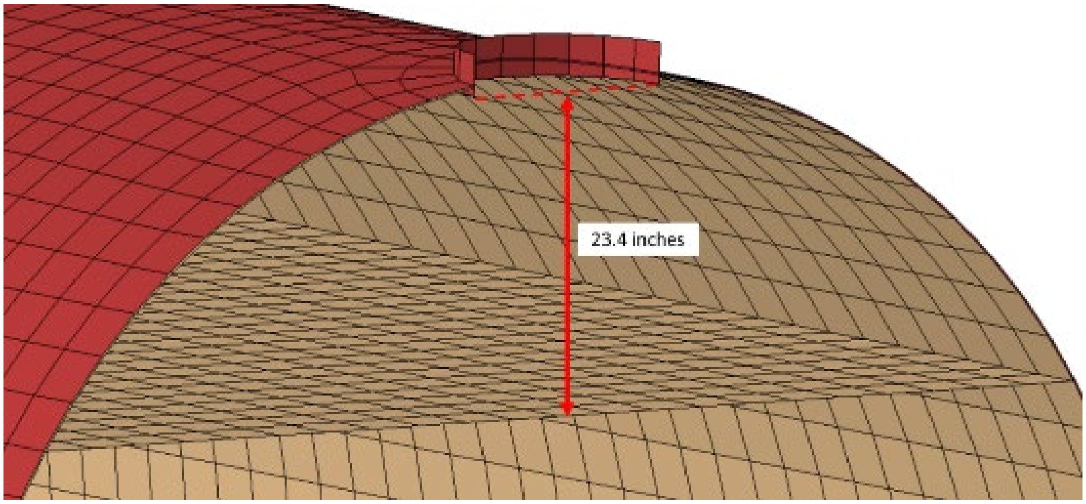

Figure D10. Reference Points for Outage Height within Membrane

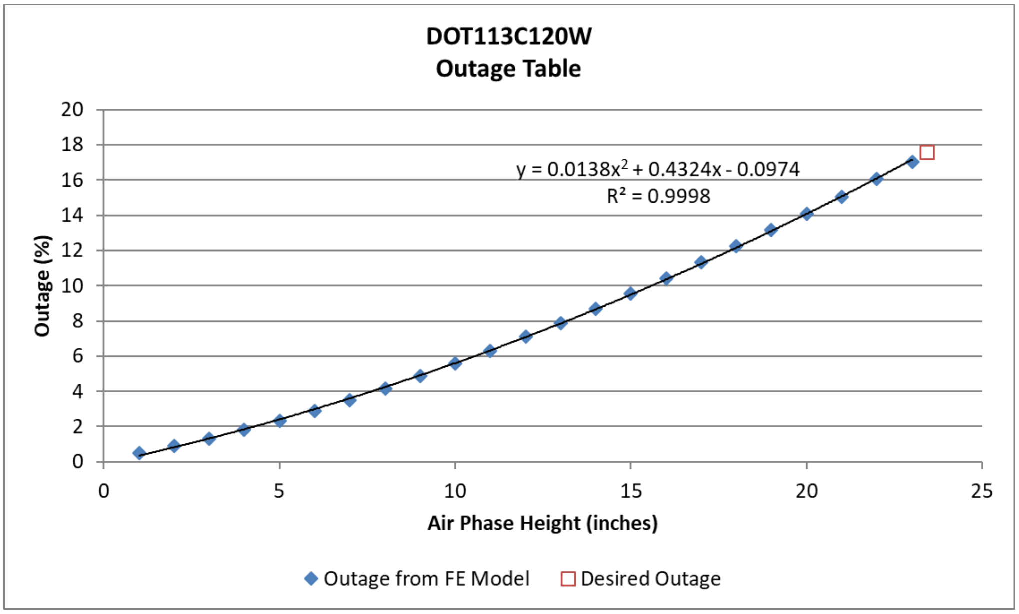

Figure D11. Outage Height Versus Outage Volume for DOT-113 Model

The membrane was also used to represent the mass of the water lading within the tank. This was done through the use of a “nonstructural mass” feature in Abaqus. The total mass of the water was calculated based on the density of water and the volume enclosed by the membrane at the desired outage level. This mass was then distributed uniformly through the membrane, including the horizontal portion of the membrane dividing the water and air phases. The properties of the membrane are summarized in Table D11 for the pre-test and post-test models.

Table D11. Properties of Membrane Mesh in FE Model

	Pre-Test Model	**Post-Test Model, Pre-Test Materials**	**Post-Test Model, Post-Test Materials**
Type of Part	Deformable, Membrane	Deformable, Membrane	Deformable, Membrane
Number of Elements	M3D4R: 23,824 M3D3: 42	M3D4R: 23,824 M3D3: 42	M3D4R: 23,828 M3D3: 34
Membrane Thickness (inches)	0.05	0.05	0.05
Material(s)	Membrane	Membrane	Membrane
Approximate Mesh Size(inches)	4	4	4
Approximate Membrane Weight (lbf)	5,350	5,350	5,350
Approximate Nonstructural Weight of Water (lbf)	227,600	227,600	227,600

Section 10. Ground

For both the pre- and post-test models, the rigid ground was modeled with all six degrees-of-freedom (DOF) fixed. The rigid ground geometry is shown in Figure D12 (left) and the rigid ground mesh is shown in Figure D12 (right). The same ground mesh and geometry was used in all FE models.

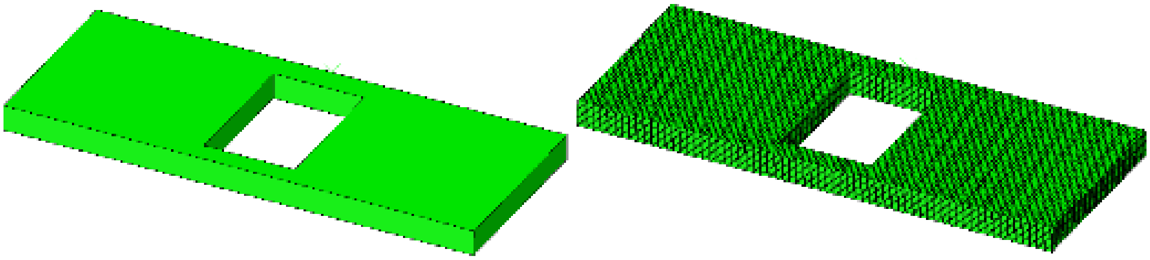

Figure D12. Rigid Ground Geometry (left) and Mesh (right)

The properties of the rigid ground mesh are summarized in Table D12.

Table D12. Properties of Ground Meshes in FE Models

Type of Part	**Rigid Body**
Number of Elements	R3D4: 11,964 RNODE3D: 9
Approximate Mesh Size	1.5 inches

Section 11. Piping

The pre- and post-test FE models included deformable shell parts representing the filling, vacuum, and drain piping. Shell elements were chosen over beam elements to allow for the pipe cross section to change in the event a pipe was crushed during the test. Some piping was constructed of carbon steel, and some piping was constructed of stainless steel. For each model, the particular material model of carbon or stainless steel used in the piping was chosen to match the respective carbon and stainless steel material used in the outer and inner tanks. The piping geometry (left) and mesh (right) are shown in Figure D13.

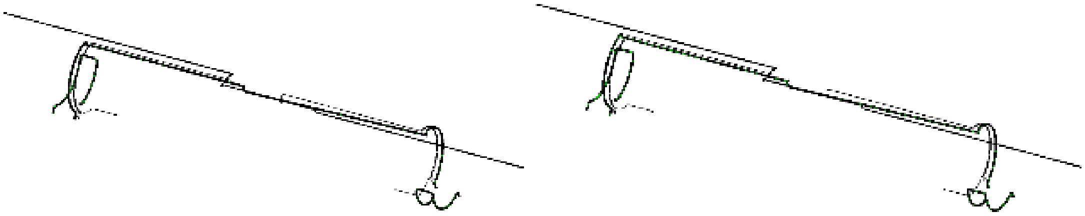

Figure D13. Piping Geometry (left) and Mesh (right)

The properties of the piping meshes used in the pre-test and post-test models are summarized in Table D13.

Table D13. Properties of Piping Meshes in FE Models

	Pre-Test Model	Post-Test Model, Pre-Test Materials	Post-Test Model, Post-Test Materials
Type of Part	Deformable, shell	Deformable, shell	Deformable, shell
Number of Elements	S4R: 32,396 S3R: 4	S4R: 32,396 S3R: 4	S4R: 32,396 S3R: 4
Approximate Mesh Size (inches)	0.3–3	0.3–3	0.3–3
Approximate Weight (lbf)	620	620	620
Material(s)	ASTM A516-70 (lower) and ASTM T304 (lower) or ASTM A516-70 (upper) and ASTM T304 (upper)	ASTM A516-70 (lower) and ASTM T304 (lower) or ASTM A516-70 (upper) and ASTM T304 (upper)	ASTM A516-70 (actual) and ASTM T304 (actual)

Section 12. Perlite (Post-Test Models Only)

The post-test FE models of the DOT-113 tank car included a deformable solid part representing the perlite between the inner and outer tanks. The development of the material properties used to define the perlite is described in Appendix F, Section 5. The perlite part introduced two new difficulties into the puncture zones using the "sandy soil" perlite material. Because the perlite was meshed with a coarse mesh but the solid patches on the outer and inner tanks featured extremely fine meshes, there was a mass mismatch between the tank nodes and the perlite nodes. Each node in the perlite part had a much larger mass associated with it than a single node in either solid patch of steel. This mass difference resulted in a localized indentation of the tank solid patches wherever a perlite part node was in contact. Separately, the perlite part experienced large distortions in the impact zone which could lead to abrupt model termination. As a means of addressing both of these issues, a rectangular cutout measuring approximately 30 inches high by 18 inches wide was made in the perlite between the two solid patches of tank elements. The perlite was removed from this area. Additionally, distortion control with a characteristic length of 0.1 was employed throughout the rest of the perlite mesh. The geometry of the perlite is shown in the top of Figure D14, and the mesh on the perlite is shown in the bottom of Figure D14. For models using the "crushable foam" material model, the cutout in the impact zone was not necessary and was filled in with perlite.

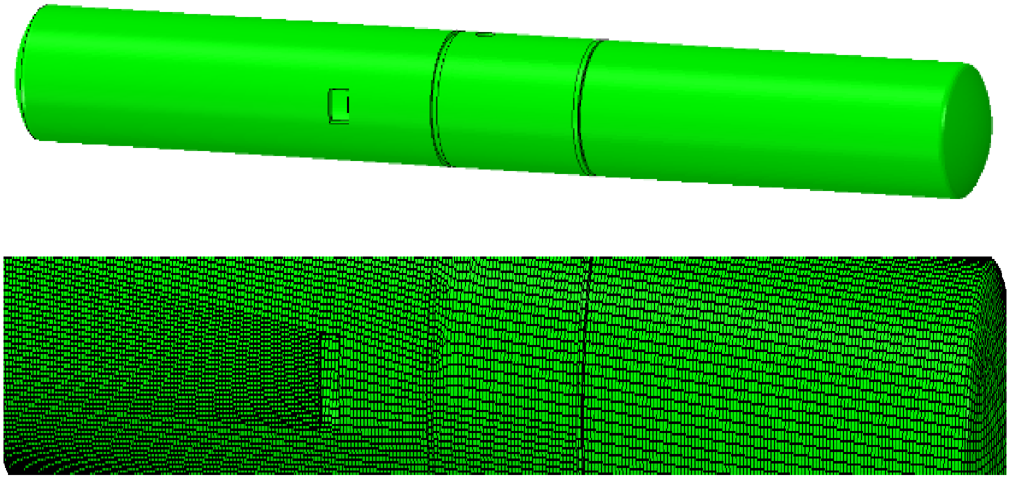

Figure D14. Perlite Geometry (top) and Mesh (bottom)

The properties of the perlite meshes are summarized in Table D14.

Table D14. Properties of Perlite Meshes

	Pre-Test Model	**Post-Test Model, Pre-Test Materials**	**Post-Test Model, Post-Test Materials, Perlite Model 1 ("Sandy Soil")**	**Post-Test Model, Post-Test Materials, Perlite Model 2 ("Crushable Foam")**
Type of Part	N/A	Deformable, solid	Deformable, solid	Deformable, solid
Number of Elements	N/A	C3D8R: 89,732	C3D8R: 78,704	C3D8R: 80,165
Approximate Mesh Size (inches)	N/A	3	3	3
Approximate Weight (lbf)	N/A	6,500	6,500	6,500
Material(s)	N/A	Drucker-Prager Perlite	Drucker-Prager Perlite	Crushable Foam Perlite

Appendix E.
Modeling Techniques Common to Pre-Test and Post-Test FE Models

This appendix describes the FE modeling techniques that were used in both the pre- and post-test models.

Section 1. Rigid Impactor Boundary Conditions

The rigid impactor was constrained against all motion except for longitudinal displacement. The impactor was stationary during the first initialization step. In the second step of the analysis, the impactor was given a constant velocity using a boundary condition that ramped up to the desired speed over the course of this acceleration step. In the third step of the analysis, the velocity boundary condition on the impactor was deactivated, leaving the impactor free to decelerate as the impact with the tank car proceeded. The pre-test models were run at various speeds, and the post-test models were run at the measured test speed of 16.7 mph.

Section 2. Rigid Wall Boundary Conditions

The rigid wall was constrained against motion in all six degrees-of-freedom (DOF).

Section 3. Rigid Ground Boundary Conditions

The ground was constrained at all six DOF.

Section 4. Inner Tank-to-Membrane Tie

The portion of the inner tank modeled using shell elements was tied to the membrane representing the interior surface of the tank using a tied constraint. Although the meshes used on both parts were similar, because they were not identical, a position tolerance of 1 inch was used.

Section 5. Outer Tank-to-Bolster Tie

The A- and B-end bolsters and cabinets were attached to the outer tank through the use of a tied constraint. A tied constraint applies to all 6 DOF between constrained nodes, representing a perfectly welded connection between nodes. A position tolerance of 5 inches was used to allow for dissimilar meshes on the tank and bolster/cabinet part. The constraint between the bolster and cabinet part at one end of the tank and the outer tank is shown in Figure E1.

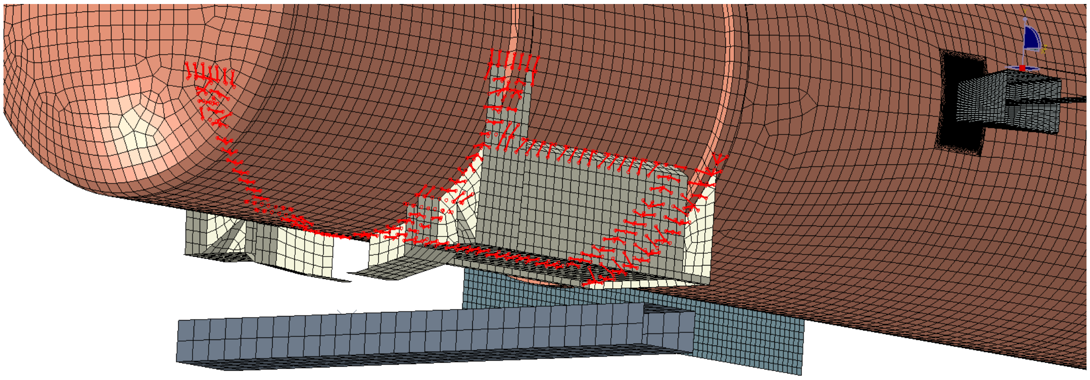

Figure E1. Tied Constraint Between Bolster/Cabinet and Outer Tank

Section 6. Piping-to-Tank Ties

A series of tied constraints were used between the piping and inner and outer tanks at each location where the piping penetrated the tank. A position tolerance of 5 inches was used on each piping-to-tank tie.

Section 7. Outer Tank-to-Skid Coupling

A beam-type multi-point constraint (MPC) was used to attach the stub sill area to the skid on each end of the tank. The rigid body reference node on the skid at each end of the tank was used as the control point of the MPC. The tank car nodes subject to this MPC included the nodes on both the bottom of the outer tank and on the bolster, where the bolster would have interfaced with the stub sill. The MPC on one end of the tank car is shown in Figure E2.

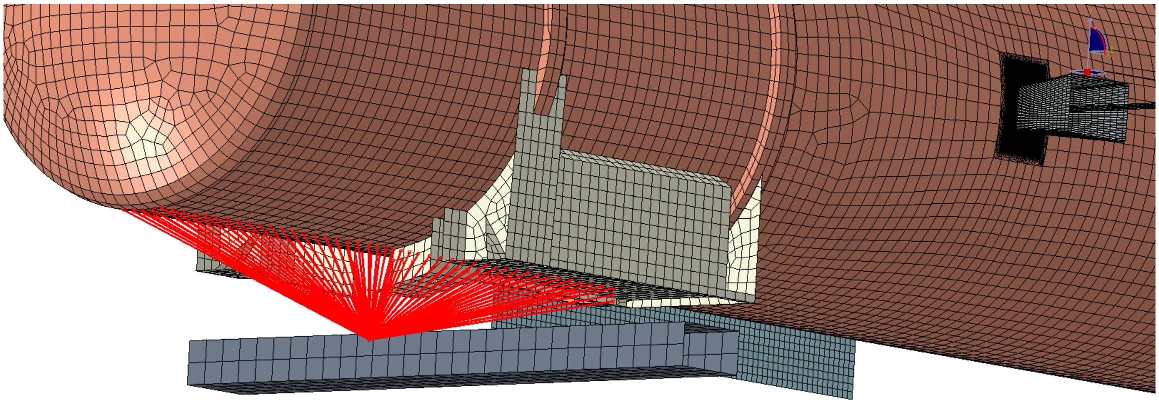

Figure E2. MPC Between End of Tank Car and Skid

Additionally, a "Cartesian" type of connector was used to constrain the motion of the skid in both the vertical and the longitudinal (i.e., direction of impactor travel) directions. A nonlinear damper was defined between the skid and ground to constrain longitudinal motion. This damper defined the longitudinal resistance force as a function of skid speed, such that the skid had to overcome an initially high force when it was moving slowly. Once this initial peak was overcome, the resistance to skid motion provided by the connector diminished as the skid moved more quickly. This simplified model was intended to approximate overcoming the effect of static friction as the skid initially began its motion, followed by a reduced resistance from kinetic friction. The longitudinal relationship used in the Cartesian connector is shown in Table E1 and plotted in Figure E3.

Table E1. Longitudinal Skid Behavior

Skid Speed ***in/s***	**Skid Force** ***kip***
-10	-0.1
-1	-38
0	0
1	38
10	0.1

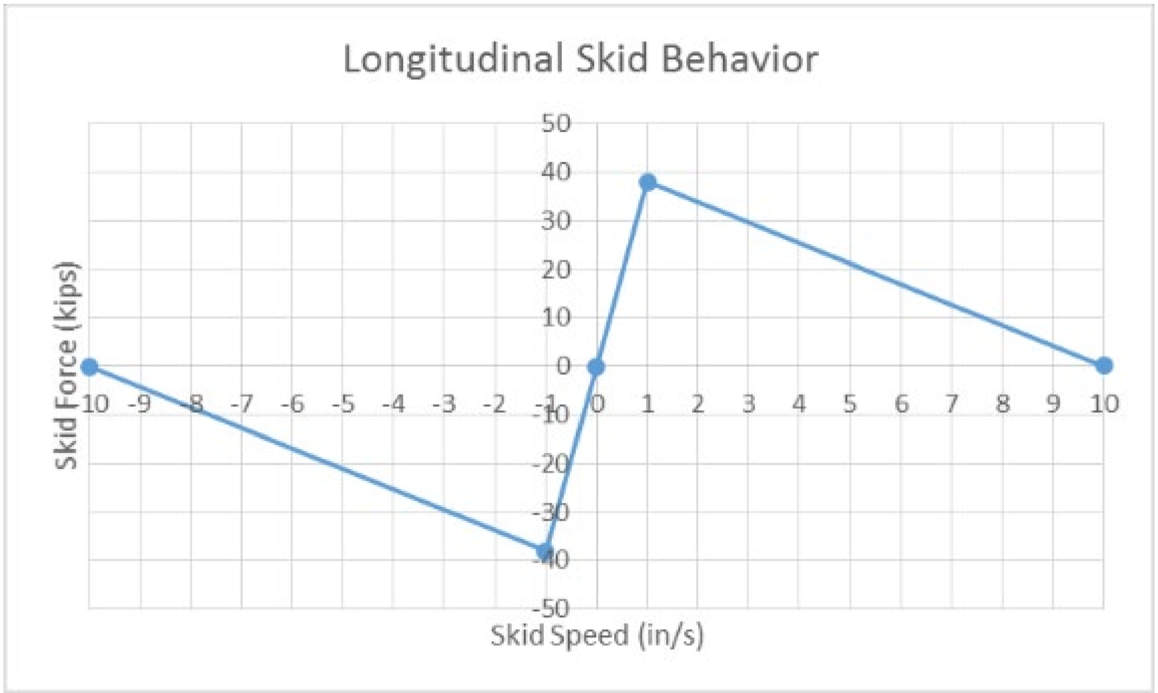

Figure E3. Longitudinal Skid Behavior

Vertically, the skid used a “Stop” behavior assigned to a connector element between the skid and the ground to limit the skid’s range of motion. The reference point of the skid was prevented from moving vertically downward, representing the ground beneath the skid. A travel limit of 100 inches was defined for vertical upward displacement. This number is arbitrary but was chosen to be larger than any anticipated vertical motion of the skid. Defining vertical stops allowing different amounts of displacement in the upward and downward directions approximated the behavior of the skid on the ground during the physical test, where the skid was prevented from moving downward due to contact with the ground but was free to lift upward if sufficient lifting forces overcame the weight resting on it.

Section 8. Inner and Outer Tanks Shell-to-solid Coupling

Shell-to-solid coupling (SSC) constraints were used on both the inner and outer tanks to attach each patch of solid elements in the vicinity of the impact zone to the rest of the shell-meshed tank. This type of constraint is necessary to ensure a smooth transition from the solid elements, which possess only translational DOF, to the shell elements, which possess translational and rotational DOF. The shell part of each tank featured a refined mesh in the vicinity of the SSC constraint. Since the shell part corresponded to the midplane thickness of the tank, the shell part was aligned with the midplane of the solid patch. The interface between solid elements and shell elements of the outer tank is shown in Figure E4. Note that this image shows the SSC region from a pre-test FE model. The post-test models used the same technique, but the dimensions of the solid patches varied from the pre-test models.

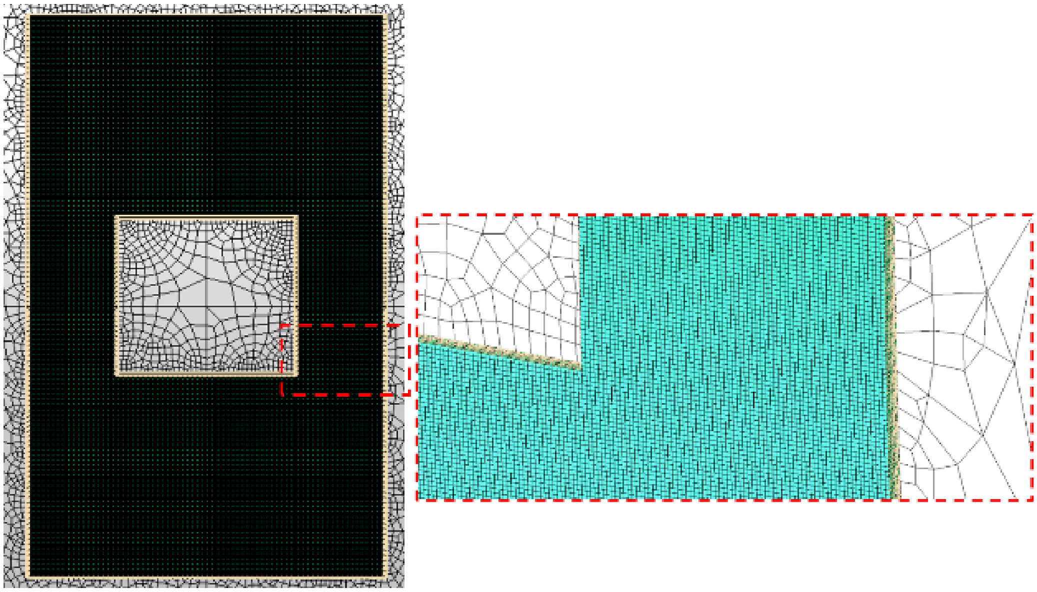

Figure E4. Entire SSC Region on Outer Tank (left) and Detailed View of Edge (right)

The interface between the inner tank's solid elements and shell elements is shown in Figure E5. Note that this image shows the SSC region from a pre-test FE model. The post-test models used the same technique, but the dimensions of the solid patches varied from the pre-test models.

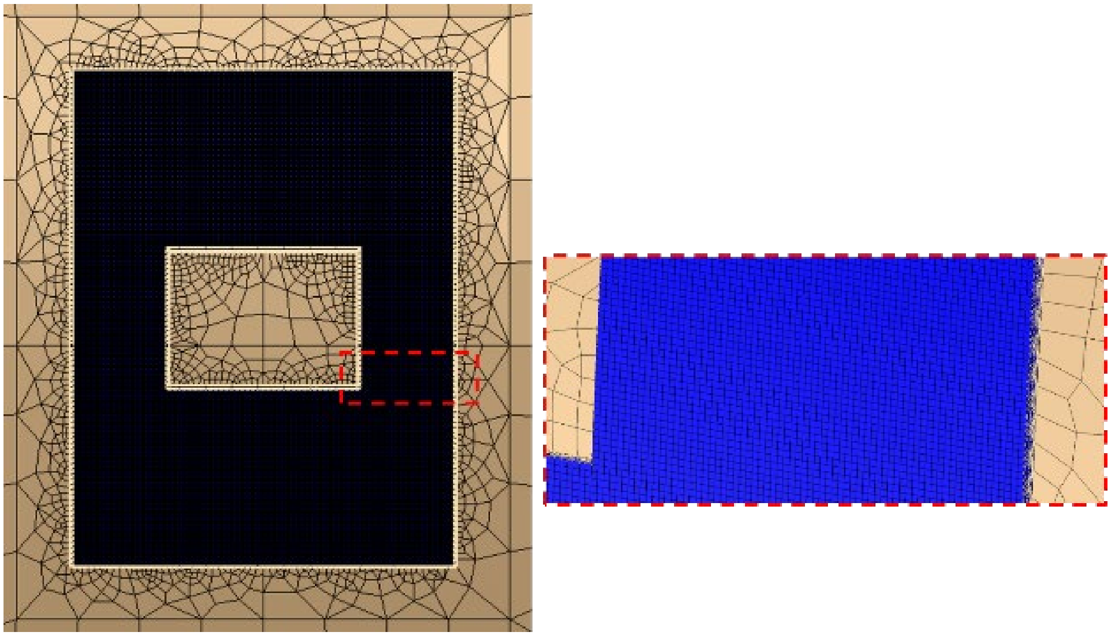

Figure E5. Entire SSC Region on Inner Tank (left) and Detailed View of Edge (right)

Section 9. Pressures, Temperatures, and Gravity

The tested DOT-113 tank car had an initial pressure above atmospheric pressure within the inner tank and had a vacuum drawn on the annular space. These two pressure conditions were intended to represent typical service conditions. The pre- and post-test FE models attempted to replicate these pressure conditions as initial conditions in the model. Initial values for lading temperature were defined in the models. Additionally, the FE models included gravity as an initial condition. Following the puncture of the outer tank, several post-test models represented the loss of vacuum using an internal pressure in the annular space.

Pressures, temperature, and gravity were applied to the model during an initial "settling" step in the simulation where the loads were allowed to stabilize prior to the time of impact. In the pre-test models, this step took 0.2 second, while in post-test models, this step was reduced to 0.1 second to cut down on runtime Internal pressure and temperature values were applied instantaneously, while gravity and external pressure used a "smooth step" amplitude curve to gradually introduce load while minimizing the dynamic overshoot associated with rapid pressurization or rapid introduction of gravity.

As the surfaces defining the boundaries of the water and gas phases deformed, the pressure was free to change in response. The water and air outage within the inner tank were each given an initial pressure of 45 psig in the pre-test models and 50 psig in the post-test models. The hydraulic cavity and pneumatic cavity definitions also require the definition of the ambient pressure outside of the cavity. A value of 12.3 psi, corresponding to atmospheric pressure [41] at Pueblo, CO, altitude of approximately 4,700 feet,[11] was used for ambient pressure. Thus, the air within the tank was initially modeled at an absolute pressure of 57.3 psi in the pre-test models and 62.3 psi in the post-test models.

The fluid cavity approach of modeling liquids and gases required the definition of an initial temperature for each cavity. Based on the average historical climate data around the planned date for the DOT-113 tank car test, an initial temperature of 39 °F was chosen for the pre-test models.[12] The post-test models used an initial temperature of 50 °F based on the actual test day temperature.

A 12.3 psi pressure load was applied to the outer surface of the outer tank. This pressure represents one atmosphere of air pressure acting on the outer tank. No pressure loads were defined in the annular space. Thus, since the outer tank had a 12.3 psi pressure acting on its outer surface and the inner tank had a 12.3 psi ambient pressure defined, the annular space was simulated as if under vacuum loading. As discussed below, these assumptions were discovered to be incorrect during preparations for Test 12.

A cross section of the DOT-113 FE model showing the absolute pressure acting on each region of the model is shown in Figure E6.

---

[11] USGS Geographic Names Information System (GNIS). *GNIS Detail – Pueblo Memorial Airport*. United States Geologic Survey.

[12] U.S. Climate Data. *Climate Pueblo – Colorado and Weather Averages Pueblo*. Daily Normals Pueblo, CO, November.

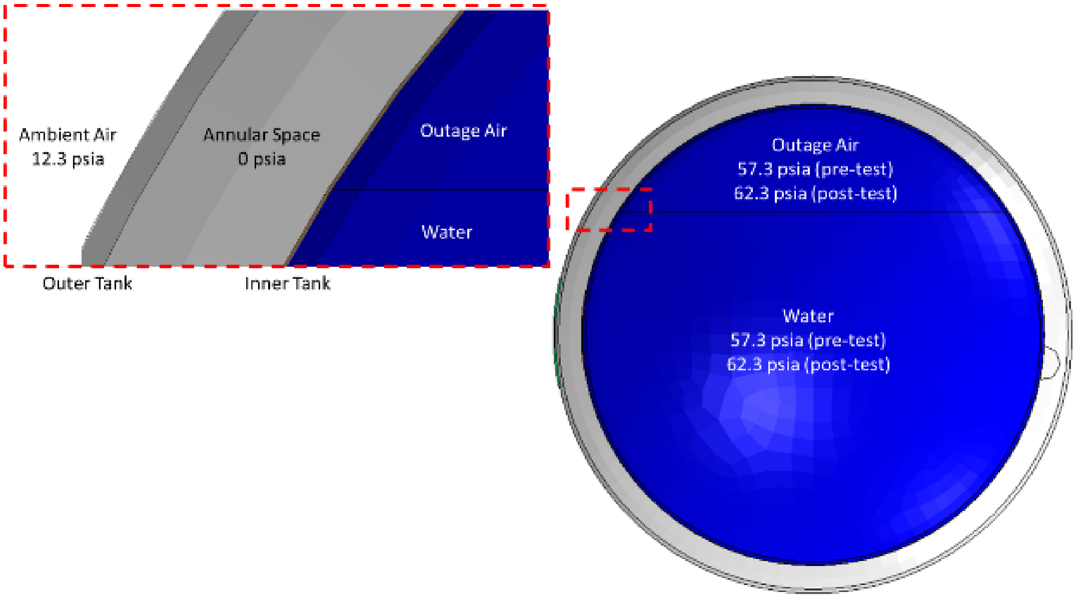

Figure E6. Pressures Acting on Different Regions of DOT-113 FE Model

For the post-test FE models using “crushable foam” perlite, the model also attempted to capture the loss of vacuum in the annular space following the tearing of the outer tank. The effect of the tearing of the outer tank was to allow air at 12.3 psia to enter the annular space and act on the inside surface of the outer tank and the outside surface of the inner tank. This behavior was manually added to the model as a prescribed pressure-time response on the two surfaces enclosing the annular space. The manual approach required an iterative approach, as the time of outer tank tearing needed to be known so the pressure-time history in the model could be defined. The simulated vacuum loss pressure-time history is shown in Figure E7. The pressure begins to rise at 0.12 second of impact time and reaches 1 atmosphere by 0.165 second.

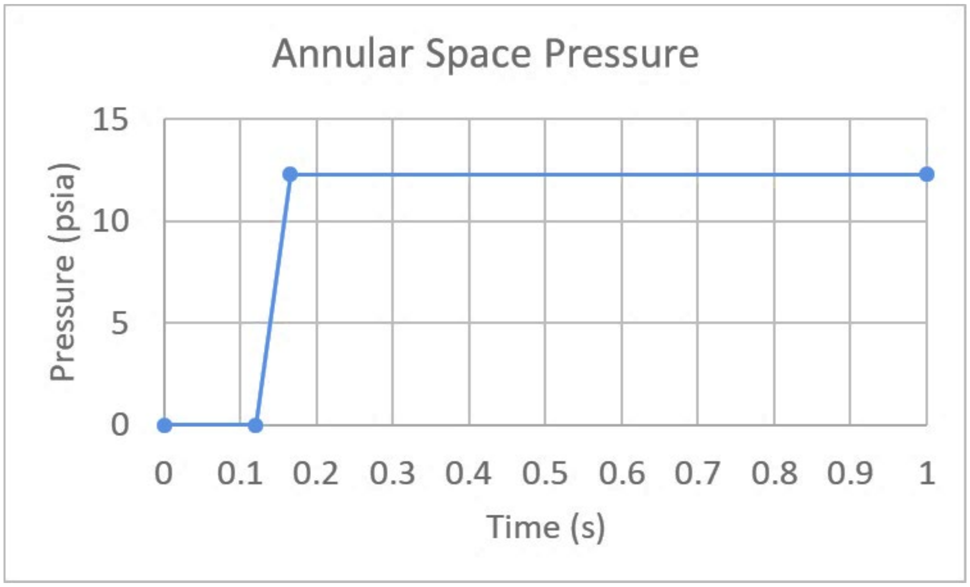

Figure E7. Prescribed Pressure-Time History for Vacuum Loss in Annular Space

During preparations for a future test of a DOT-113 surrogate tank car using LN2, the modeling team discovered that the techniques described above did not result in a zero-pressure vacuum. Rather, using an ambient pressure definition of 12.3 psia in the pneumatic and hydraulic cavities resulted in a 12.3 psi external load acting on the outer limits of the cavities which were initially co-located with the inner tank's surface. Thus, in actuality, the Test 10 models had an external pressure of 12.3 psia outside of the outer tank, 0 psia inside the outer tank, 12.3 psia outside the inner tank, and 62.3 psia inside the inner tank. This situation is not physically realistic, as the inner surface of the outer tank and the outer surface of the inner tank are both in contact with the annular space, and therefore, they must be at the same pressure.

The effects of the additional 12.3 psia load acting on the outer surface of the inner tank were investigated after the load was discovered. The post-test model was corrected to remove the 12.3 psia pressure acting on the outer surface of the inner tank. The absolute pressure in the inner tank was maintained at 62.3 psia as the gauges used in the test to read the inner tank's pressure were in communication with atmosphere. The results of this corrected model are described in Appendix C, Section 3.6.

Section 10. Mass Scaling

Variable mass scaling was used in the puncture-capable models. Because of the need for a refined mesh of solid elements in the impact zone on both the inner and outer tanks, the puncture-capable models featured a large number of very small elements. Additionally, the models were full length, as the impact zone was off center for this test. A large number of very small elements combined with a full-length model resulted in models with significant runtimes, even when executed on multiple processor workstations. Variable mass scaling was employed in the FE models to decrease the runtime without decreasing either the span or the resolution of the refined meshes. Variable mass scaling is a technique in which the user sets a target-time increment for a set of elements within the model (i.e., up to and including all elements within the model), and the Abaqus solver increases the mass of each element in an attempt to bring the minimum timestep up to the user-defined minimum. "Variable" refers to the software's ability to increase the mass of each element by a different amount, based on the material and geometry of each element. While mass scaling is an efficient way of reducing runtime without re-meshing a model, care must be exercised when using this technique with highly dynamic simulations. If an overly aggressive mass scaling is applied, the amount of artificial mass added to the model in the refined mesh area can significantly affect both the overall dynamic response as well as the puncture behavior of the model.

The material coupon models of A516-70 and T304 steels used variable mass scaling with a target-time increment of 1×10^{-6} seconds. These models also made use of an "adaptive remeshing" technique that periodically adjusts the positions of the nodes in a highly deforming mesh to attempt to prevent large element distortion.

The pre-test puncture-capable FE models used a variable mass scaling to achieve a target-time increment of 2×10^{-6} seconds over the entire model. The mass scaling factors were re-calculated for the full-scale puncture models at 50 intervals during the course of the simulation. The post-test puncture-capable FE models used a variable mass scaling to achieve a target-time increment of 9×10^{-7} seconds. This reduction in mass scaling was made to reduce the high dynamic overshoots observed in the pre-test modeling but resulted in a longer runtime for post-test models. Adaptive remeshing was not used in any of the DOT-113 impact simulations.

Section 11. Contact

A general contact definition was used in all models. The global contact used frictionless contact, except for metal-on-metal contact. A coefficient of friction of 0.3 was defined for regions of metal-on-metal contact. Furthermore, contact exclusions were defined between the shell-tank and the solid-tank patch for: 1) both the inner and outer tanks, 2) areas where piping passed through a tank, 3) areas between the piping and the perlite (in post-test models), 4) areas between the piping and the membrane, and 5) areas between the cabinet/bolster and the outer tank. A contact thickness reduction was used on the membrane mesh in the vicinity of the impact zone.

Appendix F. Material Behaviors in FE Models

Section 1. Introduction

Pre-test FE models used two A516-70 carbon steel responses for the outer tank and two T304 stainless steel responses for the cryogenic inner tank that were intended to estimate high and low ductility responses for each steel. The modeled A516-70 materials in the outer tank were based on publicly available uniaxial tensile test data [21], [29]. The modeled T304 materials in the inner tank were based on publicly available smooth and notched round bar tensile data from T304L [26] and from testing on a similar stainless steel (T316L) intended to develop failure parameters for FE model input [27].

Following the test, 2-inch gage length flat coupons were cut from both the outer and inner tanks and sent to two different test labs for mechanical testing. Post-test material models for both A516-70 and T304 used in the post-test DOT-113 impact simulations were developed using the results of the mechanical testing.

The processes used to create the pre-test and post-test material models are described in this appendix.

Section 2. Simulation of Coupon Tests

FE simulations of A516-70 and T304 uniaxial tensile coupon tests were used to calibrate the material definitions in Abaqus for the full-scale models of the DOT-113 side impact test. First, the plastic true stress-plastic equivalent strain (PEEQ) characteristic was specified. Then, the damage initiation envelope was calculated. Finally, a reasonable damage progression was empirically determined.

As the material responses developed using coupon models were planned for implementation in the full-scale DOT-113 tank car model, modeling techniques similar to the techniques planned for the side-impact analyses of the DOT-113 tank car were deliberately chosen for the coupon simulations. The same solver (Abaqus/Explicit), element types (C3D8R) and mesh sizes (approximately 0.05-inch) were chosen for the coupon models and the DOT-113 impact models. This was done to attempt to minimize the uncertainty associated with using one set of modeling techniques to calibrate a material response while using a different set of techniques to model a puncture in the full-scale tank car impact simulation. If the tank car model was run using a different solver or different mesh density, it would be expected that the material behaviors would need to be recalibrated using coupon simulations that used similar solvers and mesh densities.

For all tensile coupon simulations, a soft (1 x 10^{-6} lbf/in.) discrete spring was included in the model to represent an extensometer attached to the ends of the gage. This spring was a surrogate for an extensometer in the model and simplified the process of requesting the length change for the model's gage section.

The flat DB coupon models used for the A516-70 pre-test and post-test calibrations is shown in Figure F1. The pre-test A516-70 coupon geometry had a 2-inch gage length, 0.5-inch width, and 0.5-inch thickness. The post-test A516-70 coupon model was updated based on the measurements of the average thickness (~0.463 inch) of the coupons cut from the outer tank of the tested DOT-113, and the three planes of symmetry that were added to reduce the number of elements in the model.

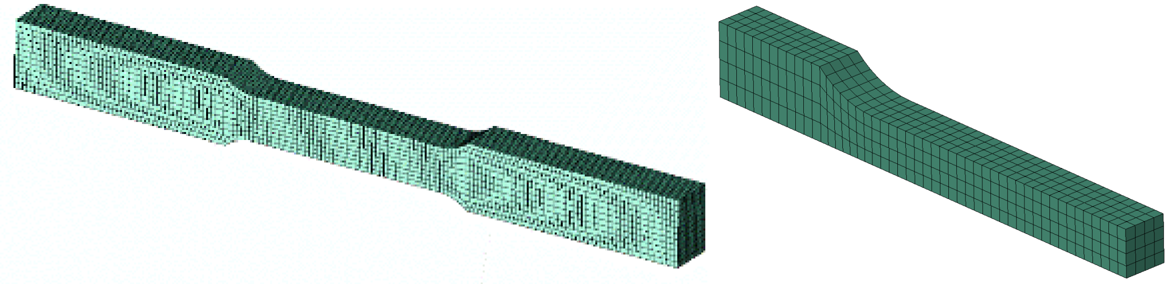

Figure F1. FE Model of A516-70 Steel Pre-Test (left) and Post-Test (right) Flat DB Tensile Coupons (0.055-inch Mesh Size; Pre-Test no symmetry, Post-Test 1/8 symmetry)

The pre-test and post-test tensile coupon models used for the T304 stainless steel calibrations are shown in Figure F2. The pre-test T304 coupon was a smooth round bar with a 2-inch gage length and 0.5-inch diameter. The post-test T304 coupon was updated to a flat DB geometry as this was the geometry used by the testing labs. The post-test DB dimensions were based on measurements from the coupons cut from the inner tank, having a 2-inch gage length, 0.5-inch width, and 0.281-inch thickness. Both geometries had a nominal mesh size of 0.05 inches and three planes of symmetry.

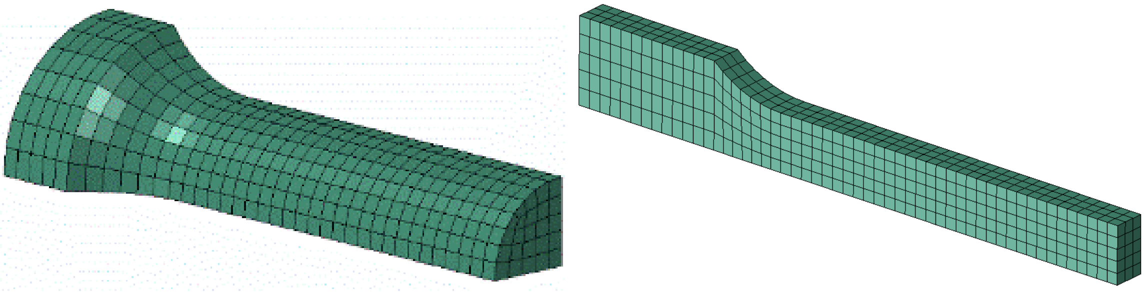

Figure F2. FE Model of T304 Stainless Steel Pre-Test (Left) and Post-Test (Right) Tensile Coupons (0.05-inch Mesh Size; 1/8 symmetry)

Previous simulations of puncture tests of tank cars used mesh sizes in the coupon and tank shell that were typically approximately 0.085 inch [11] [12] [13]. In the full-scale puncture model of the DOT-113 tank car, the 7/16-inch (0.4375) thick A516-70 outer tank shell was meshed with eight elements across the thickness, corresponding to a mesh size of approximately 0.055 inch (refer to Appendix D, Section 8). The 0.25-inch thick T304 inner tank shell was meshed with five elements across the thickness, corresponding to a mesh size of 0.05 inch (refer to Appendix D, Section 6).

Section 2.1 Plastic Hardening

Abaqus requires metal plasticity to be defined in terms of true stress and PEEQ. The plastic behavior of each steel was input to the Abaqus model as isotropic hardening using a discrete number of data points. True stress and PEEQ can be calculated from nominal stress-strain tensile coupon data according to Equation F1.

$$\sigma_{true} = \sigma_{nom} \cdot (1 + \varepsilon_{nom})$$
$$\bar{\varepsilon}^{pl} = \ln(1 + \varepsilon_{nom}) - \frac{\sigma_{true}}{E}$$

σ_{nom} nominal (engineering) stress
ε_{nom} nominal (engineering) strain
σ_{true} true stress
$\bar{\varepsilon}^{pl}$ plastic equivalent strain (PEEQ)

Equation F1. True Stress-strain Transformation

Because necking dominates the nominal stress-strain response of the tensile coupon characteristic after the max force is achieved, the true stress-PEEQ relationship was extrapolated for strains beyond the strain at max force using the inverse method. The inverse method involves iteratively adjusting the true stress-PEEQ relationship until agreement is achieved between the tensile coupon simulation and test results. In this study, two methods were used to describe the true stress-PEEQ relationships for A516-70 and T304, respectively.

The pre-test A516-70 plasticity model was calibrated by manually specifying points along the true stress-PEEQ uniaxial tensile data from zero PEEQ (at YS) to the PEEQ at max force (at UTS) and then estimating a linear extrapolation for true stress at high strains. The slope of the linear extrapolation was iteratively adjusted by rerunning the coupon FE model until the nominal stress-strain output from the model was in agreement with the test results, up to the point of crack initiation. The resulting true stress-PEEQ relationship is shown in Figure F9 for the pre-test material behavior estimates. Linear extrapolation of the true stress at high strains has been used previously in side impact tests [10] [11] [12] [13] [21].

Paredes et al. [42] applied a Mixed Swift-Voce Law hardening expression to extrapolate true stress at high strains for TC128-B. The Mixed Swift-Voce Law is a conjunction of the Swift (power) Law [43] and the Voce (exponential/saturation) Law [44] that each describe plastic hardening. The Mixed Swift-Voce Law is a function of PEEQ and is formed by combining the Swift term (σ_t^{Swift}) with the Voce term (σ_t^{Voce}) using a weighting factor (α) as shown in Equation F2.

$$\sigma_t^{Swift}(\bar{\varepsilon}^{pl}) = A \cdot (\varepsilon_0 + \bar{\varepsilon}^{pl})^n$$
$$\sigma_t^{Voce}(\bar{\varepsilon}^{pl}) = K_0 + Q \cdot \left(1 - e^{-\beta \bar{\varepsilon}^{pl}}\right)$$
$$\sigma_t^{Mixed} = \alpha \cdot \sigma_t^{Swift} + (1 - \alpha)\sigma_t^{Voce}$$

Equation F2. Swift (Power), Voce (Exponential/Saturation), and Mixed Swift-Voce Laws for Plastic Hardening

The Swift-Voce constants are calibrated using the calculated true stress-PEEQ (see Equation F1) from a tensile test and performing a least squares regression fit on the Swift and Voce equations. The Swift and Voce expressions are independently fit on the test data from a PEEQ close to zero to the PEEQ at max force because the plastic behavior of the coupon is not dominated by necking for that range of strains. After the constants for the Swift and Voce expressions are independently determined by least-squares regression, a FE model of the uniaxial tensile test is iteratively executed while varying α until the nominal stress-strain output from the model is in agreement with the test results up to the point of crack initiation.

More recent side impact tests [14] [25] used a Swift-Voce extrapolation for true-stress at high strains because the post-necking behavior of the coupon was better represented in the tensile coupon FE models. The post-test A516-70 true stress-PEEQ strain behavior shown in Figure F12 used the Swift-Voce Law for extrapolation. For T304 stainless steel, the pre-test (Figure F15) and post-test true stress-PEEQ strain behaviors also used the Swift-Voce Law for extrapolation.

For both the linear extrapolation and the Swift-Voce Law, a single parameter was varied while iteratively running the coupon simulations to achieve agreement with the test results via the inverse method. The parameter used for the A516-70 models was the linear slope of the extrapolated true stress-PEEQ curve for high PEEQs. The parameter used for the T304 models was the weight factor α which determined the amount of hardening at high strains, i.e., a high value for α resulted in more plastic hardening at high strains.

Ductile damage initiation and progression can be used in Abaqus to simulate the crack initiation and propagation experienced in an actual coupon test. The process of calibrating a damage initiation envelope and then empirically determining a suitable damage progression value is explained in the following sections. The fracture locus used for A516-70 carbon steel is discussed in Appendix F, Section 2.2, and the fracture locus used for T304 stainless steel is discussed in Appendix F, Section 2.3.

Section 2.2. Bao-Wierzbicki (B-W) Damage Initiation

Figure F3 shows a schematic of the B-W triaxiality (η) based damage initiation envelope [23] which was used in the A516-70 material failure models. "Triaxiality" is defined as the ratio of the hydrostatic stress (σ_H) divided by the von Mises stress (σ_v) as shown in Equation F3.

$$\eta = \frac{\sigma_H}{\sigma_v}$$

Equation F3. Stress Triaxiality

The B-W envelope consists of three regions: I – Ductile Fracture, II – Mixed Fracture, and III – Shear Fracture.

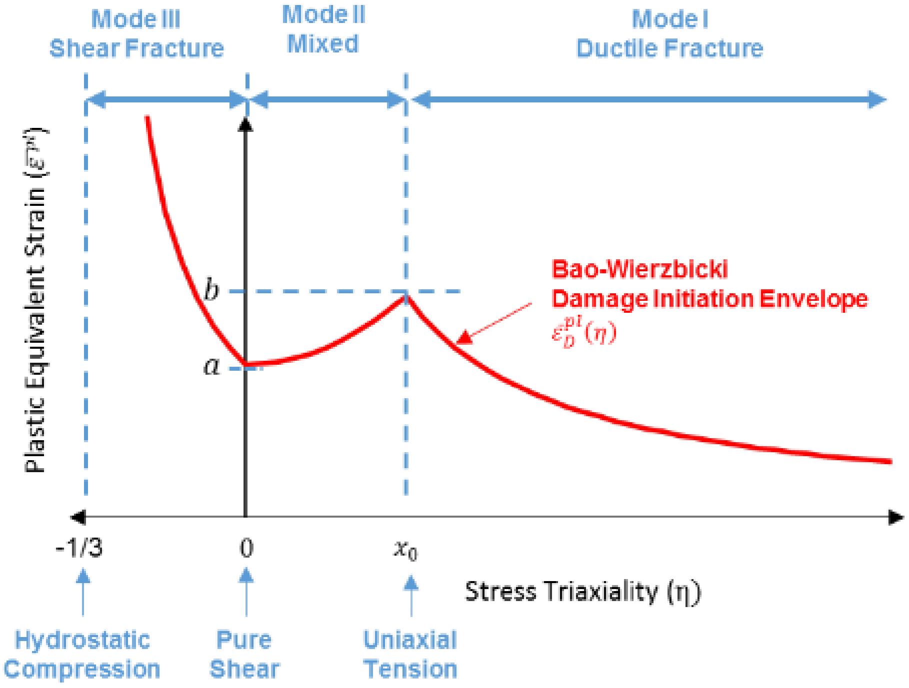

Figure F3. Schematic of Bao-Wierzbicki Damage Initiation Envelope

When $\eta < 0$ the element is in a state of compression and when $\eta > 0$ the element is in a state of tension, a triaxiality of $\eta = -1/3$ corresponds to a stress state of hydrostatic compression and $\eta = 0$ corresponds to pure shear. The cusp of the B-W fracture locus is located at the average triaxiality on the fracture surface of a smooth round bar (SRB) specimen under uniaxial tension at $\eta = x_0$ and is typically close to a value of 0.4.

Three constants (a, b, x_0) govern the shape of the B-W fracture locus (Equation F4) and are all calibrated based on coupon test results. The effective plastic strain to fracture in pure shear (a) corresponds to $\eta = 0$ (pure shear). The effective plastic strain to fracture in uniaxial tension (b) corresponds to the cusp of the B-W fracture locus when $\eta = x_0$.

$$\bar{\varepsilon}_D^{pl}(\eta) = \begin{cases} \dfrac{a}{1 + 3 \cdot \eta} & -\dfrac{1}{3} \leq \eta \leq 0 \\ (b - a) \cdot \left(\dfrac{\eta}{x_0}\right)^2 + a & 0 \leq \eta \leq x_0 \\ \dfrac{b \cdot x_0}{\eta} & x_0 \leq \eta \end{cases}$$

Equation F4. B-W Damage Initiation Envelope

The complete damage initiation envelope can be developed through a series of mechanical tests on 11 unique specimen geometries intended to cover a wide range of stress triaxialities. However, Lee and Wierzbicki [30] [31] developed a simplified "quick calibration" approach for industrial use that requires only one uniaxial tensile geometry to estimate the entire failure envelope. According to Lee, the quick calibration approach is intended to be within 10 percent agreement with a failure envelope that was developed using the complete set of 11 specimens.

The only specimen geometry that is required to calculate the B-W fracture locus using the quick calibration method is a tensile coupon. In the US, a tensile test is typically performed in accordance with ASTM E8[13] to characterize the engineering stress-strain behaviors of a metallic specimen, including the YS, UTS, EB, and reduction in area (RA). ASTM E8 includes prescribed geometries for both SRB and flat rectangular coupons (also known as DB) and contains limits on the thickness of steel plates and sheets for which each coupon geometry is applicable. The quick calibration procedure using the results of SRB tensile tests allows the calculation of the B-W fracture locus constants (a, b, x_0) by measuring the initial radius (a_0), final radius (a_f), displacement at max force (δ_d), and initial gauge length (L_0) of the tensile coupon. For flat tensile coupons, the calculation of the B-W fracture locus constants is performed by measuring initial thickness (t_0) and final thickness (t_f) instead of initial and final radius. As seen in Equation F5, the quick calibration procedure also uses the hardening exponent (n) which is used to describe the plastic hardening behavior of metals by the power law. The hardening exponent is estimated as a function of engineering strain at max force. Additional discussion of the differences between calibration using an SRB or a DB coupon can be found in [45].

SRB	**DB**
$n = \ln\left(1 + \frac{\delta_d}{L_0}\right)$	$n = \ln\left(1 + \frac{\delta_d}{L_0}\right)$
$b = 2 \cdot \ln\frac{a_o}{a_f}$	$b = \frac{2}{\sqrt{3}} \cdot \ln\frac{t_o}{t_f} + \frac{2 \cdot n}{\sqrt{3}} \cdot \left(\sqrt{3} - 1\right)$
$x_0 = \frac{1}{3} + \frac{0.22}{b} \cdot (b - n)^{1.8}$	$x_0 = \frac{1}{\sqrt{3}} - \frac{2 \cdot n}{3 \cdot b} \cdot \left(\sqrt{3} - 1\right)$
$a = b \cdot \left(\frac{\sqrt{3}}{2}\right)^{1/n}$	$a = b \cdot \left(\frac{\sqrt{3}}{2}\right)^{1/n}$

Equation F5. Quick Calibration Procedure for Smooth Round Bar (SRB) (Left) and Flat DB (Right) Uniaxial Tensile Coupons

For ductile metals in Abaqus, the damage threshold of an integration point is reached when the ductile criterion (ω_D) reaches a value of 1. According to Equation F6, ω_D is calculated by integrating the change in ε^{pl} by effective strain to fracture as a function of triaxiality, i.e., the B-W fracture locus or $\varepsilon^{pl}{}_D(\eta)$ from Equation F4.

$$\omega_D = \int \frac{d\varepsilon^{pl}}{\varepsilon_D^{pl}(\eta)}$$

Equation F6. Calculation of Ductile Criterion (DUCTCRT) in Abaqus

---

[13] ASTM E8 / E8M-16ae1, Standard Test Methods for Tension Testing of Metallic Materials, ASTM International, West Conshohocken, PA, 2016.

After ω_D reaches a value of 1 the stiffness of the element is degraded according to the damage progression in the material definition., Exponential displacement-based damage progression values were calibrated for each material. Previous puncture simulations, however, used linear energy-based damage progressions [11] [12] [13].

Section 2.3. MMC Damage Initiation

Bai and Wierzbicki [46] extended the original Mohr-Coulomb criterion, which is widely used in soil mechanics, to ductile fracture in metals in order to capture the dependence on the third invariant of the deviatoric stress tensor. As shown in Figure F4, the MMC fracture surface is a function of stress triaxiality and normalized Lode angle ($\bar{\theta}$). In comparison with the B-W fracture locus, the MMC fracture locus covers a larger range of possible three-dimensional stress states since it is more than a function of triaxiality.

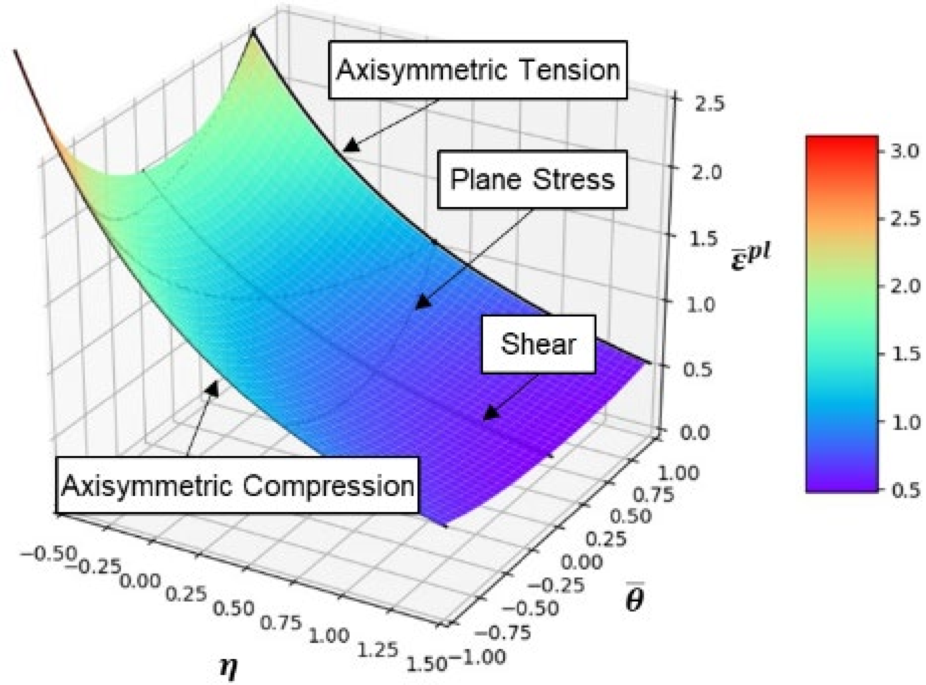

Figure F4. MMC Fracture Surface for Stainless Steel with Annotations of Various Stress States

While η is related to the first invariant (I_1) of the stress tensor ($\boldsymbol{\sigma}$) and the second invariant (J_2) of the deviatoric stress tensor (**S**), $\bar{\theta}$ is related to J_2 and the third invariant (J_3) of **S**. The relationship between the Lode angle (θ), normalized third invariant (ξ), and $\bar{\theta}$ is given in Equation F7.

$$\theta = \frac{1}{3}\cos^{-1}(\xi) = \frac{1}{3}\cos^{-1}\left[\left(\frac{J_3}{\sqrt{3J_2}}\right)^3\right]$$

$$\xi = \cos(3\theta) = \left(\frac{J_3}{\sqrt{3J_2}}\right)^3$$

$$\bar{\theta} = 1 - \frac{6\theta}{\pi} = 1 - \frac{2}{\pi}\arccos(\xi)$$

Equation F7. Lode Angle (θ), Normalized Third Invariant (ξ), and Normalized Lode Angle ($\bar{\theta}$)

Wierzbicki and Xue [47] derived an expression (see Equation F8) to relate η and $\bar{\theta}$ for plane stress states. Plane stress corresponds to J_3 and subsequently $\bar{\theta}$ and ξ being equal to zero.

$$\xi = \cos\left[\frac{\pi}{2}(1-\bar{\theta})\right] = -\frac{27}{2}\eta\left(\eta^2 - \frac{1}{3}\right)$$

Equation F8. Plane Stress Relationship between Triaxiality (η) and Normalized Lode Angle ($\bar{\theta}$) or Normalized Third Invariant (ξ)

Figure F5 shows a plot of this expression (corresponding to the dark curve) along with idealizations of different stress states in terms of stress triaxiality and Lode angle parameters. Axisymmetric tension $(J_3 = +\sqrt{3J_2})$ and compression $(J_3 = -\sqrt{3J_2})$ correspond to $\bar{\theta}$ being equal to plus and minus one respectively (shown in the blue solid lines). Based on this figure, a physical interpretation of $\bar{\theta}$ is that it is capable of discriminating between axisymmetric and plane stress states.

Figure F5 is a plot of $\bar{\theta}$ versus η which shows the different stress states of plane strain, plane stress, axisymmetric tension, and axisymmetric compression along with the initial stress states of the various specimens which can be used to estimate an MMC damage initiation envelope.

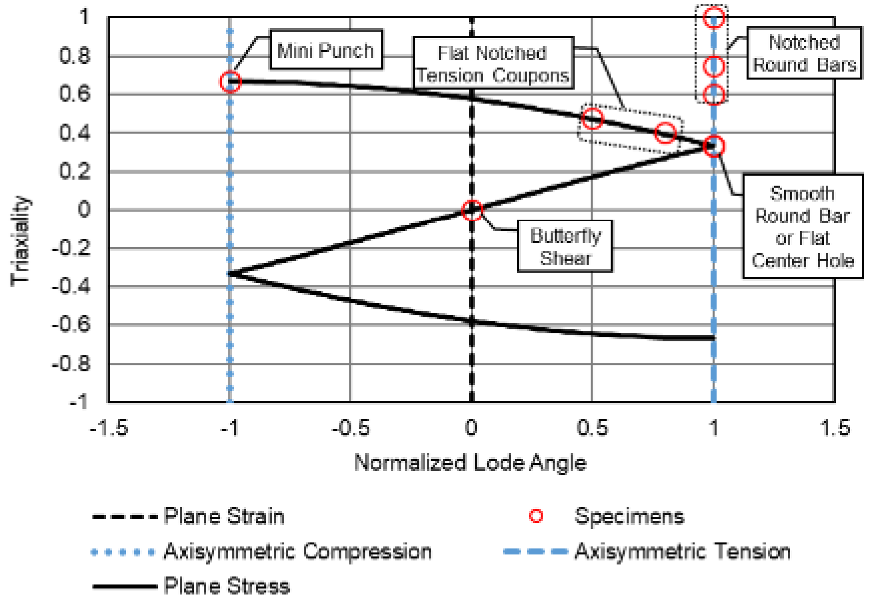

Figure F5. Schematic of Initial Stress State in Terms of Stress Triaxiality (η) and Normalized Lode Angle ($\bar{\theta}$)

Figure F6 shows FE geometries for the flat tensile coupons used in this study to fit the MMC fracture surface. Paredes et al. describe these specimens in more detail in their MMC surface calibration for TC128-B steel [42]. The notched tensile specimens have a 20 mm radius (NT20) and a 6.67 mm radius (NT6.67). The flat center hole tensile specimen has an 8 mm diameter (CH8). The specimens have a C3D8R mesh size of approximately 200 μm in the region of fracture. Three planes of symmetry were used to reduce the total number of elements.

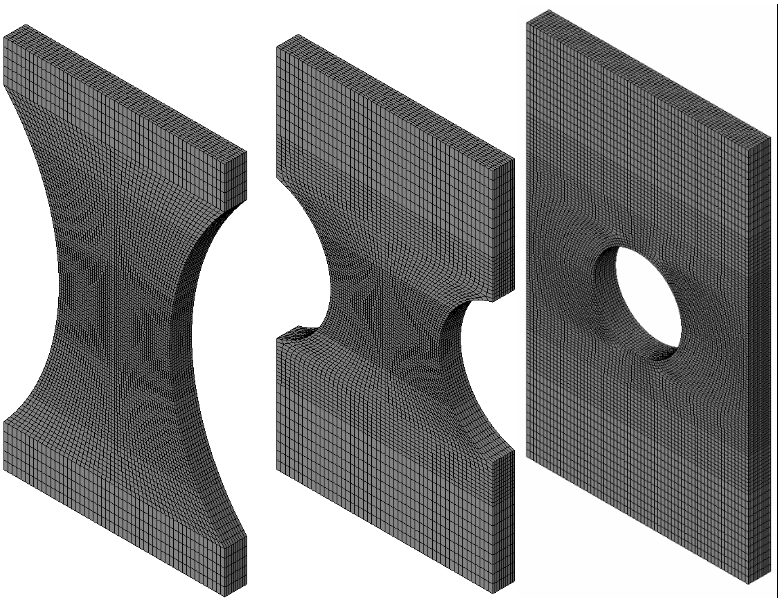

Figure F6. Flat Notched 20 mm (left), Notched 6.67 mm (center), and Center Hole 8 mm (right) FE Models Used for MMC Fracture Surface Calibration (200 μm Mesh; 1/8 Symmetry Not Shown)

Figure F7 shows the notched round bar (NRB) specimens used in this study. Kirkpatrick et al. describe these specimens in more detail in their B-W curve calibration for T304L steel [26]. The NRB specimens have notch radii of 0.20, 0.10, and 0.05 inch. The specimens have a C3D8R mesh size of approximately 0.0125 inch with three planes of symmetry to reduce the total number of elements.

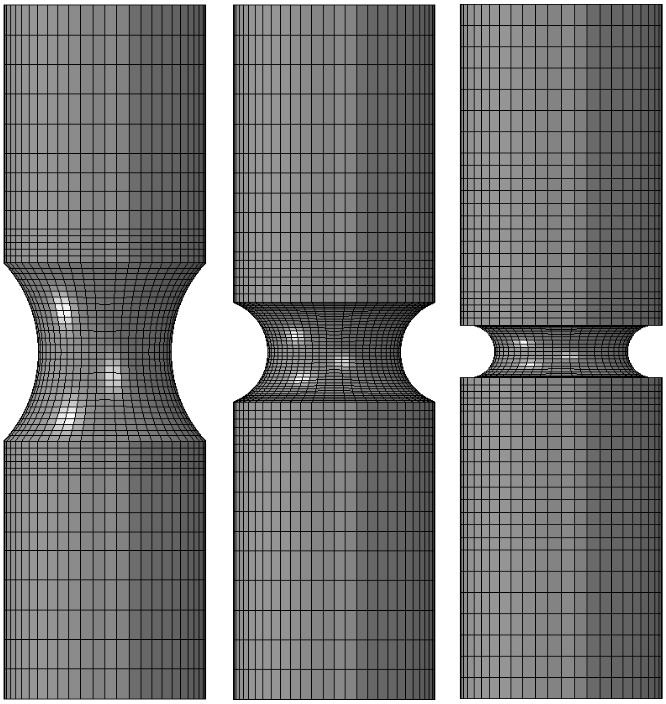

Figure F7. Notched Round Bar Geometries with 0.20-inch (left), 0.10-inch (center), and 0.05-inch (right) Radii (0.0125-inch Mesh; 1/8 Symmetry Not Shown)

Figure F8 shows the mini-punch (PU) specimen used in this study. Paredes et al. describe this specimen in more detail in their MMC surface calibration for TC128-B steel [42]. The PU specimen has a thickness of 1 mm, and the indenter has a radius of 0.25 inch. The PU specimen has a C3D8R mesh size of approximately 200 μm with two planes of symmetry to reduce the total number of elements.

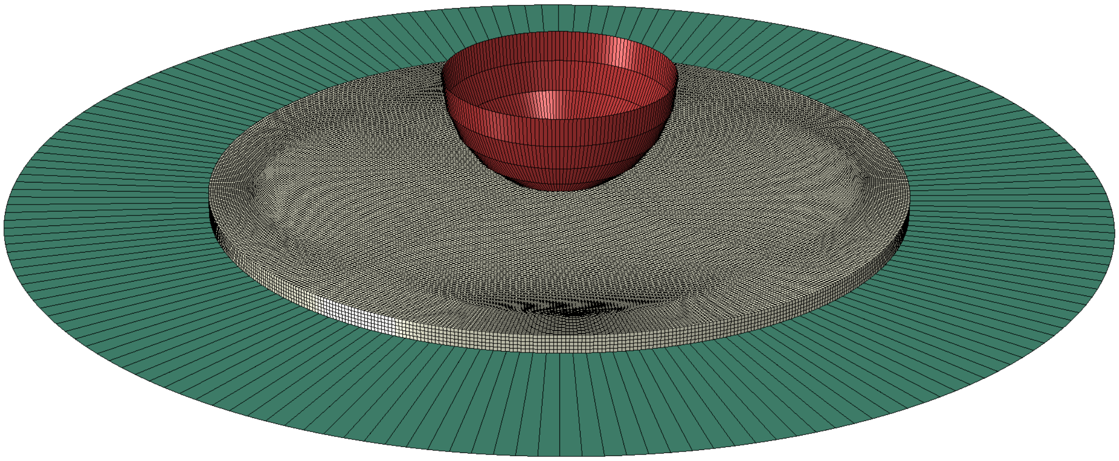

Figure F8. Mini-punch Geometry with Rigid Analytic Indenter (Red) and Plate (Green) (200 μm Mesh; 1/4 Symmetry Not Shown)

Equation F9 gives the expression of the MMC fracture surface. For proportional loading, the fracture surface is asymmetric in terms of $\bar{\theta}$ and undergoes exponential decay with respect to η (see Figure F3).

$$\bar{\varepsilon}_D^{pl}(\eta,\bar{\theta}) = \left\{\frac{A}{c_2}\left[c_3 + \frac{\sqrt{3}}{2-\sqrt{3}}(1-c_3)\left(\sec\left(\frac{\bar{\theta}\pi}{6}\right)-1\right)\right]\left[\sqrt{\frac{1+{c_1}^2}{3}}\cos\left(\frac{\bar{\theta}\pi}{6}\right)+c_1\left(\eta+\frac{1}{3}\sin\left(\frac{\bar{\theta}\pi}{6}\right)\right)\right]\right\}^{-1/n}$$

Equation F9. MMC Failure Surface [46]

Three constants (c_1, c_2, c_3) unique to the MMC model are calibrated from the mechanical tests denoted in Figure F5. The constants A and n are from the Swift Law hardening expression which relates the material's true stress-PEEQ behavior as described Appendix F, Section 2.1.

Section 3. A516-70 Steel Material Behavior

Three characterizations of A516-70 steel were developed over the course of this study. Prior to the test, high and low estimates of the ductility of A516-70 were developed based on publicly available tensile coupon data from multiple sources. After the test, a third (post-test) characterization was developed based on the measured properties of the A516-70 steel from the tested DOT-113 tank car. For comparison, the results of tensile coupon simulations with the different A516-70 material models are summarized in Table F1. The post-test material characterization revealed mechanical properties that did not meet the minimum YS or UTS for A516-70 but exceeded the EB of both the A516-70 specification and the high-ductility pre-test material estimate.

Table F1. Summary of Mechanical Properties of A516-70 from 2-inch Gage DB FE Models

Name	**YS** *ksi*	**UTS** *ksi*	**EB** *%*
Pre-test High Ductility	50	72	37
Pre-test Low Ductility	54	73	29
Post-test Actual	36	54	43[14]

Section 3.1. A516-70 Pre-Test Characterization

Because the mechanical properties of the A516-70 steel in the outer tank of the DOT-113 tank car were unknown prior to the test, material models with upper and lower pre-test estimates of ductility were developed using publicly available tensile test data. Values for the YS, UTS, EB in 2 inches, and EB in 8 inches are summarized below in Table F2. The minimum properties are included in this table both with and without the minimum properties required by the specification included in consideration of the minimum. As no published results indicated properties below the

---

[14] One sample has been excluded from this average as the reported EB in the tensile test (63%) was an outlier compared to all other measurements.

minimum requirements, the specification values are the absolute minimum values for YS, UTS, and EB. The material data summarized in Table F2 were compiled from numerous sources.[15]

Table F2. Material Properties from Published Sources for A516-70

Property	Min (including specification)	Min (excluding specification)	Average	Max
YS (*ksi*)	38	39.9	51.7	75.8
UTS (*ksi*)	70	70.9	77.2	86.4
EB in 2 inches (%)	21	28	34.1	40
EB in 8 inches (%)	17	17	23.9	30

The shapes of the pre-test A516-70 plastic stress-strain responses were developed based on stress-strain curves published in two of the identified sources of material data [21] [29]. The sources for high and low ductility tensile test results for A516-70 had similar YS and UTS results resulting in the calibrated plastic material behavior inputs being similar, as shown in Figure F9 and Table F3.

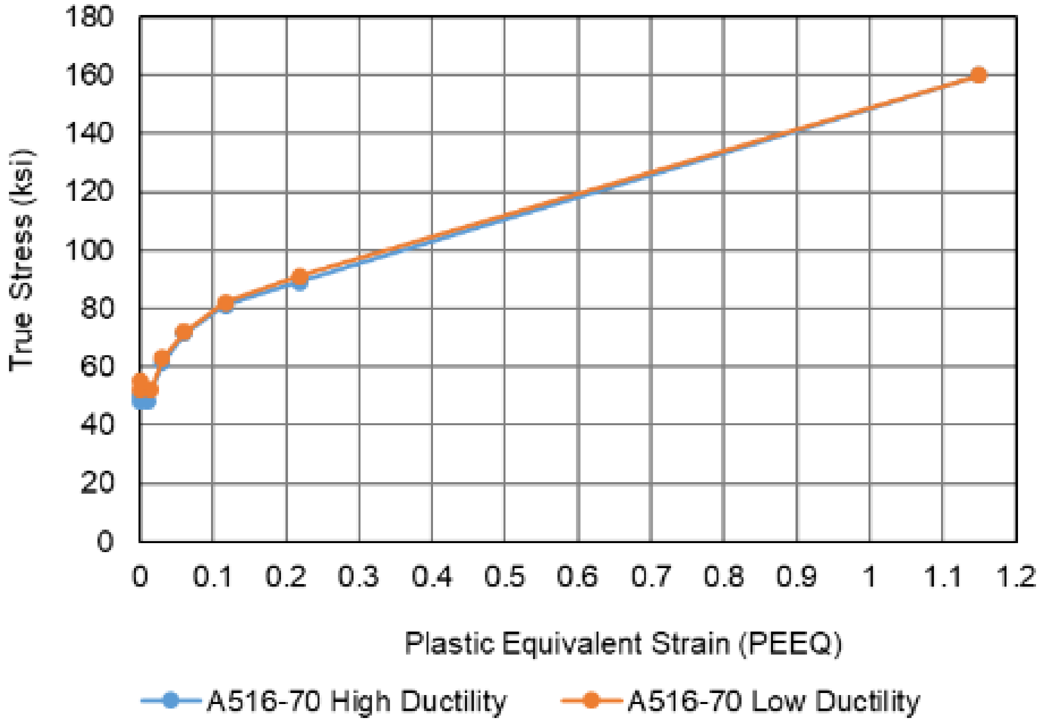

Figure F9. True Plastic Stress-Strain Behaviors for A516-70 Steel from Pre-Test Models with High and Low Estimates of Ductility

---

[15] Sources include: [26] [29] [53] [55] [56] [57] [58] [59] [60] [61]

Table F3. True Stress/True Plastic Strain Inputs for A516-70 Pre-Test Models with High and Low Estimates of Ductility

	High Ductility	**Low Ductility**
PEEQ ***in/in***	**True Stress** ***psi***	**True Stress** ***ksi***
0	50	55
0.000822	48	52
0.015	48	52
0.03	61.5	63
0.06	71.5	72
0.117	81	82
0.218	89	91
1.15	160	160

Damage initiation and progression behaviors were calibrated in the A516-70 coupon models to approximate high and low values of EB observed in the reference reports. A modified version of Lee and Wierzbicki's [30] [31] "quick calibration" approach was used to develop the pre-test A516-70 damage initiation envelopes for the upper- and lower-ductility estimates for A516-70. The damage initiation envelopes were calibrated in an iterative approach to match the EB and reduction in area from the published test reports. The pre-test B-W damage initiation envelopes for the A516-70 material definitions were much less similar when compared with their plastic hardening behavior, as the goal was to estimate high and low ductility versions of the steel for the pre-test models. The constants for the B-W damage envelopes are given in Table F4 and the resulting B-W envelopes are plotted in Figure F10.

Table F4. B-W Damage Initiation Envelope Constants for Pre-Test A516-70 High and Low Ductility Estimates

	a	b	x_0
High Ductility	0.35	0.835	0.481
Low Ductility	0.163	0.547	0.472

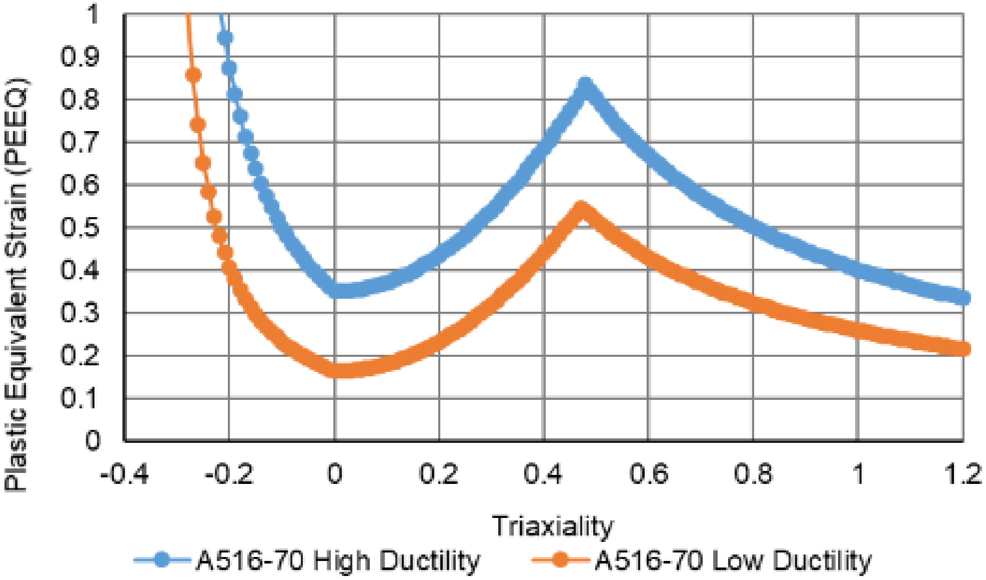

Figure F10. Damage Initiation Envelopes for A516-70 Steel from Pre-Test Models with High and Low Estimates of Ductility

Figure F11 shows the resulting engineering stress-strain responses from pre-test simulations of A516-70 DB tensile coupon geometry (Figure F1). Both the upper- and lower-ductility estimates of A516-70 used a displacement-based exponential damage progression in Abaqus/Explicit. The high ductility version had a targeted displacement of 0.03 in/in^2 and exponent of -8 while the low ductility version had a targeted displacement of 0.02 in/in^2 and exponent of -2. The damage progression was iteratively determined to match the shape and EB from the referenced sources.

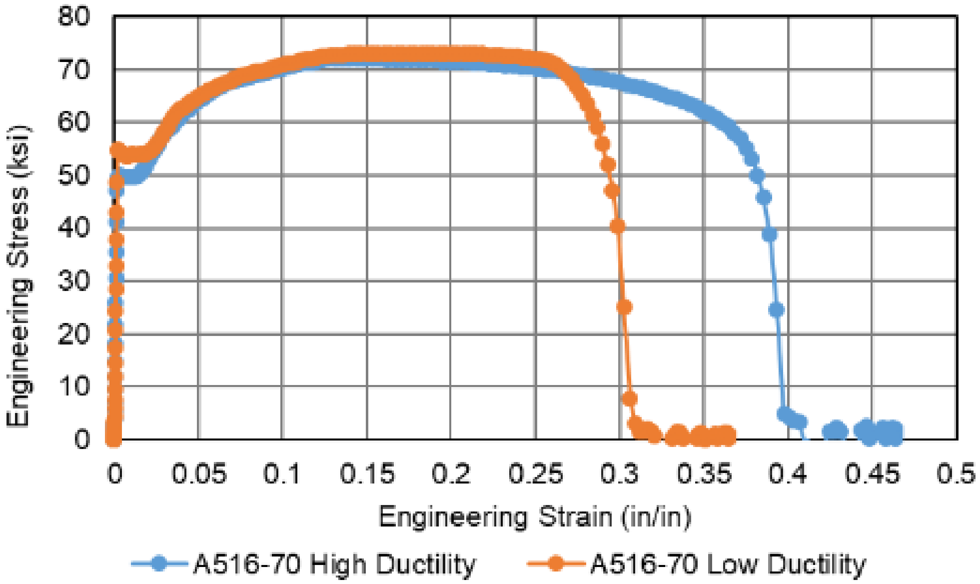

Figure F11. Pre-Test Engineering Stress-Strain Tensile Coupon FE Results for A516-70 Steel with High and Low Estimates of Ductility

Section 3.2. A516-70 Post-Test Characterization

Following the test, material coupons were excised from an undamaged area of the A516-70 steel outer tank of the tested DOT-113 tank car and sent to two different labs for tensile testing. The A516-70 steel plate was cut into 2-inch gage length DB coupons for tensile testing. The results of the tensile tests are included in Appendix B, Section 4. Additionally, the raw nominal stress-strain test data was provided to Volpe for use in developing a material response for the material in the tested tank car. Extensometer data collected during the material testing only included the initial portion of the stress-strain test.

Table F5 contains the tabular data used to define the isotropic plastic hardening of the A516-70 material in the post-test FE model. Points were manually specified in the Lüder’s (slip) band region of the curve up to a PEEQ strain of 0.04 in/in and subsequently a curve fit based on the Swift-Voce Hardening Law relationship was applied for PEEQ strains from 0.045 in/in up to 2.0 in/in at an increment of 0.005 in/in.

Table F5 gives the constants for the Swift-Voce Hardening Law (Equation F2) of post-test A516-70 for PEEQ strains greater than 0.40 in/in. The best agreement was reached with a weighting factor of 1 meaning that the exponential (Voce) term was not used in the final calibration.

Table F5. True Stress and Plastic Equivalent Strain FE Input for Post-Test A516-70 Material for Plastic Equivalent Strains Between 0 and 0.04 in/in

PEEQ *in/in*	True Stress *ksi*
0.000	34.5
0.005	34.5
0.010	34.5
0.015	34.5
0.020	38.0
0.025	40.5
0.030	42.5
0.035	44.7
0.040	46.5

Table F6. Constants for Mixed Swift-Voce Plastic Hardening of Post-Test A516-70 for Plastic Equivalent Strains Greater Than 0.04 in/in

Swift Hardening Law			Voce Hardening Law			Weighting Factor
A	ε_0	n	k_0	Q	β	α
ksi	-	-	*ksi*	*ksi*	-	-
96.183	0	0.22341	-	-	-	1

Figure F12 shows the true stress-PEEQ inputs for Abaqus in the pre-test (upper- and lower-ductility estimates of A516-70) and post-test models. The pre-test input plastic behaviors have notably higher stresses than the post-test behavior due to the difference in measured YS and UTS.

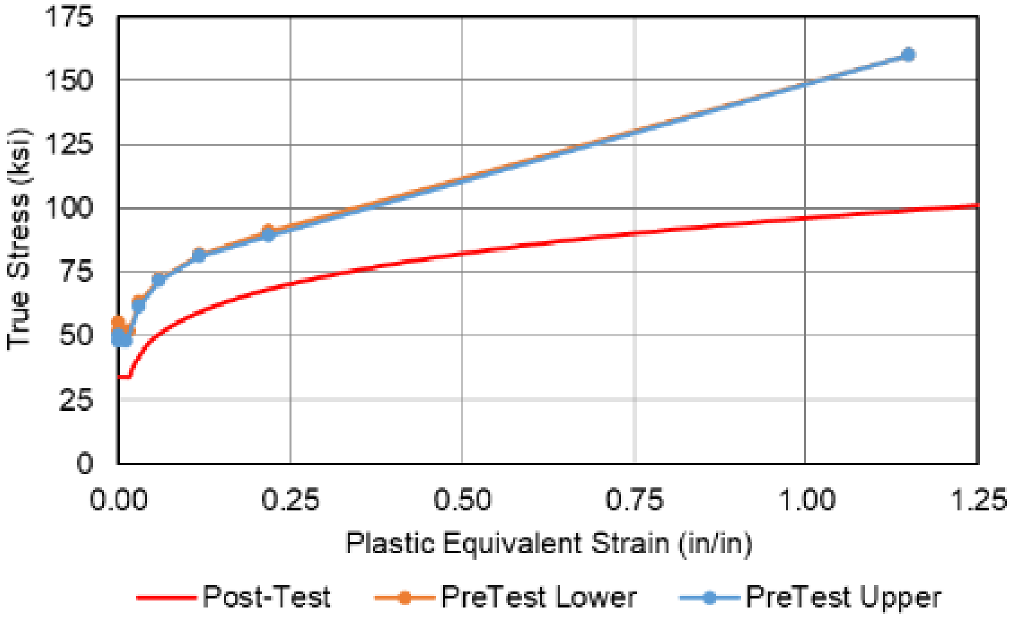

Figure F12. True Stress-Plastic Equivalent Strain A516-70 Abaqus Inputs for Post-Test Models with Pre-Test Models Shown for Comparison

Table F7 contains the B-W damage initiation envelope constants (refer to Equation F4) used to define the damage initiation envelope of the post-test A516-70 material. The damage initiation envelope was calculated based on the Lee-Wierzbicki quick calibration procedure [30], [31] using the average mechanical properties (see Appendix B, Section 4) from flat tensile coupon samples that were cut from the outer tank after the side impact test. The B-W constants were calculated according to Equation F5 for flat DB coupons. The damage progression was specified as displacement-based with exponential softening, and the targeted displacement was set to 0.022 in/in^2 with an exponent of -5.

Table F7. B-W Damage Initiation Envelope Constants for Post-Test A516-70 Material

a	b	x_0
0.375	0.732	0.434

Figure F13 compares the pre- and post-test B-W damage initiation envelopes. In shear and mixed fracture, the post-test envelope was in nearly perfect agreement with the pre-test upper estimate. In ductile fracture, the post-test envelope was between the pre-test upper and lower estimates.

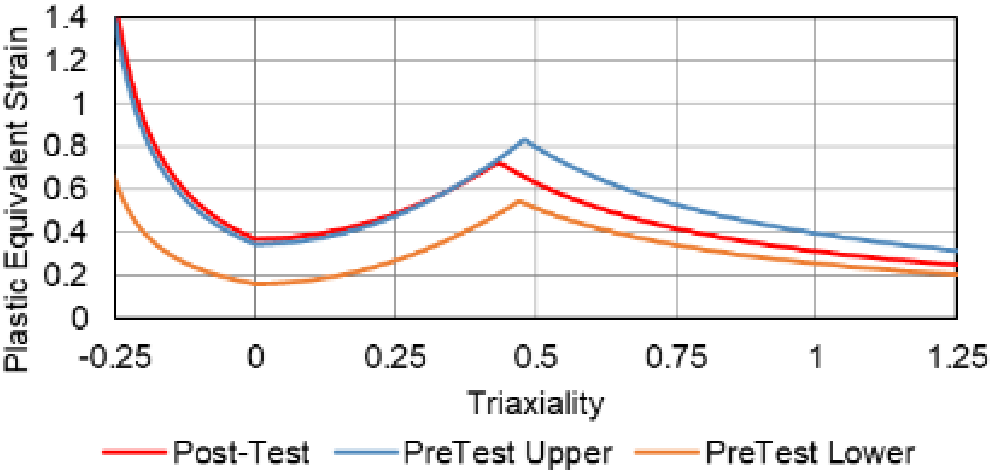

Figure F13. B-W Damage Initiation Envelopes from Post-Test A516-70 Material with Pre-Test Estimates Shown for Comparison

Figure F14 shows the engineering stress-strain responses from a simulation of the post-test flat tensile coupon geometry (Figure F1) with the pre-test upper- and lower-ductility engineering stress-strain curves shown for comparison. The post-test material exhibited a lower YS and UTS than either pre-test estimate but had an EB in excess of even the upper-ductility pre-test estimate.

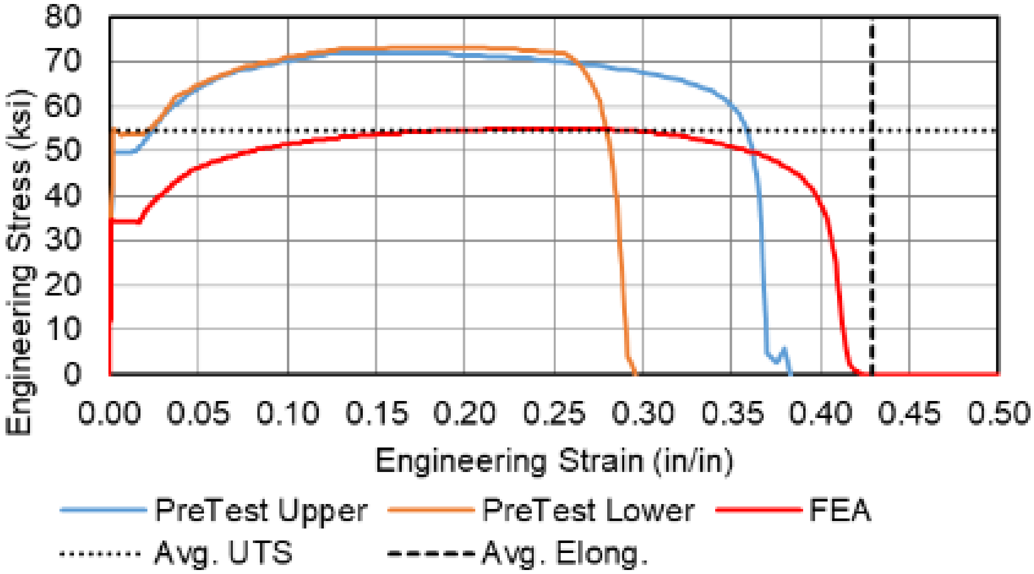

Figure F14. Engineering Stress-Strain Response from the A516-70 Post-Test Flat Tensile FE Model with Average Tensile Properties (Dashed) and Responses from Pre-Test Models Plotted for Comparison

Section 4. A240 T304 Stainless Steel Material Behavior

Five characterizations of ASTM A240 T304 stainless steel were developed over the course of this study. Prior to the test, upper and lower estimates of the ductility of T304 were developed based on coupon data available in published literature. After the test, three additional characterizations were developed to attempt to bookend the inner tank puncture response observed in the test. For comparison, the results of tensile coupon simulations with the different T304 material models are summarized in Table F8. The pre-test estimated mechanical properties of T304 were similar to the post-test actual T304 stainless steel. In particular, the estimated EB from the high- and low-ductility pre-test estimates bounded the average EB from the tensile tests.

Table F8. Summary of Mechanical Properties of T304 from Pre-Test Estimates and Post-Test Measurement

Name	**YS** *ksi*	**UTS** *ksi*	**EB** *%*
Pre-test High Ductility	46	90	79
Pre-test Low Ductility	46	90	67
Post-test MMC	44	85	74
Post-test BW (QS)	44	85	71
Post-test BW (0.1/s)	48	81	49

Section 4.1. A240 T304 Pre-Test Characterization

The mechanical properties of the T304 stainless steel composing the inner cryogenic tank of the DOT-113 tank car were unknown prior to the test so material models with high and low pre-test estimates of ductility were developed using published coupon test data from several sources.

The pre-test T304 plastic hardening behavior was developed based on smooth round bar engineering stress-strain curves for a similar stainless steel, T304L [26]. Figure F15 shows the plastic hardening pre-test material input for T304 stainless steel. The constants for the Mixed Swift-Voce expression (Equation F2) used for the pre-test T304 estimates are given in Table F9.

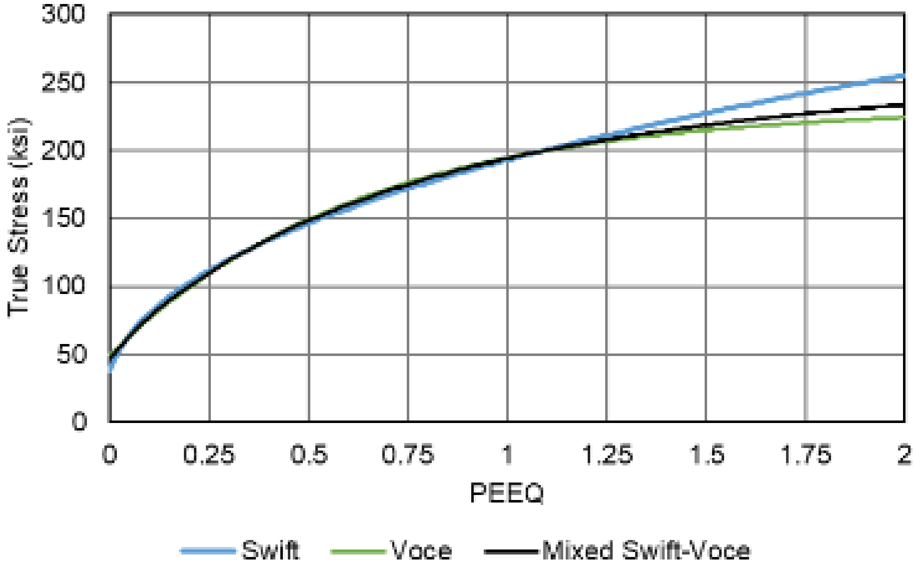

Figure F15. Mixed Swift-Voce Law for True Plastic Stress-PEEQ Strain FE Input for T304 from Pre-Test Models

Table F9. Constants for Elasticity and Mixed Swift-Voce Plastic Hardening for Pre-Test Estimates of T304 Behavior

Swift Hardening Law			Voce Hardening Law			Weighting Factor
A	***ε_0***	***n***	***k_0***	***Q***	***β***	***α***
ksi	-	-	*ksi*	*ksi*	-	-
191.4974	0.01979	0.409728	49.64786	182.1167	1.587435	0.3

A pre-test MMC damage initiation envelope was estimated for T304 steel by using coupon test results from two different sources. Tests were conducted on a similar stainless steel, T316L [27], using the coupon geometries annotated in Figure F5, and tests were conducted on T304L [26] with smooth and notched round bar geometries. The test results obtained by Paredes, et al. were available to Volpe for use in calibrating FE models [27]. Initially, each coupon geometry was simulated with the pre-test plasticity estimate for T304 steel but without damage initiation behavior. Targets for the PEEQ at damage initiation in the critical element (crack initiation point) were set for each coupon. The MMC surface was then calibrated by minimizing a residual squared error function for the plastic equivalent strain at damage (crack) initiation until agreement was reached with the various fracture specimens made from similar stainless steels and documented in the two sources identified above. This approach is similar to the approach used for calibrating an MMC fracture surface for another tank car steel, TC128-B [42].

Figure F16 shows the pre-test MMC damage initiation envelope for T304. The constants for the MMC surface are given in Table F10.

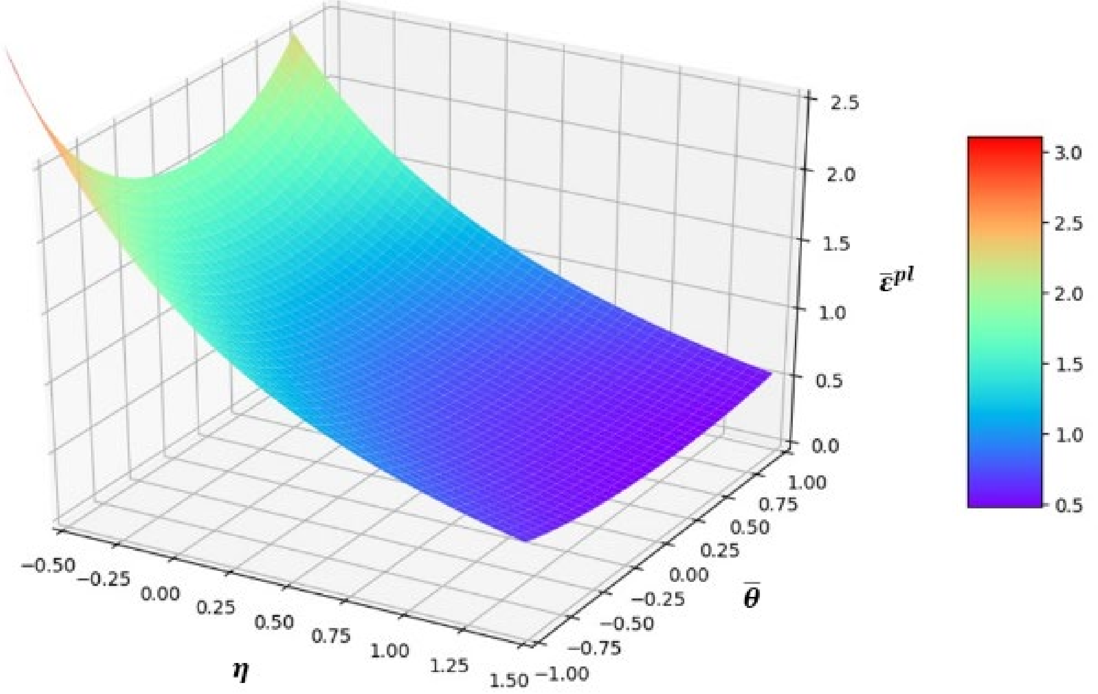

Figure F16. MMC Fracture Surface for T304 Stainless Steel from Pre-Test Models

Table F10. MMC Damage Initiation Constants for Pre-Test Estimates of T304 Fracture

A	*n*	*c₁*	*c₂*	*c₃*
ksi	-	-	*ksi*	-
191.4974	0.409728	0.163094	115.4613	0.987424

Damage progression behaviors were estimated based on the uncertainty in EB observed in the T304L smooth round bar test results. Table F10 summarizes the T304 pre-test tensile coupon FEA results with high and low estimates of ductility. To check for agreement, the coupon models were then rerun with the calibrated MMC fracture surface and a conservative damage progression, later specified as the damage progression value for the lower ductility pre-test estimate.

Figure F17 shows the nominal stress-strain results of the coupon FE fracture models with flat notched (20 mm and 6.67 mm) and center-hole (8 mm) geometries (see Figure F6) compared with the test results obtained by Paredes et al. [27]. A 20 mm gage length is used to calculate engineering strain.

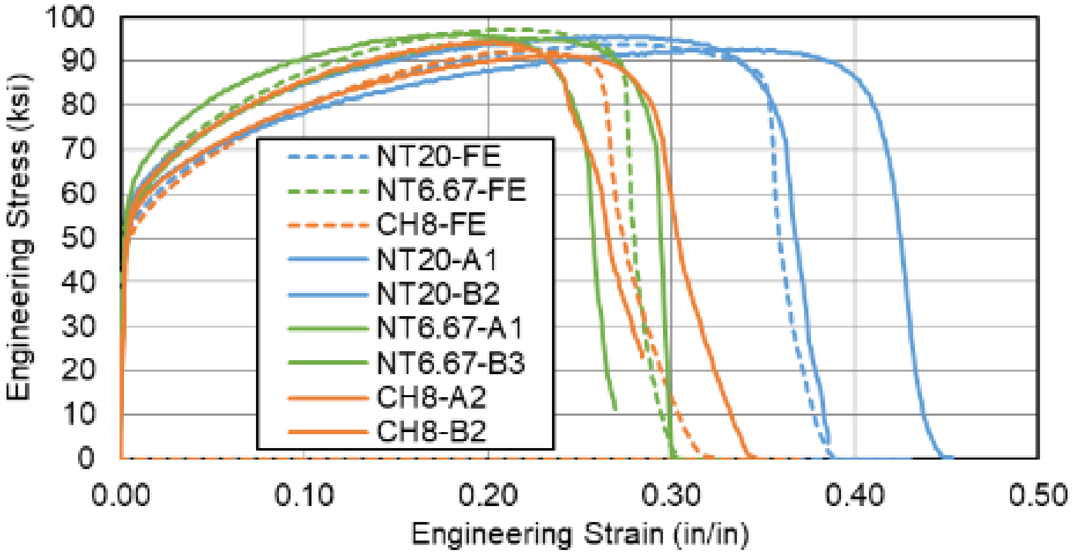

Figure F17. Flat Notched Tension (NT) and Center Hole (CH) Coupon FE Results (Dashed) with the Pre-Test Lower Ductility Estimate and Test Results (Solid) from Two Different Batches (A/B) of T316L for Comparison

Figure F18 shows the mini-punch (see Figure F8) force-deflection FE fracture results with the test results for comparison.

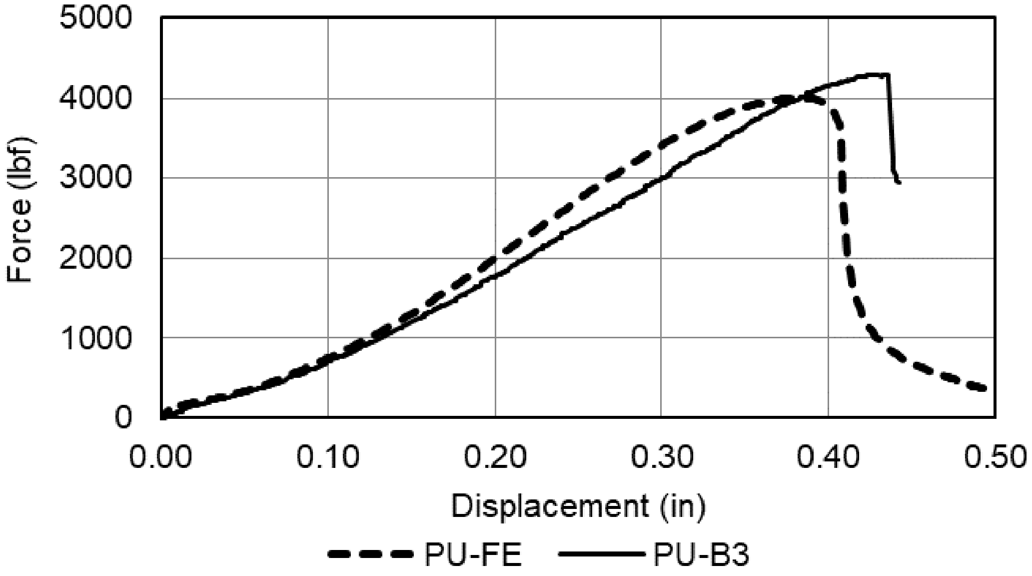

Figure F18. Mini-punch (PU) Coupon FE Results (Dashed) with Pre-Test Lower Ductility Estimate and Test Results (Solid) of T316L for Comparison

The pre-test smooth round bar coupon model (Figure F2) was simulated with the pre-test lower and upper estimates of ductility. The resulting engineering stress-strain responses are shown in Figure F19 with the engineering strains where damage initiated marked with a vertical dashed line. The high-ductility pre-test estimate of T304 used an exponential displacement-based damage progression with a targeted normalized displacement of 0.03 in/in^2 and exponent of -2 while the low ductility pre-test estimate had a targeted normalized displacement of 0.0015 in/in^2 and exponent of -2.

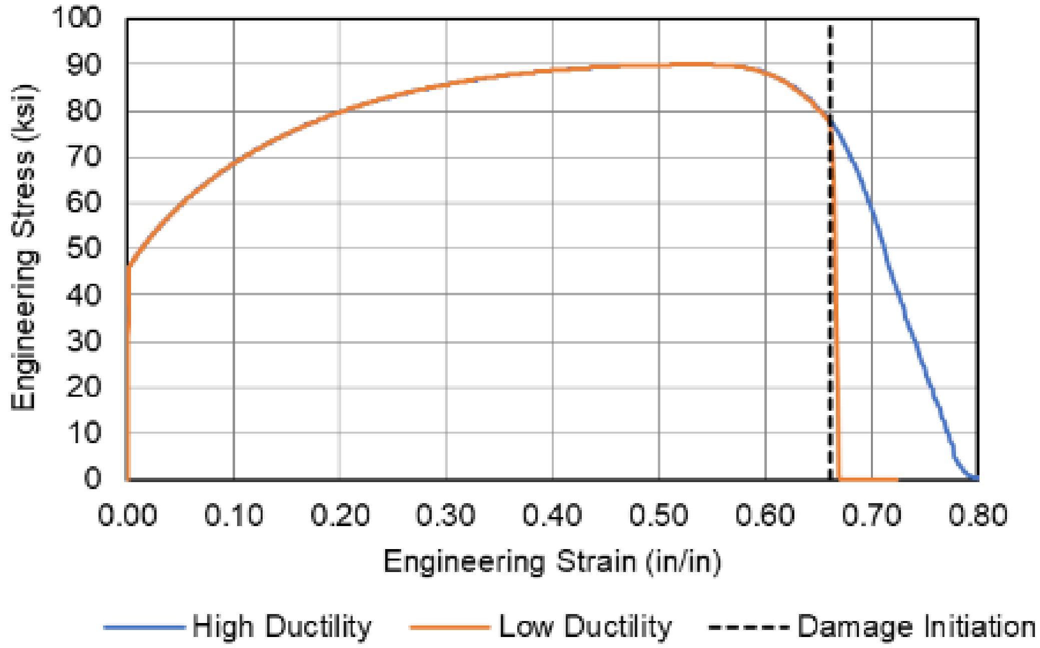

Figure F19. Pre-Test Engineering Stress-Strain Tensile Coupon FE Results for T304 with High and Low Estimates of Ductility

Section 4.2. A240 T304 Post-Test Characterization

Following the test, material coupons were excised from the T304 stainless steel inner tank of the tested DOT-113 tank car and sent to two different labs for tensile testing. The T304 steel plate was cut into 2-inch gage length DB coupons for tensile testing. The results of the tensile tests are included in Appendix B, Section 4. Additionally, the raw nominal stress-strain test data was provided to Volpe for use in developing a material response for the material in the tested tank car. Extensometer data collected during the material testing only included the initial portion of the stress-strain test.

Three post-test material behaviors were calibrated for the T304 stainless steel in the inner tank in an attempt to capture the puncture response observed during the test. The first post-test material behavior used the MMC damage initiation envelope from the pre-test model which happened to be in good agreement with the actual tensile properties measured in coupons excised from the inner tank. However, the pre-test MMC damage initiation envelope resulted in an overestimation of the puncture resistance of the inner tank. The second post-test T304 material behavior used a B-W damage initiation envelope and was closer to the actual puncture response observed in the test but still overestimated the puncture resistance. The third T304 post-test material behavior used a B-W damage initiation envelope calibrated based on tensile test results that were not QS, i.e., measured at a strain rate of 0.1 in/in/s. To differentiate the post-test material calibrations, the calibrations are named: 1) MMC QS, 2) B-W QS, and 3) B-W 0.1/s.

While the first two material models were calibrated based on QS tensile test data, research from Paik [28] and Kirkpatrick [26] showed that the mechanical properties of stainless steel are sensitive to rate effects. The third post-test material behavior used a B-W damage initiation envelope calibrated based on the tensile properties reported by Kirkpatrick [26] for T304L stainless steel tested at a rate of 0.1 in/in/s. This rate was chosen because it resulted in the lowest properties for UTS and EB out of the rates that were reported. The modeling team expected that the properties at this rate would therefore result in the lowest puncture speed in the DOT-113 FE model. This third post-test material behavior was able to book-end the inner tank response (i.e., estimate a lower puncture resistance) so the material calibration was stopped at this point.

Additional iterations of post-test material calibration could have been performed to match the response observed in the test; however, it would have been focused on model calibration (tuning) instead of model validation. The lessons learned from this test on the damage initiation models and strain rate sensitivity of stainless steel will be applied in future tests with stainless steel tanks in order to validate a DOT-113 FE model.

Figure F20 shows the engineering stress-strain response from a model of the rectangular DB coupon cut from the inner tank with each of the three post-test material calibrations applied to it alongside the average QS UTS and EB from the coupons excised from the inner tank.

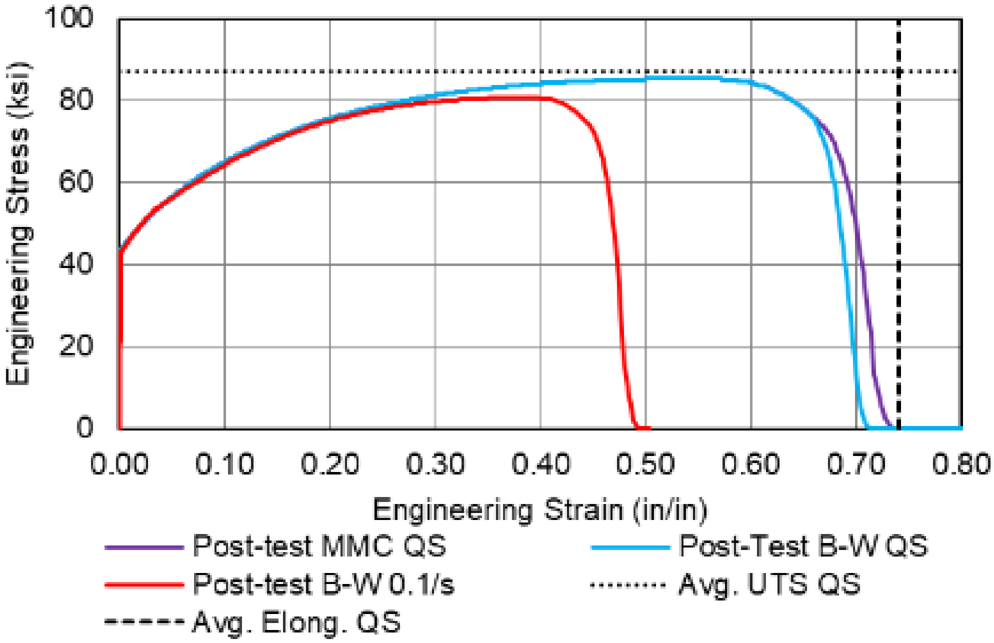

Figure F20. Engineering Stress-Strain Response from the Three T304 Post-Test Material Calibrations Applied to a Flat Tensile FE Model with Average QS Tensile Properties (Dashed) for Comparison

From Figure F20, it is apparent that the MMC QS and B-W QS post-test material calibrations resulted in a similar uniaxial tensile response; however, a difference in puncture resistance was observed (refer to Section 7.2). A significant reduction in EB was observed in the third post-test calibration based on 0.1 in/in/s tensile test data. This less-ductile response also resulted in a significant reduction in puncture resistance in the inner tank (refer to Section 7.2).

A comparison of the damage initiation envelopes is shown in Figure F21. Because the MMC envelope is a three-dimensional surface, a slice at a normalized Lode angle of -1 is taken so that it can be plotted alongside the two-dimensional B-W damage initiation envelopes which are a function of stress triaxiality. A normalized Lode angle of -1 was chosen for comparison because it corresponded to a stress state of biaxial tension which was the stress state observed under the corners of the impactor where fracture initiates. From this plot, it was clear that the plastic equivalent strain to fracture was reduced in each iteration of the post-test material calibration which resulted in a reduction in puncture resistance of the inner tank.

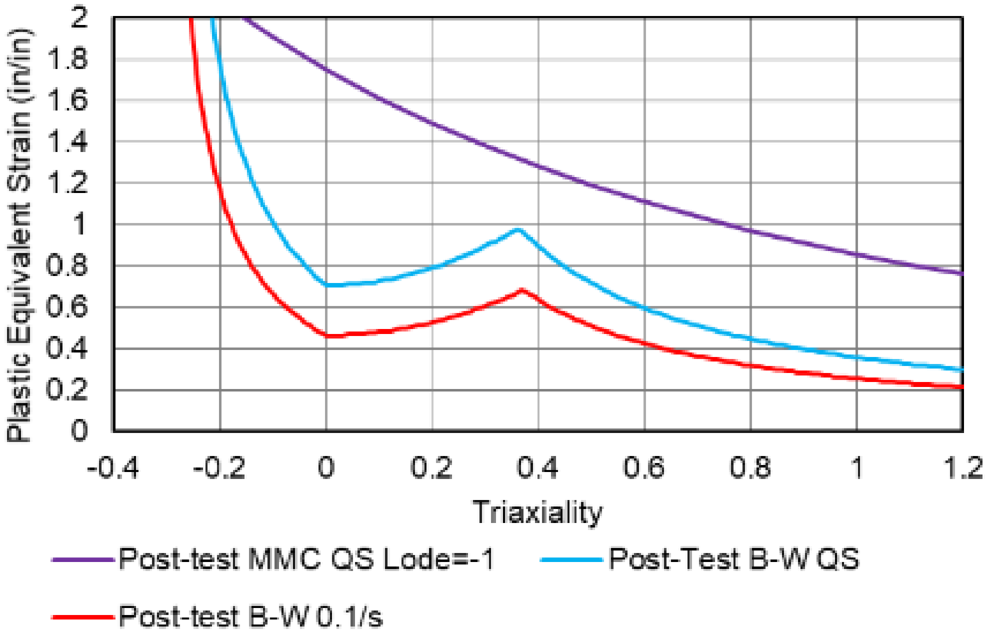

Figure F21. Post-Test T304 Damage Initiation Envelopes

Figure F22 shows the plastic hardening curves from the post-test material calibrations of T304.

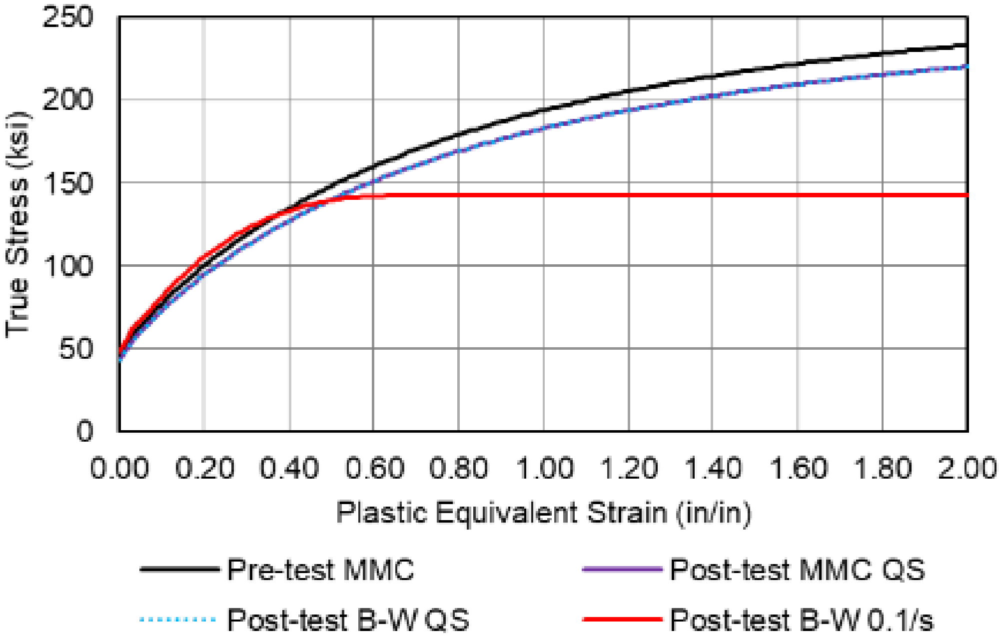

Figure F22. Pre- and Post-Test T304 Plastic Hardening Damage Initiation Envelopes

T304 Post-Test MMC QS Characterization

Due to similarity between the measured T304 properties and the estimated values used in pre-test models, the post-test 2-inch gage length DB coupons (Figure F2) were initially simulated using the pre-test FEA estimated properties for T304. The results of this approach to simulation revealed excellent agreement except that the pre-test estimate had a slightly higher YS and UTS. The true stress-PEEQ strain FE input for the pre-test model (Figure F15) was scaled by a factor of 17/18 to create the post-test true stress-PEEQ strain FE input. The constants for the Swift-Voce hardening expression are given in Table F11.

Table F11. Constants for Mixed Swift-Voce Plastic Hardening for QS Post-Test T304 Material Calibrations (MMC QS and B-W QS)

Swift Hardening Law			**Voce Hardening Law**			**Weighting Factor**
A	ε_0	***n***	k_0	***Q***	β	α
ksi	-	-	*ksi*	*ksi*	-	-
180.8587	0.01979	0.409728	46.88965	171.9991	1.587435	0.3

No modification was made to the pre-test MMC fracture surface (Figure F16). To match the average EB from the T304 tests, the damage progression was set between the pre-test lower and upper ductility targets at a normalized displacement of 0.015 in/in^2 with an exponent of -2.

T304 Post-Test B-W QS Characterization

The post-test MMC QS material calibration was modified to use a B-W damage initiation envelope because the MMC QS DOT-113 FE model overestimated the impactor travel and force at puncture of the inner tank. It was expected that a B-W damage initiation envelope would be more conservative in predicting puncture than an MMC damage initiation envelope because FE models in previous side impact tests that had used a B-W curve were conservative. A B-W damage initiation envelope was calibrated using the Lee-Wierzbicki quick calibration procedure [30] [31] on the QS post-test tensile coupon results which resulted in the B-W constants given in Table F12. The plastic hardening curve was not modified from the MMC QS calibration (see Table F12), and the same damage progression was used.

Table F12. B-W Damage Initiation Envelope Constants for Post-Test T304 B-W QS Material

a	***b***	x_0
0.706	0.985	0.363

T304 Post-Test B-W 0.1/s Characterization

Both the post-test MMC QS and B-W QS material models resulted in an overprediction of the impactor travel and force at puncture of the inner tank. Because of this, the effect of strain rate was considered for the T304 inner tank. While previous research had shown that strain rate effects did not need to be considered for TC128-B, this was the first side impact test of a tank car with a stainless-steel tank. It was expected that adding strain rate effects to the FE model would be able to capture the puncture behavior in the inner tank when QS material models were over-predicting puncture.

A literature search was conducted to find tensile test results that were conducted at elevated strain rates. Two sources [26] [28] were selected for material calibrations. The calibration at a strain rate of 0.1/s from Kirkpatrick's tensile test results was incorporated into the DOT-113 FE model because it was expected that it would result in the lowest estimate of puncture resistance in the inner tank. While better agreement could have been obtained by further investigating strain rate effects in T304, the post-test T304 material calibration was stopped at this point because an underprediction of inner tank puncture was finally achieved, and the puncture response observed in the test was bookended. Further calibration would no longer have been focused on validation of the DOT-113 FE model instead it would have been focused on model tuning.

The Swift-Voce plastic hardening constants are given in Table F13, and the B-W curve constants are given in Table F14. for the B-W 0.1/s post-test material calibration. The same damage progression (normalized displacement of 0.015 in/in^2 with an exponent of -2) was used for all post-test material calibrations.

Table F13. Constants for Mixed Swift-Voce Plastic Hardening for QS Post-Test T304 B-W 0.1/s Material

Swift Hardening Law			Voce Hardening Law			Weighting Factor
A	ε_0	***n***	k_0	***Q***	β	α
ksi	-	-	*ksi*	*ksi*	-	-
192.5029	0.039333	0.4265110	51.42653	119.0364	2.99566	-1

Table F14. Bao-Wierzbicki Damage Initiation Envelope Constants for Post-Test T304 B-W 0.1/s Material

a	***b***	x_0
0.464	0.683	0.373

A comparison of the damage initiation envelopes is shown in Figure F22. Because the MMC envelope is a three-dimensional surface, a slice at a normalized Lode angle of -1 was taken so that it could be plotted alongside the two-dimensional B-W damage initiation envelopes which are a function of stress triaxiality. A normalized Lode angle of -1 was chosen because it corresponds to a stress state of biaxial tension which is the stress state observed under the corners of the impactor where fracture initiates. From this plot, it is clear that the plastic equivalent strain to fracture was reduced in each iteration of the post-test material calibration which resulted in a reduction in puncture resistance of the inner tank.

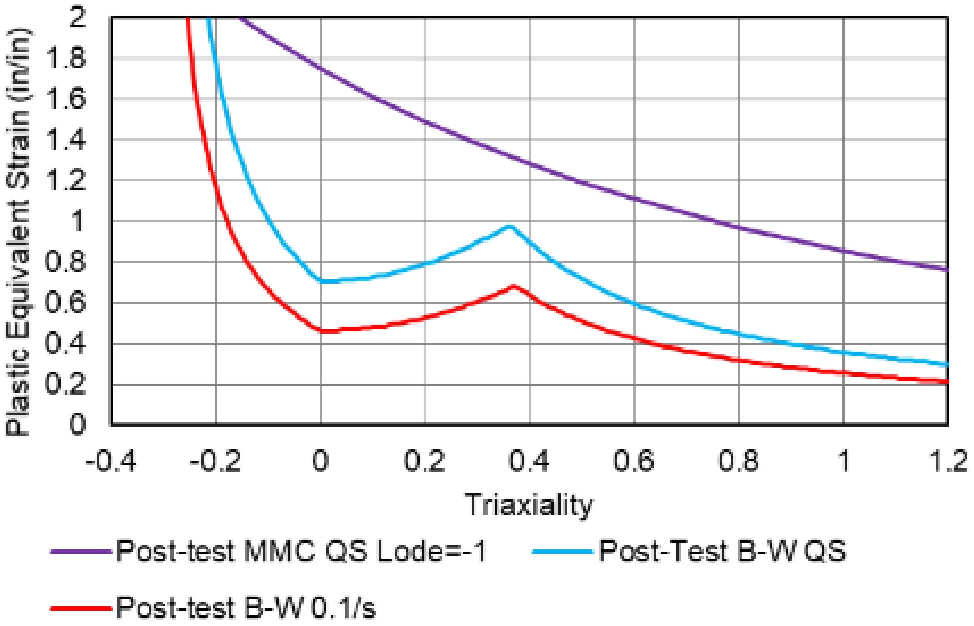

Figure F23. Post-Test Damage Initiation Envelopes

Section 5. Perlite Material

Post-test modeling sought to examine potential sources of disagreement between the pre-test FE model results and the test measurements. One potential source of disagreement was the pre-test simplification of an annual space containing only vacuum, with no effects of perlite accounted for. Post-test observation of the annular space between the two tanks indicated that the perlite in an area remote from the impact zone was relatively densely packed into the space (see Figure 29). Thus, the perlite may have had an influence on the dynamics of the DOT-113, acting to constrain the indentation of the outer tank or restricting the inner tank's ability to deflect under the impact load.

Section 5.1. Drucker-Prager "Sandy Soil" Perlite Material Model

A simplified material model for perlite was needed to examine the effects of including this material in the post-test models. As perlite is not widely used in modern DOT-113 tank car construction (in favor of MLI), a significant effort at characterizing the mechanical properties of perlite would have limited use. As a means of investigating whether the perlite could have accounted for differences between pre-test models and test observations, a simplified approach to modeling the perlite was developed using existing data.

The perlite in the tested DOT-113 tank car was a fine particulate material. This observation gave rise to the notion of adapting an Abaqus material model of sandy soil as a stand-in for perlite, an approach that had also been described in the literature [39]. A material model of sandy soil, using modified Drucker-Prager cap plasticity developed for use in Abaqus/Explicit was found in the literature [40] and adapted for the unit system of the DOT-113 model. This material model was then used to simulate a drop test into sandy soil described by a second reference [48]. Input values to the perlite material model were adjusted iteratively both to account for differences between perlite and sandy soil as well as to improve the level of agreement between the perlite drop simulations and those of the reference. The final material inputs for simplified perlite that were used in the post-test DOT-113 models are shown in Table F15.

Table F15. Summary of Material Inputs for Simplified Perlite #1

Parameter	Symbol	Value	Units	Notes
Young's Modulus	E	67.5	psi	Adjusted from value in [40] to give better agreement with drop results in [48]
Poisson's Ratio	ν	0	unitless	[40]
Mass Density	ρ	9×10^{-6}	$lbf\text{-}s^2/in^4$	Density chosen to match total weight of perlite per DOT-113 drawings (6,500 lbf) and estimated annular space volume (8,150 gal)
Angle of Friction	β	57.8	degrees	[40]
Material Cohesion	d	5.1×10^{-2}	psi	[40]
Cap Eccentricity	R	1.1×10^{-4}	unitless	Chosen to exceed Abaqus minimum of 1×10^{-4}
Initial Yield Surface Position	$\varepsilon_{vol}^{in}\|_0$	0	unitless	Arbitrary value
Transition Surface Radius	α	0	unitless	Default value
Flow Stress Ratio	K	1	unitless	Default value

Table F16. Cap Hardening Parameters Converted to DOT-113 Model Unit System [40]

Hydrostatic Yield Stress (psi)	Volumetric Plastic Strain
0.000145	0
0.725	0.014661
1.45	0.028334
2.901	0.053024
4.351	0.074619
5.802	0.093572
7.252	0.110262
8.702	0.125006
10.153	0.138069
11.603	0.149679
13.053	0. 160028
14.504	0. 16928

Hydrostatic Yield Stress (psi)	Volumetric Plastic Strain
17.405	0.185036
23.206	0.208422
30.458	0.228045
42.061	0.248232
58.015	0.266976
72.519	0.280999

Section 5.2. Crushable Foam Perlite Material Model

Many of the discrepancies between the test measurements and the FE outputs remained after implementing the sandy soil material model as a stand-in for perlite in the post-test FE models. Including a representation of perlite was found to be necessary if the post-test FE models were going to experience a puncture to the inner tank under the test impact conditions. However, discrepancies between the global model stiffness and the global stiffness measured in the test persisted even with the sandy soil material model.

To attain better agreement between the post-test FE model and the test measurements, a second material model for perlite was developed. This second material model required a more in-depth literature search to obtain better estimated properties because, for the second perlite material model, the mechanical properties of actual expanded perlite were sought, rather than trying to adapt those from a sandy soil.

In addition to finding material properties in the literature for expanded perlite, a suitable material modeling approach had to be chosen that could be implemented in Abaqus/Explicit. Where the “sandy soil” perlite material model had used a modified Drucker-Prager cap plasticity material model, the mechanical properties needed to develop such a model were not available for perlite. Thus, various other material models available in the Abaqus/Explicit software had to be examined based on the mechanical properties for the available data for perlite.

Two additional reference sources were identified that contained mechanical property measurements for expanded perlite. It should be noted that, because perlite is a naturally occurring mineral, there is expected to be some variation in both the chemical composition and the mechanical properties of expanded perlite when the perlite is obtained from different sources. The properties that were available in the literature for perlite are summarized in Table F17.

Table F17. Summary of Mechanical Properties for Perlite Found in Literature

Property	Description	Source
Bulk Density	Mass of loose perlite divided by volume of container	[49] [50] [51] Estimate for DOT-113 test
Particle Density or True Density	Mass of perlite divided by volume of particles	[49] [50] [51]
Porosity	Volume of void space divided by volume of container	[50] [51]
Young's Modulus	Elastic stiffness given as a function of perlite bulk density or porosity	[51]
Poisson's Ratio	Proportion of lateral deformation in response to a longitudinal force given as a function of perlite bulk density or porosity	[51]

The mechanical properties summarized in Table F17 were used to develop perlite material input parameters in the format required by Abaqus. The input parameters are summarized in Table F18. Each parameter is discussed in further detail in subsequent paragraphs.

Table F18. Summary of Material Inputs for Simplified Perlite #2 (Crushable foam)

Parameter	Symbol	Value	Units	Notes
Mass Density	ρ	9×10^{-6}	$lbf\text{-}s^2/in^4$	Density chosen to match total weight of perlite per DOT-113 drawings (6,500 lbf) and estimated annular space volume (8,150 gal)
Poisson's Ratio	ν	0.3	unitless	[51]
Young's Modulus in Compression	E	Tabular	psi	Adapted from values in [51]
Young's Modulus in Tension	E	Tabular	psi	Assumed same values as compression, with tensile cutoff stress
Tensile Cutoff Stress	$\sigma_{t,\ cutoff}$	40	psi	Empirical value
Linear Viscosity Parameter	μ_0	0.0001	s	Default value in Abaqus
Nonlinear Viscosity Parameter	μ_1	0.005	s	Default value in Abaqus
Exponent	α	2	unitless	Default value in Abaqus

Density and Porosity

The same mass density of perlite was defined in the post-test perlite material models (both the Drucker-Prager and the crushable foam). The density used is the "bulk density" of the material, meaning that this density is the average density of a volume containing expanded perlite and air. Since perlite is a particulate material, there is space between the individual grains that is initially filled with air, or in the case of the DOT-113, under vacuum. The engineering drawings for the DOT-113 provided prior to the test indicated 6,500 pounds of perlite were added to the annular space. In the FE model, the annular space was estimated to have a volume of approximately 8,150 gallons. Thus, the bulk density of the perlite in the FE model was approximately 6 lbf/ft^3, or 0.096 g/cm^3.

A second measure for density is the "true density" of the perlite. This density represents the mass of perlite contained within a volume if the grains could be tightly packed together, eliminating the intergranular space. According to the literature [51], this value was reported as a "unit weight" of 2.2–2.4 g/cm3 of perlite.

Dividing the bulk density by the true density and subtracting this value from 100 percent gives the porosity which is a measure of the relative amount of intergranular space in a granular material. The higher the value of porosity, the more intergranular space and the lower the bulk density of the material. For the DOT-113 used for Test 10, assuming a bulk density of 0.096 g/cm^3 and a true density of 2.4 g/cm^3, the perlite had an estimated porosity of 96 percent.

Poisson's Ratio

Values for Poisson's Ratio (ν) as a function of perlite density were obtained from the literature [51]. While ν varied with the density of the expanded perlite, a constant value of 0.3 was used in the post-test model as the variation described in the literature was minor for the range of densities examined [51].

In the crushable foam model used in Abaqus, Poisson's ratio was implemented by including the keyword "*Low Density Foam, LATERAL STRAIN DATA=YES". The lateral strain was then included as tabular data, where lateral strain is simply ν multiplied by the longitudinal strain. Note that for tensile longitudinal strains, the lateral strain defined must be negative.

Young's Modulus and Tensile Cutoff

The literature [51] provided a series of measurements of Young's Modulus at different densities/porosities of expanded perlite. within Abaqus, the crushable foam material model allows the user to define elasticity as a series of discrete stresses and strains, in both tension and compression. Thus, the values obtained from the literature needed to be converted into a format that could be input into Abaqus.

To convert the values of E at different porosities into stresses at different strains, it was assumed that the mass of perlite remained the same at each value of porosity. Thus, the porosity was only varied by compacting the perlite so that the given mass occupied a smaller volume. It was further assumed that the perlite occupied the same cross-sectional area of the container during compaction, so the change in volume was only accomplished by a reduction in the height of the perlite (uniaxial compression). These assumptions are illustrated schematically in Figure F24.

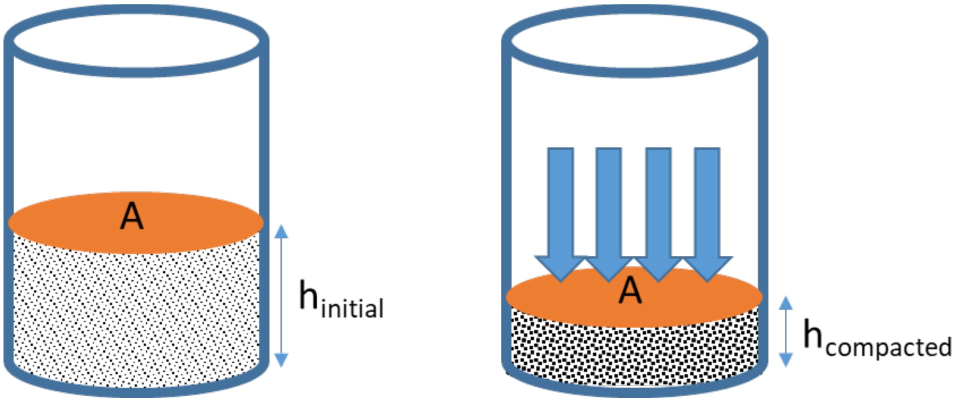

Figure F24. Schematic Illustrating Perlite Compaction Assumed in Stress-Strain Behavior Calculations

Using a value of 96 percent porosity as the initial condition of the perlite, the relative compressive strain was calculated at each value of porosity for which E was given in the literature according to Equation F10.

$$\varepsilon_{relative} = \frac{h_{initial} - h_{compacted}}{h_{initial}}$$

Equation F10. Relative Strain for Perlite

Because E is tangent to a stress-strain curve at the strain where it is being defined, the discrete values for $\varepsilon_{relative}$ and E were used to estimate both of the values of the compressive stress (σ_c) and the shape of the stress-strain response curve. Starting at a value of zero relative strain (corresponding to 96 percent porosity), stress was assumed to increase according to E_0. When $\varepsilon_{relative}$ reached a value halfway between ε_n and ε_{n+1}, the stress would begin to increase according to the next tabulated value of E, ensuring that the stress-strain curve would be tangent to ε_n once the strain reached that value.

Table F19. Relative Strain, Young's Modulus, and Estimated Stress at Different Values of Porosity

Porosity (%)	Relative Strain (in/in)	Young's Modulus (psi)	Estimated Stress (psi)
96	0	4,946	0
95	0.167	9,427	1,198
94	0.333	17,985	3,482
92	0.5	29,878	7,470.66
90	0.6	38,435	10,886.3
88	0.667	45,542	13,685.54
86	0.706	50,763	15,573.9
84	0.733	53,664	17,007.19
0	0.96	11,360,827	1,302,222

Using the values for relative strain and estimated stress in Table F19 (see above), the estimated stress-strain curve shown in Figure F25 was generated. The simplified approach used in this characterization of perlite assumed the same stress-strain response in tension as in compression, with the addition of a limit on the maximum tensile stress referred to as a tensile cutoff stress. This figure distinguishes the values of strain at which E is found to be tangent from the intermediate values of strain where a transition occurs from one value of E to the next.

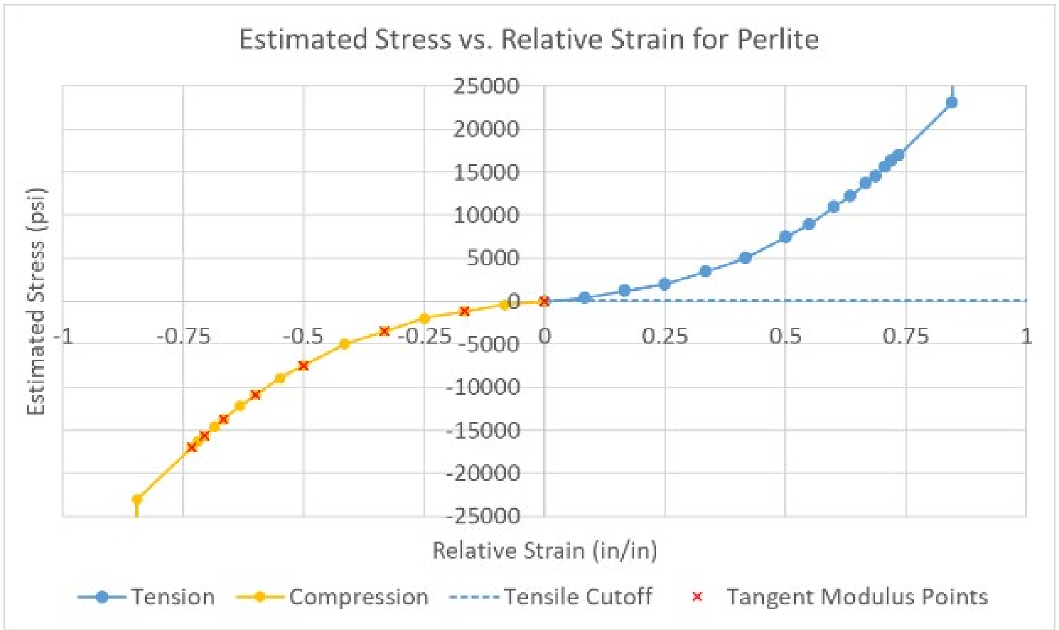

Figure F25. Estimated Stress Versus Relative Strain for Perlite Modeled as Crushable Foam

The crushable foam material model in Abaqus also includes the ability to prescribe a limit to the amount of tension a material can carry. Laboratory data on the tension-carrying ability of granular materials such as perlite are fairly limited, as loose granular materials are not capable of carrying high tensile loads. However, following the removal of sections of the DOT-113's outer and inner tanks for tensile testing, it was observed that the perlite was firmly packed into the annular space, and it did not freely "flow" out of the hole in the tank (see Figure 29). If the perlite were limited to zero tensile stress, this material would have flowed entirely out of the holes cut in the tank. At the same time, the perlite could be easily dug out of the space by hand without a need to chip away at it, indicating that its ability to carry tension was fairly limited. The post-test FE model with perlite modeled as crushable foam was run for its gravity settling step without using a tensile cutoff pressure. It was observed that the maximum tensile stress to develop in the perlite under its own weight was on the order of 30 psi. Thus, 30 psi was chosen as the lower empirical value for the tensile cutoff pressure, following the logic that the perlite material should not fail in the model prior to any impact loads being imparted. The post-test impact model was run iteratively, and a tensile cutoff value of 40 psi was found to provide the closest agreement to the test measurements. Therefore, if the tensile stress in the perlite reached 40 psi, the element was removed from the analysis. Due to the tensile stress limit, the range of tensile stress-strain points defined in the FE model was smaller than the range for the compressive stress-strain response. The tensile response is illustrated in Figure F26, showing a 30-psi tensile cutoff stress as an example.

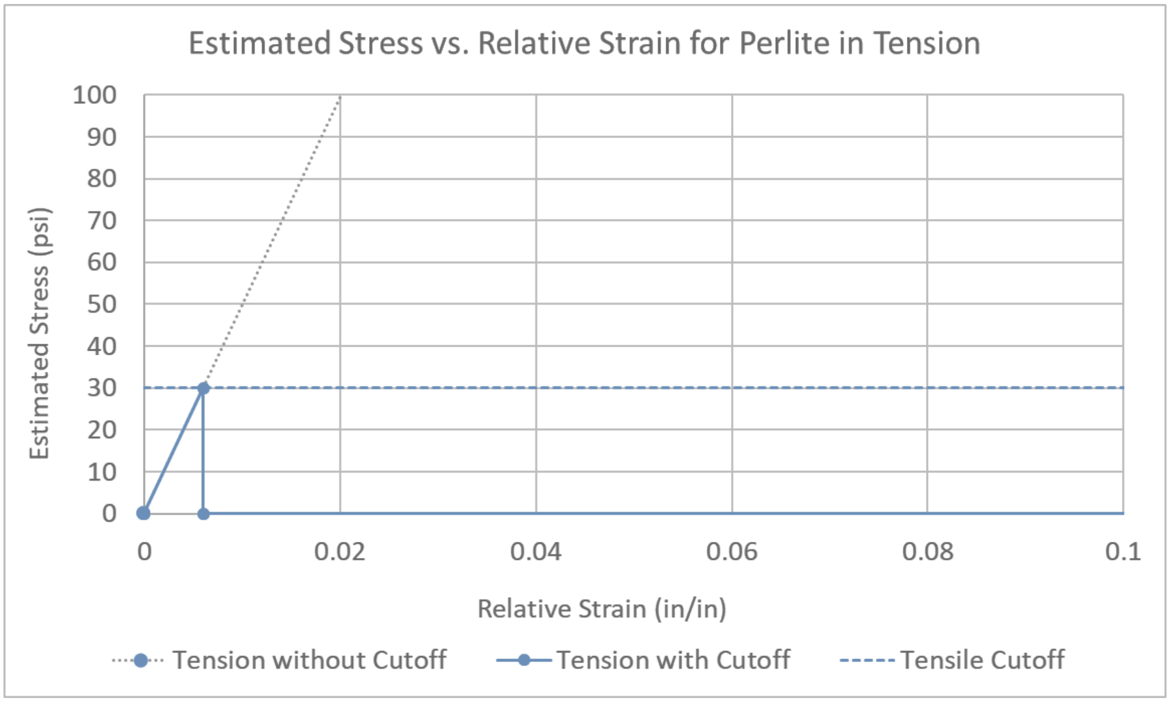

Figure F26. Estimated Stress Versus Relative Strain for Perlite Modeled as Crushable Foam in Tension, with Tensile Cutoff Used

The input values for stress, strain, lateral strain in tension and compression, and nominal strain rate defined in the post-test Abaqus model are shown in Table F20. Note that the tensile cutoff pressure and density were input separately from the stress-strain values shown in this table.

Table F20. Stress and Strain Behavior Defined in FE Model for Crushable Foam Perlite Material Model

Stress (psi)	Strain (in/in)	Lateral Strain (tension)(in/in)	Lateral Strain (compression) (in/in)	Nominal Strain Rate (in/in/s)
0	0	0.000	0	0
412	0.083	-0.025	0.025	0
1,198	0.167	-0.050	0.05	0
1,983	0.25	-0.075	0.075	0
3,482	0.333	-0.100	0.1	0
4,981	0.417	-0.125	0.125	0
7,471	0.5	-	0.15	0
8,965	0.55	-	0.165	0
10,886	0.6	-	0.18	0
12,168	0.633	-	0.19	0
13,686	0.667	-	0.2	0
14,579	0.686	-	0.206	0
15,574	0.706	-	0.212	0
16,271	0.72	-	0.216	0
17,007	0.733	-	0.220	0
23,050	0.846	-	0.254	0
1,302,222	0.959	-	0.288	0

Appendix G.
Outage Volume and Pressure Calculations

The calculations described in this appendix were made by Dr. Phani Raj of the FRA's Office of Safety. These calculations were provided to the test team during the test preparation phase to assist with choosing the fill level and pressure for the test

The "filling density" is defined as the weight ratio of the cryogenic commodity at its design temperature to water at atmospheric pressure and 60 °F. Based on this definition, using water as the test liquid required additional calculations to determine the volume of water to fill the tank. If the stipulation was that at the PRV's STDP (75 psig) condition, the volume of vapor space was to be 15 percent of the tank volume, then the mass of LNG in the tank car could be calculated knowing the saturation density of LNG at the PRV's STDP. Based on this result and the need to have the target volume of water used for this test match the weight of LNG that a DOT-113 could carry, the tank would have only been filled to 32.5 percent of its volume with water. While the mass of water in the tank would have been equal to the mass of LNG permitted by the NPRM, the height of the water in the tank would have been quite low due to the much lower volume of water compared to the volume of LNG having the same weight. Previous FRA-sponsored testing and analysis have shown that the height of the outage can have a significant effect on the structural response and puncture behavior of an impacted tank car under standardized test conditions. Thus, the filling level was chosen to match the approximate filling volume of LNG with an equivalent volume of water. Because water has a higher density than LNG, using an equivalent volume of water to LNG would result in a water-filled car that is considerably heavier than an LNG-filled car.

To calculate the volume of the tank car that would be filled with LNG using a filling density of 32.5 percent, the density of the LNG also needed to be known. The density of LNG varies with the pressure at which the LNG is stored. While a DOT-113 tank car is highly insulated, the lading will gradually heat up. As the lading heats up, it expands within the tank. This expansion simultaneously reduces the outage volume and increases the outage pressure.

This relationship between outage pressure and outage volume had to be considered when choosing either pressure or outage volume as an input to the test plan. Because LNG was not widely transported via DOT-113 tank cars at the time this test was being planned, there was no data on "typical" service conditions that could be used to select a test pressure and calculate a corresponding filling level that would commonly be encountered. The NPRM stated:

> *The maximum offering pressure of 15 psig is consistent with the 20-day transportation requirement for cryogenic materials and the estimated 3 psig per day pressure increase during transportation. The filling density is similar to the filling density requirements for cryogenic materials transported in a cargo tank motor vehicle. These requirements will provide a 15 percent vapor volume outage (at the start-to-discharge-pressure of the pressure relief valve) for the rail tank car during transportation.*

Two bounding conditions were identified. At one limit, just prior to activation of the PRV, the tank would have a pressure of 75 psig and a 15 percent outage volume. This represents the highest pressure expected to be encountered in normal service and the smallest outage volume. At the other limit, assuming a 15 psig loading pressure and a filling density (by weight) of 32.5

percent would result in a 21 percent outage by volume. This set of conditions represents the lowest pressure expected to be encountered in normal service and the largest outage volume. A higher pressure and smaller outage will result in a tank car that is stiffer and punctures with less energy absorbed than a car with a lower pressure and a larger outage. However, the magnitude of difference this range of outage volumes and pressures makes was not known.

Because typical loading conditions, transit times, and heating rates were not known due to a lack of service history for LNG transported via DOT-113 tank cars, the test outage pressure was chosen to represent a mid-range value. A 45-psig outage was chosen to represent a tank car that may be in transit but has not been in transit for so long that its PRV is imminently going to vent. Assuming a 32.5 percent filling density and a filling pressure of 15 psig, by the time the internal pressure reached 45 psig, the outage volume would be reduced to 17.6 percent.

The calculations made to determine these outage pressures and volume targets used saturated liquid methane properties obtained from [52] and are presented in Table G1.

Table G1. Assumed Properties Used in Outage Pressure and Volume Calculations

Description	Value	Unit
STDP of the PRV	75.0	psig
Minimum vapor space volume as a percentage of tank car volume at STDP condition	15.0	%
Maximum liquid volume as a percentage of tank car volume at STDP condition	85.0	%
Maximum tank car pressure at the time of offering the tank car for transportation	15.0	psig
Liquid filling density by weight[16]	32.5	% by weight

Using the filling density by weight, STDP, and minimum vapor space at STDP condition from the table above, the liquid filling density by volume was calculated for two further pressures of interest. The first pressure of interest was the initial filling pressure of 15 psig. This filling volume would represent the smallest liquid percent (by volume) expected to be encountered during normal service. The second pressure of interest was a pressure of 45 psig which is halfway between the 15 psig initial filling pressure and the 75 psig start-to-discharge pressure. A pressure of 45 psig and the corresponding liquid volume would represent a DOT-113 tank car that has been in transit for a period of time, causing it to heat up and the liquid inside to expand.

---

[16] Ratio of the weight of saturated liquid at 15 psig and the weight of water occupying the entire tank car volume at 60 °F. The density of water used in these calculations was 997.94 kg/m^3.

One assumption made in these calculations was that for each pressure examined, the LNG remained saturated. Therefore, with the total mass of LNG within the tank remaining constant at each pressure, the volume occupied by the LNG would vary because the saturated liquid density varies with pressure. As the liquid mass remains constant at each pressure, the liquid mass per unit tank volume also remains constant as the volume of the tank is also assumed to remain unchanged at each pressure.

At the STDP of 75 psig, the minimum outage of 15 percent corresponds to a liquid volume fraction of 85 percent. Thus, the liquid mass per unit tank volume at the STDP can be calculated according to Equation G1.

$$Liquid\ Mass\ per\ Unit\ Tank\ Volume\ at\ STDP = Liquid\ Volume\ Fraction\ \cdot Liquid\ Density$$

$$85\% \cdot 381.5\frac{kg}{m^3} = 324.3\frac{kg}{m^3}$$

Equation G1. Liquid Mass per Unit Tank Volume

The filling density by weight is calculated as the ratio of the liquid mass per unit tank volume to the density of water at 60 °F, as shown in Equation G2.

$$Filling\ Density = \frac{Liquid\ Mass\ per\ Unit\ Tank\ Volume}{Density\ of\ Water\ (mass\ of\ liquid\ per\ unit\ volume\ of\ liquid)}$$

$$\frac{324.3\frac{kg}{m^3}}{997.94\frac{kg}{m^3}} = 32.5\%$$

Equation G2. Filling Density

As both the liquid mass per unit tank volume and the filling density by weight remain constant across all pressures, the liquid volume fraction at the other pressures of interest are simply the ratio of the liquid mass per unit tank volume to the liquid density at each saturated gage pressure of interest. These calculations are shown in Equation G3.

$$Liquid\ Volume\ Fraction = \frac{Liquid\ Mass\ per\ Unit\ Tank\ Volume}{Liquid\ Density}$$

$$\frac{324.3\frac{kg}{m^3}}{410.6\frac{kg}{m^3}} = 79.0\%\ (at\ 15\ psig)$$

$$\frac{324.3\frac{kg}{m^3}}{393.8\frac{kg}{m^3}} = 82.4\%\ (at\ 45\ psig)$$

Equation G3. Liquid Volume Fraction

Based on these calculations, a liquid volume fraction of 82.4 percent, corresponding to a 17.6 percent outage, was used for the target test pressure of 45 psig. The liquid volume fractions at varied pressures of interest are summarized in Table G2.

Table G2. Liquid Volume Fractions at Varied Pressures of Interest

Condition	**Saturated Gage Pressure (psig)**	**Liquid Density at Saturated Gage Pressure** [52] **(kg/m^3)**	**Liquid Volume Fraction at Saturated Gage Pressure (%)**
Assumed Loading Pressure, from NPRM	15	410.6	79
Target Test Pressure	45	393.8	**82.4**
Start-to-discharge Pressure, from NPRM	75	381.5	85

Abbreviations and Acronyms

ACRONYMS	EXPLANATION
ASTM	American Society for Testing and Materials
AAR	Association of American Railroads
B-W	Bao-Wierzbicki
CFC	Channel Frequency Class
CFR	Code of Federal Regulations
DOF	Degrees of Freedom
DB	Dogbone
EB	Elongation at Break
EOS	Equations of State
FRA	Federal Railroad Administration
FEA	Finite Element Analysis
FE	Finite Element
HMR	Hazardous Materials Regulations
HD	High Definition
HHFT	High-hazard Flammable Trains
LIDAR	Light Detection and Ranging
LNG	Liquefied Natural Gas
LN2	Liquid Nitrogen
MLI	Multi-layer Insulation
MMC	Modified Mohr-Coulomb
MW	Molecular weight
NPRM	Notice of Proposed Rulemaking
NRB	Notched Round Bar
PEEQ	Plastic Equivalent
PHMSA	Pipeline and Hazardous Materials Safety Administration
PRV	Pressure Relief Valve
QS	Quasi-static
ROW	Right-of-Way
SSC	Shell-to-solid Coupling
SPH	Smoothed Particle Hydrodynamics

ACRONYMS	**EXPLANATION**
SRB	Smooth Round Bar
SAE	Society of Automotive Engineers
SCFM	Standard Cubic Feet per Minute
STDP	Start-to-discharge Pressure
TRIAX	Stress Triaxiality
TC	Transport Canada
TTC	Transportation Technology Center
TTCI	Transportation Technology Center, Inc.
UTS	Ultimate Tensile Strength
Volpe	Volpe National Transportation Systems Center
YS	Yield Strength